DATE ISSUED: OCT 21 1970

581

ORNL
MASTER COPY
265

ORNL-4584
UC-41 — Health and Safety

HEALTH PHYSICS DIVISION
ANNUAL PROGRESS REPORT
FOR PERIOD ENDING JULY 31, 1970

OAK RIDGE NATIONAL LABORATORY
operated by
UNION CARBIDE CORPORATION
for the
U.S. ATOMIC ENERGY COMMISSION

ChemRisk Document No. 581

Printed in the United States of America. Available from
National Technical Information Service,
U.S. Department of Commerce, Springfield, Virginia 22151
Price: Printed Copy $3.00; Microfiche $0.65

LEGAL NOTICE

This report was prepared as an account of Government sponsored work. Neither the United States, nor the Commission, nor any person acting on behalf of the Commission:

A. Makes any warranty or representation, expressed or implied, with respect to the accuracy, completeness, or usefulness of the information contained in this report, or that the use of any information, apparatus, method, or process disclosed in this report may not infringe private-owned rights; or

B. Assumes any liabilities with respect to the use of, or for damages resulting from the use of any information, apparatus, method, or process disclosed in this report.

As used in the above, "person acting on behalf of the Commission" includes any employee or contractor of the Commission, or employee of such contractor, to the extent that such employee or contractor of the Commission, or employee of such contractor prepares, disseminates, or provides access to, any information pursuant to his employment or contract with the Commission, or his employment with such contractor.

ORNL-4584
UC-41 — Health and Safety

Contract No. W-7405-eng-26

HEALTH PHYSICS DIVISION ANNUAL PROGRESS REPORT

For Period Ending July 31, 1970

K. Z. Morgan, Director

W. S. Snyder, Assistant Director
E. G. Struxness, Assistant Director

OCTOBER 1970

OAK RIDGE NATIONAL LABORATORY
Oak Ridge, Tennessee
operated by
UNION CARBIDE CORPORATION
for the
U. S. ATOMIC ENERGY COMMISSION

Reports previously issued in this series are as follows:

ORNL-2384	Period Ending July 31, 1957
ORNL-2590	Period Ending July 31, 1958
ORNL-2806	Period Ending July 31, 1959
ORNL-2994	Period Ending July 31, 1960
ORNL-3189	Period Ending July 31, 1961
ORNL-3347	Period Ending July 31, 1962
ORNL-3492	Period Ending July 31, 1963
ORNL-3697	Period Ending July 31, 1964
ORNL-3849	Period Ending July 31, 1965
ORNL-4007	Period Ending July 31, 1966
ORNL-4168	Period Ending July 31, 1967
ORNL-4316	Period Ending July 31, 1968
ORNL-4446	Period Ending July 31, 1969

Contents

SUMMARY ix

PART I. RADIOACTIVE WASTE DISPOSAL

1. FATE OF TRACE ELEMENTS AND RADIONUCLIDES IN TERRESTRIAL ENVIRONMENT 1
   - Evaluation of Zonal Centrifugation Techniques 1
   - Applications of Zonal Centrifugation 4
   - Distribution of ^{137}Cs in Soil of a *Liriodendron* Forest 8
   - Water Quality Studies in Walker Branch Watershed 9
2. DISPOSAL BY HYDRAULIC FRACTURING 11
   - Investigations at Oak Ridge 11
   - Investigations in New York State 11
3. DISPOSAL IN NATURAL SALT FORMATIONS 16
   - Design Criteria and Facility Description 16
   - Detailed Information Developed in Support of Facility Design 18
4. ENGINEERING, ECONOMIC, AND SAFETY EVALUATIONS 37
   - Siting and Operation of Nuclear Facilities 37
   - Routine Atmospheric Releases of Radioactive Materials 37
   - Pathway Analysis 38
   - Regional Planning 39
5. EARTHQUAKES AND REACTOR SAFETY 41
   - ORNL Seismograph Station ORT 41
6. DOSE ESTIMATION STUDIES RELATED TO PEACEFUL USES OF NUCLEAR EXPLOSIVES 42
   - Utilization of Natural Gas from Nuclearly Stimulated Wells 42
   - Development of Radiation Safety Guides for Transient Exposures 49
   - Dose Estimation Studies Related to Construction of an Interoceanic Canal with Nuclear Explosives 53

10. PHYSICS OF TISSUE DAMAGE 87

Electron-Slowing-Down Studies 87

Optical Properties of Some Organic Liquids 88

11. ELECTRON AND ION COLLISION PHYSICS 92

Electron Impact Excitation and Ionization of the Rare Gases 92

Threshold Electron Impact Excitation of Some Simple Molecules 94

Interaction of Electrons with Substituted Benzenes, Substituted Pyridines, and Pyrizine 95

Attachment Rate of Thermal Electrons to SF_6 96

Thermal-Electron Attachment Rates and Negative-Ion Lifetimes of Other Molecules 97

Quadrupole Ion-Mass Analysis of Swarm Experiments 98

Collisions of Slow Cesium Atoms with Electronegative Gases 98

Low-Energy Negative-Ion–Molecule Reactions 100

12. ATOMIC AND MOLECULAR RADIATION PHYSICS 105

Thermal-Electron Scattering by Polar Molecules 105

Electron Attachment and "Carrier Gas" Energy Distribution Functions 108

Cross-Section Functions for Thermal-Peaking Electron Attachment Resonances 108

Electron Attachment to Sulfur Hexafluoride 114

Electron Attachment to Organic Molecules 116

Capture of Slow Electrons by Organic Molecules in the Field of an Excited Electronic State 118

Lifetimes of Long-Lived Polyatomic Negative Ions Formed by Electron Capture in the Field of the Ground Electronic State 118

Energy Dependence of the Lifetime of Long-Lived Transient Negative Ions 119

Electron Attachment to Halogenated Hydrocarbons 121

Threshold-Electron Excitation Spectra of Organic Molecules; Location of Triplet and Compound Molecular Negative-Ion States 121

Emission and Decay of Fluorescent Organic Liquids Under Electron Impact 121

Photophysical Studies of Liquids 122

On Molecular Parameters of Physical, Chemical, and Biological Interest 123

Stopping Powers of Slow Electrons in Hydrocarbons 123

Resonance Radiation Imprisonment Phenomena 123

Comparison of Direct and Photosensitized Ionization Efficiencies 124

13. GRADUATE EDUCATION AND VOCATIONAL TRAINING 125

PART III. RADIATION DOSIMETRY RESEARCH

GENERAL OBJECTIVES AND ACTIVITIES 128

14. DOSIMETRY FOR HUMAN EXPOSURES AND RADIOBIOLOGY 129

Japanese Dosimetry Program 129

Leakage Studies for "Fat Man" and "Little Boy" 134

Dose Distributions in Cylinders Exposed During Operation HENRE 135

Depth-Dose Distributions in Small Animals 137

Californium-252 138

15. SPECTROMETRY RESEARCH AND DEVELOPMENT 152

An Extrapolation Chamber for the Measurement of Dose Distributions at Bone-Tissue Interfaces 152

Dose Distributions at Bone-Tissue Interfaces 153

Purification of Sulfur by Zone Refining 155

Experimental Measurements of LET 155

Unusual X-Ray Sources 157

Description of Neutron Leakage from the Operation HENRE Neutron Generator 159

Organic Scintillator Experiment 159

DOSAR Portable Scaler Modification 161

Nuclear Data Analyzer Tape Conversion 161

TSEE and Spark-Counter Preamplifiers 162

Measurement of the Neutron Spectrum from the HPRR Between 50 keV and 450 keV 164

16. APPLIED DOSIMETRY RESEARCH 165

TSEE Research 165

Nuclear Track Registration in Polymers 180

17. HPRR AND ACCELERATOR OPERATIONS 187

Neutron Generator Target Research $D(d,n)^3He$ and $T(d,n)^4He$ Reactions 187

HPRR Operations 189

Intercomparison Studies 191

Van de Graaff Operations 197

18. INTERACTION OF CHARGED PARTICLES WITH MATTER 198

PART IV. INTERNAL DOSIMETRY

19. INTERNAL DOSE ESTIMATION 200

Estimates of Dose to Red Bone Marrow from Monoenergetic Sources of Photons in Lungs and Other Organs 200

Estimation of Dose to Gonads from Gamma Emitters Present in the Body 203

Estimation of Dose and Dose Commitment to Bladder Wall from a Radionuclide Present in Urine 206

Application of Berman's Ten-Compartment Model for Human Iodine Metabolism to Estimation of Microcurie-Days Residence of ^{123}I, ^{124}I, ^{125}I, ^{126}I, and ^{131}I 208

Application of the Mammillary Compartment Model to Estimation of Microcurie-Days Residence of ^{232}Th, ^{228}Ra-^{228}Ac, ^{228}Th, and ^{224}Ra in Man 214

Scattered Energy Spectrum for a Monoenergetic Gamma Emitter Uniformly Distributed in an Infinite Cloud 216

20. STABLE ELEMENT METABOLISM 223

Elemental Intake and Excretion in Long-Term Balance Studies 223

Gross Composition of Bone and Cartilage 223

THESES, PAPERS, PUBLICATIONS, AND LECTURES

THESES 227

PAPERS 228

PUBLICATIONS 233

LECTURES 242

Summary

PART I. RADIOACTIVE WASTE DISPOSAL

1. Fate of Trace Elements and Radionuclides in Terrestrial Environment

Banding of several reference clay minerals was evaluated in a continuous density-gradient solution using zonal centrifugation. Variables examined were particle sizes, cationic saturations, and centrifugal forces. Zonal centrifugation was also used to segregate mineral fractions of several environmental samples, and then these were investigated for phosphate or radionuclide distribution. For phosphate distribution, samples were obtained from the bottom and suspended sediments of the ORIC pond and a soil whose runoff drains into the pond. The principal finding is that most of the phosphate is present in the iron and aluminum phosphate forms.

For radionuclide distribution samples, bottom sediments from White Oak Lake Bed and Creek were examined. Cesium-137 was found primarily in the clay mineral band; ^{90}Sr was found in most bands, including the bands containing calcium carbonate, which tentatively confirms earlier conclusion. Distribution of ^{137}Cs in a soil from previously tagged trees (*Liriodendron* forest) suggests that the mineral illite plays a dominant role in fixing this radionuclide.

Water quality studies of Walker Branch Watershed were continued. Water temperatures were measured continuously at several locations in the two streams which drain the watershed. Differences in water temperatures were observed with time and location, and the differences were not predictably uniform. The differences are discussed, with reference to the source of groundwater and to air temperatures.

2. Disposal by Hydraulic Fracturing

Operational waste injection ILW-6 was made in June 1969. Some 80,000 gal of waste, containing nearly 100,000 Ci of activity, were disposed of without incident.

The work in New York State is well under way. The injection well and the four surrounding observation wells have been completed, and two test injections have been made. Both injections were into the same slot at a depth of 1450 ft. The first was made with water only in October 1969, and apparently made a dominantly horizontal but complex fracture. The second, containing 2.7 Ci of ^{95}Zr-^{95}Nb, was made on June 26, 1970, and is already known to be horizontal. A dye, Rhodamine B, was mixed with the radioactive tracer to make a visible marker.

3. Disposal in Natural Salt Formations

The principal effort in the current program is a study leading to the development of a conceptual design (and the required safety analyses) of a combined solidified high-level power reactor fuel-reprocessing waste repository and low-activity alpha-contaminated waste repository. This one facility should be capable of handling all waste of these two types until about the end of this century.

For the high-level wastes a total (gross) salt mine area of about 850 acres, all newly mined for the purpose, will be required. The present design for the low-level facility calls for the use of an existing inactive mine which has around 40 million cubic feet of space already mined. The tentatively selected location is near Lyons, Kansas.

A geologic and hydrologic study based on available information indicates that the central Kansas area meets the criteria established for the location of the first demonstration repository (e.g., salt beds at least 200 ft thick and lying at depths of no more than 2000 ft). Also the Arbuckle formation appears to be suitable for disposal of excess salt as brine. However, contacts with local salt producers have indicated the possibility for sale of the salt either as brine or as rock salt. Therefore, sale of the excess salt is considered to be the desirable disposal method, with the Arbuckle formation as a backup.

A number of preliminary studies of temperatures (due to radioactive decay heat) at mine level and in the rock formations around the mine have been carried out. Based on all considerations (such as mine stability, aquifer temperature rises, etc.), it appears that 200°C peak salt temperature is neither too conservative nor too liberal for at least the initial stages of a high-level disposal facility operation.

A study of salt tectonics in relation to the disposal of solidified high-level waste was made. Considering the specific case of the formation at Lyons, Kansas, it was concluded that the possibility of extensive salt deformation affecting the safety of the disposal area for a period of a few hundred thousand years can be excluded. Also the heating caused by the decay heat generated in the high-level waste would be of such short duration (from a geologic point of view) that no significant consequences would be expected.

4. Engineering, Economic, and Safety Evaluation

Investigation has continued of factors involved in the siting and operation of nuclear facilities. Radioactive production and decay processes can now be included directly in computer calculation of downwind air concentrations that result from routine release of gaseous effluents. After deposition, the movement of radionuclides in food chains can be simulated by the preliminary computer program PATHWAY. An example is used to illustrate application of this program. Information has been assembled on nuclear power plant locations and the surface waters contiguous to each site for use in discussions on regional planning.

5. Earthquakes and Reactor Safety

Routine operation of the ORNL seismograph station has continued during the year, including the regular reporting of data to the U.S. Coast and Geodetic Survey and the periodical issuance of a station bulletin. In addition, a seismic history of the southeast region of the United States was compiled and a study of the seismicity of this area made.

6. Dose Estimation Studies Related to Peaceful Uses of Nuclear Explosives

The concentration of tritium and ^{85}Kr in gas samples from the Gasbuggy well, the first nuclearly stimulated natural gas well, declined exponentially as contaminated gas was removed during flaring operations and diluted with uncontaminated formation gas. The ratio of these radioactive impurities in the gas to the concentration of carbon dioxide and hydrogen also diminished for reasons that are not clear at present. Recent census data were used for an estimate of the home occupancy factor, the fraction of the time that an average home is occupied, to aid calculations of home exposure to radioisotopes in contaminated gas used for heating and other purposes.

Data on gas consumption in two West Coast metropolitan areas, Los Angeles and San Francisco, have been combined with meteorological information to provide estimates of the hypothetical doses resulting from the use of contaminated natural gas in these areas. Calculated concentrations of radioisotopes in the atmosphere were higher in Los Angeles than in San Francisco, but the hypothetical doses resulting from the maximum exposures were almost the same in both areas (2.2 and 2.5 millirems/year respectively) because of greater domestic use of gas in the cooler region.

In addition to potential radiation exposures from home and industrial combustion of contaminated natural gas, the hypothetical exposure of users of gas by-products has been considered, including carbon black, fertilizer ammonia, tritiated alcohol, and hydrogenated fats and oils. In all cases the hypothetical exposure to consumers of these products was shown to be negligible at the levels of radioactivity anticipated in large-scale use of nuclear explosives for stimulation of natural gas production.

Considerable effort has been directed toward the development of radiation safety guides for transient exposures because of the need to evaluate the possible hazard of radioactive releases from peaceful uses of nuclear explosives at or near the earth's surface. Cumulative exposure guides (CUE's), based either on ICRP maximum permissible annual doses or on maximum permissible organ burdens, have been calculated for short-term inhalation exposures in terms of concentration (microcuries per cubic centimeter) and time (hours). These transient exposure guides, calculated by means of computer programs, are useful for "first-cut" assessment of the possible impact of short-term releases of radioactive materials to the environment.

Other exposure modes which are, in general, more difficult to evaluate than inhalation, have also been considered in calculating CUE's. A computer program is available for calculating the exposure resulting from immersion in radioactive clouds for short periods. A simplified model has also been developed to describe one exposure pathway, the fallout-milk-man food chain, that can aid evaluation of ingestion hazards resulting from either transient or long-term fission product deposition on vegetation.

Potential doses to indigenous populations along Route 17 in eastern Panama and Route 25 in northwestern Colombia were estimated for a combination of hypothetical exposures to radiation. The studies attempted to determine when it might be appropriate for populations to reenter areas adjacent to the two routes.

7. Related Cooperative Projects

Representatives of other agencies continued to participate in the Radioactive Waste Disposal Section's studies. One alien guest was in residence during the year. One member served as assistant news editor for the United States for *Health Physics* and as an assistant editor of *Nuclear Safety*. One member of the Section served on the Southern Governors' Conference Task Force for Nuclear Power Policy. Members of the Section participated part time in the Nuclear Safety Information Center, the Civil Defense Research Project, and the agroindustrial complex study.

PART II. RADIATION PHYSICS

8. Theoretical Radiation Physics

A critical appraisal has been made of quantities and units in radiation protection work, and a different approach has been suggested for establishing permissible limits of radiation exposure.

A Monte Carlo method has been developed for determining LET spectra from energy-proportional pulse-height measurements, and work has begun to use this method to develop a more convenient and more reliable means of determining LET distributions.

Work is in progress in collaboration with the experimental Health Physics Group at CERN on the dosimetry of high-energy pions. Calculations are being tailored to simulate actual experimental conditions such as beam density profile, energy distributions, and target size, shape, and composition, and initial results have been in good agreement with experiment.

A new theoretical investigation has been made of electron binding to a finite dynamic dipolar system where the Hamiltonian operator in the Schrödinger equation contains, in addition to the electron kinetic energy, the rotational energy of the dipole. Approximate Hartree-Fock energies have been calculated for autoionizing states in neon and argon atoms. A new variational method has been formulated and applied to the determination of elastic scattering phase shifts. A generalization of the oscillator strength of a molecular system which includes nuclei as well as electrons has been enunciated. A rapid method of obtaining the potential energy of a diatomic molecule has been devised. An expression for the mean free path of a swift charged particle for plasmon excitation, valid for relativistic energies of the particle, has been given. A theoretical treatment of the difference in stopping power of a charged particle and its antiparticle has been made using a semiclassical approach. Working in the RPA, a formula for the mean free path for double-plasmon excitation by a fast charged particle has been derived. Festenberg's experimental results showing anomalously large damping of volume plasmons in polycrystalline aluminum have been explained in terms of elastic scatter of the plasmon on the grain structure. A theory has been advanced to account for the decrease in optical reflectance of a metal in the neighborhood of the surface plasmon energy. A revised formulation of the macroscopic Maxwell theory has been made. The concept of energy as it enters kinetic plasma theory has been reexamined, and a revised version of the theory has been postulated.

9. Interaction of Radiation with Liquids and Solids

With a Seya-Namioka vacuum ultraviolet monochromator the optical properties of cesium have been measured just above the plasma energy and the data interpreted in terms of a plasmon-assisted interband transition. The recently installed soft-x-ray monochromator has been used to extend measurements of the optical properties of MgF_2 and MgO, previously made with a Seya-Namioka monochromator, up to 66 eV. Further refinements have been made to the ultrahigh vacuum-ellipsometer, and optical constants were obtained for palladium from 3000 to 20,000 Å.

Investigations have been continued of the optical emission spectra from metal films bombarded with high-energy electrons. The radiative decay of volume plasmons in magnesium and beryllium has been used to calculate basic parameters associated with these materials. In addition, the radiative decay of "nonradiative" surface plasmons in aluminum has been confirmed. Experimental confirmation of the theory of radiation damping of surface plasmons from aluminum-coated concave diffraction gratings has been obtained, and the results of diffusion pump oil contamination of diffraction gratings have also been investigated and compared with theory.

Abnormally high exoelectron emission currents from magnesium have been observed on exposure to O_2 or H_2O gas. The emission currents, which achieved maxi-

mum values in times comparable with times estimated to form monolayer coverages on the surface, are believed to be associated with a lowering of the work function of the magnesium and a formation of unstable chemical bonds on the metal surface.

10. Physics of Tissue Damage

The electron flux in an irradiated semiconductor (^{71}Ge) was measured and compared with that in metal irradiated similarly. When data were reduced to eliminate differences due to high-energy stopping powers, densities, and source strengths, identical spectra were found at the higher energies (~5 keV), but the flux in the semiconductor rose to about twice that in the metal at low energies (10 eV), possibly due to reduced semiconductor stopping power near the band gap energy.

An attempt was made to see if the electron flux in an irradiated medium is enhanced substantially by absorption of photons released in the medium by deexcitation, x-ray production, and bremsstrahlung. Thin and thick (compared with most photon attenuation lengths) sources of ^{185}W were examined with the Keplertron (electrostatic spectrometer), but no differences in electron spectra were found. The possibility remains, however, that extremely low-energy photons (less than 1 keV) may be important, and still thinner sources will have to be studied to check this.

The optical constants of the organic liquids CCl_4, C_6H_{14}, C_6H_{12}, C_6H_{10}, C_6H_8, and C_6H_6 have been measured in the energy range from 4.0 to 10.7 eV using the closed-cell semicylinder method. In the course of this work satisfactory techniques were developed for cleaning the semicylinder cell windows, enabling consistent data to be obtained. The data have been interpreted in terms of $\pi \rightarrow \pi^*$, $n \rightarrow \sigma^*$, and $\sigma \rightarrow \sigma^*$ molecular electronic excitations.

11. Electron and Ion Collision Physics

The cross-section behavior for the production of slow electrons (0 to 0.5 eV) upon electron impact ionization of the rare gases, water vapor, and benzene has been studied for the first time using the SF_6 scavenger technique and the trapped-electron method. For the rare gases the cross section for the production of slow electrons abruptly rises at the ionization potential and remains relatively constant up to an energy in excess of 100 eV. The cross sections for water vapor and benzene are found to steadily increase beginning at their ionization potentials in contrast to the flatness exhibited by the rare gases. Absolute cross-section measurements of these inelastic scattering processes will be helpful in interpreting electron-slowing-down spectra in gases.

Negative-ion formation in a large number of organic and inorganic molecules has been studied in considerable depth with both electron swarm and electron beam techniques. The major part of our effort has been devoted to the study of (1) negative-ion lifetimes, (2) temporary negative-ion resonances, (3) dissociative attachment cross sections, (4) thermal energy electron attachment rates, (5) negative-ion mobilities, and (6) mass analysis of negative ions formed in electron swarm experiments. Input data from all these experiments provide a quite detailed description of electron attachment mechanisms.

An apparatus has been constructed to mass identify the positive- and negative-ion products resulting from collisions of fast neutral cesium atoms with molecules. Measurements of the threshold for ion pair production in collisions of cesium atoms with electronegative molecules afford a determination of the lower limit to the electron affinity of molecules. Using this technique we have shown that the electron affinity of nitrogen dioxide is greater than or equal to 2.2 ± 0.2 eV. Mass analysis of ions formed in collisions of high-energy cesium atoms (~30 eV) with Br_2 shows that both Br_2^- and Br^- are produced. Mass analysis of ions formed in collisions of cesium with molecules is providing a wealth of new information about the formation of negative ions due to the complex adiabatic nature of the collision.

Reaction products and rates of reaction of low-energy (0–2 eV) O^- ions with acetylene, ethylene, ethane, and benzene (and their deuterated analogs) have been investigated. The absolute magnitudes of the ion-molecule reaction cross sections, their dependence on O^- energy, and branching ratios and isotope effects have been compared with existing theory.

12. Atomic and Molecular Radiation Physics

The scattering of thermal electrons by highly polar molecules has continued. The dependence of the drift velocity of thermal electrons traveling through polar gases has been investigated, and the data have been used to determine the magnitude and the velocity dependence of the momentum transfer cross section. The data have been discussed within the Born approximation and with relevance to a number of factors which can distinctly affect the scattering. Measurements have been made also of electron diffusion coefficients and mobilities in hydrocarbon vapors. These yielded stopping

powers of electrons less than ~2 eV which were remarkably insensitive to structural variations.

An accurate and exhaustive experimental test has been made of electron swarm energy distribution functions $f(\epsilon, E/P)$ for the carrier gases C_2H_4, N_2, and Ar used in electron attachment studies. A standard set of $f(\epsilon, E/P)$ has been established and recommended. A method has been developed whereby both the magnitude and the energy dependence of thermal-peaking electron attachment resonances is obtained from electron swarm data alone. The method has been applied successfully to many molecules (e.g., CCl_4, SF_6, anthracene, 1,2-benzanthracene). Lifetimes and cross sections for long-lived polyatomic negative ions have been measured and have been related to electronic and geometrical structure. Estimates of electron affinities were obtained for some molecules.

Electron capture by an organic molecule with simultaneous excitation of one of the orbiting electrons resulting in a long-lived parent negative ion has been observed for the first time. Also, the first energy dependence of the autoionization lifetime of long-lived negative ions has been found for both nuclear- and electron-excited Feshbach resonances, and it clearly showed the effect of increase in internal energy of the ion on the autodetachment rate. A systematic study has been made of electron attachment to molecules of the form $C_nH_{2n+1}Br$ (n = 1 to 10) which allowed a deeper understanding of the energetics and quantitative aspects of dissociative electron attachment to polyatomic molecules. A new high-resolution experimental arrangement has been constructed and built which enables threshold-electron and compound negative-ion excitation studies.

New information of great significance has also been obtained on the emission and decay of organic liquids under electron impact, photophysical studies of liquids, transport of resonance radiation in gases, and sensitized ionization of molecules.

13. Graduate Education and Training

The Health Physics Training Program included fellowship students from Vanderbilt University, The University of Tennessee, the University of Kansas, the University of California, and Georgia Institute of Technology. These reported to ORNL for summer on-the-job instruction in applied and research health physics.

Division personnel visited 17 colleges and universities to give seminars on various research problems of current interest and also to help recruit qualified students in the fellowship program.

The Health Physics Division provided research facilities and advisors for 20 Oak Ridge Graduate Fellows, AEC Fellows, and USPHS Fellows who were conducting thesis research. A total of 41 university personnel ranging from undergraduates to professors spent the summer in the Division.

Teaching assistance was given to The University of Tennessee for its program in Radiation Physics and to Vanderbilt University for its course in Radiation Physics. Lectures and tours were given for several university groups visiting ORNL.

Assistance and consultation were given to eight schools that were interested in establishing health physics courses or programs in their science departments.

The Division cooperated with ORAU in the presentation of a ten-week course in Applied Health Physics and in the screening of applicants for AEC Fellowships.

PART III. RADIATION DOSIMETRY RESEARCH

14. Dosimetry for Human Exposures and Radiobiology

Calculations of depth-dose distributions for neutrons were extended into areas of practical application, especially for the use of ^{252}Cf in cancer therapy. Dose and LET distributions for line, point, and disk-shaped sources of neutrons having the energy spectrum of ^{252}Cf were calculated. The calculations of dose and LET distributions due to neutrons were also made for two small cylinders chosen to approximate the size of rats and rabbits respectively. Preliminary calculations were also made for the dose distributions in human fetuses exposed to radiation from the nuclear bombs exploded over Hiroshima and Nagasaki. Close liaison has been maintained with the Atomic Bomb Casualty Commission (ABCC) in Japan. Emphasis this year has been given to computation of the radiation doses received by those persons exposed near the bombs who survived because of the radiation and blast protection afforded by seismic reinforced buildings.

15. Spectrometry Research and Development

Experimental measurements of dose distributions in man-sized tissue-equivalent media were made to test the recently calculated values. A special extrapolation chamber was developed and used for measuring the dose distribution near bone-tissue and tissue-bone interfaces in phantoms irradiated by the Health Physics Research Reactor (HPRR). Other experiments were directed to the measurement of LET in neutron-

irradiated tissue phantoms utilizing recently developed counters. Measurement of the HPRR spectrum in the energy range below 0.5 MeV was accomplished. A variety of electronic instruments related to spectrometry research were developed or improved, and zone-refining techniques were used for the purification of detector materials.

16. Applied Dosimetry Research

The emphasis on thermally stimulated exoelectron emission (TSEE) has continued, with major advances made in the sensitivity and stability of detectors, especially sintered BeO. Initial studies of neutron response characteristics have been completed, and the response per unit dose as a function of photon energy has been measured for several detector types. TSEE techniques were also applied to samples of lunar material with the objective of learning more about the thermal and radiation history of the moon.

Registration of charged-particle tracks in insulating solids has proved to be of increasing practical value, with application in autoradiography with alpha particles and radon monitoring. More basic studies of track registration were made, with emphasis on alpha-particle registration in cellulose nitrate.

17. HPRR and Accelerator Operations

Results from a new target assembly promise greater neutron yields and longer life for tritium targets for accelerators, especially those used for the $T(d,n)^4He$ reaction. The DOSAR Low Energy Accelerator (DLEA) and the 3-MV Van de Graaff are used extensively in these studies and in most other dosimetry research.

The HPRR was operated routinely and without fault. The annual disassembly and inspection revealed no detectable change in the core materials. In July 1970, the seventh intercomparison study in dosimetry was held, using the HPRR as the radiation source, and participants included dosimetrists from four foreign countries.

18. Interaction of Charged Particles with Matter

Transfer of equipment from the University of Kentucky to the 3-MV Van de Graaff was completed, and installation and testing were initiated. Initial studies include the intensities, lifetimes, and wavelengths of the electromagnetic radiations emitted from noble gases irradiated by fast protons as well as the W values of pure gases and gas mixtures.

PART IV. INTERNAL DOSIMETRY

19. Internal Dose Estimation

Estimates of dose to red bone marrow are difficult to obtain because of the complex distribution of red bone marrow within the body. Yet it is a tissue of particular importance, because the dose limits recommended for purposes of radiation protection are lower (5 rems/year for occupational exposure) than for most tissues. The anthropomorphic phantom and Monte Carlo computer program reported here previously for estimation of dose due to photons have been adapted to take account of the distribution of red marrow. Only doses from a monoenergetic photon emitter present in lungs are reported here. As might be expected, the dose is highest for the red marrow in the rib cage and certain portions of the spine. The pelvic region contains a considerable fraction of the total red marrow, and the dose to this portion is much less, often by an order of magnitude.

The Monte Carlo computer program mentioned above has been used to estimate doses in many body organs. However, in some cases the estimates are statistically unreliable, particularly for small organs such as gonads or thyroid when they are far from the source organ. A buildup factor for dose in an infinite medium of water has been reported, and despite the finiteness and heterogeneity of the body, the use of this buildup factor seems to be accurate within a factor of 2 in all cases tested against the Monte Carlo code. This result is being tested further, and if the limit of error is this small, the method may be useful in estimating dose to small organs.

Since many radionuclides are excreted in urine, the bladder wall is irradiated by radiation originating in the urine, which constitutes a pool of variable size. The dose per photon varies markedly as the bladder contents increase, partly because wall thickness is changing and also because of the inverse-square relation of dose and distance. The basic data on dose per photon are estimated for a range of bladder sizes ranging from 0 to 500 ml content.

A compartmental model for metabolism of iodine has been given by Berman, but because of its complexity, it has not been directly compared with more conventional models. This is done here, and for ^{131}I the comparison is rather close. For some compartments and isotopes of iodine, differences by a factor of 2 may occur.

The thorny question of what happens to a radium atom when produced in bone by decay of a thorium parent continues to demand attention, because the estimate of dose to bone will vary greatly depending on

the model assumed. Last year's report contained calculations corresponding to some hypotheses, and these are supplemented here by further cases ranging from immediate transfer of the radium atom to blood to the assumption that it remains fixed in situ until its decay.

Although immersion in an infinite cloud of radioactive emitter has been a standard case considered in the past, no good estimates of the energy spectrum produced in such a case have been available. Due to this fact, no reliable estimates of dose at various depths within the body have been produced. The energy spectrum resulting from a monoenergetic photon source distributed uniformly in an infinite space of air is given here. It is expected that a correction for ground effect will be forthcoming in next year's report.

20. Stable Element Metabolism

The elemental balance for intake and excretion of certain elements commonly present in diets is reported here for two adult subjects who ate ad libitum. The study is almost unique in that these individuals were studied over a period of several years, and many minor fluctuations appear to "cancel out" over such a period of study.

The gross compositions of bone and cartilage are reported here. The data on cartilage are essentially new and help fill one sizable gap in our knowledge of the composition of the body.

Part I. Radioactive Waste Disposal

K. E. Cowser

1. Fate of Trace Elements and Radionuclides in Terrestrial Environment

Tsuneo Tamura

W. P. Bonner F. S. Brinkley
C. W. Francis E. R. Eastwood
A. L. D'Andrea[1]

EVALUATION OF ZONAL CENTRIFUGATION TECHNIQUES

In order to better understand environmental systems, it is frequently desirable to segregate a sample into its individual components for identification as well as to establish associations of interested elements or radionuclides with different components of the matrix. Recent developments in zonal centrifugation techniques suggest several applications of this tool in physically separating environmental samples into their various inorganic components.[2]

Zonal centrifugation consists in preparing a continuous density-gradient solution in a tube, layering the test sample on the gradient solution, and centrifuging the tubes to allow each component to collect at its isodensity, or isopycnic, point. The time required for minerals to collect at their isodensity point is a function of a number of variables, including centrifugal force, size and shape of particles, density of particles, density of suspending medium, and viscosity of the medium.

The density of minerals will vary depending on the nature of the minerals and their interaction with the gradient medium or dispersing agent. Thus the measured density is the "buoyant density" and not necessarily the original compositional density. The theoretical times required for isopycnic banding of particles, varying in size and density, are given in Table 1.1 for the conventional centrifuge and the ultracentrifuge used in our tests. The times listed assume sedimentation follows Stokes' law and setting the approach to ideal isopycnic density to within 0.05 g/cc as the limit. Note that with the conventional centrifuge at 1500 rpm speed, 1-μ-diam particles reach isopycnic density in less than about 32 hr; smaller particles require inordinate times. With the ultracentrifuge at 10,000 rpm, isopycnic density is reached in less than three days even for the smaller particles and long travel distance in the tube as required for the particles with 2.61 g/cc density.

The importance of high centrifugal force is especially apparent in separating fine-size particles such as bentonites. With 1500 rpm and 40 hr [19,000 gravity × hours (gh)], two bands are observed with $<0.2\ \mu$ bentonite; but with 10,000 rpm and 14 hr (200,000 gh), only one band is observed with the same mineral (Table 1.2). The occurrence of the higher density band

[1] ORAU summer participant.

[2] K. Z. Morgan *et al.*, *Health Phys. Div. Ann. Progr. Rept. July 31, 1969*, ORNL-4446, pp. 1–8.

Table 1.1. Hours[a] Required for Isopycnic Banding of Particles of Varying Sizes and Densities

Particle Diameter (μ)	Particle Density (g/cc)					
	Conventional[b]			Ultracentrifuge[c]		
	2.11	2.46	2.61	2.11	2.46	2.61
5	0.628	1.08	1.29	0.013	0.023	0.027
2	3.92	6.78	8.05	0.083	0.146	0.173
1	15.77	27.15	32.21	0.332	0.584	0.692
0.2	392	678	805	8.30	14.6	17.3
0.1	1570	2710	3220	33.2	58.4	69.3

[a]Assuming sedimentation follows Stokes' law and allowing 0.05 g/cc difference between density of liquid and particle.

[b]International Equipment Company model PR-2 refrigerated centrifuge with No. 253 rotor at 1500 rpm.

[c]Beckman Instruments, Inc., Spinco Division, model L-2 refrigerated ultracentrifuge with No. SW25.2 swinging bucket rotor at 10,000 rpm.

Table 1.2. Influence of Rate of Centrifugation, Cation Saturation, and Particle Size in Isopycnic Banding of Wyoming Bentonite, API No. 26

Band density range and median density[a] in g/cc

Particle Diameter (μ)	Number of Gravities Times Hours[b]					
	200,000			19,000		
	Saturating Cation					
	Na	K	Cs	Na	K	Cs
			Bentonite Bands			
<2	1.87–2.03 (1.95)	1.98–2.19 (2.08)	2.02–2.18 (2.10)	1.88–1.98 (1.93)	2.06–2.12 (2.09)	2.10–2.14 (2.12)
2.0–0.2	1.92–2.00 (1.96)	2.08–2.18 (2.13)	(2.12–2.19) (2.15)	1.86–1.92 (1.89)	2.03–2.14 (2.08)	2.06–2.15 (2.10)
<0.2	1.87–1.95 (1.91)	1.90–2.07 (1.99)	1.98–2.10 (2.04)	1.52–1.72 (1.62)	1.57–1.78 (1.67)	1.50–1.79 (1.64)
	1.87–1.96 (1.91)[c]			1.85–1.89 (1.87)	2.02–2.08 (2.05)	2.09–2.15 (2.12)
			Quartz Bands			
<2	2.47–2.51 (2.49)	2.46–2.52 (2.49)	2.50–2.56 (2.53)	2.43–2.53 (2.48)	2.41–2.48 (2.44)	2.41–2.47 (2.44)
2.0–0.2	2.41–2.51 (2.46)	2.46–2.55 (2.50)	2.49–2.54 (2.51)	2.39–2.51 (2.45)	2.40–2.47 (2.43)	2.43–2.52 (2.47)
<0.2	No quartz band in <0.2-μ clay					

[a]Median density is in parentheses.

[b]Comparison between an ultracentrifuge at 10,000 rpm for 14 hr (200,000 gh) and a conventional refrigerated centrifuge at 1500 rpm for 40 hr (19,000 gh).

[c]568,000 gh – ultracentrifuge at 10,000 rpm for 90 hr.

observed with 19,000 gh, especially with the potassium- and cesium-saturated bentonite, indicates formation of peptized floccules which are stable at 19,000 gh. The difference in cation saturation results in banding of the bentonite at different densities but seems to have no significant effect in banding the quartz fraction. The median densities of the bentonite differ little between potassium and cesium saturation, indicating that interlayer relationship plays a more dominant role than the additional mass associated with the mass of the saturating cation.

With Kentucky metabentonite (API No. 42), two clay bands and a quartz band (band 3) were observed (Table 1.3). Both clay bands showed 10-Å *c*-axis spacing when x-rayed using glycerol solvation. The spacing is the same as that observed with the mineral illite. On comparing the densities of the bands with those of illite, both minerals have components with densities of 2.3 to 2.4 g/cc; but the lighter band of the metabentonite (2.2 to 2.3 g/cc) is heavier than that observed in illite (1.95 g/cc).

The bands recovered from kaolinite from Macon, Georgia, are given in Table 1.4. With the sodium-saturated <2-μ particles, two bands were recoverable; however, with particles less than 0.2 μ, only one wide band was found. With cesium saturation only one band was observed. Sodium- and cesium-saturated kaolinite of less than 2 μ diameter centrifuged for 40 hr in a conventional centrifuge (1500 rpm) showed only a highly dispersed suspension and no discernible bands.

Table 1.4. Influence of Particle Size and Cation Saturation on Isopycnic Banding of Kaolinite, from Macon, Georgia[a]

Particle Diameter (μ)	Saturating Cation	
	Na	Cs
<2	2.12–2.15 (2.13)	
	2.34–2.51 (2.42)	2.40–2.52 (2.46)
2.0–0.2	2.39–2.56 (2.47)	2.46–2.57 (2.52)
<0.2	2.18–2.55 (2.36)	2.33–2.50 (2.41)
<0.2[b]	2.26–2.47 (2.36)	

[a]250-mg samples centrifuged at 10,000 rpm for 14 hr – 200,000 gh.
[b]100-mg samples centrifuged at 10,000 rpm for 40 hr – 568,000 gh.

The results obtained thus far lead to several conclusions. First, isopycnic zonal centrifugation of particles less than 0.2 μ is not practical in conventional refrigerated centrifuges (1500 rpm). Second, dispersion of clays even less than 0.2 μ in diameter can be maintained for periods as long as 40 hr in nonaqueous density gradient (20 ± 3°C). Third, cesium saturation increases the buoyant density of the minerals as compared with sodium saturation; the increase is greater for bentonite

Table 1.3. Influence of Rate of Centrifugation and Cation Saturation in Isopycnic Banding of Kentucky Metabentonite, API No. 42

Band density range and average density[a] in g/cc

Particle Diameter (μ)	Number of Gravities Times Hours[b]					
	200,000			19,000		
	Saturating Cation					
	Na	K	Cs	Na	K	Cs
			Band 1			
<2	2.14–2.20 (2.17)	2.20–2.29 (2.25)	2.28–2.33 (2.30)	2.15–2.21 (2.18)	2.17–2.24 (2.20)	2.18–2.38 (2.28)
			Band 2			
<2	2.28–2.32 (2.30)	2.33–2.40 (2.36)	2.36–2.41 (2.39)	2.28–2.32 (2.30)	2.31–2.36 (2.33)	2.41–2.44 (2.42)
			Band 3			
<2	2.48–2.51 (2.49)	2.49–2.56 (2.52)	2.48–2.50 (2.49)	2.45–2.49 (2.47)	2.49–2.52 (2.49)	2.47–2.52 (2.49)

[a]Average density is in parentheses.
[b]Comparison between an ultracentrifuge at 10,000 rpm for 14 hr and a conventional refrigerated centrifuge at 1500 rpm for 40 hr.

(8% increase in mean density) and metabentonite (5% increase) than for kaolinite (2% increase). This order of increase is consistent with the ability of the mineral to solvate.

APPLICATIONS OF ZONAL CENTRIFUGATION

Phosphate Distribution in Soils and Sediments

This technique should be useful in separating calcium carbonate (density, 2.7 g/cc) from other components in soils and sediments, thus eliminating problems which have been encountered in determining the forms of phosphate in these media (attributable to this mineral). Three environmental media were selected which would serve to develop the technique and evaluate its potential, as well as provide information on forms of phosphates. These included (1) a calcareous bottom sediment (ORIC pond) typical of sediments found in many lakes in the southeastern United States, (2) the suspended sediment from which the bottom sediment is derived, and (3) a noncalcareous soil (Lower Hill soil) whose products of erosion are the source of sediment in this pond.

The gradient system used in this study consisted in varying proportions of tetrabromoethane (TBE) and ethyl alcohol (EtOH), the latter containing 10% by weight of polyvinylpyrrolidone (PVP K-30) as a dispersant for the clays. The density range chosen was 1.8 to 2.8 g/cc.

Initially, pond sediment which had received no prior size segregation was separated by zonal centrifugation.

[3]K. Z. Morgan *et al.*, *Health Phys. Div. Ann. Progr. Rept. July 31, 1968*, ORNL-4316, pp. 1–4.

[4]J. D. H. Williams, J. K. Syers, and T. W. Walker, "Fractionation of Soil Inorganic Phosphate by a Modification of Chang and Jackson's Procedure," *Soil Sci. Soc. Am. Proc.* 31, 736–39 (1967).

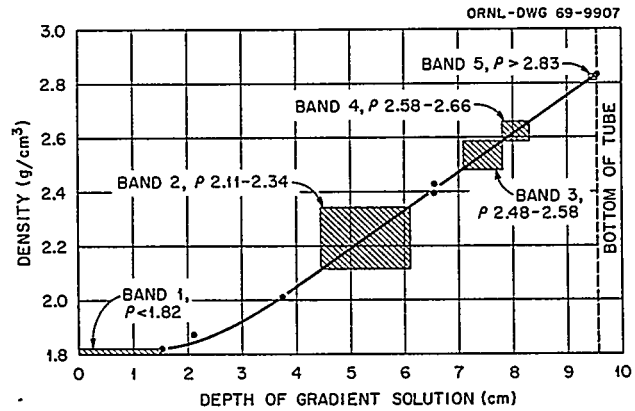

Fig. 1.1. Shape of the Reconfirmed Density Gradient Showing the Location and Density Range of the Bands Recovered from Isopycnically Banding a Calcareous Pond Sediment.

The density of the material recovered in each of the five bands was obtained from its location within the reconfirmed density gradient shown in Fig. 1.1. Note that bands 1 and 5 contain materials having densities outside the limits of the gradient.

When the phosphorus extraction procedure described by Jackson[3] and modified by Williams *et al.*[4] was applied to the banded as well as the unbanded sediment, contrasting results were obtained. The data presented in Table 1.5 give the concentration of various forms of phosphate in milligrams in the unbanded sample and in each of the recovered bands. The extractants used are those which selectively dissolve different forms of phosphates. The NH_4Cl removes easily exchangeable forms, NH_4F dissolves easily soluble aluminum phosphate, the NaOH which follows NH_4F extraction dissolves easily soluble iron phosphate, and the H_2SO_4 used last removes calcium phosphate. Each value shown is the average of values obtained by analyzing four 0.15-g samples which were

Table 1.5. Distribution of Weight and Extractable Phosphorus in the Banded and Unbanded Sample of Bottom Sediment

Band	Weight (g)	Extracting Reagent, PO_4 (mg)				Sum
		NH_4Cl	NH_4F	NaOH	H_2SO_4	
1	0.0008	0.00148	0.0008	0.00056	0.00089	0.00381
2	0.0468	0.00145	0.01543	0.00731	0.00530	0.02949
3	0.0783	0.00100	0.00635	0.00076	0.00809	0.01620
4	0.0114	0.00077	0.00766	0.00040	0.00925	0.01808
5	0.0046	0.00071	0.00404	0.00145	0.00949	0.01569
Sum 1–5	0.1419	0.00541	0.03436	0.01048	0.03302	0.08327
Unbanded	0.1500	0.00125	0.01503	0.00090	0.07062	0.08780

individually banded. Values for the unbanded sample are the averages of four replicates of the same sample. Statistical analysis of the values showed no reason for rejecting values; consequently, it was assumed that values from like fractions were from the same population and therefore averaged.

Note that, although the total phosphate recovered from both the banded and unbanded sample agrees within 5%, the distribution of the different forms is grossly different. The typical weight distribution included in Table 1.5 suggests that the 5% error could be due to loss of material during banding. For each of the first three extractants, the phosphate concentration is lower for the unbanded sample than for the sum of bands 1 through 5 of each extractant of the banded sample. This is reasonable since the presence of calcium carbonate is known to influence the phosphate fractionation procedure through the formation of calcium phosphate.[4] Thus, when calcium carbonate is present, the phosphorus extraction procedure underestimates the iron and aluminum phosphate and overestimates calcium phosphate. The lower value for iron phosphate in pond sediment is most likely due to the release of iron-bound phosphate under reducing conditions found in pond sediment.

The distribution of the various forms of phosphate among the several bands is also noteworthy. Band 2 contains most of the aluminum and iron phosphate forms which would be expected to occur in the fraction containing predominantly clays.

Calcium phosphate, however, is found in several bands in nearly equal quantities. Initially, calcium phosphate was expected to be found predominantly in band 4; however, several forms of calcium phosphate are known to have a density within the range of 2.2 to 2.8. Preliminary data obtained from the fractionation of a calcareous soil suggest that different forms of calcium phosphate exist in this sediment.

Lower Hill soil, a fertilized noncalcareous soil, was banded just as the pond sediment. To one series of samples was added 17% calcium carbonate in order to demonstrate the effect, if any, that banding has upon the distribution and forms of phosphate in a calcareous and a noncalcareous environmental medium. The results are shown in Fig. 1.2. Note that the addition of calcium carbonate to the sample which was subsequently banded produced no increase in the H_2SO_4 extractable fraction of Lower Hill soil. This is in contrast to results obtained when calcium carbonate is added to unbanded samples.[2] The values observed for the banded and unbanded samples are also in good agreement. These data are grossly different from those obtained from

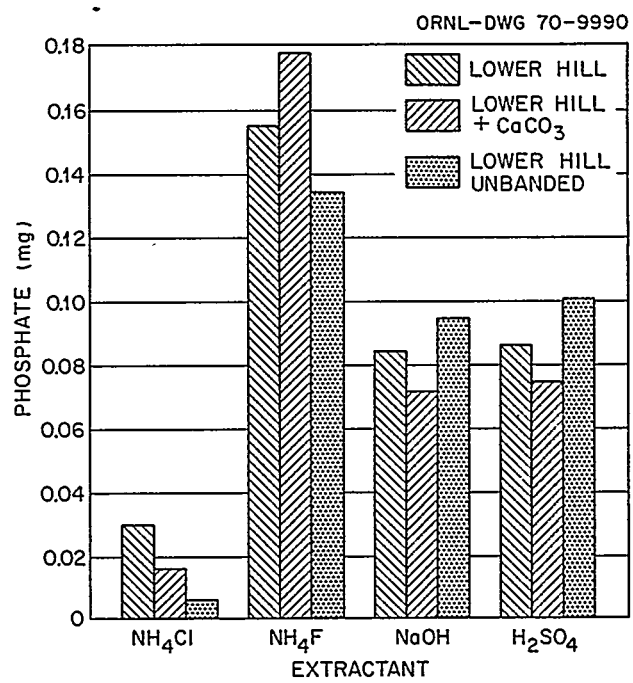

Fig. 1.2. Forms and Concentration of Phosphate in the Unbanded Acid Soil and in the Banded Soil With and Without Added Calcium Carbonate.

unbanded pond sediment, in which the H_2SO_4 extractable phosphate in the unbanded sample was shown to be more than double that found in the banded (calcium carbonate segregated) sample. This clearly demonstrates the influence of calcium carbonate on the phosphorus extraction procedure.

The distribution and forms of phosphate in the banded and unbanded Lower Hill soil are given in Table 1.6. These data show that aluminum, iron, and calcium phosphate are more abundant in band 3 (density, 2.4 to 2.5). The greater proportion of calcium phosphate associated with lower density material is different from that observed for pond sediment, where calcium phosphate was more evenly distributed between bands having a density greater than 2.4. This is probably due to the formation of calcium phosphate in the vicinity of clay particles possessing a high concentration of calcium ions and to the absence of calcium carbonate in the soil.[5]

The third environmental component was pond suspended solids. In this case it was necessary to separate the solids from the liquid prior to zonal centrifugation. Solids were separated into four size groupings by centrifugation, assuming an average particle density of 2.5 g/cc. These groupings were silt, greater than 2 μ;

[5] C. A. Black, *Soil-Plant Relationships*, Wiley, New York, 1968.

Table 1.6. Forms and Distribution of Phosphorus in Banded and Unbanded Lower Hill Soil

Band	Density (g/cc)	Weight (g)	Extracting Reagent, PO_4 (mg)				Sum
			NH_4Cl	NH_4F	NaOH	H_2SO_4	
1	<1.8	0.0067	0.00460	0.01250	0.00440	0.00310	0.02460
2	2.07–2.22	0.0247	0.00840	0.03690	0.02330	0.01150	0.08010
3	2.41–2.50	0.0279	0.00850	0.06940	0.03710	0.03840	0.15340
4	2.50–2.60	0.0190	0.00345	0.02150	0.00780	0.01130	0.04405
5	2.60–2.67	0.0521	0.00347	0.01140	0.00860	0.01060	0.03407
6	>2.79	0.0029	0.00165	0.00390	0.00360	0.01150	0.02065
Sum 1–6		0.1333	0.03007	0.15560	0.08480	0.08640	0.35687
Unbanded		0.150	0.00860	0.13650	0.09270	0.11570	0.3535

Table 1.7. Forms and Distribution of Phosphorus in Pond Suspended Solids

Particle Size Range (μ)	Band	Weight (g)	Extracting Reagent, PO_4 (mg)				Sum
			NH_4Cl	NH_4F	NaOH	H_2SO_4	
>2	1	0.0038	0.00056	0.00073	0.00043	0.00010	0.00182
	2	0.0680	0.00124	0.01050	0.00746	0.00200	0.21210
	3	0.0329	0.00089	0.00354	0.00185	0.00109	0.00737
	4	0.0046	0.00035	0.00040	<0.00013	0.00023	0.00111
	5	0.0015	0.00018	0.00033	<0.00013	0.00023	0.00087
	Total		0.00322	0.01550	0.01000	0.00365	0.03237
0.2–2	1	0.0045	0.00725	0.00609	0.00160	0.00030	0.01524
	2	0.0158	0.0313	0.01409	0.00539	0.00081	0.02342
	3	0.1126	0.00290	0.03961	0.03265	0.00789	0.08305
	4	0.0061	0.00099	0.00226	0.00064	0.00070	0.00459
	Total		0.01427	0.06205	0.04028	0.00970	0.12630
0.08–0.2	1	0.0009	0.00013	0.00017	0.00007	0.00097	0.00047
	2	0.0807	0.00113	0.01286	0.00097	0.00139	0.01635
	Total		0.00126	0.01303	0.00104	0.00149	0.01682
0.01–0.08	1	0.0215	0.00417	0.00500	0.00160	0.00017	0.01094
	2	0.0020	0.00042	0.00056	0.00008	0.00010	0.00116
	Total		0.00459	0.00556	0.00168	0.0027	0.01210
	Total all bands		0.02334	0.09614	0.05300	0.01511	0.18759

coarse clay, 2 to 0.2 μ; medium clay, 0.2 to 0.08 μ; and fine clay, 0.08 to 0.01 μ. The sample received no pretreatment prior to size separation; thus the separation should represent the particle size distribution found in the natural state. The particle size distribution obtained is as follows: silt, 25.5%; coarse clay, 62.3%; medium clay, 9.1%; and fine clay, 3.1%.

Material from each of the particle size groupings was then banded in density 1.8 to 2.8 TBE-EtOH, and the bands were recovered for phosphorus extraction. The results of extraction are given in Table 1.7. The values shown are calculated on the basis of 0.15 g of total suspended solids prior to separation from pond water. Note that most of the phosphate exists in the iron and aluminum forms. Inasmuch as calcium carbonate was identified in the >0.2-μ fractions, the results of phosphate fractionation are in marked contrast to those of pond sediment, where calcium phosphate was observed to be approximately equal to aluminum phosphate. The low calcium relative to iron and aluminum phosphate in suspended solids was not expected, since calcium phosphate is relatively insoluble under alkaline conditions. Calcium carbonate was identified in the suspended solids, and the pond sediment contained approximately equal quantities of iron plus aluminum and calcium phosphate. The difference could be that, upon settling, the iron-bound phosphate was released under reducing conditions of pond sediment, forming calcium phosphate in the sediment.

The distribution of phosphorus as a function of particle size is also of interest. Although most of the phosphorus was found in the 0.2-to-2-μ (coarse clay)

fraction, a significant quantity was found in the <0.2-μ fraction. In water quality studies, particles passing a 0.4- or 0.2-μ filter are considered to be solution. The data show that approximately 15% of the phosphate is associated with particles in the <0.2-μ fractions. Thus a significant quantity of phosphate is being incorrectly ascribed to the solution phase.

The fact that most of the calcium phosphate observed in soil, sediment, and suspended solids occurs in bands having a density less than that of calcium carbonate seems noteworthy. Its presence could be attributed to fertilization of the soil or formation of calcium phosphate under the alkaline, high-calcium conditions in the water regime without immediate formation of apatite (3.0 g/cc density).

Collectively, these data show that zonal configuration offers a technique for the separation of environmental media into components which lend themselves to more meaningful study. Calcium carbonate, the component of calcareous media which is most troublesome in phosphorus extraction, is removed by this banding technique, thus permitting a more detailed look at the distribution of the forms of phosphorus and the components with which they are associated. The data show that the forms of phosphate are not altered during zonal centrifugation of a calcareous medium in a gradient of TBE and EtOH. The data also confirm that calcium phosphate exists in forms which are not directly associated with calcium carbonate. Some of the forms have a density of less than 2.7 g/cm^3 (density of calcium carbonate). These could be forms which are important in agriculture. The successful application of this technique to soils, sediments, and suspended solids facilitates study of the forms and availability of phosphorus in environmental media and the changes which occur as normally acid soils are eroded into an alkaline water regime.

Radionuclide Distribution in White Oak Creek Sediments

Tests with samples obtained from the Clinch River and White Oak Creek had suggested that most of the ^{137}Cs was associated with clays and that a significant portion of the ^{90}Sr was associated with limestone.[6] To test this tentative conclusion and to further evaluate zonal centrifugation as a technique to segregate specific radionuclides in multicomponent systems, sediment samples were obtained from the mouth of White Oak Creek entering the Clinch River (creek sample) and from White Oak Lake (lake bed sample).

These two samples were segregated using the same system as described for phosphate analysis. The ^{137}Cs was counted directly in a multichannel analyzer, and the ^{90}Sr was determined by the Analytical Chemistry Division by extracting the sample with 2 M HNO_3 and counting in an anticoincident beta counter after radiochemical separation. Although seven bands were recovered in the creek sample, only six were recovered from the lake bed sample; in the creek sample sufficient indication of a distinct band was present at the 2.41-to-2.47-g/cc density range which warranted separate recovery, whereas in the lake bed sample no such distinction could be made. From x-ray diffraction analysis, the occurrence of the distinct band is the presence of a large amount of feldspar in the creek sample.

Results of the radionuclide distribution are shown in Table 1.8. The total ^{90}Sr content is similar in the two samples, about 3.7×10^{-4} μCi/g. A higher ^{137}Cs concentration was found in the creek sample (5.8×10^{-3} μCi/g) than in the lake bed sample (1.9×10^{-3} μCi/g). The band with the highest ^{137}Cs concentration had a density of 2.30 to 2.47 g/cc; minerals in this band in both samples were primarily the clay minerals illite (50%) and kaolinite (25%). In the creek sample approximately 37% of the ^{137}Cs was in this band, which represents 18% of the total weight; in the lake bed sample 40% was in this band, and the band accounted for 36% of the weight.

In the earlier Clinch River study, it was found that ion exchange mechanism accounted for about 77% of the ^{90}Sr retention in the Clinch River sample at the mouth of White Oak Creek and 35% in the White Oak Lake Bed sample.[6] It was further suggested that calcium carbonate was responsible for sorbing the remainder of the radionuclide. In the lake bed sample, the calcite (calcium carbonate) was identified mainly in band 6 with a small amount in band 5, and dolomite (calcium-magnesium carbonate) was found in band 7. In the creek sample dolomite was readily identified in band 7, but little evidence for calcite was found in band 6. The ^{90}Sr in bands 6 and 7 of the lake bed sample is about 40% of the total present, and in band 7 of the creek sample the ^{90}Sr content is about 15%. Although no leaching tests were performed to establish the amount of ion-exchanged ^{90}Sr, these results are encouraging in that different bands contain different amounts of this radionuclide and thus may permit better definition of reaction mechanisms in environmental samples.

[6] R. J. Pickering *et al.*, "Radioactivity in Bottom Sediment of the Clinch and Tennessee Rivers," pp. 57–88 in *Disposal of Radioactive Wastes into Seas, Oceans, and Surface Waters*, IAEA Proceeding Series STI/PUB/126, 1966.

Table 1.8. Distribution of ^{90}Sr and ^{137}Cs from Sediments Collected in White Oak Lake Bed and the Mouth of White Oak Creek

Band	Density (g/cc)	Weight (g)	Percent Weight	^{90}Sr (counts/min)	Percent in Band	^{137}Cs (counts/min)	Percent in Band	Band Characteristics
				White Oak Creek				
1	1.86	0.0025	1.8	15	11.7	15	1.2	Amorphous material
2	1.86–2.30	0.0072	5.6	16	12.5	118	9.7	Amorphous material
3	2.30–2.41	0.0230	17.7	33	25.8	456	37.4	Clay minerals
4	2.41–2.47	0.0220	17.0	10	7.8	212	17.4	Clay minerals with feldspars
5	2.47–2.56	0.0562	43.3	25	19.5	281	23.1	Primarily quartz; some clay minerals
6	2.56–2.78	0.0143	11.0	10	7.8	77	6.3	Mica and chlorite (?)
7	2.78	0.0045	3.5	19	14.8	59	4.8	Heavy minerals, including dolomite
Total		0.1287		128		1218		
Unbanded		0.1500		132		1326		
				White Oak Lake Bed				
1	1.86	0.0013	1.0	5	3.8	8	2.2	Amorphous material
2	1.86–2.30	0.0012	0.9	7	5.3	23	6.3	Amorphous material
3	2.30–2.47	0.0486	35.8	37	28.0	148	40.5	Clay minerals includes band 4
4								Clay minerals includes band 4
5	2.47–2.59	0.0552	40.6	30	22.7	101	27.7	Primarily quartz; some calcite and clay minerals
6	2.59–2.78	0.0267	19.17	44	33.3	65	17.8	Primarily calcite
7	2.78	0.0029	2.1	9	6.8	20	5.5	Heavy minerals, including dolomite
Total		0.1359		132		365		
Unbanded		0.1500		105		406		

DISTRIBUTION OF ^{137}Cs IN SOIL OF A *LIRIODENDRON* FOREST

This section, as well as that following, represents contributions from the Health Physics Division to the Ecological Sciences Division's joint cooperative projects. Only the summary of the findings is reported here; the more detailed report will be found in the Ecological Sciences Division Annual Report.[7]

Since the *Liriodendron* forest was tagged in 1962, the soil radioactivity has continued to increase; and in October 1967 approximately 65% of the initial inoculation had accumulated in the soil.[2] Studies have continued on the distribution of the ^{137}Cs in the soil and to evaluate the distribution of ^{137}Cs among the soil separates. Analysis of a composite sample (20 cores) revealed that the soil compartment contained approximately 50% of the ^{137}Cs; this value, as compared with a higher 1967 value, cannot be explained at this time. Approximately 50% of the ^{137}Cs was found in the 0- to 4-cm depth and decreased with depth until only about 2% was found at 16 to 20 cm.

After separating the soil into different particle size fractions and a separate root fraction, the highest ^{137}Cs concentration was found in the roots (about 15 pc/mg). Concentration of ^{137}Cs in the root was constant with depth, in sharp contrast to the mineral fractions, which decreased with depth. Of the mineral fractions the clay size fraction contained the highest concentration of ^{137}Cs per unit weight.

To ascertain the distribution of ^{137}Cs in clay separates, the clay fraction was banded using zonal centrifugation. Although the separations of individual clay minerals were not complete, the higher concentrations of ^{137}Cs in bands containing illite suggest that this mineral plays a predominant role in sorbing this element (Table 1.9).

[7] S. I. Auerbach *et al.*, *Ecological Sciences Div. Ann. Progr. Rept. July 31, 1970* (in preparation).

Table 1.9. Zonal Centrifugation of the Clay Separate of an Emory Silt Loam from the ^{137}Cs-Tagged *Liriodendron* Forest[a]

	Density Range (g/cc)	Weight Fraction (%)	Activity pc/ml	Activity %	Band Description
Band 1	1.80–2.03	1.0			Amorphous-organo-clay
Band 2	2.03–2.19	34.0	6.1	17.9	Principally kaolinitic clay
Band 3	2.19–2.52	19.1	31.3	52.1	Illitic and kaolinitic clay in ratio approximately 70:30
Band 4	2.52–2.65	40.6	8.1	28.6	Quartz and illite in ratio approximately 90:10
Bottom	>2.75	8.3	3.3	1.5	Heavy minerals

[a]Depth of 4 to 9 cm.

WATER QUALITY STUDIES IN WALKER BRANCH WATERSHED

One of the objectives of the Walker Branch Watershed project is to relate the water quality and productivity of the stream to the characteristics of the adjacent terrestrial ecosystem.[2] Anomalies noted during the sampling of water from springs and segments of both east and west forks of Walker Branch have been tentatively explained on the basis of the soil characteristics.[2] Since water reaches varying depths in the soil, it was felt that a better indication (short of core drilling and tracer studies) of groundwater movement could be obtained from temperature measurements of water from springs and streams. The locations of the recorders along with the mean monthly temperature observed at each location from November 1969 through May 1970 are shown in Fig. 1.3.

Temperatures observed at springs S3E and S3W are relatively constant and slightly higher than those observed at other locations during this period. In contrast to the relatively constant temperatures in these springs, spring S4E shows a fluctuation of 5.8°C during this period. As the water flows downstream the temperature decreases or increases with seasonal and diurnal changes in air temperature (compare readings at 1500 ft with S4E, which is a larger contributor to the Walker Branch). As the water flows underground from 1440 to 980 ft (S1E), a moderating effect is noted.

These findings strengthen the hypothesis that water emerging from S4E is derived from shallow sources, the restricted percolation downward being caused by the fragipan in the soils of the area. The gross differences in stream temperature and the changing chemical composition,[2] especially in the east fork, suggest that different biotic species might be observed in this reach.

To attempt to correlate water quality with geologic factors without core drilling, samples of rocks were obtained either as part of a rock outcrop or loose rock, and analysis for selected elements was performed. Analysis revealed that dolomitic rocks (calcium-magnesium carbonate) are present near the weir sites and in the stream bed above the weirs. These rocks were found to possess approximately the same calcium to magnesium ratio as found in the stream water.[3] The absence of dolomitic rocks in the upstream areas suggests that "hard" waters emerging from springs in these areas must be of deeper origin and that water emerging from S4E could be derived from a much wider area than suggested by the Tarklin soil. Confirmation of this hypothesis would require measurement of vertical and lateral water permeability of the surrounding soils.

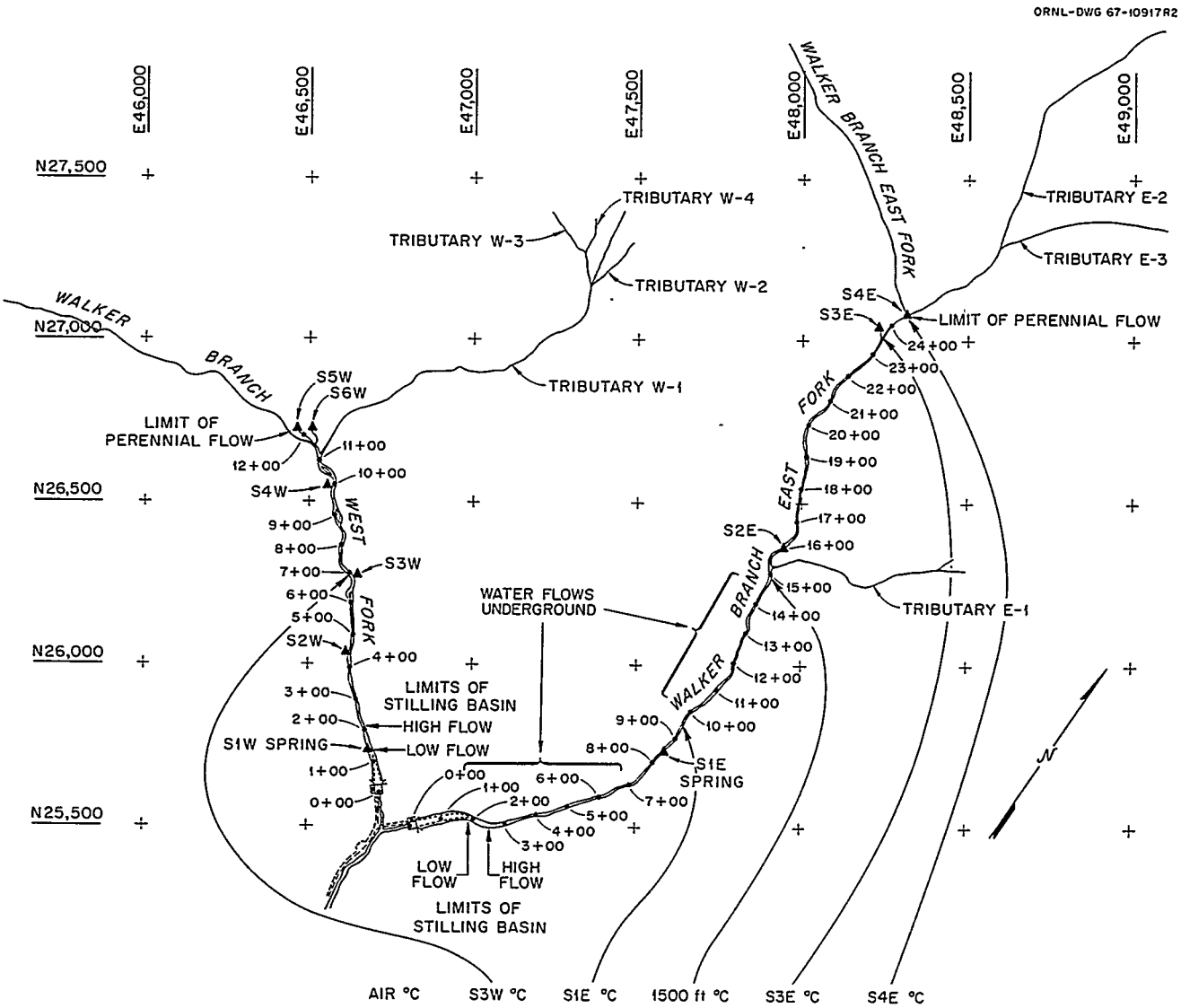

	AIR °C	S3W °C	S1E °C	1500 ft °C	S3E °C	S4E °C
NOVEMBER	5.5	13.1	13.3	8.5	13.2	10.1
DECEMBER	0.5	13.1	12.9	8.9	12.5	8.2
JANUARY	−1.4	13.0	10.8	4.9	11.9	8.7
FEBRUARY	2.0	12.9	10.0	7.6	12.7	9.0
MARCH	5.5	13.1	10.9	9.6	12.9	10.0
APRIL	14.0	13.3	11.3	11.9	13.2	
MAY	17.9	13.4	13.1	14.5	13.7*	14.0*

*FLOW EXTREMELY LOW

Fig. 1.3. Horizontal Traverse of Walker Branch Showing Water Temperature at Selected Locations.

2. Disposal by Hydraulic Fracturing

Wallace de Laguna Tsuneo Tamura
K. E. Cowser O. M. Sealand

INVESTIGATIONS AT OAK RIDGE

Operational waste injection ILW-6 was made June 11, 1969, and comprised 79,350 gal of waste and 12,400 gal of water, which with the solid ingredients mixed up to 126,331 gal of slurry. The waste contained 89,000 Ci of ^{137}Cs, 8900 Ci of ^{90}Sr, 100 Ci of ^{106}Ru, and 200 Ci of ^{60}Co, making it the most radioactive waste solution disposed of so far at the hydraulic fracturing plant. During the injection there was a steady rise in the pressure of the water in rock-cover monitoring well NW 175, but not in the other four rock-cover monitoring wells then in operation. This suggests that the fracture moved out to the northwest. The injection went smoothly and required about 10½ hr of pumping.

During the course of the summer, five more rock-cover monitoring wells were completed, bringing the total to nine. All these wells have now been pressure tested. Several of the old monitoring wells have been retested, and these show no change in the permeability of the rock cover.

Preparations have been made to repair the two plugged observation wells used for gamma-ray logging. We also hope to drill four more observation wells for logging, which will bring the total number of such wells up to 11.

INVESTIGATIONS IN NEW YORK STATE

The "five-spot" well pattern, a central injection well and four surrounding observation wells, was completed at the test site in New York. The observation wells are located at the corners of a square, about 150 ft out from the injection well. The first hole drilled, the core hole, was cased with 1¼-in. tubing and now forms the east observation well. The other three were drilled 6½ in. in diameter and cased with 2-in. tubing. The observation wells were all installed prior to any injection, so that they might be logged after each injection and in this way all doubt removed as to which injection was responsible for which logging peak or fracture. Also, using this plan, there will be no need to log in a contaminated hole.

The general plan for the injection remains much the same, although there have been some minor changes. All four injections will consist of water containing one-tenth of a pound of Grundite (illite) clay to the gallon. The total volume of each injection will be about 100,000 gal, to which 2.7 Ci of ^{95}Zr-^{95}Nb will be added. The depths of the four injections, as measured in the injection well, will be 1450, 1245, 1010, and 520 ft.

Water Injection Test

A preliminary injection of plain water, with no radioactive tracer, was made at a depth of 1450 ft on October 9, 1969. The total volume injected was 114,000 gal. The pressures during the injection were low, around 1040 to 1100 psig, as measured at the surface, and varied very little as the pumping rate was varied from 100 to 400 gpm. We have no explanation for this. The pressure-decay curve was consistent with the formation of a horizontal fracture but suggested a complex fracture pattern.

The conclusions reached from a study of the pumping pressures were as follows (First Fracturing Test, West Valley, New York, ORNL-CF-69-12-54):

1. In the test at New York there is only a trivial difference between the injection pressures at the several flow rates. This can only be interpreted as meaning that the situation at the New York site is so different from conditions at Oak Ridge that there is no basis for comparison. These constant injection pressures at the various flow rates are by far the most puzzling aspect of these results.

2. The injection pressure was constant as a function of volume injected. If it were not for item 1 above, it would be tempting to conclude from this that the fracture was *not* both circular and horizontal, that is, that it was either horizontal and very elongated, or nonhorizontal.
3. The unusual pressure behavior following a 45-min period of no pumping suggests that the fracturing process did not begin again at the point where it ceased but in some way changed its configuration. This, in turn, suggests that a group or network of fractures may have been formed rather than a single fracture.
4. From a study of the pressure-decay curve, one may conclude that the fracture pattern at the New York test site is different from the pattern at Oak Ridge. It is also more complex. Inasmuch as we know that the fracture pattern at Oak Ridge is comparatively simple and nearly horizontal, this is almost equivalent to saying that the fractures at New York are complex. A possible interpretation of the pressure-decay data is that part of the fracture pattern is horizontal.

Tests to be run in the summer of 1970 will use a radioactive tracer to help reveal the actual pattern of the fractures.

Evaluation of ^{95}Zr-^{95}Nb Tracer in Hydraulic Fracturing Test

To determine the direction and position of the fracture in the shale at the New York State site, mixed ^{95}Zr-^{95}Nb tag will be used as a tracer in a clay-water slurry. The tag will be added to a 30-gal stainless steel drum filled with approximately 10 gal of a dye solution; the solution will be fed directly to the well casing by means of a high-pressure pump delivering approximately 1.5 gph (see Fig. 2.1). The tagged solution will be mixed with a clay-water slurry in the wellhead and pumped down the well and into the fracture at a rate of approximately 12,000 gph (200 gpm). Later, measurements will be taken at the four observation wells using a gamma probe to determine the intersection of the tagged slurry. Following the completion of injection, the well will be shut, and pressure readings will be taken over an extended period until the pressure drop is relatively insignificant.

To ensure that radioactivity will be delivered to the wellhead, to determine the reaction of the tag with the clay-water slurry, and to characterize the behavior of the slurry in the fracture as well as on the ground surface in the event of a mishap, several laboratory tests were performed. The results of these tests are summarized in Tables 2.1 and 2.2.

ORNL-DWG 69-7292

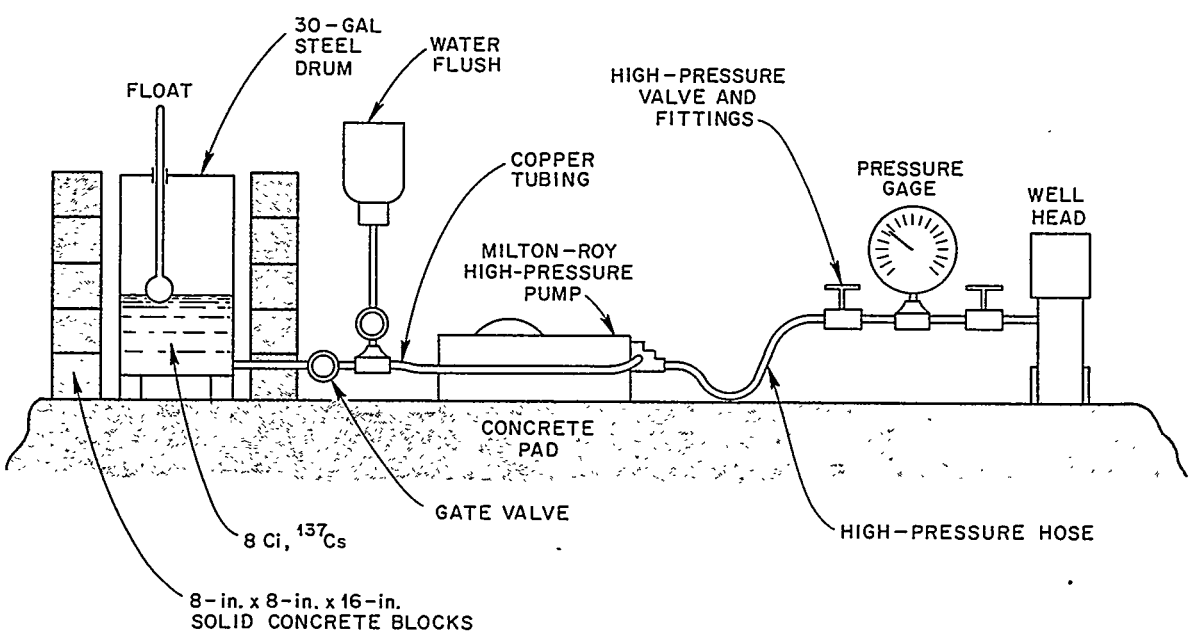

Fig. 2.1. Schematic Diagram of Tag Feed System for Hydraulic Fracturing Test.

Since ^{95}Zr-^{95}Nb is known to plate out on surfaces, it was first necessary to know its behavior when added to the 30-gal drum. The results of adding the tag solution to both glass and stainless steel containers of near-equal surface area are summarized in Table 2.1. The initial ^{95}Zr-^{95}Nb is added as a 5% solution of oxalic acid (normally used solution for packaging this element). Initially, distilled water was used; but, since the water at the test site contains calcium and magnesium ions, later tests were made using Oak Ridge tap water with approximately 25 ppm calcium and 10 ppm magnesium. Tests with this tap water showed that approximately 25% of the tag was removed from solution; the white precipitate suggested that calcium oxalate formed and carried with it the ^{95}Zr-^{95}Nb. Calculations of the solubility of calcium oxalate in a medium of 25 ppm calcium and 1.5×10^{-3} *M* oxalate ions (100 ml of 5% oxalic acid solution diluted to 10 gal) show that a precipitate will be formed under these conditions. Hence, to keep the ^{95}Zr-^{95}Nb in solution, 0.1 *N* HNO_3 was recommended.

Table 2.1. Adsorption (counts min^{-1} ml^{-1}) of ^{95}Zr-^{95}Nb by Glass and Stainless Steel Containers in Selected Solutions[a]

Time (hr)	Pyrex Glass	Stainless Steel
	Distilled Water	
0.5	22,700	
1	22,900	
6	22,900	
24	22,300	
	5% Oxalic Acid	
0.5	24,900	24,900
1	24,900	24,700
6	25,200	25,100
24	25,200	25,600
	0.1 *N* HNO_3	
0.5	24,900	24,800
1	25,100	24,800
6	25,400	25,400
24	25,400	25,300
	1 *N* HNO_3	
0.5	24,300	24,300
1	24,300	24,300
6	24,700	24,800
24	24,800	24,800
	Tap Water	
0.5		20,043
1		20,199
19		14,753
91		14,185

[a]Tagging solution is in 5% oxalic acid as normally packaged.

The ^{95}Zr-^{95}Nb tag will be pumped to the wellhead and there mixed with a clay-water slurry. With an 8000:1 dilution, and the buffering capacity of the clay, the pH of the slurry will be approximately 7. To determine the radionuclide distribution and settling characteristics of the slurry, the tag-clay-water slurry was blended in the Waring blender (a procedure used in water-cement slurry preparation to simulate mixing) and placed in a cylinder. After a specified time the slurry was sampled and the activity measured. Both bentonite (montmorillonite) and Grundite (illite) clay slurries were prepared (Table 2.2). The bentonite slurry remained in suspension longer, and the activity only slowly decreased with time; in contrast, the Grundite settled more rapidly and carried most of the activity with it. Note that about 85% of the activity is associated with the clay and 15% is in the liquid phase.

One of the considerations in conducting the tracer test to establish fracture orientation is the contingency that a vertical fracture might form and intercept the glacial till that forms the ground cover of approximately 180 ft thickness or that the operation might release slurry at the ground surface. To evaluate the decontaminating property of consolidated till, the slurry was filtered through media approximating New York site soil. Ottawa sand (porosity 30%) was used as the till equivalent, and Captina silt loam (porosity 40%) was used as a test sample of material with higher porosity but smaller pore size. The result of passing slurry through the column is given in Table 2.2. In the Ottawa sand column, bentonite passed freely through the column and little or no filtration or ion exchange occurred. With Grundite, even Ottawa sand filtered the solids and removed approximately 99% of the activity. In passing through Captina silt loam, both clays were effectively filtered; however, Grundite slurry permitted faster movement of the liquid through the column – 50 ml in 16 hr for bentonite. Since Grundite settles fast, it is less likely to be carried in the water phase if the slurry should reach a stream or well. With this in mind, Grundite clay is recommended for preparing the slurry.

Evaluation of Dye Addition in Hydraulic Fracturing Test

It was suggested by officials of the New York State Department of Health that a nontoxic dye in the slurry would serve as an added precaution to prevent the

Table 2.2 Characteristics of Bentonite and Grundite Slurries Tagged with ^{95}Zr-^{95}Nb

Suspension Characteristics

Bentonite Slurry[a]			Grundite Slurry[a]		
Time (hr)	Activity in Suspension[b] counts min^{-1} ml^{-1}	(%)	Time (hr)	Activity in Suspension[b] counts min^{-1} ml^{-1}	(%)
0.1	215	100	0.1	1985	100
0.5	193	90	0.3	510	26
1	176	82			
2	165	77	17	327	16

Filtration Characteristics

Bentonite Slurry		Grundite Slurry	
Ottawa sand (215 counts min^{-1} ml^{-1})	Captina s.l. (2385 counts min^{-1} ml^{-1})	Ottawa Sand (2044 counts min^{-1} ml^{-1})	Captina s.l. (1985 counts min^{-1} ml^{-1})
205 counts min^{-1} ml^{-1} suspension which flushed through	7 counts min^{-1} ml^{-1} in 15 ml collected in 16 hr	13 counts min^{-1} ml^{-1} in 50 ml collected in 2 hr	10 counts min^{-1} ml^{-1} in 50 ml collected in 16 hr

[a]Distribution of activity was 85% on solid and 15% in liquid for both bentonite and Grundite.
[b]Activity measured at 1-in. depth in cylinder of 20 in.

possible ingestion of small quantities of radioactive tracer in the unlikely event of its migration off site into shallow water wells. Tests were conducted to evaluate several dyes for use in the test.

Initial tests included fluorescein, Rhodamine B, Rhodamine Wt, and All-Purpose Rit (scarlet) dyes. Of these, Rhodamine B and Rhodamine Wt were most effective in maintaining their color (red) after the addition and settling of the clay. Initial volume of dye to be added is limited by the feed source; this feed source is the 30-gal tank which contains 10 gal of water plus radionuclide (Fig. 2.1). Since the concentrated dye is viscous, dilution with water at 4:1 is needed to make it ready for pumping. Hence, 2 gal of dye plus 8 gal of water tracer is recommended. To maintain ^{95}Zr-^{95}Nb in solution in the tank, the system must be acidic. On the other hand, Rhodamine Wt "curdles" in an acidic medium; hence, Rhodamine B was selected as the dye for use.

Since Rhodamine B is in a highly acidic solution, the need for 0.1 N HNO_3 solution to maintain ^{95}Zr-^{95}Nb in solution was questioned. Tests were run to determine whether ^{95}Zr-^{95}Nb would be lost from solution if the nitric acid was omitted from the feed makeup as was recommended earlier. After 3½ days of contact time, 100% of the activity remained in solution; it was therefore concluded that the nitric acid addition was unnecessary.

At a pumping rate of 12,000 gph of slurry and 1.5 gph of dye plus radioactive "tag" solution, dilution of the tag solution will be 8000:1. At this concentration the slurry, as well as the liquid after the clay settles, is visibly pink. Hence, in the unlikely event of discharge to the ground surface, the slurry would be visible to the naked eye.

If the slurry should reach a well, visibility of the dye will depend on the dilution. Since most of the dye becomes attached to the clay, the lower limit of visual detection after the clay settles is 100:1 dilution; greater dilution will mean that the color is undetectable with the naked eye. Immediately upon mixing with well water, however, detectability would be increased because of the color of the "red" clay; the lower level of detection in this situation (no settling) is at a dilution of about 750:1. Obviously, less dilution would be detectable, and it might be assumed that if the dye slurry entered the well, individuals would not drink the water. With 750:1 dilution the dye-slurry mixture would contain 9.5×10^{-6} μCi/ml of ^{95}Zr-^{95}Nb. The nonoccupational MPC_w for this radionuclide is 6×10^{-5} μCi/ml.

Hypothetical Dose Equivalents Through Ingestion

The first tagged slurry to determine the orientation of the fracture will be injected at a 1450-ft depth;

preliminary water injection suggested a horizontal fracture of a complex pattern. If further work confirms the horizontal fracture pattern, the likelihood of any radioactivity reaching potable water is extremely remote. However, in the unlikely event that the slurry should reach potable water, the dose equivalent to anyone drinking the contaminated water should be assessed.

One source of potable water is Buttermilk Creek, which flows into Cattaraugus Creek. The other source is a few shallow wells located outside the Nuclear Fuel Services plant boundary whose depth may be as much as 250 ft, but most of them are about 25 to 50 ft.

The first hypothetical and unlikely situation assessed was one in which it was assumed that the tagged slurry was pumped directly into Buttermilk Creek at a rate of 200 gpm for an 8-hr period. The concentration of slurry at the point of discharge would be 7.1×10^{-3} μCi/ml; with complete mixing in water from Buttermilk Creek (41 cfs), the concentration would be reduced to 7.7×10^{-5} μCi/ml. During an 8-hr day, "standard" man's intake of water is 1100 cc; under these conditions, he could ingest 0.085 μCi from Buttermilk Creek. The dose equivalent to the critical organ (GI tract) from ingestion of a unit amount (1 μCi at $t = 0$) of initially pure ^{95}Zr is shown in Fig. 2.2. From this figure, the dose equivalent from this hypothetical ingestion is calculated to be 2.8 millirems. Similar calculations for Cattaraugus Creek (358 cfs) show the hypothetical dose equivalent to be 0.31 millirem.

The second hypothetical situation assessed was one in which it was assumed that a water supply well becomes contaminated by the slurry. Up to 750:1 dilution the red color of the dye will be detectable, and, hopefully, individuals would not drink the water. In addition to the red color, the slurry would be "muddy," and this also would make the water objectionable for drinking. At a dilution of dye slurry greater than 750:1, it must be assumed that the water could be consumed without fear or suspicion. It was further assumed that any recharge will bring in the same 750:1 diluted dye-slurry mixture and no credit could be taken for filtration and sorption of the radionuclide as it moves through the soil. (Column studies show that in fact filtration is an effective means of removing radionuclides from the slurry.) In contrast to the surface water situation described above, it was assumed that the well water would be consumed daily and that the consumption would be 2200 cc/day. Using the data in Fig. 2.2, the total calculated dose to the GI tract would be about 18 millirems. If the clay settles in the well, the limit of detection would be 100:1; but, since 95% of the radioactivity would be associated with the settled clay, the intake would be less than that in the 750:1 dilution case, and the calculated dose would be about 7 millirems.

The maximum annual dose to the GI tract for members of the public is 1500 millirems; thus the hypothetical dose received in the unlikely situations described above (that is, drinking water from Buttermilk Creek and Cattaraugus Creek or from a shallow groundwater supply) would be a small fraction of the permissible annual dose to the GI tract.

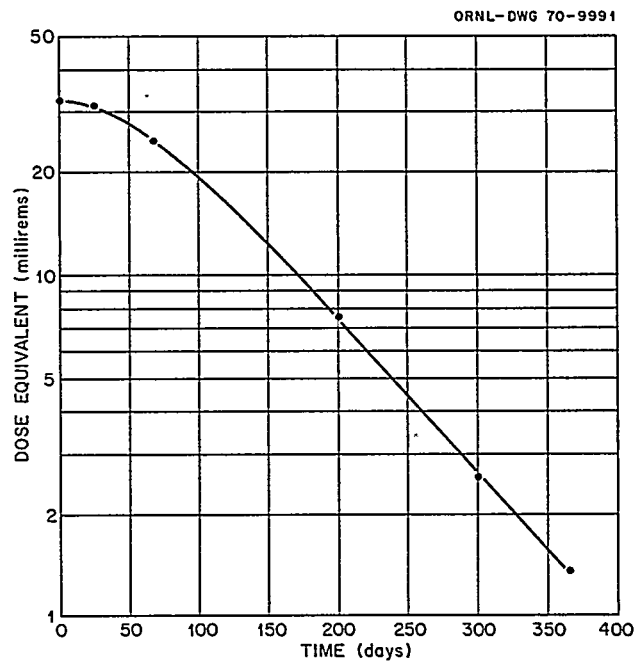

Fig. 2.2. Dose Equivalent to GI Tract from Ingestion of Unit Amount (1 μCi at $t = 0$) of Initially Pure ^{95}Zr.

3. Disposal in Natural Salt Formations

R. L. Bradshaw
J. O. Blomeke[1]
F. M. Empson
Ferruccio Gera[2]
T. W. Hodge, Jr.
B. L. Houser
T. F. Lomenick
W. C. McClain
G. W. Renfro[3]
H. J. Wyrick

One of the principal efforts in this program has been a study leading to the development of a conceptual design of a high-level waste repository. Most of the actual design has been carried out by the General Engineering and Construction Division under the joint direction of the Health Physics and Chemical Technology Divisions. This facility was to be capable of handling all the solidified high-level wastes from the commercial reprocessing of fuels from the civilian nuclear power economy for a period of at least 20 years. As the conceptual design was nearing completion, instructions were received to enlarge the scope of waste repository operation to provide facilities for handling packaged low-specific-activity, alpha-contaminated materials, most of which would originate at AEC installations. Conceptual design of such a "combined" waste repository is still in progress.

DESIGN CRITERIA AND FACILITY DESCRIPTION

For high-level wastes a total salt mine area of about 850 acres, all newly mined for the purpose, will be required. The solidified wastes will be sealed in cans and transported in casks from the reprocessing plants to the repository by both rail and truck. Facilities will be provided at the surface level of the repository for unloading the cans, for inspecting them and either decontaminating or recanning them if necessary, and for lowering them to the mine working level approximately 1000 ft below the surface. At the mine level the cans will be placed in casks, carried by motorized transporters to rooms, and buried in the floor. The spacing between cans in the floor will be gaged so that the radioactive decay heat will be dissipated without causing the temperature of the intervening salt to exceed 200°C at any point; and after the floor area of a room has been utilized, the room will be backfilled with crushed salt and sealed.

Facilities will be provided for handling up to 300 cans of solidified waste per week, based on a three-shift five-day/week operation. The waste cans will be fabricated of either carbon steel or stainless steel and may vary from 6 to 24 in. in diameter and from 2 to 10 ft in length; when filled with waste they may weigh up to 6000 lb each. Shipping casks containing either water or air as a primary coolant and weighing up to 100 tons, with a maximum diameter of 8 ft and a maximum length of 15 ft, will be accepted. Detailed requirements of the can and cask designs will be specified for purposes of standardizing the mechanical handling equipment at the repository. The solidified wastes will be physically, chemically, and radiolytically stable up to 900°C, and their radiation spectrum for shielding considerations will not exceed that of a one-year-old fission product mixture from fuel irradiated to 33,000 MWd/ton at 30 MW/ton. The tentative maximum acceptable heat-generation rates are 4100 W per can for 6-in.-diam cans, 5400 W for 12-in. cans, and 8000 W for 24-in. cans. A water-bath calorimeter will be used to check the heat-generation rate of each can before it is lowered into the mine for burial. Biological shielding in the process areas will be of sufficient thickness to limit radiation dosages to a maximum of 1 millirem/hr at the outer surfaces.

A complete irradiation and processing history of the original fuel and the solidified waste will be required

[1] Chemical Technology Division.

[2] Visiting scientist on leave from Italian National Committee for Nuclear Energy.

[3] General Engineering and Construction Division.

from each shipper as a prerequisite to acceptance and disposal. Before a cask is opened, the primary coolant will be sampled and analyzed to determine if it meets the contamination specifications of 10 CFR 71. If these requirements are satisfied, only a cursory visual in-cell inspection of the cans will be performed before disposition in the mine. If the contamination exceeds these limits, in-cell liquid decontamination facilities will be utilized for removing the loosely adhering contaminants from the surfaces of the cans and/or recanning the waste as may be required.

Waste cans will be unloaded from the casks into a shielded cell in air, individually, and moved either to the shaft and loaded into a cage for subsequent lowering to the mine working level or to a storage area for temporary holdup. The storage area will provide capacity for one week's inventory of waste cans at the maximum mine operating capacity (300 6-in.-diam cans) and will have the capability for removing 4,200,000 Btu/hr of heat. Empty casks will be closed, checked for contamination, and moved to the docking area for return to the shippers. Rail spur and trailer parking space will be provided near the dock for twenty-five 100-ton casks.

Facilities will be provided for lowering the waste cans from the topside hot cell into a transporter at the mine working level at a maximum rate of three cans per hour. The transporter will carry the can to a disposal room, deposit it in a vertical hole in the floor, and backfill the hole with crushed salt. A cased shaft, 33 in. in inside diameter, will be provided for lowering the waste cans, individually, in a cage designed to prevent contact between cans and the shaft casing during transfer. Both shaft and hoist will meet the requirements of 30 CFR 57 for a man-riding hoist. The receiving station will be designed to provide secondary containment as the cans are removed from the cage at the bottom of the shaft and loaded into a shielded cask mounted on a motorized transporter. The transporter will carry one can at a time to the disposal area. The transporter will be designed to maneuver in a 30-ft-wide corridor, to index the shielded can over a vertical hole in the mine floor, lower the can into the hole, and backfill the hole with crushed salt. The transporter cask will be designed to limit radiation exposures to 1 millirem/hr at 1 ft from its surface.

In the underground portion of the repository, the rooms and corridors of the waste disposal area will, in general, resemble a normal producing salt mine, and no special procedures or equipment for salt excavation will be required. In the interest of efficiency, the industry standard of undercutting, drill and shoot, load and haul, is recommended. Backfilling of the waste disposal rooms can be accomplished in any suitable way, but a "ramp building" technique using an ejector-equipped scoop loader appears to be advantageous.

The salt excavation rate at any given time will depend upon the rate at which mined space is being used by the waste disposal operations. The salt excavation in any area must be completed before waste disposal operations can commence in that area in order to maintain complete isolation of the ventilation air supplies for the two activities. A detailed mine plan giving the excavation sequences, excavation rate (based on anticipated maximum waste deliveries), and layout of support facilities (especially mine ventilation patterns) for the entire lifetime of the facility will be prepared in advance in order to assure that all safety criteria will be satisfied at all times.

All of the excavation equipment, the various other systems in the mine (ventilation, power distribution, communications, etc.), and the mine itself will meet the specifications set forth in the Federal Regulations, Title 30. The equipment must also be approved by the U.S. Bureau of Mines and must undergo regular and routine inspections by both the U.S. Bureau of Mines, Health and Safety Branch, and the Mine Safety Office of the Kansas Department of Labor.

The underground air-flow pattern will be from a large salt-hoisting and ventilation shaft to the active excavation area of the mine, since more machinery will be at work there. This air will be exhausted through special ventilation shafts. It will not flow through portions of the mine where waste has been, or is being, buried. Control of the flow patterns will be by use of dual corridors and curtain walls (brattices).

Portable blowers and ducts will be used as needed to force air from the main corridors into dead-end individual rooms or corridor faces where excavation is occurring.

Based on men and machine requirements, part of the fresh-air supply will be channeled into the active waste burial area of the mine. Administrative controls will be used to ensure that personnel do not enter the air stream after it has passed through the active burial area. Burial of waste products will begin in rooms farthest from the fresh-air supply. As rooms are filled with buried waste, the burial operations will proceed upstream toward the air supply. Backfilling with salt will begin as soon as possible after the maximum amount of waste has been put in a room. As a precautionary measure, active burial rooms and those being backfilled will be kept at a negative pressure, with air flowing into the rooms from the corridor. This will

be done by portable fans and ducts, placed so the air intake is near the dead end of each room. The air from these rooms will be blown down the corridor to a safe distance beyond the farthest active room before being exhausted back into the corridor air stream. From this point the air will move to an exhaust shaft without passing through any occupied portion of the mine.

Air monitors will be located in the active burial rooms and in the corridor downstream from the active and filled rooms. If any radioactivity is detected, the supply air fan will be shut down, all machines will be shut down, and personnel will be evacuated. Simultaneously, the air being exhausted from the burial area will be diverted through a high efficiency particulate absolute (HEPA) filter bank. This air flow quantity will be reduced to that amount required to maintain a negative pressure in the burial area. Under this emergency condition, all air flow in the mine will be into the burial area and then out through the HEPA filters. Discharge will be from a stack high enough to disperse and dilute the exhaust air.

Other facilities required at the surface include offices, changerooms and lavatories, a small laboratory for radiochemical analysis, a counting room, decontamination and maintenance areas, and a storage area for nonradioactive materials and supplies.

The present design of the facilities for disposing of alpha-contaminated wastes will utilize an existing nonproducing salt mine which provides at least 40 to 50 million cubic feet of available space which, in the interest of economy and efficiency, should be adjacent to the high-level facility. The alpha facility will have a capability of handling and storing approximately 1 million cubic feet of waste per year, based on three-shift, 5-day/week operation. Waste packages received for routine handling must have dimensions not exceeding 4 by 6 by 6 ft and must weigh less than 5 tons.

The surface structure for receiving these wastes will be alpha contained, earthquake and tornado resistant, and equipped to unload waste containers from commercial carriers, repackage them if necessary, and lower them into the mine. Space will be provided outside the containment areas for maintenance of equipment, offices, a counting room, changerooms, toilets, and a lunchroom.

Since an unused existing mine has been assumed in this design, it was also assumed that the facility will be served by an existing rail spur and will utilize an existing mine shaft and hoist after some renovation. The extent of renovation will be determined following an evaluation of the shaft and hoist by qualified consultants. Extensive cleanup of the existing mine no doubt will be necessary to provide access and safe working conditions for handling and storage of the waste.

Supporting space for the alpha-waste-receiving building will include offices, counting rooms, and changerooms and will be located outside the alpha-contained area.

DETAILED INFORMATION DEVELOPED IN SUPPORT OF FACILITY DESIGN

In addition to direct contributions to the conceptual design of the demonstration waste repository facilities, a considerable effort has been expended in developing detailed information on specific aspects. Some of this information was required for the conceptual design, and some was prepared in anticipation of required safety analysis and reviews. The following sections are summaries of this information.

Geologic and Hydrologic Features Related to the Utilization of Rock Salt Deposits in Central Kansas as a Repository for Radioactive Wastes

T. F. Lomenick H. J. Wyrick

Nature and Extent of Salt

The salt deposits of central Kansas lie in the northernmost extension of the Permian basin, which stretches from central Kansas through the Oklahoma Panhandle and into western Texas and eastern New Mexico. In general, salt deposits within the basin become progressively younger, thicker, and deeper toward the southwest. The thickest and most widespread salt deposit in Kansas is the Hutchinson salt member of the Wellington formation (Fig. 3.1), a part of the Sumner group of gently westward-dipping Upper Permian rocks. Salt deposits have also been found in the younger Nippewalla group of Permian rocks toward the southwest, but their distribution and thickness are not precisely known.

The Hutchinson salt, as seen in Fig. 3.1, underlies central and south-central Kansas and extends southward into Oklahoma. The eastern edge of the salt body lies approximately 400 ft below the land surface. Near its western edge in Kansas, it is found at a depth of more than 1500 ft. Thicknesses of the unit in the state range up to 700 ft.[4] In general, the Hutchinson consists of a

[4] R. O. Kulstad, "Thickness and Salt Percentage of the Hutchinson Salt," *Symposium on Geophysics in Kansas,* Kansas Geological Survey Bulletin 137, 1959.

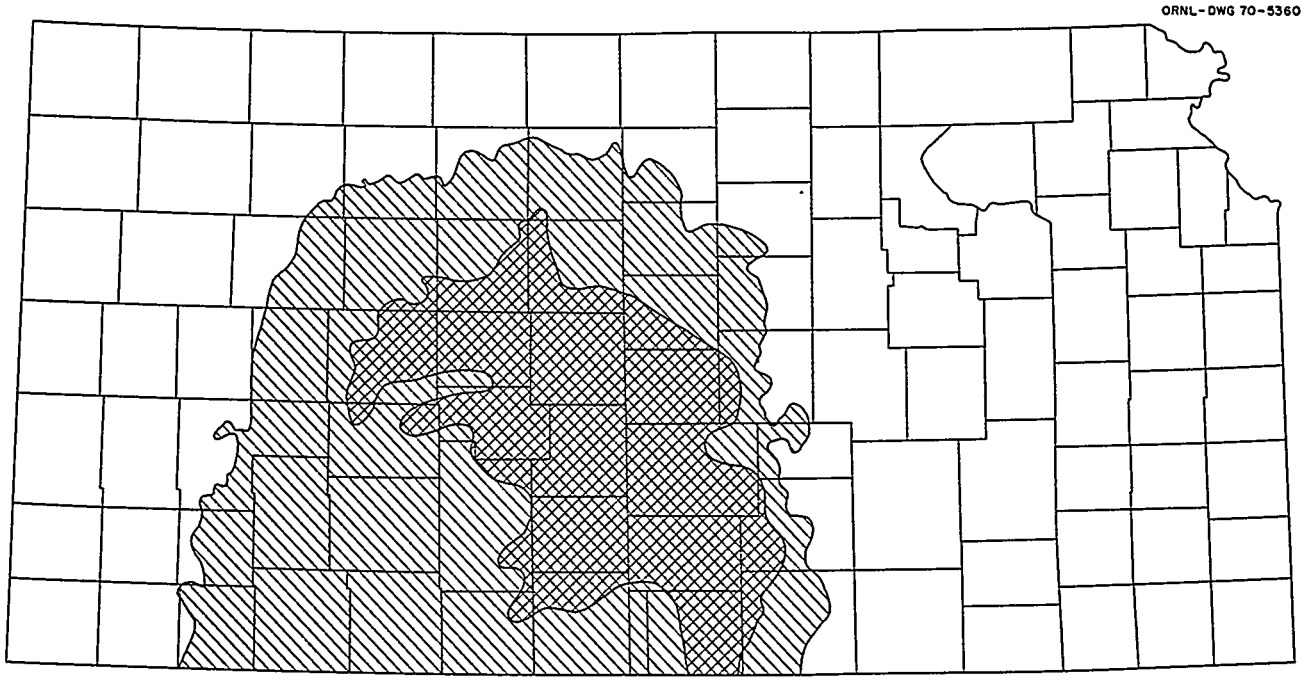

Fig. 3.1. Map of Kansas Showing Area Underlain by the Hutchinson Salt. Double-cross-hatched area represents the extent of the deposit having a salt percentage of at least 60 and a thickness greater than 200 ft. After R. O. Kulstad, "Thickness and Salt Percentage of the Hutchinson Salt," *Symposium on Geophysics in Kansas,* State Geological Survey of Kansas Bulletin 137, 1959.

complex mixture of salt, anhydrite, and shale, with salt being the predominant fraction throughout most of its extent in Kansas. In addition to showing the general distribution of the Hutchinson salt, Fig. 3.1 shows the percentage of salt in the member. Note that about half of the total area underlain by the Hutchinson has a salt percentage greater than 60%. Figure 3.1 also shows that the thickness of salt beds in this area (the double-cross-hatched area) is greater than 200 ft, and the top of the Hutchinson is less than 2000 ft deep.

It is not absolutely necessary that salt beds used for repositories lie at depths less than 2000 ft; however, at greater depths increasingly greater amounts of salt must be left as pillar support, and shaft costs are higher. Both of these factors, of course, would significantly affect the economics of waste disposal operations in salt. In general, the minimum depth of storage is governed by geohydrological factors. In Kansas and elsewhere, salt does not outcrop at the surface but has been dissolved to depths of several hundred feet by groundwater action. In other areas, such as the Gulf Coast area and parts of the arid west, rock salt outcrops at or near the ground surface. To ensure long-term integrity, at least several hundred feet of shale or some other impermeable rock should overlie the salt, and the excavation itself should be located vertically well within the salt deposit, perhaps 100 ft or more.

Brine Disposal into Deep Porous and Permeable Formations

Brine injection into deep permeable and porous formations is an important consideration for disposal of the excess salt mined in the construction of a radioactive waste repository. In central Kansas, the excess mined salt could be dissolved and the resulting brine injected into the Arbuckle formation at a depth of about 3500 ft. The Arbuckle group of rocks is a thick sequence of mainly dolomitic sediments of Cambrian-Ordovician age that underlies a large portion of Oklahoma, Missouri, and Kansas. The type locality for the group is in the Arbuckle Mountains of southeastern Oklahoma, where about 8000 ft is exposed.[5] In Kansas and Missouri the section thins out considerably and is about 1000 ft thick in downwarped depressions or basins within those states and about 300 to 400 ft thick over uplifted and arched areas. In central Kansas the Arbuckle is from 500 to 700 ft thick.[6] During the deposition of these rocks in central Kansas, the dominant structural feature was the southeast Nebraska Arch. Apparently, this prominent uplift centered to-

[5] J. A. Taff, U.S. Geological Survey Folio 79, 1902.

[6] Lee Wallace, *Stratigraphy and Structural Development of the Salina Basin Area,* Kansas Geological Survey Bulletin 121, 1956.

ward the northeast supplied much of the source material for the Arbuckle sediments. As a consequence, the group thins and feathers out toward the northeast and thickens to the southwest. In Kansas the Arbuckle may be subdivided (oldest to youngest) into the Bonneterre dolomite and Eminence dolostone, Gasconade, and Van Buren formations, Roubidoux formation, and Jefferson City and Cotter dolostones. Major unconformities exist at the contacts of these units, revealing the many fluctuations of the land surface above and below sea level during that time. Locally, the Arbuckle group is not commonly subdivided since similarities in the units are difficult to differentiate from well cuttings.

In central Kansas the Arbuckle generally lies conformably on the Regan sandstone of Cambrian age and is unconformably overlain by a thin section of Mississippian shales and carbonates. The Regan, which may be grouped with the Arbuckle as a single hydrologic unit for brine disposal,[7] is best described as a granite wash deposit immediately overlying the weathered Precambrian basement rocks. It averages about 50 ft in thickness and grades upward into the dolomitic sediments of the Arbuckle. The carbonate sediments of the Arbuckle indicate a long period of submergence with warm shallow sea deposition periodically interrupted by periods of uplift and erosion followed by repeated deposition of clastics and nonclastics. Silurian and Lower and Middle Devonian rocks which originally covered the Arbuckle and later Ordovician rocks are not present in the rock column over most of central Kansas now. After their deposition, repeated periods of uplift and erosion along the central Kansas uplift caused these rocks to be worn away. Thus the Arbuckle is unconformably overlain by shales and limestone of Upper Devonian or Mississippian age that were subsequently thinned by erosion before the deposition of Pennsylvanian rocks. Some knowledge of the complex history of cyclic uplift, erosion, and submergence during and immediately after the deposition of the Arbuckle is essential to explain its geohydrologic characteristics. It was during these periods of land- and sea-level fluctuations that the unusually high permeabilities and porosities of the group were developed. It is an ideal salt-water-disposal aquifer.

The Arbuckle is widely used throughout the mid-continent region for the disposal of oil-field brines and other liquid wastes. The porosities and permeabilities of this group are known to be high, but exact values are difficult to establish because of the heterogeneous nature of carbonate rocks and the lack of adequate cores taken from it. Many disposal wells in the Arbuckle are known to accept from 200,000 to 500,000 gpd for periods of 10 to 20 years without pump pressures.[8]

In central Kansas the top of the Arbuckle is generally found at depths of 3000 to 3500 ft. Assuming that the underlying granite wash or Regan sandstone and the Arbuckle sequence would function as a single hydrologic unit, about 400 to 700 ft of aquifer could be utilized for salt water disposal. The static level of water in wells that penetrate the Arbuckle within the area is about 700 to 1500 ft below ground surface;[9] thus at least several hundred thousand gallons per day could probably be discharged through a single well at ground surface into the formation without application of pressure at the wellhead.

Most brine disposal wells in the Arbuckle are located in the oil-producing regions of the central Kansas uplift. In addition to the many oil field disposal wells within the area, several industrial disposal wells are in operation. Apparently most if not all of these wells have operated satisfactorily, and none are taxing the input possibilities of the formation.[7] These disposal wells were developed and tested for 1000 bbl or less per day, and, consequently, the usual length of open hole is only a part of the total formation thickness available. The American Salt Company's industrial brine disposal well at Lyons, Kansas, was tested with no loss of vacuum for an input of 300 gpm (10,000 bbl per day) into only 150 ft of open hole in the Arbuckle. According to the Continental Oil Company, which operates several brine disposal wells in central Kansas, the greatest input for a single well is 29,000 bbl/day (1,200,000 gpd).[7] This well is located in Ellis County.

The concentration of sodium chloride in oil field brine (1 to 3%) is considerably less than that of the highly saturated salt water (about 30%) that will be produced at the proposed demonstration repository. However, there is considerable experience in Kansas with the disposal of highly saturated brines from "washed out" caverns in rock salt that are utilized for liquefied petroleum gas storage. In general, continuous

[7] Bruce Latta, Director, Oil Field Section, State Department of Health, Topeka, personal communication, 1970.

[8] *A Study of Deep Well Disposal of Desalination Brine Waste,* Office of Saline Water, Research and Development Progress Report No. 456, June 1969.

[9] Ronald B. Martin, *Relationship Between Quality of Water in the Arbuckle Group and Major Structural Features in Central and Eastern Kansas,* unpublished thesis for the degree of Master of Science, University of Kansas, 1968.

circulation rates of 100 to 200 gpm for periods of up to several hundred days are used to "wash out" the cavities.[10] Generally, the saturated brine is discharged into the Arbuckle.

Once brine is discharged into the Arbuckle, there is, of course, a need for determining the rates and directions of its movement. In general, the direction of flow in this aquifer is from north to south or toward the Anadarko basin in southern Kansas and northern Oklahoma; however, there are numerous "highs" and "lows" of the piezometric surface in central Kansas that may reflect the withdrawal of fluids in oil-producing areas.[9] By measuring the piezometric head of the Arbuckle in and around a waste disposal site and relating it to the regional configuration of that aquifer, reasonable estimates could be made of the fate of the brine. A more attractive scheme would be to withdraw slightly brackish water from the Arbuckle at the repository site and utilize it for dissolving the excess mined rock salt. The salt-saturated Arbuckle water could then be returned to the Arbuckle in nearby disposal wells with little change in the volume of liquids and therefore with only very minor perturbations of the pressure relationships in the aquifer.

In summary, all evidence short of actual site testing suggests that the Arbuckle group could be utilized for the disposal of the large quantities of brine expected from the repository operation. Considering the vast quantities of oil field brines currently disposed of in this manner in the area, there appear to be no technical objections to such an operation.

Tectonics and Seismicity

Central Kansas is located within the "stable interior," a region where earthquakes occur rather infrequently. Furthermore, the area has not been subjected to intense deformation in the geologic past, but prominent structural basins and arches were developed slowly and apparently without intense earthquake activity. Figure 3.2 shows the location of historic earthquakes and their relationships to the major structural features in Kansas. Note the almost complete absence of earthquakes along the central Kansas uplift. The earthquakes that have occurred in the central Kansas area range up to a modified Mercalli intensity scale rating of VI (damage small). These shocks, as well as others in Kansas, have occurred at rather shallow depths (16 to 38 miles) and probably represent minor adjustments in the underlying granitic crustal rocks.[11] Epicentral locations of many of the earthquakes, including the two most damaging, were centered along the Nemaha anticline in eastern Kansas. This apparent correlation of earthquakes and structure indicates that the structure is probably still tectonically active and that minor adjustments are occurring in the deep-seated rocks beneath it. Based on the recent seismic history of all the other structures in Kansas, it is likely that they are tectonically inactive.

Occurrences of Oil and Gas

Oil and gas were discovered in Kansas in 1860, but no production was reported for about 20 years. Through 1966 nearly 4 billion barrels of crude oil have been produced and about 13 trillion cubic feet of natural gas.[12] The oil and gas industry of Kansas has made important contributions to the state's economy; however, crude oil production peaked in 1956 and has been steadily declining since, while natural gas production appears to have stabilized.

Oil and gas accumulations are naturally associated with structural and stratigraphic features. In central Kansas the controlling structures are the central Kansas uplift and its southernmost extension, the Pratt anticline, and the Hugoton Embayment area of the Anadarko basin (Fig. 3.2). There are several producing zones of reservoirs within this area that range in age from Precambrian to Lower Permian; however, the most proliferous zones are those of the Arbuckle dolomite (Cambro-Ordovician) and the Lansing–Kansas City (Pennsylvanian). The general stratigraphic relationships of these important oil-producing formations and others to the Hutchinson salt member are shown in Fig. 3.3. It is observed that almost 2000 ft of sedimentary rock separates the salt deposits from the deeper oil and gas deposits in this part of central Kansas. The Arbuckle and Lansing–Kansas City groups are largely carbonate reservoir rocks, while sandstone constitutes the principal source rock for the Simpson formation and several other producing formations in central Kansas. In the Arbuckle zone, the uppermost 100 ft of the formation in any given area provides essentially all of the oil production.[13] Thus, in the unlikely event that

[10] J. M. Jewett, *L.P.G. Storage in Kansas Salt Beds in Kansas*, Geological Society Guidebook, 18th Field Conference, 1955.

[11] D. F. Merriam, *History of Earthquakes in Kansas*, Seismological Society of America Bulletin, vol. 46, No. 2, 1956.

[12] Margaret O. Oros and D. L. Beene, *Oil and Gas Development in Kansas During 1966*, State Geological Survey of Kansas Bulletin 190, 1968.

[13] P. L. Hilpman, *Producing Zones of Kansas Oil and Gas Fields*, State Geological Survey of Kansas, Oil and Gas Investigation No. 16, 1958.

ORNL-DWG 70-9992

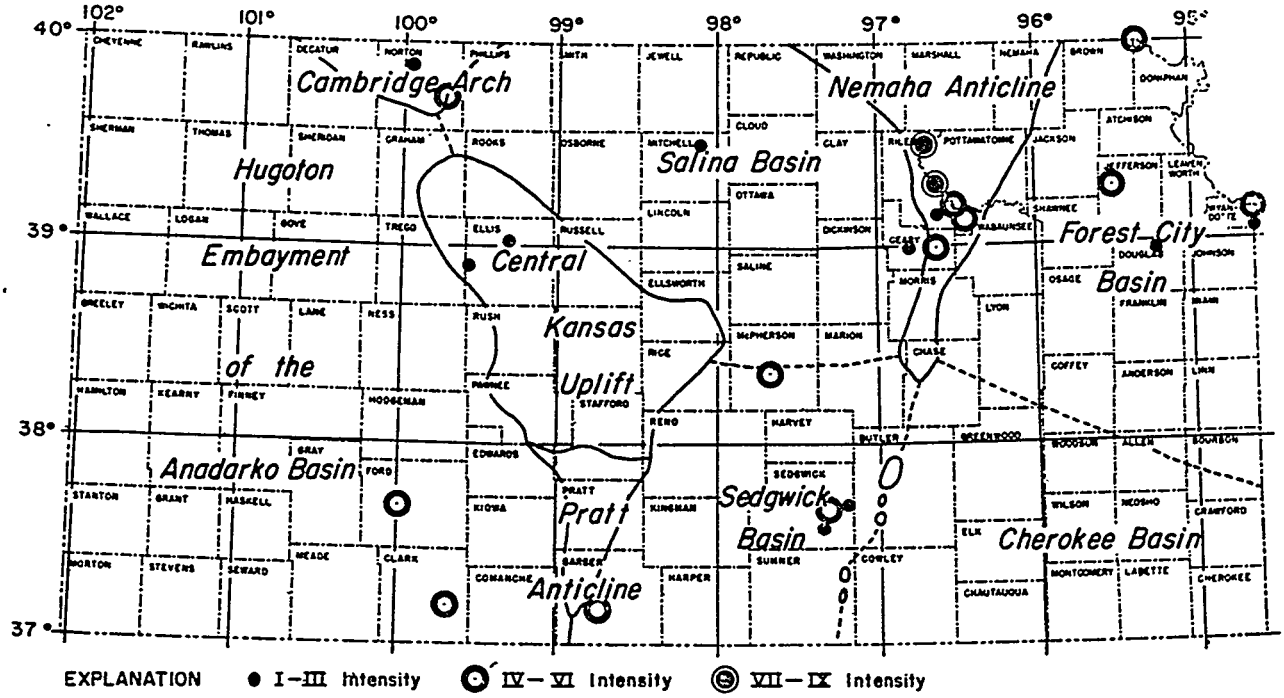

Fig. 3.2. Map of Kansas Showing Major Structural Features and Location of Earthquake Epicenters. After D. F. Merriam, *History of Earthquakes in Kansas,* Seismological Society of America Bulletin, vol. 46, No. 2, 1956, pp. 87–96.

oil were produced from the Arbuckle at a location where brine is being pumped into the same unit, it is conceivable that oil could be withdrawn from the uppermost part of the Arbuckle, while brine is being discharged into its lowest part.

Occurrences and Characteristics of Groundwater

In general, the thick deposits of gravel and coarse sand that fill the large stream valleys are the source beds for the principal supplies of groundwater in central Kansas. Perhaps the most important source bed is found in the Great Bend region, which lies within the general area of the Arkansas River valley from Kiowa County on the west to Reno County on the east. This region is underlain mostly by sand and gravel deposits of Tertiary and Quaternary age that may be as much as 300 ft thick. Overlying sand dunes provide an excellent surface for recharge. Depth to groundwater within the area is generally less than 100 ft. Supplies in excess of 1 million gallons per day from these deposits are commonly developed.[14]

The sedimentary rocks of Cretaceous age that underlie most of the northern half of central Kansas are relatively unimportant sources of groundwater.[14] Locally, small supplies of water are available from outcropping sandstone beds and from patches of Tertiary and Quaternary deposits, but only the large river valleys contain sand and gravel deposits in sufficient quantities to provide commercial supplies of groundwater.

Impermeable beds of shale and siltstone of Permian age underlie parts of extreme south-central Kansas. In general, the water from these rocks is poor in quality and limited in quantity, being sufficient only for domestic or stock use.[14]

Concerning the relationship of groundwater supplies to rock salt beds in central Kansas, it is seen in Fig. 3.3 that the salt is separated from the Pleistocene (Quaternary) beds at the surface by about 700 ft of impermeable shales and siltstones. In areas where ancient streams have cut channels into the Permian section of rocks which were later filled with water-bearing sediments of Tertiary and Quaternary age, the separation between the salt and the groundwater supplies is at least several feet. In the rock section

[14] S. W. Lohman *et al., Groundwater Supplies in Kansas Available for National Defense Industries,* State Geological Survey of Kansas Bulletin 41, 1942.

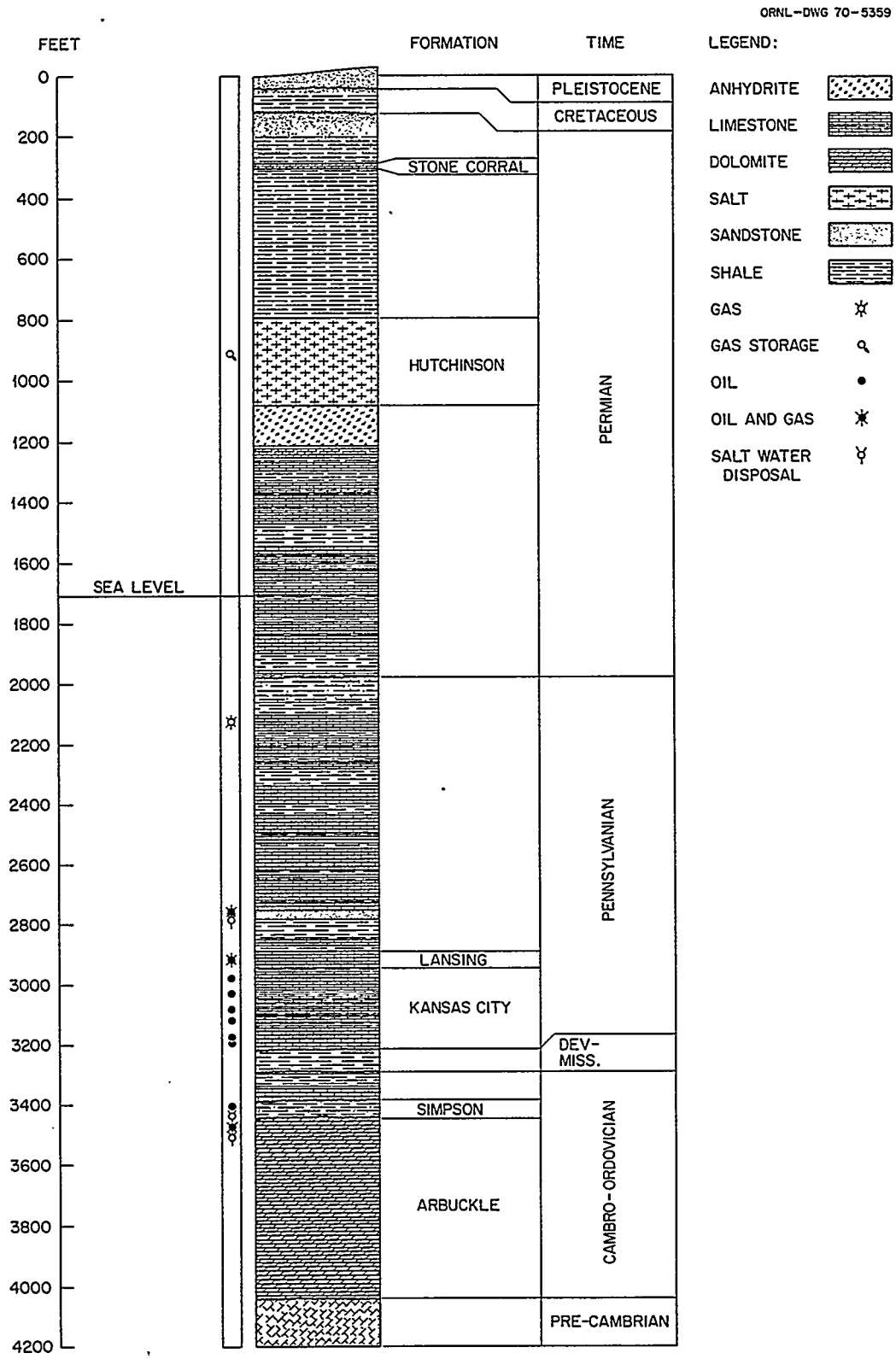

Fig. 3.3. Generalized Geologic Section, Rice County, Kansas. After *Type Log for Rice County*, Catalog No. 20-19-8w, published by Kansas Geological Society.

below the salt, several beds in the Pennsylvanian and older rocks contain salt water and/or oil and gas. Porous beds thus lie several hundred to a thousand feet or more below the salt deposits.

Subsurface Leaching of Rock Salt Deposits

As seen in Fig. 3.1 the Hutchinson salt member of the Wellington formation underlies south-central Kansas and extends southward into Oklahoma. Toward the southeast, west, north, and northeast, there is a gradual thinning of the salt bed which undoubtedly represents the original limits of salt deposition; however, along the eastern boundary of the deposit from Saline County to northwestern Sumner County (see Fig. 3.2 for county locations), the salt deposit ends abruptly, and a series of subsidence ponds and salt water springs overlying the present stratigraphic position of the salt member suggests that the original limits of the salt deposit extended somewhat farther east. In northwest Saline County precise dating of subsidence features indicates that the salt front has retreated a distance of 5 miles or less in the last 1 million years (or throughout the Pleistocene), while in McPherson and Harvey counties westward, migration of the salt has been 13 and 12 miles, respectively, from Delmore (Pliocene) to Kansas (a time span of about 5 million years).[15] According to Fent, the natural leaching of the salt body by circulating groundwater depends on the development of secondary permeability in the overlying shales, which, in turn, is brought about by erosion when the protective Cretaceous shales and clays are removed.[15] In areas where the overlying shale section is complete, which includes essentially all of the central Kansas salt area west of the eastern boundary of Rice County, it may be considered to be protected for geologic time periods of at least 1 million years or for about the time span of the Pleistocene.[15]

In addition to the series of salt water springs along the eastern limit of the Hutchinson salt member, brine flows have been observed in Barton and Stafford counties; however, in these counties it has been established that the brine is issuing from Cretaceous sandstones which lie stratigraphically well above the Hutchinson.[15]

Several sinkholes and depressions in central Kansas have been ascribed to subsurface solution within the underlying salt beds; however, in the case of some that have been studied intensively, it has been shown that other geologic processes have caused them. For instance, the Cheyenne Bottoms, located in northern Barton County, was once thought to be due to solution of the underlying Hutchinson salt followed by collapse of the overlying rocks. Later test drilling within the area, however, has demonstrated that this large undrained depression is simply a buried Pleistocene valley.

Salt Deformation

In general, all salt deposits buried to any appreciable depth in the geologic past show some deformation. Of course, the extent of deformation varies greatly, ranging from slight postdepositional thickening and thinning, such as may have been the case in the central Kansas deposits, to the forming of salt domes from deep-lying "mother" salt beds, as in the Gulf Coast Embayment. Salt beds, like other rocks, will deform by folding and even by faulting where subjected to lateral or vertical tectonic forces; however, unlike other rocks, salt flows plastically under relatively low temperatures and pressures; thus salt is commonly squeezed from the limbs of folds into the structurally higher apices of anticlines when subjected to compressional forces. It is unlikely that tectonically induced folding or faulting of the central Kansas salt deposits will occur since the major structures are presently inactive and the geologic past of the area is one of tectonic stability.

It seems clear that tectonic forces alone would not have been sufficient for the formation of the salt domes in the Gulf Coast Embayment. Rather, the forces responsible for these structures are gravitational in nature. The static weight of several miles of heavy sediments on the bedded salt is considered adequate to cause it to flow upward. Of course, the salt can only rise when the force applied by it exceeds the shear strength of the overburden; thus the physical properties of the overburden are also important in the process. In view of the large volumes of salt present in individual domes within the Gulf Coastal region and the limited extension of the source area from which the salt was derived, it is clear that this process requires a thick "mother" bed. In the Gulf Coast area the "mother" bed is probably at least several thousand feet thick. The rate of growth of salt domes and other diapiric structures is not accurately known, but there is good evidence that growth is generally slow and occurs unevenly and whenever conditions are appropriate.

Considering the conditions under which salt domes have been formed in the Gulf Coastal area, it seems clear that the rock salt in central Kansas is much too shallow and too thin to deform in a similar fasion. In

[15] O. S. Fent, Consulting Geologist, Salina, Kansas, personal communication, 1970.

addition, the cover rock is competent and relatively free from faults and other zones of weakness through which the salt could move. Certainly, the increase in temperature of the salt due to decay heat generated in the waste will increase the plasticity of the salt within the confines of the repository, but the limited area affected and the geologically short heating period (a few thousand years) will almost certainly limit the ensuing deformations to the mined openings.

Summary

Rock salt, because of its plastic flow characteristics, is impervious to the passage of groundwater and thus is the preferred geologic formation for repositories containing radioactive wastes. Rock salt is also widely distributed, underlying portions of 24 of the 50 states. For selected areas within the Salina basin of the northeastern states and the Permian basin, which underlies a portion of several southwestern states, thick deposits of essentially flat-lying beds of rock salt are known to lie at depths that would be suitable for development as waste repositories. In the case of several of the remaining deposits, accurate data are not available as to their distribution and occurrence, while other salt deposits are too deep to be mechanically mined. Finally, a few of the deposits exist as domal or anticlinal structures. Based on the desirable characteristics of its salt deposits and other geological and hydrological features, central Kansas, which lies within the Permian basin, is extremely well suited as the location of the first demonstration repository for radioactive wastes.

South-central Kansas is located in the stable interior of the country. The rocks in this region are all of sedimentary origin and flat lying for the most part. In general, a thin blanket of unconsolidated sands, silts, and gravels of Pleistocene age covers the land surface. This is generally underlain by Cretaceous age sandstones, while Permian rocks are found beneath the Cretaceous deposits. The salt member lies within the Permian rocks and is as great as 700 ft thick and lies from about 400 to 1700 ft below the land surface. Pennsylvanian and Cambro-Ordovician sediments comprise most of the rock section below the salt, with the Precambrian basement lying at depths of about 3500 to 4000 ft. Beginning some several hundred feet to a thousand feet below the salt bed, the rocks contain numerous permeable and porous beds that contain salt water and locally gas and oil. In general, the only important supplies of fresh water are found in the thick accumulations of sand and gravel in stream valleys. Some water may also be obtained from Cretaceous and Permian beds that outcrop at the surface, but the quality of the water is generally poor and the quantities small. Thus the salt beds are separated from freshwater aquifers above, as well as oil and gas reservoirs below, by several hundred to a thousand feet or more of impermeable shales and other sedimentary rocks.

The Arbuckle group of rocks is commonly used in the midcontinent region as a disposal medium for oil field brines. In central Kansas it is 400 to 700 ft in thickness and lies between 3000 and 3500 ft below the surface. The porosity and permeability of this largely dolomitic group of rocks are extremely high, and all indications are that it is capable of receiving large quantities of excess salt as brine from the operation of a waste repository in central Kansas.

Because of the long history of tectonic stability in the central Kansas area and the characteristics of the salt beds, it is unlikely that the salt will deform or be eroded appreciably during the effective lifetime of the waste.

Effect of Heating on Geological Environment

R. L. Bradshaw

As mentioned in prior reports, a flexible computer program (called the "Mine Management Program") capable of estimating required spacing for waste containers of various sizes and nuclide spectra coming into the mine at varying rates is needed for operation of a waste disposal facility. Development of such a program is progressing. In the meantime, there are a number of other thermal considerations which are important to the design and safety analyses of the proposed disposal facility.

General Thermal Considerations

Most of the earlier studies were made with computer programs for two equations: (1) an infinite array of finite-length line heat sources and (2) a finite-length line source. Both required the assumption of an infinite homogeneous medium. These programs have been rewritten for use with the IBM 360 computers and have been used in some of the current studies.

R. S. Dillon and others of the Chemical Technology Division have developed a computer program which combines the finite line source and a finite plane source. Temperatures in a room are obtained by summing the contributions from line sources in the room and from adjacent rooms treated as plane sources. It is still necessary to assume an infinite homogeneous

medium. This program is being used primarily to develop waste management cost estimates.

Turner and others have developed a program called "Heating"[16] which can handle two- and three-dimensional problems with considerable flexibility using finite difference techniques. This program, which can handle problems with spatial variation in thermal and heat-generating properties, as well as various boundary conditions, has been used to provide most of the results reported herein.

For current calculations the Diablo Canyon reactor fuel-reprocessing waste characteristics are being used as representative of LWR wastes. The assumed fuel irradiation history is 33,000 MWd/ton at 30 MW/ton (three years in the reactor). The waste is assumed to contain all fission products, ½% of the plutonium and uranium, and all of the remaining actinides. Each cubic foot of solid waste contains the products of 10,000 MWd of reactor operation.

One item of interest is how far away heat sources must be considered in establishing the spacing of containers within a room. If this is known and the rate at which waste is received at the disposal facility is also known, then the length of time into the future which the waste characteristics must be predicted can be established. Based on a comparison of calculations with the infinite array and with single line sources in a circular array (for a source spectrum which is dominated by 30-year half-life material, the maximum case), 1% accuracy on peak salt temperature rise can be obtained by considering all sources to a radius of 500 ft. Results are accurate within 10% if sources beyond 300 ft are neglected. Even smaller distances can be used for wastes containing large quantities of short-half-life nuclides and whose peak temperature is reached in a few hundred hours to a couple of years.

The Heating code normally requires the heat generation to be uniform within the heat-generating zone in the floor of the rooms (normally taken to be 10 ft thick). For wastes dominated by 30-year-half-life nuclides, the peak temperature rise in the center of this heat-generating slab was found to be about 10% lower than at the wall of a discrete 6-in.-diam can in the center of the room. For short-cooled wastes the difference would be expected to be greater. Thus it was concluded that for Diablo Canyon wastes about three years old and older, the Heating code calculations would be adequate for establishing the effects of other variables on the peak salt temperatures, as well as for the temperatures in the geologic formation.

Disposal rooms will be backfilled with crushed salt, and it is necessary to take this into account in thermal calculations. No information on thermal properties of crushed salt was found in the literature; so the thermal conductivity of mine-run salt from the Hutchinson, Kansas, mine was both measured and calculated using methods outlined by Godbee.[17] The measured value was 0.13 and the calculated value was 0.36 Btu hr^{-1} $(°F)^{-1}$ ft^{-1}. The calculated value is believed to be the most accurate, but the measured value has been used in the salt temperature calculations since it gives about 3% higher peak temperature rises. With ten-year-old Diablo Canyon waste, the calculated temperature rise when the room was filled with crushed salt was about 11% higher than if the room were assumed to be solid salt.

Another point of interest is how far vertically the thermal properties of the formation affect the peak temperature in the floor of the mine. Peak temperatures are reached in 40 years or less for Diablo Canyon wastes of 100 years or less age at burial. Heating code calculations indicate that if upper and lower boundaries are set at 400 or 500 ft from the heat-generating zone, there is essentially no effect. Boundaries at 300 ft showed a drop of about 1% in the peak temperature rise. Thus 400 ft was used for subsequent calculations of temperatures at the mine level.

Although the Heating code is capable of handling thermal properties which vary with temperature, the computer time may become excessive. Therefore the effect of using constant salt thermal properties was investigated. Peak salt temperatures calculated using 100, 200, and 300°C salt thermal properties all occurred at about 35 years after burial of ten-year Diablo Canyon waste. The 200°C properties peak was about 12% higher than the 100°C, and the 300°C peak was about 12% higher than the 200°C. (A solid salt formation was assumed.) Therefore it was decided to use the 200°C salt thermal properties in most calculations.

Two-dimensional Heating code computer runs are cheaper than three-dimensional runs; so most are made in two dimensions. Thus the assumption is made that rooms and pillars are infinite in length. A check with a three-dimensional Heating code and another check by summing line sources indicated that the calculated peak rise (with ten-year-old Diablo Canyon waste) is about 6

[16] W. D. Turner and J. S. Crowell, *Notes on Heating – an IBM 360 Heat Conduction Program,* Computing Technology Center, Oak Ridge, Tennessee, CTC-INF-980 (November 1969).

[17] H. W. Godbee, *Thermal Conductivity of Magnesia, Alumina, and Zirconia Powders in Air at Atmospheric Pressure from 200°F to 1500°F,* ORNL-3510 (1966).

to 9% too high for rooms 50 ft wide by 300 ft long having 50-ft barrier pillars at each end. If the rooms were shorter and the end pillars the same, the error would be even greater. For short-cooled wastes the error would be less.

For study purposes the general stratigraphy of central Kansas was selected, and it would be expected to be about the same over a fairly large area. Therefore, since the detailed stratigraphy of the Lyons site was determined for Project Salt Vault, this was used for investigating the general effects which may be expected in the central Kansas area. In the nominal 300-ft salt member at Lyons, the thickness of salt is about 172½ ft out of 290 ft total, or about 60%. The rest is mostly shale, with a small percentage of anhydrite and limestone. For thermal considerations it has all been considered to be shale. For both 4½- and 10-year-old Diablo Canyon waste, the shale and salt formation with crushed salt in the room produced calculated peak temperature rises about 20% higher than a formation of solid salt with crushed salt in the room. For both waste ages the rise with shale was about 34% higher than for the case of solid salt in the room also. The effects of the shale should be less pronounced with short-cooled wastes.

Most calculations have been done with 50-ft-wide rooms and pillars. With ten-year-old waste in 30-ft rooms with 30-ft pillars (assuming salt, crushed salt, and shale), the temperature rise was about 6% less. With 50-ft rooms and 30-ft pillars, the temperature rise was 23% higher when the same heat generation per unit floor area was used but about the same if the heat input per unit *gross* area (room plus pillar) was used as in the 50-ft–50-ft case.

For temperatures in the formation at distances from the heat-generating zone of more than about 100 ft, a different type of calculation was used. When vertical temperature profiles were desired, the heat generation was assumed to be uniformly distributed over the area beneath the room and one pillar. The crushed salt in the room was neglected, and all the salt was lumped into one zone. This would result in calculations which allowed more than the normal amount of heat to flow up and less to flow down. Also, a geothermal flux of 10^{-6} cal cm^{-2} sec^{-1} (1.33×10^{-2} Btu hr^{-1} ft^{-2}) was introduced below the mine level. When horizontal and vertical temperatures were desired, a three-dimensional configuration was used, with the mine assumed to be circular. The heat generation per unit area in this case was assumed to be one-third of that in the rooms, since only about one-third of the gross mine area will actually contain waste. Thus, these calculations as well as those for the vertical profiles will not be accurate for temperatures in or near the heat-generating zone.

Effects of Peak Salt Temperature

The higher the allowable peak temperature rise in the salt around the waste containers in the mine floor, the closer the containers may be spaced and the cheaper the operation. Early considerations indicated 200°C as about the maximum desired salt temperature. Recent studies confirm this, as indicated in the following considerations: (1) shattering of unrestrained salt at around 250 to 350°C, (2) temperature and thermal stress transfer effects on mine stability during operation, (3) possible instability in whole geologic formation, (4) temperature rise in freshwater aquifers, and (5) temperatures beyond the boundary of the mine.

Salt Decrepitation. – Brine in small cavities will be released at temperatures above 250°C, but field tests indicate no hazard if small masses of salt around the cans in the floor reach 300°C or greater. Long-term large-mass temperatures this high might be undesirable from the standpoint of the larger quantities of water released.

Temperature Effects on Stability. – Elevated temperatures increase the flow rates of salt (on 4-to-1 width-to-height pillars, flow rates go up with about the tenth power of absolute temperature). Figure 3.4 shows the effects of temperature on model pillars at 4000 psi average vertical stress. In a disposal mine operation,

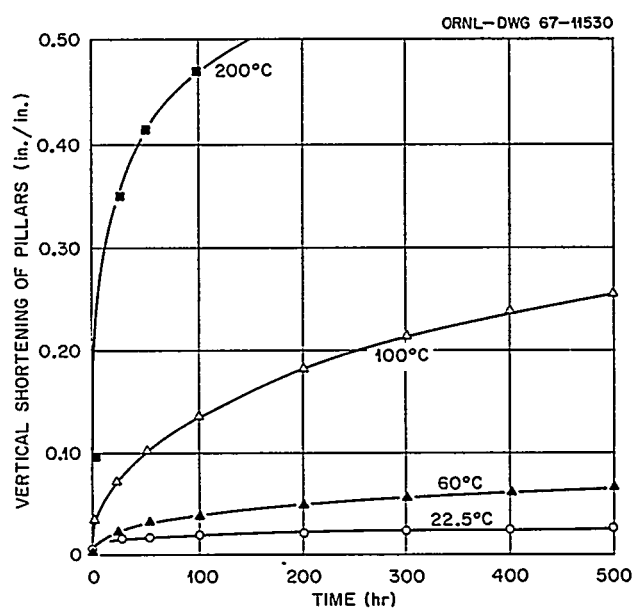

Fig. 3.4. Deformation of Pillar Models at 4000 psi.

stresses would probably be limited to around 2000 psi, but the effects would be similar, although the curve slopes would be about an order of magnitude less, since creep rates change with about the third power of the stress ratio.

Figure 3.5 shows calculated temperatures in and around a disposal room at the time the peak temperature is reached (assuming a ten-year-old waste). Notice the large area beneath the room and in the pillar which is above 170°C. Figure 3.6 shows the simplified stratigraphy used in the calculations. Figure 3.7 shows the temperature rise at various points as a function of time after burial of the waste. Notice that temperatures at all points are above 100°C by the end of ten years. From Figs. 3.5 and 3.7, it is apparent that 200°C maximum salt temperature is not unduly conservative from the standpoint of stability during operation. Yet, it should be adequate to achieve the desired room closure and recompaction of the backfilled salt. Also, salt starts to behave quite plastically at temperatures around 300°C. If a large area of salt were to approach

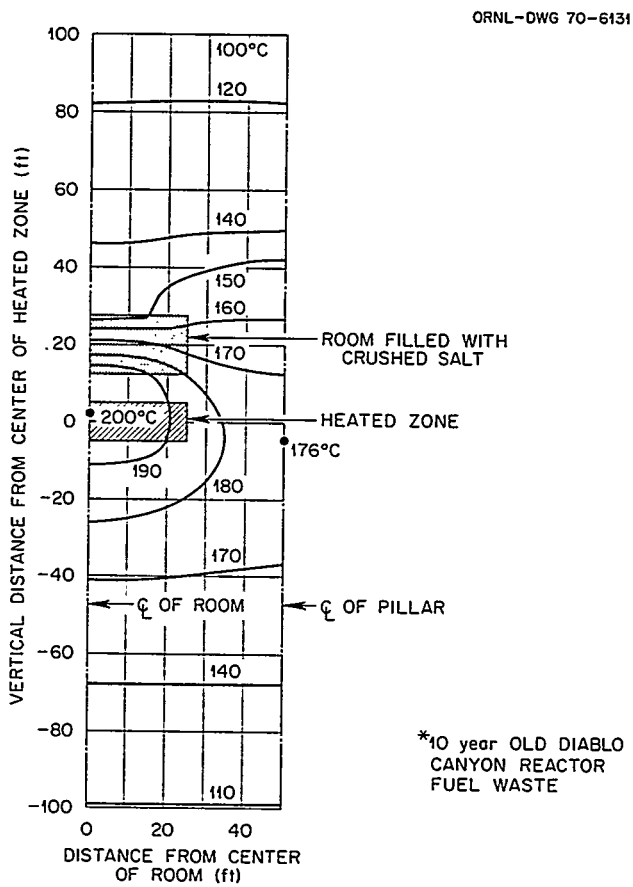

Fig. 3.5. Temperatures in Formation at Time of Peak in Heated Zone (About 34 Years After Burial).

300°C while operations were still under way in a mine, that area could possibly fail to support its overburden load, thus transferring excessive loads to the current operating area.

Stress Transfer Effects. – In Project Salt Vault, thermal stresses produced by sources in the floor were found to transfer essentially instantaneously around the room and, in this respect, to be more important in determining localized stability conditions during the initial stages of operation than the change in creep properties of salt due to rising temperatures.

In the Project Salt Vault array rooms the most noticeable and significant effect was a sudden fivefold increase in the rate of sag of the 2-ft-thick salt layer in the immediate roof. This stress transfer mechanism is illustrated in Fig. 3.8.

Consideration of all the effects in both the array rooms and the heated pillar rooms tends to indicate that the effects are roughly proportional to the heat input *rate* per unit of floor area. The rates in the array rooms were initially about 20 Btu hr^{-1} ft^{-2} and in the heated pillar rooms, about 23½ Btu hr^{-1} ft^{-2}. For a ten-year-old Diablo Canyon waste, the heat input rate to reach 200°C maximum temperature will also be about 20 Btu hr^{-1} ft^{-2}; so it appears that the thermal stress transfer effects will be at least as great as in Project Salt Vault. Thus, based on the experimental results, it would appear that an initial heat-generation rate per unit area which will ultimately produce a maximum salt temperature of 200°C is about as high as desirable (at least for the initial stages of operation) for the first disposal facility.

Formation Stability. – As may be noted in Fig. 3.5, at the time of peak salt temperature in the floor, about 100 ft of formation above and below the center of the heat-generating zone will be heated to in excess of 100°C. Thus, some shale beds will reach temperatures in excess of 100°C. At these temperatures, it can be concluded that the shale and the small quantity of water in its pores may expand somewhat, but the net effect should be no more than an increase in the rate of closure of the rooms. On the other hand, if the temperatures were allowed to go much higher, it is conceivable that some type of unknown behavior could be encountered.

Another suggested effect of elevated salt formation temperature is the possibility of large-scale tectonic deformation. This diapiric action is covered in another section of this report.

Aquifer Temperature Rises. – Figure 3.9 shows temperatures in the entire formation for a condition where the peak salt temperature in the floor of a room

ORNL-DWG 70-9993

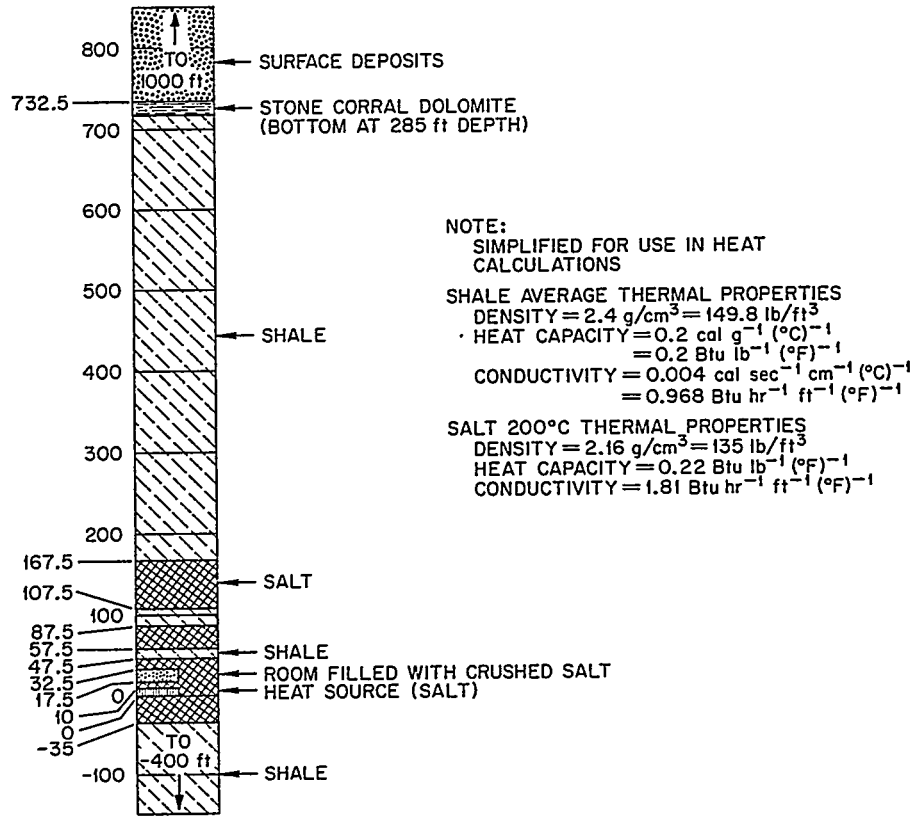

Fig. 3.6. Approximate Lyons Stratigraphy.

ORNL-DWG 70-6132

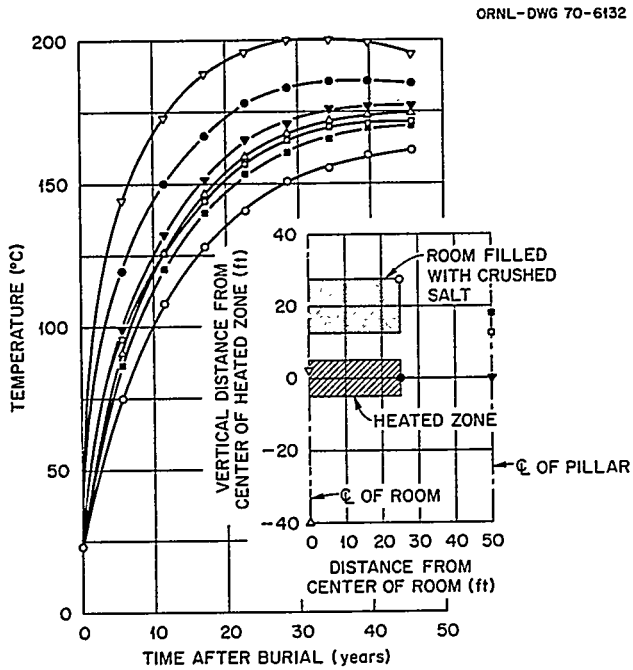

Fig. 3.7. Temperatures in Floor and Pillar.

reaches 200°C with a ten-year-old waste. The peak is reached at 25 to 50 years after burial, but this type of calculation is not accurate for temperatures in and near the heat-generating zone, since the heat input is distributed beneath both the room and the adjacent pillar. This figure indicates that the heat front will reach the Stone Corral formation (depth, about 285 ft) after about 100 years and that the peak rise would reach a maximum of about 32°F after 800 years (assuming no flow in the aquifer). Portions of similarly stagnant aquifers at depths near 100 ft would experience temperature rises of about 14°F at about the same time.

Figure 3.9 also indicates that there would be little to be gained from operating at two levels in the salt formation and that use of the same formation for a second disposal operation would not be practical for about 2000 years. Another point is that the peak flux at the ground surface, due to the decay heat, will be no more than six or seven times the normal geothermal flux. On the other hand the average annual solar flux reaching the ground is three to four orders of magni-

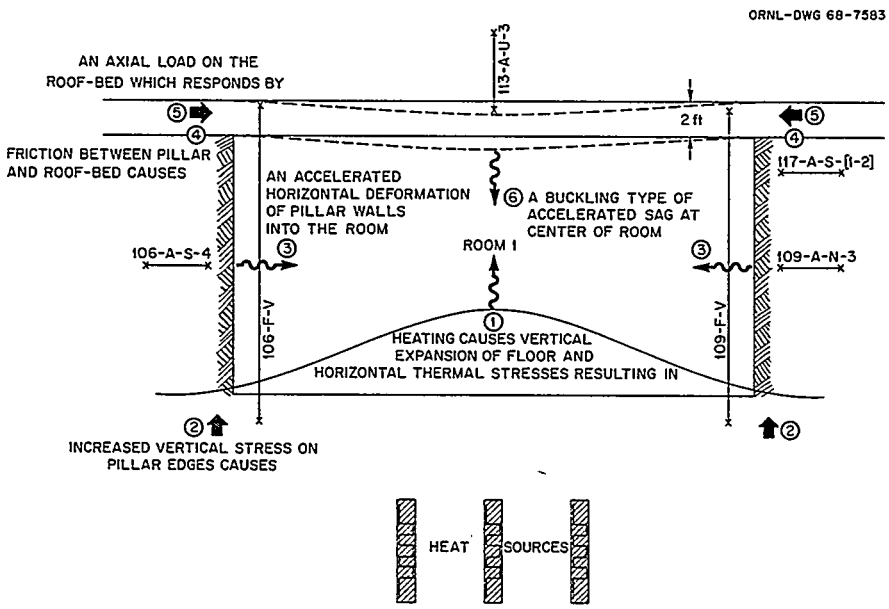

Fig. 3.8. Mechanism of Stress Transference from Floor to Ceiling; Numerical Sequence.

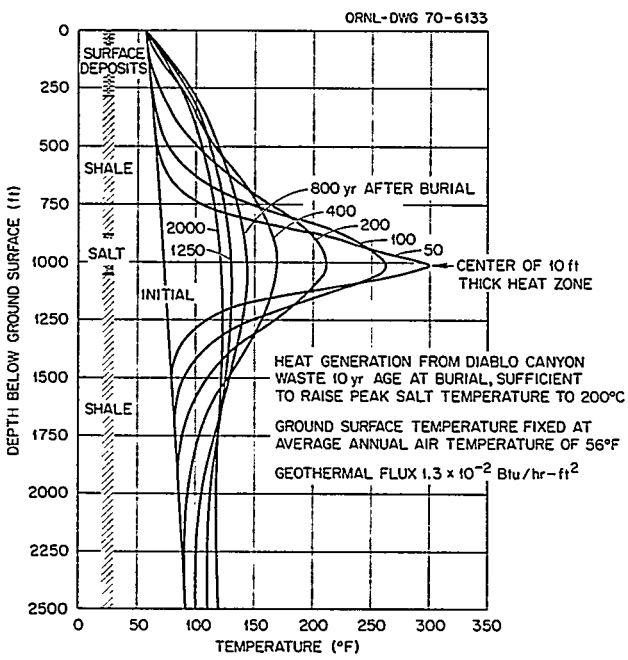

Fig. 3.9. Temperatures in Formation at Lyons.

tude greater than the geothermal flux;[18] so the decay heat should have essentially no effect on the local climate.

[18]Sidney Paige, "Sources of Energy Responsible for the Transformation and Deformation of the Earth's Crust," p. 338 in *Crust of the Earth*, Poldervaart, ed., July 1955.

Temperatures Around Mine. – A somewhat more simplified model was used for estimating the temperatures in the formation around the mine. In this case the mine was assumed to be a disk 7000 ft in diameter (about 880 acres) with a 10-ft-thick heat-generating zone. Since only about one-third of the mine will actually contain wastes, the heat generation per unit area of mine was taken as one-third of that per unit area of disposal room floor.

The somewhat simplified stratigraphy may be seen in Fig. 3.10, which shows the temperatures after 1000 years. Ground surface temperature was fixed at 56°F, and the geothermal flux was introduced 1000 ft below the mine. The 70°F contour indicates that the heat front has moved out about 1900 ft from the edge of the mine. A more meaningful measure is the 10°F rise contours shown in Fig. 3.11. After 1000 years the 10°F rise contour has only moved out horizontally about 500 ft.

Another point of interest is the temperature rise at 100 ft out from the edge. This is illustrated in Fig. 3.12. The maximum rise of about 49°F occurs about 75 years after placement of the waste. After about 1000 years the rise above ambient is still about 20°F.

Conclusions. – Based on all considerations, it appears that 200°C peak salt temperature is neither too conservative nor too liberal for at least the initial stages of a disposal facility operation. Operating experience may indicate higher allowable temperatures, which would produce a more economical operation.

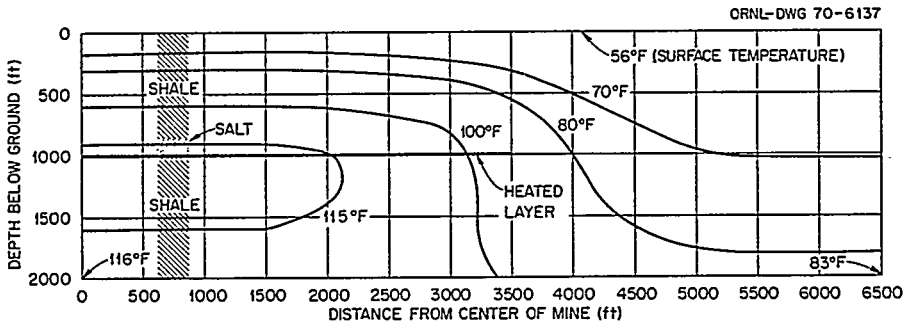

Fig. 3.10. Temperature in Formation After 1000 Years.

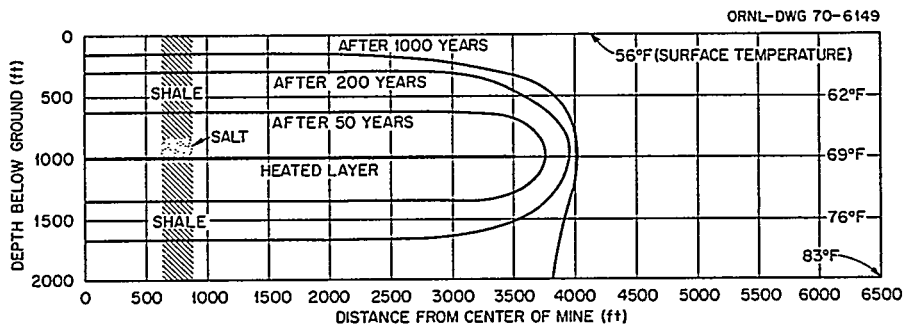

Fig. 3.11. 10°F Temperature-Rise Contours.

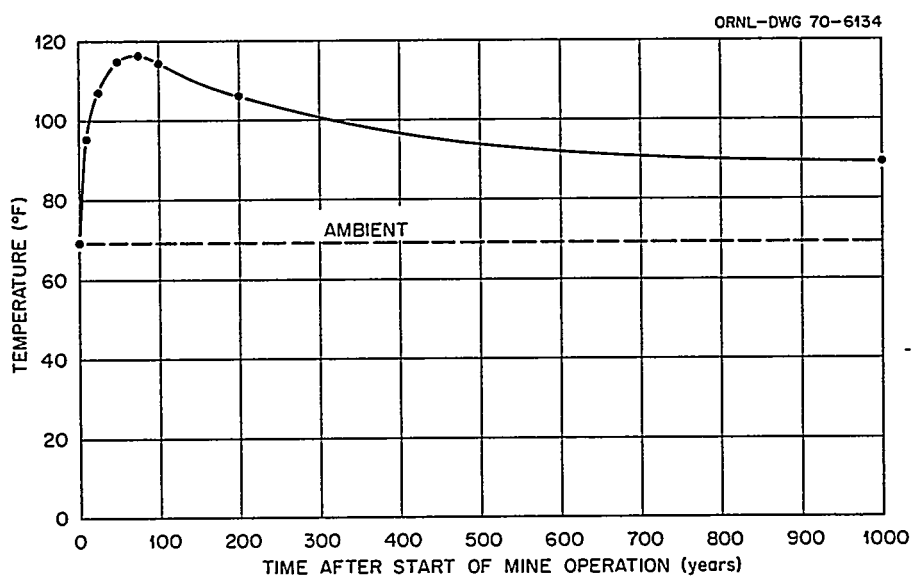

Fig. 3.12. Temperature 100 ft from Edge of Mine.

Salt Tectonics Considered in Relation to the Disposal of Radioactive Waste in Bedded Salt Formations

Ferruccio Gera

In order to evaluate the possibility of failure of waste containment because of deformation of the disposal formation, a good understanding of salt tectonics is necessary. The main questions that need to be answered in relation to the disposal of radioactive waste are: (1) what are the forces and mechanisms responsible for salt deformation and (2) what are the rates of salt deformation?

Salt Deformation

The relative mobility of rock salt in relation to other geologic materials is a consequence of its high plasticity. The deformation of salt specimens in the laboratory permits the evaluation of some of the parameters affecting the physical behavior of salt.[19,20] The temperature is the parameter with the largest effect on the physical properties of halite. Besides the increase of deformation rates, the progressive reduction of the strain-hardening effect with increasing temperature is geologically very important. At 300°C the strain-hardening effect disappears completely. Since such temperature would be reached naturally only at depths of the order of 900–10,000 m, most salt deformation is expected to occur in the presence of some strain hardening. The rate of deformation of salt varies inversely with the confining pressure; however, this effect is very secondary with respect to the effect of temperature.[21] Therefore, plasticity of salt increases with depth. In addition, the deformation rate is proportional to the stress difference and is influenced by the rate of stress variation. Other parameters affecting salt deformation are the grain size, the nature and amount of impurities, and the presence of fluids. Because of uncertainties in assessing the effect of the interplay of all these parameters and because of the uncertainties introduced by the time element, laboratory experiments are of limited help in understanding the geologic behavior of salt.

[19] H. Odé, "Review of Mechanical Properties of Salt Relating to Salt Dome Genesis," pp. 543–95, in *Saline Deposits*, Geol. Soc. Am. Spec. Paper, No. 88, 1968.

[20] P. LeComte, "Creep in Rock Salt," *J. Geol.* 73, 469–84 (1965).

[21] J. Handin and R. V. Hager, Jr., "Experimental Deformation of Sedimentary Rocks Under Confining Pressure: Tests at High Temperature," *Bull. Am. Assoc. Petrol. Geologists* 42, 2892–2934 (1958).

From the observation of saline deposits of the world, it is apparent that evaporites that are or have been buried to a certain depth usually show some deformation. The range of possible deformation is extreme, varying from moderate postdepositional thickening of the salt beds to well-developed piercement structures.

The forces responsible for the deformation of salt are mainly gravitational in nature. Locally, tectonic forces can be active and squeeze the salt along lines of minimum resistance, but the phenomenon of diapirism is essentially caused by flow of salt under the differential load of the overburden. All salt beds are exposed to some degree of differential loading because of variation in the overburden thickness or specific gravity, or both. But not all salt beds show signs of plastic flow; therefore a critical value of the pressure difference must exist below which no deformation occurs. The critical pressure difference is not constant in the various geologic environments but varies as a function of all parameters affecting the physical behavior of salt. Once the pressure difference on the salt bed is sufficient to cause salt flowage, all the strata, from the salt upward, begin to deform. The flowage of salt from high- to low-pressure areas requires that the overburden be uplifted over the zones of salt accumulation; strata must be downwarped or grabens formed over the areas from which salt is squeezed out.

Once salt flowage has resulted in variations in thickness of the mother bed, the density contrast between salt and overlying sediments begins to play a part that increases progressively in importance with the salt accumulation. If we consider an ideal horizontal reference plane in the salt bed and two points located on it – a in the high-pressure area from which salt flows and b in the low-pressure area where salt accumulates – it is clear that the pressure difference $\Delta P = P_a - P_b$ increases with the increase of the thickness of salt over b. This is true only if the accumulating salt replaces the heavier sediments and as long as the surface is maintained horizontal by differential accumulation, or erosion of the uplift, or both. Figure 3.13 shows the diagrammatic development of a salt structure.

Piercement of the overburden and intrusion of the salt can only occur when the stresses exerted by the rising salt exceed the shear strength of the overburden. The physical properties of the overburden are, therefore, important for the development of the diapiric process. The diapiric salt rises as a plug pushed from underneath.

The upper portion of a typical salt diapir has a horizontal section from circular to oval and an average diameter that can vary from less than 2 to more than 8

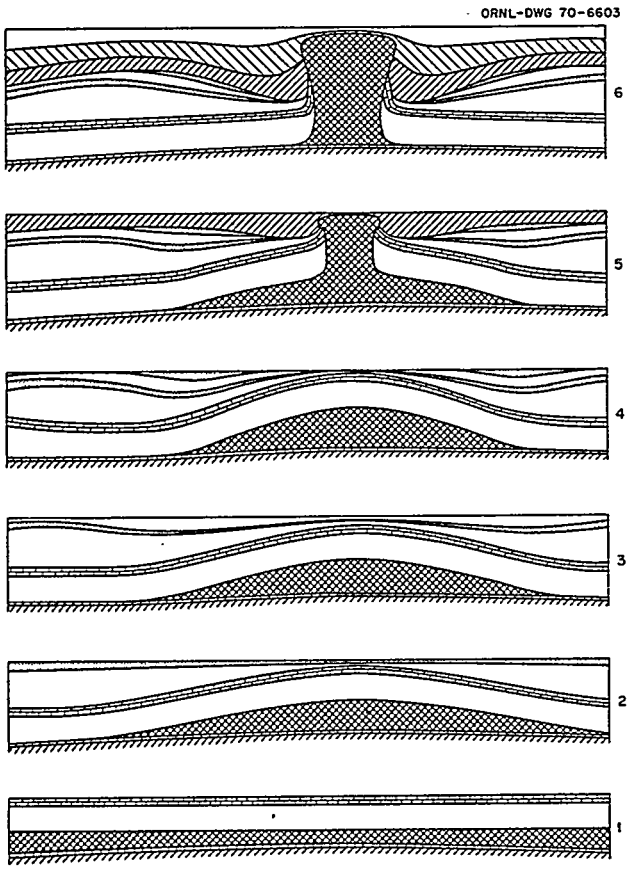

Fig. 3.13. Diagrammatic Development of a Salt Structure.

km. The shape in depth is either cylindrical or conical or a combination of the two. Occasionally, overhanging flanks are observed. The depth of the mother bed is quite variable from one geological region to the other. In the Gulf Coast area of the United States, the depth of the mother bed is at least 8000 to 9000 m, while in the eastern Texas and northern Louisiana synclines the depth of the Louann salt ranges from 3000 to more than 4500 m.[22,23] Considering the large volume of salt present in individual diapirs and the limited extension of the source area, from which the salt was drained, it seems clear that diapirism requires a thick bed of salt.[24] The critical thickness is unknown; but, in the areas where salt diapirs have developed, the original thickness of the mother bed must have been in excess of 300 to 400 m.

There is no clear-cut minimum depth of the salt bed that separates deformable salt from competent salt. For example, in some areas of the German Zechstein basin, there is good geologic evidence that salt deformation started when salt was only 2000 to 2500 m deep.[25] But north-northwest of Hamburg there is a large area where Zechstein salt, about 1000 m thick, covered by 3000 to 4000 m of sedimentary overburden, shows no sign of deformation.[26] While the ease of deformation of salt increases with depth, because of the increase in temperature, the only critical factor of the deformation process is the pressure difference to which salt is exposed.

Rate of Salt Deformation

In relation to the proposed disposal of radioactive waste in bedded salt, the most important aspect of salt deformation is the rate of the process in its various stages. If the time necessary for an unacceptable deformation of the salt bed should largely exceed the time required for decay of ^{239}Pu (300,000 to 400,000 years), the whole question of the plastic deformation of salt would have little relevance to the disposal of radioactive waste. Most geologists believe that salt deformation is a slow process, progressing at a rate comparable with the rate of other geologic processes, such as subsidence, mountain building, sediment accumulation, etc.[27]

The rate of salt movement is not the same in all phases of salt deformation; it is probably at a maximum in the late stage, when diapirs are approaching or reaching the surface. In fact, in this phase the pressure difference due to the salt-sediment density contrast is close to its maximum, and the resistance offered by the overburden to the rising salt is reduced or even nil when salt is exposed at the surface.

In the prepiercement stage of salt deformation the pressure differences are much less and the resistance of

---

[22] W. C. Gussow, "Salt Diapirism: Importance of Temperature and Energy Source of Emplacement," pp. 16–52 in *Diapirism and Diapirs,* Memoir No. 8, American Association of Petroleum Geologists, 1968.

[23] G. I. Atwater, "Gulf Coast Salt Dome Field Area," pp. 29–40 in *Saline Deposits,* Geol. Soc. Am. Spec. Paper No. 88, 1968.

[24] G. I. Atwater and M. J. Forman, "Nature of Growth of Southern Louisiana Salt Domes and Its Effect on Petroleum Accumulation," *Bull. Am. Assoc. Petrol. Geologists* 43, 2592–2622 (1959).

[25] A. Roll, "Zur Strukturgeschichte der Salzstocke von Wesendorf U. Hohenhorn," *Geotekton. Symposion,* F. Lotze, ed., Stuttgart, 1956.

[26] D. Sannemann, "Salt-Stock Families in Northwestern Germany," pp. 261–70 in *Diapirism and Diapirs,* Memoir No. 8, American Association of Petroleum Geologists, 1968.

[27] H. Borchert and R. O. Muir, *Salt Deposits: The Origin, Metamorphism and Deformation of Evaporites,* D. Van Nostrand, London, 1964.

the overburden is higher; therefore, rates of movement should be markedly less than the likely rate of growth for a well-developed diapir approaching the surface.

Evidence about the rate of salt deformation can be obtained considering several aspects of salt structures. The main points are:

1. The cap-rock formation present on many diapirs has been formed by the dissolution of salt by groundwater and accumulation of the insoluble impurities (mainly anhydrite) contained in the salt. If the composition of the salt is known, it is possible to calculate the volume of dissolved salt from the volume of cap rock. In many cases a thickness of salt of many thousands of meters must have been dissolved to accumulate the cap rock.[28] Since the known geologic relationships prove that the top of the salt diapir has never been thousands of meters higher than the present top of the cap-rock formation, the only logical explanation is continuous growth of the diapir during dissolution of the salt. The rates of the two processes for a great part of the diapir growth must have been roughly similar.

2. Seismic profiles through the bottom sediments of the Gulf of Mexico and other sea basins show many structures that suggest growing diapirs. For one of the Sigsbee knolls, located in the deepest part of the Gulf of Mexico, the diapiric nature has been proven by recent deep-sea drilling. The lack of terrigenous sediments on top of the knoll since at least Upper Miocene time and the thinning of sediments on the flanks strongly suggest a rate of diapir growth of the same order of magnitude as the rate of sedimentation.[29]

3. If the evolution of rim synclines through geologic time can be reconstructed, as is often the case in Germany, the rate of deformation of the salt bed can be estimated. The downwarping of the sedimentary strata into the space vacated by the flowing salt is necessarily contemporaneous with the accumulation of salt in the area of uplift. From the evidence furnished by many German diapirs, it can be concluded that the time necessary for the accumulation of Zechstein salt in salt pillows and salt anticlines has been of the order of 20 to 60 million years. In several cases the diapiric phase of salt deformation can be dated, and stages of diapirism that have lasted as much as 10 to 40 million years are indicated.[26,30] In such long time periods the rate of growth of the diapir certainly was not uniform, and long periods of stasis may have occurred, but the very slow rate of salt movement is evident.

The average rate of salt movement obtained from the study of German salt structures is about 0.3 mm/year. However, the measurement of present movements and the geologic evidence in cases of recent growth indicate that the rate of uplift of a well-developed diapir approaching the surface can be as high as a few millimeters per year. For example, Lotze (1957) mentions that a relative uplift of 1 to 2 mm per year has been measured on salt stocks of the Caspian depression.[31] Trusheim (1960) reports Teichmuller's conclusion that the rise of the salt stock of Segeberg, in Holstein, northern Germany, has been about 2 mm/year in the last 20,000 years.[30] From observations by Lees and Falcon, Trusheim has calculated a rate of salt movement of 2.4 mm/year in salt structures located in Iraq.[30]

Sheets (1947) reports that active movement has been measured at Hoskins Mound, Brazoria County, Texas.[32] An area of 100 acres located in the central part of the diapir has apparently risen a maximum of 18 cm in a 23-year period (1922–1945). The resulting rate of uplift at the surface is about 8 mm/year. However, due to the known subsidence of the surrounding area, this rate of uplift is likely to be an overestimate. A similar salt spine has been, and probably still is, rising underneath Jefferson Island, Louisiana; the rate of growth in this case has been estimated at 2 to 4 mm/year. In many other cases there is strong evidence of present movement even if data are insufficient to calculate the rate of growth.[33]

Finally, there is the observation that of the thousands of salt structures known throughout the world, none has ever been observed to undergo the rapid growth that has been postulated by a few authors.[22,34] Since all stages of development of salt structures can be

[28] M. Bornhauser, "Geology of Day Dome (Madison County, Texas) – A Study of Salt Emplacement," *Bull. Am. Assoc. Petrol. Geologists* 53, 1411–20 (1969).

[29] C. A. Burk *et al.*, "Deep-Sea Drilling into the Challenger Knoll, Central Gulf of Mexico," *Bull. Am. Assoc. Petrol. Geologists* 53, 1338–47 (1969).

[30] F. Trusheim, "Mechanism of Salt Migration in Northern Germany," *Bull. Am. Assoc. Petrol. Geologists* 44, 1519–40 (1960).

[31] F. Lotze, *Steinsalz und Kalisalze,* pt. I, 466 pp., Gebruder Borntraeger, Berlin, 1957.

[32] M. M. Sheets, "Diastrophism During Historic Time in Gulf Coastal Plain," *Bull. Am. Assoc. Petrol. Geologists* 31, 201–26 (1947).

[33] F. E. Vaughan, "The Five Islands, Louisiana," *Bull. Am. Assoc. Petrol. Geologists* 9, 756–97 (1925).

[34] H. D. Outmans, "Discussion on Theory of Gravity Instability with Variable Overburden and Compaction," *Geophysics* 31, 829–31 (1966).

observed, it seems that only two conclusions are possible. The first is that the geologic process of salt diapirism either has been eliminated or only occurs when nobody is looking. The second possibility is that salt diapirism is regularly occurring, whenever conditions are appropriate, but only accurate measurements or geologic observations can provide evidence of the slow rate of movement.

Conclusions

From this review of the tectonics of salt, it is clear that the risk of waste release because of the plastic deformation of a bedded salt formation is negligible. The heating caused by the decay heat generated in the high-level waste would only affect a limited area of the salt formation and, from a geologic point of view, would be of such short duration that no consequences would be expected. In fact, it has been calculated that in a few thousand years the temperature variation due to the heat generated by decay of the fission products would be negligible. The heating of the geologic formations due to the decay of long-lived alpha emitters would last for a substantially longer time period; however, the peak temperature in the alpha-waste section of the repository is not expected to exceed 70 to 80°C, at the most.

Considering the specific case of the salt formation at Lyons, Kansas, it is clear that the possibility of extensive salt deformation affecting the safety of the disposal operation can be excluded for a number of reasons.

1. The differential loading on the salt bed is very limited, due to the subhorizontal position of the strata and the limited relief of the area.
2. The thickness of the salt bed is insufficient to produce sizable salt structures.
3. The salt bed is only 300 m deep; therefore, ambient salt temperature is low and pressure differences required to maintain salt deformation would be high.
4. The area is tectonically stable, and no tectonic forces would be expected to complicate the picture.
5. The overburden is mainly composed of fairly indurated Permian shales that would be expected to offer substantial resistance to the deformation of the salt bed.
6. Even if the pressure differences on the salt bed were increased either by erosional unloading of part of the formation or by tectonic movements, the amount of deformation expected in a time period of a few hundred thousand years would be limited.

Disposal of Excess Salt

F. M. Empson T. F. Lomenick
W. C. McClain

Some concern has been expressed about the possibility of utilizing brine injection for the disposal of the excess salt in the conceptual design of the radioactive waste repository. The original concept involved brining the excess mined salt and injecting the resulting brine into the Arbuckle formation at a depth of about 3500 ft, at the site. Following the expression of concern, this concept was reexamined along with alternatives and the conceptual design slightly modified.

Possible Sale of Excess Salt in Local Markets

The commercial sale of the excess salt produced by waste disposal operations, either as rock salt or as brine, was examined as a possible (and highly attractive) alternative to deep-well injection. Such a possibility has been discussed with three salt producers in the central Kansas area. Two of these, the American Salt Corporation of Lyons and The Carey Salt Company of Hutchinson, operate both rock salt mines and evaporating plants. The Morton Salt Company operates an evaporating plant in Hutchinson and purchases a limited amount of rock salt from Kansas producers for resale to their customers. All three of these companies have expressed interest in discussing the proposed sale and in entering into negotiations if it should be of mutual interest to do so.

Certain inferences may be drawn from these expressions of interest. Salt is produced very cheaply by brining, and it is doubtful if the brining costs are a significant part of the overall cost of producing evaporated salt. This means that salt sold as brine will be sold very cheaply. Further, prospective customers will be limited by their location with respect to the waste repository. If the repository is located near Lyons, American Salt may be the only customer for brine. A site near Hutchinson would bring three companies into the market for brine, Carey Salt, Morton Salt, and Barton Salt Company. (Barton, a relatively small producer, has not been contacted.) Telephone conversations left an impression that American Salt was the most interested of the three companies contacted in the possible purchase of the salt as brine.

Exact location would probably not be a significant factor if the salt were marketed as rock salt. Snow- and

ice-control salt is shipped by truck and rail. Loading facilities at the repository could serve any producer buying for sale during the peak load period. The effect of impurities on the salability has not been established.

All three companies contacted were about equally interested in the purchase of rock salt. Morton may consider it a way of getting into the area market for snow control. Carey and American salt companies are currently providing large aboveground storage buildings for rock salt. They propose to mine at a relatively constant rate, filling the storage building during summer and selling from it during the snow months. The availability of this storage capacity may affect the American and Carey interest in rock salt.

It would appear that the interest of these companies in purchase might be increased if one were selected as the mining contractor. However, this possibility has not been discussed with them.

Status of Excess Salt Disposal in Conceptual Design

Based on the favorable response to inquiries about the possible sale of the excess salt in local markets, the original conceptual design has been modified to incorporate this as the prime salt disposal method. These modifications include arrangements for hoisting the entire volume of excess salt to the surface. Facilities at the surface will be provided to divert whatever proportion can be sold as rock salt to either truck or rail car loading equipment. Facilities will also be provided on the surface to dissolve the rock salt for possible sale as brine. These brining facilities will be sized to handle the maximum salt production rate.

The possibilities of using the Arbuckle group as a reservoir formation for injected brine are discussed in a previous section. The examination of this technique revealed no reason why the excess salt which cannot be disposed of in local markets could not be brined and injected into this porous formation. Therefore, such a system has become the backup method of salt disposal rather than the prime method and has been modified to include use of Arbuckle water for brining and injection from the surface.

4. Engineering, Economic, and Safety Evaluation

D. G. Jacobs Ferruccio Gera[2]
K. E. Cowser R. V. O'Neill[3]
M. Reeves III[1] O. M. Sealand
P. G. Fowler[1]

SITING AND OPERATION OF NUCLEAR FACILITIES

The intent of this program has been to develop information and a rationale that may be used to assess some of the factors involved in planning both local and regional expansion of nuclear power. Of particular current interest is the management and control of radioactive effluents and the need for a coherent model to simulate the dynamic behavior of radionuclides in the environment. Previous annual reports have described progress made in developing techniques to calculate downwind air concentrations (with corrections for washout and fallout) resulting from routine airborne releases, to predict radionuclide movement through some environmental pathways leading to man, and to estimate dose to man due to various modes of exposure.[4–6]

ROUTINE ATMOSPHERIC RELEASES OF RADIOACTIVE MATERIALS

In siting and operating nuclear facilities it is desirable to predict the transport of radioactive materials. We consider a routine situation in which radioactive materials are being continuously emitted into the atmosphere rather than an accidental situation. Hence only average annual concentrations are to be determined. Some releases will contain relatively short-lived members of radioactive decay chains.

This circumstance necessitates the consideration of several factors. For example, radioactive production and decay processes will occur both in the atmosphere and on the ground. Also the washout and fallout processes by which the materials reach the surface will be characterized in general by different washout coefficients and deposition velocities for different members of the decay chain. In addition, processes such as erosion, seepage, and translocation, which remove radioactive materials from the ground on which they were deposited, may differ for each member.

Our basic formulas are based on the Gaussian plume formula developed by Gifford.[7] The average annual ground-level air concentration (Ci/m^3) for nuclide i of the decay chain is[4]

$$X_i(x, \theta) = \sum_{p=1}^{n_s} \sum_{r=1}^{n_w} \frac{2.032 F_{pr}(\theta)\, \overline{Q}_{ipr}(x)}{\sigma_p(x)\, u_r x} \times \exp\left[-\frac{h^2}{2\sigma_p^2(x)}\right]. \quad (1)$$

Here $\sigma_p(x)$ (m) is the vertical dispersion coefficient for stability p at distance x from the stack, u_r (m/sec) is the wind speed for speed group r, h (m) is the stack height, and $F_{pr}(\theta)$ is the frequency of stability p and wind speed u_r in direction θ.

Implicit in Eq. (1) are the use of an image source to account for reflection at the earth's surface and a cross-wind average[8] which attributes uniformly over a

[1] Computing Technology Center, Oak Ridge.

[2] Visiting scientist on leave from Italian National Committee for Nuclear Energy.

[3] Ecological Sciences Division.

[4] *Health Phys. Div. Ann. Progr. Rept. July 31, 1967*, ORNL-4168, pp. 39–43.

[5] *Health Phys. Div. Ann. Progr. Rept. July 31, 1968*, ORNL-4316, pp. 47–51.

[6] *Health Phys. Div. Ann. Progr. Rept. July 31, 1969*, ORNL-4446, pp. 20–22.

[7] F. A. Gifford, Jr., *Meteorology and Atomic Energy 1968*, D. H. Slade (ed.), TID-24190 (July 1968).

[8] W. M. Culkowski, *Sixth Air Cleaning Conference, July 7–9, 1959*, TID-7593 (October 1960).

22.5° arc. (The angle θ is allowed to assume only the 16 different compass directions.)

Effects of washout, fallout, and radioactive decay are taken into account by the effective emission rate (Ci/sec):[4]

$$\bar{Q}_{ipr}(x) = W_w\, Q^w_{ipr}(x) + W_f\, Q^f_{ipr}(x)\ , \qquad (2)$$

where W_w and W_f are washout and fallout frequencies respectively. Also

$$Q^w_{ipr}(x) = Q_{ipr}(x,\ \Lambda_i,\ v_i = 0) \qquad (3)$$

and

$$Q^f_{ipr}(x) = Q_{ipr}(x,\ \Lambda_i = 0,\ v_i)\ , \qquad (4)$$

where Λ_i (sec^{-1}) is the washout coefficient, v_i (m/sec) is the deposition velocity,

$$Q_{ipr}(x,\ \Lambda_i,\ v_i) = \begin{cases} Q^0_{1pr}(x,\ v_i)\exp(-q_1 x/u_r)\ , & i = 1\ , \\ Q^0_{2pr}(x,\ v_2)\exp(-q_2 x/u_r) + Q^0_{1pr}(x,\ v_1)\lambda_2 \dfrac{\exp(-q_1 x/u_r) - \exp(-q_2 x/u_r)}{q_2 - q_1}\ , & i = 2\ , \end{cases} \qquad (5)$$

$$Q^0_{ipr}(x,\ v_i) = Q_{i0}\exp\left[-v_i\, g_p(x)/u_r\right]\ , \qquad (6)$$

and

$$g_p(x) = (2/\pi)^{1/2}\int_0^x dx' \times \exp\left[-\frac{h^2}{2\sigma_p(x')}\right]/\sigma_p(x')\ . \qquad (7)$$

The quantity $q_i = \Lambda_i + \lambda_i$ (sec^{-1}) is the sum of the washout coefficient and the decay constant, and Q_{i0} (Ci/sec) is the actual stack emission rate. Because of its complexity, we do not give the general expression in Eq. (5). This term may be obtained by generalizing Turner's expression.[9]

Equations (1) to (7) define the ground-level air concentration (Ci/m^3). We are also interested in deposition rates ω_i (Ci m^{-2} sec^{-1}) and ground concentrations ϕ_i (Ci/m^2). They are given by

$$\omega_i(x,\ \theta) = \sum_{p=1}^{n_s}\sum_{r=1}^{n_w}\frac{F_{pr}(\theta)}{\sigma_p(x)\,u_r x}\left\{2.543\Lambda_i W_w Q^w_{ipr}(x) + 2.032 v_i W_f \exp\left[\frac{-h^2}{2\sigma_p^2(x)}\right] Q^f_{ipr}(x)\right\} \qquad (8)$$

and

$$\phi_i(x,\ \theta) = \begin{cases} \dfrac{1}{\lambda_1 + \mu_1}\,\omega_1(x,\ \theta) & i = 1 \\ \dfrac{1}{\lambda_i + \mu_i}\left[\lambda_i\,\phi_{i-1}(x,\ \theta) + \omega_i(x,\ \theta)\right] & i = 2, 3, \ldots \end{cases}\ , \qquad (9)$$

where $\mu_i\phi_i$ (Ci m^{-2} sec^{-1}) is the material lost by, say, erosion, seepage, and translocation. Concepts presented by Briggs[10] are used in the development of Eq. (8). In the derivation of Eq. (9) a steady state is assumed so that as much of material i is being gained through deposition and decay from $i - 1$ as is being lost by radioactive decay and other natural processes.

Equations (1) to (9) have been programmed in double-precision FORTRAN IV, and the calculations of this code have been successfully checked against five different hand calculations. In this, the initial version of our code, we do not consider branching in the decay scheme. In order for the vertical dispersion coefficients $\sigma_p(x)$ to be input for unequally spaced intervals, a generalization[11] of Simpson's rule appropriate for such intervals is used to obtain $g_p(x)$, Eq. (7). Values of $g_p(x)$ for which x is located between mesh points of $\sigma_p(x)$ are obtained by linear interpolation. Finally, values for the effective emission rate $\bar{Q}_{ipr}(x)$, Eqs. (2) to (6), are obtained from the previously mentioned subroutine CHAIN.

PATHWAY ANALYSIS

Systems analysis techniques can be used to simulate the movement of radionuclides in food chains. The

[9] W. D. Turner, *The Exrem II Computer Code for Estimating Doses to Populations from Construction of a Sea-Level Canal with Nuclear Explosives*, CTC-8 (July 1969).

[10] G. A. Briggs, *Meteorology and Atomic Energy 1968*, D. H. Slade (ed.), TID-24190 (July 1968).

[11] R. E. Funderlic, *The Programmer's Handbook*, K-1729 (February 1968).

PATHWAY model, programmed in FORTRAN IV, represents a preliminary attempt to predict the concentration of ^{131}I, ^{90}Sr, and ^{137}Cs in a variety of foods following a unit surface deposition.[12] Models like those described in the previous section and PLUME generate the source term (surface deposition) for PATHWAY.[13] The equations describing the behavior of this compartmented system are based on a discrete-time approximation assuming 24-hr equilibrium in compartments for which only concentration factors are known. Many of the transfer coefficients needed for a continuous time model are not readily available.

Figure 4.1 is a simple schematic diagram of an agricultural system used to illustrate the application of PATHWAY. The example assumes four sites downwind from the source as follows: (1) a truck farm growing potatoes and leafy vegetables, (2) a reservoir providing drinking water and fish, (3) a farm producing grain products, and (4) a dairy farm yielding beef and milk. The hypothetical source term is exponential in character and scaled so that depositions decrease by factors of 1, $1/4$, $1/16$, and $1/32$ from site 1 to site 4. Parameters used to quantify the model were listed previously.[6] Figure 4.2 shows the predicted concentration of ^{90}Sr in food items. With data on the diet of residents the daily intake of radionuclides would be calculated and INREM used to estimate internal dose.

[12] R. V. O'Neill, internal memorandum, ORNL-CF-70-3-25 (Mar. 19, 1970).

[13] F. T. Binford, F. B. Kahn, and J. Barrish, *Information on Radiation Doses Following a Reactor Accident,* ORNL-4086 (1967).

ORNL-DWG 69-6536

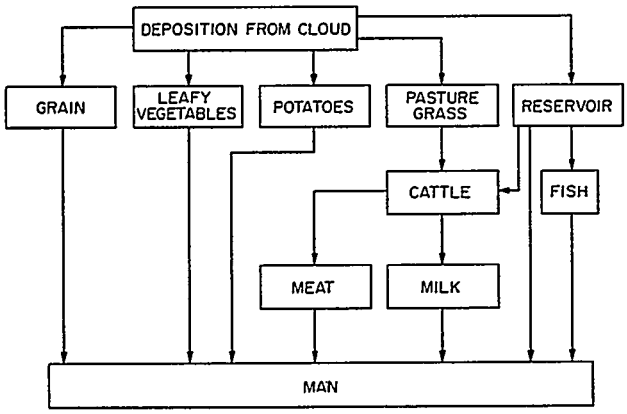

Fig. 4.1. Food Chains Leading to Man. The diagram is not intended to represent all possible pathways, only those used in the present example.

ORNL-DWG 69-6540R2

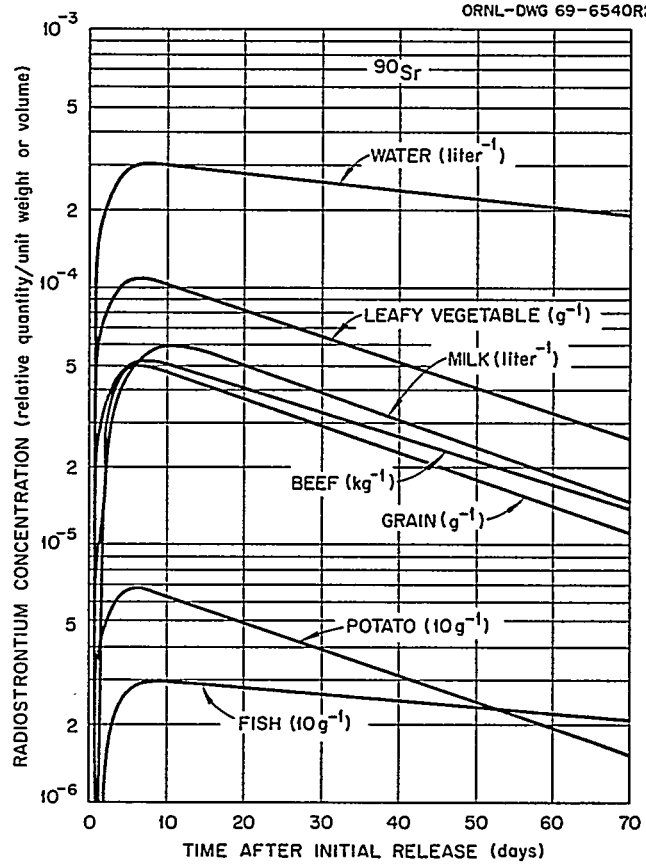

Fig. 4.2. Estimated Relative Concentrations of ^{90}Sr in Human Foods Following an Arbitrarily Defined Release.

REGIONAL PLANNING

Many factors must be considered in selecting sites for steam power plants. Those that relate directly to the environment have been enumerated and described most recently in a report sponsored by the Energy Policy Staff, Office of Science and Technology. As indicated, planning for area use will take on greater significance with the increased demand for electric power, especially in view of the estimated 255 new sites needed for thermal plants (both nuclear and fossil-fueled generating units) by 1990.[14]

The requirements for adequate water supplies to serve steam power plants will also increase as plant size and demand increase. We have limited our initial search for information to the potential use of surface waters associated with nuclear power production and planning.

[14] *Considerations Affecting Steam Power Plant Site Selection,* a report sponsored by the Energy Policy Staff, Office of Science and Technology, U.S. Government Printing Office, 1968.

A convenient starting point is the present status of nuclear power plants; and for this purpose we chose a recent AEC news release that reports on plants operable, being built, or planned.[15]

Information is summarized on nuclear power plant locations and the surface waters contiguous to each site. Preliminary safety analysis reports are the principal source of the latter information. Plant location is also listed by the eight geographical power supply regions of the Federal Power Commission[16] as well as principal drainage basins in the continental United States.[17] This information is intended to serve as a basis for further discussions on regional planning.

---

[15] USAEC News Release, Jan. 13, 1970, *Status of All Nuclear Power Plants as of December 31, 1969.*

[16] United States Federal Power Commission, *National Power Survey*, parts 1 and 2, U.S. Government Printing Office, Washington, D.C. (1964).

[17] D. W. Miller, J. J. Geroghty, and R. S. Collins, *Water Atlas of the United States*, plate 9, Water Information Center, Inc., Port Washington, Long Island, N.Y.

5. Earthquakes and Reactor Safety

ORNL SEISMOGRAPH STATION ORT

W. C. McClain O. H. Myers

Station ORT is a reporting station in the U.S. Coast and Geodetic Survey network, reporting seismic events to the National Earthquake Information Center. The reported events include local and worldwide seismic events and underground nuclear detonations.

A vertical long-period seismometer and its amplifying equipment has been added to the station. This equipment is more likely to continue operating during small local earthquakes or more distant large seismic events than the short-period instrument. An improved time-keeping system has also been installed.

Among the local events reported to the National Earthquake Information Center (NEIC) by station ORT is the East Tennessee earthquake of July 13, 1969. Earth motion at the ORT short-period vertical seismometer, when amplified, was strong enough to drive the recorder off scale. Small aftershocks from this quake, centered in the Knoxville area, were recorded by ORT during the two days following the initial shock. Even though the Richter magnitude listed by the U.S. Coast and Geodetic Survey was only about 3.5, it was reported by 25 seismograph stations throughout the country. Some of these were as far away as New York, New Mexico, and Colorado. The felt area included parts of North Carolina, Virginia, and Kentucky, as well as Tennessee.

The most prominent nuclear detonation recorded by the station during fiscal year 1970 was the underground shot on Amchitka Island in the Aleutians at 22 06 00.0 GMT on October 2, 1969. This 1-megaton "Milrow" event was reported to have been detonated at a depth of 1.77 km. Body wave magnitude computed from the initial p-wave registered 6.5 on the Richter scale. There had been opposition to this explosion because of the fear of triggering a damaging earthquake in the Alaskan or Aleutian fault areas. Several countries objected, including the Soviet Union, Japan, and Canada, as well as numerous United States scientists and political figures. However, no damaging seismic disturbances resulted from the shot. It produced only a ground roll on desolate Amchitka Island.

A study of seismicity in the southeastern United States was made and a seismic history of the southeast region compiled, mainly from published literature.[1] The seismic history was computerized in such a manner that lists of the seismic events for specific areas, states, or geologic provinces can be retrieved. This history should be useful in facility siting as well as in describing seismicity of the region and furthering earthquake prediction efforts.

A bulletin covering the operation of Station ORT and closely related seismic data, informative subjects of special interest, and current developments in seismology is also published semiannually.[2]

---

[1] W. C. McClain and O. H. Myers, *Seismic History and Seismology of the Southeastern Region of the United States*, ORNL-4582, 43 pp. (June 1970).

[2] O. H. Myers, internal memorandum, ORNL-CF-69-10-55, 33 pp. (October 1969).

6. Dose Estimation Studies Related to Peaceful Uses of Nuclear Explosives

C. J. Barton[1] M. J. Kelly[1]
R. S. Booth[2] J. P. Lund[4]
K. E. Cowser B. F. Roberts[1]
D. G. Jacobs P. S. Rohwer
S. V. Kaye[3] W. S. Snyder
E. G. Struxness

UTILIZATION OF NATURAL GAS FROM NUCLEARLY STIMULATED WELLS

C. J. Barton D. G. Jacobs
M. J. Kelly

Concentration of Tritium and ^{85}Kr in Gasbuggy Gas as a Function of Gas Flow

The concentrations of radionuclides in gas removed from the Gasbuggy cavity have been decreasing with time.[5] Data on the concentration of tritium and ^{85}Kr in Gasbuggy chimney gas as a function of gas flow through August 1969 are shown in Fig. 6.1. Although there are deviations between the data and the line representing the expected exponential decrease in concentration based on the initial volume of 128 million cubic feet (M^2cf) of gas, the rate of decrease in both concentrations seems to agree reasonably well with the theoretical curve. The bottom hole pressure, which varied from 64 to 73 atm during the initial shut-in period, dropped to about 18 atm during the long-term low-flow-rate test at constant pressure. The slope of the line during this period corresponds to a cavity volume of 35 M^2cf, in fair agreement with the volume (34 M^2cf) calculated by adjusting the initial volume for the difference in cavity pressure. It is estimated that an additional 50 Ci of tritium, 8 Ci of ^{85}Kr, and 0.5 Ci of ^{14}C could be produced from the well based on the August 1969 radionuclide concentrations and the reported bottom hole pressure. These estimates agree reasonably well with Holzer's figures of 40 Ci of tritium and 7 Ci of ^{85}Kr, based on October 1969 data.[6]

Ratios of Radioactive Contaminants to Nonradioactive Contaminants in Gasbuggy Gas

The principal radionuclides in Gasbuggy gas are ^{85}Kr and ^{3}H, while the principal nonradioactive impurities are CO_2 and H_2. Since none of these species was present to any appreciable extent in the formation gas that entered the Gasbuggy cavity as the contaminated gas was removed, it would be expected that the ratio of the radioactive to nonradioactive components of the gas would be constant. The principal value of such ratios is the indication that they give of analytical errors and of unexpected behavior of any of the gas components.

Several ratios were calculated and compared with those reported by Holzer,[6] which were presented as a function of time. Results of the calculations involving ^{85}Kr are shown in Fig. 6.2 as a function of cumulative gas flow and are quite similar to those obtained involving tritium. There was an increase in the ^{85}Kr/H_2 ratio during the initial high-flow-rate test (0.4 to 55.4

[1] Reactor Chemistry Division.

[2] Instrumentation and Controls Division.

[3] Ecological Sciences Division.

[4] Analytical Chemistry Division.

[5] C. F. Smith, Jr., *Project Gasbuggy Gas Quality Analysis and Evaluation Program, Tabulation of Radiochemical and Chemical Analytical Results,* UCRL-50635, rev. 1 (November 1969).

[6] A. Holzer, "Gasbuggy in Perspective," *Proceedings of the ANS Topical Meeting, Engineering with Nuclear Explosives, Las Vegas, Nevada, January 1970,* CONF-700101, vol. I, p. 62 (1970).

M^2cf) compared with values observed during the initial shut-in period. Although the scatter in data makes the slope of the line rather uncertain, there appears to be a drop-off of about 22% in the ratio during removal of the first 200 M^2cf of gas from the well. This has been followed by a more rapid rate of decrease during the final long-term flow test. The slope of this part of Fig. 6.2 shows that removal of 50 M^2cf of gas caused a factor of 2 reduction in the $^{85}Kr/H_2$ ratio. For the $^{85}Kr/CO_2$ data the corresponding value was 58 M^2cf. This ratio was the only one that failed to show an increase over the average value for the initial shut-in period.

Holzer[6] has hypothesized that the decrease in CH_3T/CO_2 and $^{85}Kr/CO_2$ ratios was due to CO_2 initially dissolved in water being evolved and mixed with the cavity gas. This obviously is not the correct explanation since the CH_3T/H_2 and $^{85}Kr/H_2$ ratios are quite similar to those for CO_2 and since H_2 has very limited solubility in water.

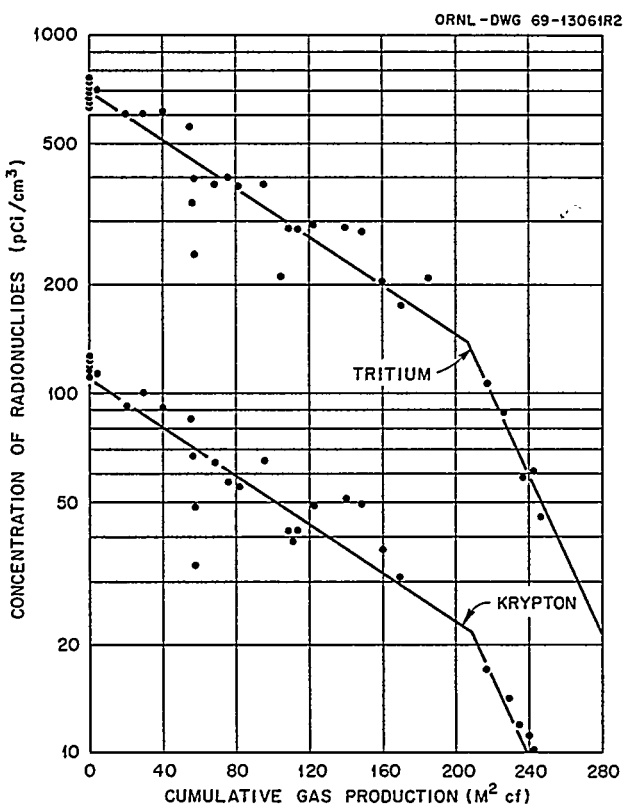

Fig. 6.1. Concentrations of Tritium and ^{85}Kr in Gasbuggy Gas as a Function of the Total Volume of Gas Produced. The straight lines represent the predicted concentrations based on complete mixing of 128 M^2cf of gas in the chimney up to 210 M^2cf production and mixing of 35 M^2cf of gas thereafter.

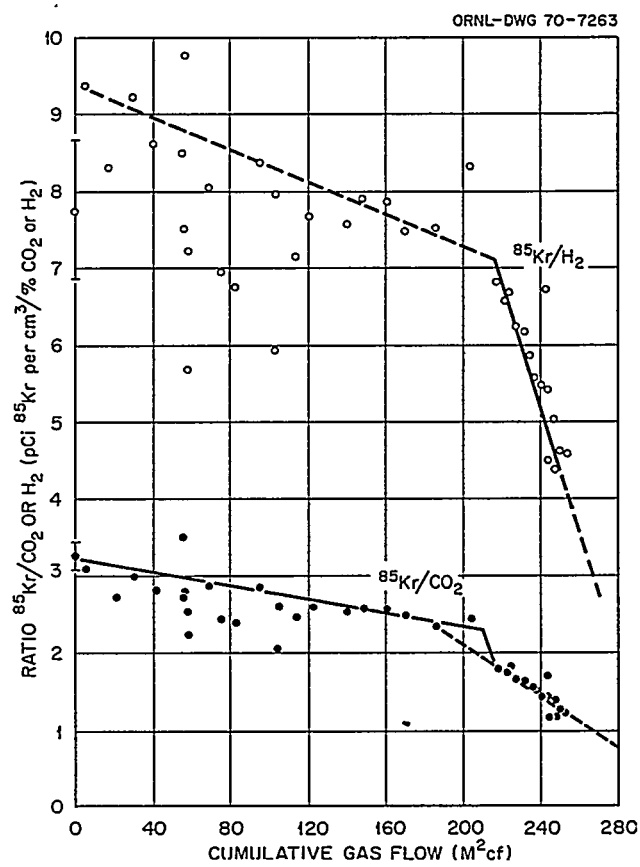

Fig. 6.2. Ratio of ^{85}Kr to H_2 and CO_2 Concentrations.

One possible explanation for the observed variation in ratios is lack of perfect mixing in the cavity during gas withdrawal. The low flow rates that prevailed during the long-term production test (160 to 500 Mcf/day) may have accentuated the problem of inhomogeneity since flow of uncontaminated formation gas from a section near the top of the Gasbuggy well may be a significant fraction of the total flow. However, this explanation requires that mixing be a function of diffusion rate, and one would expect a larger difference than was observed between CO_2 and H_2 ratios.

Estimate of Home Occupancy Factor

The home occupancy factor, the fraction of the time a home is occupied, must be considered in estimating doses to occupants of a home heated with natural gas from a nuclearly stimulated well.[7] An estimate of the

[7]M. J. Kelly *et al.*, *Second Quarterly Progress Report on the Theoretical Evaluation of Consumer Products from Project Gasbuggy*, ORNL-TM-2513 (March 1969).

home occupancy factor during the heating season was based on the following assumptions:

1. average time at home for housewives, preschool children, and retired men – 21 hr/day,
2. average time at home for working wives and husbands – 14 hr/day,
3. average time at home for school children – 15 hr/day.

Using the latest available census figures[8] on the makeup of the average family, we can estimate the person-hours of home occupancy as shown in Table 6.1. The home occupancy factor is

$$\frac{61.3}{24 \times 3.66} = 0.70 .$$

There appears to be no way at present to verify the assumed hours per day spent at home by the various family members. These estimates are undoubtedly higher than the true values for most parts of the country, so that calculations based on this home occupancy factor will be conservative.

The most important (or critical) age groups are the preschool children and housewives because of the high fraction of time they spend in the home.

[8] U.S. Bureau of the Census, *Statistical Abstract of the United States: 1969* (90th ed.), Washington, D.C., 1969.

Table 6.1. Average Person-Hours per Day Spent in the Home

Family Member	Average Number per Family	Average Person-Hours per Day
Preschool children (<5 years)	0.37	7.8
School children (5 to 17 years)	1.03	15.5
Retired people (>65 years)	0.38	8.0
Housewives	0.53	11.1
Working adults	1.35	18.9
Total	3.66	61.3

Hypothetical Population Exposures in Metropolitan Areas

Gas leaving the Blanco Plant of El Paso Natural Gas Company is mixed with gas from other basins during its transmission to consumer areas. Some of the principal population centers using gas processed through the Blanco Plant are listed in Table 6.2. About 88% of the gas processed at the Blanco Plant is sold in California, with about 60% going to Pacific Gas and Electric Company, which serves the central valley and San Francisco Bay areas, and 28% going to the southeastern part of the Los Angeles Basin. These areas differ with respect to dilution of Blanco gas, to heating requirements, and to the number of people that could be potentially exposed from the hypothetical use of gas from the Gasbuggy well. Dose equivalents from the hypothetical exposure to tritium from domestic use of Gasbuggy gas during the entire lifetime of this single well have been estimated for individuals living in these areas. The exposure conditions considered were for nonvented heating in a normally constructed home of 1000-ft^2 floor area and an occupancy factor of 1. Previous calculations have shown that tritium is the critical radionuclide and that hypothetical radiation

Table 6.2. Potential Dose Equivalents to Various Population Groups from the Hypothetical Use of Gasbuggy Gas

City	Heating Requirements (degree-days/year)	Further Dilution Factor for Blanco Gas	Dose Equivalents from Tritium (millirems)
San Francisco	2950	6.0	0.15
Peninsula Cities	2700	6.0	0.14
San Jose	2450	6.0	0.14
Bakersfield	2100	3.2	0.25
Fresno	2490	3.2	0.27
Salinas	2700	3.2	0.28
Arrowhead Lake	5400	5.3	0.23
San Fernando Valley	1700	16	0.05
Southeastern Los Angeles Basin	1700	5.3	0.14

doses from ^{85}Kr are much smaller than those from tritium.[9]

Natural gas is used in metropolitan areas for operation of steam plants to generate electricity and for a wide variety of industrial and commercial applications, as well as for domestic consumption. Releases of combustion products from steam plants are through tall stacks, and they represent elevated point sources, while releases from most industrial and domestic gas users can be considered to be ground-level sources. Both types of release require use of data on local meteorological conditions for determining ground-level air concentration of the pollutants. Hanna and Gifford[10] have provided ground-level air concentrations for the combustion products from natural gas in the Los Angeles Basin and in the San Francisco Bay area based on average daily usage of gas in these areas. Results of their calculations are displayed in Figs. 6.3 and 6.4 in terms of the combustion products of a given volume of gas in cubic centimeters per cubic meter of air.

In the Los Angeles Basin (Fig. 6.3) there are three grids (16-mi^2 areas) which have relatively high concentrations of combustion products at ground level due to releases from tall stacks. The peak concentration of combustion products in the air at ground level was estimated to be equivalent to that amount produced from combustion of 100 cm^3 of natural gas per cubic meter of air. It is estimated that the population-weighted mean concentration would be 13 cm^3/m^3 in the Los Angeles Basin. In the San Francisco Bay area (Fig. 6.4) the peak concentration is due primarily to ground-level sources and is estimated to be 13 cm^3/m^3. The population-weighted mean concentration is estimated to be 3.7 cm^3/m^3.

In Table 6.3 are tabulated the potential dose equivalents that could be attained in these two major metropolitan areas from the continuous use of natural gas having a concentration of 1 pCi/cm^3 of tritium. This represents a steady-state concentration of tritium that seems attainable for multiple well stimulation by

[9] D. G. Jacobs, E. G. Struxness, and C. R. Bowman, "A Preliminary Assessment of the Radiological Implications of Commercial Utilization of Natural Gas from a Nuclearly Stimulated Well," *Proceedings of the ANS Topical Meeting, Engineering with Nuclear Explosives, Las Vegas, Nevada, January 1970*, CONF-700101, vol. I, p. 831 (1970).

[10] S. R. Hanna and F. A. Gifford, Air Resources Atmospheric Turbulence and Diffusion Laboratory, Environmental Science Services Administration, Oak Ridge, Tennessee, private communication with D. G. Jacobs, October 1969.

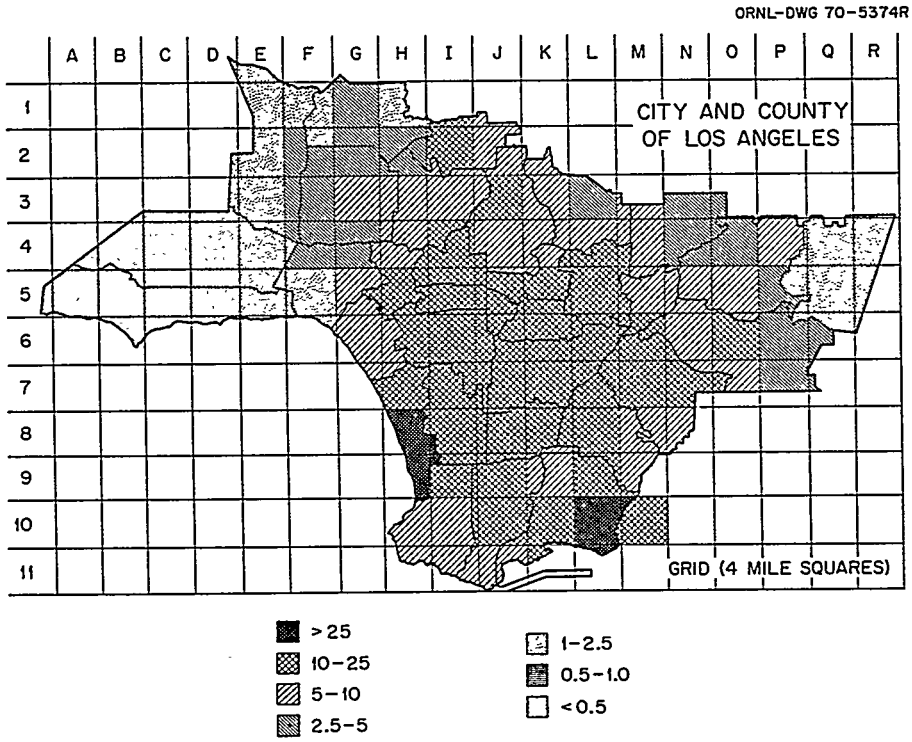

Fig. 6.3. Concentration of Combustion Products from Natural Gas in Air at the Ground Surface. The concentration is expressed as the equivalent content of the combustion products from the gas in cubic centimeters per cubic meter of air.

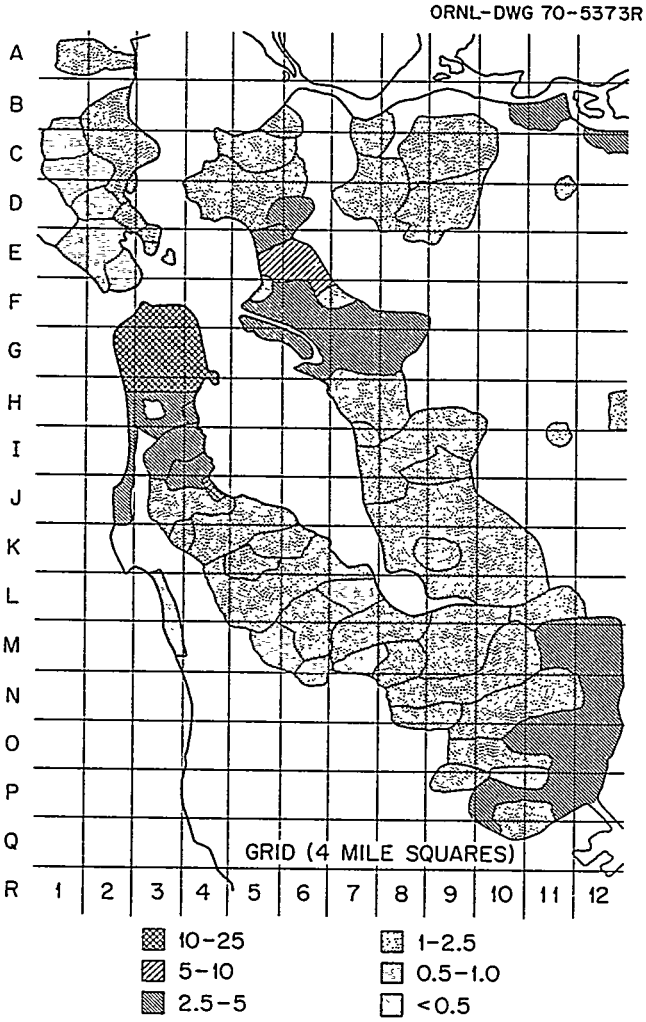

Fig. 6.4. Concentration of Combustion Products from Natural Gas in Air at the Ground Surface. The concentration is expressed as the equivalent content of the combustion products from the gas in cubic centimeters per cubic meter of air.

nuclear detonations. From these comparative numbers, it is seen that the major exposure would be expected to occur due to domestic consumption of gas.

In considering the values of dose equivalents presented in Table 6.3, we must remember that, although these hypothetical radiation exposures would give rise to potential doses of less than 170 millirems/year, the use of natural gas from nuclearly stimulated wells represents only one potential source of exposure. Also, in this part of the preliminary analysis, only direct modes of exposure through inhalation, submersion, and absorption through the skin have been considered. Additional efforts are being directed at other modes of exposure, such as ingestion, which may involve less direct exposure pathways. The recommendations of the ICRP[11] and other authorities[12,13] specifically require that radiation exposures from all sources, other than natural background and medical sources, be considered in any radiological safety evaluation.

Hazard of Exposure to Petrochemicals and Other Nonfuel Products from Contaminated Natural Gas

Although combustion is the predominant disposition of natural gas, a large and rapidly growing quantity of natural gas components is converted into a variety of chemical products. Some petrochemicals are marketed without further treatment, but others serve as intermediates in the manufacture of large-tonnage products such as synthetic rubber, detergents, fibers, resins, plastics, plasticizers, and fertilizers. Two major products not considered as petrochemicals are hydrogen and carbon black.

Figure 6.5 shows the disposition of natural gas hydrocarbons in 1956.[14] Although some recent trends in utilization of these hydrocarbons have been noted, such as increased recovery of ethane and higher hydrocarbons for chemical use, this diagram gives an approximate indication of the present use of natural gas hydrocarbons.

A number of years will be required to develop widespread exploitation of nuclearly stimulated natural gas reservoirs. Therefore a projection of future gas use is needed to evaluate the hazard of certain aspects of contaminated gas usage. The 1969 edition of *Gas Facts*[15] has such a projection to 1990. We selected the projected 1980 total sales figure of 27.1 billion therms, equivalent to 25.2 trillion cubic feet of gas, to calculate the hazard of the combustion products formed during the manufacture of carbon black from radioactive natural gas.

---

[11] International Commission on Radiological Protection, *Recommendations of the International Commission on Radiological Protection* (Report of Committee 2), ICRP Publication 2, Pergamon, London, 1959.

[12] National Commission on Radiation Protection, *Maximum Permissible Body Burdens and Maximum Permissible Concentrations of Radionuclides in Air and Water for Occupational Exposure,* National Bureau of Standards Handbook 69 (June 5, 1969).

[13] Federal Radiation Council, *Background Material for the Development of Radiation Protection Standards,* Federal Radiation Council Report No. 5 (July 1964).

[14] V. B. Guthrie, ed., *Petroleum Products Handbook,* pp. 12–15, McGraw-Hill, New York, 1960.

[15] American Gas Association, Inc., *1969 Gas Facts,* New York, 1969.

Table 6.3. Dose Equivalents from the Hypothetical Use of Natural Gas Containing 1 pCi/cm^3 of Tritium in the Los Angeles Basin and in the San Francisco Bay Area

Source of Exposure	Dose Equivalents (millirems/year)	
	Los Angeles Basin	San Francisco Bay Area
Atmosphere		
At point of peak concentration	0.19	0.024
Population-weighted average	0.024	0.007
Domestic use		
Nonvented heating and appliances[a]	2.0	2.5
All appliances vented except range	0.27	0.27
Weighted average[b]	0.45	0.49
Total		
Maximum exposure	2.2	2.5
Weighted average[b]	0.47	0.50

[a]Assumes 1700 degree-days of heating for Los Angeles and 2950 for San Francisco and a 1000-ft^2 residence of normal construction.
[b]Assumes nonvented heating for 10% of the population.

If we assume that a steady-state situation will exist in 1980, with newly stimulated gas wells brought into production as the quantity of gas available from older wells declines, and that only fission devices are used, average concentrations of 1 pCi/cm^3 for tritium and 0.5 pCi/cm^3 for ^{85}Kr seem reasonable.

Carbon Black

The total production of carbon black from natural gas and liquid hydrocarbons in 1966 was 2.6×10^9 lb. It is obvious that the only radioisotope that will be found in carbon black is ^{14}C. From the reported concentration of 0.5 pCi of $^{14}CH_4$ per cubic centimeter in Gasbuggy gas,[16] we estimate a value of 10^3 pCi of ^{14}C per gram in carbon black produced from undiluted Gasbuggy gas. About 0.4 to 0.5% of the carbon black produced in 1964 and 1965 was used as a chemical or in food production. It seems unlikely that the concentration of carbon black in food products would exceed a few tenths of a percent, but at 1% the ^{14}C content of the food material would be 10 pCi/g.

The daily intake of carbon-containing food is about 500 g. At this intake rate the ^{14}C ingested would amount to 5×10^{-3} μCi/day, and continuous consumption would give 0.085 μCi for the resulting body burden of ^{14}C. This body burden would give rise to a whole-body dose rate of 1 millirem/year.

We must also consider the hazard from exposure to the radioisotopes in the combustion products evolved in manufacturing carbon black. Assuming that the distribution shown in Fig. 6.5 applies to 1980 gas production, the yearly consumption of natural gas for carbon black production (assuming that only gas is used) is projected to be 4.5×10^{11} ft^3, which would hypothetically contain 1.3×10^4 Ci of tritium and 6.5×10^3 Ci of ^{85}Kr. This is equivalent to 35 Ci/day of tritium and 18 Ci/day of ^{85}Kr. If we further assume no change in the number of United States carbon black plants in the interval 1966–1980 and that all 34 plants[17] are equal in size, each plant would emit 1 Ci of tritium and 0.5 Ci of ^{85}Kr per day. The annual tritium production rate of 1.3×10^4 Ci from carbon black production is quite small compared with the natural production rate of 4 to 8×10^6 Ci/year. The plant emission rates are quite low, and the radioisotopes would be greatly diluted by use of plant stacks.

Ammonia Fertilizer

Ammonia is produced by reaction of hydrogen from natural gas with nitrogen. Hydrogen production from

[16]C. F. Smith, Jr., *Project Gasbuggy Gas Quality Analysis and Evaluation Program – Tabulation of Radiochemical and Chemical Analytical Results*, UCRL-50635, rev. 1 (November 1969).

[17]U.S. Bureau of Mines, *Minerals Yearbook – 1967*, vols. I and II, pp. 263–72, Washington, D.C., 1968.

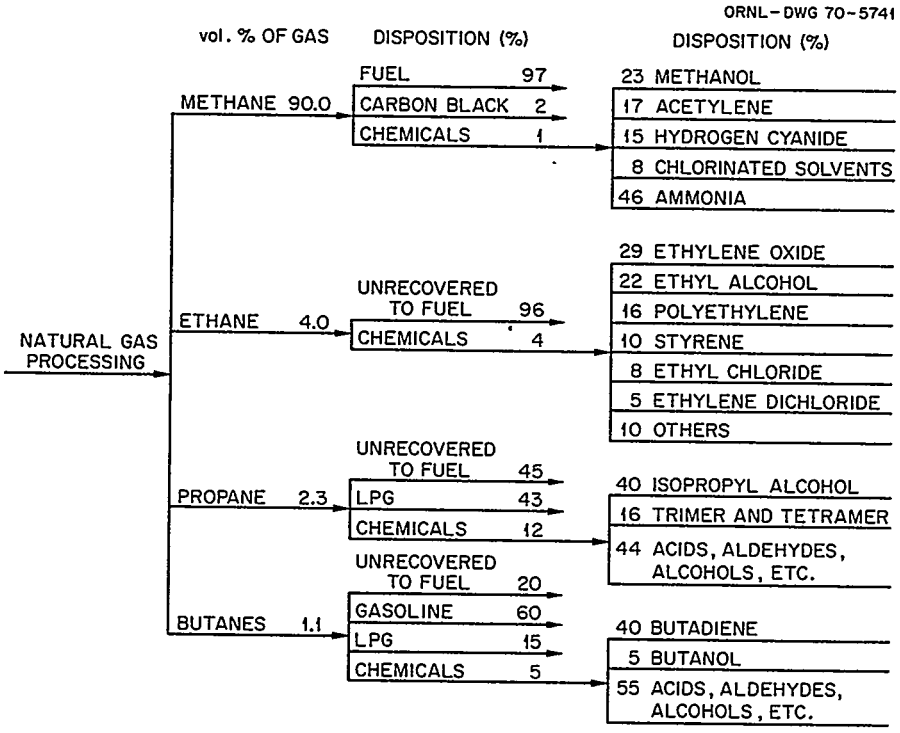

Fig. 6.5. Disposition of Natural Gas Hydrocarbons in 1956.

all sources was recently reported[18] to be 2.5×10^{12} ft^3. The same publication showed that hydrogen was being produced from methane at a cost of \$0.21/Mcf compared with \$4.00/Mcf by electrolysis. It seems safe to assume, therefore, that all synthetic NH_3 used in fertilizers comes from natural gas. It was also reported that 35% of the hydrogen (8.75×10^{11} ft^3/year) was used to make ammonia. Since two volumes of hydrogen are produced from each volume of methane, assuming 100% conversion, 4.4×10^{11} ft^3/year of CH_4 would be required to produce this amount of hydrogen. This is equivalent to 5.8×10^{11} ft^3/year of NH_3 or 2.8×10^{10} lb of NH_3 per year.

If we assume that the tritium concentration in natural gas is 1 pCi/cm^3 and that all the tritium is present as CH_3T, the resulting tritium concentration in NH_3 would be 0.43 μCi/lb. For the calculation of tritium absorption in fertilized food materials, we assume an ammonia application rate of 100 lb/acre-year, annual rainfall of 40 in. (4000 m^3/acre), uniform dilution of tritium, and grain production of 100 bu/acre at 60 lb/bu. Dilution of the tritium with incident rainfall would result in a tritium concentration in the groundwater of about 10^{-2} μCi/m^3. If the grain produced is 20% moisture by weight, the tritium content of the grain as moisture would be about 9×10^{-7} μCi/lb. Incorporation of tritium into carbohydrates would add about 2.2×10^{-6} μCi/lb for a total content of 3.1×10^{-6} μCi of ^3H per pound. Daily consumption of the equivalent of 2 liters of water plus 1 lb of grain would correspond to a daily tritium intake of 2.3×10^{-5} μCi and would be contributed mainly by the water. Continuous consumption would result in a body burden of 4×10^{-4} μCi of tritium, corresponding to an annual dose rate of about 2 microrems to body tissue.

Hydrogenated Fats and Oils

Another hazard that must be considered from the use of natural gas contaminated with tritium is the use of hydrogen gas for hydrogenation of foodstuff. Approximately 10^9 ft^3 of H_2 was used in the hydrogenation of fats and oils in 1967.[19] If we assume that the natural gas from which the hydrogen was produced had a tritium concentration of 1 pCi/cm^3 and that oleic acid with a molecular weight of 282 is typical of unsaturated fats and oils, we can calculate the hypothetical tritium

[18] J. H. Finneran and P. J. Mazur, "Plant Size and Feed: Key to Lower Hydrogen Costs," *Oil Gas J.* 67(29), 70–74 (July 21, 1969).

[19] *Chem. Eng. News* 45, 20 (Nov. 27, 1967).

content of the hydrogenated product. Since 2 moles of H_2 are produced from 1 mole of CH_4, the principal constituent of natural gas, the concentration of tritium in the hydrogen would be about 0.5 pCi/cm^3, or 1.4 X 10^4 pCi/ft^3. It follows then that 1 lb of hydrogenated oleic acid would contain 0.018 μCi. Daily consumption of ¼ lb of hydrogenated product would result in the attainment of a body burden of tritium amounting to 0.08 μCi, corresponding to an annual dose rate of 0.4 millirem to body tissue.

Ethyl Alcohol

Although a large fraction of the ethyl alcohol produced from natural gas is undoubtedly used to manufacture other products such as synthetic rubber, we must consider the possibility that tritiated ethanol might be drunk by human beings. We have assumed that the contaminated natural gas has the chemical composition of Gasbuggy gas in June 1969[20] with an ethane concentration of 6.95% and that 16% of the hypothetical tritium concentration (1 pCi/cm^3) is C_2H_5T. Then we can calculate that 1 μCi of tritium could be contained in 1000 g or 1300 cm^3 of ethanol product. A concentration of 0.15% of alcohol in the blood is a generally accepted definition of intoxication level. For an average-sized individual containing 5.2 liters of blood, this corresponds to 7.8 cm^3 alcohol. If we assume that all body water has this concentration of alcohol, approximately 90 cm^3 of ethanol would be required to intoxicate a 150-lb adult. A person in a continual state of drunkenness could attain a body burden of 1.2 μCi of tritium and receive an annual radiation dose to body tissue of 6 millirems.

Other Products

Although other compounds in addition to those considered here may find use in foods or beverages, it seems unlikely that the hazard of human consumption of such products will be significantly greater than that of tritiated fats or of beverage alcohol. Other products such as plastics, resins, and synthetic rubber would present only the hazard of external radiation. Since tritium emits only beta particles with a maximum energy of 18 keV, it appears probable that the hazard of all noningested tritium-contaminated products is negligibly small. Their combustion products could be absorbed by the body, but this is not an ordinary treatment of most materials manufactured from petrochemicals.

[20] C. F. Smith, Jr., *Project Gasbuggy Gas Quality Analysis and Evaluation Program, Tabulation of Radiochemical and Chemical Analytical Results,* UCRL-50635, rev. 1 (November 1969).

DEVELOPMENT OF RADIATION SAFETY GUIDES FOR TRANSIENT EXPOSURES

P. S. Rohwer E. G. Struxness
S. V. Kaye R. S. Booth
J. R. Lund B. F. Roberts

The continuing promise of peaceful applications of nuclear explosives for excavations, and the radioactivity release potential of these applications, has stimulated interest in the development of radiation safety guides specific for transient exposure situations. The transient exposures envisioned involve potential radiation dose contributions from radionuclides which may be internal and/or external to the body. Duration of the radionuclide intake and external exposure, in this context, may extend up to a few hundred hours. The exposure is assumed to be attributable to a specific excavation event; if this event specificity is lost, the radioactive materials become a part of worldwide fallout and, as such, are subject to other radiological safety considerations. Transient exposure guides are to facilitate first-cut assessments of environmental releases of radioactivity from Plowshare events on the basis of total radiation doses which may be received by the individuals exposed. The aim is to interpret time-integrated radionuclide concentrations in air, measured during passage of the radioactive cloud, in terms of appropriate radiation safety standards. These interpretations will then support judgments concerning the need for protective actions or the testing of compliance with regulations governing environmental releases of radioactivity.

General Approach

The primary standards recommended by the ICRP are specified in terms of a maximum permissible annual dose (rems/year).[21] For internal dose purposes a secondary guide (maximum permissible organ burden) is estimated on the basis of the primary standard. This secondary guide is used in calculating maximum permissible radionuclide concentrations in air and water such

[21] International Commission on Radiological Protection, *Recommendations of the International Commission on Radiological Protection (Report of Committee 2 on Permissible Dose for Internal Radiation),* ICRP Publication 2, Pergamon, London, 1959.

that the maximum permissible annual dose rate to the reference organ would not be exceeded during 50 years of continuous exposure. A similar approach was used to develop transient-exposure guides.[22] The important difference is the relatively short period during which the individual is exposed externally or during which there is intake of radioactive material into the body. The primary standards used ("selected annual dose limits") are adapted from the radiation safety standards recommended for members of the public by recognized authorities. Selected annual dose limits should reflect an apportionment of the permissible radiation dose to members of the public from all sources excluding medical exposures and natural background.

Guide Format

Visualize downwind movement of a radioactive cloud at ground surface as the source for a transient exposure. Individuals submerged in that cloud immediately incur a dose commitment due to radionuclide intake as well as an external radiation dose. Radiation doses to be expected due to inhaled radioactivity can be estimated from a knowledge of cloud concentration and duration along with certain metabolic and physiological parameters (standard man)[21] characterizing the individuals exposed. Radiation doses to be expected due to some other exposure modes of potential importance (e.g., external exposure to contaminated land surface, external exposure due to submersion in contaminated surface water, and internal exposure resulting from ingestion of contaminated foods and beverages) cannot be estimated on the basis of standard man and cloud parameters alone; such doses will be influenced by many environmental and behavioral factors which are difficult to evaluate. Therefore, initial development of transient-exposure guides was limited to consideration of only the dose resulting from radionuclide inhalation.

Radionuclide intake must be evaluated to assess an event evolving internal dose commitments. Intake for an inhalation exposure is a function both of radionuclide concentration in the inhaled air and of intake duration. This suggested use of a factor with units of concentration (microcuries per cubic centimeter) and time (hours) when giving general guidance for exposure via inhalation. As a result a transient-exposure guide CUE (CUmulative Exposure) with units of microcurie-hours per cubic centimeter is under development. CUE is defined as a time-integrated radionuclide concentration in air based on radiation safety standards intended to limit dose to members of the public from all exposure modes. These transient-exposure guides are intended for use in the first-cut assessment of releases of radioactive materials to the environment.

Calculation of CUE

Two methods for calculating CUE are under development in an attempt to suggest CUE's which permit optimal distribution of dose among potential dose-contributing events and, at the same time, prevent accumulation of dose commitments which could hamper Plowshare activities in future years.

The first method for calculating CUE is based on an organ-burden limitation. The initial step in this method is determination of the organ burden consistent with the selected annual dose limit.[23] The organ burden estimate is used in conjunction with an uptake fraction and an inhalation rate to determine CUE ($CUE^{inh.}$) for a single-mode (inhalation) exposure as follows:

$$CUE_{ij}^{inh.} = \frac{b_{ij}}{(f_a)_{ij}\, 8.33 \times 10^5}, \qquad (1)$$

where

$CUE_{ij}^{inh.}$ = transient-exposure guide (μCi-hr/cm^3) for ith radionuclide based on exposure of jth organ via inhalation only,

b_{ij} = burden (μCi) for ith radionuclide in jth organ, consistent with selected annual dose limit,

$(f_a)_{ij}$ = fraction of inhaled ith radionuclide reaching jth organ,

8.33×10^5 = inhalation rate (cm^3/hr).

Control of an exposure situation to meet this time-integrated radionuclide concentration in air ($CUE^{inh.}$) will restrict the inhalation dose to the jth organ in accordance with an organ burden consistent with the annual dose limit selected for that organ. Depending upon the effective half-time of a radionuclide in the reference organ, a transient exposure equivalent to $CUE^{inh.}$ limited by the organ burden may yield a dose

[22] E. G. Struxness and P. S. Rohwer, "An Approach to the Development of Guidelines for Plowshare," presented at the 2nd Session of U.S.–U.S.S.R. Technical Talks in Moscow, Feb. 10–18, 1970.

[23] P. S. Rohwer and E. G. Struxness, *Quarterly Progress Report on Radiological Safety of Peaceful Uses of Nuclear Explosives: Development of Transient-Exposure Guides*, ORNL-TM-2810 (May 1970).

which is less than the selected annual dose limit. When that situation exists (radionuclides with short effective half-times) additional exposures equivalent to the $CUE^{inh.}$ may be permitted within the same year. The maximum number of events permitted within one year or within a lifetime is inversely related to the effective half-time of radionuclide in the reference organ. For radionuclides with very long effective half-times, only one transient exposure equivalent to a $CUE^{inh.}$, limited by the organ burden, is permitted within a lifetime; such an exposure is not recommended because it leaves no reserve for future exposures, expected or unexpected. The second method for calculating CUE provides more conservative guidance for radionuclides with long effective half-times in reference organs.

The second method for calculating CUE is based on a dose commitment limitation. "Dose commitment" is defined as the total dose an individual will accrue within his lifetime as the result of a radionuclide intake. A $CUE^{inh.}$ calculated with the following method is intended to restrict intake via inhalation such that the resulting dose commitment will not exceed the selected annual dose limit.

$$CUE_{ij}^{inh.} = \frac{R_j}{d_{ij}^{inh.}\, 8.33 \times 10^5}\ \mu\text{Ci-hr/cm}^3\ , \qquad (2)$$

where

R_j = selected dose limit (rems/year) for jth organ, as apportioned to type of exposure under consideration,

$d_{ij}^{inh.}$ = dose commitment to jth organ per microcurie of ith radionuclide inhaled [rems/lifetime (years)/μCi],

8.33×10^5 = inhalation rate (cm^3/hr),

and $CUE_{ij}^{inh.}$ is defined as for Eq. (1). $CUE^{inh.}$ values obtained with this method are less restrictive (larger) for radionuclides with short (less than a few months) effective half-times and are more restrictive (smaller) for radionuclides with long (years) effective half-times. Dose commitment ($d_{ij}^{inh.}$) to the reference organ is estimated with the INREM computer code.[24] Only one event resulting in an exposure equivalent to a $CUE^{inh.}$ determined with Eq. (2) would be permitted in one year. However, because dose commitment incurred per event does not exceed the selected annual dose limit, similar events would be permitted in succeeding years, even for radionuclides with very long effective half-times.

Adjustment for Additional Exposure Modes

An exposure equivalent to $CUE^{inh.}$ would result, according to present dose estimates, in a dose or dose commitment via inhalation which is equal to the selected annual dose limit. Any dose or dose commitment from other exposure modes would result in a total dose or dose commitment exceeding that limit. For that reason, $CUE^{inh.}$ must be reduced proportionately, depending upon dose contributions from other exposure modes. $CUE^{inh.}$ values from Eqs. (1) and (2) may be adjusted in the following manner:

$$CUE_{ij} = CUE_{ij}^{inh.} \frac{R_j}{R_j + (D_{ij} - D_{ij}^{inh.})}\ , \qquad (3)$$

where

CUE_{ij} = transient exposure guide (μCi-hr/cm^3) for ith radionuclide based on exposure of jth organ via all exposure modes,

D_{ij} = dose or dose commitment (rems/year) to jth organ from ith radionuclide via all exposure modes for an exposure equivalent to $CUE_{ij}^{inh.}$,

$D_{ij}^{inh.}$ = dose or dose commitment (rems/year) to jth organ from ith radionuclide via inhalation only for an exposure equivalent to $CUE_{ij}^{inh.}$,

and $CUE_{ij}^{inh.}$ and R_j are as defined previously. Omission of any exposure mode which contributes significantly to D_{ij} will result in a CUE_{ij} value which is too large, and individuals exposed will be subject to doses or dose commitments exceeding the selected annual dose limit.

Modification of $CUE^{inh.}$ to incorporate external dose contributions resulting from submersion in a radioactive cloud is one of the easier adjustments. External dose via the submersion mode, assuming a uniform cloud, is a function primarily of radionuclide concentration in the cloud and cloud residency time. Doses to be expected via this mode can be estimated with the EXREM computer code.[24]

Adjustment of $CUE^{inh.}$ to include possible dose contributions resulting from ingestion of radioactive materials is more difficult. In this case, doses cannot be estimated on the basis of standard man and cloud

[24] W. D. Turner, S. V. Kaye, and P. S. Rohwer, *EXREM and INREM Computer Codes for Estimating Radiation Doses to Populations from Construction of a Sea-Level Canal with Nuclear Explosives*, K-1752 (Sept. 16, 1968).

parameters alone; as mentioned earlier, such doses will be influenced by many environmental and behavioral factors which are difficult to evaluate. Initial effort in this area was limited to one exposure pathway, the fallout-milk-man food chain, shown in Fig. 6.6 in its simplified form. The objective was to quantitate transfer of radioactive iodine, cesium, and strontium from a given concentration in air 1 m above a pasture to milk produced by cows which forage that pasture. This potential exposure situation may be represented by a series of compartments which when coupled together with appropriate transfer coefficients form a series of pathways from air to milk. However, the only pathway of importance appears to be the one shown in Fig. 6.6. Incentive for this study is the need to accurately predict radioactivity concentrations in milk from time-dependent radionuclide sources in air, measured at the time of cloud passage, with a model that allows wide variation in such parameters as source specification, transfer coefficients, weather conditions, and countermeasures. This latter objective is accomplished by an analog solution to equations written for each compartment of the model. Emphasis of previous work by others in this area was either to determine the maximum possible concentration in milk or to model specific experiments. Particular attention is given to those experiments in this work since the aim is to predict an experimental value under widely varying ecological conditions. Transfer coefficients are derived completely from experimental measurements, and the test of the model is against experiments. Special attention is given to ensure that the model obeys obvious, but mathematically powerful, constraints

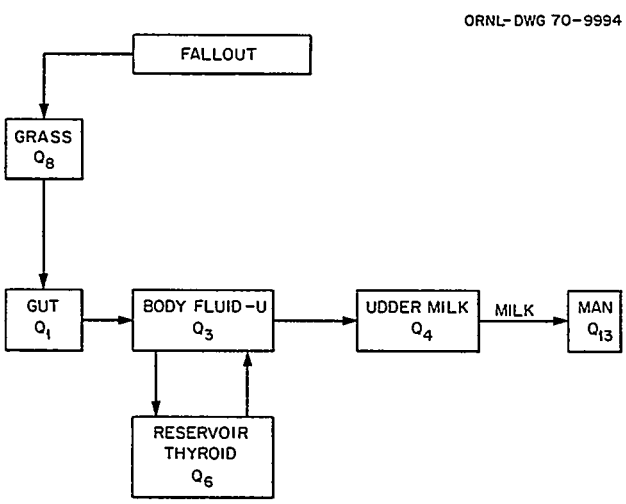

Fig. 6.6. Simplified Block Diagram of the Fallout-Milk-Man Food Chain.

which include conservation of amounts of radioactivity introduced into the system and conservation of mass in each compartment. Experience has shown that this model, which is not nearly as complicated as the system it represents, is able to describe the dynamics of the transfer of radioisotopes through the milk pathway. Time-dependent concentrations of radioactivity in milk lead to daily radionuclide intakes which are inputs to the INREM computer code for estimating dose to man. Resulting dose estimates are used to calculate CUE values for exposure situations which include the milk pathway.

Use of CUE

The CUE for each radionuclide is calculated assuming no other radionuclides are present. Assessment of a one-radionuclide event in terms of selected annual dose limit is accomplished by a direct comparison of the time-integrated exposure (microcurie-hours per cubic centimeter) with the appropriate CUE. Assessment of an event involving a mixture of radionuclides requires an additional calculation. A multiradionuclide event must satisfy the following condition for each organ if the total dose expected from all radionuclides is not to exceed the selected annual dose limitations:

$$\sum_{i=0}^{n} \frac{E_i}{\mathrm{CUE}_{ij}} \leqslant 1 , \qquad (4)$$

where E_i is the time-integrated exposure for the ith radionuclide, and CUE_{ij} is defined as for Eq. (3). If three or more organs each yield a value greater than 0.5 for Eq. (4), the exposure should also be considered excessive. These suggestions for handling multiradionuclide and multiorgan exposures are adapted from ICRP recommendations for occupational workers.[22,25]

Future Development of CUE

Consideration of additional elements for study in the fallout-milk-man food chain and additional pathways for exposure modes already discussed (e.g., ingestion via vegetables, fruits, and meats) is in a preliminary stage of development. Plans also include addition of other exposure modes; submersion in contaminated water, exposure to contaminated land surface, and exposure

[25] International Commission on Radiological Protection, *Recommendations of the International Commission on Radiological Protection* (adopted Sept. 17, 1965), ICRP Publication 9, Pergamon, London, 1966.

due to contaminated body surfaces are examples. The goal is to include all principal exposure modes and pathways in a simple guide for transient exposures – a quest to generalize – and yet retain flexibility to adjust to the unique features of each exposure situation.

Heavy reliance is placed upon metabolic parameters developed for standard man and the continuous (50 years) exposure situation. Suitability of these parameters for transient exposure situations should be verified, particularly for radionuclides with long effective half-times and intricate redistribution patterns in the body. Several of these parameters are age dependent. CUE's could be calculated for various age groups, depending upon the availability of data to evaluate age-dependent parameters. Protection of the most radiosensitive age groups within the exposed populations is the desired end result.

The need to identify radionuclides quantitatively before appropriate CUE's can be applied is recognized. This could require a sophisticated air monitoring system with tedious and time-consuming data analysis in some cases. Unfortunately, development of a CUE for unidentified radionuclides, a possibility to be considered, is not foreseen at present.

Actual calculation of CUE's for possible suggestion as guides for transient exposures awaits further development and analysis of the concept.

DOSE ESTIMATION STUDIES RELATED TO CONSTRUCTION OF AN INTEROCEANIC CANAL WITH NUCLEAR EXPLOSIVES

S. V. Kaye P. S. Rohwer

This report summarizes contributions of the Health Physics Division to the Bioenvironmental Radiological Safety Feasibility Study of a sea-level canal excavated with nuclear explosives. External exposure to contaminated landscape and internal exposure from ingestion of contaminated foods and beverages were the only modes of exposure considered. Parameters in internal dose models were adjusted to differentiate five age groups within each of four indigenous populations and nine reference organs. These populations were further differentiated on the basis of diet and estimates of time- and age-dependent concentrations of radioactivity in dietary items. Intake functions (microcuries ingested per day) for internal dose estimates were average values for watersheds with highest initial areal concentration

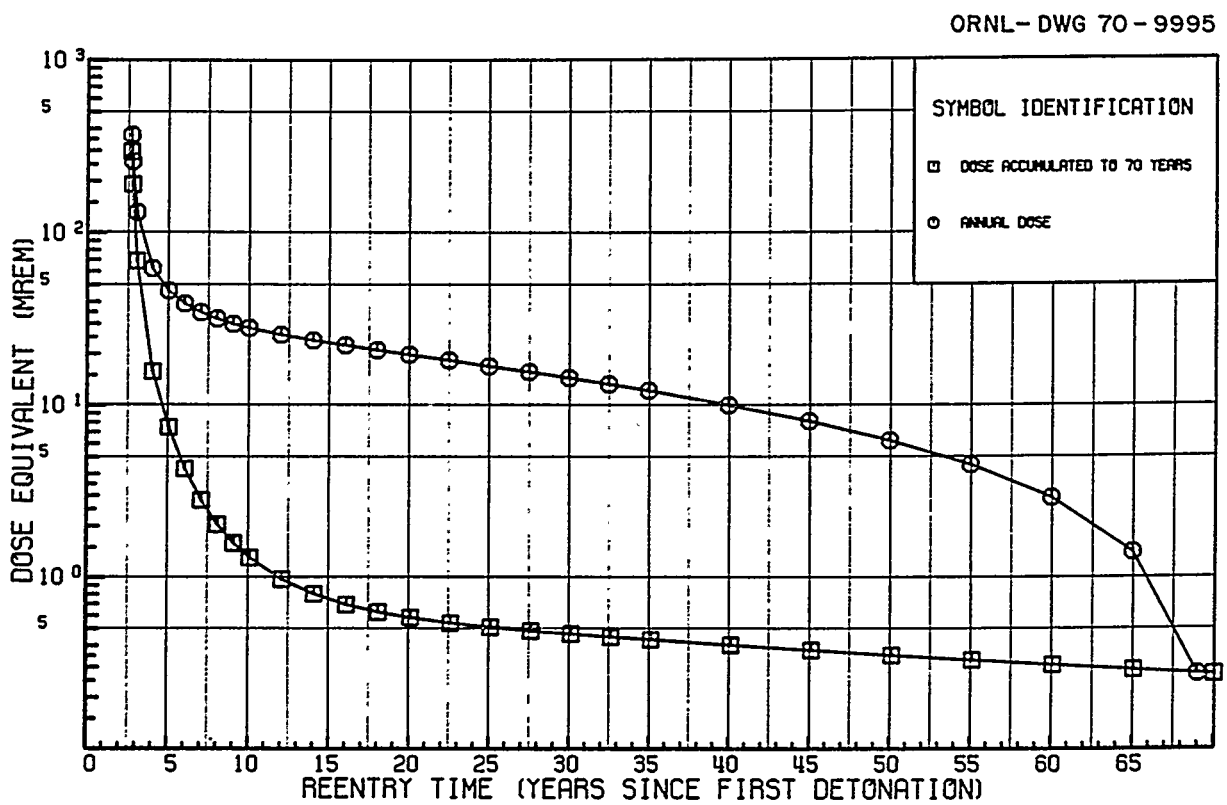

Fig. 6.7. External Gamma Dose 1 m Above Landscape at Chepigana, Panama, Plotted as a Function of Reentry Time.

of fallout along each route, whereas external doses were computed for 13 locations (towns and villages) in watersheds of the exclusion zone of Route 17 only. Estimates of potential external doses were based on 170 radionuclides; only 31 radionuclides were considered in detail for estimation of potential internal doses, with an approximate estimate of total dose from radionuclides not included in the list of 31.

Estimates of potential total doses (internal dose from ingestion plus external dose from landscape) were assessed in terms of radiation safety criteria recommended for members of the public by recognized authorities. The basic criteria were: annual dose limit to total body of 0.17 rem/year and a genetic dose limit of 5 rems in 30 years.

Estimates of potential external gamma dose (millirems) accumulated to 70 years after the initial detonation and the estimates of yearly dose rates (millirems/year) are shown in the cathode ray tube (CRT) plots of Fig. 6.7 for Chepigana, one of the 13 locations in Panama for which dose estimates were made. The first point on the graph represents 30 days after the last detonation (2.65 years after the first detonation), which is the earliest reentry time considered. At Chepigana, approximately 98.7% of the potential 0-to-70-year dose (5.21 rems) is accrued the first 3 years after the initial detonation (approximately six months after the last detonation). A great reduction in potential external dose could be realized at all of the locations studied if reentry is delayed long enough to allow for the decay of relatively short-lived radionuclides.

The estimated instantaneous dose rate (rems per hour) as a function of reentry time for Chepigana is shown in Fig. 6.8. Dose rates were estimated for all 13 locations, but only one example is shown here. Dose rates below 10^{-6} rem/hr are plotted at 10^{-6} rem/hr (8.8 millirems/year) for convenience in the CRT graphical output. These graphs indicate the potential dose rates that construction personnel might experience in the exclusion area. The nine "spikes" in this CRT plot correspond to the approximate time of arrival of fallout from individual detonations.

Estimated dose commitment to the total body from ingestion of contaminated foods and beverages is shown in Fig. 6.9 as a function of reentry time to watershed 5

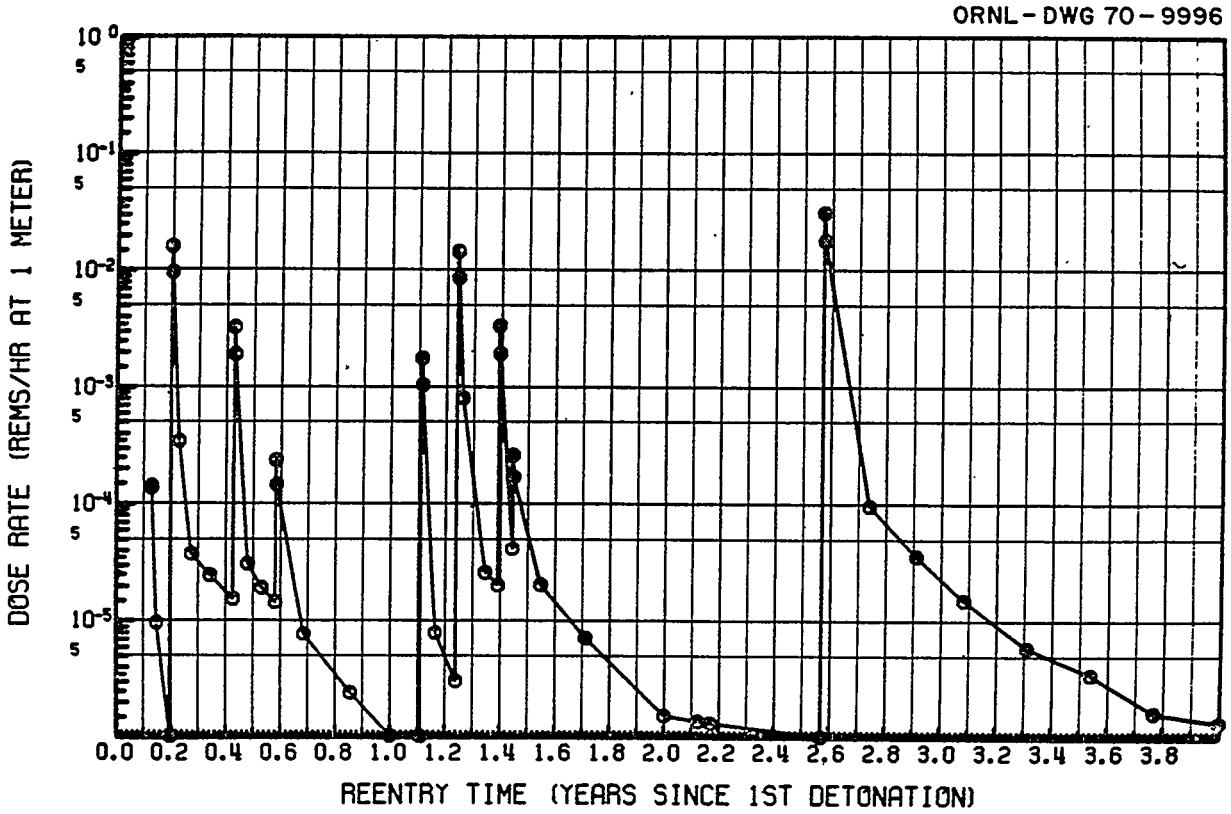

Fig. 6.8. Instantaneous External Dose Rate 1 m Above Landscape at Chepigana, Panama.

ORNL- DWG 70-9997

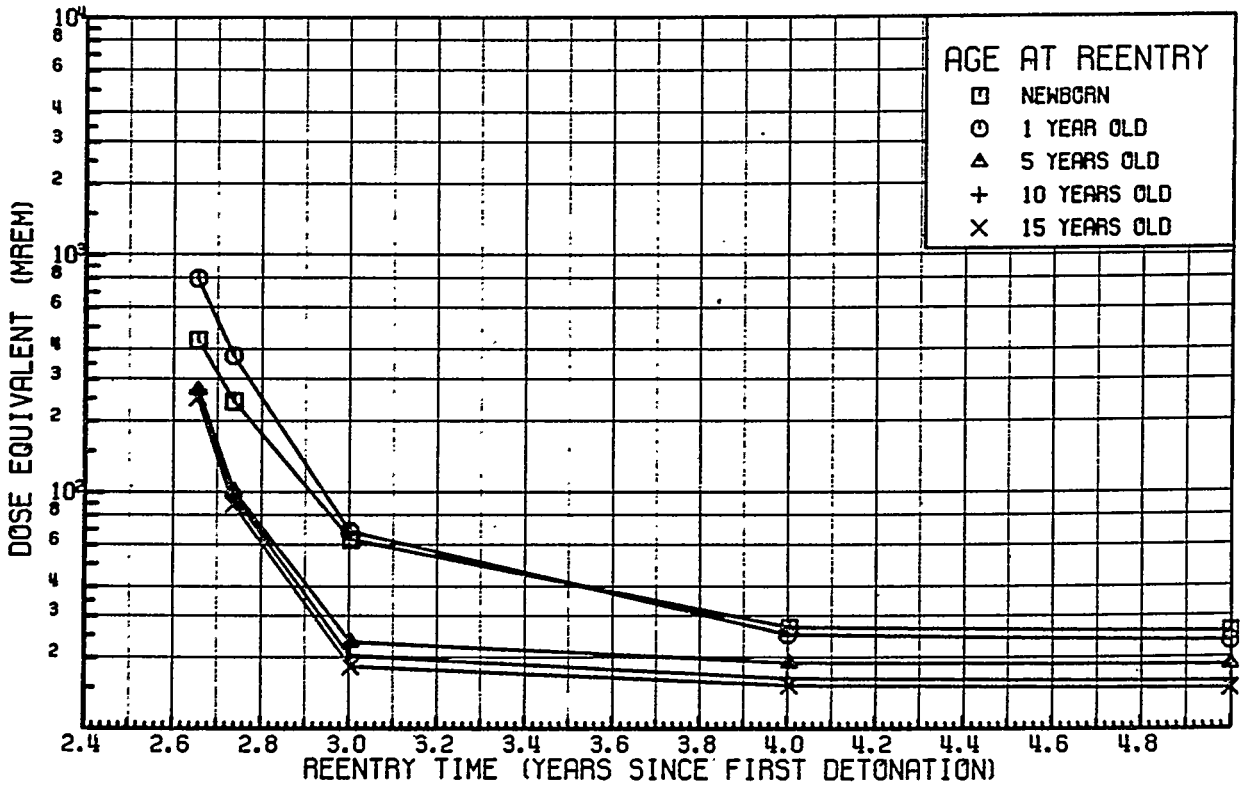

Fig. 6.9. Dose Commitment to the Total Body of Choco Indians from Ingestion of Contaminated Foods and Beverages, Watershed 5, Panama.

in Panama for five age groups of Choco Indians. Dose commitment is an estimate of the maximum internal dose an individual can receive due to radionuclides taken into the body (i.e., the dose already received plus the dose to be received in his remaining lifetime). Figure 6.9 is an example of the type of dose estimates made for all reference organs, age groups, and ethnic groups considered for Panama and Colombia. Interpopulation variations for a given age group and reference organ were attributable to dietary differences, because daily radionuclide intake was the only parameter used to differentiate the four populations. Intrapopulation variations, on the other hand, reflected the influence of the five parameters used to differentiate age groups. Only the first four years after the first detonation are shown in the CRT plots of dose commitment of Fig. 6.9, because the differences among age groups for later times are negligible. Estimated annual dose rates had a similar behavior and declined to less than 10 millirems/year soon after the last detonation.

The sum of potential internal dose to the whole body and potential external dose to the whole body from a contaminated land surface is plotted in Fig. 6.10 for watershed 5 of Panama. Although external dose was dominant at all postevacuation times, that dominance increases for later reentry times. One probable explanation for this increasing dominance of external dose is the fact that radioactive decay was the only parameter considered as reducing the external exposure as a function of time.

Assessments based on somatic doses suggest reentry to the watershed receiving the highest initial areal contamination may be appropriate eight to ten years after the last detonation. Children less than five years of age at the time of reentry may be the critical age group among those age groups for which doses were estimated. Within this age group, no single ethnic group emerged as the most critical. Assessments based on genetic dose appear to be less limiting, suggesting reentry may be possible within months following the last detonation. These assessments are based on comparisons with the total doses allowed under the radiation safety criteria. In actual practice, apportionment of these criteria would be likely. Such an apportionment would be undertaken by countries involved.

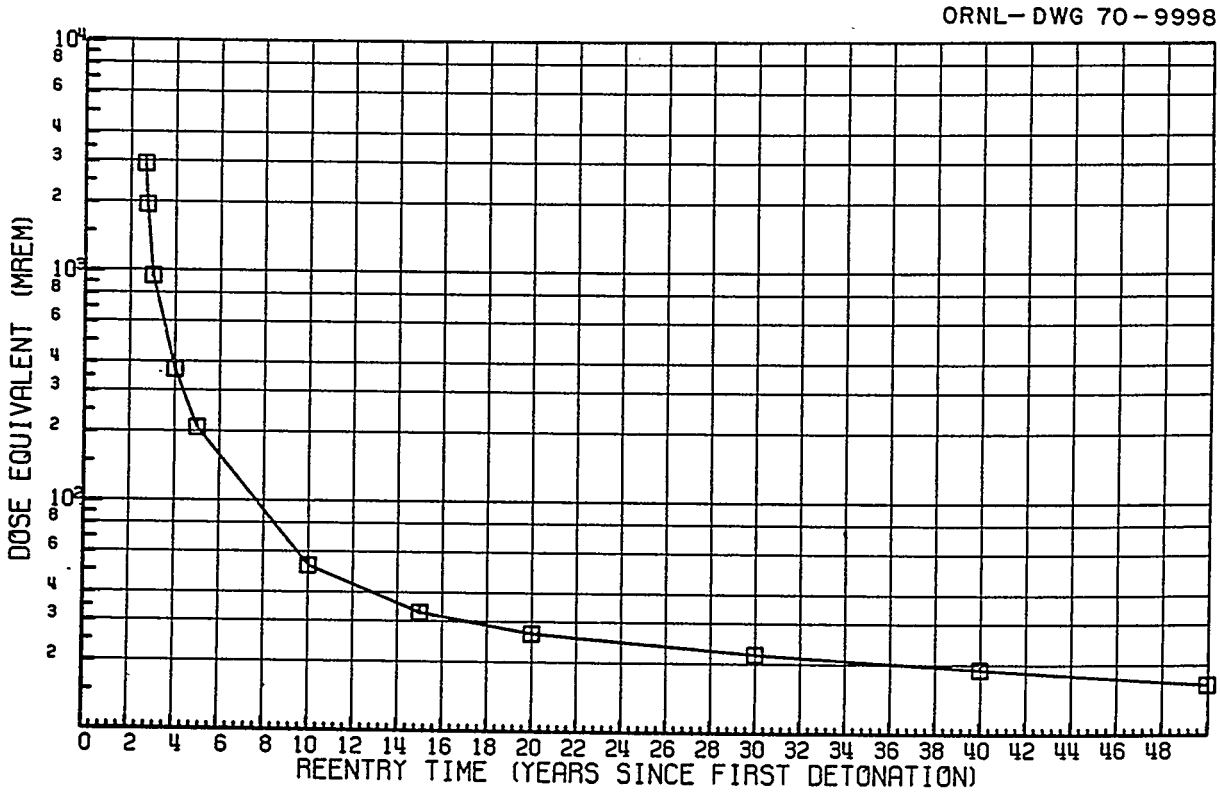

Fig. 6.10. Annual Dose to Total Body from the Two Modes of Exposure Considered (Ingestion of Contaminated Foods and Beverages and Exposure to a Contaminated Landscape), Watershed 5, Panama.

7. Related Cooperative Projects

COOPERATION OF OTHER AGENCIES IN ORNL STUDIES

The research and development program of the Radioactive Waste Disposal Section is of special interest to various public and private agencies. Several study projects provide an opportunity for others to participate, both to supplement the Laboratory's research effort and to gain information and experience of value to the other agency. The ways in which another agency may cooperate include: assignment of on-loan personnel as temporary additions to the ORNL staff, performance of specific work under cooperative agreements to augment ORNL programs, work authorized under ORNL subcontracts and performed by the contracting agency, and coordination of related work projects with ORNL projects for mutual benefit.

Waste Management Studies

Agencies participating in these programs during the past year have included The Carey Salt Company of Hutchinson, Kansas, and the New York State Atomic and Space Development Authority. Results of the cooperative program with the former agency are included in Sect. 3, "Disposal in Natural Salt Formations," and of the latter agency in Sect. 2, "Disposal by Hydraulic Fracturing."

VISITING INVESTIGATORS FROM ABROAD

During the year, one noncitizen guest participated as a temporary member of the research staff of the Section.

NUCLEAR SAFETY REVIEW

One member of the Section served on the staff of *Nuclear Safety* as assistant editor. During the year, several individuals in the Section contributed review articles which were published under the category "Consequences of Activity Release."

PARTICIPATION IN EDUCATIONAL PROGRAMS AND COOPERATION WITH OTHER AGENCIES

A series of lectures was presented on Health Physics Aspects of Radionuclides Released to the Environment at a health physics training course sponsored by ORAU. One member of the Section served as a member of the Southern Governor's Conference Task Force for Nuclear Power Policy on a group devoted to public health (administered by the Southern Interstate Nuclear Board).

LABORATORY PROJECTS

Several members of the Section served as part-time staff members of the Nuclear Safety Information Center, the Civil Defense Research Project, and the agroindustrial complex study.

Part II. Radiation Physics

R. D. Birkhoff R. H. Ritchie

8. Theoretical Radiation Physics

Jacob Neufeld
R. H. Ritchie
V. E. Anderson[1]
J. C. Ashley
W. Brandt[2]
J. J. Cowan[3]
Julian Crowell[2]
Joice Doolittle[4]
J. M. Elson[5]
Kenneth Fox[2]
W. R. Garrett
R. N. Hamm
Vinod Krishan[6]
Betty McGill
H. C. Schweinler
S. Y. Shieh[2]
W. S. Snyder
J. E. Turner[7]
R. B. Vora[8]
H. A. Wright

RADIATION QUANTITIES AND THEIR SIGNIFICANCE IN HEALTH PHYSICS

A critical appraisal is made of quantities and units in radiation protection work, and a different approach is suggested for establishing permissible limits of radiation exposure. There is an ambiguity in the current health physics terminology, particularly with reference to such quantities as the dose equivalent. It is pointed out that dose equivalent has been specified for a macroscopically small volume element Δv around a point r in a medium which can be a phantom or a human body. In such case the dose equivalent has been assumed to vary from one point to another; it is therefore a field quantity, representing a condition spatially distributed in the medium. There exists, however, another quantity erroneously called "dose equivalent" which is not a field variable but a single numerical entity. This other quantity, which for all practical purposes has remained anonymous, represents the "amount" of exposure and is related to what is known to be the maximum permissible dose (MPD).[9]

There is also confusion in speaking about the quality factor (QF). The name "quality factor" is currently used to represent several quantities, conceptually different one from the other, and the usefulness of some

[1] On loan from Computing Technology Center (ORGDP).

[2] Consultant.

[3] Radiological Health Physics Fellow; consultant.

[4] Postdoctoral Fellowship.

[5] Oak Ridge Graduate Fellow.

[6] Graduate student, University of Tennessee.

[7] Presently on assignment to Health Physics Group, CERN, 1211 Geneva 23, Switzerland.

[8] World Health Organization Fellow from Bhabha Atomic Research Centre, Bombay-74, India.

[9] *ICRP Publication 9*, p. 14, Pergamon, London, 1966.

interpretations of the (QF) is open to question. In one case (QF) applies to charged particles and represents a "weighting factor," directly dependent on the linear energy transfer. It can therefore be represented as $(QF)_{LET}$. In the other case, (QF) denoted as $(QF)_{DE}$ is defined by the relationship

$$(QF)_{DE} = \frac{DE}{D},$$

where D is the absorbed dose and DE is the dose equivalent. In estimating the effects of exposure to neutrons or high-energy protons, DE is expressed in terms of $(QF)_{LET}$. Consequently, $(QF)_{DE}$ is a function of $(QF)_{LET}$. It has been shown that $(QF)_{LET}$ and $(QF)_{DE}$, when applied to protons having an energy of several hundred MeV, represent two different concepts. The $(QF)_{LET}$ depends on the energy loss of the proton *itself*, whereas the $(QF)_{DE}$ depends on various other factors, including the energy loss of *other* particles (electrons, secondary protons, alpha particles, recoil nuclei, etc.) which are generated within the tissue by the primary protons.

Moreover, the relationship between the dose equivalent and the quality factor, recommended by the International Commission on Radiation Units and Measurements (ICRU), is not the one which is used in health physics calculations; there is, therefore, a discrepancy between the "official" and "nonofficial" point of view. One can clarify the situation by analyzing the derivation of the quality factor and of other similar concepts from an operational and more particularly from an instrumental point of view. It can be seen that the requirements for radiation protection have not been adequately systematized, and in order to give a more complete account of what is considered to be the responsibility of a health physicist, an alternative, anticipatory approach to the interpretation of radiation quality is presented. It is proposed to define a "quality index,"

$$Q = \frac{D_e^{\text{eff}}}{D_r},$$

where D_r is the "reference dose" to be used in monitoring a radiation field and D_e^{eff} is the "effective dose equivalent," which is the name given in this analysis to the "amount" of exposure. The reference dose is expressed as

$$D_r = \frac{\Delta E_r}{\Delta m_r},$$

where ΔE_r is the energy imparted by ionizing radiation to the matter having "standard" chemical composition (approximating that of soft tissue) in a volume element Δv and Δm_r is the mass of matter in that volume element. Since radiation protection procedures are anticipatory, the measurements of the reference dose should be made in an unperturbed radiation field, whereas the effective dose equivalent should be obtained from a perturbed field, the perturbation being produced by a phantom, introduced in a locale in which the measurement of the reference dose has been previously made. The suggested anticipatory point of view is intended to supplement rather than to replace the one in which "simultaneous" measurements are made, as with dosimeters and other instruments worn by workers in the radiation field.

A detailed account of this analysis will be published in the August 1970 issue of *Health Physics.*

DOSIMETRY OF HIGH-ENERGY NUCLEONS AND PIONS

An understanding of the various interactions that high-energy particles (e.g., protons, neutrons, and pions) undergo with matter and, particularly, with tissue is essential in assessing the hazards from these radiations. During the last few years various theoretical models of the interaction have been developed and used to compute absorbed dose and dose equivalent under idealized conditions such as an infinite slab tissue phantom, uniform broad monoenergetic beams, etc. Work is in progress in collaboration with the experimental Health Physics Group at CERN (European Organization for Nuclear Research), Geneva, Switzerland, on the dosimetry of high-energy radiation, and one member of the staff is in Geneva this year. Calculations are being tailored to simulate actual experimental conditions, and factors such as beam density profile, energy distributions, and target size, shape, and composition are being taken into account.

Initial results have been obtained for depth-dose curves in water resulting from beams of negative and positive pions having momenta in the range 160 to 220 MeV/c. The Monte Carlo computations have taken into account inelastic nuclear interactions of pions in flight, the absorption of stopped negative pions by oxygen nuclei, decay of stopped positive pions into muons, and the subsequent decay of muons into positrons. Results are shown in Figs. 8.1 and 8.2 for pions with a Gaussian distribution of momenta with mean 173 MeV/c and such that 50% of the pions have momenta within ±2% of the mean. The pions were considered incident at one point along the axis of a 50-cm-radius cylinder of water.

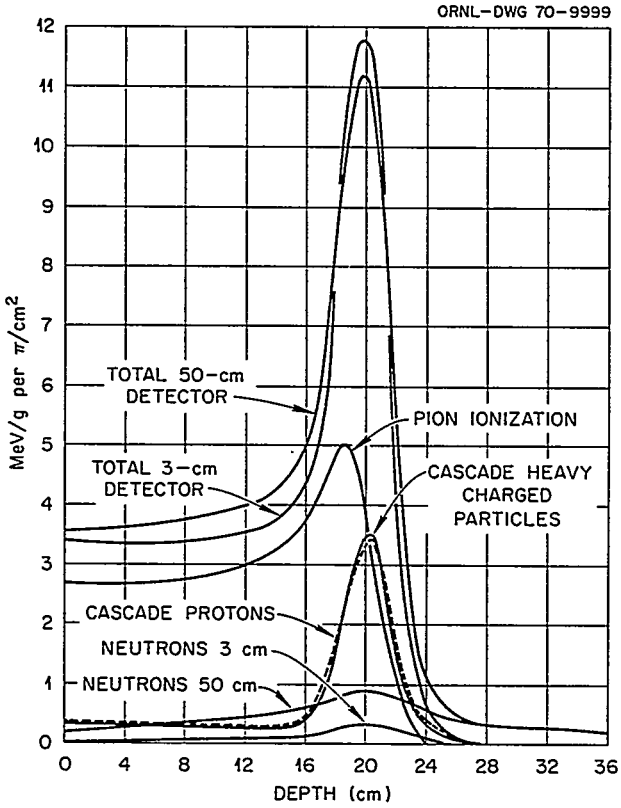

Fig. 8.1. Energy Deposited, as a Function of Depth, in a Water Absorber by π^- with a Mean Momentum of 173 MeV/c.

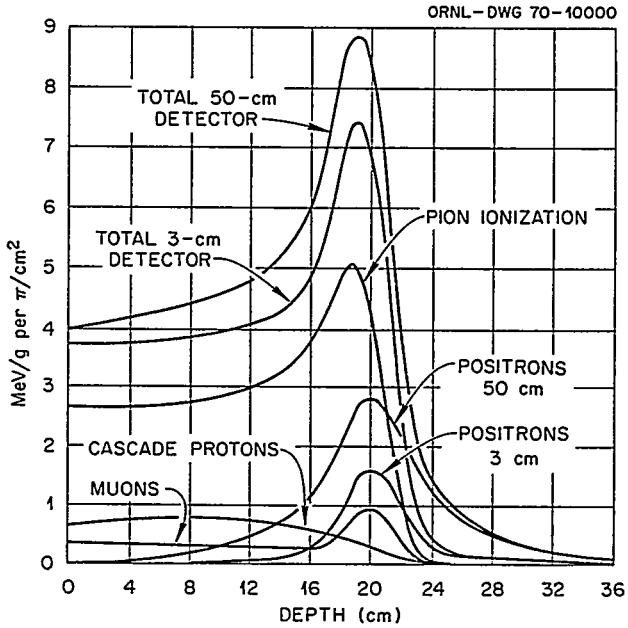

Fig. 8.2. Energy Deposited, as a Function of Depth, in a Water Absorber by π^+ with a Mean Momentum of 173 MeV/c.

The curves represent the total energy that would be absorbed, as a function of depth, in a 3-cm-radius detector and a 50-cm-radius detector, as well as a breakdown of the total energy into various components. The locations, heights, and widths of the peaks in the curves for total dose and stopped-pion dose and also the location and relative intensity of the high-LET contribution to absorbed dose have been studied for incident pion beams with various momentum spreads. Good agreement has been obtained between measured and calculated depth-dose curves. The possibility of using beams of negative pions for therapy has been studied by several groups during the past few years, and is hoped that the joint work of the experimental group at CERN and the theoretical group at ORNL will shed new light on the subject.

Calculations are also being made to correlate with biological irradiation experiments in progress at CERN using beams of high-energy neutrons. The beams are obtained from neutrons emitted in the forward direction when 397-MeV protons from the accelerator impinge on a beryllium target. Calculations are being made to estimate the energy distribution of the neutrons in the beam and to compute depth-dose curves to compare with the experimental results.

DETERMINATION OF LET SPECTRA FROM ENERGY-PROPORTIONAL PULSE-HEIGHT MEASUREMENTS

A Monte Carlo method of unfolding LET spectra from energy-proportional pulse-height measurements[10,11] was reported in the 1969 annual report.[12] Work has begun jointly with the Radiation Dosimetry Section to utilize this method to develop a more convenient and more reliable means of determining LET distributions than is currently being used. The method presently employed for this purpose was developed by Rossi[13] and uses a spherical proportional counter.

As discussed in the Radiation Dosimetry section of this report (Part III), pulse-height measurements made by spherical and cylindrical counters have been unfolded to determine LET distributions from a source of

[10] R. D. Birkhoff *et al.*, *Health Phys.* 18, 1 (1970).

[11] J. E. Turner *et al.*, *Health Phys.* 18, 15 (1970).

[12] *Health Phys. Div. Ann. Progr. Rept. July 31, 1969*, ORNL-4446.

[13] H. H. Rossi and W. Rosenzweig, *Radiology* 64, 404 (1955).

neutrons from Am-Be and also from the Health Physics Research Reactor. Good agreement was obtained from the Am-Be source, but poor agreement was obtained from the reactor source. The Rossi method is based on the assumption that the track length distribution in the spherical chamber is triangular, the most probable track length being the diameter of the sphere. The track length distribution will be triangular if the radiation is isotropic (or a broad uniform parallel beam) and if each particle leaving a track traverses the entire spherical chamber. The distribution will deviate from triangular if some of the charged particles stop or are born within the gas in the spherical chamber. Some estimates have been made of the errors involved in the use of the triangular track length distribution for low-energy neutrons.[14]

A simple model has been developed in order to estimate the effect of "stoppers" and "starters" on the track length distribution in spheres irradiated by neutrons. The model assumes the neutrons interact only by isotropic scattering (in the center-of-mass system) with hydrogen, and the resulting recoil protons are allowed to slow down according to the stopping-power formula. The results obtained are shown in Fig. 8.3. The triangular distribution which would result if no particles stop or start within the gas is shown as well as the distribution of tracks obtained by this model when the incident particles are 2- and 0.5-MeV neutrons. In the case of 0.5-MeV incident neutrons, more than one-third of the tracks did not traverse the entire counter chamber (which was assumed to be a 2-in.-diam sphere filled with cyclopropane at a pressure of 2 cm Hg), and, consequently, the track length distribution deviates substantially from triangular.

[14]R. F. Dvorak, *Health Phys.* 17, 279 (1969).

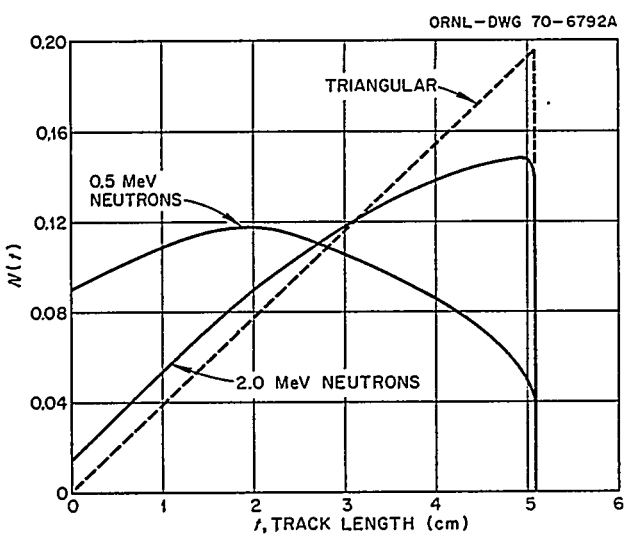

Fig. 8.3. Distributions of Track Lengths of Recoil Protons Through a Spherical Rossi Counter Irradiated by 0.5- and 2.0-MeV Neutrons. The dashed curve represents the theoretical triangular distribution.

Improvements are now being made in the model to allow other types of interactions of the incident neutrons to occur. Work is continuing, jointly with the Radiation Dosimetry Section, to try to determine the limitations of the currently used methods and to utilize the Monte Carlo procedure to permit the use of more convenient counter geometries than the sphere and to take into account the computed nontriangular track length distributions in the LET unfolding procedure.

CRITICAL DIPOLE MOMENTS FOR ELECTRON BINDING TO A NONSTATIONARY DIPOLAR SYSTEM

Earlier investigations at ORNL and elsewhere have shown that an electron is bound to a finite fixed dipole only if the dipole moment exceeds a certain critical value (1.625×10^{-18} esu cm). No bound states exist for dipole moments, D, smaller than this value, and an infinity of states exists for a fixed dipole whose moment exceeds this critical value. The existence of this critical moment and the nature of the accompanying bound states in the dipole field have important implications for low-energy-electron scattering by polar molecules. However, in the realistic problem of electron binding to a polar molecule, the source of the field is not fixed in space but is, itself, a part of the dynamical system and should be treated as such in determining the critical moment necessary for binding. A new investigation has been made of electron binding to a finite dynamic dipolar system where the Hamiltonian operator in the Schrödinger equation contains, in addition to the electron kinetic energy, the rotational terms of the dipole.[15]

Consider an electron with coordinate r measured from the center of mass of a finite dipole having charges $\pm q$ separated by distance $R = 2s$ and possessing a moment of inertia I about the origin as in Fig. 8.4. In Rydberg atomic units the Schrödinger equation for the total system can be written as

$$[H_R - \nabla_r^2 + V(\mathbf{r},\hat{s})]\ \Psi(\mathbf{r},\hat{s}) = E\ \Psi(\mathbf{r},\hat{s})\ , \qquad (1)$$

[15]W. R. Garrett, "Critical Binding of an Electron to a Non-Stationary Electric Dipole," *Chem. Phys. Letters* 5, 393 (1970).

ORNL—DWG 70—1081A

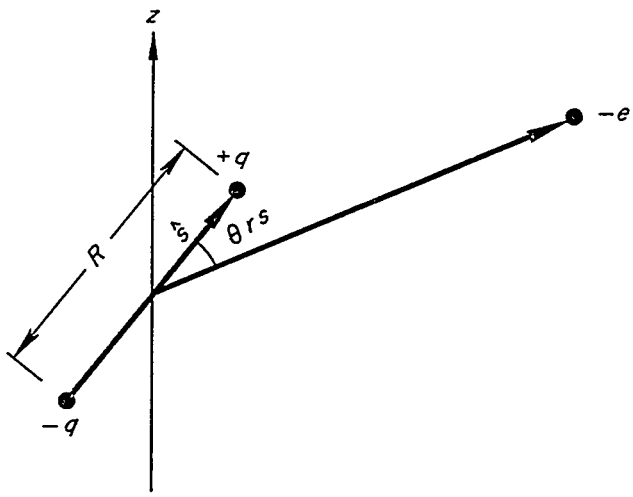

Fig. 8.4. Coordinate System for Electron-Dipole Problem.

where $-\nabla_r^2$ is the kinetic energy operator of the electron and H_R is the rotational energy operator for the dipole. The rotational operator H_R has eigenfunctions $Y_j^{m_j}(\hat{s})$ which satisfy the equation

$$\left[H_R - \frac{j(j+1)}{2I}\right] Y_j^{m_j}(\hat{s}) = 0 . \tag{2}$$

The interaction potential $V(\mathbf{r}, \hat{s})$ is that of the electron due to the charges at $\pm\hat{s}$. In the absence of the electron, the dipolar masses satisfy Eq. (2) with rotational quantum numbers $j(j+1)$ and rotational energy $j(j+1)/2I$. In the total system, which includes the electron, j is no longer a good quantum number. We thus couple the angular momentum $\mathbf{j}$ of the nuclei to that of the electron, designated as $\mathbf{l}$. The total angular momentum $\mathbf{J} = \mathbf{j} + \mathbf{l}$ and z component $M = m_l + m_j$ are then good quantum numbers. To utilize this fact we introduce the coupled spherical harmonics

$$\mathcal{Y}_{jl}^{JM}(\hat{r}, \hat{s}) = \sum_{m_j} \sum_{m_l} (jl\, m_j\, m_l | jl\, JM)\, Y_j^{m_j}(\hat{s})\, Y_l^{m_l}(\hat{r}) , \tag{3}$$

which are eigenfunctions of J^2 and J_z. The terms $(jl\, m_j m_l | jl\, JM)$ are the usual Clebsch-Gordan coefficients. We now expand the total wave function for the system in terms of the set (3):

$$\Psi^{JM}(\mathbf{r}, \hat{s}) = \sum_j \sum_l \frac{U_{jl}(r)}{r} \mathcal{Y}_{jl}^{JM}(\hat{r}, \hat{s}) , \tag{4}$$

where $U_{jl}(r)$ is the reduced radial function to be determined from the Schrödinger equation (1). We also expand the interaction term V in the form

$$V(\mathbf{r}, \hat{s}) = \sum_{\lambda=1,3,\ldots} \frac{2eqr_<^\lambda}{r_>^{\lambda+1}} P_\lambda(\cos\theta_{rs}) = \sum_{\lambda=1,3,\ldots} \frac{eDr_<^\lambda}{sr_>^{\lambda+1}} , \tag{5}$$

where θ_{rs} is the angle between $\mathbf{r}$ and $\hat{s}$ and $r_<$ is the lesser and $r_>$ the greater of r and s. The sum extends over odd powers of λ, and the dipole moment is $D = 2qs = qR$. (Here D is in ea_0 units.)

The substitution of expansions (4) and (5) into Eq. (1) with the performance of a scalar multiplication over angular variables leads to the set of coupled radial equations

$$\left[\frac{d^2}{dr^2} - \frac{l'(l'+1)}{r^2} - \frac{j'(j'+1)}{2I} + E\right] U_{j'l'}(r) = \sum_\lambda \sum_{jl} \frac{2eqr^\lambda}{s^{\lambda+1}} f_\lambda(j'l', jl; J)\, U_{jl}(r) \text{ (for } r < s) , \tag{6a}$$

$$\left[\frac{d^2}{dr^2} - \frac{l'(l'+1)}{r^2} - \frac{j'(j'+1)}{2I} + E\right] U_{j'l'}(r) = \sum_\lambda \sum_{jl} \frac{2eqs^\lambda}{r^{\lambda+1}} f_\lambda(j'l', jl; J)\, U_{jl}(r) \text{ (for } r > s) . \tag{6b}$$

The f_λ on the right-hand side are constants which result from the angular integration.[15]

The critical dipole moment for a dipolar system of moment of inertia I and dipole length $R = 2s$ can be obtained by solving the coupled set (6a, b) for bounded solutions in the limit where the total energy $E \to 0$. An iterative method of achieving solutions has been developed and described elsewhere.[16]

Results for the ground state of the electron-dipolar system are shown graphically in Fig. 8.5.

We note four important consequences of the inclusion of the nuclear motion into the finite-dipole problem. First, as can be seen in Fig. 8.5, the minimum moment is everywhere larger than that for the fixed-dipole

[16] W. R. Garrett, J. E. Turner, and V. E. Anderson, *Analysis of Ground State Energy Eigenfunctions for Finite Dipole in Spherical Coordinate Systems*, ORNL-4431 (February 1970).

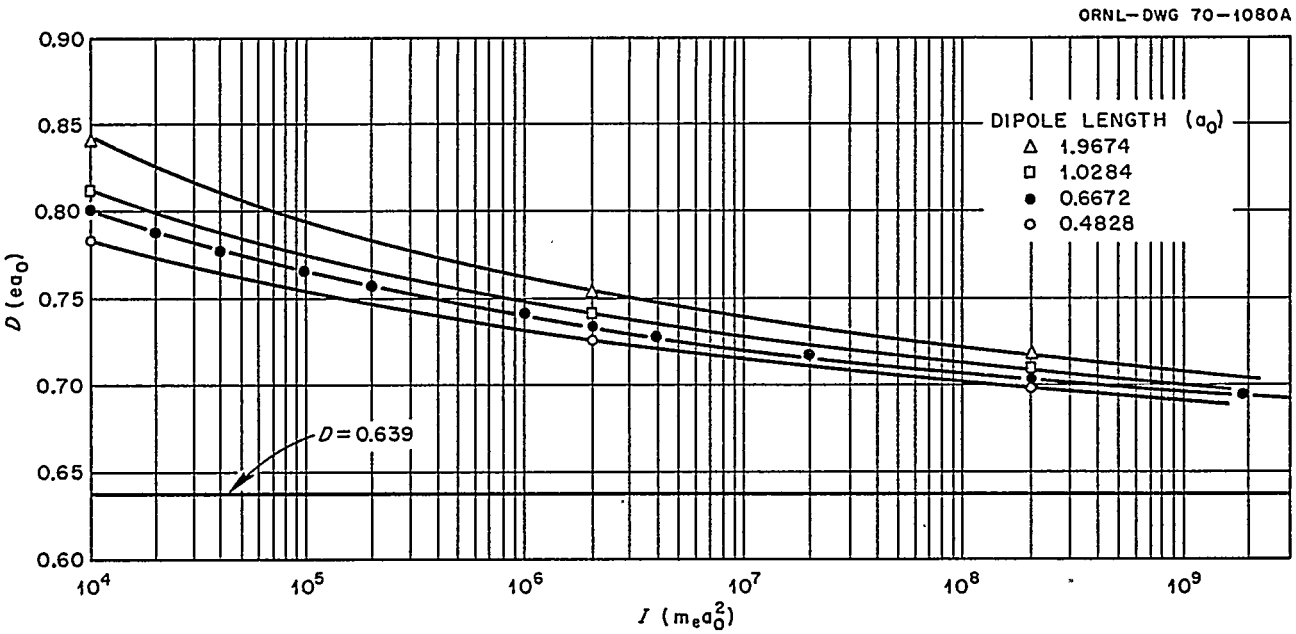

Fig. 8.5. Critical Dipole Moment as a Function of Moment of Inertia I for Dipole Lengths R = 0.4828, 0.6672, 1.0284, and 1.9674 a_0.

problem. Second, the free dipole is unlike the stationary dipole in that the critical moment is no longer independent of the dipole length. Third, the minimum moment for an infinitely massive system, corresponding to the fixed dipole, is approached very slowly with increasing molecular moment of inertia. Finally, we note that in the case of the nonstationary dipole there is no accumulation point in the energy spectrum at E = 0 as for the fixed dipole, and thus an infinite number of bound states do not appear at the critical moment.

The present results have important implications for the problem of low-energy electron scattering by polar molecules.

APPROXIMATE HARTREE-FOCK ENERGIES FOR AUTOIONIZING STATES IN NEON AND ARGON

Prompted by a critical need for the positions of a number of autoionizing states in the study of threshold excitation spectra of noble gases, an attempt was made to carry out Hartree-Fock (H.F.) calculations for states in which an inner-shell electron is excited to an unfilled H.F. orbital and for states in which two outer-shell electrons are simultaneously excited to higher unfilled H.F. orbitals. Repeated attempts to obtain complete H.F. results for neon and argon were all unsuccessful due to a lack of convergence in the orthogonalization procedure.[17] However, by utilizing an angular-momentum-averaged exchange procedure investigated earlier,[18] it was possible to carry out approximate H.F. calculations for all states attempted. Extensive calculations have shown[18] that the definition of an average exchange potential for each set of orbitals of a given symmetry leads to very close agreement with complete H.F. results with the great simplification of reducing the radial equations to homogeneous rather than inhomogeneous differential equations and with the essential feature that all orbitals are automatically orthogonal. This latter feature allowed the highly excited autoionizing states to be readily calculated.

The average energy for a given configuration was evaluated in the computer program according to the scheme of Slater.[19] Specific term values for a given multiplet were obtained by calculating the appropriate splitting from the average energy of the configuration as discussed by Slater.

These approximate H.F. energy levels greatly facilitated the assignment of threshold spectral features in

[17] Charlotte Froese, *Phys. Rev.* 137, A1644 (1965).

[18] W. R. Garrett and L. D. Mullins, *J. Chem. Phys.* 48, 4140 (1968).

[19] J. C. Slater, *Quantum Theory of Atomic Structure*, vol. 1, chap. 14, McGraw-Hill, New York, 1960.

both neon[20] and argon.[21] We note also that the ease with which calculations proceeded in the l-averaged H.F. calculations as compared with the complete H.F. treatment rather clearly demonstrated the usefulness of the technique and of the existing computer program.

VARIATIONAL BOUND METHOD FOR ELASTIC SCATTERING PHASE SHIFTS

In all continuum variational methods of the Kohn-Hulthen type,[22] one utilizes the stationary property of a certain variational integral to obtain an approximation to the eigenfunction φ_l for the lth partial wave component of the total wave function describing a scattering problem. The variational treatment of the continuum problem differs from the analogous stationary expression for the energy of a discrete bound state problem in that an error in the trial function within the stationary integral leads to a second-order term whose algebraic sign cannot be determined. Thus the variationally determined phase shift η_l^f is neither an upper nor a lower bound on the true phase shift, and consequently an increase in the number of terms in a trial function does not necessarily lead to an improvement in the resultant phase. Furthermore, the resultant phase shift may be larger or smaller than the true value.

In practice a trial function φ_l^f depends on $n + 1$ linear variational parameters, $d_1, d_2, \ldots, d_n$, and η_l^f. The stationary property

$$\delta\left[\int \varphi_l (H - F_2)\varphi_l \, d\tau - k\eta_l\right] = \delta(I_l - k\eta_l) = 0 \qquad (7)$$

allows the determination of the parameters from the conditions

$$\frac{\partial I_l}{\partial d_i} = 0, i = 1, 2, \ldots, n\,, \qquad (8)$$

$$\frac{\partial I_l}{\partial \eta_l^f} = k\,. \qquad (9)$$

In addition, the condition

$$I_l = 0 \qquad (10)$$

should be satisfied.[22] Since there are only $n + 1$ unknowns, the $n + 2$ equations in (8), (9), and (10) cannot be satisfied unless φ_l^f is an exact solution to the Schrödinger equation. In the method of Hulthen[22] Eq. (12) is omitted, and in that of Kohn[22] Eq. (13) is dropped and the parameters are determined from the remaining $n + 1$ equations. The magnitude of the errors involved in these techniques is inferred from the behavior of the calculated phase shift as one or more nonlinear parameters in the trial function are varied. In all applications of the Kohn or Hulthen procedures the variational calculations are repeated until a trial function is found which is "smooth" with respect to small changes in a nonlinear parameter or to an increase in the number of linear variational terms.[23]

We suggest a new method of selecting a "best" trial function in an extension of a variational method which was introduced for scattering problems involving long-range interactions.[24] The new method leads to a lower bound on the true scattering phase shift.

First we expand a trial function in a series of angular momentum eigenfunctions. We illustrate with an example of singlet and triplet s-wave scattering of electrons on atomic hydrogen. We have

$$H = -\nabla_1^2 - \nabla_2^2 - \frac{2}{r_1} - \frac{2}{r_2} + \frac{2}{r_{12}}\,, \qquad (11)$$

and we write the trial function as:

$$\varphi_l^+(\mathbf{r}_1, \mathbf{r}_2) = A(1,2)\left\{\left[\frac{P_{1s}(r_1)}{r_1}\frac{1}{4\pi} + \mathcal{D}_N r_2\, e^{-(r_1+r_2)}\, \mathcal{Y}^{\infty}_{l_1 l_1}(\hat{r}_1, \hat{r}_2)\right]\frac{U_0(r_2)}{r_2} + \sum_{l_2=0}\sum_{p,q=1} \mathcal{D}^{l_2}_{pq}\, \mathcal{Y}^{\infty}_{l_2 l_2}(\hat{r}_1, \hat{r}_2)\, r_1^{p+l_2}\, r_2^{q+l_2}\, e^{-\beta(r_1+r_2)}\right\}. \qquad (12)$$

The factor $A(1, 2) = [1 \pm P(1, 2)]$ is the exchange operator where $P(1, 2)$ exchanges coordinates $\mathbf{r}_1$ and $\mathbf{r}_2$. $P_{1s}(r_1)$ is the ground-state hydrogen radial function, and the angular momentum eigenfunctions are defined as

$$\mathcal{Y}^{Jm}_{l_1 l_2} = \sum_{m, n_2} C(l_1 l_2 J, m_1 m_2 M)\, Y^{m_1}_{l_1}(\hat{r}_1)\, Y^{m_2}_{l_2}(r_2)\,, \qquad (13)$$

[20] J. T. Grissom, W. R. Garrett, and R. N. Compton, *Phys. Rev. Letters* 23, 1011 (1969).

[21] J. T. Grissom, R. N. Compton, and W. R. Garrett, *Electron Impact Excitation and Ionization Studies of the Rare Gases*, ORNL-TM-2618 (1970).

[22] For a summary of variational methods in scattering theory see: N. F. Mott and H. S. W. Massey, *The Theory of Atomic Collisions*, 3d ed., chap VI, Oxford Press, London, 1965.

[23] C. Schwartz, *Ann. Phys.* 16, 36 (1961).

[24] W. R. Garrett, p. 768 in *Proc. Sixth Intern. Conf. Phys. Elec. Atomic Collisions*, MIT Press, Cambridge, Mass., 1969.

where C is the usual Clebsch-Gordan coefficient. The $\mathfrak{D}$'s are linear variational parameters, and the function $U_0(r)$ is a numerical function which is the regular solution to the equation

$$\left[\frac{d^2}{dr^2} - V_t(r) + k^2\right] U_0(r) = 0 . \tag{14}$$

$V_t(r)$ is a "trial" scattering potential of the new variational method described elsewhere.[24] Finally, β is a nonlinear variational parameter of the type discussed in connection with the Kohn or Hulthen procedure.

Now suppose that two trial functions have been found, each of which satisfies the stationary conditions of Eqs. (8) and (9). Then since Eq. (10) is satisfied exactly by the true wave function, one can choose, in a variational search procedure, to define the "better" of two trial functions as that which results in a value of I_l which lies closer to zero. In fact, it has been found that by varying a nonlinear parameter in the usual variational search method, it is possible to find a trial function which satisfies all $n + 2$ conditions of Eqs. (9), (10), and (11). Now it was noted above that this latter condition is possible only if the trial function is a true solution to the Schrödinger equation. However, it can be shown[25] that the use of a finite number of terms in the angular momentum representation of Eq. (12) is equivalent to a truncation of the total Hamiltonian. Thus, what one gets in the present procedure is an exact solution (within numerical roundoff) to a problem in which a part of the total interaction potential has been deleted. This exactly satisfies a theorem of Gailitis,[26] who shows that such a solution provides a lower bound on the true scattering phase shift.

[25] W. R. Garrett, *J. Phys. B* (submitted).

[26] M. Gailitis, *Zh. Eksperim. i Teor. Fiz.* 47, 160 (1965); translation *Soviet Phys. JETP* 20, 107 (1965).

[27] Y. Hahn, T. F. O'Malley, and L. Spruch, *Phys. Rev.* 130, 381 (1963).

Results of the present technique applied to a sample problem of electron scattering by atomic hydrogen are shown in Table 8.1. The present results agree exactly with a different and more difficult variational bound method of Hahn *et al.*[27]

OSCILLATOR STRENGTH

A slight generalization of oscillator strength which includes particles other than electrons (such as the protons in methane, CH_4) is provided by the operator

$$\Omega^{\alpha\beta}_{mm'} = [X^{\alpha}_{m'} (m\hbar^{-2}H, X^{\beta}_{m'})] ,$$

in which

$$X^{\alpha}_{m} = \sum_i x^{i\alpha}\, \delta(m_i, m)$$

is the sum of the α component ($\alpha = 1, 2, 3$ or x, y, z) of the coordinates of all particles of mass m, H is the Hamiltonian operator for the system, $2\pi\hbar$ is Planck's constant, and $[A, B] = AB - BA$ is the commutator bracket of operators A and B. It can be proved from the coordinate-momentum commutation relations that

$$\Omega^{\alpha\beta}_{mm'} = n_m\, \delta(\alpha, \beta)\, \delta(m, m'),$$

where n_m is the number of particles of mass m and $\delta(r, s) = 1$ if $r = s$, 0 otherwise. Ω, which is evidently a tensor of the second rank in the components α and β, can be split into a traceless tensor of the second rank

$$\Omega^{(2)\alpha\beta}_{mm'} = \Omega^{\alpha\beta}_{mm'} - \frac{1}{3}\sum_{\gamma=1}^{3} \Omega^{\gamma\gamma}_{mm'}\, \delta(\alpha, \beta)$$

and a remainder

$$\Omega^{(0)\alpha\beta}_{mm'} = \frac{1}{3}\sum_{\gamma=1}^{3} \Omega^{\gamma\gamma}_{mm'}\, \delta(\alpha, \beta) ;$$

Table 8.1. Electron-Hydrogen $l = 0$ Phase Shifts

$ka_0 = 0.4$

States Included	Singlet		Triplet	
	Variational Bound[a]	Present	Variational Bound[a]	Present
s	1.2695	1.2690	2.2920	2.290
$s+p$	1.4029	1.402	2.2922	2.292

[a] I. Aronson *et al.*, *Phys. Rev.* 153, 73 (1967).

it is found that $\Omega^{(2)}$ is identically zero and that $\Omega^{(0)}$ is a constant operator. The matrix elements of $\Omega^{(0)}$ with respect to energy eigenstates provide the generalization of oscillator strength referred to in the first sentence above.

The isotope shift in atoms provides an oscillator strength sum rule, namely, the sum of oscillator strengths weighted by the energy difference between states entering the oscillator strength. We can write for the Hamiltonian of an atom of mass M

$$H = H^{\infty} + H'' ,$$

where H^{∞} is the Hamiltonian for a similar atom of infinite mass and

$$H'' = \frac{P^2}{2M} = \sum_{\alpha=1}^{3} \left(\sum_{j=1}^{n} p_{j\alpha} \right)^2 \Big/ 2M$$

is the correction; here P is the nuclear momentum, equal to the negative of that of the electrons. From first-order perturbation theory applied to state I, we find after a simple calculation

$$E_I - E_I^{\infty} \cong \langle I|H''|I\rangle = (3m/4M)\, S_1 ,$$

where m is the electronic mass and

$$S_1 = \sum_J (E_J^{\infty} - E_I^{\infty})\{f_{JI}^{xx} + f_{JI}^{yy} + f_{JI}^{zz}\}/3$$

is the sum referred to in the first sentence, in which

$$f^{xx} = 2m\hbar^{-2}(E_j^{\infty} - E_I^{\infty})|\langle J|\Sigma x_i|I\rangle|^2 ,$$

and so on. For H, D, and T the results coincide with known formulas of Bethe.

POTENTIAL ENERGY CURVES FOR DIATOMIC MOLECULES

A rapid method of obtaining the potential energy of a diatomic molecule has been devised, using only the experimentally determined energy as a function of vibrational and rotational quantum numbers ν and J. At each internuclear spacing r the sum of centrifugal potential energy $J(J+1)\hbar^2/2\mu r^2$ and true potential energy $U_e(r)$ is less than the total energy by the radial kinetic energy, so we have the relation

$$\frac{J(J+1)\hbar^2}{2\mu r^2} + U_e(r) \leqslant E\left[\nu + \frac{1}{2}, J(J+1)\right] .$$

(Here μ is the reduced mass of the two atoms which make up the diatomic molecule.) Equality holds only when the radial kinetic energy is zero, corresponding to the extrapolated value $\nu = -\frac{1}{2}$ of the vibrational quantum number. Under orbiting conditions (when r takes on the constant value $\bar{r}$), the equality above holds for the square of the orbiting angular momentum $\overline{p_\phi^2}$, and we have

$$U_e(\bar{r}) = E\left(\nu + \frac{1}{2} = 0, \frac{\overline{p_\phi^2}}{\hbar^2}\right) - \frac{\overline{p_\phi^2}}{2\mu\bar{r}^2} ; \tag{15}$$

for all other values of $\overline{p_\phi^2}$, $U_e(\bar{r}) < E(0, p_\phi^2/\hbar^2) - p_\phi^2/2\mu\bar{r}^2$. A very simple formula then results:

$$U_e(\bar{r}) = \max_{-\infty < p_\phi^2 < \infty} \left\{ E\left(\nu + \frac{1}{2} = 0, \frac{p_\phi^2}{\hbar^2}\right) - \frac{p_\phi^2}{2\mu\bar{r}^2} \right\} . \tag{16}$$

Physically, the square of the orbital angular momentum is positive; its extension to negative values in the above equation must be viewed as an analytic continuation of the experimental energy surface $E(\nu + \frac{1}{2}, p_\phi^2/\hbar^2)$; it does, however, give correct results for the two soluble problems which were described in earlier reports. The method gave only fair results when applied to $H^{81}Br$, probably because the experimental energy formula for high $J(J+1)$ is not very accurate.

THE MEAN FREE PATH OF RELATIVISTIC ELECTRONS FOR PLASMON EXCITATION

An analytic expression for the mean free path of a charged particle for plasmon excitation has been known for several years. General theoretical arguments indicate that this expression, calculated for a nonrelativistic incident particle, should also hold in good approximation if the incident particle is relativistic. However, there is some uncertainty as to just what variables are appropriate in the relativistic case. For example, should the mean free path be expressed in terms of the momentum or velocity of the incident particle? To answer these questions we have derived the mean free path for plasmon excitation using ab initio a relativistic incident electron. The medium containing free electrons is described using a quantum-hydrodynamical model, and the wave functions of the incident particle are solutions of the Dirac equation. First-order perturbation theory is used to calculate the rate of excitation of plasmons by the incident electron; the excitation rate leads to the mean free path. Assuming no dispersion in the plasmon energy, we find the inverse mean free path to be given by

$$\lambda_p^{-1} \frac{e^2 \omega_p}{\hbar v_0^2} \ln \left[\left(\frac{\hbar k_c}{p_0 - \sqrt{p_0^2 - 2\gamma_0 m\hbar\omega_p}} \right) \right] , \quad (17)$$

where e, m, v_0, and p_0 are, respectively, the charge, mass, velocity, and momentum of the incident particle, $\hbar\omega_p$ is the plasmon energy, k_c is a cutoff wave number, and $\gamma_0 = [1-(v_0/c)^2]^{-1/2}$. If the energy of the incident particle is large compared with the plasmon energy, we recover the well-known result

$$\lambda_p^{-1} = \frac{e^2 \omega_p}{\hbar v_0^2} \ln \frac{v_0 k_c}{\omega_p} . \quad (18)$$

Including dispersion of the plasmon energy produces, in this same limiting case, relatively small changes in the mean free path.

Z_1^3 EFFECT IN THE STOPPING POWER OF CHARGED PARTICLES

In some recent experiments[28,29] the ranges of π^+ and π^- mesons were found to differ such that the stopping power for the positive particles is higher by ~10% than that of the negative particle. Standard stopping-power theory, derived in the first-order Born approximation, gives the result that the stopping power is proportional to the square of the charge of the incident particle $(Z_1 e)^2$. We are presently completing an extension of stopping-power theory to include corrections to the semiclassical impulse approximation which yields a term proportional to $(Z_1 e^2)^3$. We consider the interaction of a particle of charge $Z_1 e$ incident at a given impact parameter with an electron bound isotropically and harmonically with a frequency ω to a nucleus of charge $Z_2 e$ located at the origin. The force exerted by the incident particle on the bound electron during the collision is calculated at the actual position of the bound electron. Using a perturbation expansion that assumes the displacement of the bound electron is small compared with the impact parameter and integrating over the impact parameter from some minimum value a to infinity, we are led to an expression for the stopping power. The leading term in this expansion proportional to $(Z_1 e^2)^2$ is the usual result for this type of model, while the second term gives us the $(Z_1 e^2)^3$ correction. For a medium of atomic density n_2 with Z_2 electrons per atom, we find this stopping-power correction due to electrons bound with a frequency ω to be given by

$$\Delta\left(-\frac{dE}{dx}\right)_\omega = \frac{4\pi n_2 Z_2 F_\omega \omega}{m^2 v_1^5} (Z_1 e^2)^3 I(\xi) , \quad (19)$$

where m is the electron mass, v_1 is the speed of the incident particle, F_ω is the fraction of electrons in the medium bound with frequency ω, and $I(\xi)$, with $\xi \equiv a\omega/v_1$, is a complicated double integral which has been evaluated by computer for the range of values of ξ which are of interest. $I(\xi)$ is shown in Figs. 8.6 and 8.7. The integrations in $I(\xi)$ can be carried out in limiting cases and give

$$I(\xi) \approx -2\pi \ln \xi + \text{const} , \quad \xi \ll 1 , \quad (20)$$

and

$$I(\xi) \approx \frac{4\pi}{\xi^2} e^{-2\xi} , \quad \xi \gg 1 . \quad (21)$$

Since the charge number of the incident particle Z_1 enters as Z_1^3 in this equation, we see that this correction term increases the stopping power for positively charged incident particles and decreases the stopping power for negatively charged incident particles. Preliminary calculations indicate that this Z_1^3 correction term is of the proper size to account for the observed differences between the stopping powers of a charged particle and its antiparticle.

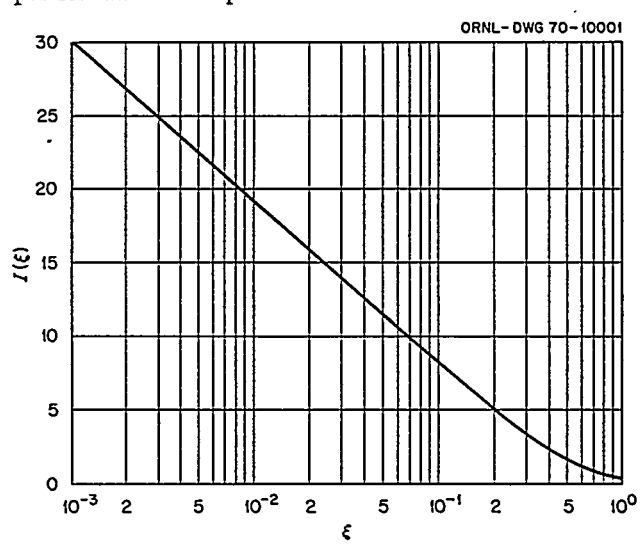

Fig. 8.6. Plot of $I(\xi)$ (as Calculated by Computer) as a Function of ξ.

[28] H. H. Heckman and P. J. Kindstrom, *Phys. Rev. Letters* 22, 871 (1969).

[29] W. H. Barkas, W. Z. Osborne, W. G. Simon, and F. M. Smith, CERN Report No. CERN 65-4 (1965), vol. II (unpublished).

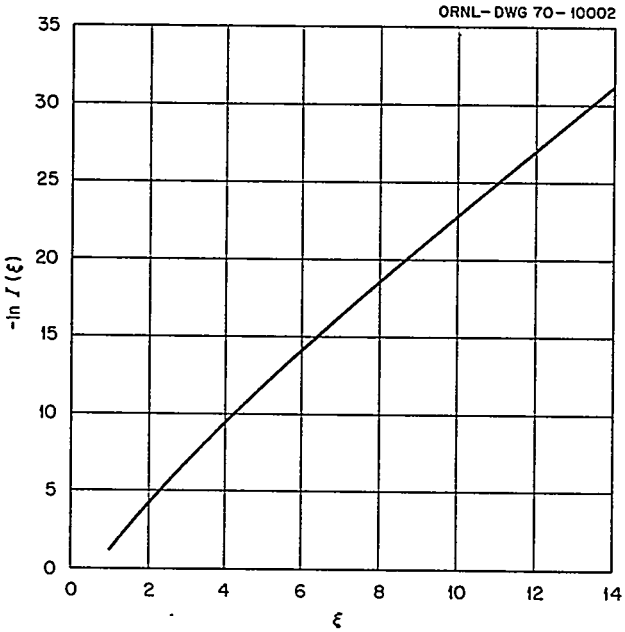

Fig. 8.7. Plot of $-\ln I(\xi)$ vs ξ from $I(\xi)$ as Evaluated by Computer.

DOUBLE-PLASMON EXCITATION IN A FREE-ELECTRON GAS

The interaction of a fast charged particle with a free-electron gas has been described in the random-phase approximation, and the mean free path for the second-order process of double-plasmon excitation has been calculated. If the energy of the incident particle is large compared with the plasmon energy, we find for the inverse mean free path for double-plasmon excitation, λ_{2p}^{-1}, the result

$$\lambda_{2p}^{-1} = \frac{9k_c^5\hbar}{2^7\pi^2 nm\omega_p}\lambda_p^{-1} , \tag{22}$$

where the inverse mean free path for the single-plasmon excitation process is given by

$$\lambda_p^{-1} = \frac{e^2\omega_p}{\hbar v_0^2}\ln\left(\frac{v_0 k_c}{\omega_p}\right). \tag{23}$$

In these equations, e and v_0 are, respectively, the charge and speed of the incident particle, m is the electron mass, ω_p is the plasma frequency for the electron gas of density n, and k_c is the cutoff wave number. If we take the Pines-Bohm value, $k_c = \omega_p/v_F$, where v_F is the Fermi velocity for the electron gas, we find

$$\lambda_{2p}^{-1} = 0.0103 r_s^2 \lambda_p^{-1} . \tag{24}$$

Here r_s is the radius, measured in units of Bohr radii, of the sphere containing on the average one electron in the electron gas. To estimate the importance of double-plasmon excitation let us suppose that multiple single-plasmon and double-plasmon excitation events are the predominant energy loss mechanisms for the incident particle. If we define an effective mean free path for these two loss processes, λ, by $\lambda^{-1} = \lambda_p^{-1} + \lambda_{2p}^{-1}$, then the probability for the incident particle to lose no energy in traversing a distance t in the medium is given by $P_0(t) = e^{-t/\lambda}$. A simple calculation gives, for the probability of an energy loss $\hbar\omega_p$,

$$P_1(t) = \frac{t}{\lambda_p} e^{-t/\lambda} , \tag{25}$$

and the probability of an energy loss $2\hbar\omega_p$ is given by

$$P_2(t) = \frac{1}{2}\left(\frac{t}{\lambda_p}\right)^2 e^{-t/\lambda} + \frac{t}{\lambda_{2p}} e^{-t/\lambda} . \tag{26}$$

If we consider a group of incident particles that has lost an energy $2\hbar\omega_p$, then the fraction of the particles found in this group due to double-plasmon excitation is

$$f = \frac{1}{P_2(t)}\frac{t}{\lambda_{2p}} e^{-t/\lambda} , \tag{27}$$

or using the expression for λ_{2p}, we find

$$f = \left(1 + \frac{1}{0.0206 r_s^2}\frac{t}{\lambda_p}\right)^{-1} . \tag{28}$$

For $t \approx \lambda_p$, $f \approx 0.08$ for $r_s = 2$ (Al), $f \approx 0.25$ for $r_s = 4$ (Na), and $f \approx 0.40$ for $r_s = 5.7$ (Cs). Thus, under suitable conditions a rather large fraction of the incident particles losing energy $2\hbar\omega_p$ may be due to the double-plasmon emission process, and indeed this may lead to a measurable effect in certain experimental work, for example, characteristic energy loss measurements.

ANOMALOUS DAMPING OF VOLUME PLASMONS IN POLYCRYSTALLINE METALS

Festenberg[30,31] has carried out a series of elegant measurements of the half width ΔE of volume plasmon

[30] C. von Festenberg, *Phys. Letters* 23, 293 (1966).

[31] C. von Festenberg, *Z. Physik* 207, 47 (1967).

energy losses by 50-keV electrons in polycrystalline foils of aluminum metal. The experiments were done for various known angular deflections θ of the fast electron and for foils composed of various crystallite sizes. He found that when foils are used for which the crystallite dimensions are $\gtrsim$250 Å, the ΔE vs θ values are described quite well by the free-electron gas theory of Ninham, Powell, and Swanson;[32] a constant must be added to their theoretical damping values to account for Drude-type processes involving thermal effects, disorder, interband effects, etc. When crystallites of smaller dimensions were involved, a strongly augmented damping was observed in the region of small angular deflections ($\theta \lesssim 1$ milliradian). This contribution decreases monotonically to zero at a rather steep rate as θ increases, beginning at a value for $\theta = 0$ which may be several times larger than the comparable damping in a foil composed of large crystallites. This grain-size-dependent damping seems to be unexplained to date.

A possible explanation of this phenomenon is presented herewith. One argues that a polycrystalline metal may be regarded as a random assemblage of crystallites in electrical contact over portions of their surfaces, but separated by regions having electronic composition different from that of the bulk metal. The interstices may be vacant or partially filled with smaller aggregates of matter. In a homogeneous isotropic electron gas the momentum of a plasmon is a constant of the motion. By contrast, if the system is weakly inhomogeneous the plasmon may scatter elastically on inhomogeneities from an initial state of given momentum to any of a large number of states of different momenta on the energy shell. This scattering should evince itself as lifetime broadening of a plasmon state created by a fast electron. We suggest that plasmon damping in polycrystalline media may be due in part to such scattering processes.

We have constructed a theory of this process, using a quantum-hydrodynamical model of a weakly inhomogeneous plasma[33] and assuming that the inhomogeneities may be described adequately by the correlation function $\langle f(\mathbf{r})f(\mathbf{r}+\mathbf{r}_0)\rangle = \langle f^2\rangle G(r_0)$, where $f(\mathbf{r}) = \delta n(\mathbf{r})/\langle n(\mathbf{r})\rangle$ is the fractional deviation of the electron density at $\mathbf{r}$ from its mean value averaged over all of the metal. If we employ a Gaussian autocorrelation function, that is, $G(r) = e^{-(r/\sigma)^2}$, we find that the damping rate γ of a volume plasmon with wave number q_0 due to the postulated process is

$$\frac{\gamma}{\omega_p} = \frac{5}{12}\left[\frac{\pi}{2}\right]^{1/2} \langle f^2\rangle \left(\frac{\sigma\omega_p}{v_F}\right)^2 g(\sigma q_0/2)\,, \qquad (29)$$

where

$$g(x) \equiv x^{-5}\,[(2-2x^2+x^4)-(2+2x^2+x^4)e^{-2x^2}]\,,$$

ω_p is the volume plasma frequency, and v_F is the Fermi velocity for the plasma. We have also been able to derive a somewhat more general equation for the damping rate which includes the effect of individual electron-hole pair excitations. The latter processes are felt to be relatively unimportant in the present connection, however.

In Fig. 8.8 we compare the increase in damping rate due to crystallite size from Festenberg's data with the predictions of Eq. (29) above, both as a function of the angle θ, choosing σ = 210 Å. The experimental data were obtained from Fig. 5 of ref. 31 and represent the difference in the damping half width between Festenberg's solid points, obtained for nominally 70-Å crystallite sizes, and the open circles represent the energy half width appropriate to large crystallites. These differences are plotted as the points in Fig. 8.8. The solid

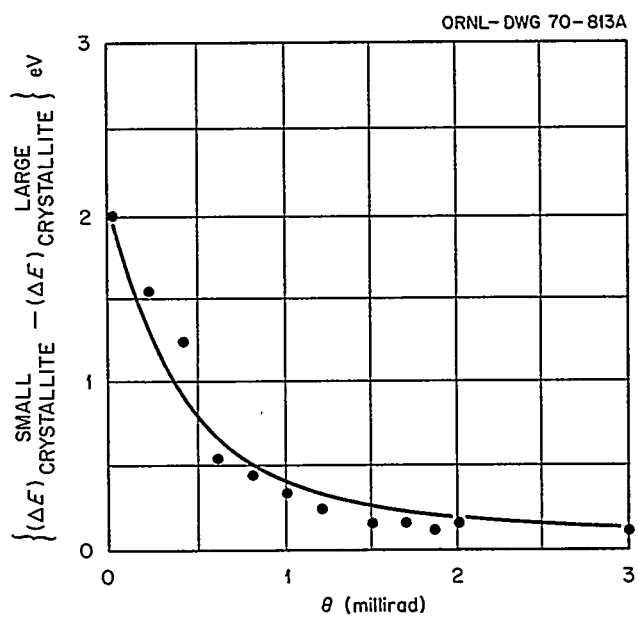

Fig. 8.8. Augmented Plasmon Damping Width Due to the Polycrystalline Structure of Aluminum Metal. The points were taken from Festenberg's data (ref. 31, Fig. 5). The smooth curve was calculated from Eq. (29).

[32] B. F. Ninham, C. J. Powell, and N. Swanson, *Phys. Rev.* 145, 209 (1966). See, however, D. F. DuBois and M. G. Kivelson, *Phys. Rev.* 186, 409 (1969).

[33] R. H. Ritchie and R. E. Wilems, *Phys. Rev.* 178, 372 (1969) (errata note, August 1969).

theoretical curve is normalized to the point at $\theta = 0$ and is obtained by taking $q_0 = [(\omega_p/v)^2 + (k\theta)^2]^{1/2}$, where v is the velocity of the 50-keV electron and k is its wave number.

We note that Festenberg's technique may be quite useful in studying the long-range electronic structure of polycrystalline metals as well as that of other condensed matter. The volume plasmon may be a potentially valuable diagnostic probe of certain kinds of matter in a sense comparable with the x ray and the fast electron.

An account of this work has been published recently.[34]

PHOTON–SURFACE-PLASMON COUPLING AT A DIELECTRIC SOLID

The coupling of photons with surface plasmons on a thick metal foil through the presence of structural irregularities at the surface has been studied experimentally by several workers. Theoretical treatments of this process neglecting the effect of retardation on the surface plasmon field have been given by Fedders[35] and Ritchie and Wilems.[33] Crowell and Ritchie[36] have extended the theory to include retardation in case of the plasmon on a semi-infinite electron gas separated from vacuum by a plane bounding surface.

Determination of the optical constants of solids through reflectivity measurements may be vitiated by the photon–surface-plasmon coupling effect unless the surface is extremely smooth or unless the effect may be allowed for theoretically. We have constructed a theory which is valid for photons incident normally upon a "weakly" rough surface between vacuum and a medium characterized by a wave-vector-independent dielectric constant $\epsilon(\omega) = \epsilon_1(\omega) + i\epsilon_2(\omega)$, such that $|\epsilon_1| \gg |\epsilon_2|$ in the range of frequencies ω of interest.

We quantize the surface plasmon (SP) field on the plane surface $z = 0$ by setting the total plasmon energy

$$H_0 = \frac{1}{8\pi c^2}\int d^3x \left\{\left(\tilde{\epsilon} + \frac{\omega}{2}\frac{d\tilde{\epsilon}}{d\omega}\right)\dot{\mathrm{A}}^2 + \frac{\omega^3}{2}\frac{d\tilde{\epsilon}}{d\omega}\mathrm{A}^2 + c^2(\nabla\times\mathrm{A})^2\right\} = \sum_\kappa \hbar\omega_\kappa b_\kappa^* b_\kappa\,, \quad (30)$$

where the integral runs over all space; $\tilde{\epsilon} = 1$ in vacuo ($z < 0$) and takes the (real) value $\epsilon_1(\omega)$ in the dielectric ($z > 0$). We assume that damping of the plasmon field is small enough that it may be treated by means of perturbation theory. The vector potential of the SP is chosen such that ϕ, the electric scalar potential, of the SP field is identically zero. The field amplitudes (b_κ, b_κ^*) become (annihilation, creation) operators after quantization according to the usual procedure.[35] The SP eigenfrequency ω_κ is the solution of $\kappa^2 = (\omega_\kappa^2/c^2)\{\epsilon_1(\omega_\kappa)/[1+\epsilon_1(\omega_\kappa)]\}$.

After quantization, we write the vector potential operator of the SP field corresponding to the plane-bounded dielectric as

$$\hat{\mathrm{A}} = \sum_\kappa \left[\frac{4\pi\hbar c}{L^2 p_\kappa}\right]^{1/2}\left[i\hat{\kappa} - \mathrm{sgn}(z)\frac{\kappa}{\nu}\hat{z}\right] \times e^{-\nu|z|}(b_\kappa + b_{-\kappa}^*)\,, \quad (31)$$

where $\nu(z) = (\kappa^2 - \omega^2\tilde{\epsilon}/c^2)^{1/2}$ and $\hat{\kappa}$ is a unit vector in the direction of the SP wave vector κ, parallel to the plane $z = 0$. The function $\mathrm{sgn}(x) \equiv x/|x|$, and $\hat{z}$ is a unit vector in the direction of the positive z Cartesian coordinate axis. The quantity

$$p_\kappa = (1-\epsilon_1)[-(1+\epsilon_1)]^{1/2}\,\epsilon_1^{-2} \times \left[\epsilon_1(\epsilon_1+1) + \frac{\omega}{2}\frac{d\epsilon_1}{d\omega}\right], \quad (32)$$

where $\epsilon_1(\omega)$ is understood to be evaluated at $\omega = \omega_\kappa$.

The equation satisfied by the state vector $|\psi\rangle$ of the SP field in the Schrödinger picture when a light beam is incident normally on the surface is

$$\left\{H_0 + H_1 - i\hbar\frac{\partial}{\partial t}\right\}|\psi\rangle = 0\,. \quad (33)$$

The Hamiltonian H_1 describes interaction between the light wave and the SP field due to the deviation of the surface from planeness.

Solving Eq. (33) by first-order perturbation theory for the case in which a photon is normally incident upon the surface, we find $\Delta R_S(\omega)$, the reflectivity decrease for photon energy $\hbar\omega$ due to surface plasmon generation,

[34] Vinod Krishan and R. H. Ritchie, *Phys. Rev. Letters* 24, 1117 (1970).

[35] P. A. Fedders, *Phys. Rev.* 165, 580 (1968).

[36] J. Crowell and R. H. Ritchie, *J. Opt. Soc. Am.* 60, 794 (1970).

values of k and ω are now expressed by complex values $k - i\alpha$ and $\omega - i\beta$. Substituting the expression for an unperturbed wave into Maxwell's equations in which $\sigma = 0$ and the corresponding expression for a perturbed wave into Maxwell's equations in which $\sigma \neq 0$ and assuming that $|\alpha| \ll k$ and $|\omega| \gg \beta$, we obtain two equations:

$$F = F(k, \omega) = (c^2k^2/\omega) - \omega\epsilon = 0$$

and

$$\alpha(\partial F/\partial k) + \beta(\partial F/\partial \omega) + 4\pi\sigma = 0,$$

which provide relationships between k, ω, α, and β.

If the medium is nonabsorbing, an electromagnetic disturbance is usually a specified mixture of homogeneous plane waves ("unperturbed" wave packet). It can then be expressed as

$$E^0 = \mathcal{E}^0(\psi) \exp i(kx - \omega t),$$

where $\exp i(kx - \omega t)$ is a carrier wave, $\mathcal{E}^0(\psi)$ is a modulating function, $\psi = x - v_g t$, and $v_g = d\omega/dt$ is the group velocity. The corresponding formulation for a "perturbed" wave packet (in an absorbing medium) is then obtained by applying the operator $\hat{K}$ to each homogeneous plane wave in the unperturbed wave packet. This results in the substitution of $k - i\alpha$ for k and $\omega - i\beta$ for ω. The total effect of absorption can then be obtained by summing the nonhomogeneous plane waves in the same manner as homogeneous plane waves are summed in the unperturbed wave packet. The perturbed wave packet then has the form $E = \mathcal{E}(\psi) \exp i(kx - \omega t)$, where $\mathcal{E}(\psi) = \exp(\alpha x - \beta t)\, \mathcal{E}^0(\psi)$ is the modulating function and $\exp(\alpha x - \beta t)$ is the attenuation factor.

In order to extend the meaning of the propagation velocity to absorbing media, we assume that the disturbance can be localized at a point $M(x_M, t_M)$ at which its intensity is maximum and consider the velocity of this point as the velocity of the disturbance. Then the velocity of the perturbed wave packet can be shown to be the same as the velocity of the unperturbed wave packet and to be equal to $v_g = v^0{}_g = d\omega/dk$. Using the equality $\psi = x_M - v_g t_M = 0$ and expressing t_M in terms of x_M or, conversely, x_M in terms of t_M, we obtain two alternate representations for a wave packet which are $E = (\exp \lambda x)E^0$ and $E = (\exp \delta t)\, E^0$, where $E^0 = \mathcal{E}^0(\psi) \exp i(kx - \omega t)$ and x, t, and ψ are the values at the point M. The expression $E = (\exp \lambda x)\, E^0$ shows how the disturbance localized at M decays with x, whereas the expression $E = (\exp \delta t)\, E^0$ shows how it decays with time. The attenuation parameters λ and δ are

$$\lambda = -\frac{4\pi\sigma}{\partial F/\partial k} \text{ and } \delta = \frac{4\pi\sigma}{\partial F/\partial \omega}; \qquad [F = (c^2k^2/\omega) - \omega\epsilon]\,. \qquad (36)$$

It has been shown in this analysis that by taking into account absorption, the energy density becomes $\overline{U} = \overline{U^0} \exp 2\lambda x$ or $\overline{U} = \overline{U^0} \exp 2\delta t$, the energy flow becomes $\overline{S} = \overline{S^0} \exp 2\lambda x$ or $\overline{S} = \overline{S^0} \exp 2\delta t$, and the velocity of the energy transport $v_u = \overline{S}/\overline{U}$ is the same as the kinematic velocity $v_g = d\omega/dk$, even if there is absorption.

A detailed account of the revised formulation of the macroscopic Maxwell theory has been recently published.[39]

REVISED FORMULATION OF THE KINETIC PLASMA THEORY

Using the Maxwellian macroscopic approach and analyzing the expression for the dielectric constant, it has been shown that the concept of energy has not been properly incorporated into the kinetic plasma theory. If one attempts to rephrase the Boltzmann-Vlasov theory in terms of the Maxwellian macroscopic formulation, one obtains an expression for energy which is not consistent with the meaning of this concept in generalized dynamics.[39]

The purpose of this investigation is to propose a revised version of the kinetic plasma theory in which the concept of energy is incorporated in accordance with the necessary requirements of the theory. In the revised version developed in this analysis the Boltzmann collisional operator $(\partial f/\partial t)_{\text{coll}}$ has been eliminated, and instead an appropriate collisional operator is introduced which is believed to describe more adequately collisional processes in a plasma.

To simplify the treatment, we assume that there is no Landau damping, and therefore there are no electrons traveling at or near the velocity of the wave. Then considering the macroscopic Maxwellian point of view we represent the effect of collisions by conductivity σ and assume that σ is a small perturbation. When $\sigma = 0$ we represent the collisionless unperturbed plasma in the usual manner by means of the Vlasov equations,

[39] Jacob Neufeld, *Nuovo Cimento* 65B, 33 (1970); 66B, 51 (1970).

9. Interaction of Radiation with Liquids and Solids

E. T. Arakawa
R. D. Birkhoff

A. J. Braundmeier[1]
Barbara G. Brooks[1]
T. A. Callcott[2]
J. J. Cowan[2]
L. C. Emerson
T. F. Gesell[1]
R. N. Hamm
W. F. Hanson[3]
J. A. Harter
R. A. MacRae[2]
Linda R. Painter[2]
B. L. Sowers[4]
U. S. Whang[2]
Mary W. Williams[2]

COLLECTIVE EFFECTS IN THE OPTICAL PROPERTIES OF CESIUM

There has been extensive interest recently in the optical properties of the alkali metals. Much of the work has been devoted to the lighter metals, sodium and potassium, and to the energy region below the plasma frequency. However, several recent theoretical studies suggest that excitation of collective modes makes an important contribution to the optical absorption above the plasma frequency.[5-7] Sutherland, Hamm, and Arakawa[8] have reported structure in the optical constants of sodium and potassium that is consistent with these predictions but does not distinguish between the absorption process suggested by Hopfield[5] as opposed to those of Lundqvist and Lydén[6] and Janow and Tzoar.[7] We have now extended our measurements of optical and dielectric constants to include cesium at photon energies above the plasma energy. Absorption in this region is attributed, at least partially, to a plasmon-assisted interband transition.

Reflectance measurements were made at the interface of cesium films evaporated onto quartz and CaF_2 substrates with light incident through the substrate. Since oxidation proceeds from the vacuum side of the cesium film, measuring times of many hours were available before oxidation of the film penetrated to the interface. The reflectance was measured as a function of angle of incidence, and the optical constants were derived from the behavior of the reflectance near the angle for total internal reflection. When $n \cong 1$ and $k \lesssim 0.05$, the real part of the complex refractive index, n, is determined from the angular position of the critical angle for total internal reflection after making a small correction in angle for finite k, the imaginary part of the refractive index. To a good approximation the critical angle is the angle where the slope of the reflectance vs angle of incidence curve is a maximum. The value of k is calculated from the slope of the reflectance curve at the critical angle, which has only a weak dependence on n. Data points from 3.6 to 9.6 eV and smoothed curves of n and k are shown in Fig. 9.1. The optical conductivity $\sigma = \omega nk/2\pi$, calculated from the smoothed curves of n and k, is shown in Fig. 9.2, along with lower-energy data of Ives and Briggs,[9] Smith,[10] and Mayer and Hietel.[11] The conductivity is a

[1] USAEC Health Physics Fellow.
[2] Consultant.
[3] Radiological Health Physics Fellow.
[4] Oak Ridge Graduate Fellow.
[5] J. J. Hopfield, *Phys. Rev.* 139A, 419 (1965).
[6] B. I. Lundqvist and V. S. Lydén, to be published.
[7] R. Janow and N. Tzoar, to be published.
[8] J. C. Sutherland, R. N. Hamm, and E. T. Arakawa, *J. Opt. Soc. Am.* 59, 1581 (1969).
[9] H. E. Ives and H. B. Briggs, *J. Opt. Soc. Am.* 27, 395 (1937).
[10] N. V. Smith, to be published.
[11] H. Mayer and B. Hietel, *Optical Properties and Electronic Structure of Metals and Alloys*, ed. by F. Abelés, North Holland, Amsterdam, 1966.

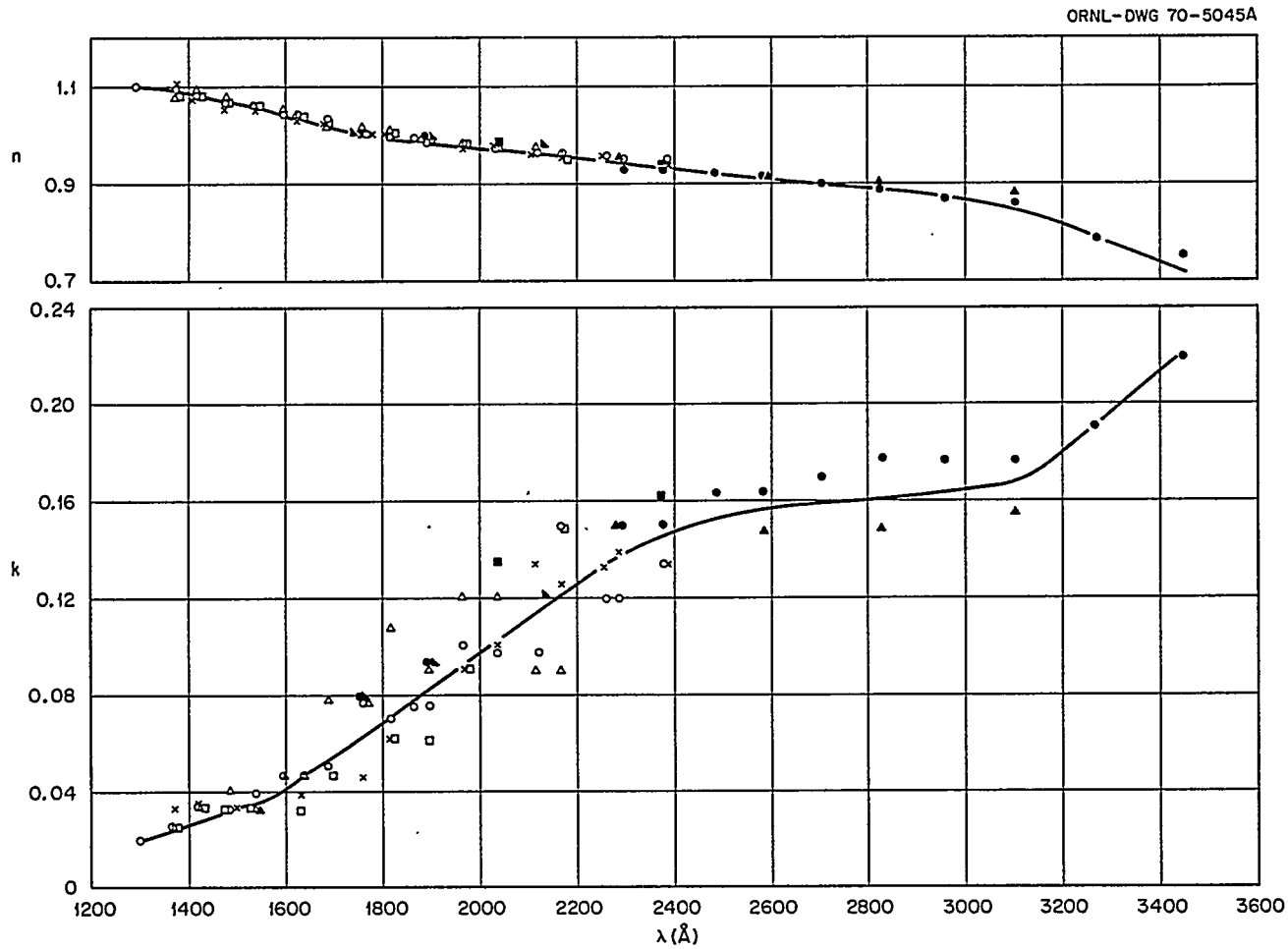

Fig. 9.1. Experimentally Determined n and k Values for Cesium Plotted Against Photon Wavelength. Film A, ○; film B, △; film C, □; film D, ×; film F, ●; film F, ▲; film G, ■; and film H, ▶. Solid lines give the smoothed average values.

direct measure of the optical energy absorption of the material. For cesium the plasma energy $\hbar\omega_p$ is at 2.9 eV, and absorption below this energy has been attributed to an interband transition. Absorption above the plasma energy, shown by a broad peak in σ with a threshold at 3.5 to 4 eV and a maximum at 5 eV, is the new feature seen from our observations. Band structure calculations indicate that this absorption at 5 eV cannot be explained as an interband transition. Several authors[5-7] have described absorption mechanisms involving collective effects that may provide absorption processes comparable in strength with interband transitions in the alkali metals where interband absorption is weak. Of these an appreciable increase in free carrier absorption as one passes through the plasma frequency[5] has to be ruled out for cesium. A plasmon-assisted interband transition[6,7] with a threshold at $\hbar\omega_p + \hbar\omega_g$, where ω_g is the threshold for interband transitions, is a possibility. The observed absorption seems to fit this description very well with a threshold between 3.5 and 4 eV as compared with $\hbar\omega_p + \hbar\omega_g$ = 3.5 to 3.8 eV, depending on the value taken for ω_g. The peak at 5 eV is very close to the plasmon energy plus the energy of the interband absorption peak. Lundqvist and Lydén[6] predict a magnitude for the absorption as measured by the value of σ of 30 to 50% of the interband peak for sodium. For cesium we observe relative values closer to 75%. If the interpretation in terms of plasmon-assisted transitions proves to be correct, this magnitude of the absorption and the fact that this absorption is larger in cesium than in sodium will have to be explained. It is interesting to speculate that the absorption apparently becomes stronger for alkali metals of higher atomic number. We are currently measuring rubidium to see if such a trend does in fact exist.

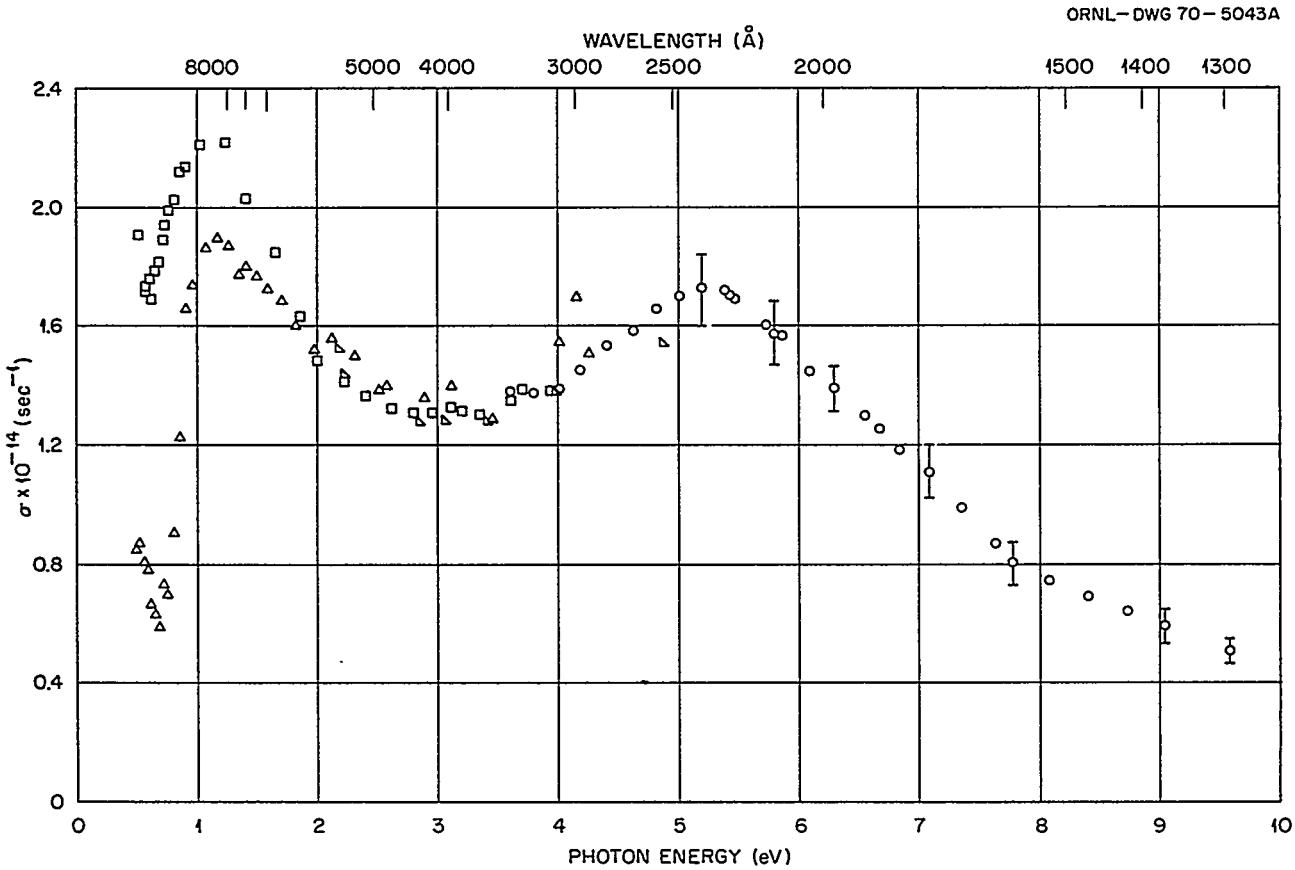

Fig. 9.2. Optical Conductivity σ vs Photon Energy. Present data, •; Smith, ▫; Mayer and Hietel, ▲; and Ives and Briggs, △.

OPTICAL PROPERTIES OF MgO AND MgF_2 IN THE SOFT-X-RAY REGION

The optical properties of MgO and MgF_2 have been obtained from 20 to 66 eV by measuring reflectance as a function of angle of incidence on single crystals and transmittance of thin films. The incident radiation in this energy region was produced by a high-voltage capillary discharge in air. A 2.2-m grazing incidence spectrometer with a resolution of approximately 1 Å was used. The thin film samples were vacuum evaporated onto self-supporting thin aluminum films and then transferred into the sample chamber. The aluminum substrate films were approximately 1500 Å thick. Two thin film samples were made for each of the two materials. The two MgF_2 films were each approximately 450 Å thick. One of the MgO films was approximately 280 Å thick and the other approximately 780 Å.

Figures 9.3 and 9.4 show the real part ϵ_1 and the imaginary part ϵ_2 of the complex dielectric constant as a function of the incident photon energy for MgO and MgF_2 respectively. In both cases the curves shown represent a composite of the values obtained from multiangle reflectance and transmittance data. In addition, normal incidence reflectance was used to perform a Kramers-Kronig analysis for the MgO. We see in both materials that ϵ_1 is approaching unity and ϵ_2 becoming small as the photon energy increases. This is to be expected in this energy region.

In Fig. 9.3 it is seen that ϵ_2 for MgO shows structure at 24, 30 to 41, and 52 to 60 eV. Cohen *et al.*[12] have determined the electronic band structure of MgO using a pseudopotential method. Although no strong 24-eV interband transitions are predicted by this calculation,

[12]Marvin L. Cohen *et al.*, *Phys. Rev.* 155, 922 (1967).

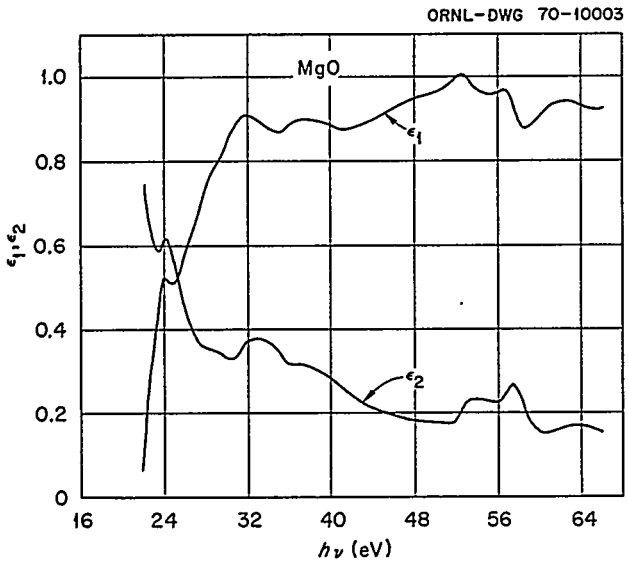

Fig. 9.3. Dielectric Constants for MgO vs Photon Energy.

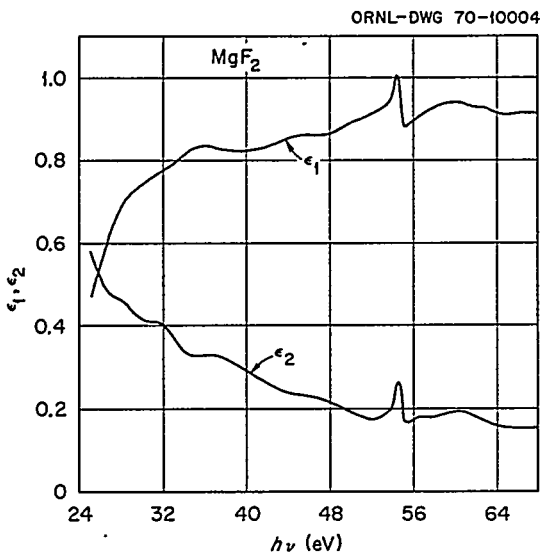

Fig. 9.4. Dielectric Constants for MgF_2 vs Photon Energy.

which was carried out for only a few directions in k space, we interpret the structure at 24 eV in terms of a transition or transitions, from the valence to the conduction band in MgO. As discussed below, the first energy level below the valence band is the oxygen 2*s* level, which lies between 22 and 23 eV below the top of the valence band. Since MgO has a band gap of 7.9 eV,[13] it is not energetically possible for the 24-eV structure to be attributed to anything but a valence to conduction band transition. The structure in ϵ_2 from 30 to 41 eV is identified with interband transitions from the 2*s* (L_I) level of oxygen to the conduction band. The 2*s* level in atomic oxygen is at 23.7 eV.[14] Correlation of the structure in ϵ_2 with that given by Cohen *et al.* for the conduction band and for the 2*s* oxygen level places this level 22 to 23 eV below the top of the valence band. Similarly, the structure seen in ϵ_2 between 52 and 60 eV can be qualitatively explained in terms of interband transitions from the 2*p* (L_{II}, L_{III}) magnesium level (assumed flat) to the conduction band. This places the 2*p* magnesium level 45 eV below the top of the valence band, whereas in atomic magnesium it lies at 49.5 eV[13] below the Fermi level. These data on MgO show good agreement with electron energy loss measurements[15–18] and with absorption measurements on thin films made by burning magnesium and catching the smoke on nitrocellulose.[19]

In Fig. 9.4 it is seen that ϵ_2 for MgF_2 shows structure from 27 to 38 eV and from 52 to 62 eV. The structure from 27 to 38 eV is assumed to be associated with interband transitions from the 2*s* shell in fluorine (at 31 eV in atomic fluorine)[14] to the conduction band, although there is no band theory available to corroborate this. The structure from 52 to 62 eV is associated with the 2*p* electron states of magnesium. The sharpness and strength of the 54.5-eV peak suggests an exciton level there, while the weaker structure from 56 to 62 eV is identified as due to interband transitions from the magnesium 2*s* state to the conduction band. The dielectric constants for MgF_2 determined by Stephan *et al.*[20] out to 45 eV from a single-crystal sample of MgF_2 using the multiangle reflectance method agree well with our values except in the 27-to-33-eV region, where their structure is much more pronounced. As with MgO, these data for MgF_2 are also consistent with electron energy loss measurements.[21]

---

[13] M. W. Williams and E. T. Arakawa, *J. Appl. Phys.* 38, 5272 (1967).

[14] J. A. Bearden and A. F. Burr, *Rev. Mod. Phys.* 39, 125 (1967).

[15] G. W. Jull, *Proc. Phys. Soc. (London)* B69, 1237 (1956).

[16] H. Watanabe, *J. Phys. Soc. Japan* 9, 920 (1954); *Phys. Rev.* 95, 1684 (1954).

[17] E. Rudberg, *Proc. Roy. Soc. (London)* A127, 111 (1930).

[18] C. J. Powell and J. B. Swan, *Phys. Rev.* 118, 640 (1960).

[19] V. A. Formichev and I. I. Zhukova, *Soviet Phys.–Solid State* 10, 2992 (1969).

[20] G. Stephan *et al.*, *J. Phys. Chem. Solids* 30, 601 (1969).

[21] Claude Gout, Beatrice Lahaye, and Pierre Perrier, *Compt. Rend. Acad. Sci. Paris* 265, 1460 (1967).

STUDY OF THE OPTICAL PROPERTIES OF SOLIDS BY ELLIPSOMETRY

In order to measure the change in ellipticity of light caused by the reflection process at a specimen surface, it is necessary to eliminate from the optical train any element which affects the polarization characteristics of the light beam. Since the use of front-surface films requires a vacuum environment, considerable effort was expended in locating and installing fused quartz entrance and exit windows which were free of inherent strain birefringence. It has been found that the strain introduced by the atmospheric pressure differential across the windows during pumpdown is sufficient to materially affect the polarization measurements. Since this problem can probably never be completely eliminated, the proper course of action would be to attempt to correct for the effect.

One technique which can be used to obviate this problem consists in preparing the specimen surface as usual on the face of a strain-free and transparent prism and then making the measurements at the specimen-prism interface. These measurements can then be carried out at atmospheric pressure with the windows removed. A simple test for the absence of strain birefringence in the prism has been suggested.[22]

The results of a series of such measurements on a palladium film evaporated on a strain-free quartz prism are shown in Fig. 9.5. The data below 9000 Å were obtained using an EMI 9558Q photomultiplier with a cooled photocathode to reduce dark current. Above this wavelength the data were obtained with a lead sulfide photoconductive cell and phase detection techniques. The scatter of points at the longer wavelengths results from noise in the detection system and not from any structure in the optical constants. The short-wavelength cutoff at 3250 Å is caused by the onset of the absorption edge in the mica wave plate used in this ellipsometric technique.

It is possible to measure the polarization ellipse directly without using a wave plate, in which case the short-wavelength cutoff would be extended to 2500 Å, which represents the transmission limit of the silicone fluid used in the prism polarizers. The technique consists in determining the amplitude ratio of the reflection coefficients, $\tan \psi = r_p/r_s$, and the relative phase change during reflection Δ by direct measurement and from these to calculate values of the optical constants n and k. With the polarizing prism (before the

[22] J. N. Hodgson, *J. Phys. Chem. Solids* 24, 1213 (1963).

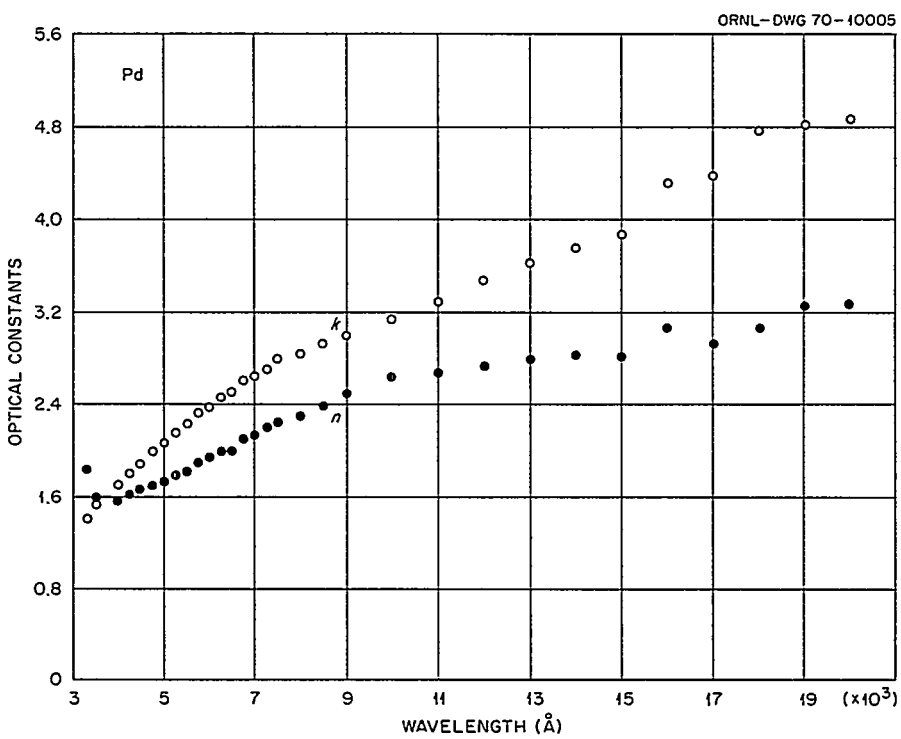

Fig. 9.5. Optical Constants of Palladium vs Wavelength.

specimen surface) set with its transmission axis at 45° from the plane of incidence, the angles ψ and Δ may be obtained from

$$\tan \psi = (c/d)^{1/2} , \quad (1)$$

$$\tan \Delta = \tan 2\eta / \sin 2\gamma , \quad (2)$$

where

$$\tan \eta = (b/a)^{1/2} . \quad (3)$$

In terms of the polarization ellipse the quantities a and b are intensities along the major and minor axes, respectively, while c and d are intensities parallel and perpendicular to the plane of incidence respectively. The angle γ is the displacement of the minor axis from the plane of incidence. An independent check on ψ may be obtained from the relation

$$\cos 2\psi = \cos 2\eta \cos 2\gamma . \quad (4)$$

The optical constants n and k are then obtained from the relation

$$n + ik = n_0 \tan \phi \left[1 - \frac{4\rho \sin^2 \phi}{(\rho + 1)^2} \right]^{1/2} , \quad (5)$$

where $\rho = \tan \psi \, e^{i\Delta}$, ϕ = angle of incidence, and n_0 = index of refraction of the immersion medium. Despite the apparent simplicity of this method, however, we have been unable to obtain better, more accurate dielectric constants with it.

RADIATIVE DECAY OF COLLECTIVE OSCILLATIONS IN METALS

Investigations have been continued of the optical emission spectra from metal films bombarded with high-energy electrons.[23]

Volume plasmon (normal surface plasmon) radiative decay is contained within the classical transition radiation theory for a planar foil and had previously been identified experimentally for several metals. During the past year, volume plasmon radiative decay measurements have been made on three metals, beryllium, magnesium, and aluminum.

There were no previous transition radiation measurements for beryllium; thus we thought it would be interesting to look at this metal. However, beryllium is very toxic and, with a high boiling point, is hard to evaporate. Figure 9.6 shows the transition radiation measured at 30° from the film normal for evaporated beryllium films bombarded by 80-keV electrons at normal incidence. There is a strong emission peak at 650 Å (19.1 eV) with a line width of 5.2 eV. By use of the optical constants measured by Toots *et al.*,[24] the

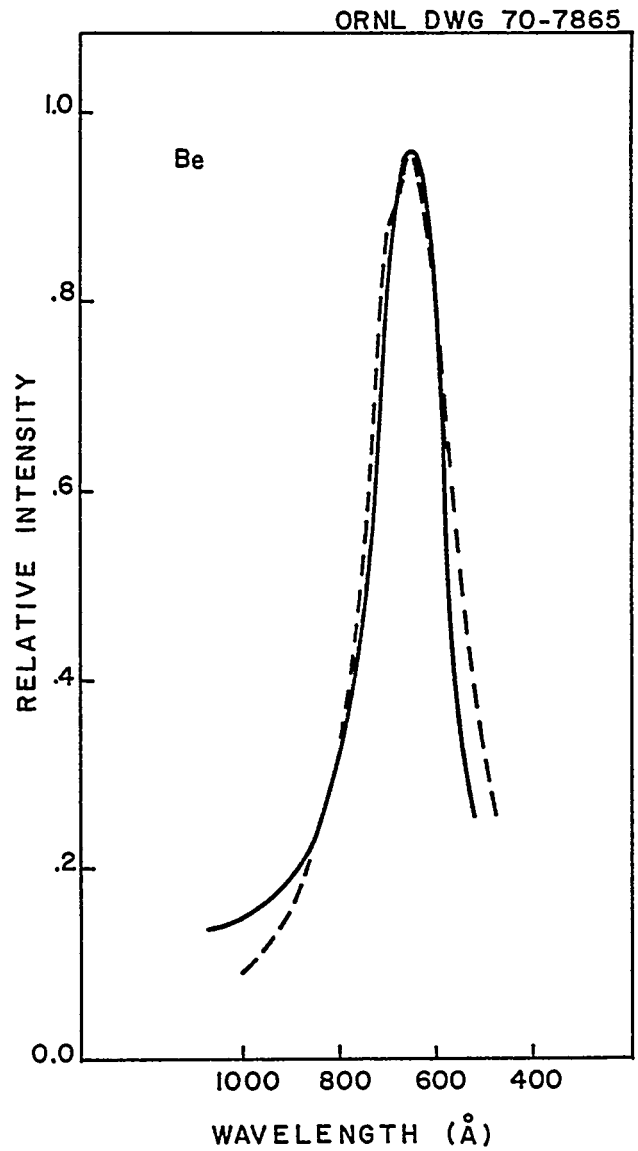

Fig. 9.6. Volume Plasmon Radiative Decay Spectrum from a Thin Be Film Bombarded with 80-keV Electrons. The spectrum was measured at 30° from the film normal and is compared with a theoretical spectrum for a 100-Å-thick film.

[23] E. T. Arakawa *et al.*, *Health Phys. Div. Ann. Progr. Rept. July 31, 1969*, ORNL-4446, pp. 187–88.

[24] J. Toots, H. A. Fowler, and L. Marton, *Phys. Rev.* 172, 670 (1968).

theoretical transition radiation spectra were calculated for various film thicknesses using the theory of Ashley.[25] Figure 9.6 shows the theoretical transition radiation spectrum for a 100-Å film with the maximum intensity adjusted to the experimental data. The beryllium film was known to be "thin," but its exact thickness was not known. It is seen that reasonable agreement is obtained between experiment and the transition radiation theory. The volume plasmon energy of 19.1 eV and the half width of 5.2 eV are comparable with the values of 18.4 eV and 4.7 eV, respectively, obtained by Toots *et al.*[24]

Recently, Feuerbacher and Fitton,[26] investigating optically induced volume plasmon resonances in thin (≅50 Å) metallic films by means of measurements of photoelectric yield, found an anomalous dispersion for magnesium. We have studied what is basically the inverse of the photoelectric yield experiment. The radiative decay spectra of volume plasmon oscillations have been observed for various angles of observation during bombardment of a 220-Å-thick magnesium film by 80-keV electrons incident nearly normal to the film. Figure 9.7 shows the spectra for angles of observation from 5 to 20° from the normal on the electron beam entrant side of the film. Assuming a free-electron-gas model for the electrons participating in the collective oscillation, it can be shown[27] that the resonance width at half maximum is given by

$$\Delta\lambda = \frac{\lambda_p}{\tau_d \omega_p} + \pi t \sin\theta \tan\theta \,, \qquad (6)$$

where τ_d^{-1} is the intrinsic damping rate, ω_p the plasma frequency, λ_p the plasma wavelength ($\omega_p \lambda_p = 2\pi c$), t the film thickness, and θ the angle of observation relative to the film normal. Figure 9.8 shows a plot of $\Delta\lambda$ vs $\sin\theta \tan\theta$ with the straight line satisfying a least-squares fit to the experimental points. The slope of this line gives a film thickness of 217 Å. The energy at which the plasma resonance for a free-electron gas occurs is given by

$$E = E_p \left(1 + \frac{\omega_p^2 t^2}{8c^2} \tan^2\theta\right) , \qquad (7)$$

where $E_p = \hbar\omega_p$.

[25] J. C. Ashley, *Phys. Rev.* 155, 208 (1967).

[26] B. Feuerbacher and B. Fitton, *Phys. Rev. Letters* 24, 499 (1970).

[27] R. A. Ferrell, *Phys. Rev.* 111, 1214 (1958).

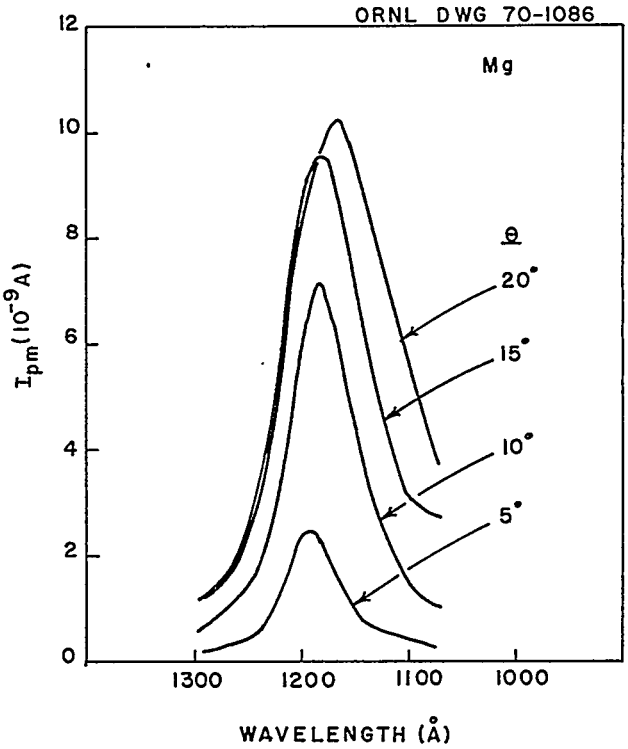

Fig. 9.7. Radiative Decay Spectrum from a 220-Å-thick Mg Film Bombarded with 80-keV Electrons.

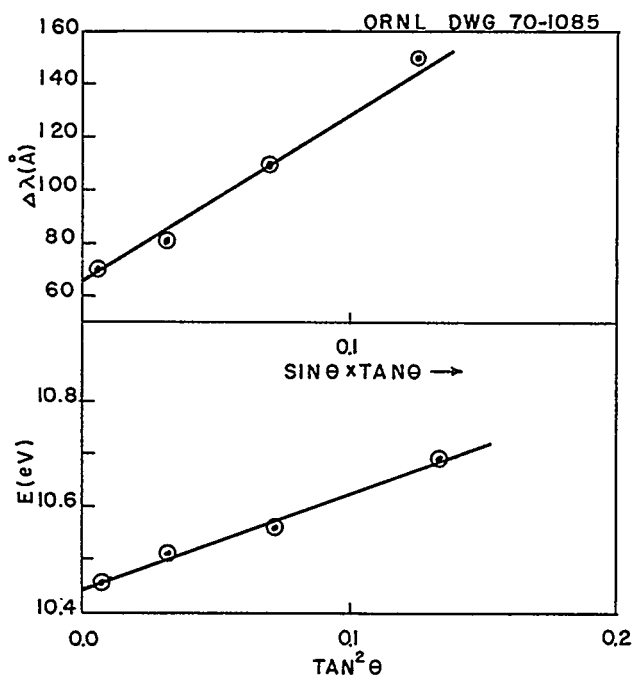

Fig. 9.8. Width at Half Maximum vs $\sin\theta \tan\theta$ and Peak Energy vs $\tan^2\theta$.

Figure 9.8 also shows a plot of the energy E at which the radiative decay is a maximum vs $\tan^2 \theta$. The slope is positive, as expected from Eq. (7), and thus the dispersion is normal, as opposed to the result found by Feuerbacher and Fitton.[26] The intercept gives a plasmon energy of 10.43 ± 0.03 eV, and substitution of this value into the slope equation gives a film thickness of 223 Å. In addition, using E_p = 10.43 eV, the intercept of $\Delta\lambda$ vs $\sin\theta \tan\theta$ gives $\tau_d = (1.14 \pm 0.11) \times 10^{-15}$ sec [Eq. (6)]. The energy width at half maximum as a fraction of the peak energy, $\Delta E/E$, is 0.055. These values are comparable with those obtained by Feuerbacher and Fitton in their photoemission experiment at room temperature:[26] E_p = 10.21 eV, $\tau_d = 1.09 \times 10^{-15}$ sec, and $\Delta E/E = 0.059$ for a 50-Å-thick film. Optical transmission measurements[28] at −196°C using a 160-Å-thick magnesium film yielded E_p = 10.1 eV and $\tau_d = 2.8 \times 10^{-15}$ sec.

Surface plasmon (tangential surface plasmon) radiative decay is not contained within the classical transition radiation theory for a planar foil since the phase velocity of these oscillations is less than that of light, and they are unable to couple with the radiation field. However, surface irregularities on real experimental foils can enable conservation of energy and momentum to be satisfied at the surface and the surface plasmon to couple with the radiation field. In general, experimental foils possess surface irregularities, so surface plasmon radiation is expected. Unambiguous identification of the radiative decay of surface plasmons has not been made previously for any material. This year we have measured plasma radiation from thin unoxidized films of aluminum bombarded by nonnormally incident 80-keV electrons. For each angle of incidence of the electrons, both surface and volume plasmon decay can be identified in the same spectrum, allowing unambiguous identification of the surface plasmon radiative decay. Previous attempts[23] to observe surface plasmon decay in aluminum were unsuccessful owing to the rapid formation of an oxide layer. In order to hinder the growth of an oxide layer on the film, a liquid-nitrogen trap was constructed to surround the fresh film almost completely during electron bombardment. Without this liquid-nitrogen trap, the pressure in the vicinity of the film was ~1 × 10^{-6} torr, and tangential surface plasmon radiative decay was not seen.

Experimental spectra of radiation emitted by a 300-Å-thick aluminum film bombarded by electrons at 60° from the film normal are shown in Fig. 9.9. The spectrometer was set to accept photons emitted at right angles to the incident electron beam, that is, 30° from the film normal. Spectra are shown for various times after evaporation of the aluminum onto the substrate. The intensity peak at 825 Å (15 eV) is explained as radiation due to decay of volume plasmons excited in the film. The prominent intensity peak near 1220 Å (10.2 eV) is believed to result from the radiative decay of surface plasmons excited by the incident electrons. The basis for this identification is the location of the peak wavelength and the rapid decrease in intensity of the radiation with time. These results are consistent with the electron energy loss measurements of Powell and Swan.[18] In addition, Powell and Swan found a loss peak at about 7 eV which increased in intensity with increasing oxide thickness. Unfortunately, our Cu-Be dynode photomultiplier has a very low response below 9 eV, and the spectra in the region of 7 eV could not be investigated.

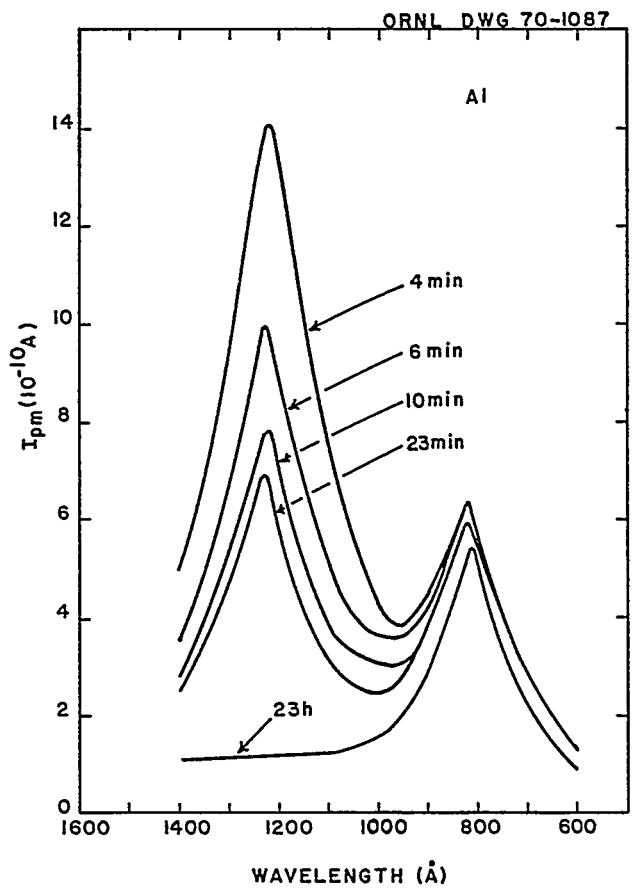

Fig. 9.9. Spectra of Radiation Emitted from a 300-Å-thick Al Film Bombarded by 80-keV Electrons at 60° from the Film Normal. The angle of observation was 90° from the electron beam direction. Spectra are shown for various times after preparation of the film. The beam current was 1 μA.

[28] H. O. Tittel, *Phys. Letters* 26A, 145 (1968).

RADIATION DAMPING OF SURFACE PLASMONS FROM ALUMINUM-COATED CONCAVE DIFFRACTION GRATINGS

Previqus studies of anomalous peaks in polarization data from the first-order diffraction spectra of monochromator concave gratings have yielded information on the dispersion of surface plasmons in the metal and dielectric coatings of the gratings.[29] To construct a theory of surface plasmon dispersion to compare with experimental results, one needs as an input parameter the real part of the dielectric constant (ϵ_1) of the overcoating metal. The experimental dispersion curve is found from the wavelengths of the anomalous polarization peaks in the diffraction spectra. Our previous work has shown excellent agreement between theory and experiment.

With this technique one should thus be able to measure an unknown ϵ_1 of a given overcoating metal from the peak wavelengths. If the imaginary part of the dielectric constant (ϵ_2) could also be measured, one would have complete information on the optical properties of the given metal. We believe this can be done by measuring the widths at half maximum of the polarization peaks. The widths are due to two effects: radiation damping and electronic damping. Electronic damping is proportional to ϵ_2 and could be measured directly if the radiation damping were known or could be calculated.

We have performed a quantum-mechanical calculation of radiation damping where consideration has been made of the decay of an intermediate-state surface plasmon into a diffracted photon using quantized radiation and plasmon fields and the groove profile geometry in an interaction Hamiltonian. This analysis yields a damping or width for a given branch value of the experimental data at a given wavelength.

Figure 9.10 shows typical experimental data for the anomalous polarization spectra. The branch values, which have been discussed in our earlier work,[29] are labeled with positive and negative integers. One notes, for example, that the peaks for the +1 branch are broader than those for the −4, −5, or −6 branches and that the +2 peak has an intermediate width.

In Fig. 9.11 are plotted the peak widths, as a function of branch value and wavelength, for +1 and +2 after electronic damping (of about 30 Å average width) has been subtracted. The dotted lines are the theoretical results. As far as general trends are concerned there is

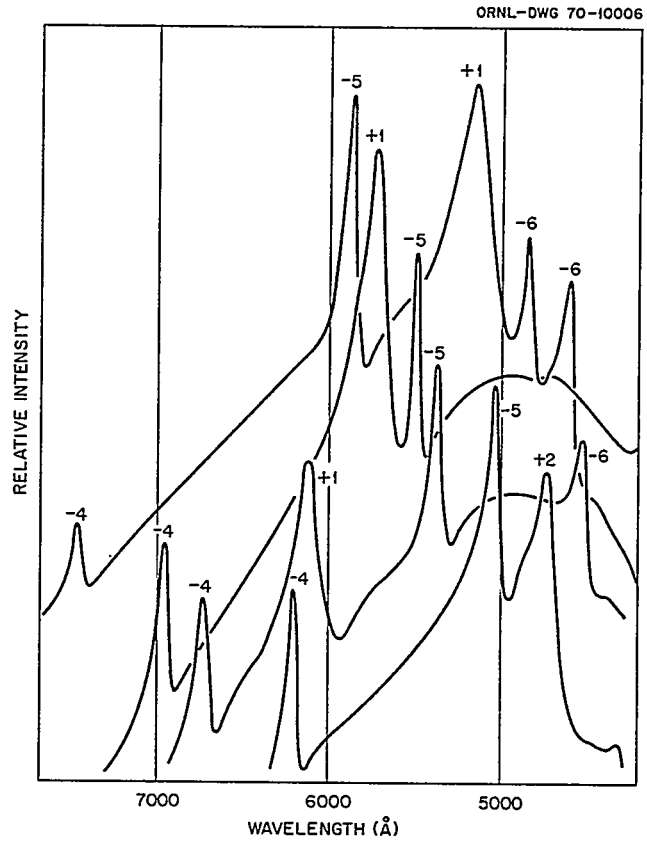

Fig. 9.10. Anomalous Polarization Peaks in First-Order On-Blaze Diffraction Spectra from Al-Coated Diffraction Grating for Various Source-Detector Angles.

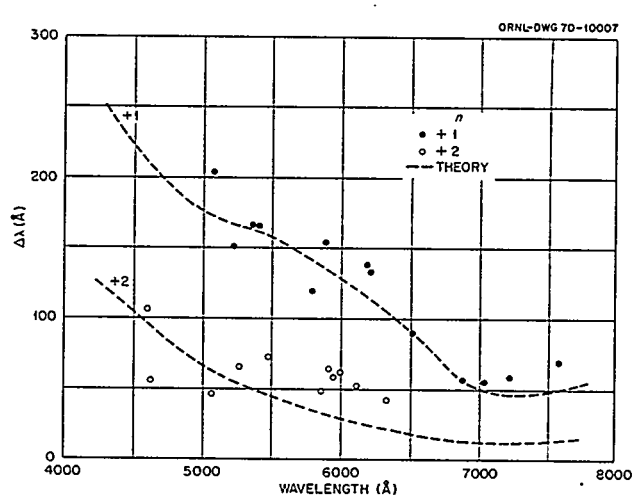

Fig. 9.11. Anomalous Peak Widths in Diffraction Spectra of Al-Coated Grating Due to Radiation Damping.

[29] E. T. Arakawa *et al.*, *Health Phys. Div. Ann. Progr. Rept. July 31, 1969*, ORNL-4446, pp. 188–96.

good agreement between theory and experiment. More careful measurements on the experimental widths are planned which we hope will yield better quantitative agreement.

EFFICIENCY OF DIELECTRIC-COATED CONCAVE DIFFRACTION GRATINGS

Measurements have been made of the efficiency of aluminized concave diffraction gratings (Bausch and Lomb, 600 lines/mm, 1500-Å blaze) when coated with diffusion pump oil of thicknesses from zero to several hundred angstroms. Previous studies had shown that diffusion pump oil contamination of monochromator gratings was responsible in part for certain anomalous polarization effects in the diffraction spectra in the visible through the vacuum ultraviolet spectral regions.[29]

Figure 9.12 shows the results of efficiency measurements from 1000 to 2500 Å for a grating coated with vacuum-evaporated Dow Corning 705 pump oil whose thickness at the time of deposition was determined with a quartz crystal monitor. The decrease in reflectance is most pronounced for small layers (20 Å) at short wavelengths. As the layer thickness is increased (150–250 Å), the decrease in reflectance becomes larger at the longer wavelengths. This is in accordance with expected behavior since optical absorption varies inversely with wavelength and directly with the absorption coefficient. For DC-705 the absorption coefficient is zero at wavelengths longer than 2500 Å and is finite at shorter wavelengths, reaching a maximum at 1000 Å.

The grating coated with 250 Å of oil was left in the vacuum system for 48 hr, and the efficiency measured at the end of this time is shown in Fig. 9.13. The increase in efficiency is attributed to evaporation from the grating of the oil at 10^{-6} torr. Visual inspection of the grating seemed to verify this, since thick layers are clearly discernible and thin layers are not. The anomalous *p*-polarized first-order on-blaze spectra of the grating in the visible region are shown in Fig. 9.14. The shift of the polarization peaks to longer wavelengths for increasing dielectric thickness is predicted by the surface plasmon resonance interaction theory.[29] The magnitude of the wavelength shifts gives calculated dielectric thicknesses in fairly close agreement with the measured values. Note that after evaporation the peaks shift back to values characteristic of thin layers.

The results of these measurements indicate that grating contamination can be monitored simply by measuring the shift in anomalous polarization peak wavelengths. This could have applications, for example, in the space program, where grating spectrometers subject to contamination in spacecraft could be calibrated in flight by scanning the diffraction spectrum.

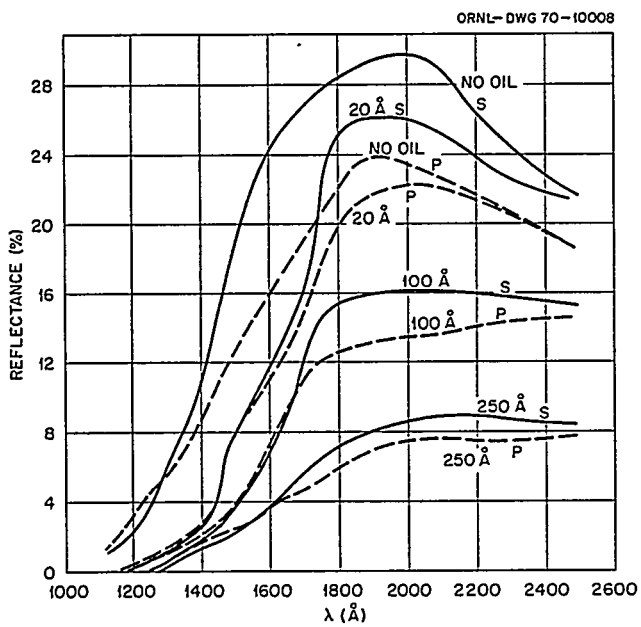

Fig. 9.12. Diffraction Grating Efficiency vs Wavelength for Various DC-705 Pump Oil Thicknesses.

OBSERVATIONS OF SURFACE ROUGHNESS

An optically smooth surface reflects a beam of light in the direction specified by geometrical optics. A small

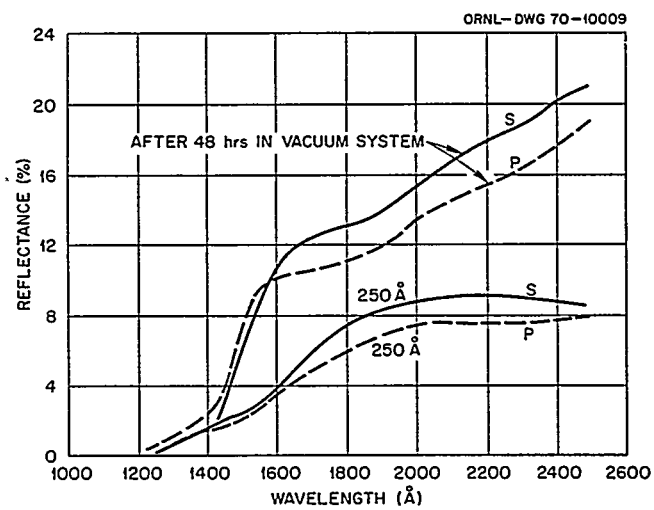

Fig. 9.13. Grating Efficiency vs Wavelength for a Thick DC-705 Oil Layer.

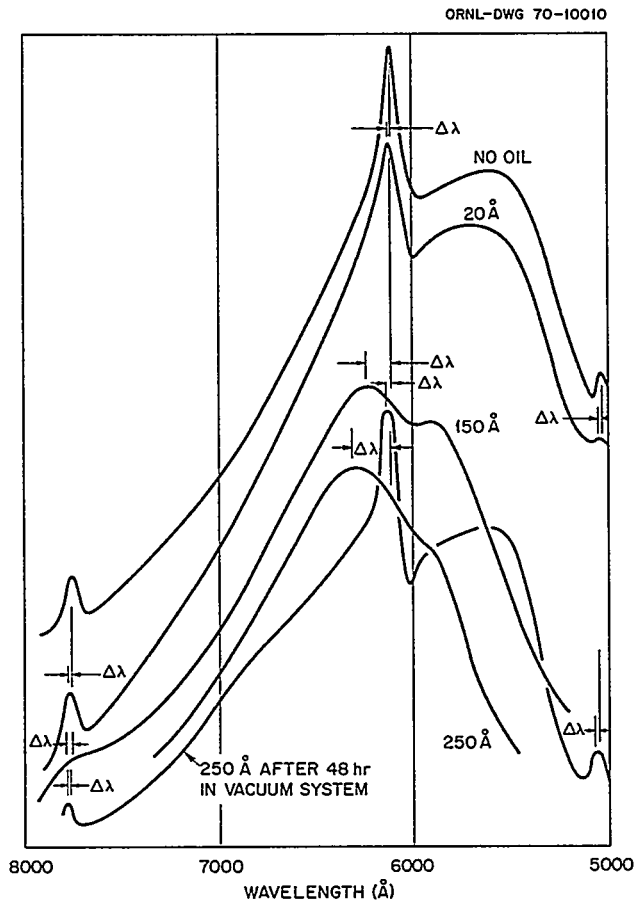

Fig. 9.14. Anomalous Polarization Peak Shift with DC-705 Oil Layer Thickness.

intensity of light is propagated in other directions owing to diffraction at the edges of the beam. If the surface is not perfectly smooth, some light will also be diffusely reflected by the surface irregularities. The degree of smoothness necessary to give specular reflection can be estimated by a consideration of the behavior of a reflection grating. Consider a parallel beam of light incident at angle θ_1 to the normal on a grating of constant d. The directions θ, measured from the normal, of the principal maxima in the diffracted light are given by the grating equation:

$$d(\sin\theta - \sin\theta_1) = \pm m\lambda\,, \tag{8}$$

where m is an integer or zero. The specularly reflected beam corresponds to zero order, $m = 0$. If the incidence is normal, $\theta_1 = 0$, the nonzero orders will not occur when $\lambda/d > 1$ because no real values of θ satisfy Eq. (8). Therefore, at normal incidence the transition to specular reflection occurs when $d = \lambda$; for smaller d the surface is optically smooth.

A polished surface does not have the regularity of a grating, but the structure of the surface can be represented by a surface profile function $h(x, y)$. Here x and y are coordinates in the mean surface, assumed plane, and h is the local height above the mean surface. A Fourier transformation of $h(x, y)$ gives the spectrum of surface roughness $H(k)$. Optical methods can be used to investigate the components of $H(k)$ with wave numbers in the range $k \leqslant 2\pi/\lambda$, where λ is the wavelength of light. Components of roughness in this range are important for the coupling of light waves with surface plasmons. The optical reflectance of a metallic surface is also dependent to some extent on the internal scattering of conduction electrons at the surface. The de Broglie wavelengths of these electrons are ~10 Å, and the degree of specular reflection is determined by surface structure of this order of magnitude. Since atomic diameters are ~2 Å, the atomic structure of the surface must be considered, and the problem is related to x-ray diffraction by an array of atoms. A surface may be quite rough for optical wavelengths but reflect conduction electrons specularly because it consists of regular crystal planes.

The surface profile function $h(x, y)$ for a single surface can be deduced from specular and diffuse reflectance measurements,[30] and the combined $h(x, y)$ for two surfaces from multiple-beam Fizeau fringes. A further, proposed method which should give a quantitative measure of the combined $h(x, y)$ for two surfaces consists in the photometric observation of two-beam fringes. Consider interference in light reflected from a wedge-shaped gap between uncoated glass surfaces as shown in Fig. 9.15. The gap thickness is given by

$$S = x\theta + h(x, y)\,. \tag{9}$$

[30] H. E. Bennett and J. O. Porteous, *J. Opt. Soc. Am.* 51, 123 (1961).

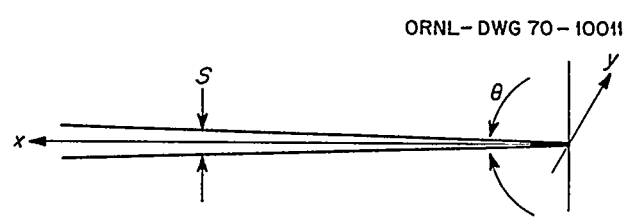

Fig. 9.15. Experimental Arrangement for Measuring Surface Roughness.

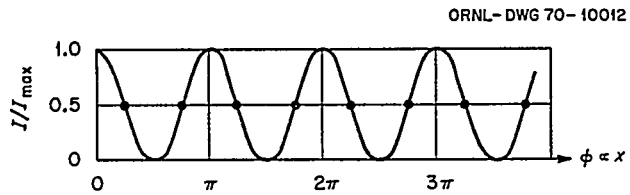

Fig. 9.16. Variation of Intensity with Distance Along Wedge.

The fringes are effectively two-beam[31] with a distribution of intensity given by

$$I = \frac{1}{2} I_{max} \, (1 + \cos 2\phi) \, ,$$

where I_{max} is the peak intensity and 2ϕ is the phase difference between reflected beams. If the surfaces are smooth, $h(x, y) = 0$ and

$$\phi = 2\pi x\theta/\lambda \text{ (normal incidence assumed)} \, . \qquad (10)$$

The variation of I with x is illustrated in Fig. 9.16. When $\phi = (\pi/4)\,(2m - 1)$, where m is an integer, $dI/d\phi$ has a maximum value. For a constant $x = x_0$ corresponding to a value of $\phi = (\pi/4)\,(2m - 1)$, the intensity in the y direction varies as

$$I = \frac{1}{2} I_{max} \left\{ 1 \pm \sin \left[\frac{4\pi}{\lambda} h(x_0, y) \right] \right\} \, , \qquad (11)$$

or

$$I \cong \frac{1}{2} I_{max} \left[1 \pm \frac{4\pi}{\lambda} h(x_0, y) \right] \, . \qquad (12)$$

A scan of I in the y direction gives the variation of $h(x_0, y)$ with y. Thus, a 1% variation in I corresponds to a variation of 5 Å in $h(x_0, y)$ for $\lambda = 6000$ Å. This should be measurable with a photomultiplier tube attached to a microscope.

EXOELECTRON EMISSION DURING OXYGEN AND WATER CHEMISORPTION ON FRESH MAGNESIUM SURFACES

The term exoelectron emission has been applied to a small electron emission current from a solid when the process supplying energy to excite internal electrons over the surface barrier is not clearly related to external stimuli. For metals, some authors have attributed most reported results to low levels of photoemission from stray light, but others claim small currents in the absence of light. It is well established, for metals, that exoelectron emission is strongly dependent on the type and pressure of the background gas in which the sample is immersed, but the exact processes supplying energy to the escaping electrons are not generally agreed upon. Usually the emission currents recorded have been of the order of 10^{-17} to 10^{-15} A/cm^2.

We have found exoelectron emission[32] currents as high as 2×10^{-11} A/cm^2 on exposing a fresh magnesium surface to water vapor or oxygen in the range from 5×10^{-10} to 1×10^{-6} torr partial pressure. The experiments were performed in complete darkness and at room temperature in a liquid-nitrogen-trapped valveless stainless steel vacuum system pumped with a 4-in. oil diffusion pump using Dow Corning 705 and capable of 1.5×10^{-8} torr without baking. The sample area was about 5 cm^2. The electrons were collected at +8 V on a 7-in.-diam stainless steel grid. The current was measured with a Keithley 417 picoammeter connected directly to the sample. To make a measurement the partial pressure was set by admitting the desired gas via a high-vacuum leak valve while monitoring the total pressure with an ionization gage connected to a strip-chart recorder. The difference in total pressure was taken as a reasonable measure of the partial pressure of the added gas. The ionization gage was then turned off and covered with a light-tight cover. The fresh surface was prepared either by vacuum evaporation (from a tungsten filament) or by abrading a bulk sample for 10 sec with a stainless steel wire brush operated through a rotary feedthrough. Following evaporation or abrasion, the picoammeter and the recorder were switched on to record the current. Current vs time curves taken at the same pressure were quite reproducible.

Figure 9.17 shows the time development of the exoelectron emission of abraded magnesium exposed to various partial pressures of oxygen. The two maxima in the exoelectron current for the intermediate pressure indicate that the process is not a simple one. Figure 9.18 shows the time development of the exoelectron emission of abraded magnesium exposed to various partial pressures of water vapor. For similar pressures the exoelectron emission induced by water vapor took somewhat longer to reach a maximum and persisted longer than the emission induced by oxygen. No double

[31] See, for example, S. Tolansky, *Multiple Beam Interferometry*, Oxford, 1948, and *Surface Micro-Topography*, Interscience, 1960.

[32] T. F. Gesell, E. T. Arakawa, and T. A. Callcott, *Surface Sci.* 20, 174 (1970).

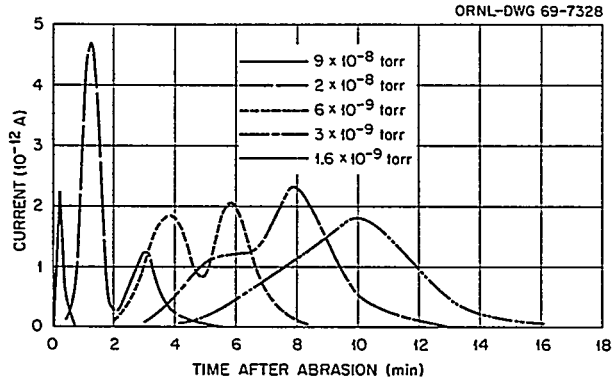

Fig. 9.17. Time Development of Exoelectron Emission for Oxygen on Magnesium at Various Pressures.

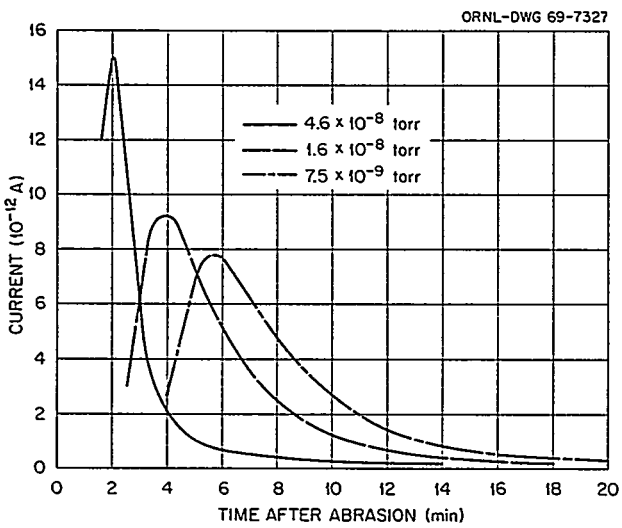

Fig. 9.18. Time Development of Exoelectron Emission for Water Vapor on Magnesium at Various Partial Pressures.

maxima have been observed with water vapor. Several other gases were tested on magnesium. No measurable emission was found with ethanol, nitrogen, acetone, isopropyl alcohol, or hydrogen, but a small emission was found with methanol. In separate experiments it was determined that there is a correlation between exoelectron emission and the work function of the surface, the work function going through a minimum when the emission current goes through a maximum. In addition, the maxima in the emission occur at times which are close to monolayer formation times calculated assuming a unit sticking coefficient. For an oxygen partial pressure of 1.1×10^{-8} torr, the maximum yield is 1.2×10^{-6} electron per molecule assuming 100% collection efficiency. The yield for electron ejection due to chemisorption of water on magnesium is of the same order of magnitude as the yield for chemisorption of oxygen on magnesium.

We feel that the energy for the ejection of the electrons comes from the energy released by the chemisorption of the oxygen or water molecules on the fresh magnesium surface. One possible mechanism for the electron ejection, first suggested to us by Ehrlich,[33] is that the incoming molecule is adsorbed, and then emits an Auger electron in the process of chemically uniting with the magnesium to form MgO. Although more work will be necessary before the detailed mechanism of the emission can be explained, the high currents available make the magnesium-oxygen and magnesium-water systems particularly well suited for studying emission during chemisorption of gases on metals.

[33] G. Ehrlich, private communication.

10. Physics of Tissue Damage

E. T. Arakawa
R. D. Birkhoff
L. C. Emerson W. J. McConnell
R. N. Hamm L. R. Painter[1]
H. C. Schweinler
B. L. Sowers[2]
M. R. Williams[1]

ELECTRON-SLOWING-DOWN STUDIES

This year we decided to investigate the electron flux in an irradiated semiconductor to see if the flux in this type of solid is similar to that in the metals previously investigated, or whether the presence of a band gap results in a change in the number of low-energy electrons. The semiconductor germanium was chosen in the form of single crystals 50 mils thick. When irradiated in a reactor, germanium produces two radioactive isotopes of substantial half-life, ^{71}Ge, which decays by *K* capture with 7.8-keV *KLL* and 0.9-keV *LMM* Auger electrons emitted, and ^{77}Ge, which has an 11.3-hr half-life and a complicated beta- and gamma-ray spectrum. We were interested in the longer-lived activity, with the monoenergetic Auger electrons providing essentially delta-function electron sources for producing electrons which would cascade in numbers and be followed down to energies of the order of the band gap. Unfortunately, the first irradiation produced an insufficiently intense source after we had allowed the short-lived ^{77}Ge activity to die away. A new source was constructed and placed in the reactor for a much longer activation period, which increased the activity of the ^{71}Ge by a factor of 10.

The flux emerging from the double-disk source of ^{71}Ge is shown in Fig. 10.1, along with the same from a source of ^{51}Cr. The flux from the germanium is higher than the flux from the chromium due to the higher energy of the *KLL* Auger electron in the case of the germanium (7.8 keV). The flux in the chromium generated by the 4.3-keV *KLL* Auger lies consistently about a factor of 2 below the germanium data above 100 eV, in part because the stopping power is higher at the lower electron energy, thus depressing the flux. General shapes of the two curves are very similar, however, indicating that the flux emerging from a

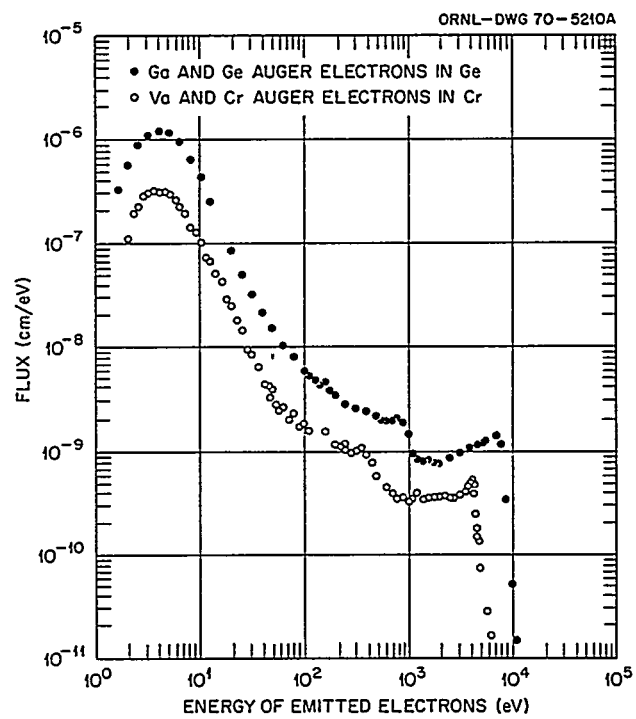

Fig. 10.1. Electron Fluxes Emerging from ^{71}Ge and ^{51}Cr Sources.

[1]Consultant.
[2]Oak Ridge Graduate Fellow.

semiconductor differs only slightly from that from a metal. This observation tends to verify what we have come to assume for some time, namely, that the slowing-down spectrum of electrons in an irradiated solid is rather independent of the electronic structure of the solid, at least above a few electron volts. At the lowest energies the flux from the germanium increases faster than that from the chromium, due possibly to the reduced stopping power in the semiconductor near the band gap.

All the data taken on electron slowing down in metallic media, while agreeing with the Spencer-Fano formulation in the energy region above 10 keV, have shown consistently more electrons below this energy by as much as a factor of 4. A careful look at various possible systematic errors in the experiment has revealed none, which implies that the Spencer-Fano theory utilizing electron production by electron-electron collisions only may, in fact, be neglecting one or more important sources of electrons. It is well known that in any irradiated medium roughly comparable amounts of energy go into ionization and excitation of the medium. It would seem possible that the energy going into excitation might somehow reappear in the form of electrons.

In an ancient paper Edwards and Poole[3] irradiated various metallic media with beta rays and measured the spectrum of the photons generated using an absorption technique. They found a very large apparent low-energy photon flux (which could, however, at least in part be ascribed to an increase of the sensitivity of their ion chamber at low energies). Thus we were led to speculate that there might be a photon cascade in an irradiated solid as a companion to the electron cascade. The thought here is that the energy might be transferred back and forth from electrons to photons many times in the slowing-down process.

To check this idea, we constructed a source of tungsten which when irradiated yielded two isotopes, ^{185}W and ^{187}W, the first with a 74-day half-life and a 0.43-MeV beta ray and the second with a 24-hr half-life and a complicated beta- and gamma-ray spectrum. The shorter-lived isotope was allowed to decay away, leaving the pure beta spectrum of ^{185}W as the source of electrons. The source is in two parts, a thin disk only slightly thicker than the beta-ray range and a thick disk whose thickness is equal to the $1/e$ attenuation length of the bremsstrahlung corresponding to the highest-energy beta ray.

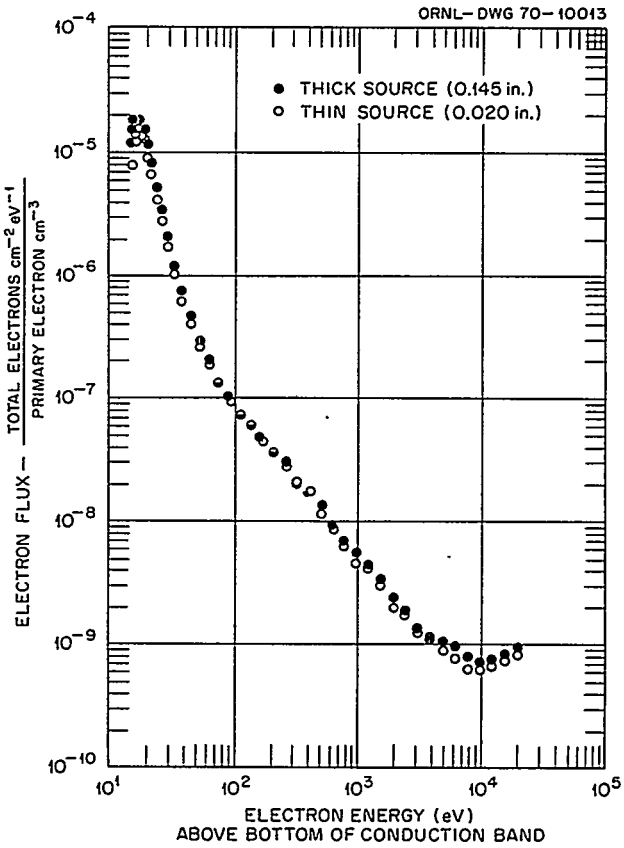

Fig. 10.2. Electron Fluxes in Thin and Thick Sources of ^{185}W.

Electron flux measured from these thin and thick tungsten sources is shown in Fig. 10.2. It can be seen that these fluxes are indistinguishable within the experimental accuracy of about ±10%. Thus, it would seem that the photons generated in an irradiated medium are relatively ineffective in creating electrons as compared with those created directly by the beta rays in the medium. Thus, we will have to look elsewhere for sources of electrons to explain the discrepancy between our observations on many metals and a semiconductor, and the Spencer-Fano-Attix theory.

OPTICAL PROPERTIES OF SOME ORGANIC LIQUIDS

Reflectance measurements of some representative organic liquids and diffusion pump oils in the vacuum uv have been continued[4] in order to further clarify the

[3] G. E. Edwards and M. L. Poole, *Phys. Rev.* 69, 549 (1946).

[4] E. T. Arakawa *et al.*, *Health Phys. Div. Ann. Progr. Rept. July 31, 1969*, ORNL-4446, pp. 180–82.

processes that occur in this energy range. Some improvements have been made in the procedure to enable better and more consistent data to be obtained. A family of simple organic liquids from cyclohexane to benzene have been measured from 4.0 to 10.65 eV. It is hoped that this work will lay the foundation for interpreting the results from the more complicated molecules.

In the past, problems have arisen with the consistency of data in measuring optical properties of liquids in the vacuum uv using the semicylinder method. In this method we assume an optically flat crystal giving a plane liquid-crystal interface at which reflectance takes place. Most of the crystals used are fluoride salts, which are fragile and soluble in most liquids; therefore harsh cleaning procedures cannot be used. It became evident that the condition of the crystal surface was causing the problems of reproducibility of the data. After much experimenting it has been found that the fluoride crystals can be cleaned sufficiently without destroying the optically polished surface. We use freshly distilled vapor from a Freon 113 or isopropyl alcohol bath. Freon is better in some cases because of its lower boiling point. In this way the optical surfaces are never touched with lens tissues, which seem to deposit a layer of dirt or grease on the crystal, making the experimental conditions inconsistent with the theoretical assumptions.

A Teletype system has also been added to the experimental equipment which records the data directly onto paper tape compatible with the computer. This eliminates the process of reading chart paper with the possibility of the visual bias of the experimenter.

Because there is so little theoretical foundation on the optical properties of liquids in this energy region, most of the liquids chosen for study are simple in structure. Carbon tetrachloride, CCl_4, is a tetrahedral molecule. Reflectance measurements have been taken from 4.0 to 10.65 eV. Figure 10.3 shows the optical constants n and k for CCl_4. The optical absorption at 9.7 eV corresponds to a $\sigma \rightarrow \sigma^*$ transition. The dashed curve is absorption obtained by us from transmission measurements and occurs at approximately the same energy as absorption in the vapor.[5] Here k is very small ($\cong$0.05) and cannot be measured by the reflectance method; however, there is slight structure in n, indicating some absorption. This absorption at 7.0 eV is attributed to an $n \rightarrow \sigma^*$ transition involving the nonbonding chlorine electrons.[5] There is also evidence of strong absorption above 10.7 eV. These data should enable group theoretical calculations to be made to identify more precisely these molecular transitions.

Measurements of the optical properties of n-hexane, C_6H_{14}, which is a linear chain, and benzene, C_6H_6, which is a six-member C ring with three π bonds, have been reported previously.[4] Recently, other six-member C ring hydrocarbons have been measured, including

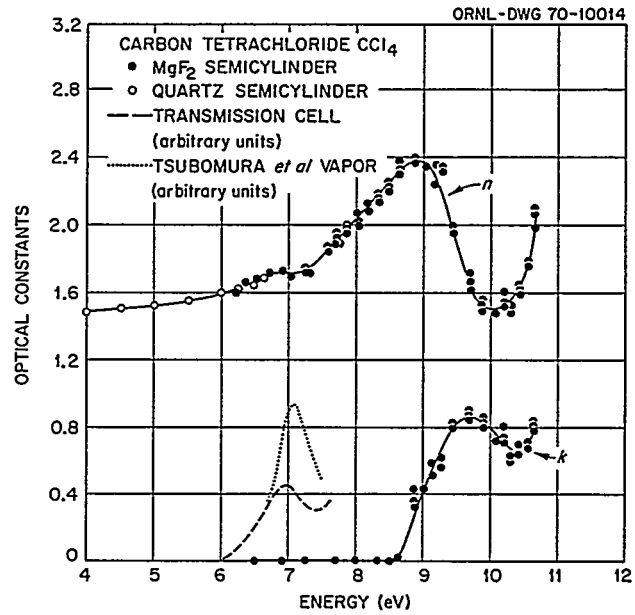

Fig. 10.3. Optical Constants of CCl_4 vs Photon Energy.

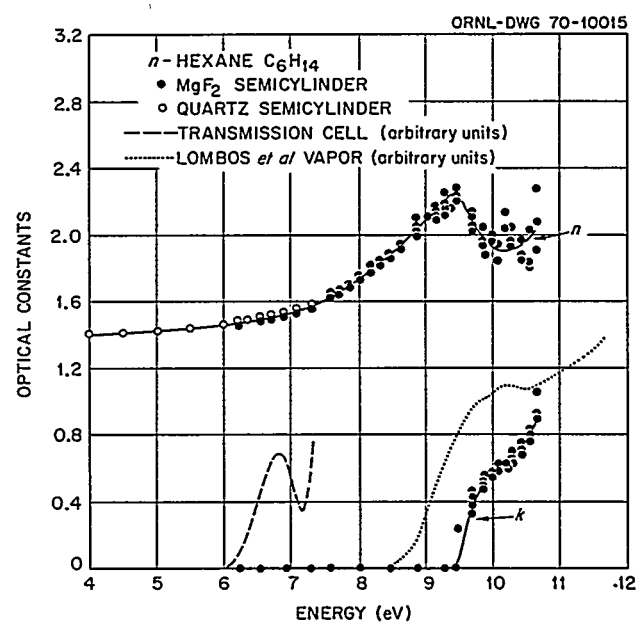

Fig. 10.4. Optical Constants of C_6H_{14} vs Photon Energy.

[5] H. Tsubomura *et al.*, *Bull. Chem. Soc. Japan* 37, 422 (1964).

cyclohexane, C_6H_{12} (no π bonds), cyclohexene, C_6H_{10} (one π bond), and cyclohexadiene, C_6H_8 (two π bonds). *n*-Hexane and benzene have both been remeasured using the improved experimental methods. Figures 10.4–10.8 show the most recent optical constants of these five molecules. All five molecules show a characteristic absorption beginning at 9.5 eV. This is attributed to $\sigma \rightarrow \sigma^*$ transitions for the C–C or C–H bonds. In Fig. 10.4 the peak in C_6H_{14} at 6.8 eV was found from transmission data. The origin of this absorption, which is small, is not known. In Fig. 10.5 (C_6H_{12}), the small structure in *n* at 8.0 eV presumably corresponds to the peak in the vapor data[6] at 8.5 eV. Figure 10.6

[6] J. W. Raymonda and W. T. Simpson, *J. Chem. Phys.* 47, 441 (1967).

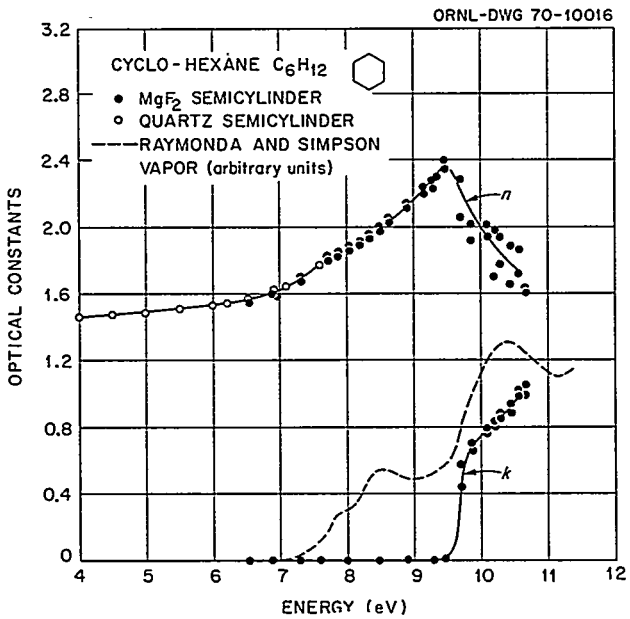

Fig. 10.5. Optical Constants of C_6H_{12} vs Photon Energy.

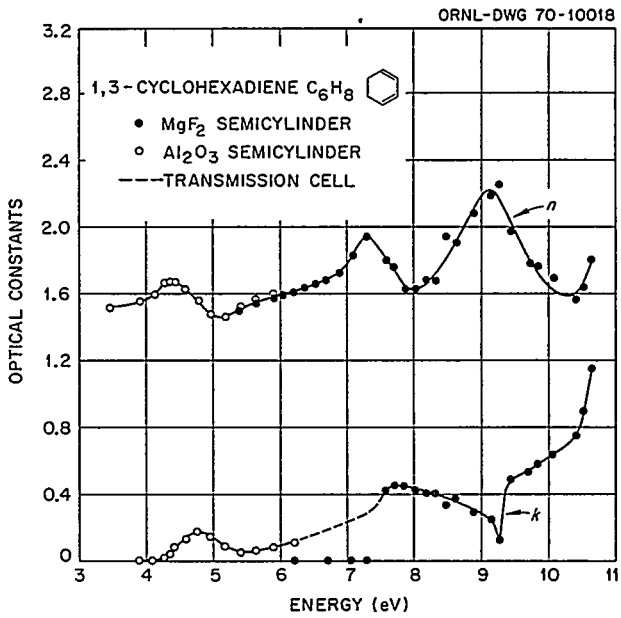

Fig. 10.7. Optical Constants of C_6H_8 vs Photon Energy.

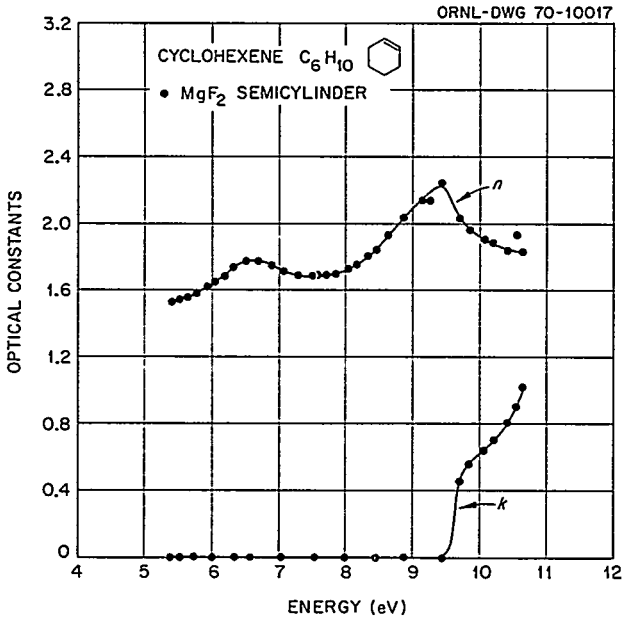

Fig. 10.6. Optical Constants of C_6H_{10} vs Photon Energy.

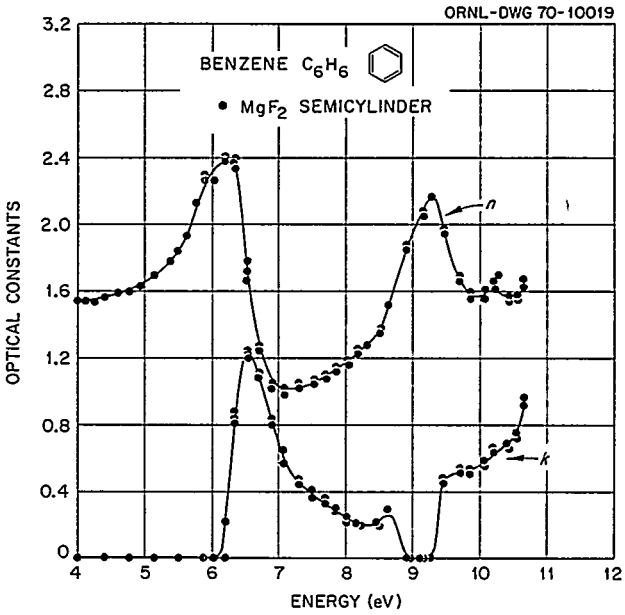

Fig. 10.8. Optical Constants of C_6H_6 vs Photon Energy.

(C_6H_{10}) shows structure in n at 6.5 eV, the corresponding k again being too small to be measured by reflectance methods. We attribute the structure in n to the excitation of the π electrons, but this is not as intense as in C_6H_6 (Fig. 10.8) because of the smaller number of π electrons. Figure 10.7 (C_6H_8) shows structure in n and k in the region of 7 to 8 eV, similar to that in C_6H_{10} and C_6H_6, with an intermediate intensity corresponding to the intermediate number of π electrons. Some new structure has been found in C_6H_6 at 8.6 eV, as shown in Fig. 10.8, but has not been identified.

With this body of knowledge for the simple liquids, we are continuing our work with more complicated molecules such as diffusion pump oil and body fluids.

11. Electron and Ion Collision Physics

R. N. Compton

V. E. Anderson[1]
Ada Carter
C. D. Cooper[2]
F. J. Davis
W. R. Garrett
J. T. Grissom[3]
J. A. Harter
G. S. Hurst[2]
W. T. Naff[4]
S. J. Nalley[3]
D. R. Nelson
P. W. Reinhardt
H. C. Schweinler
J. A. Stockdale

ELECTRON IMPACT EXCITATION AND IONIZATION OF THE RARE GASES

Two complementary techniques are presently being used to study inelastic electron scattering in gases: the trapped-electron method and the SF_6 scavenger technique. In studies of He,[5] Ne,[6] and Ar, negative-ion resonances associated with autoionizing states are observed in trapped-electron spectra of the cross section for the production of slow electrons resulting from ionizing collisions. As an example, Fig. 11.1 shows evidence for new negative-ion states in neon at 44.51 eV associated with an autoionizing state of the form $2s^2 2p^4 nln'l'$ or $2s2p^6 nl$, and at 49.86 eV associated with an autoionizing state of the form $2s^2 2p^4 nln'l'$. The latter negative-ion state represents the first observation of a triply excited negative-ion state for any atomic system other than helium. Triply excited negative-ion resonances have also been observed as "dips" in the positive ionization cross section of helium. The two resonances shown in Fig. 11.2 occur at 57.2 and 58.3 eV and correspond to He^- terms of $2s^2 2p(^2P)$ and $2s2p^2(^2D)$ respectively.

Figure 11.3 shows the trapped-electron spectrum of helium from the first excited state at 19.83 eV up to approximately 90 eV. Right at the ionization potential (24.6 eV) both of the final-state electrons have zero kinetic energy, so that the trapped-electron current abruptly increases. The spectrum is noted to remain relatively constant over a broad energy range. The

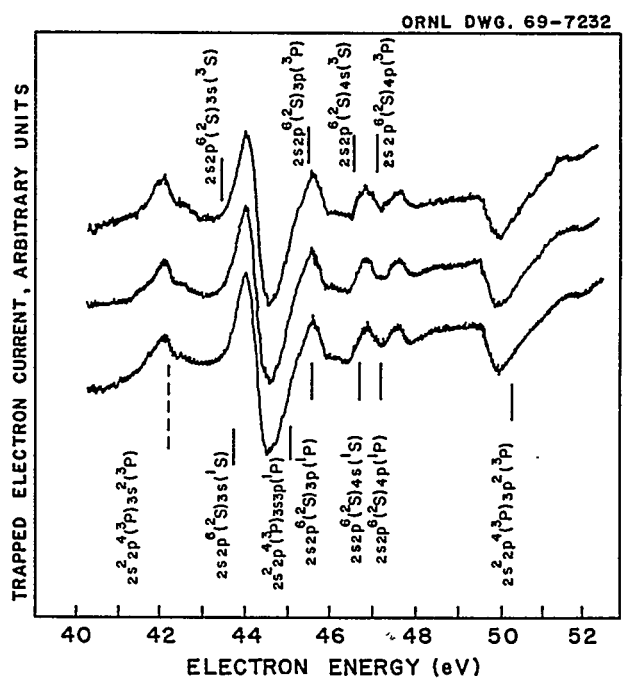

Fig. 11.1. Neon Trapped-Electron Spectra in the Energy Region of Doubly Excited Autoionizing States.

[1] On loan from Computing Technology Center (ORGDP).

[2] Consultant.

[3] Radiological Health Physics Fellow.

[4] Oak Ridge Graduate Fellow.

[5] J. T. Grissom, R. N. Compton, and W. R. Garrett, *Phys. Letters* 30A, 117 (1969).

[6] J. T. Grissom, W. R. Garrett, and R. N. Compton, *Phys. Rev. Letters* 23, 1011 (1969).

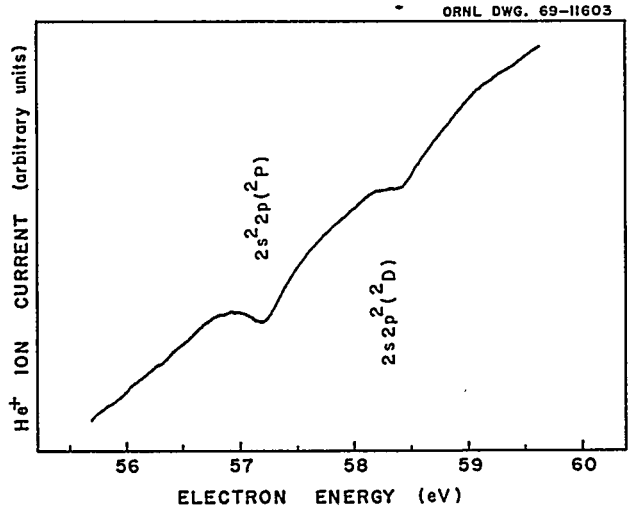

Fig. 11.2. Negative-Ion Resonances in the Helium Ionization Cross Section.

overall shape of the trapped-electron spectrum in the ionization region is only slightly dependent on the depth of the potential well. Figures 11.4 and 11.5 show the SF_6 scavenger and the trapped-electron spectra, respectively, of argon. Again note the relatively flat cross section for production of slow electrons. Structure in the energy region from 20 to 30 eV is attributed to both autoionizing states and temporary negative-ion resonances. The rise in the cross section at ~30 eV is attributed to ionization of a $3p$ electron accompanied by excitation and/or ionization of a $3s$ intershell electron. It seems rather surprising that the cross section for producing slow electrons in ionizing collisions exhibits such a small variation over an energy region in which the ionization cross section is changing so rapidly. The relative flatness of the slow-electron

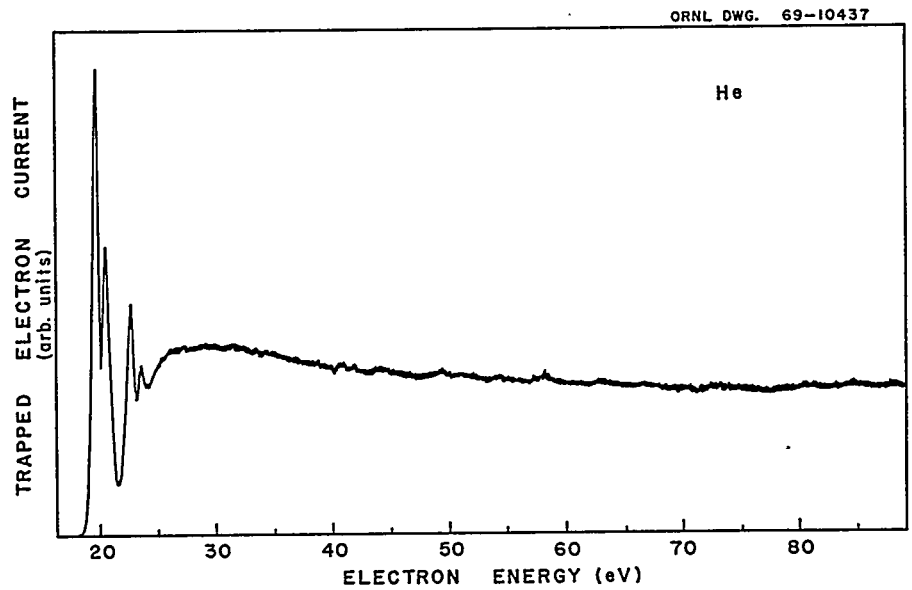

Fig. 11.3. Helium Trapped-Electron Spectrum.

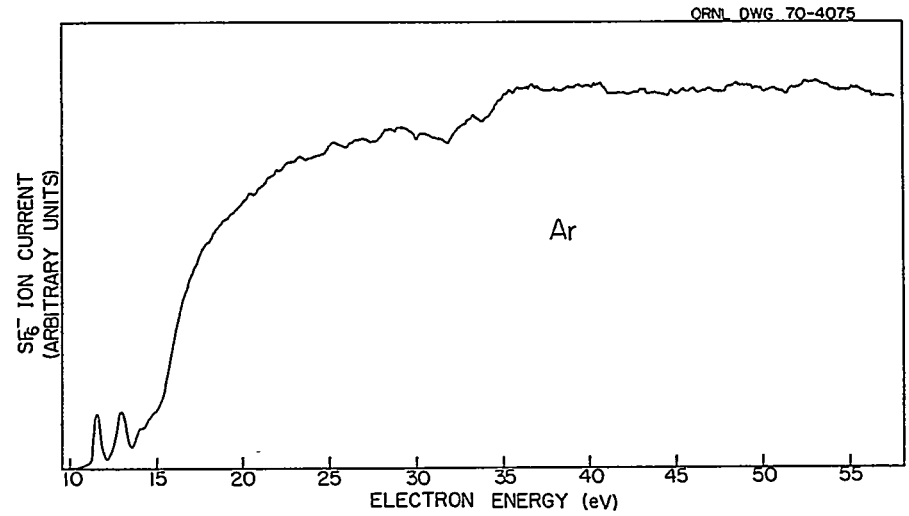

Fig. 11.4. SF_6^- Scavenger Spectrum of Argon.

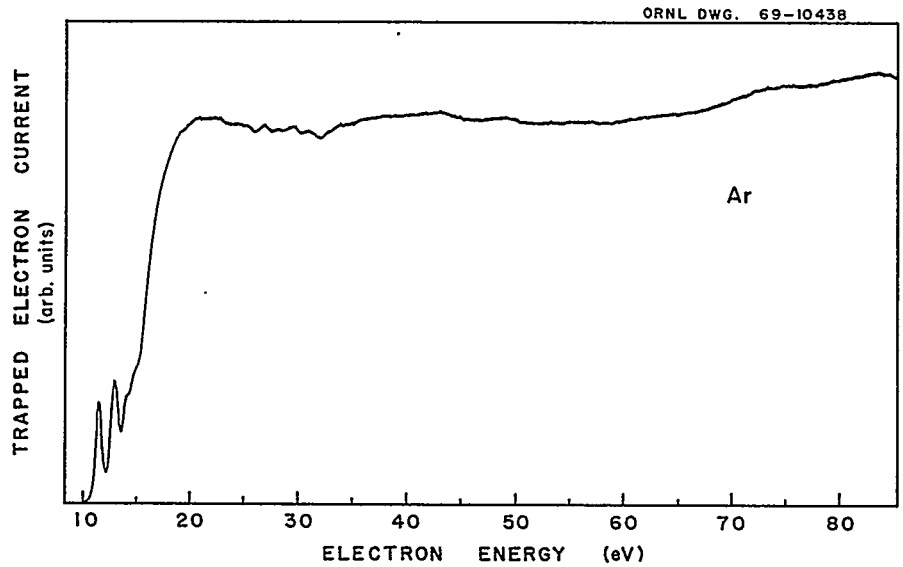

Fig. 11.5. Trapped-Electron Spectrum of Argon.

production cross sections has not been explained theoretically.

The cross sections for the production of slow electrons above the ionization potential are being investigated, and attempts are being made to relate these measurements to electron-slowing-down spectra in helium.

THRESHOLD ELECTRON IMPACT EXCITATION OF SOME SIMPLE MOLECULES

The SF_6 scavenger technique has been employed to study threshold excitation and the slow electrons produced upon ionization of water vapor, boron trichloride, boron trifluoride, acetone, benzene, biphenylene, and triphenylene. In this connection the productions of ion fragments from water and benzene were recorded as functions of the electron beam energy in order to aid in interpreting the slow-electron production cross sections. Contrary to the results for the rare gases discussed in the previous section, the cross section for production of slow electrons above the ionization potential increases with electron energy up to ~80 eV. The general increase in the slow-electron cross section may be explained by the introduction of other channels of ionization, that is, dissociation into ionized fragments.

The threshold excitation spectrum of BCl_3 is shown in Fig. 11.6. A number of electronic states are observed as well as temporary negative-ion resonances. Dissociative attachment to BCl_3 and BF_3 showed some striking differences: Cl^-/BCl_3 occurred at ~0.9 eV and F^-/BF_3 peaked at the unusually high electron energy of ~11 eV. These results indicate that rather dramatic differences must exist in the attachment of electrons to the simple boron halides. Perhaps the resulting BF_2 is electronically excited when an electron is dissociatively attached to BF_3.

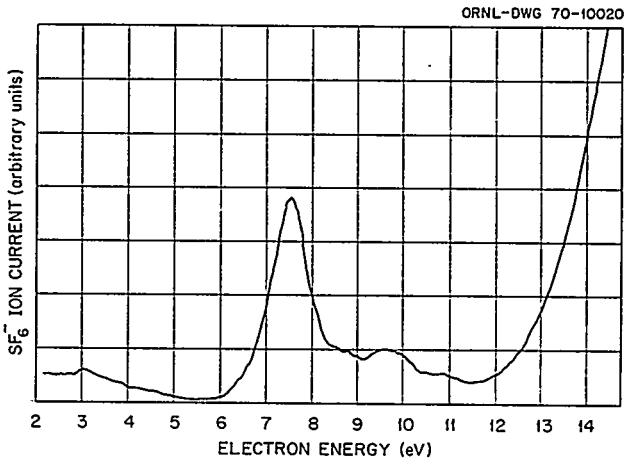

Fig. 11.6. Threshold Electron Impact Excitation Spectrum of BCl_3.

The threshold excitation of biphenylene shows an intense broad peak at ~2 eV. Although the lowest triplet state of this important molecule has never been detected, it is believed that the 2-eV peak in the

threshold excitation spectrum can be attributed to this electronic state. Presently the dissociative attachment processes in chlorobiphenylene are being investigated to further identify this peak.

INTERACTION OF ELECTRONS WITH SUBSTITUTED BENZENES, SUBSTITUTED PYRIDINES, AND PYRIZINE

Nondissociative thermal-electron attachment was observed in the following aromatic species with measured autodetachment lifetimes (in microseconds) shown in parentheses: C_6F_5Br (29), C_6F_5Cl (17.6), C_6F_5CN (17), C_6F_5CHO (36), C_6H_5CN ($\approx$5), $C_6H_5NO_2$ (17.5), $C_6D_5NO_2$ (22), *m*-$C_6H_4ClNO_2$ (47), and perfluoronaphthalene (123). Figure 11.7 shows the measured negative-ion lifetimes for some highly fluorinated compounds plotted vs the number of degrees of vibrational freedom along with those of a previous study[7] (previous study results are open circles). The approximate linearity of the plot with the present data supports our previous model describing long-lived negative ions. Deuteration was observed to increase the lifetime of nitrobenzene, which is also in qualitative agreement with the lifetime model. Monochlorination of nitrobenzene (*m*-$C_6H_4ClNO_2$) essentially doubled the measured value of the lifetime, which can be explained by assuming the electron affinity is increased. Neither C_6F_5I nor *m*-$C_6F_4INO_2$ formed long-lived parent states, dissociation dominating at thermal incident electron energy, which reflects the relatively weak bond strengths of iodine compared with other halogens.

Dissociative attachment as a function of incident electron energy was studied in all of the above molecules using the automatic retarding potential difference (RPD) technique. In molecules of the form C_6F_5X (X = Cl, Br, I) ion currents of X^- and $C_6F_5^-$ were observed for incident electron energies of <0.1 eV. The current ratios of $Cl^-/C_6F_5^-$, $Br^-/C_6F_5^-$, and $I^-/C_6F_5^-$ were 100/1, 30/1, and 1/3 respectively. Since in C_6F_5Br and C_6F_5Cl a long-lived parent ion current was observed at energies overlapping dissociative attachment, a study was made to determine whether or not long-lived parent ion states underwent dissociation. It was determined that all measurable dissociation occurred within 1 μsec after electron impact. Parent ion states which lived longer than 1 μsec did not dissociate but decayed through autodetachment only. This would imply that dissociation occurred from a different resonant state than the long-lived state.

Figure 11.8 shows negative-ion breakdown curves for *m*-chloronitrobenzene. Dissociation producing both Cl^- and NO_2^- occurred at two resonances having energies close to those producing NO_2^- in nitrobenzene. Dissociation appears to occur from two virtual states with the incident electron captured into π-electronic orbitals. In a study of *m*-iodonitrobenzene, I^- was observed at

[7]W. T. Naff, C. D. Cooper, and R. N. Compton, *J. Chem. Phys.* 49, 2784 (1968).

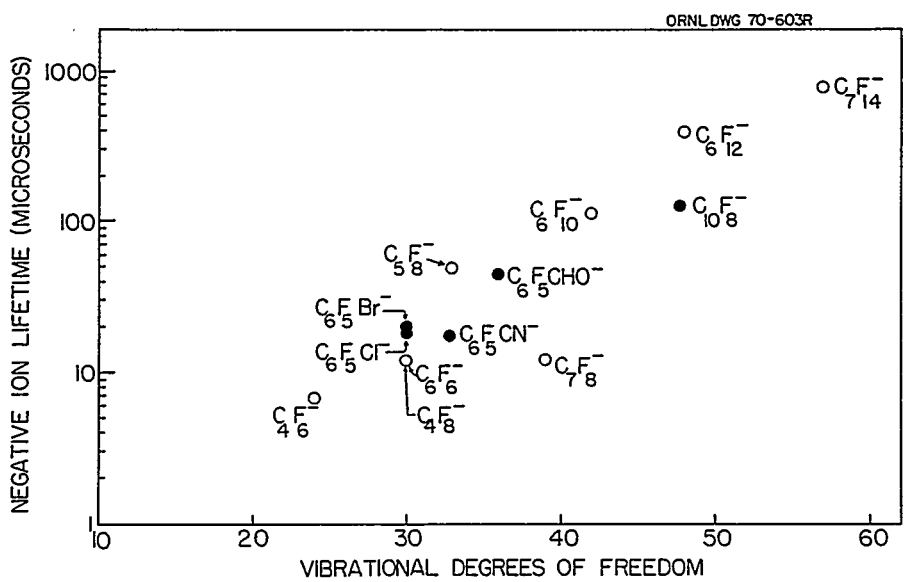

Fig. 11.7. Dependence of Negative-Ion Lifetimes of Highly Fluorinated Parent Ions on the Number of Degrees of Vibrational Freedom.

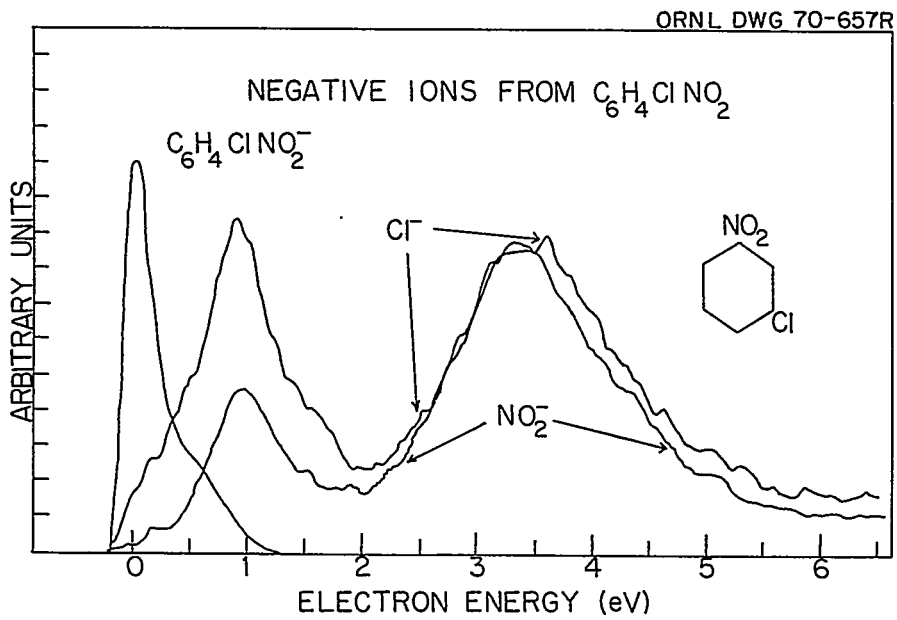

Fig. 11.8. Negative-Ion Yields from *m*-Chloronitrobenzene.

thermal energy with a small peak in the I^- current at 0.8 eV in addition to a broad I^- resonance at 4.1 eV.

The SF_6 scavenger technique was employed in detecting a temporary negative-ion resonance (TNIR) at ~0.8 eV in pyrizine. This was the only peak in the scavenger spectrum below 4 eV. *o*-Chloropyridine was observed to dissociate producing Cl^- at ~0.5 eV, with a TNIR detected with the scavenger technique at ~0.4 eV. Pyridine, on the other hand, showed two temporary negative-ion resonances.[8] Br^- from *o*-bromopyridine was observed at ~0.15 eV. The TNIR in bromopyridine could not be detected with the SF_6 scavenger technique since it was expected to lie at an energy too close to that for the primary SF_6^- current.

ATTACHMENT RATE OF THERMAL ELECTRONS TO SF_6

It has been pointed out[9,10] that the model for electron attachment followed by either stabilization or detachment, which was proposed by Mahan and Walker[11] and cited as a possible explanation for SF_6 attachment results,[12] is invalid. Briefly, Mahan and Walker proposed a two-body-capture process of an electron e by a molecule X to produce an unstable excited state ion X^{-*},

$$e + X \underset{k_a}{\overset{k_1}{\rightleftharpoons}} X^{-*}, \tag{1}$$

which autodetaches with a mean lifetime k_a^{-1}. In the presence of a third body M (carrier gas), X^{-*} can collide with M to promote either electron detachment from or stabilization of the ion through

$$X^{-*} + M \begin{array}{l} \overset{k_2}{\rightarrow} X + M + e \\ \overset{k_3}{\rightarrow} X^- + M. \end{array} \tag{2}$$

This model then predicts a measured rate of loss of electrons given by

$$-\frac{d[e]}{dt} = \frac{k_1 k_3 [M][e][X]}{k_a + (k_2 + k_3)[M]}, \tag{3}$$

where the brackets indicate concentration. Mahan and Walker assumed that if the lifetime of the unstable ion

[8] R. H. Huebner, R. N. Compton, and H. C. Schweinler, *Chem. Phys. Letters* 2, 407 (1968).

[9] C. E. Klots, *J. Chem. Phys.* (in press).

[10] C. E. Klots, private communication.

[11] B. H. Mahan and I. C. Walker, *J. Chem. Phys.* 47, 3780 (1967).

[12] F. J. Davis and D. R. Nelson, *Chem. Phys. Letters* 3, 461 (1969).

is sufficiently long, then the autodetachment rate $k_a \ll (k_2 + k_3)[M]$. The result is then a rate-of-electron-loss model which predicts a first-order (pseudo) attachment rate dependent upon the nature of the third body. However, Klots[9] has shown that the above assumption violates microscopic reversibility, which requires $k_1/k_a = k_{-2}/k_2$, where k_{-2} is the three-body attachment rate.

Because of the above considerations, the authors reexamined the previous study[12] of thermal-electron attachment to SF_6 in various carrier gases. It was found that a failure to adjust the calculated concentrations for the nonideal compressibility of the carrier gases at the high pressures used in the premixing cylinders accounts for the previously reported (attachment rate) differences determined with CO_2 and C_2H_4. The previous[12] and here corrected thermal-electron attachment rates (αw) for SF_6 in 14 carrier-gas mixtures are given in the first two columns of Table 11.1. These αw values are an average of those found for each mixture, of which the number investigated is given in parentheses. The SF_6 used in this study was CP grade (99.8% – Matheson). Recently, two mixtures of CH_4 with instrument-grade (99.99% – Air Products) SF_6 gave an average thermal-electron attachment rate value of 6.73×10^9 sec^{-1} $torr^{-1}$, which indicates that the investigations using CP-grade SF_6 were not in error due to a lack of purity.

The average thermal-electron attachment rate of SF_6 and its experimental standard deviation, obtained by weighting the corrected αw values of column 2 in Table 11.1 according to the number of mixtures studied, is $(6.85 \pm 0.14) \times 10^9$ sec^{-1} $torr^{-1}$. This value is in excellent agreement with the value of 7.1×10^9 sec^{-1} $torr^{-1}$ reported by Fehsenfeld[13] and in fairly good agreement with the value of 7.8×10^9 sec^{-1} $torr^{-1}$ reported by Chen *et al.*[14] It would appear that the recent values of 8.7×10^9 and 9×10^9 sec^{-1} $torr^{-1}$ (N_2 and C_2H_4, respectively, used as the carrier gas) obtained by Christophorou and co-workers[15] and the value of 10×10^9 sec^{-1} $torr^{-1}$ reported by Mahan and Young[16] are too high. However, there is probably agreement of these methods within the experimental error.

Table 11.1. Thermal Energy (300°K) Electron Attachment Rates for SF_6 in Different Carrier Gases

Previous αw[a] (sec^{-1} $torr^{-1}$)	Corrected αw (sec^{-1} $torr^{-1}$)	Carrier Gas
$\times 10^9$	$\times 10^9$	
6.90 (3)	6.85 (3)	He
6.4 (1)	6.80 (1)	1% CH_4 + 99% Ar
6.5 (1)	6.94 (1)	11% CH_4 + 89% Ar
7.1 (1)	6.97 (1)	H_2
6.7 (1)	6.71 (1)	N_2
7.0 (2)	7.18 (2)	CO
3.74 (3)	6.74 (3)	CO_2
5.86 (6)	6.78 (6)	CF_4
6.8 (1)	7.13 (1)	CH_4
6.8 (1)	6.93 (1)	C_2H_2
2.46 (3)	6.84 (4)	C_2H_4
6.0 (1)	6.60 (1)	C_2F_6
5.8 (1)	6.81 (1)	*cis*-C_4H_8
6.5 (1)	6.83 (1)	C_4H_{10}

[a]F. J. Davis and D. R. Nelson, *Chem. Phys. Letters*, accepted for publication in August 1970.

THERMAL-ELECTRON ATTACHMENT RATES AND NEGATIVE-ION LIFETIMES OF OTHER MOLECULES

Thermal-electron attachment rates are shown in Table 11.2 for 11 molecules. The first six fluorinated hydrocarbons were studied by Naff *et al.*[17] for the lifetime of the parent negative ion. Further measurements of thermal-electron attachment to other fluorinated cyclic

[13]F. C. Fehsenfeld, *Bull. Am. Phys. Soc.* 15, 419 (1970). The thermal-electron attachment rate for SF_6 of 2.7×10^{-7} cm^3/sec given in the abstract was revised to 2.2×10^{-7} cm^3/sec when the paper was presented at the Twenty-Second Annual Gaseous Electronics Conference.

[14]E. Chen, R. D. George, and W. E. Wentworth, *J. Chem. Phys.* 49, 1973 (1968).

[15]L. G. Christophorou, private communication.

[16]B. H. Mahan and C. E. Young, *J. Chem. Phys.* 44, 2192 (1966).

[17]W. T. Naff, C. D. Cooper, and R. N. Compton, *J. Chem. Phys.* 49, 2784 (1968).

Table 11.2. Thermal-Electron Attachment Rates

Molecule	Thermal Attachment Rate (sec^{-1} $torr^{-1}$)
C_4F_8	3.5×10^8
C_5F_8	3.8×10^9
C_6F_6	3×10^9
C_7F_8	7.7×10^8
C_6F_{10}	1×10^{10}
C_7F_{14}	1.3×10^9
CCl_4	1.1×10^{10}
SO_2F_2	1.9×10^7
$(CH_3CO)_2$	1.3×10^8
C_8H_8	3×10^7
O_2	2.0×10^3 sec^{-1} $torr^{-2}$

hydrocarbons are continuing in order to obtain a better understanding of the physics of electron attachment by correlating the lifetime and attachment rate measurements. Studies of perfluorocyclobutane (C_4F_8) in the electron beam experiments show two resonance states in the $C_4F_8^-$ ion current, one at thermal energies and another at ~1.0 eV. The second state also acts as an energy loss resonance, as evidenced by the SF_6 scavenger technique.

Thus far, CCl_4 has been the highest thermal-electron-attaching molecule studied. The value of 1.1×10^{10} sec^{-1} $torr^{-1}$ is probably about 10% higher than other values found in the literature, but the agreement is within experimental error. The only molecule studied which exhibits a pressure squared dependence of (three-body) attachment for thermal electrons was oxygen. The present value of 2.0×10^3 sec^{-1} $torr^{-2}$ is in perfect agreement with the value reported by Pack and Phelps.[18] There has been particular interest in the attachment rate of cycloöctatetraene (C_8H_8) since this molecule is known to form a double negative parent ion in the condensed phase. Further studies are under way to determine whether or not a double negative ion might also be found in the gaseous state. The negative-ion lifetime of $C_8H_8^-$ has been found to be quite short, 7 ± 0.2 μsec.

QUADRUPOLE ION-MASS ANALYSIS OF SWARM EXPERIMENTS

Some obvious and serious problems of electron attachment in swarm experiments are: What ions result after the initial electron attachment process, was the attachment dissociative or nondissociative, and what further charge-exchange and/or ion-molecule reactions occur before a stable ion results? And, depending upon the ultimate ions, there also may be radicals produced whose ultimate fate is very important in understanding the total disposition of charge and energy. In order to answer these important questions we have constructed an apparatus designed to mass analyze ions formed in high-pressure swarm experiments. A quadrupole ion-mass analyzer has been incorporated at the detection end of an electron swarm attachment experiment, as shown in Fig. 11.9. Photoelectrons are generated at the emitter plate by incident light emitted from a xenon-mercury discharge lamp. The ions which result from electron attachment, charge transfer, or ion-molecule reactions are swept out of the top plate aperture to the quadrupole ion-mass analyzer and multiplier detector.

The relative intensities of ions formed can be studied as a function of pressure, energy (E/P), and time. Figure 11.10 gives the results of the preliminary study of the ions observed in SF_6 as a function of E/P. For the first time in an electron swarm experiment the SF_5^- ion was observed to have a peak coincident with the SF_6^- ion at zero or near-zero energies. This is in agreement with the recent temperature-dependence studies of the SF_5^- ion formed in SF_6 by Chen and Chantry[19] with a beam experiment whereby SF_5^- is formed by attachment to vibrationally excited SF_6. The approximate equality of numbers of SF_6^- and SF_5^- ions at the peak intensity of the SF_5^- ions ($E/P \sim 100$) is in good agreement with the Townsend discharge observations of McAfee and Edelson.[20]

Preliminary studies of mass analysis of ions formed in electron swarms with CCl_4, C_4F_8, C_6F_6, and N_2O have been performed. Studies of these and others are being continued.

COLLISIONS OF SLOW CESIUM ATOMS WITH ELECTRONEGATIVE GASES

An apparatus has been constructed to mass identify the positive- and negative-ion products resulting from collisions of fast neutral cesium atoms with molecules. The threshold for production of a positive-and-negative-ion pair, that is,

$$Cs + X \rightarrow Cs^+ + X^- , \qquad (4)$$

would be

$$E_{\text{thres}} = \frac{M_{Cs} + M_X}{M_X} \left[IP(Cs) - E_A(X) + E' \right] , \qquad (5)$$

where M_{Cs} and M_X are the respective masses of cesium and X, IP(Cs) is the ionization potential of cesium, $E_A(X)$ is the electron affinity of X, and E' represents any excitation energy which may reside in X^- plus any activation energy required to make the reaction proceed. Thus a measurement of the threshold for ion pair production in collisions of cesium atoms with electro-

[18] J. L. Pack and A. V. Phelps, *J. Chem. Phys.* 44, 1870 (1966).

[19] C. L. Chen and P. J. Chantry, *Bull. Am. Phys. Soc.* 15, 461 (1970).

[20] K. B. McAfee and D. Edelson, *Proc. Phys. Soc.* 81, 382 (1963).

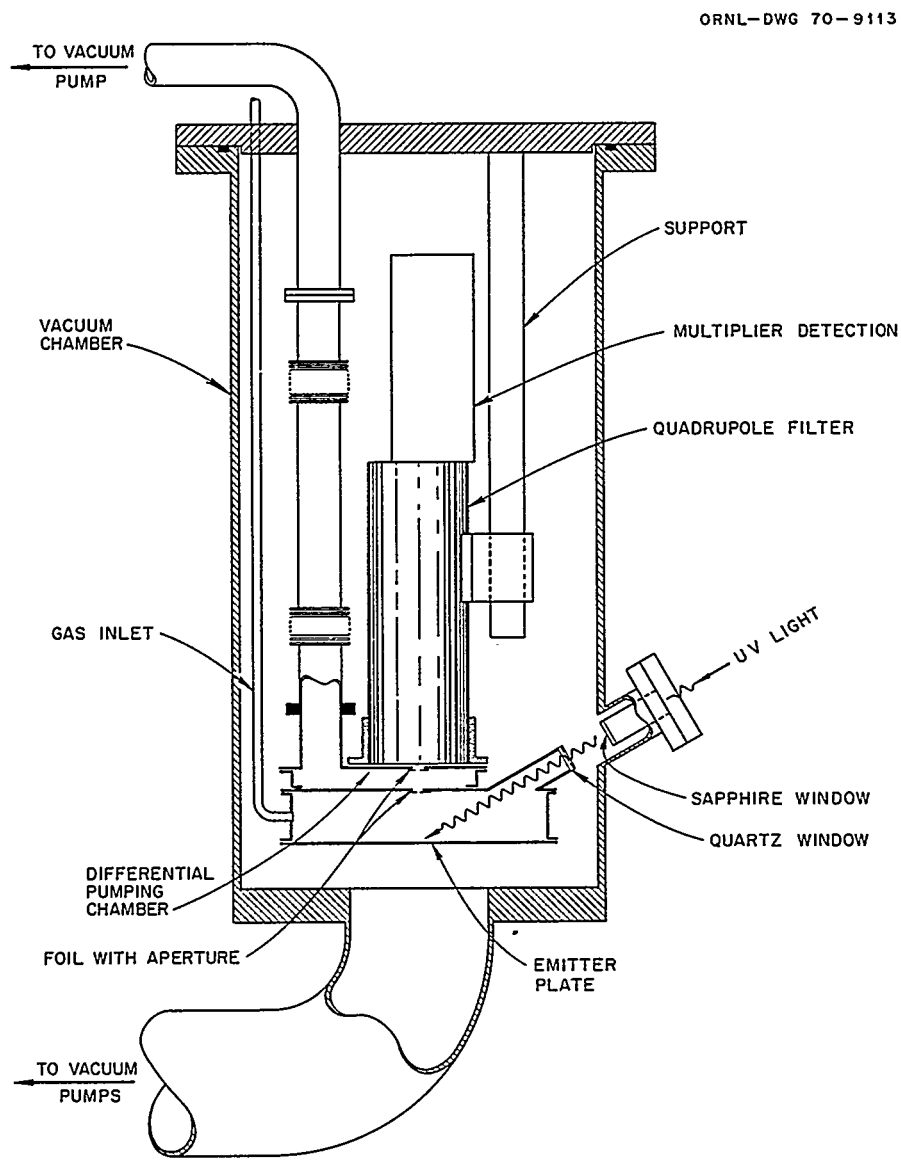

Fig. 11.9. Tandem Mass Spectrometer and Electron Swarm Chamber Designed to Mass Identify Negative-Ion Products from Electron Swarm Experiments.

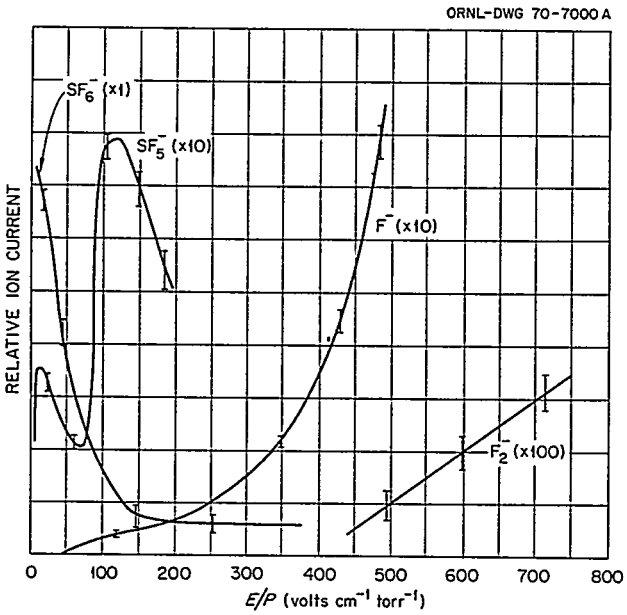

Fig. 11.10. Mass-Identified Electron Swarm Product Yields as a Function of the Electric Field to Pressure Ratio in Pure Sulfur Hexafluoride at a Pressure of 0.33 Torr.

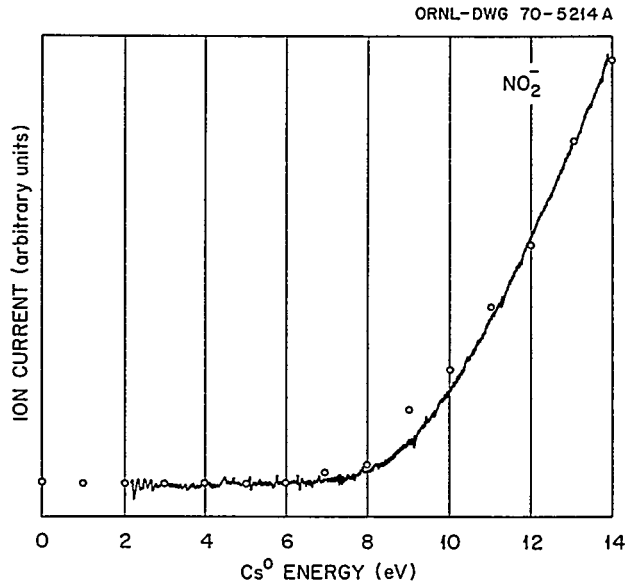

Fig. 11.11. Measurement of the NO_2^- Ion Current as a Function of the Incident Cesium Energy Resulting from the Reaction $Cs + NO_2 \rightarrow Cs^+ + NO_2^-$. The threshold for the reaction places a lower limit of 2.2 ± 0.1 eV for the electron affinity of nitrogen dioxide.

negative molecules affords a determination of the lower limit to the electron affinity of molecules. Electron affinity values for molecules are fundamental quantities which are greatly needed to interpret many chemical, physical, and biological effects. Unfortunately, electron affinity values for molecules are extremely inaccurate, and there appears to be no present method which is satisfactory to obtain them. Indeed, in many cases the sign of the electron affinity is in dispute.

Preliminary measurements of the threshold required to produce positive or negative ions through reaction (4) have been performed for Br_2 and NO_2. Figure 11.11 shows the negative-ion current of NO_2^- as a function of the Cs^0 energy. The single dots and continuous trace represent data taken about one year apart. The threshold is consistent with an electron affinity of 2.2 ± 0.2 eV for NO_2. Atomic oxygen negative ions are produced for cesium energies above ~20 eV. The mean kinetic energy and energy distribution of the cesium beam are accurately determined by a time-of-flight method. The full width at half height is a small percentage of the mean energy, approximately 1% at 10 eV and 3% at 50 eV.

Mass analysis of the ions formed in collisions of high-energy cesium atoms (~30 eV) with Br_2 shows that both Br_2^- and Br^- are produced. Mass analysis of ions formed in collisions of cesium with molecules should provide a wealth of new information about the formation of negative ions simply because of the complex adiabatic nature of the collision. A search for the existence of previously unobserved ions is another primary objective of the experiment.

LOW-ENERGY NEGATIVE-ION–MOLECULE REACTIONS

Reaction products and rates of reaction of O^- ions with C_2H_2, C_2D_2, C_2H_4, C_2H_6, C_6H_6, and C_6D_6 have been investigated at various points in the O^- energy range between 0 and 2 eV[21] using the pulsed-source mass spectrometer method described previously.[22] The energy dependence of primary negative-ion formation by dissociative electron attachment to these molecules was also studied.[23] Table 11.3 lists the chief reaction

[21] J. A. D. Stockdale, R. N. Compton, and P. W. Reinhardt, ORNL-TM-2546 (1969); this report contains a review of experimental work in this energy region.

[22] J. A. D. Stockdale, R. N. Compton, and P. W. Reinhardt, *Phys. Rev.* 184, 81 (1969).

[23] J. A. D. Stockdale, R. N. Compton, and P. W. Reinhardt, *Intern. J. Mass Spec. Ion Phys.* (in press); contains a discussion of these data.

Table 11.3. Reactions of O^- with C_2H_2, C_2D_2, C_2H_4, C_6H_6, and C_6D_6

Reaction	Source of O^-	O^- Energy (eV)	Rate Constant (molecules^{-1}cm^{3}sec^{-1})	Cross Section (cm^2)
$O^- + C_2H_2 \rightarrow C_2H^- + OH$	O^-/NO_2 [a] 1st peak	$\lesssim 0.3$ [a]	$(1.4 \pm 0.3) \times 10^{-9}$	
	O^-/NO_2 [a] 2nd peak		$(2.4 \pm 0.7) \times 10^{-9}$	
	O^-/NO_2 [a] 3rd peak		$(1.3 \pm 0.4) \times 10^{-9}$	
	O^-/N_2O	0.39 [b]	$(2.6 \pm 0.8) \times 10^{-9}$	$(1.2 \pm 0.4) \times 10^{-14}$
	O^-/NO	0.8 [c]	$(1.9 \pm 0.6) \times 10^{-9}$	$(6.1 \pm 1.8) \times 10^{-15}$
	O^-/O_2	1.6 [d]	$(4.2 \pm 1.3) \times 10^{-9}$	$(9.5 \pm 2.8) \times 10^{-15}$
$O^- + C_2D_2 \rightarrow C_2D^- + OD$	O^-/NO_2 1st peak	$\lesssim 0.3$	$(7.8 \pm 2.0) \times 10^{-10}$	
	O^-/NO_2 2nd peak		$(1.0 \pm 0.3) \times 10^{-9}$	
	O^-/NO_2 3rd peak		$(8.6 \pm 3.0) \times 10^{-10}$	
	O^-/N_2O	0.39	$(1.8 \pm 0.6) \times 10^{-9}$	$(8.3 \pm 2.5) \times 10^{-15}$
	O^-/NO	0.8	$(2.5 \pm 0.8) \times 10^{-9}$	$(8.0 \pm 2.4) \times 10^{-15}$
	O^-/O_2	1.6	$(3.2 \pm 1.0) \times 10^{-9}$	$(7.3 \pm 2.2) \times 10^{-15}$
$O^- + C_2H_2 \rightarrow C_2OH^- + H$	O^-/NO_2 1st peak	$\lesssim 0.3$	$(4.6 \pm 1.5) \times 10^{-11}$	
	O^-/NO	0.8	$(6.7 \pm 2.0) \times 10^{-11}$	$(2.2 \pm 0.7) \times 10^{-16}$
	O^-/O_2	1.6	$(9.0 \pm 3.0) \times 10^{-11}$	$(2.1 \pm 0.6) \times 10^{-16}$

Table 11.3 (continued)

Reaction	Source of O^-	O^- Energy (eV)	Rate Constant (molecules^{-1}cm^{3}sec^{-1})	Cross Section (cm^2)
$O^- + C_2D_2 \rightarrow C_2OD^- + D$	O^-/NO_2 1st peak	$\lesssim 0.3$	$(4.2 \pm 1.5) \times 10^{-11}$	
	O^-/NO_2 2nd peak		$(8.3 \pm 2.5) \times 10^{-11}$	
	O^-/NO_2 3rd peak		$(5.3 \pm 1.6) \times 10^{-11}$	
	O^-/N_2O	0.39	$(6.8 \pm 2.0) \times 10^{-11}$	$(3.1 \pm 0.9) \times 10^{-16}$
$O^- + C_2H_2 \rightarrow C_2H_2O^-$	O^-/NO_2 1st peak	$\lesssim 0.3$	$(6.0 \pm 1.8) \times 10^{-12}$	
$O^- + C_2H_4 \rightarrow C_2H_2^- + (H_2O)$	O^-/NO	0.8	$\leq (4.2 \pm 1.3) \times 10^{-10}$	$\leq (1.4 \pm 0.4) \times 10^{-15}$
$O^- + C_6H_6 \rightarrow C_6H_4^- + (H_2O)$	O^-/NO_2 1st peak	$\lesssim 0.3$	$(1.1 \pm 0.3) \times 10^{-10}$	
$O^- + C_6D_6 \rightarrow C_6D_4^- + (D_2O)$	O^-/NO_2 1st peak	$\lesssim 0.3$	$(2.6 \pm 0.7) \times 10^{-10}$	
$O^- + C_6H_6 \rightarrow C_6H_5O^- + H$	O^-/NO_2 1st peak	$\lesssim 0.3$	$(8.4 \pm 2.5) \times 10^{-11}$	
$O^- + C_6D_6 \rightarrow C_6D_5O^- + D$	O^-/NO_2 1st peak	$\lesssim 0.3$	$(1.7 \pm 0.5) \times 10^{-10}$	

[a] J. A. D. Stockdale, R. N. Compton, and P. W. Reinhardt, Phys. Rev. 184, (1969) 81.

[b] P. J. Chantry, J. Chem. Phys., 51, (1969) 3369.

[c] P. J. Chantry, Phys. Rev., 172, (1968) 125.

[d] P. J. Chantry and G. J. Schulz, Phys. Rev., 156, (1967) 134.

rate constants obtained. It is interesting to note that no significant isotope effects were observed in reactions of O^- with C_2H_2 and C_2D_2 but that large isotope effects were seen in O^- reactions with C_6H_6 and C_6D_6. The former observation is not inconsistent with the classical theory of ion-molecule reactions,[24] but there is at present no adequate explanation of the latter.

In studies of the reaction of O^- ions at thermal energies with hydrocarbons, Bohme and co-workers[25] found that ion-molecule reactions proceeded most favorably by proton abstraction to yield OH and a

[24] P. Langevin, *Ann. Chem. Phys.* 5, 245 (1905); G. Gloumousis and D. P. Stevenson, *J. Chem. Phys.* 29, 294 (1958).

[25] D. K. Bohme and F. C. Fehsenfeld, *Can. J. Chem.* 47, 2717 (1969); D. K. Bohme and L. B. Young, private communication (to be published).

carbanion in the case of unsaturated hydrocarbons and by hydrogen atom abstraction to yield OH^- with saturated hydrocarbons. The present work tends to support this generalization with some exceptions. Neither of the two reactions observed in benzene, for instance, corresponds to either of these processes. Table 11.4 lists upper limits to OH^- production for a number of cases. Figure 11.12 shows rate constants plotted against O^- energy for the reaction $O^- + C_2H_2 \rightarrow C_2H^- + OH$ and its deuterated analog. Figure 11.13 shows average rate constants and cross sections for this process obtained from the data of Fig. 11.12. The trend of the cross section may be somewhat less steep than $1/v$, where v is the O^- ion velocity.

Table 11.4. Upper Limits to OH^- Production in Reactions of O^- with C_2H_2 and C_2H_4

Reaction	Source of O^-	O^- Energy (eV)	Upper Limit to Rate Constant (molecules^{-1} cm^3 sec^{-1})
$O^- + C_2H_2 \rightarrow OH^- + C_2H$	O^-/NO_2 1st peak	$\lesssim 0.3$	3.5×10^{-10}
	O^-/NO_2 2nd peak		3.0×10^{-10}
	O^-/NO_2 3rd peak		3.2×10^{-10}
	O^-/NO	0.8	6.4×10^{-11}
	O^-/O_2	1.6	1.8×10^{-10}
$O^- + C_2H_4 \rightarrow OH^- + C_2H$	O^-/NO_2	$\lesssim 0.3$	6.0×10^{-11}

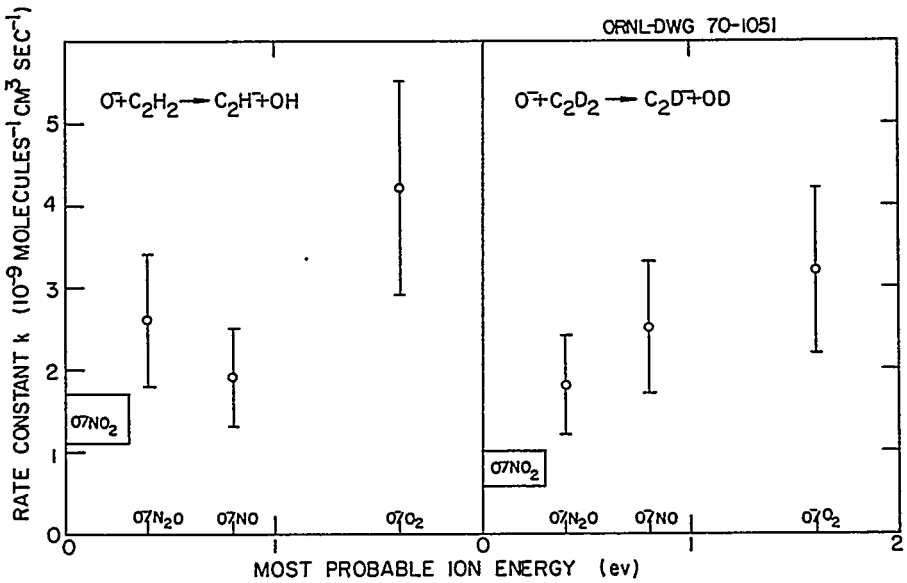

Fig. 11.12. Rate Constants vs Ion Energy for the Reaction of Negative Oxygen Ions with Acetylene and Deuterated Acetylene.

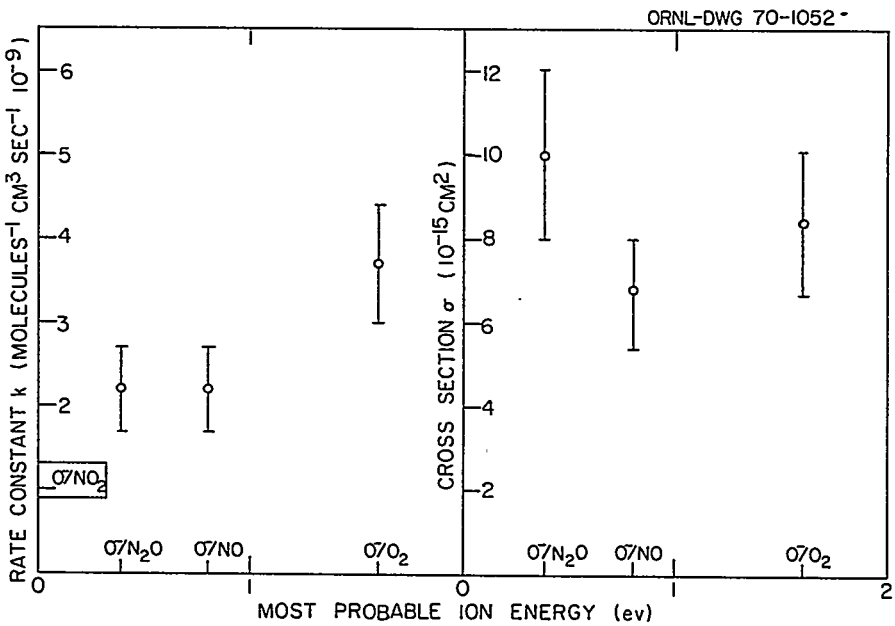

Fig. 11.13. Rate Constants and Converted Cross Sections vs Incident Ion Energy for the Reaction $O^- + C_2H_2 \rightarrow C_2H^- + OH$.

12. Atomic and Molecular Radiation Physics

L. G. Christophorou

V. E. Anderson[1]
J. B. Birks[2]
R. P. Blaunstein[2]
Ada Carter
J. G. Carter
E. L. Chaney[3]
A. A. Christodoulides[4]
P. M. Collins[5]
J. T. Cox
C. E. Easterly[6]
A. Hadjiantoniou[7]
J. A. Harter
C. E. Klots
D. L. McCorkle[8]
Betty McGill
M. N. Pisanias[4]
D. Pittman

THERMAL-ELECTRON SCATTERING BY POLAR MOLECULES[9]

The scattering of thermal electrons by highly polar molecules has been under intense experimental and theoretical study. As we continued our effort, we investigated the temperature dependence of the drift velocity w of thermal electrons traveling through polar gases. The $w(T)$ measurements were performed as previously discussed.[10] In the present study, however, we have restricted our measurements to sufficiently low-pressure reduced electric fields E/P for which w varies linearly with E/P and the electron swarm energy distribution function can be approximated by

$$f_0(v) = \left(\frac{m}{2\pi kT}\right)^{3/2} e^{-mv^2/2kT}, \qquad (1)$$

where k is the Boltzmann constant and T is the absolute temperature.

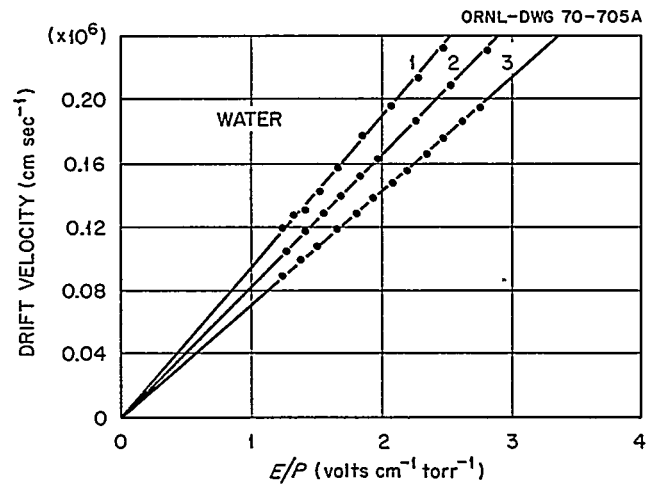

Fig. 12.1. Electron Swarm Drift Velocity vs E/P_{298} for H_2O at Three Different Temperatures: 1 (440°K), 2 (375°K), and 3 (298°K).

In Fig. 12.1 typical data on w vs E/P at three different temperatures are given for water. At all temperatures the pressures were normalized to 298°K. Data similar to those shown in Fig. 12.1 for water have been obtained for all other compounds studied (see Table 12.1) and have been used to determine by a least-squares fitting the slope S [$\equiv w/(E/P)$] as a function of T. Figures 12.2 and 12.3 show $S(T)$ for a number of polar molecules. From the $S(T)$ data we have determined the power α of v for the momentum transfer cross section $\sigma_m(v)$, expressed as

$$\sigma_m(v) = \frac{A_\alpha}{v^\alpha}, \qquad (2)$$

[1]On loan from Computing Technology Center, Union Carbide Corporation, Nuclear Division.

[2]Consultant.

[3]Oak Ridge Graduate Fellow.

[4]Graduate Student, University of Tennessee.

[5]Radiological Health Physics Fellow.

[6]USAEC Health Physics Fellow.

[7]Graduate Assistant, University of Tennessee, and alien guest from the Greek Atomic Energy Commission.

[8]National Defense Education Act Fellow.

[9]L. G. Christophorou and D. Pittman, *J. Phys. B* (in press).

[10]L. G. Christophorou and A. A. Christodoulides, *J. Phys. B* 2, 71 (1969).

Table 12.1. Data on Polar Molecules

Molecule	μ^a (D)	A_α	α	$\langle\sigma_m(v)\rangle_{v\alpha} \times 10^{14b}$ (cm^2)	$\langle\sigma_m(v)\rangle_{v2} \times 10^{14b}$ (cm^2)	$\langle\sigma_m(v)\rangle_A \times 10^{14c}$ (cm^2)	R^d
Dimethylamine	1.0	13.79	1.79	3.89	5.16	3.8083	1.02
Chlorobenzene	1.61	3944	2.375	34.2	18	9.871	3.46
Butyl alcohol	1.63	3.07	1.955	13.42	14.45	10.12	1.33
n-Propyl alcohol	1.66	0.966	1.887	11.82	13.85	10.49	1.13
Methyl alcohol	1.7	37.98	2.113	15.26	13.00	11.006	1.39
Ethyl alcohol	1.7	8.923	2.025	13.62	13.43	11.006	1.24
Water	1.85	175.6	2.17	30.44	23.67	13.034	2.34
Chloromethane	1.88	1545	2.315	31.67	18.39	13.459	2.35
1-Chlorobutane	2.08	419	2.232	28.96	20.22	16.476	1.76
Propionaldehyde	2.74	985	2.27	39.5	26.49	28.589	1.38
Acetone	2.87	1466	2.285	46.83	29.5	31.369	1.49
Cyclopentanone	3.3	96.1	2.115	37.67	31.00	41.47	0.91
Acrylonitrile	3.89	7.71	1.946	38.59	42.71	57.627	0.67
1-Butyronitrile	4.06	417	2.184	59.1	44.2	62.774	0.94

[a]See detailed values in Christophorou and Christodoulides, *J. Phys. B* 2, 71 (1969).
[b]For $T = 298°K$.
[c]$\langle\sigma_m(v)\rangle_A = 3.8083 \times 10^{-14}\ \mu^2$ [cm^2 (μ in debyes)].
[d]$R \equiv \langle\sigma_m(v)\rangle_{v\alpha}/\langle\sigma_m(v)\rangle_A$.

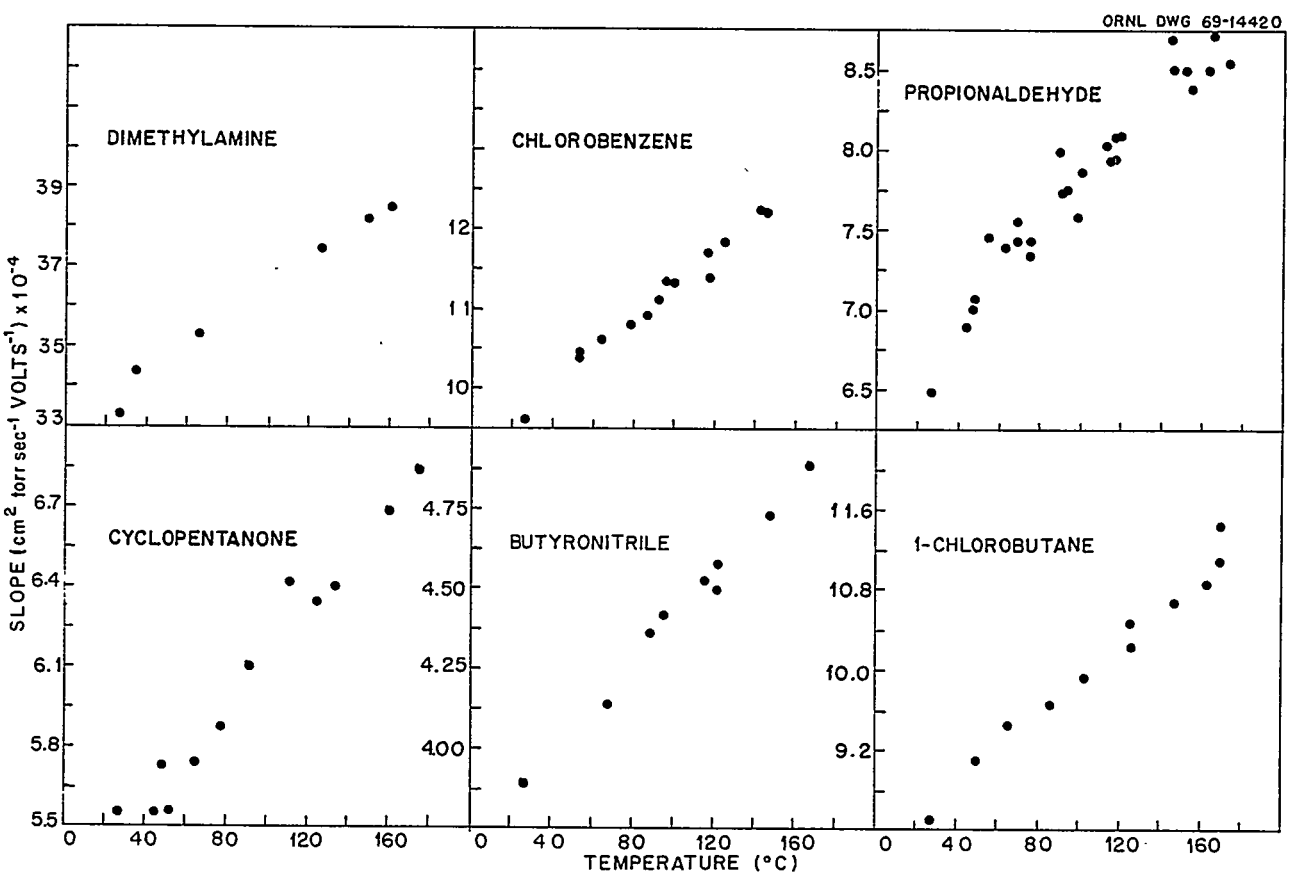

Fig. 12.2. Variation of the Slope $S = w/(E/P)$ with Temperature T for the Polar Molecules Dimethylamine, Chlorobenzene, Propionaldehyde, Cyclopentanone, Butyronitrile, and 1-Chlorobutane.

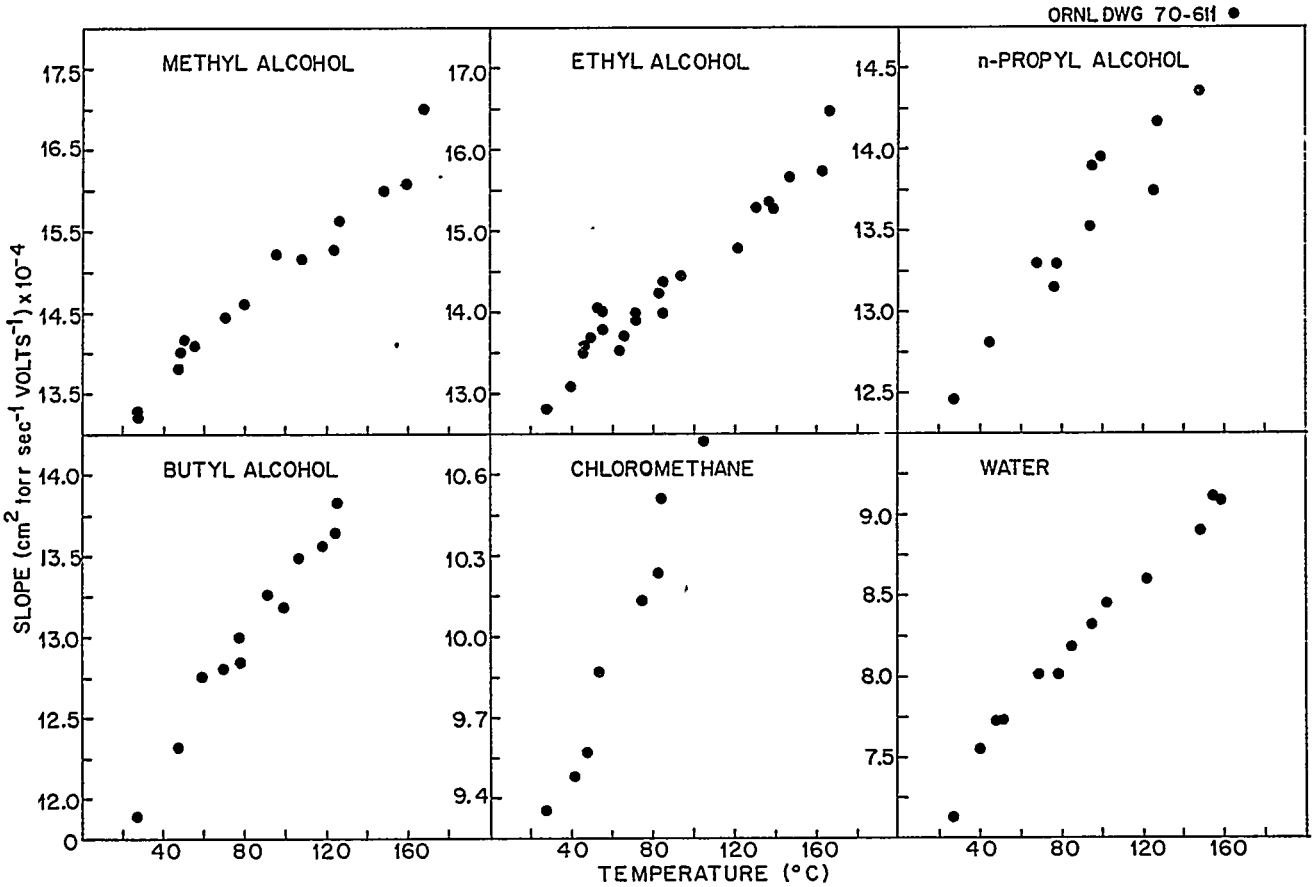

Fig. 12.3. Variation of the Slope $S = w/(E/P)$ with Temperature T for the Polar Molecules Methyl Alcohol, Ethyl Alcohol, *n*-Propyl Alcohol, Butyl Alcohol, Chloromethane, and Water.

using for the electron energy distribution Eq. (1) and for $\sigma_m(v)$ the equation[11]

$$w = -\frac{4\pi e}{3mN}\frac{E}{P}\int_0^\infty \frac{v^2}{\sigma_m(v)}\frac{df_0}{dv}\,dv\,, \tag{3}$$

where N is the gas density at 1 torr and 298°K and e/m is the electron charge to mass ratio. This has been done through a least-squares analysis whereby an optimum value for α and A_α is found for which the differences between the calculated and the experimental S as a function of T are minimized. A typical set of data showing this procedure is shown in Fig. 12.4, where the residuals

$$\text{res} = \sum_i (S_{\text{exp}} - S_{\text{cal}})^2 \tag{4}$$

are plotted as a function of the power α of v; i refers to the ith temperature. The improvement over the previous assumption ($\alpha = 2$) can be seen clearly from the data presented in Fig. 12.4.

The final values of α and A_α were used to determine $\langle\sigma_m(v)\rangle_{v\alpha}$, defined by

$$\langle\sigma_m(v)\rangle_{v\alpha} \equiv 4\pi\int_0^\infty \sigma_m(v)\,f_0(v)\,v^2\,dv\,. \tag{5}$$

The quantities α, A_α, $\langle\sigma_m(v)\rangle_{v\alpha}$ (for $T = 298$°K), and μ are listed in Table 12.1. In the table $\langle\sigma_m(v)\rangle_{v^2}$ (= 17.176×10^{-9} sec^{-1}) for $\alpha = 2$ and $\langle\sigma_m(v)\rangle_A$ [= $3.8083 \times 10^{-14}\ \mu^2$ (cm^2; μ in debyes)] as determined from the Born approximation calculation of Altshuler[12] are given also for comparison.

It is seen from Table 12.1 that the values of α are around its Born approximation value of 2, showing, as we concluded earlier, that most of the scattering can be

[11] W. P. Allis, *Handbook of Physics* 21, 413 (1956).
[12] S. Altshuler, *Phys. Rev.* 107, 114 (1957).

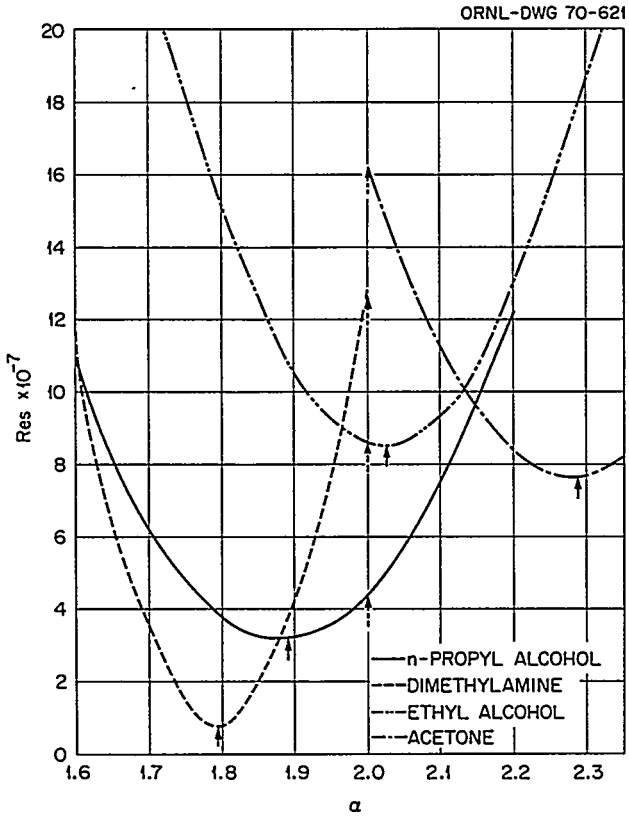

Fig. 12.4. Dependence of the Residuals (See Text) on the Power α of the Electron Velocity v for *n*-Propyl Alcohol, Dimethylamine, Ethyl Alcohol, and Acetone.

accounted for by considering the direct effect of the magnitude of the electric dipole moment. However, the magnitude of $\langle\sigma_m(v)\rangle_{v^\alpha}$ and its variation with μ clearly demonstrate the inadequacy of the Born approximation for pure dipole scattering to describe the experimental results in detail.

It is evident that the majority of the molecules we have been able to study in this work have very much higher cross sections than those predicted by the Altshuler calculation in the region $1.65 \lesssim \mu \lesssim 3$ D. The observed enhancement in the measured cross section in the region $1.65 \lesssim \mu \lesssim 3$ D over the value of the cross section in the Born approximation for a pure dipole has been discussed with relevance to a number of factors which can distinctly affect the scattering:

1. bound states for a thermal or epithermal electron when $\mu > \mu_{min}$,
2. potential resonance,
3. rotational resonances,
4. induced moments,
5. other factors such as dipole length, π-electron structures, etc.

The exceptionally high cross section for chlorobenzene, for example, can be attributed to its π electrons and high induced moments resulting from the ease of polarization of the π-electron system (such induced moments would lower the value of μ_{min}).

ELECTRON ATTACHMENT AND "CARRIER GAS" ENERGY DISTRIBUTION FUNCTIONS

Additional experimental data have been obtained which strongly support our earlier conclusion[13] as to the correctness of the electron energy distribution functions $f(\epsilon, E/P)$ for the gases C_2H_4, N_2, and Ar used in electron attachment studies. A typical example is shown in Fig. 12.5, where the electron attachment rates in a number of brominated hydrocarbons, measured independently in each of the carrier gases C_2H_4, N_2, and Ar, are plotted as a function of the mean electron energy $\langle\epsilon\rangle$ for the respective carrier gas. The mean electron energies for Ar have been calculated from the revised distribution functions of Ritchie and Whitesides,[14] those for N_2 have been calculated from the data of Engelhardt *et al.*,[15] and those for C_2H_4 have been determined[13] from D/μ data using a Maxwellian form of the electron energy distribution function. It is seen from Fig. 12.5 that the measured attachment rates in the three carrier gases are in excellent agreement when plotted vs $\langle\epsilon\rangle$ obtained from ref. 14 for argon, from ref. 15 for N_2, and from D/μ data using a Maxwellian form for the distribution function for C_2H_4.[13] These three carrier gases, with the respective distribution functions just mentioned, are recommended as standard carrier gases for electron attachment work.

CROSS-SECTION FUNCTIONS FOR THERMAL-PEAKING ELECTRON ATTACHMENT RESONANCES[16]

A large number of polyatomic molecules have been found to capture electrons nondissociatively for long

[13] L. G. Christophorou, E. L. Chaney, and A. A. Christodoulides, *Chem. Phys. Letters* 3, 363 (1969).

[14] R. H. Ritchie and G. E. Whitesides, ORNL-3081 (1961); revised distributions by G. E. Whitesides and D. R. Nelson (private communication).

[15] A. G. Engelhardt, A. V. Phelps, and C. G. Risk, *Phys. Rev.* 135, A1566 (1964); A. V. Phelps (private communication).

[16] L. G. Christophorou, D. L. McCorkle, and J. G. Carter, *J. Chem. Phys.*, in press.

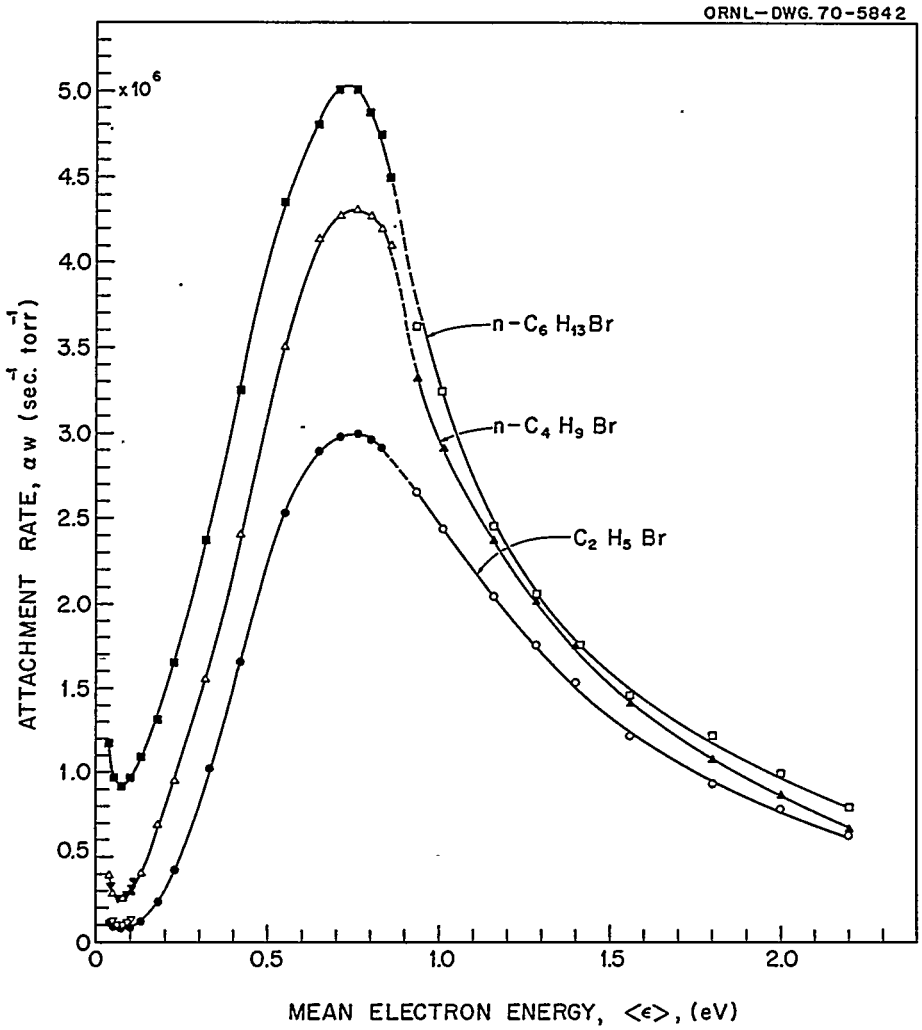

Fig. 12.5. Electron Attachment Rates as a Function of Mean Electron Energy for a Number of Brominated Aliphatic Hydrocarbons. Note the excellent agreement between the data in the carrier gases C_2H_4, N_2, and Ar:

C_2H_5Br: ▽(C_2H_4), •(N_2), ○(Ar)

n-C_4H_9Br: ▼(C_2H_4), △(N_2), ▲(Ar)

n-$C_6H_{13}Br$: ▪(N_2), □(Ar)

The total pressures in the three carrier gases were 250, 400, and 500 torrs for C_2H_4, N_2, and Ar respectively.

periods of time (>10^{-6} sec).[17-20] In most cases (see, e.g., refs. 17–20) such processes peaked sharply at thermal energies, and neither the electron swarm nor the electron beam technique gave accurately the magnitude of the cross-section function or its energy dependence. The shapes of the negative-ion currents as a function of electron energy as obtained in electron beam studies are, quite generally, instrumental in such cases.

A simple procedure to obtain both the magnitude and the energy dependence of thermal-peaking cross-section functions from swarm experiments alone is given below. Let us assume that αw has been measured for a number of E/P values in a carrier gas where $f(\epsilon, E/P)$ are known down to very low E/P values (see preceding section). Let us further make the assumption that for an initial energy region the attachment cross section $\sigma_a(\epsilon)$ can be represented by

$$\sigma_a(\epsilon) = \frac{A_\gamma}{\epsilon^\gamma}. \tag{6}$$

Then, expressing the rate αw (in $\sec^{-1}$ torr^{-1}) of electron attachment to a molecule by

$$\alpha w = N(2/m)^{1/2} \int_0^\infty \epsilon^{1/2}\, \sigma_a(\epsilon) f(\epsilon, E/P)\, d\epsilon \tag{7}$$

and considering the values of the constants involved, we have

$$\alpha w = 1.52 \times 10^{30} \int_0^\infty \epsilon^{1/2} f(\epsilon, E/P)\, A_\gamma\, \epsilon^{-\gamma}\, d\epsilon\,. \tag{8}$$

In Eqs. (7) and (8), α is the electron attachment coefficient, w is the electron swarm drift velocity, v and ϵ are, respectively, the electron velocity and energy, and N (= 3.241×10^{16}) is the number of attaching gas molecules per cubic centimeter per torr at 298°K. Hence, when αw is measured in a carrier gas for which $f(\epsilon, E/P)$ are known down to very low E/P values (see previous section), γ and A_γ can be determined by a least-squares procedure whereby for each set of values of γ and A_γ, αw is calculated as a function of E/P and compared with the experimental results until the residuals

$$\sum_i [(\alpha_i w_i)_{\text{exp}} - (\alpha_i w_i)_{\text{cal}}]^2 \tag{9}$$

are minimized. The optimum values of γ and A_γ yield both the energy dependence and the magnitude of the attachment cross section for the assumed cross section form [Eq. (6)].

As an example of this analysis we present here the results of our work on sulfur hexafluoride, 1,4-naphthoquinone, anthracene, and 1,2-benzanthracene. In Table 12.2 we list the optimum values of γ, A_γ, and σ_a (ϵ = 0.05 eV) and in the last column the energy range over which $\sigma_a(\epsilon)$ can be approximated by Eq. (6) with the values of A_γ and γ listed in the table.

A comparison of $(\alpha_i w_i)_{\text{exp}}$ with $(\alpha_i w_i)_{\text{cal}}$ – the latter have been calculated for the optimum values of γ and A_γ shown in Table 12.2 – is given in Fig. 12.6. It is seen that the calculated values of the attachment rates for the optimum values of γ and A_γ fit very well the experimentally determined attachment rates plotted vs E/P or $\langle\epsilon\rangle$.

The values of $\sigma_a(\epsilon)$ are plotted in Fig. 12.7 as a function of ϵ. On the same figure αw is plotted as a function of $\langle\epsilon\rangle$. It is very interesting to note the rapid variation of σ_a with electron energy. Very clearly γ is now seen to be much greater than the value of 0.5 which was originally suggested for SF_6.[18]

Additionally, a straightforward way to check the validity of the assumed simple exponential behavior of

[17] L. G. Christophorou, *Atomic and Molecular Radiation Physics*, chaps. 4 and 6, Wiley, New York and London, in press.

[18] R. N. Compton *et al.*, *J. Chem. Phys.* 45, 4634 (1966).

[19] E. L. Chaney *et al.*, *J. Chem. Phys.* 52, 4413 (1970).

[20] P. M. Collins *et al.*, *Chem. Phys. Letters* 4, 646 (1970).

Table 12.2. Values of γ, A_γ, σ_a (0.05 eV), δ, and $\frac{1}{2} + \delta$

Compound	γ	A_γ (ergs$^\gamma$ cm^2)	σ_a(0.05 eV) (cm^2)	δ	$\frac{1}{2} + \delta$	Energy Range[a] (eV)
Sulfur hexafluoride	1.12	2.5×10^{-29}	1.17×10^{-14}	0.64	1.13	≤0.11
1,4-Naphthoquinone	1.412	7×10^{-34}	2.17×10^{-15}	0.863	1.363	≤0.5
Anthracene	1.1484	9.1×10^{-32}	1×10^{-16}	0.622	1.122	≤0.3
1,2-Benzanthracene	1.0307	1.66×10^{-29}	5.2×10^{-16}	0.521	1.021	≤0.35

[a] This is the energy range over which ln αw varies linearly with ln $\langle\epsilon\rangle$ and in which region σ_a can be approximated by Eq. (6) with the values of A_γ and γ listed in this table.

ORNL DWG.70-1084

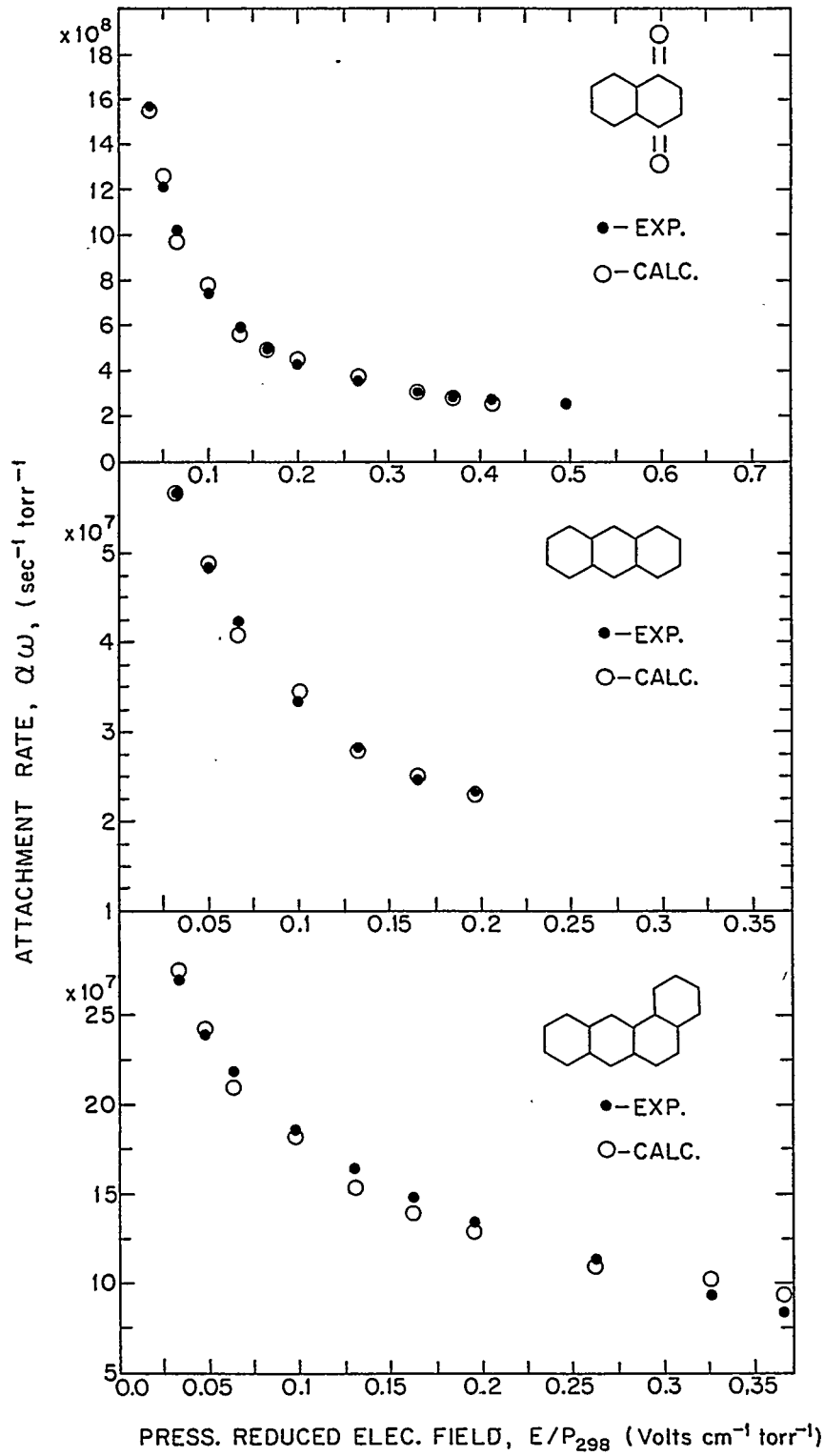

Fig. 12.6. Comparison of $(\alpha_i w_i)_{exp}$ with $(\alpha_i w_i)_{cal}$ for 1,4-Naphthoquinone, Anthracene, and 1,2-Benzanthracene (See Text).

ORNL DWG.70-1083R

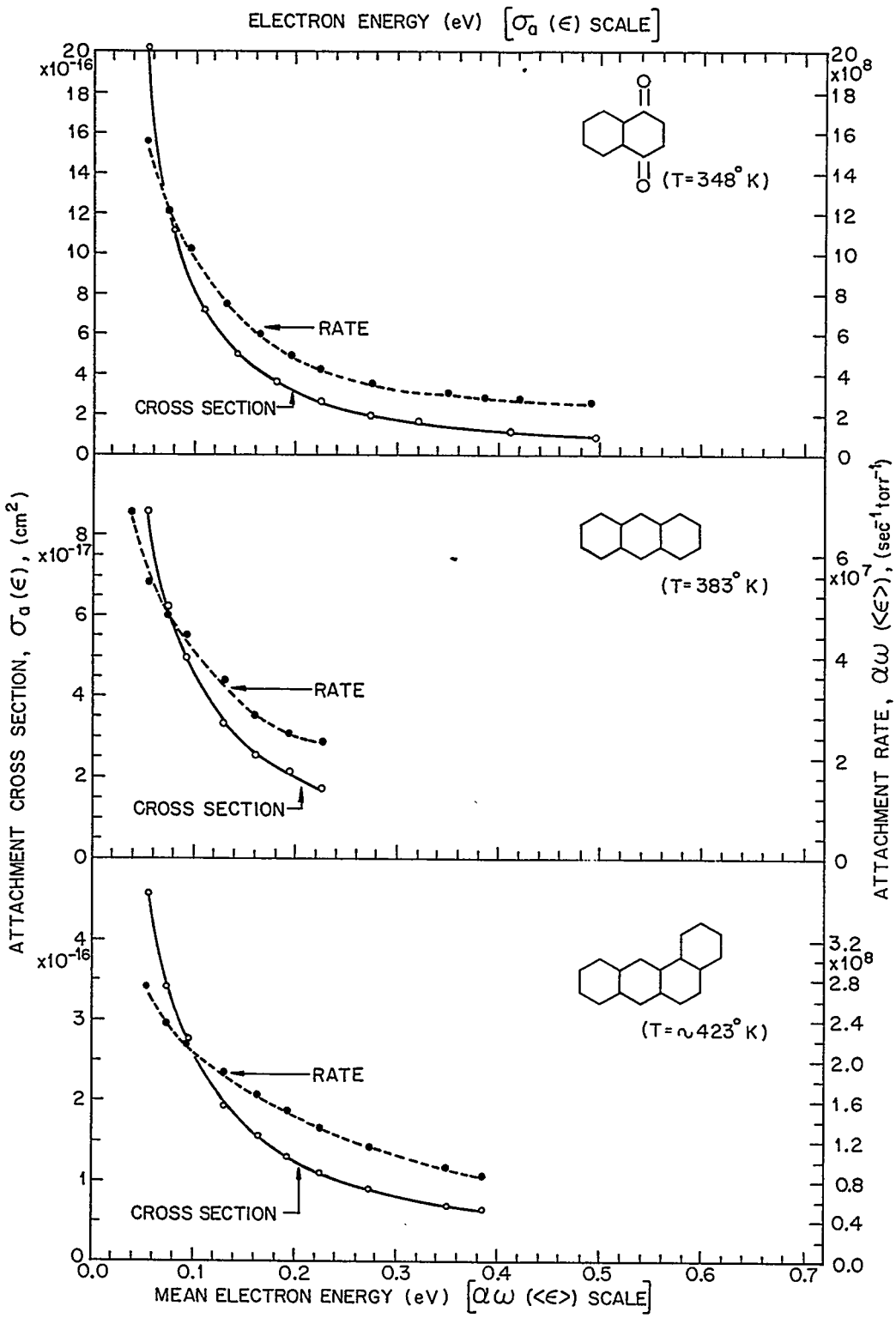

Fig. 12.7. Electron Attachment Cross Section as a Function of Electron Energy and Electron Attachment Rate as a Function of the Mean Electron Energy for 1,4-Naphthoquinone, Anthracene, and 1,2-Benzanthracene.

ORNL DWG. 70-4079

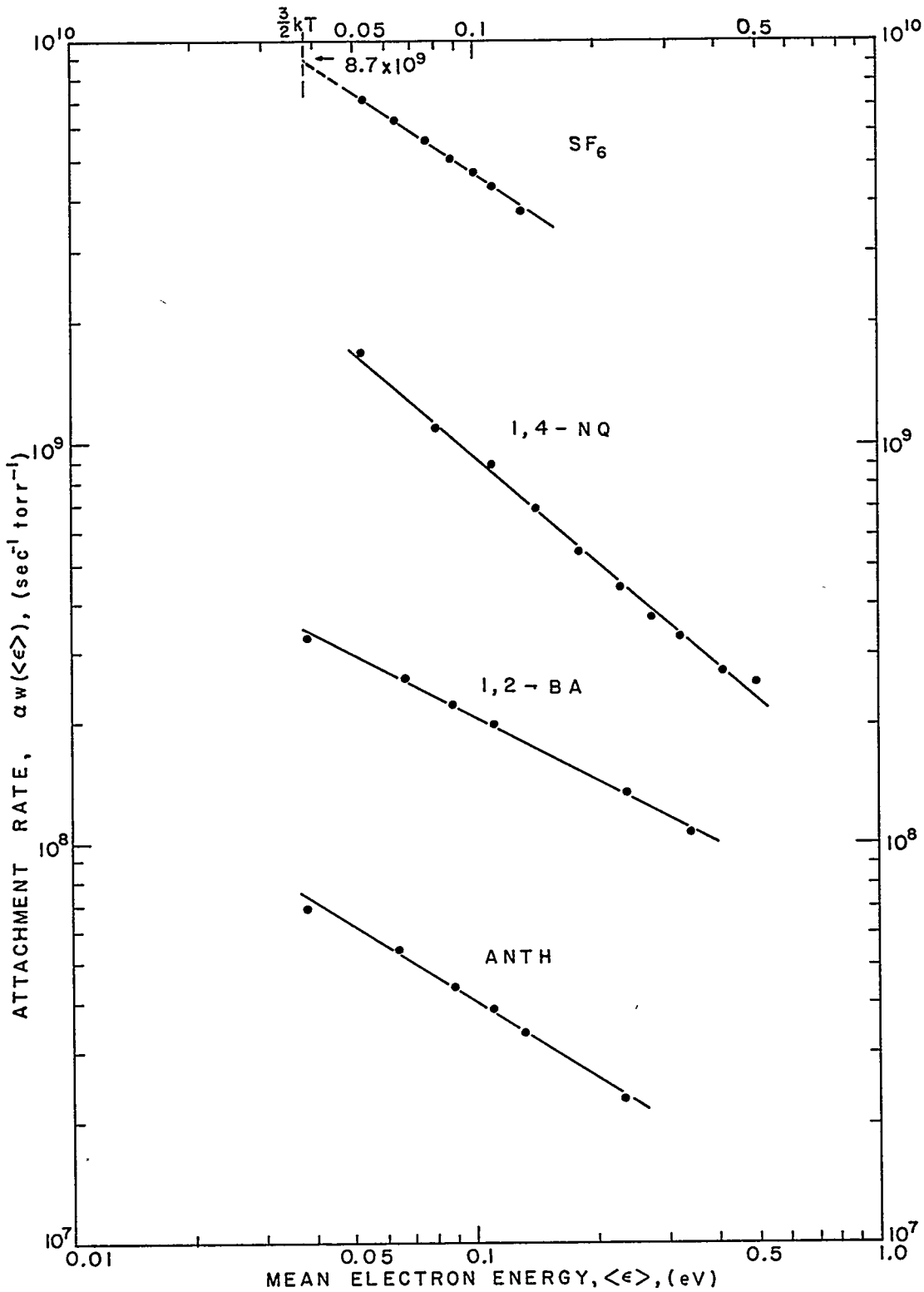

Fig. 12.8. αw vs $\langle\epsilon\rangle$ for Sulfur Hexafluoride (SF_6), 1,4-Naphthoquinone (1,4-NQ), 1,2-Benzanthracene (1,2-BA), and Anthracene (ANTH) for the Energy Region in Which σ_a Can Be Approximated by Eq. (6). For SF_6 the value (8.7×10^9) of αw at $\frac{3}{2}\ kT$ is shown.

$\sigma_a(\epsilon)$ [Eq. (6)] and to find with less labor the power γ of ϵ is shown in Fig. 12.8, where αw vs $\langle\epsilon\rangle$ are plotted on a log-log graph. It is seen that below a certain value of $\langle\epsilon\rangle$ the data can be fitted to a straight line, showing that the attachment rate can be represented by

$$\alpha w = \text{const}\ \langle\epsilon\rangle^{-\delta} . \tag{10}$$

The values of δ obtained this way by a least-squares fitting to the data in Fig. 12.8 are listed in column 5 of Table 12.2. If we now take

$$\alpha w \propto \sigma\langle\epsilon\rangle^{1/2} , \tag{11}$$

we have

$$\sigma_a \propto \langle\epsilon\rangle^{-(1/2)-\delta} . \tag{12}$$

The values of $\frac{1}{2} + \delta$ listed in column 6 of Table 12.2 are seen to be in good agreement with the values of γ listed in column 2. Hence, from measurements of αw vs E/P in N_2 and the $\langle\epsilon\rangle$ vs E/P data for N_2,[13] one can obtain from a log-log plot of αw vs $\langle\epsilon\rangle$ a good estimate of both the velocity dependence and the magnitude of $\sigma_a(\epsilon)$ at near thermal energies quickly and without the need of a computer and a detailed knowledge of $f(\epsilon, E/P)$.

ELECTRON ATTACHMENT TO SULFUR HEXAFLUORIDE

Electron attachment to sulfur hexafluoride (SF_6) has been the subject of many studies which have employed a variety of methods. The thermal and near-thermal electron attachment process to SF_6 has been described as

$$SF_6 + e \underset{\tau_a^{-1}}{\overset{\sigma_0}{\rightleftharpoons}} SF_6^{-*} \begin{cases} \xrightarrow{p_{st}} SF_6^- & (a) \\ \xrightarrow{p_{da}} SF_5^- + F & (b) \end{cases} \tag{13}$$

The SF_6^{-*} ion is metastable with a mean autoionization lifetime of ~30 μsec.[18,20] The cross-section function for process (13) is large and very narrow with a maximum at thermal energies. The relative abundances of SF_6^- and SF_5^- (at ~0.0 eV) are strongly dependent on temperature.[21] At room temperature SF_6^- is the predominant ion.[21,22] However, neither the magnitude nor the energy dependence of the cross section for SF_6^- has been known accurately. In this section we (1) present the results of a swarm study on SF_6 in mixtures with the carrier gases C_2H_4 and N_2 at room temperature (restriction of the study to room temperature ensures that SF_6^- is the predominant ion formed at energies $\lesssim$0.1 eV), (2) derive a functional form for the cross section for SF_6^- at near-thermal energies, (3) summarize all available data on the thermal (300°K) attachment rate for SF_6, and (4) derive a cross-section function for SF_5^- at room temperature.

Attachment Rate and Cross Section for SF_6^- as a Function of Electron Energy

The electron attachment rates (average of six runs) for SF_6-N_2 mixtures at 298°K are shown in Fig. 12.9, where they are plotted as a function of $\langle\epsilon\rangle$ (Fig. 12.9*a*) and E/P (Fig. 12.9*b*). The SF_6 was of a quoted purity of 99.997%. From the data in Fig. 12.9 a thermal value for the electron attachment rate equal to 8.7×10^9 sec^{-1} $torr^{-1}$ has been obtained (see also Fig. 12.8). Applying the procedure described in the preceding section and making use of the measured attachment rates in N_2 below 0.11 eV (see Figs. 12.8 and 12.9), we determined the values of γ, A_γ, and σ_a (0.05 eV) listed in Table 12.2.

The data in Figs. 12.8 and 12.9 clearly show that $\sigma_a(\epsilon)$ for SF_6^- decreases with ϵ much faster than it was originally indicated from the $\alpha w(T)$ studies.[18] At energies $\epsilon \lesssim 0.1$ eV, Eq. (6) describes the experimental results reasonably well, and one obtains for SF_6^- the cross-section values listed in Table 12.3 using the values of γ and A_γ shown in Table 12.2 for SF_6.

Attachment Rates and Cross Sections for SF_5^- as a Function of Electron Energy

The attachment rates plotted in Fig. 12.9 show the contribution of SF_5^- to the measured rates at $\langle\epsilon\rangle \gtrsim 0.1$ eV. Electron beam data (see, e.g., refs. 21 and 23) have shown that the SF_5^-/SF_6 current peaks at ~0.37 eV and that at this energy the SF_5^- current is very much greater than the SF_6^- current. We then conclude that the observed bump at $\langle\epsilon\rangle \cong 0.35$ eV in Fig. 12.9*a* reflects predominantly the contribution of SF_5^- to the measured attachment rates. We have been able to deduce from the experimental data shown in Fig. 12.9

[21] C. L. Chen and P. J. Chantry, *Abstracts of Gaseous Electronics Conference*, Gatlinburg, Tennessee, Oct. 27–31, 1969, paper J3, p. 39.

[22] F. C. Fehsenfeld, *Abstracts of Gaseous Electronics Conference*, Gatlinburg, Tennessee, Oct. 27–31, 1969, paper J4, p. 39.

[23] P. M. Collins, L. G. Christophorou, and J. G. Carter (unpublished results).

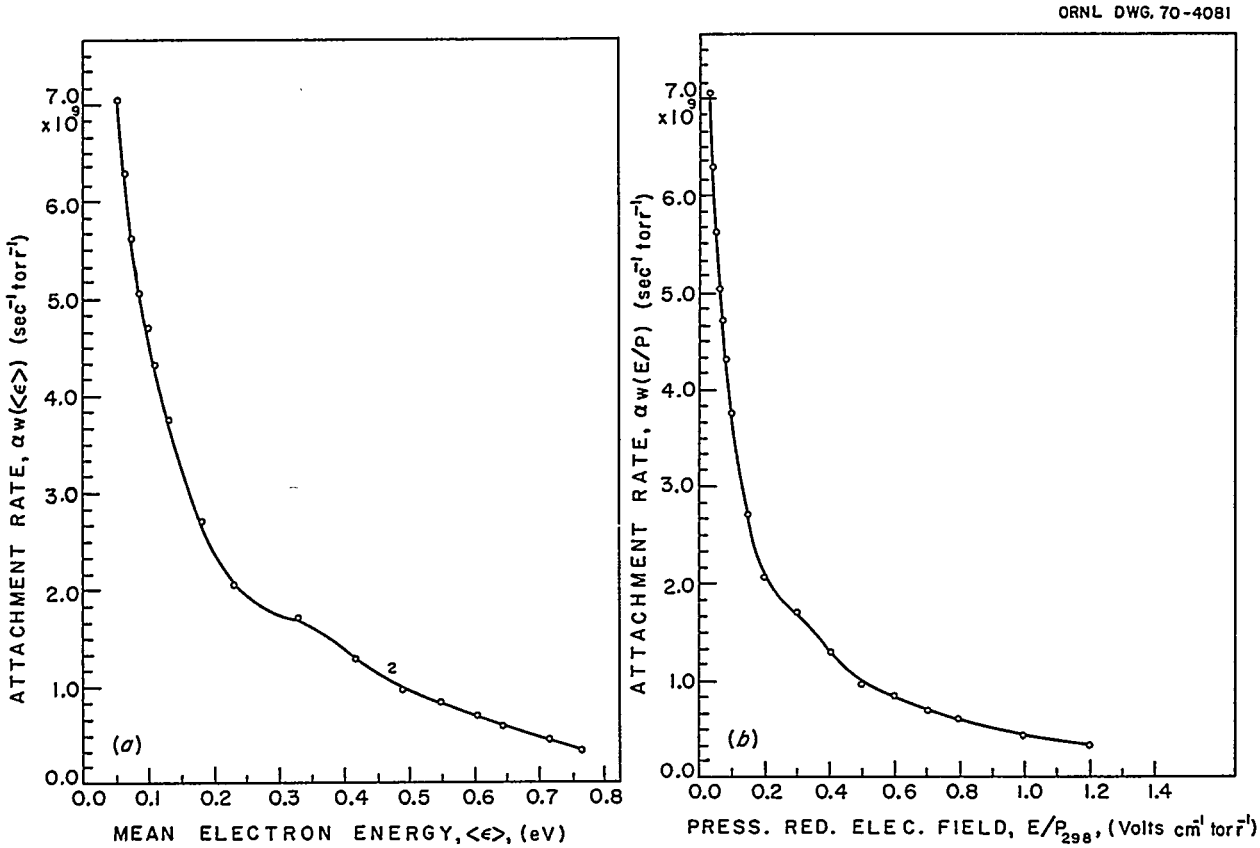

Fig. 12.9. (*a*) αw vs $\langle\epsilon\rangle$, P_{N_2} = 400 Torrs, $1 \lesssim P_{SF_6} \leq 7 \times 10^{-5}$ Torr; (*b*) αw vs E/P.

Table 12.3. Values of $\sigma_a(\epsilon)$ for SF_6^- ($\epsilon \leq 0.1$ eV)

ϵ (eV)	$\sigma_a(\epsilon)$ ($cm^2 \times 10^{-14}$)
0.03	2.07
0.04	1.5
0.05	1.17
0.06	0.95
0.08	0.69
0.10	0.54

the cross section for the formation of SF_5^- at room temperature assuming (1) that the energy scale calibration[21,23] and the shape[23] of the SF_5^-/SF_6 dissociative attachment resonance shown in Fig. 12.10 are correct and (2) that the measured attachment rates at $E/P \geq 1.1$ V cm^{-1} $torr^{-1}$ are entirely due to the production of SF_5^-. Hence, using the measured rates at $E/P = 1.1$ and 1.2 V cm^{-1} $torr^{-1}$, we have determined the absolute cross-section scale in Fig. 12.10 using the swarm-beam technique of Christophorou *et al.*[24] At the peak energy (= 0.37 eV) the cross section is equal to 4.9×10^{-17} cm^2.

The Thermal (~300°K) Value of the Electron Attachment Rate for SF_6

The many values reported for the thermal-electron attachment rate $(\alpha w)_{th}$ for SF_6 are summarized in Table 12.4. In view of the large discrepancies observed and the low values of $(\alpha w)_{th}$ for SF_6-C_2H_4 mixtures, we performed, in addition to our experiments with N_2, five new experiments on SF_6-C_2H_4 mixtures at 298°K; the results of these measurements are shown in Fig. 12.11. For $E/P \to 0$, $\alpha w = 9 \times 10^9$ sec^{-1} $torr^{-1}$, which is in excellent agreement with our value for $(\alpha w)_{th}$ determined from the SF_6-N_2 mixtures and also with the other most reliable data listed in Table 12.4.

[24] L. G. Christophorou *et al.*, *J. Chem. Phys.* 43, 4273 (1965).

Excluding the data of refs. *f* and *j* in Table 12.4, the rest of the experimental values listed in the table yield $(\alpha w)_{th} = 8.8 \times 10^9$ sec^{-1} torr^{-1} for SF_6. This value is ~0.75 times the maximum rate, that is, the rate which corresponds to $\pi\lambda\!\!\!^{-2}$, where λ (= $2\pi\lambda\!\!\!^{-}$) is the de Broglie wavelength for an electron of velocity $v = (3kT/m)^{1/2}$.

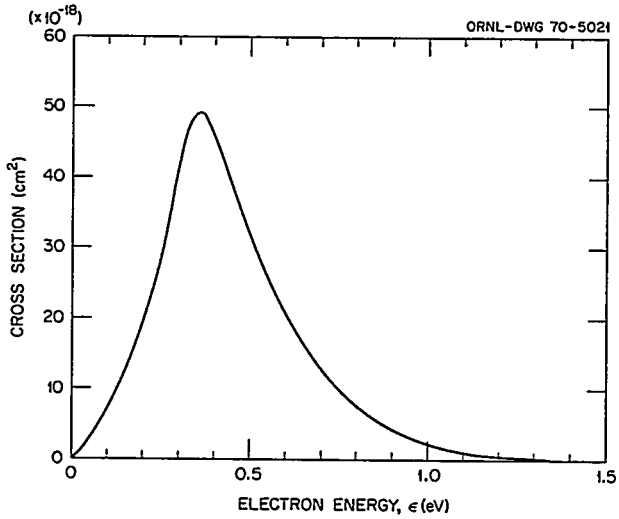

Fig. 12.10. Cross-Section Function for SF_5^-/SF_6. The shape of the resonance is the average of 12 runs. The cross-section scale was determined as discussed in the text.

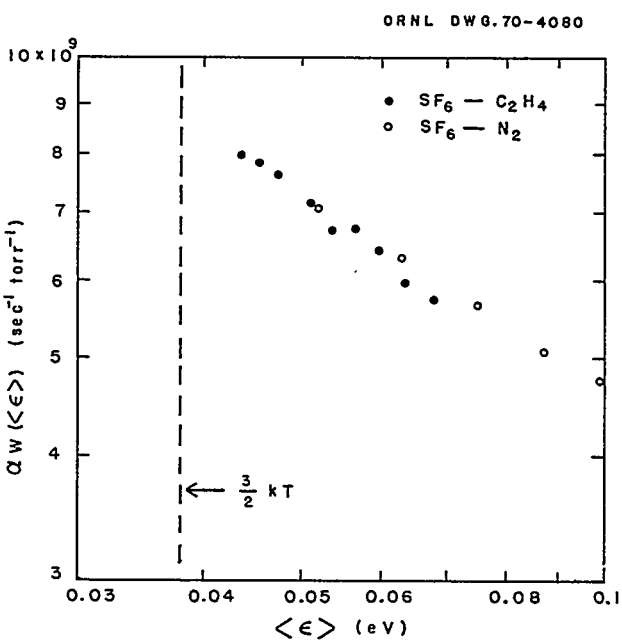

Fig. 12.11. Attachment Rates αw as a Function of $\langle\epsilon\rangle$ for SF_6 in the Carrier Gases C_2H_4 and N_2. At $\langle\epsilon\rangle = \frac{3}{2}kT$ the data in N_2 give an attachment rate equal to 8.7×10^9 sec^{-1} torr^{-1}, while those in C_2H_4 give a value of 9×10^9 sec^{-1} torr^{-1}.

Table 12.4. Values of the Thermal (~300°K) Attachment Rate for SF_6 Measured by Various Methods and in a Number of Carrier Gases

αw[a] (sec^{-1} torr^{-1})	Carrier Gas	Method and Reference
10×10^9	He	Microwave[b]
8.7×10^9	He	Microwave[c]
7.8×10^9	90% Ar + 10% CH_4	Pulse sampling[d]
6.5×10^9[e]		Swarm[f]
8.7×10^9[g]		Flowing afterglow[h]
6.7×10^9	N_2	Swarm[f]
8.7×10^9	N_2	Present work
1.24×10^9[i]	C_2H_4	Swarm[j]
2.46×10^9[k]	C_2H_4	Swarm[f]
9×10^9	C_2H_4	Present work
1.17×10^{10}		$\pi\lambda\!\!\!^{-2}$ for $v = (3kT/m)^{1/2}$

[a]Not included in the table are a value of 9.7×10^4 sec^{-1} torr^{-1} (T = 380°K) reported by G. R. Freeman, *Radiation Res. Rev.* 1, 1 (1968) and a microwave value of 9.3×10^3 sec^{-1} torr^{-1} (T = 300°K) reported by J. B. Hasted and S. Berg, *Brit. J. Appl. Phys.* 16, 74 (1965).

[b]B. H. Mahan and C. E. Young, *J. Chem. Phys.* 44, 2192 (1966).

[c]C. E. Toung, University of California Radiation Laboratory Report UCRL-17171 (1966).

[d]E. Chen, R. D. George, and W. E. Wentworth, *J. Chem. Phys.* 49, 1973 (1968).

[e]F. J. Davis and D. R. Nelson, *Chem. Phys. Letters* 3, 461 (1969). Average of a series of values obtained in various gases with the exception of those in the carrier gases C_2H_4 and CO_2, which were not included in the averaging because they were distinctly lower. The data of these authors seem to be generally lower than the most reliable results listed above.

[f]F. J. Davis and D. R. Nelson, *Chem. Phys. Letters* 3, 461 (1969).

[g]The same value for αw was reported at T = 530°K.

[h]F. C. Fehsenfeld, *Abstracts of Gaseous Electronics Conference,* Gatlinburg, Tennessee, Oct. 27–31, 1969, paper J4, p. 39.

[i]This value is low because of errors in the pressure measurement.

[j]R. N. Compton *et al., J. Chem. Phys.* 45, 4634 (1966).

[k]This value has been revised by F. J. Davis and D. R. Nelson (private communication, 1970) who now give a value of ~6.5×10^9 sec^{-1} torr^{-1}.

ELECTRON ATTACHMENT TO ORGANIC MOLECULES

Our studies on capture of thermal and epithermal electrons by organic molecules of direct biological interest continued, with special emphasis on a number of NO_2 and oxygen-containing benzene and naphtha-

lene derivatives as well as other aromatic hydrocarbons such as azulene and 1,2-benzanthracene. A number of these systems have been found to capture thermal and epithermal electrons nondissociatively for long periods of time ($>10^{-6}$ sec). For these systems the lifetime of the temporary negative ion as well as the cross section for its formation have been measured and were related to the molecular electronic and geometrical structure. These studies provided values on the electron affinity of such systems, which are of unique radiobiological interest. Thus the study of NO_2-containing compounds aids the understanding of charge-transfer complex formation in organic liquids. The direct measurement of the electron-accepting capacity of aromatic hydrocarbons has a profound implication to current theories of chemical carcinogenicity, while our data on naphthalene find direct application to the interpretation of the pulse radiolysis results on this system.

As an example of the data obtained, we present in Fig. 12.12 the variation of the measured electron attachment rate with mean electron energy (curve *A*) for the azulene molecule. The variation of αw with $\langle\epsilon\rangle$ (or E/P) shown in Fig. 12.12 for this molecule is distinctly different from that for other aromatic molecules known to capture electrons via a nondissociative process at thermal energies.[17,25] While the thermal-peaking attachment rate for other aromatic molecules rapidly decreases when $\langle\epsilon\rangle$ exceeds its thermal value, the same is seen not to be so for azulene. From a detailed study of the azulene molecule by both the electron swarm and the electron beam method and a careful analysis of the swarm data, it was concluded that azulene attaches thermal and near-thermal-energy electrons, forming a long-lived parent negative ion in the field of the ground electronic state with a mean autoionization lifetime of 7 ± 1.5 μsec and a mean thermal attachment cross section of 3.5×10^{-15} cm^2. The sharp cross-section function for the thermal process is shown in Fig. 12.13.

Additionally, azulene was found to attach electrons via a weaker process which peaks between 0.22 and 0.37 eV. This process is clearly indicated from the analysis of the electron swarm data, and the rates represented by curve *C* in Fig. 12.12 are attributed to this latter process. The 0.22- to 0.37-eV process was not seen in the beam experiment. The latter observation and the slight dependence of αw on argon pressure above ~1 eV suggest that the negative ion formed at

[25] L. G. Christophorou and R. P. Blaunstein, *Radiation Res.* 37, 229 (1969).

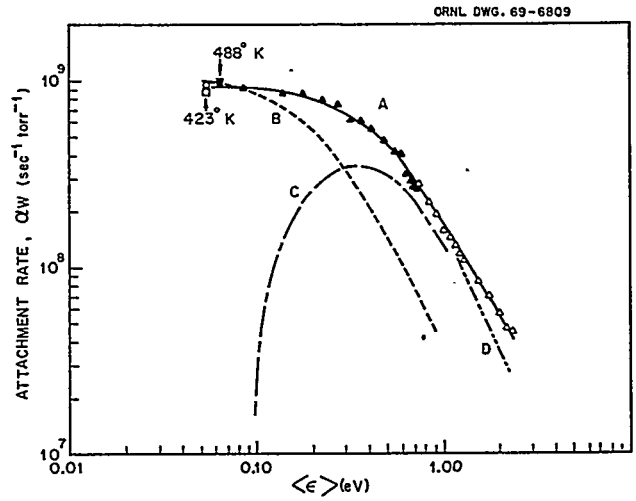

Fig. 12.12. Electron Attachment Rate αw. Curve *A:* αw vs mean electron energy $\langle\epsilon\rangle$ for (1) CO_2, 500 torrs, ○ 423°K; C_2H_4, 500 torrs, □ 423°K and ■ 488°K; (2) N_2, 750 torrs, ▲ 423° and 488°K; (3) Ar, 1000 torrs, △ 423° and 488°K. Curve *B:* Calculated αw using a thermal-peaking cross-section function such as shown in Fig. 12.13. Curve *C:* Curve *B* subtracted from curve *A*. Curve *D:* Approximate extrapolated values of αw in Ar.

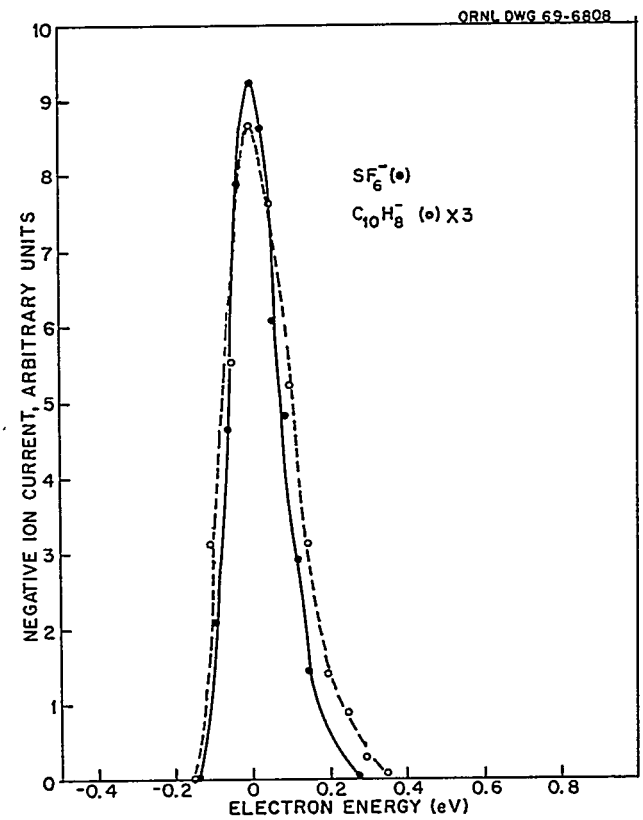

Fig. 12.13. Comparison of SF_6^- and $C_{10}H_8^-$ Negative-Ion Currents at Thermal Energies.

epithermal and higher energies autoionizes in less than 1 μsec.

If the capture process suggested by us between 0.22 and 0.37 eV is associated with electron attachment in the field of the first excited triplet state of azulene, then spectroscopic data[26] indicate an electron affinity for azulene in the first triplet state T_1 of ~0.8 eV, which is much higher than that of 0.46 eV calculated by us for the ground-state azulene molecule, using our measured values of αw and τ in connection with the vibrational frequencies of ref. 27 and the simple theoretical treatment of ref. 18. Biphenyl, aniline, and acenaphthene were found to capture thermal electrons very weakly.

CAPTURE OF SLOW ELECTRONS BY ORGANIC MOLECULES IN THE FIELD OF AN EXCITED ELECTRONIC STATE

Electron capture by an organic molecule with simultaneous excitation of one of the orbiting electrons resulting in a long-lived negative ion has been observed.[20,28] An electron capture process at 2.1 eV observed in *p*-benzoquinone has been associated with electron capture in the field of the lowest triplet state T_1, resulting from an $n \rightarrow \pi^*$ transition at ~2.35 eV. The cross section for this process is shown in Fig. 12.14*a*. For this process the lifetime τ of the long-lived ion varied from 48 μsec at 1.7 eV to ~8 μsec at 3.2 eV (see Fig. 12.14*b*).

A similar capture process but with $\tau < 1$ μsec has been observed (see preceding section) for azulene between 0.22 and 0.37 eV and has been associated with electron capture in the field of the first triplet state for this molecule. These results, especially those on *p*-benzoquinone (quinones are known for their active role in metabolism) are of direct biological interest. The role of triplet states and $n \rightarrow \pi^*$ transitions in electron attachment is under study.

LIFETIMES OF LONG-LIVED POLYATOMIC NEGATIVE IONS FORMED BY ELECTRON CAPTURE IN THE FIELD OF THE GROUND ELECTRONIC STATE

The following organic molecules have been found to capture thermal electrons nondissociatively and to form metastable parent negative ions: *o*-nitrotoluene, *m*-nitrotoluene, *p*-nitrotoluene, 1-naphthaldehyde, 2-naphthaldehyde, and cinnamaldehyde. The lifetimes τ of these negative ions have been measured with a time-of-flight mass spectrometer (TOFMS) in two ways. First, they were determined directly from the formula

$$\tau = \frac{t}{\ln (N_0/N^-)} , \qquad (14)$$

[26] P. M. Rentzepis, *Chem. Phys. Letters* 9, 717 (1969).

[27] A. van Tets and H. H. Günthard, *Spectrochim. Acta* 19, 1495 (1963).

[28] L. G. Christophorou, J. G. Carter, and A. A. Christodoulides, *Chem. Phys. Letters* 3, 237 (1969).

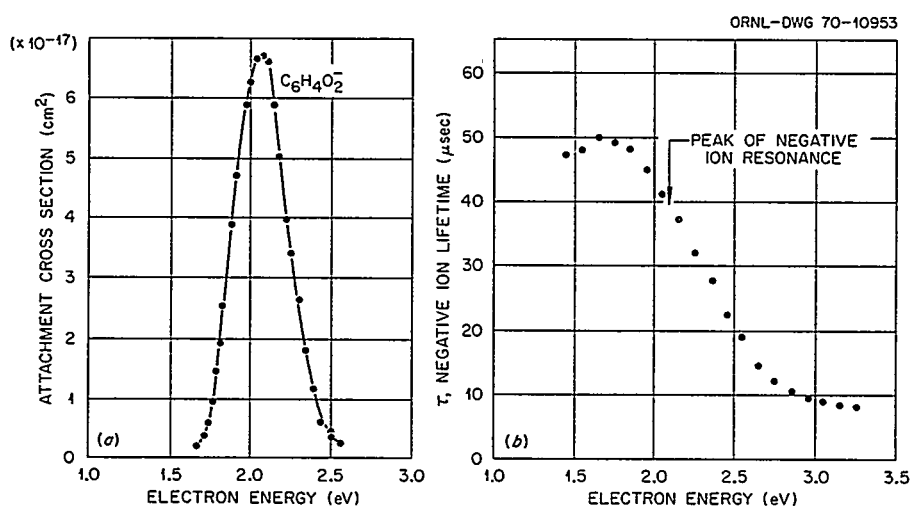

Fig. 12.14. (*a*) Electron Capture Cross Section as a Function of Electron Energy for *p*-Benzoquinone; (*b*) Negative-Ion Lifetime as a Function of Electron Energy for *p*-Benzoquinone.

where t is the time of flight, N_0 is the number of metastable ions at $t = 0$, and N^- is the number of metastable ions which have not decayed after the time t. When the lifetimes were measured this way, the SF_6^{-*} lifetime was also measured before and after each measurement of the unknown lifetime to ensure proper operating conditions. Second, they were measured from the slope of a $-\ln(N^-/N_0)$ vs t plot (see Fig. 12.15). In this case the straight line should pass through the origin. The results obtained through both methods are in excellent agreement, as can be seen from the data plotted in Fig. 12.15 and those listed in Table 12.5. None of the lifetimes listed in the table showed any dependence on the electron energy. Measurements of the attachment rates for some of these compounds are in progress, and the lifetime as well as the attachment cross-section data are currently being combined with molecular structure and the vibrational frequencies of these systems to calculate, through the formula[18]

$$\sigma_a = \frac{\pi^2 \hbar^3}{\tau \epsilon m\, \Gamma(N) \prod_{i=1}^{N} h\nu_i} \times [\epsilon + \mathrm{EA} + (1 - \beta\omega)\epsilon_z]^{N-1}\,, \quad (15)$$

the molecular electron affinity and to investigate the role of τ and σ_a in studies of molecular structure. In Eq. (15), ν_i are the vibrational frequencies of the attaching molecule with N degrees of freedom,

$$\epsilon_z = \frac{1}{2}\sum_{i=1}^{N} h\nu_i\,,$$

ϵ is the electron energy, $1 - \beta\omega$ is a correction factor, EA is the electron affinity, and m is the electron mass. Electron affinities obtained this way for the ground electronic state of a number of molecules are listed in Table 12.6.

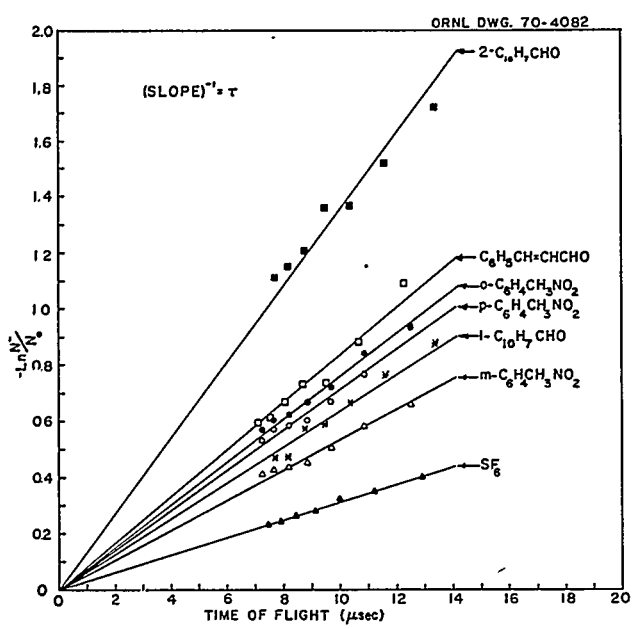

Fig. 12.15. $-\mathrm{Ln}(N^-/N_0)$ vs t for o-, m-, and p-Nitrotoluene, 1- and 2-Naphthaldehyde, and Cinnamaldehyde (See Text).

Table 12.5. Negative-Ion Lifetimes

Compound	τ_{slope} (μsec)	$\langle\tau\rangle$ (μsec)	Number of Runs
o-Nitrotoluene	13.1	13.1	3
m-Nitrotoluene	18.8	18.7	3
p-Nitrotoluene	13.9	14.0	3
1-Naphthaldehyde	15.7	14	6
2-Naphthaldehyde	7.4	7.5	8
Cinnamaldehyde	11.9	12.0	4
Sulfur hexafluoride	32.1	32.4	8

Table 12.6. Electron Affinity for Some Molecules

Compound	EA (eV)
Sulfur hexafluoride	≥1.30
1,4-Naphthoquinone	≥0.6
Nitrobenzene	≥0.5
Azulene	≥0.45
Biacetyl	≥0.40
p-Benzoquinone	≥0

ENERGY DEPENDENCE OF THE LIFETIME OF LONG-LIVED TRANSIENT NEGATIVE IONS

The mean autoionization lifetime of a parent negative ion formed by electron capture in the field of the ground electronic state (nuclear-excited Feshbach resonance[29]) or in the field of an excited electronic state (electron-excited Feshbach resonance[29]) has been found, for the first time, to vary with electron energy. As we have reported earlier,[20,28] p-benzoquinone (BQ)

[29] J. N. Bardsley and F. Mandl, *Rept. Progr. Phys.* 31, part 2, 471 (1968).

has been found to capture electrons via an electron-excited Feshbach resonance at ~2.1 eV. The mean autoionization lifetime for the BQ^{-*} ion due to this capture process has been found to vary with electron energy ϵ over the negative-ion resonance (Fig. 12.14*a*), as shown in Fig. 12.14*b*. These data were taken without application of the retarding-potential-difference (RPD) method. However, use of the RPD method has produced data consistent with those plotted in Fig. 12.14*b*. The lifetime was independent of BQ pressure (1×10^{-5} to 1.5×10^{-4} torr) and filament current (1.6 to 2.5 A). Each lifetime measurement for BQ^{-*} was preceded by a measurement of τ for SF_6^- to ensure proper operation of the TOFMS. No variation of τ with ϵ was detected over the sharp SF_6^- resonance at ~0.0 eV.

Additionally, the lifetime of a long-lived parent negative ion formed by electron capture in the field of the ground electronic state (nuclear-excited Feshbach resonance) has been found to vary with ϵ. Figure 12.16*a* shows αw vs $\langle\epsilon\rangle$ for 1,4-naphthoquinone (NQ) measured at 348°K in mixtures with C_2H_4 (400 and 1000 torrs), N_2 (400, 750, and 1000 torrs), and Ar (400, 750, and 1000 torrs). The NQ pressures ranged from 3×10^{-4} torr in C_2H_4 and N_2 to 10^{-3} torr in Ar. No dependence on carrier gas pressure was observed, and measurements at 363°K indicated no change in the attachment rate. Above 363°K reliable data could not be obtained due to decomposition of NQ. In Fig. 12.16*b* the beam data on this molecule are shown and are seen to be in agreement with the swarm data (Fig. 12.16*a*).

The variation of the negative-ion current for NQ^- obtained with the RPD method is shown in Fig. 12.16*b*. There is a possibility of some structure, which was reproducible in all ten runs made. This possible structure corresponds to excitation of skeletal deformation modes of NQ. We have calculated[20] a thermal value of 6.2×10^{-15} cm^2 for the cross section for this process.

In Fig. 12.17 the NQ^- current without the RPD method is shown with the SF_6^- current recorded under identical conditions. The peak currents have been normalized to the same value. The resonances coincide, with the NQ^- current indicating a slight tail. Both resonances are seen to be wider than those observed employing the RPD method. Also shown in Fig. 12.17 is the lifetime for NQ^- measured simultaneously with the

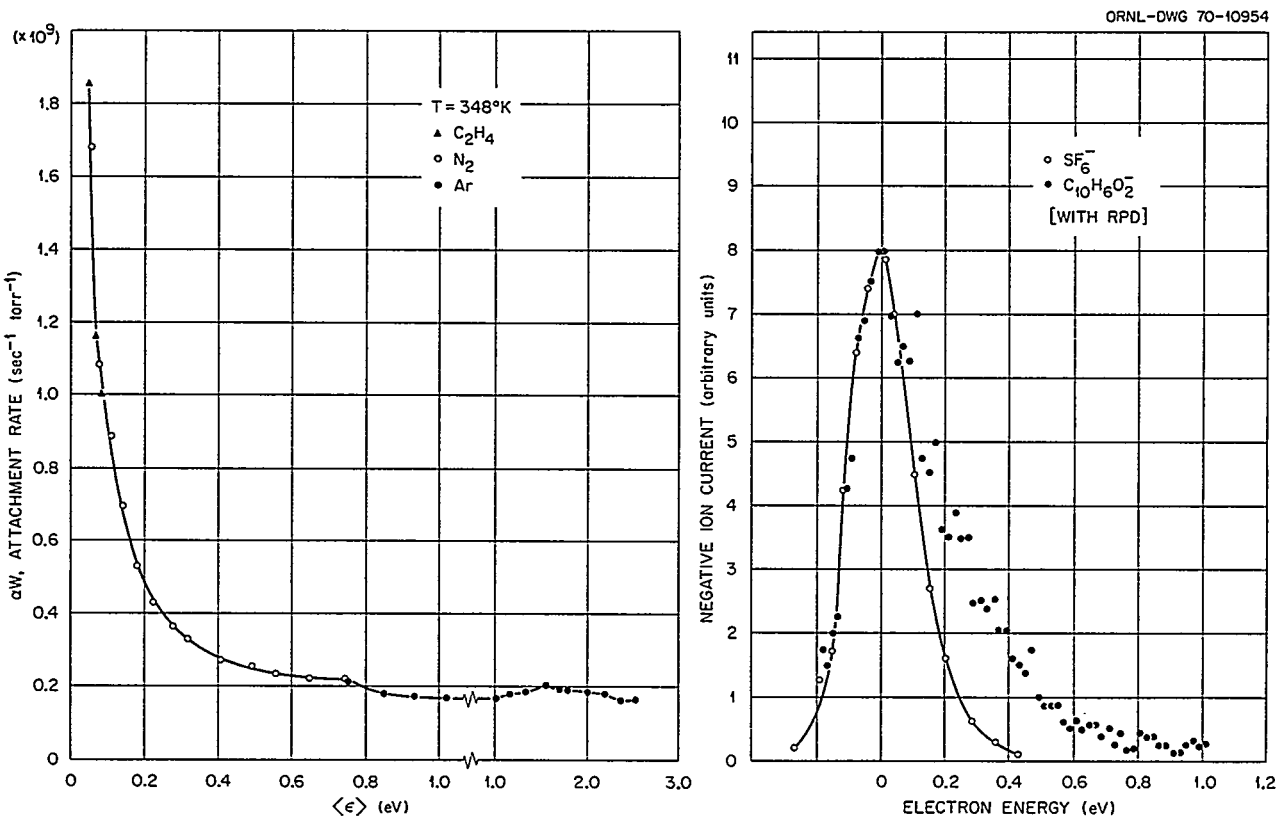

Fig. 12.16. (*a*) Attachment Rate as a Function of Mean Electron Energy for 1,4-Naphthoquinone; (*b*) Negative-Ion Current as a Function of Electron Energy for 1,4-Naphthoquinone.

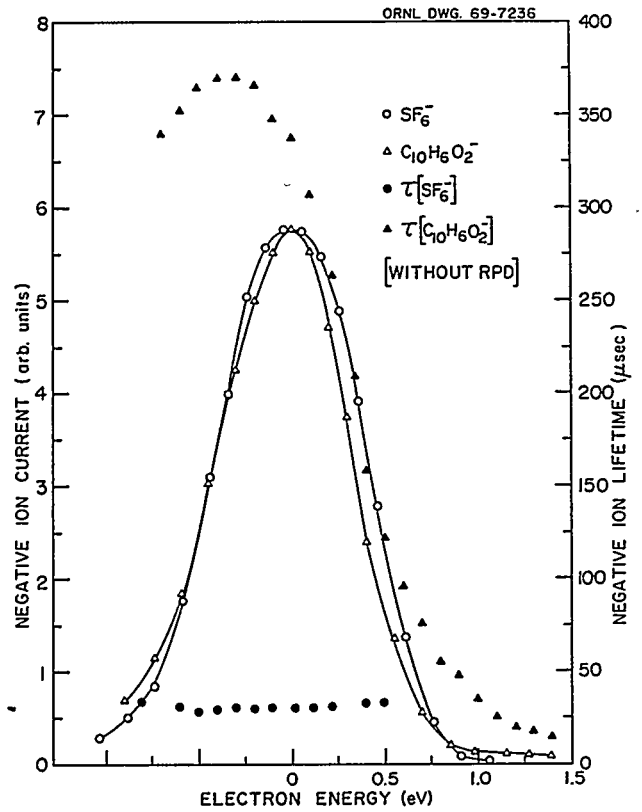

Fig. 12.17. Negative-Ion Current as a Function of Electron Energy for Sulfur Hexafluoride and 1,4-Naphthoquinone, and Negative-Ion Lifetime as a Function of Electron Energy for Sulfur Hexafluoride and 1,4-Naphthoquinone.

NQ^- current and the lifetime for SF_6^- measured both preceding and following the NQ^- current measurement. As is seen from Fig. 12.17, no variation of τ for SF_6^- could be seen. This may be attributed to the sharpness of the resonance for this molecule. Due to the low counting rates the RPD method could not be employed in measuring τ. It is believed, however, that the variation of τ is more drastic than indicated in Fig. 12.17. The sharp decrease in τ for NQ^{-*} with increasing electron energy is attributed to the increase in excess energy of the molecular negative ion, which enhances autodetachment. The small decrease in τ at low energies is attributed to experimental factors (see Discussion in ref. 20). A constant background of neutral counts could cause such an effect.

ELECTRON ATTACHMENT TO HALOGENATED HYDROCARBONS

A systematic study has been made of electron attachment to molecules of the form $C_nH_{2n+1}Br$ for n = 1 to 10, using both electron swarm and electron beam techniques. The magnitudes and widths of the dissociative attachment cross-section functions for the production of Br^- have been found to depend in a very characteristic fashion on n and thus on the reduced mass of the dissociation fragments. Figure 12.18 shows the cross-section functions obtained for the production of Br^- from $C_nH_{2n+1}Br$ molecules for n = 2 to 6. This study allowed also determination of the compound negative-ion states for these systems as well as a deeper understanding of the energetics and quantitative aspects of dissociative electron attachment to complex molecules. The results may also prove useful in efforts to relate electron attachment to the toxic action of molecules. A complete analysis of these data is in progress.

THRESHOLD-ELECTRON EXCITATION SPECTRA OF ORGANIC MOLECULES; LOCATION OF TRIPLET AND COMPOUND MOLECULAR NEGATIVE-ION STATES

A new high-resolution experimental arrangement has been designed and built which enables both an improvement and an expansion of our studies on organic molecules using threshold-electron beams. The apparatus is in the final stages of testing and will be employed for studies of optically forbidden electronic transitions as well as of compound molecular negative-ion states in organic molecules of biological interest which have low vapor pressures at room temperature.

EMISSION AND DECAY OF FLUORESCENT ORGANIC LIQUIDS UNDER ELECTRON IMPACT

Our studies on the dependence of the optical emission from organic liquids on the intensity of the exciting electron beam have continued. The experimental arrangement is currently being modified to allow a simultaneous measurement of the spectra and the lifetimes of excited electronic states under a pulsed-electron excitation. For low electron beam intensities the emission is identical to that observed under ultraviolet excitation, but as the electron beam intensity increases the emission is dominated by that due to excimers and eventually by that due to radiation products.

It has been found[30] that measurements of the true lifetime require extreme caution to remove dissolved

[30] O. E. Wagner, L. G. Christophorou, and J. G. Carter, *Chem. Phys. Letters* 4, 224 (1969).

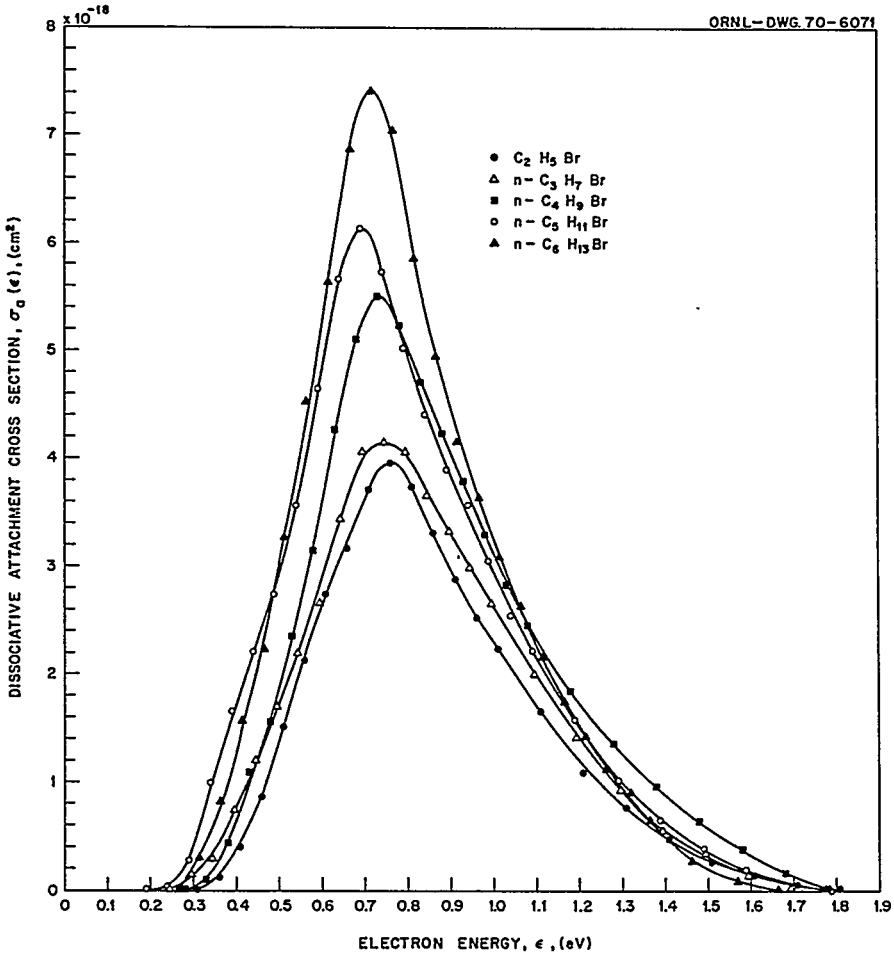

Fig. 12.18. Cross Sections for the Production of Br^- from $C_nH_{2n+1}Br$ for $n = 2$ to 6. C_2H_5Br(•), n-C_3H_7Br (Δ), n-C_4H_9Br (■), n-$C_5H_{11}Br$ (○), n-$C_6H_{13}Br$ (▲).

oxygen and traces of impurities from the liquids under study. Our measurements on liquid benzene, toluene, and mesitylene suggest that previously published data on lifetimes of organic molecules in the liquid state or in solution may be lower limits to their true values. Our values[30] for the lifetimes of liquid benzene, toluene, and mesitylene at 25°C are, respectively, greater than or equal to 30.3, 41.2, and 44.2 nsec.

Additionally, a weak emission band on the short-wavelength side of the usual $S_{1,0} \rightarrow S_{0,n}$ fluorescence emission has been observed for liquid benzene, toluene, and ethylbenzene under electron impact and has been attributed to emission from a higher excimeric state of these liquids. For the case of benzene this excimeric state has been identified as B_{2g}.

PHOTOPHYSICAL STUDIES OF LIQUIDS

A very sensitive double ultraviolet monochromator has been put into operation and has allowed detection of very weak emissions from organic and other molecules in the liquid state and in solution. Experimental data provided evidence for an emission from the second excited state of the pyrene and 3,4-benzopyrene molecules in solution. A study of other organic molecules is in progress.

An effort has been made also to detect phosphorescence emission from liquid H_2O and D_2O. The results, although interesting, are still inconclusive. It might be noted that upon excitation of liquid H_2O and D_2O with the mercury 2537-Å line, a distinct emission

was observed from both H_2O and D_2O peaking at 2780 and 2175 Å. However, auxiliary experiments have indicated that this emission must be associated with Raman scattering. Such Raman scattering "lines" may be responsible for some "anomalies" in certain spectra in the literature.

ON MOLECULAR PARAMETERS OF PHYSICAL, CHEMICAL, AND BIOLOGICAL INTEREST[31]

In view of the fact that in recent years there has been a large increase in basic research on interactions between polyatomic molecules and hence a need for measured or calculated molecular parameters, a thorough review has been completed of the present literature values of molecular ionization potentials, electron affinities, and electron capture cross sections. The values obtained for each molecular parameter have been discussed as to the physical process involved (e.g., photon-molecule interaction as compared with electron-molecule interaction) and the experimental methods employed (e.g., photoionization, photoabsorption, electron impact, charge transfer, and electron attachment-detachment).

It has been concluded from this review of the reported values of ionization potentials that, although extensive and accurate measurements (particularly photoionization measurements) of this quantity have been achieved for a large number of inorganic and organic molecules, much has yet to be reported for the large aromatic and heterocyclic molecules which form the basis of biological systems.

The values of molecular electron affinities are, in general, not in good agreement, particularly those of the large polyatomic molecules. More work is needed, especially with promising methods such as those based on photodetachment and electron-molecule interactions.

Direct measurements of the cross sections for electron-molecule and ion-molecule interactions are of extreme interest and should continue in order to supplement photophysical and theoretical data.

It was concluded also that at least part of the failure of the various attempts to explain the biological action of certain chemicals on the basis of physical quantities, such as the ionization potential, electron affinity, etc., may lie in the lack of accurate knowledge of these quantities.

[31] R. P. Blaunstein and L. G. Christophorou, *Radiation Res. Rev.* (in press).

STOPPING POWERS OF SLOW ELECTRONS IN HYDROCARBONS

Measurements of the radiation-induced conductivity in a number of liquid hydrocarbons have revealed several anomalies.[32] The observed conductivities, and hence the implied ranges of the ejected electrons, are found to be remarkably sensitive to structural variations among the hydrocarbons. In order to delineate the origin of these anomalies, stopping powers of slow electrons in several hydrocarbon vapors have been investigated. This has been accomplished obliquely by measuring mobilities and diffusion coefficients of electron swarms in the vapors in the presence of an electric field. A straightforward combination of these transport parameters yields the desired stopping rate as a function of characteristic energy.

Figure 12.19 indicates the relation obtained for several such vapors. These results are pertinent insofar as they provide data for absolute range calculations. Of more immediate interest is the fact that no differences are obtained which can be correlated with the liquid-phase conductivities. We conclude that the conductivity anomalies are not associated with intrinsic molecular parameters but arise rather through the condensation process and thus reflect an effect of phase on stopping power.

RESONANCE RADIATION IMPRISONMENT PHENOMENA

While an electronically excited atom may fluoresce quite rapidly, the emitted photon can be reabsorbed many times before finally escaping from a finite volume. This phenomenon of "imprisonment" arises in many natural and laboratory settings and was the object of an early investigation by Holstein.[33] Because of the stochastic nature of the absorption-reemission sequence, the Monte Carlo technique is an ideal theoretical method for its study. This course has been followed with considerable success. Certain results of Holstein, whose work was restricted to quite simple geometries, have been reproduced. Thus the probability $P(t)$ that a quantum is still imprisoned within a system at some time after its initial release is given by

$$P(t) = \sum_i \alpha_i \exp(-\beta_i t) .$$

[32] W. F. Schmidt and A. O. Allen, *Science* 160, 301 (1968); *J. Chem. Phys.* 72, 3730 (1968).

[33] T. Holstein, *Phys. Rev.* 72, 1212 (1947); 83, 1159 (1951).

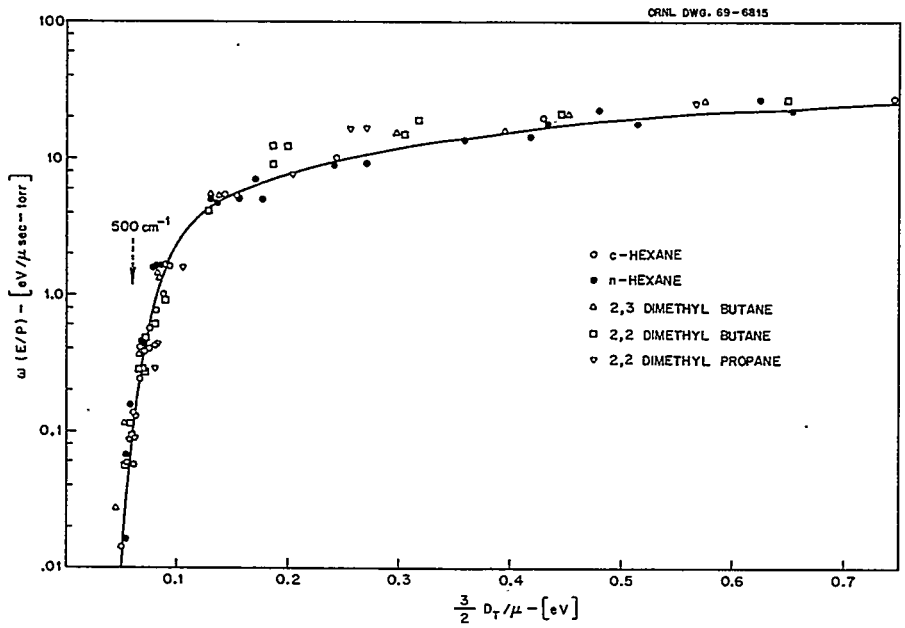

Fig. 12.19. Energy-Loss Rates in Hydrocarbon Vapors as a Function of Characteristic Electron Energy.

The coefficients α_i, β_i are obtained as simple functions of the geometry and the absorptivity of the medium. For more complicated geometries, or where reflection at the walls occurs, the Monte Carlo method is unique in providing these coefficients. Associated problems, such as the spectral dispersion of the emitted radiation and the probability of quenching by impurities within the medium, follow naturally from the calculations.

COMPARISON OF DIRECT AND PHOTOSENSITIZED IONIZATION EFFICIENCIES

Because of the pervasiveness of energy transfer phenomena, it is of interest to compare the chemical consequences of such transfer with those obtaining when an identical quantum is absorbed directly from a photon flux. Studies in this laboratory have been directed at a comparison of the ionization efficiency of a molecule when excited by collisions with a $^3P_1$ or $^1P_1$ argon atom and the analogous efficiency when a 1067- or 1048-Å photon is absorbed. Photons at each of these wavelengths are used to excite the argon atoms. These quanta are then effectively imprisoned and so may be transferred at leisure to an impurity molecule.

We find that in the great majority of cases the ionization efficiency of the acceptor molecule is the same as when the quantum is supplied directly by the light source. This is interpreted as corroborating the dipole-dipole resonance mechanism of energy transfer. Yet in the case of a few acceptor molecules, bearing a high degree of symmetry, this equivalence between the two mechanisms is not found. A hitherto unsuspected role of symmetry in energy transfer mechanisms is implicated.

13. Graduate Education and Vocational Training

K. Z. Morgan
M. F. Fair

R. D. Birkhoff
L. G. Christophorou
R. N. Compton
L. C. Emerson
W. R. Garrett
C. E. Klots
R. H. Ritchie
H. C. Schweinler
J. E. Turner
H. A. Wright

The field training program at ORNL during the summer months is open to all AEC Fellowship students who have completed their first academic school year under the fellowship program. In the past most of the Fellows have come from Vanderbilt University and The University of Tennessee; in recent years students have come from 16 other schools participating in the program. The field training consists of two major phases, applied health physics and research health physics. The university program cannot, in itself, produce the desired product. The summer training program is absolutely essential in the education of a health physicist.

Seven Fellows participated in the summer training program at ORNL during July and August 1969 – two from Vanderbilt, two from The University of Tennessee, one from the University of Kansas, one from the University of California, and one from Georgia Institute of Technology.

The summer training began with a three-day orientation program which was followed by five weeks with the applied health physics group and five weeks with the research health physics groups. One week was spent at the Special Training Division (ORAU) doing health physics experiments. Numerous seminars were held throughout the summer highlighting recent advances in health physics and closely allied fields. Many of the seminar speakers were from laboratories and universities from around the world.

In the applied health physics training, the student gains practical experience in all phases of radiation protection under the supervision of a senior health physicist. The student learns of all the protection services that are provided for the Physics Division, Reactor Chemistry Division, Metals and Ceramics Division, Solid State Division, Chemical Technology Division, Tracer Facilities, High-Level Radiochemical Development Laboratory, Fission Products Pilot Plant, Waste Disposal Group, and the Ecology Research Group. In addition, he learns of personnel monitoring, instrument calibration, counting facilities, bioassay techniques, and whole-body counting.

In health physics research the students are first given a brief summary of all the research projects in progress in the Division. They then choose the group in which they remain for a five-week period. They become part of the team and are truly engaged in doing health physics research under senior scientist supervision. The fields of investigation include: interaction of radiation with gases, solids, and liquids; theoretical radiation physics; health physics research reactor; dosimetry; radioactive waste disposal; and internal dose calculations.

The summer program gives the student sufficient experience in applied health physics to enable him to take a position in this field, where with only a little additional experience he will soon qualify for a position of responsibility in radiation protection. Also, he learns of the tremendous breadth in research health physics and is made aware of the diverse problems available for thesis work should he decide to continue his education for the M.S. or the Ph.D. degree under the AEC Fellowship.

Eighteen students were enrolled in the course in General Health Physics (Physics 4710-20-30) taught by a member of the Division at The University of Tennessee. This was a three-quarter course which met 3 hr/week. A course in Applied Radiation Physics

(Physics 234) at Vanderbilt University was taken by three AEC Fellows and four physics majors. This was a one-semester course which met 4 hr/week.

Universities and colleges at which ORNL health physics research and educational activities were discussed are listed below:

Alderson-Broaddus College
Davis and Elkins College
East Tennessee State University
Fairmont State College
Knoxville College
Marshall University
University of Florida
University of Georgia
University of Hawaii
University of Houston
University of Kentucky
University of Pennsylvania
University of Tennessee
Vanderbilt University
West Virginia State
West Virginia Wesleyan
Southern Missionary College

There were a number of Oak Ridge Graduate Fellows, AEC Fellows, and USPHS students in the Division working on theses as partial requirements for advanced degrees. Their thesis titles and universities are listed below:

1. A. J. Braundmeier, Jr., "Experimental Investigations of Surface Plasmon Radiation from Aluminum" (UT)
2. Barbara G. Brooks, "Measurement of Optical Constants by Ellipsometry" (UT)
3. E. L. Chaney, "Electron Attachment to Polyatomic Molecules" (UT)
4. A. A. Christodoulides, "Resonant Electron Attachment Processes in Polyatomic Molecules" (UT)
5. P. M. Collins, "Investigation of Negative Ions with Electron Beams" (UT)
6. J. J. Cowan, "The Surface Plasmon Resonance Effect in Grating Diffraction" (UT)
7. J. M. Elson, "Collective Excitations in Inhomogeneous Plasmas" (Univ. of Kentucky)
8. C. E. Easterly, "Study of Aromatic Hydrocarbons in Relation to Carcinogenesis" (UT)
9. T. F. Gesell, "Photoelectric Properties of Magnesium in the Vacuum Ultraviolet" (UT)
10. J. T. Grissom, "Electron Impact Excitation and Ionization Studies of the Rare Gases" (UT)
11. W. F. Hanson, "Optical Properties of Solids in the Extreme Ultraviolet" (UT)
12. D. L. McCorkle, "Interactions of Low-Energy Electrons with Polyatomic Systems" (UT)
13. S. J. Nalley, "Charge Exchange Between Fast Atoms and Molecules" (UT)
14. W. T. Naff, "Slow Electron Collisions with Molecules" (Univ. of Georgia)
15. M. N. Pisanias, "Inelastic Scattering of Slow Electrons by Organic Molecules" (UT)
16. B. L. Sowers, "Optical Constants of Several Liquids in the Vacuum Ultraviolet Region" (UT)
17. J. A. Stockdale, "Studies of Negative Ion–Molecule Reactions in the Energy Region from Zero to Three Electron Volts" (UT)
18. R. B. Vora, "Calculation of Stopping Power at Extreme Relativistic Energies" (UT)
19. U. S. Whang, "Optical Constants of Cesium for Photons of Energy 5 to 9.6 eV" (UT)
20. A. Hadjiantoniou, "Electron Attachment Cross Sections and Negative Ion Lifetimes of Polyatomic Molecules" (UT)

The Division provided assistance to the staff at The University of Tennessee in updating and revising its graduate curriculum in health physics. This included courses in General Health Physics, Radiation Chemical Physics, Physics of Polyatomic Molecules, Interaction of Electrons with Gases, Interaction of Electrons with Solids, and Interaction of Radiation with Matter. This curriculum has attracted Fellows who desire education to the master's level and also those who wish to pursue the Ph.D. degree. Help was provided The University of Tennessee in conducting the co-op program with ORNL leading to the B.S. degree in Health Physics. This type of assistance and consultation is available to any school desiring to set up a health physics program or institute courses in this field. For example, queries have been received from Georgia Institute of Technology, Southern Technical Institute, Texas Woman's University, Auburn University, Oklahoma State University, Loyola University, and Wake Forest University with regard to setting up courses in Health Physics. Assistance was given Vanderbilt University in the preparation of qualifying examinations in Health Physics. Visits to ORNL with lectures and tours were provided for classes in Health Physics from the University of Arkansas and the University of North Carolina.

One member of the Education Group of the Health Physics Division helped in the screening of applicants

for the 1969–1970 USAEC Fellowship Program. This work was done at the Oak Ridge Associated Universities (ORAU). Assistance was also given to ORAU in the presentation of a ten-week course in Health Physics and several courses for medical personnel entitled "Medical Radioisotopes."

Eight student trainees from ORAU were assigned to the Division for the summer, and five faculty members spent the summer in the Division as research participants sponsored by ORAU. One student spent the summer in the Division under the Summer Science and Engineering Program for students from predominantly Negro colleges. A two-day course was given for firemen, policemen, and civil defense workers at the request of the USAEC.

Several staff members of the Radiation Physics Section of the Health Physics Division worked with The University of Tennessee faculty in preparing preliminary examinations for the Ph.D. degree and in grading the examinations. Four of our staff hold Ford Foundation appointments at the University and in this capacity participated in student advising on matters of curricula and research. They were also active on the University Committee on Graduate Education. Our staff played prominent roles in the faculty meetings of the UT Physics Staff.

The demands for education in health physics have continued to rise. Although emphasis will be on education to the Ph.D. level to provide personnel for positions of leadership in industrial, academic, and medical institutions, education will continue to be offered during the summer at the master's level to provide vocational training which includes a knowledge of health physics principles and procedures. The needs of the reactor industry must be met by these and other efforts.

Part III. Radiation Dosimetry Research

J. A. Auxier

GENERAL OBJECTIVES AND ACTIVITIES

The major objective of the Radiation Dosimetry Research program is the development of dosimetry theories, systems, and techniques for describing the radiation fields in which human exposures have occurred (or might occur) or in which animals or other specimens for radiobiological research are exposed. For practical applications the Health Physics Research Reactor (HPRR) is the most powerful irradiation facility. However, the HPRR, the DOSAR Low-Energy Accelerator (DLEA), and the 3-MV Van de Graaff are all used for the combined applied and basic studies required by the program's objectives. The emphasis is always on development of practical systems and techniques based on the fundamental principles of the many disciplines making up this interdisciplinary field. Each component of a coexistent multicomponent radiation field is measured separately, and parameters such as energy, angular, and spatial (both macroscopic and microscopic) distributions are assumed to be the minimal requirements for the ultimate correlation of biological effect with radiation environment.

The studies include general applications, such as depth-dose studies; spectrometry research and development for neutrons and gamma rays; several solid-state detector studies; irradiation facility design, construction, and operation; and basic studies to provide otherwise unavailable information for the other categories. Great care is exercised in maintaining close liaison with dosimetry-related research throughout the world, and an information center (as yet informal) has been maintained for many years.

Considerable research and study are not reported specifically in order to conserve space. In particular, members of the program staff serve on numerous national and international committees, panels, and review boards. Critical reviews in most fields of dosimetry have been prepared over the past years, and the latest of these can be found listed in the "publications" section of this report.

14. Dosimetry for Human Exposures and Radiobiology

J. W. Poston

J. S. Cheka
W. L. Chen[1]
W. F. Fox
H. H. Hubbell, Jr.
J. E. Jackson
T. D. Jones
E. M. Robinson
W. H. Shinpaugh
W. S. Snyder
E. B. Wagner

JAPANESE DOSIMETRY PROGRAM

Close liaison was maintained between the Radiation Dosimetry Research Section and the Atomic Bomb Casualty Commission (ABCC) during the year. Three representatives from this section completed a liaison trip. Their initial objective was a case-by-case evaluation of the shielding histories of all survivors who developed leukemia plus a statistically representative number of the control population. The total number of leukemia cases in Hiroshima and Nagasaki is approximately 185, and a 10% sample was arbitrarily chosen from the control population. A total of about 2500 shielding histories were studied.

Doses for several other cases of persons exposed inside heavy shielding structures are to be calculated by the Japanese shielding technicians using procedures developed by this section. The method consists in applying the globe (spherical coordinate projector)[2] and using new techniques to calculate approximate values for the doses in concrete buildings. In order to convert the attenuation curves needed for concrete into more useful forms, the following equations were developed on the basis of preliminary data. The neutron transmission factor for Hiroshima and Nagasaki is

$$T_n = 1.140 \exp(-0.106t) ,$$

where t is the thickness of concrete in centimeters and must be $\geqslant 1$ cm. The gamma transmission factor for Hiroshima is

$$T_\gamma = 1.353 \exp(-0.0390t)$$

where the thickness of concrete was >10 cm. For 6 cm $< t \leqslant 10$ cm, $T_\gamma = 0.95$ and for $t \leqslant 6$ cm, $T_\gamma = 1.05$. The gamma transmission factor for Nagasaki is

$$T_\gamma = 1.311 \exp(-0.0421t)$$

where the thickness of concrete is >10 cm. For 6 cm $< t \leqslant 10$ cm, $T_\gamma = 0.9$ and for $t \leqslant 6$ cm, $T_\gamma = 1.0$. A more accurate procedure is desirable, and studies are under way to develop one.

At ABCC there are three types of "reliability" ratings which are used to judge a portion of the overall certainty of the final dose estimate to a given survivor. These "reliability factors" are for the most part independent of each other, and any single type of "reliability" is usually a poor indication of the overall reliability of a given dose estimate. Our representatives urged the use of a new total reliability scheme consisting of the following classes:

Good – Those cases which were first-person accounts and were rated as having good reliability in all present methods (except for children in utero, where the mother's account must be a first-person account).

Fair – Those cases which were first-person accounts or in which the history was given by a member of the family who was exposed with the individual and having good or fair rating of all three types of reliability.

Poor – All other cases, including all those survivors who have ever changed the designation of their location "at time of bombing" (ATB) more than 100 m. There exist several cases such that, in nonmedical records, people have changed their reported places of exposure several times, usually due to a financial motivation.

[1] Alien guest.

[2] H. H. Hubbell, Jr., *Health Physics Division of ORNL and ABCC Liaison Pool Activities for Period from May 1 to August 31, 1960,* Nov. 25, 1960.

One point of concern to the group was the attempt, currently under way by the Statistics Group of ABCC, to determine a "biological hypocenter." It is of concern because they are holding in abeyance the use of the hypocenters recommended by Hubbell[3] pending verification with biological data. However, this represents an attempt to determine a sensitive independent parameter from a measure of an insensitive dependent variable (i.e., using an assumed biological response to dose, a relation which is largely unknown and at best is assumed to be a relatively linear relationship, and attempting to determine a location from dose where dose varies inversely as the square of, and exponentially with, distance from the epicenter; moreover, the dose varies slowly over a circle of 50 m radius about the hypocenter because the slant range from the epicenter varies slowly for these dose distances). It also builds into the analysis a supposition concerning dose vs biological effect which the analysis should be designed to elucidate. Further, there was inhomogeneity of shielding as a function of location relative to the hypocenter. The initial population density was not uniform because there were two rivers and a cemetery close to the hypocenter on the western side of the area. It is hoped that further consideration of the problem will cause a reversal of their position.

In relation to the leukemia study, a second draft of a TR manuscript entitled "Leukemia in Atomic Bomb Survivors, Hiroshima and Nagasaki, 1 October 1950–30 September 1966" was reviewed. The liaison group disagrees with the assumptions and conclusions expressed in the manuscript and hopes it will not be published in its present form. The most unsatisfactory assumption is that RBE of neutrons for the production of leukemia is constant for all levels of exposure, and this becomes the basis for the derivation of a single RBE of neutrons with respect to production of leukemia.

We attempted to do a very crude analysis of RBE values for the production of leukemia using the basic assumption that RBE values may vary with radiation exposure level. By looking at exposure levels of the survivors who contracted leukemia, a few facts can be used to set up principles for the following analysis. The factors influencing the analysis are:

1. Exposure levels range from zero to over 500 rads, with the occurrence rate of leukemia so small that the datum points are not statistically well behaved.
2. At high doses the occurrence rates in Hiroshima and Nagasaki approach a constant limiting value.
3. The survivors who had the highest exposures and then contracted leukemia were exposed to about the same high total ($D_n + D_\gamma$) dose level in both Hiroshima and Nagasaki. [Factors 2 and 3 together imply that at exposure levels of more than 400 rads, neutrons are not significantly more effective than gamma rays in the production of leukemia. Another way of expressing this is: Although the ratios of D_γ/D_n vary by extreme factors (approximately two orders of magnitude) between Hiroshima and Nagasaki, the highest total exposure levels causing leukemia are not much different for the two cities. If neutrons are always more significant in the production of leukemia, then the highest exposures in Hiroshima should be significantly lower than the highest exposures in Nagasaki.]
4. If the data are plotted as a cumulative distribution of occurrence as a function of dose (i.e., fraction of survivors stricken by leukemia exposed to doses below a given dose level), then some of the oscillations are removed, and it appears that above the 450-rad level no differences are noted. If neutrons and gamma rays have different degrees of effectiveness, then it must be for lower exposures.
5. If the data are smoothed by an elementary smoothing process and then plotted as occurrence vs dose as shown in Fig. 14.1, then factor 4 is still true. Further, if it is assumed that biological damage in Nagasaki was due entirely to gamma rays (this approximation is justifiable because of the large ratio of D_γ/D_n in Nagasaki) and that RBE is a variable, and if the data are then replotted, then the curve for Hiroshima keeps crossing the curve for Nagasaki at lower exposures for higher values of RBE (the solution to the problem is an RBE that brings the curves together throughout the range of the abscissa). However, this technique raises the highest Hiroshima RBE doses to a much higher level than the highest Nagasaki RBE doses. All of this implies that this procedure is also inadequate.

From all of this it appears that a constant RBE of any magnitude provides no unique solution to all of these problems; however, there can be a unique solution to these problems if the RBE is allowed to vary over the range of exposures.

A study of many dose estimates for survivors in Hiroshima revealed values of D_γ/D_n to be about 2.7 for exposure levels below 100 rads, for most classes of

[3] H. H. Hubbell, Jr., T. D. Jones, and J. S. Cheka, *The Epicenters of the Atomic Bombs in Japan II. Reevaluation of All Available Data and Our Recommended Values,* ABCC TR 3-69 (to be published).

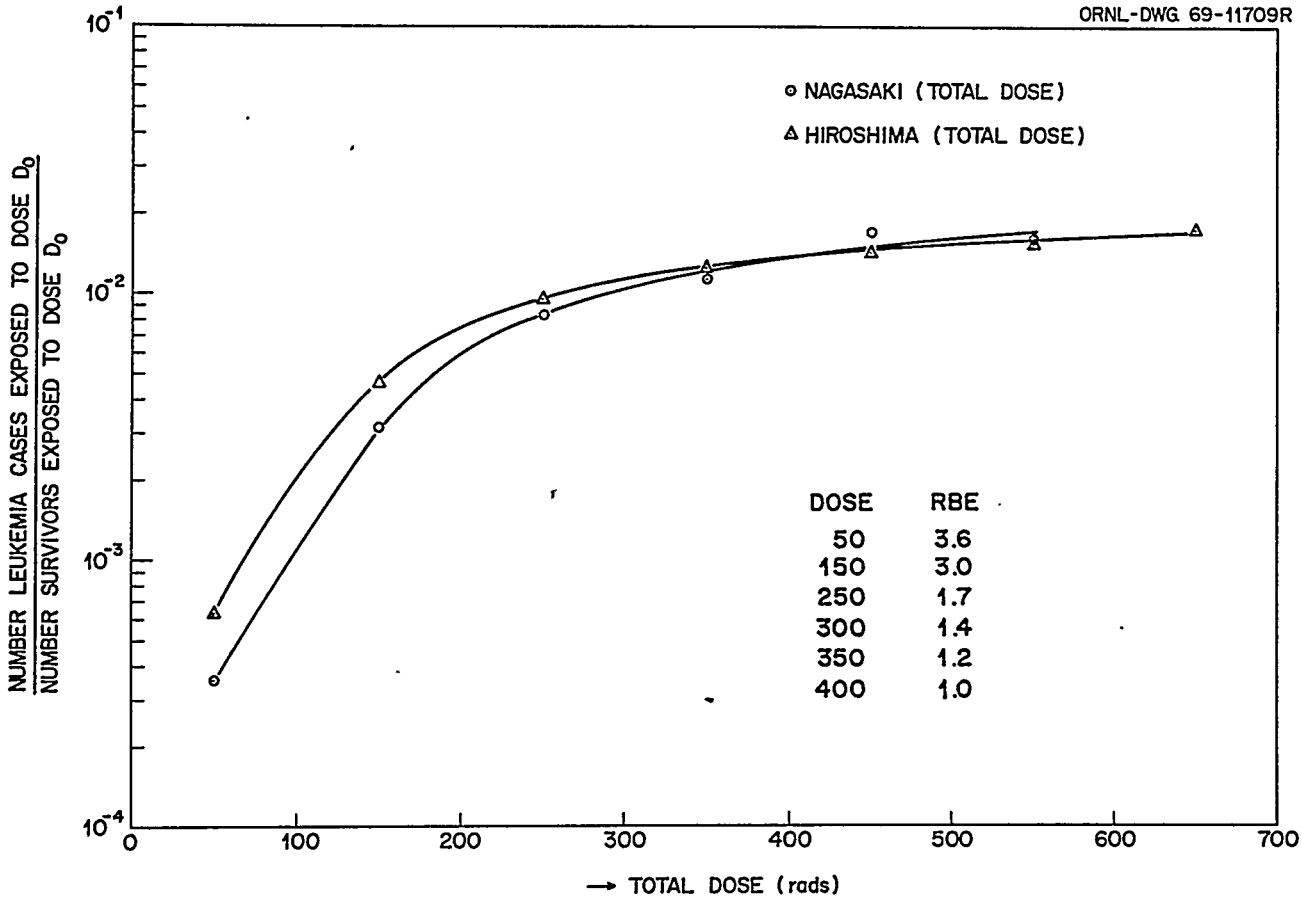

Fig. 14.1. Incidence of Leukemia in Hiroshima and Nagasaki as a Function of Dose.

Table 14.1. Fetal Dimensions at Different Stages of Development

Time (weeks)	Dimensions[a]					Dimensions[b]	
	Total Length (cm)	Crown-Rump Length (cm)	Radius (cm)	Cylinder Length (cm)	Weight (g)	Length (cm)	Weight (g)
4		0.4				1.0	
6		0.8					
7		1.5					
8		3.0	0.5	3.0		2–3	4
12		5.5	1.0	5.5		7–9	20
16	15	10.0	2.0	10.0		16.0	120
20	23	15.0[c]	2.5	15.0		25.0	250–350
24	30	20.0[c]	3.0	20.0		30.0	600–700
28	35	23.0[c]	4.0	23.0	1500	35.0	1000–1200
36	45	30.0[c]	5.0	30.0	2000–2500	45.0	2000–2500

[a]*Gray's Anatomy, Descriptive and Applied,* 32d ed., Johnson, Davies, and Davies, Longmans, Green and Co.
[b]*Obstetrics,* ed. by Dr. S. Fujimori (1960 ed.), a Japanese textbook furnished by Dr. Maki of ABCC.
[c]Estimated from assumed ratio of leg length/total length = $\frac{1}{3}$.

survivors, and $D_\gamma/D_n = 3.6$ for higher exposures. From the equation

$$(\text{leukemia rate})_\gamma\,(\text{dose})_\gamma + (\text{RBE})_n\,(\text{leukemia rate})_\gamma \times (\text{dose})_n = (\text{leukemia rate})_{(\gamma + \text{RBE} \times n)},$$

the values of RBE shown on Fig. 14.1 are obtained.[4] (Leukemia rate is occurrence per unit dose.)

The two classes of survivors for which it has been most desirable to obtain dose distributions as functions of depth inside the body are (1) children who were in utero ATB and (2) survivors developing carcinomas or nodules in the thyroid glands. The first class is of widespread interest because of the sensitivity to radiation of the fetus during its development period, especially the first trimester. The second class has received much attention because of the large number of occurrences and of the ease of detection of these abnormalities during autopsy.

Table 14.1, obtained from the indicated references and by interpolation, gives fetal dimensions at different stages of development.

Figure 14.2 shows how fetal geometries were simplified. For the first seven weeks a spherical geometry was assumed, and thereafter the fetus was assumed to be cylindrical in shape. Figure 14.3 shows the results of such geometrical simplifications. For the spherical geometries the crown-to-rump length was assumed to correspond to half of a circumference of a great circle (i.e., πR). All fetuses were assumed to be centrally located in a sagittal plane of the mother's torso.

The Monte Carlo LET code,[5,6] used for many previous calculations, was used to calculate dose and LET in cylinders having heights of 60 cm and radii of 12 and 15 cm and thus corresponding to the adult torso. The calculations consist of three components: (1) the contribution from the neutron field, (2) the

[4] S. Jablon *et al.*, "RBE of Neutrons in Japanese Survivors," presented at the Symposium on Neutrons in Radiobiology, Oak Ridge, Tennessee, November 11–14, 1969; to be published in the proceedings.

[5] J. A. Auxier, W. S. Snyder, and T. D. Jones, "Neutron Interactions and Penetration in Tissue," pp. 275–316 in *Radiation Dosimetry*, vol 1, 2d ed., ed. by F. H. Attix and W. C. Roesch, Academic, New York, 1968.

[6] W. S. Snyder, "The LET Distribution of Dose in Some Tissue Cylinders," in *Biological Effects of Neutron and Proton Irradiations*, vol 1, IAEA, Vienna, 1964.

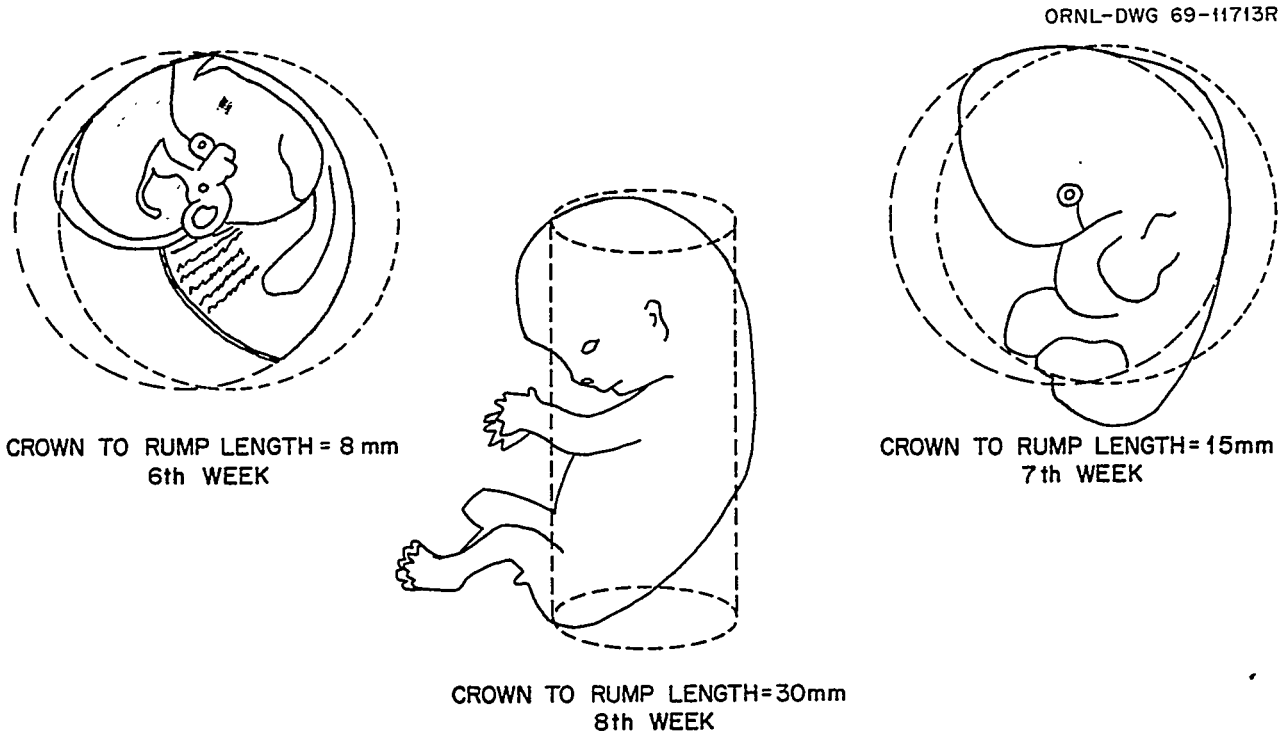

Fig. 14.2. A Human Embryo (from *Gray's Anatomy*).

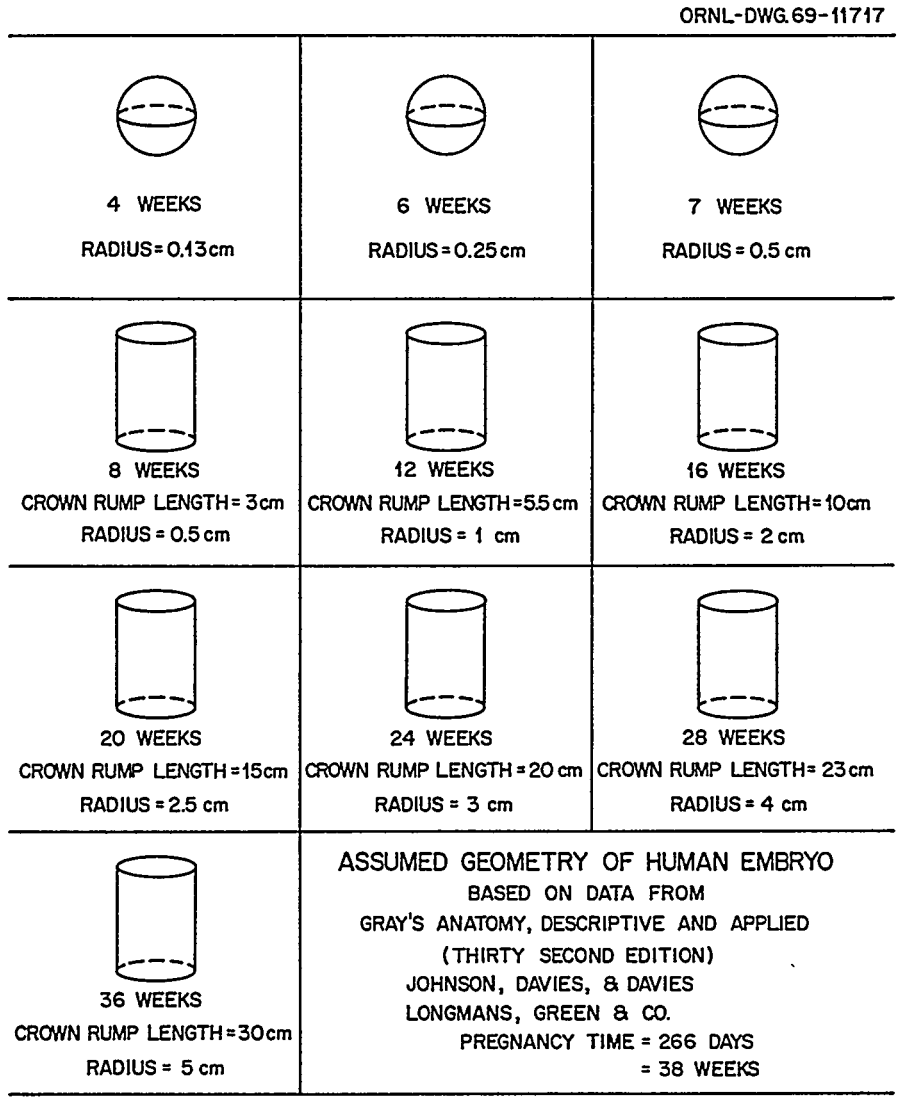

Fig. 14.3. Assumed Geometry of Human Embryo.

contribution from gamma rays produced by neutron interactions inside the phantom, and (3) the contribution from the gamma field external to the phantom. In addition to the above phantoms, a smaller, 6-cm-radius, phantom was used for estimation of dose to parts of the thyroid. Figures 14.4–14.6 show the results of the first two contributions. Calculations for the third component are still under way and will be reported later.

The neutron field was assumed to have an energy distribution similar to that of the HPRR (see Sect. 17) and an angular distribution similar to that measured during Operation HENRE.[7] From the results obtained thus far, fetal size and directional orientation of the mother are relatively unimportant because the dose distribution curves are relatively flat across the fetus, ensuring a constant exposure level to all parts of the fetus. The thyroid gland is not centered in a sagittal plane through the neck, and consequently, unlike the fetus, the gland is not exposed uniformly. However, orientation of the survivor is still not important because the first two contributions to the radiation field are nearly symmetrical with respect to direction. At the present, doses from gamma rays produced external to the phantom have not been calculated, and therefore the shapes of the distributions are unknown.

[7] J. S. Cheka, *Distribution of Radiation from a 14 MeV Neutron Source in and near Structures,* CEX-65.13 (May 1969).

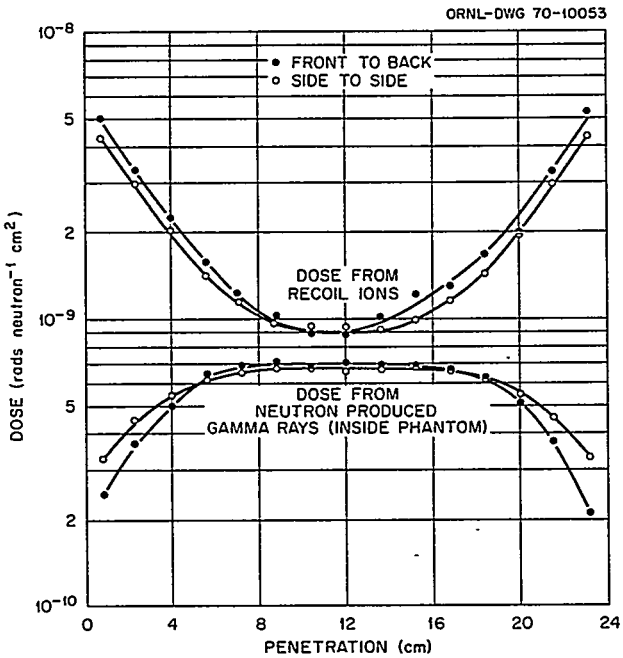

Fig. 14.4. Calculated Dose in a Small Torso from Radiation Produced by a Fission Source.

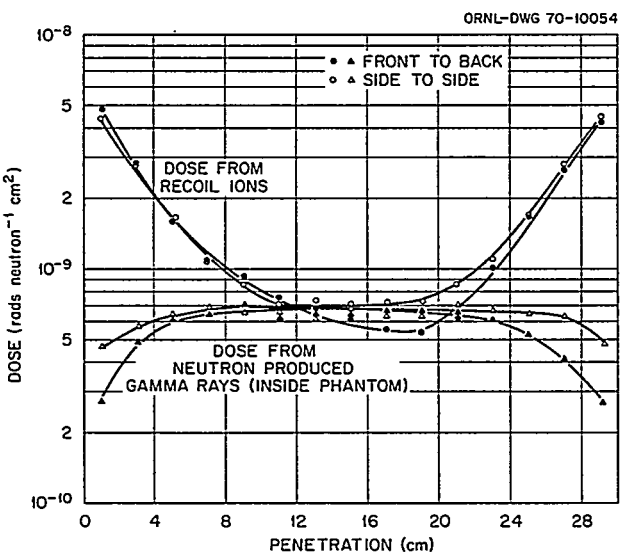

Fig. 14.5. Calculated Dose in a Large Torso from Radiation Produced by a Fission Source.

LEAKAGE STUDIES FOR "FAT MAN" AND "LITTLE BOY"

A considerable effort has been expended over the last several years to eliminate as many uncertainties as possible regarding the radiation leakage from the weapons which were detonated over Hiroshima and

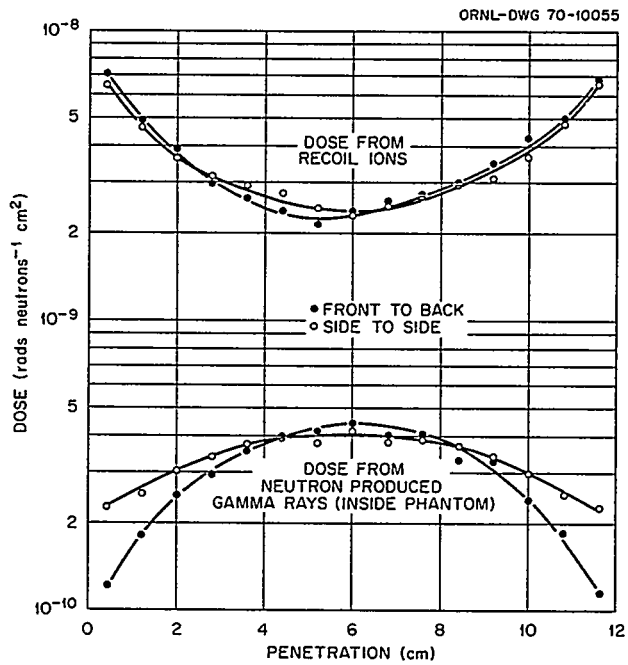

Fig. 14.6. Calculated Dose in a Neck-Sized Phantom from Radiation Produced by a Fission Source.

Nagasaki, Japan. Two years ago, an exact duplicate of each of these two weapons was sent to the Burlington, Iowa, arsenal for certain modifications so that a series of leakage studies could be performed. These were reported last year. Even after this series of experiments, there were several areas of interest which still had not been covered sufficiently. First, attempts at measuring the leakage spectrum during the studies at Burlington had not been satisfactory because of detector sensitivity. In addition, there were several developments in the Radiation Dosimetry Research Section which made it possible to measure the fission density in substitute ^{238}U parts. In order to accomplish this set of measurements, the weapons were moved to a more accessible location. Measurements of the fission density as a function of distance, in the substitute parts, from the center of a 200-μg ^{252}Cf source were made for each weapon. It was found that the fission density decreased exponentially through the uranium with a relaxation length of 2.1 cm. These data are presented in detail elsewhere.[8] An attempt was made to measure the neutron energy spectrum using a modified Hurst threshold detector and the 200-μg source. The detectors were in the form of thin electrodeposited fission fragment

[8] F. F. Haywood and W. F. Fox, "Determination of Fission Densities in Selected Group of Fissionable Material," Classified (to be published).

radiators positioned adjacent to pieces of 10-μ-thick kimfoil[9] in which the fission products actually penetrate leaving holes which may be counted with a "jumping spark" detector. Although the irradiations were made over a weekend, the source intensity was insufficient to provide adequate counting statistics. Plans are currently under way to repeat the same set of measurements using an 800-μg source. When these are complete, it is expected that a reasonable histogram-type spectrum for leakage neutrons from each weapon will be available.

[9]W. Cross, "Rapid Reading Techniques for Nuclear Particle Damage Tracks in Insulating Foils," in *Proceedings of the International Topical Conference on Nuclear Track Registration in Solids* (ed. by D. Isabelle and M. Monnin), Laboratory of Nuclear Physics, University of Clermont, 1969.

DOSE DISTRIBUTIONS IN CYLINDERS EXPOSED DURING OPERATION HENRE

The calculations of dose distributions inside cylindrical-shell H_2O-filled phantoms were continued. Some of the results and a brief description were given in last year's annual report and will not be duplicated here except to state that the calculations were done for cylindrical shells of different sizes, which are given in Figs. 14.7–14.9. E. A. Straker's DOT[10] description of the neutron field was used to describe the neutron source at the phantom, and a summary of these results is shown in Fig. 14.7. These results generally agreed

[10]F. R. Mynatt, *A User's Manual for DOT, a Two-Dimensional Discrete Ordinates Transport Code with Anisotropic Scattering,* K-1694 (to be published).

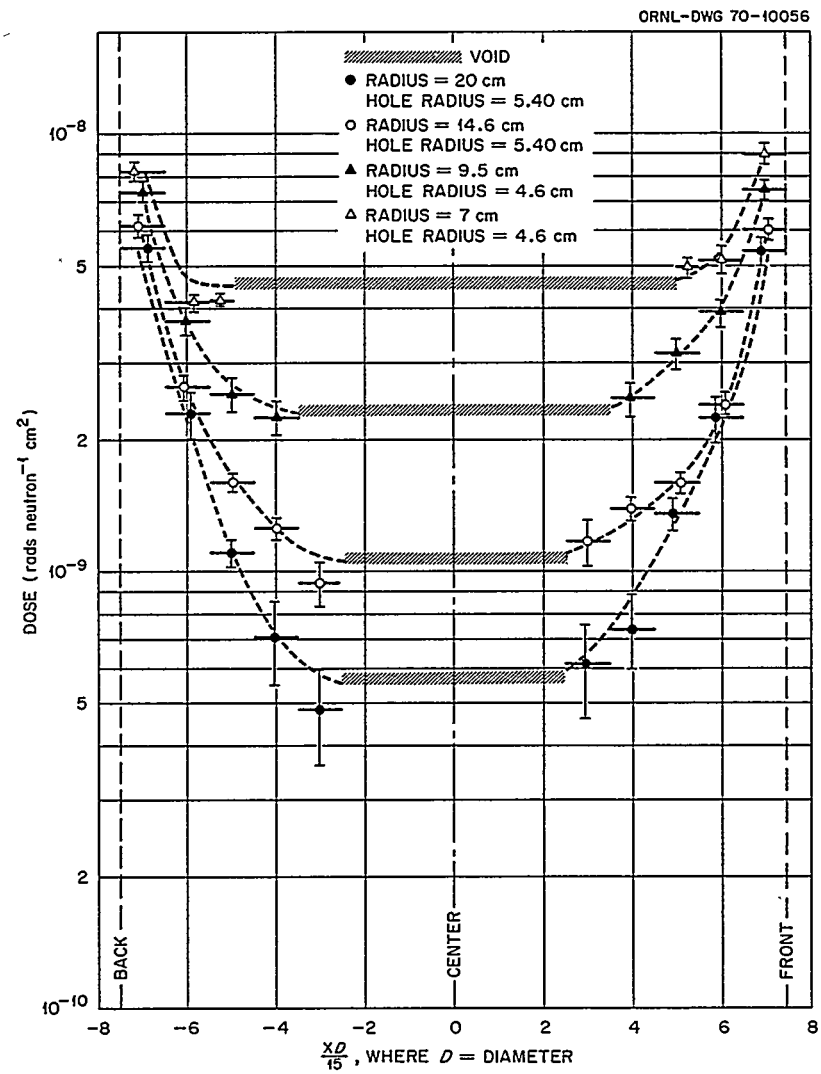

Fig. 14.7. Doses from Recoil Ions in H_2O-Filled Cylindrical Shells Due to Neutrons Having Energy Greater than 150 keV.

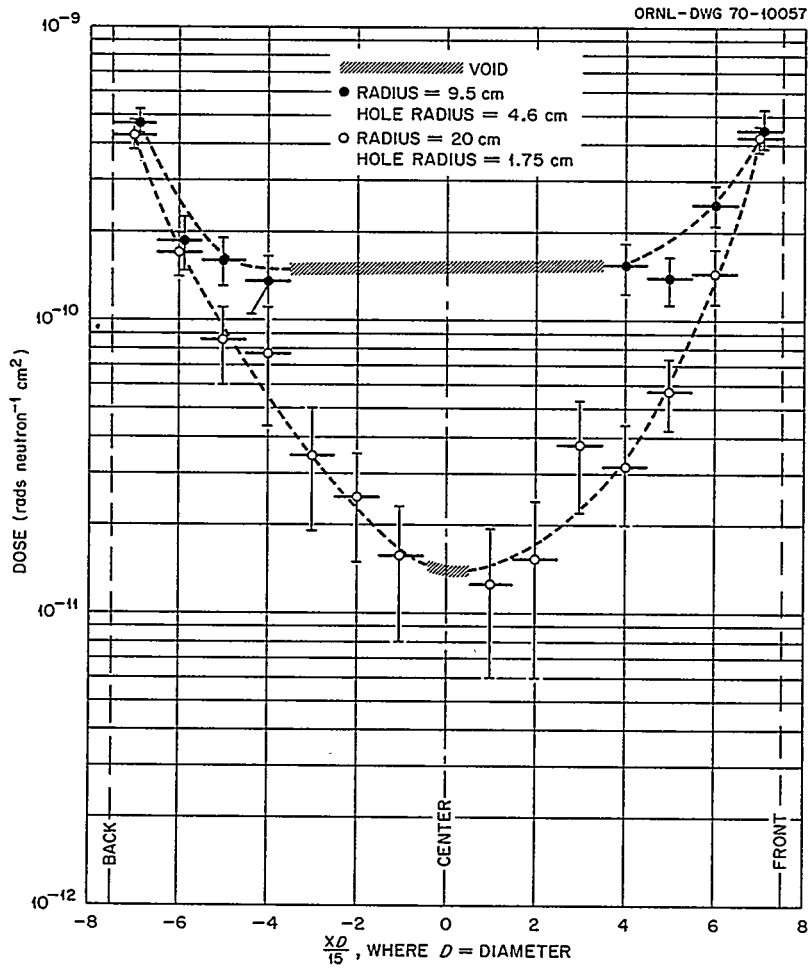

Fig. 14.8. Doses from Recoil Ions in H_2O-Filled Cylindrical Shells (Neutrons Allowed to Become Thermalized).

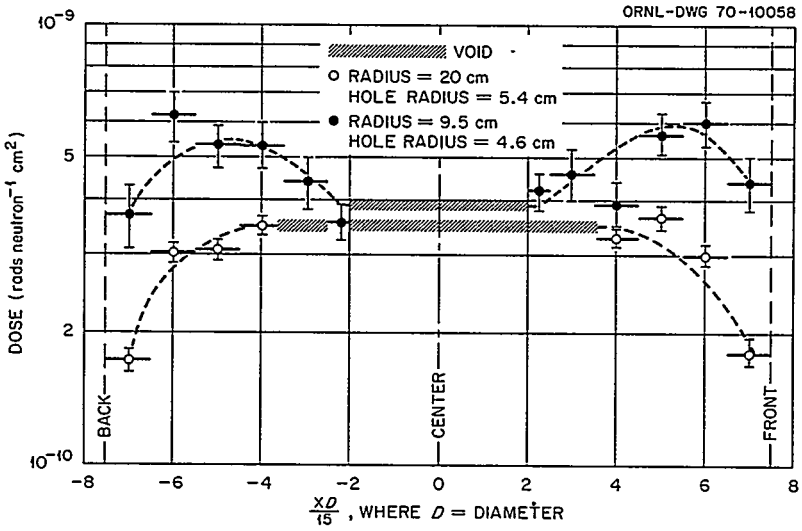

Fig. 14.9. Doses from Neutron-Produced Gamma Rays Inside H_2O-Filled Cylindrical Shells. Doses from gammas produced externally are shown in Fig. 14.10.

with the experimental results measured during HENRE to within less than 5%.

To compute dose contributions due to gamma-ray interactions inside the phantom, it is necessary to consider (1) the neutron-produced gamma rays inside the phantom amd (2) those gamma rays produced by the source and by neutrons in the air around the phantom. The neutron portion of the code[5,6] was used to generate gamma-ray histories inside the phantom, with the neutron results shown in Fig. 14.8 coming as a by-product. The corresponding gamma results are shown in Fig. 14.9, and Fig. 14.10 shows dose contributions from the gammas produced by the source and in the air around the phantom. These calculations are based on data from Straker's ORNL-4464. A comparison of the experimentally measured D_n/D_γ with calculated data showed agreement to within 23% for the two extreme cases.

DEPTH-DOSE DISTRIBUTIONS IN SMALL ANIMALS

Because of several requests for data, doses from neutron-produced recoil ions, doses from neutron-produced gamma rays inside the phantom, and the corresponding LET curves were computed for phantoms corresponding in size to those of a rat and a rabbit. Curves were generated for neutron energies of

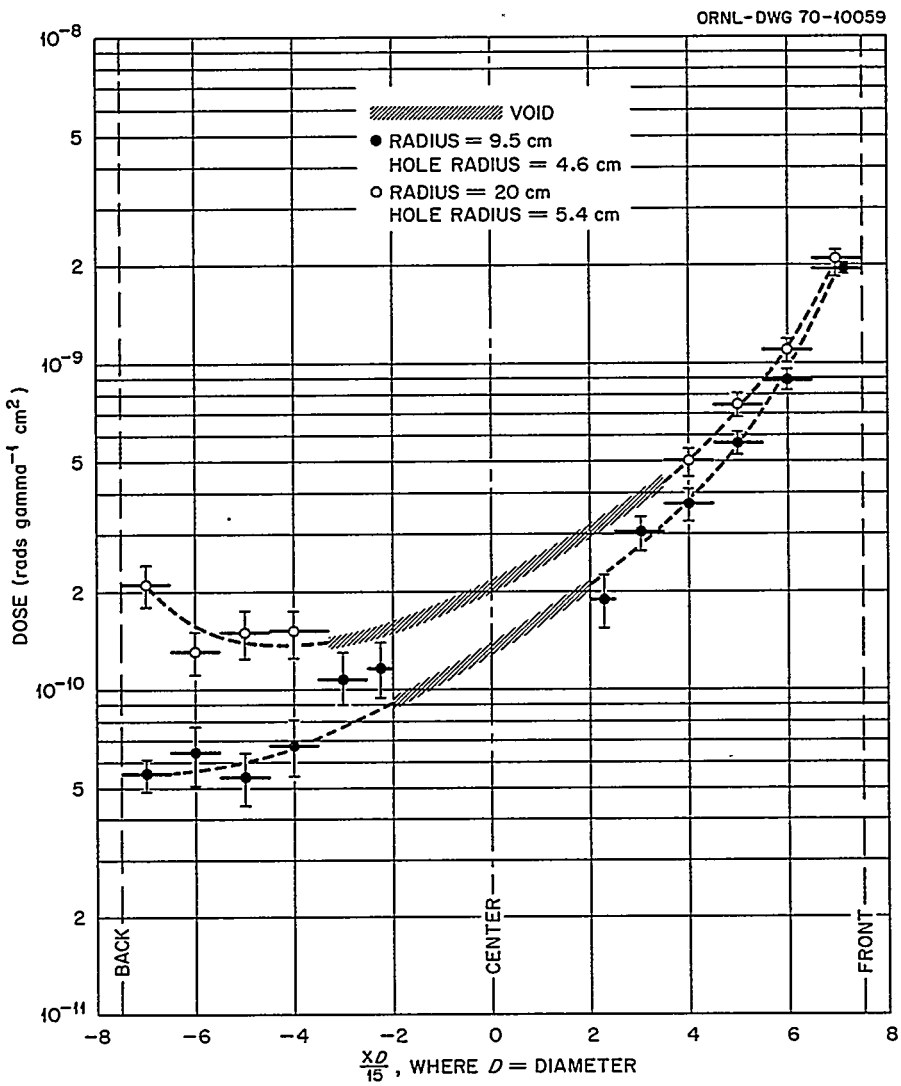

Fig. 14.10. Doses from Gamma Rays Produced Outside the H_2O-Filled Cylindrical Shells.

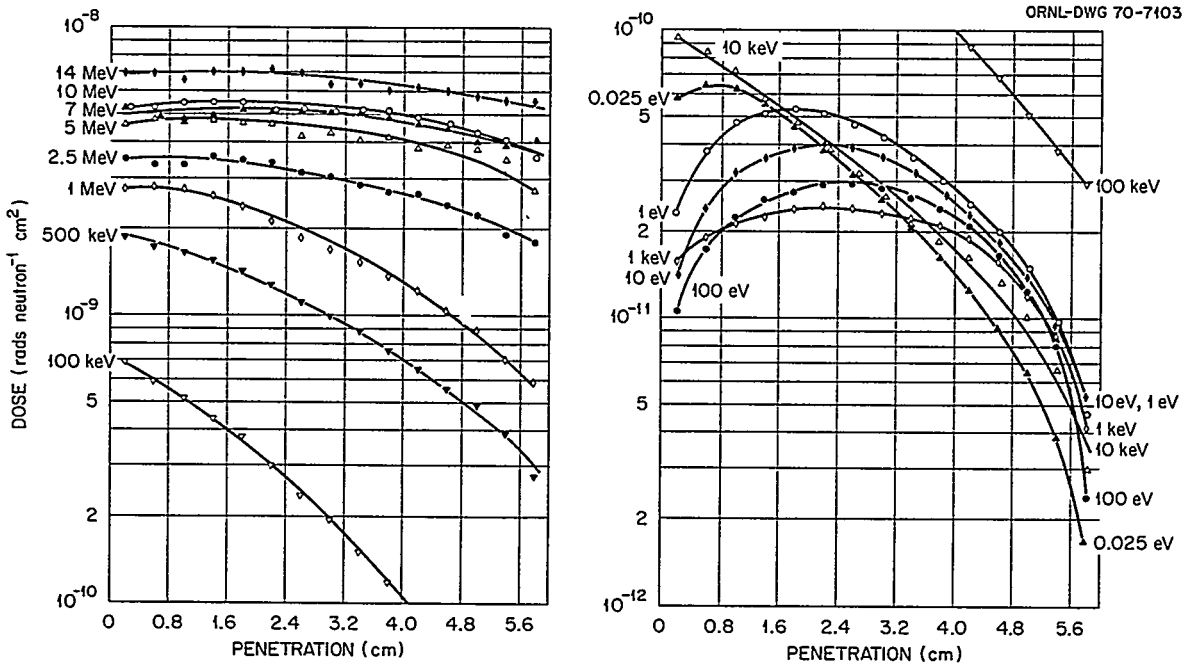

Fig. 14.11. Dose from Recoil Ions as a Function of Penetration Depth in a Rat-Sized Phantom (Radius = 3 cm, Height = 13 cm).

0.025 eV, 1 eV, 10 eV, 100 eV, 1 keV, 10 keV, 100 keV, 500 keV, 1 MeV, 2.5 MeV, 5 MeV, 7 MeV, 10 MeV, and 14 MeV. The results of the calculations of doses from neutron-produced recoil ions are shown in Figs. 14.11 and 14.12, Figs. 14.13 and 14.14 show the dose contributions from neutron-produced gamma rays, and LET distributions are shown in Figs. 14.15 and 14.16. No discussion of this material will be given here because of the close similarity to discussions of other data in both this and last year's annual report.

CALIFORNIUM-252

Calculations were made[5,6] of the absorbed dose (D), the dose equivalent (DE), and the linear energy transfer (LET) in tissue due to neutrons from a ^{252}Cf source.[11] A broad parallel beam of neutrons was incident from one direction perpendicular to the axis of a 30-cm-diam cylinder of 60 cm length. In addition, these distributions were computed for a 5-cm-diam beam of neutrons incident in the same direction at the midpoint of the cylinder, as shown in Fig. 14.17. All of the reactions shown in Table 14.2 and the neutron energy spectrum for ^{252}Cf given by Hyde[12] (Fig. 14.18) were used.

Absorbed dose as a function of depth (depth is defined as the distance from the front of the phantom measured along a diameter) is given in Fig. 14.19 for the broad-beam irradiation. Curves for D from (n,γ) reactions and from positive ions (protons and heavier ions) are given separately.

In radiation protection applications, uniform whole-body irradiations are seldom encountered. Further, there is an increasing interest in the use of ^{252}Cf in therapy. Consequently, the calculations for a small-diameter beam of neutrons incident on the cylinders were made with these practical considerations in mind. Figure 14.19 also shows the absorbed dose as a function of depth along the 2.5-cm-radius beam; the increasingly lower curves show D as a function of depth for annuli of increasing radius as indicated on the key sketch. The highest absorbed doses in the annuli outside the beam are less than in the beam by factors of from 4 to 40 for the first to fourth, respectively, and these relative values do not change appreciably for the DE curves.

[11] T. D. Jones and J. A. Auxier, "Neutron Dose, Dose Equivalent, and Linear Energy Transfer from ^{252}Cf Sources," *Health Phys.*, in press.

[12] E. K. Hyde, *A Review of Nuclear Fission. Part I. Fission Phenomena at Low Energy*, UCRL-9036 (1960).

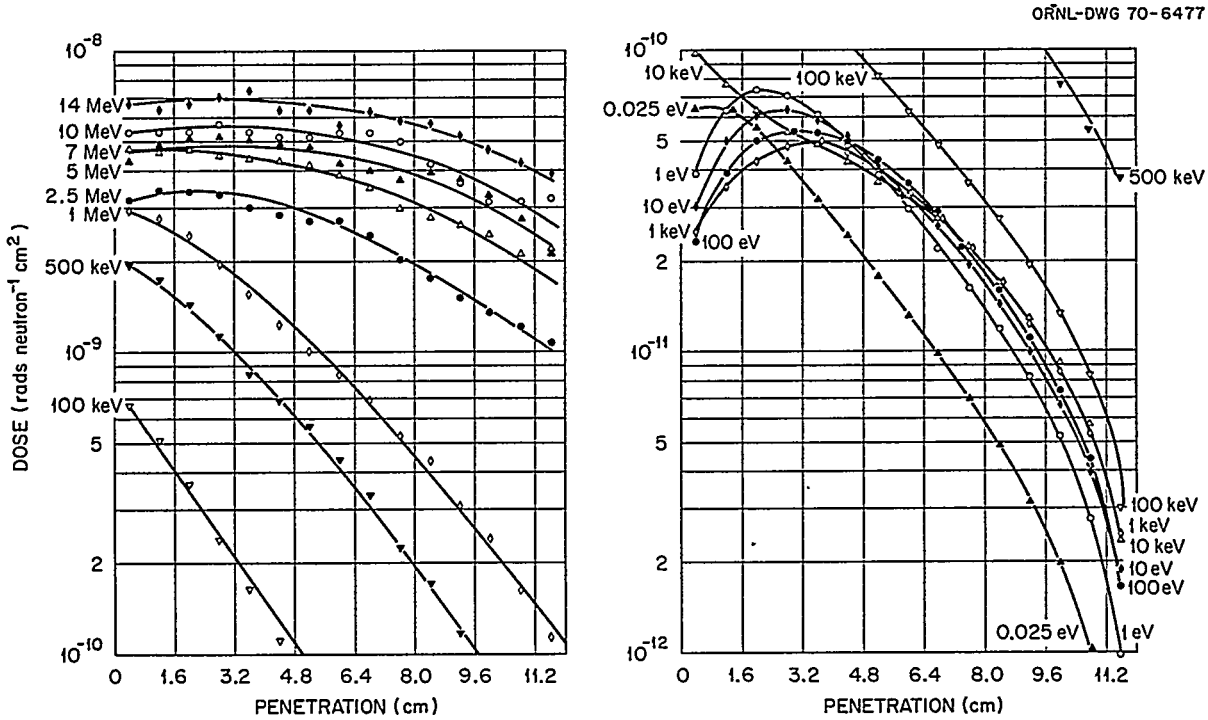

Fig. 14.12. Dose from Recoil Ions as a Function of Penetration Depth in a Rabbit-Sized Phantom (Radius = 6 cm, Height = 31 cm).

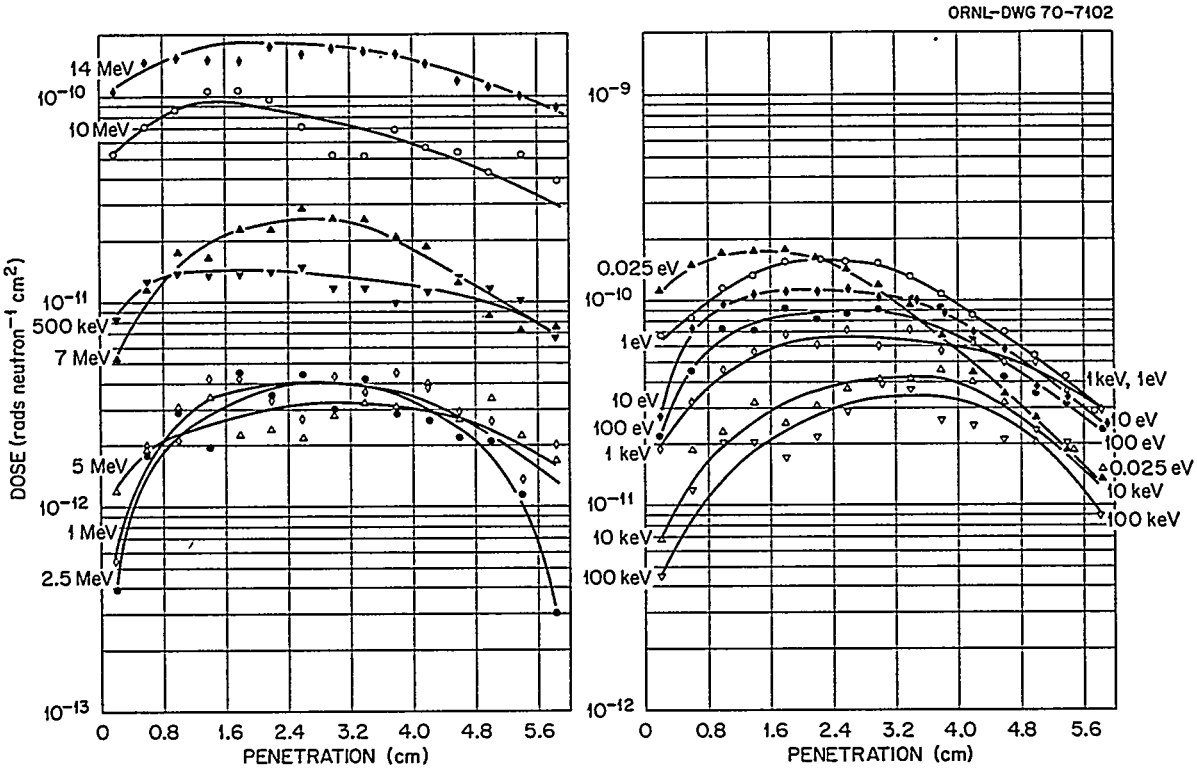

Fig. 14.13. Dose from Neutron-Produced Gamma Rays as a Function of Penetration Depth in a Rat-Sized Phantom (Radius = 3 cm, Height = 13 cm).

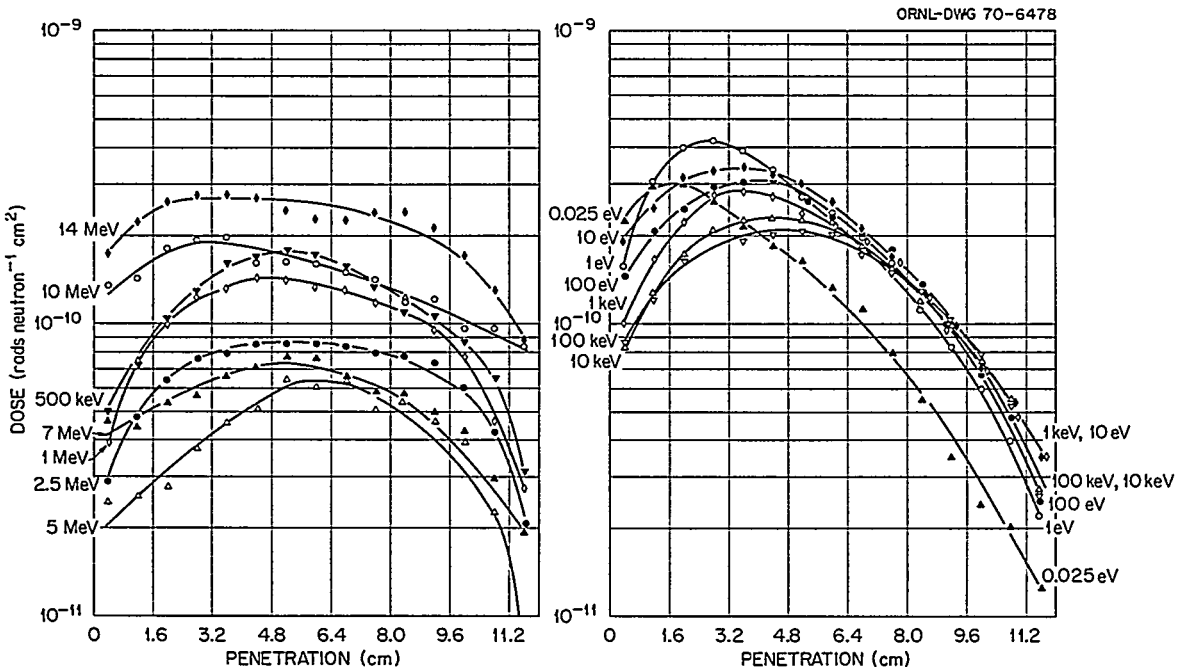

Fig. 14.14. Dose from Neutron-Produced Gamma Rays as a Function of Penetration Depth in a Rabbit-Sized Phantom (Radius = 6 cm, Height = 31 cm).

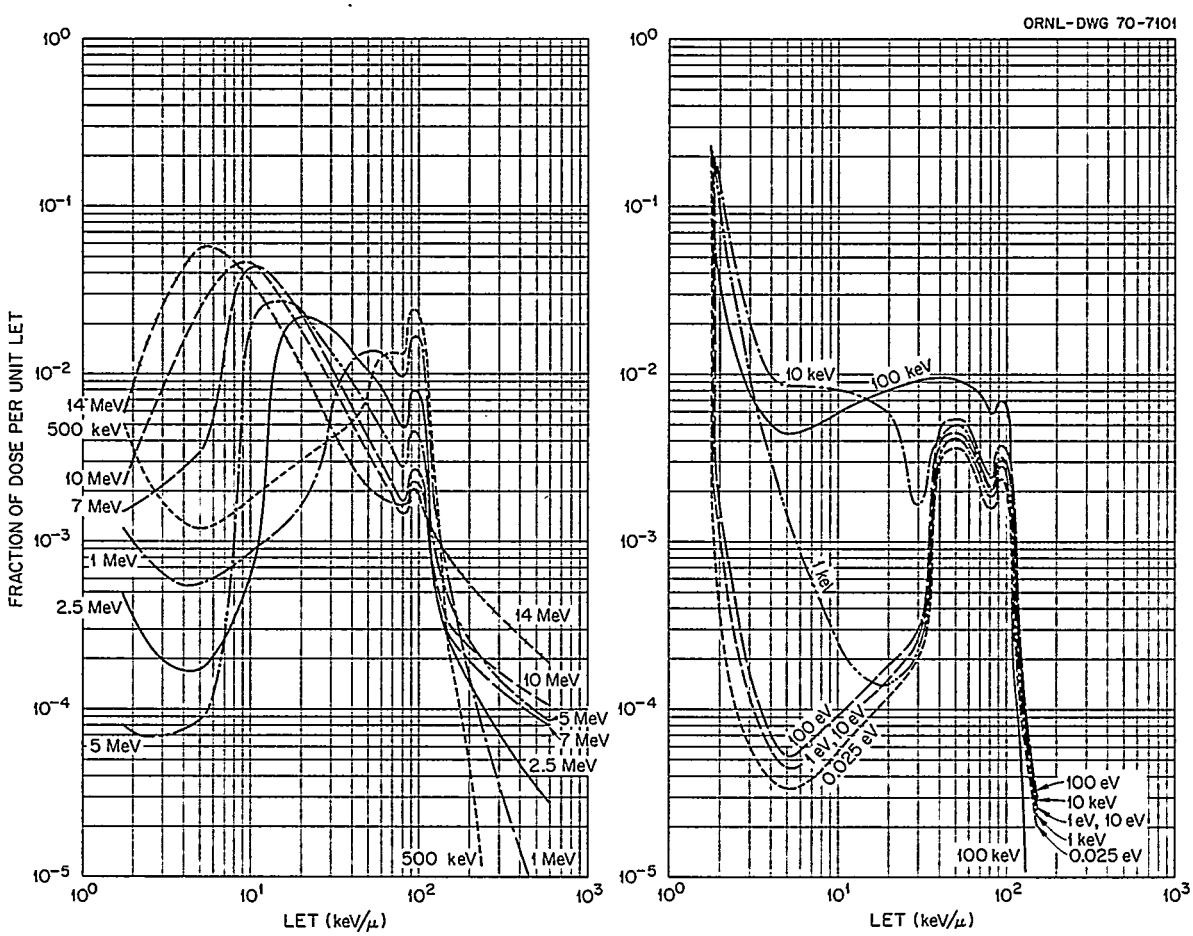

Fig. 14.15. Fraction of Dose per Unit LET at the Midpoint of a Rat-Sized Phantom (Radius = 3 cm, Height = 13 cm).

The dose as a function of LET is shown in Figs. 14.20 and 14.21 for the broad and limited beams, respectively, for volume elements at the front, center, and rear of the phantom. For the broad-beam case, the increasingly deep dip at 5 keV/μ with increasing depth in the phantom is due to the decreasing number of higher-energy protons (i.e., those whose energy is high enough to provide LET in the range of 5 to 10 keV/μ). The contribution of electrons from gamma rays produced by (n,γ) reactions, primarily $^1H(n,\gamma)^2H$, increases with increasing depth, hence the increase in dose in the LET interval below 5 keV/μ. The distribution in LET of the protons ranges from less than 10 to nearly 100 keV/μ; this proton continuum does not vary much, percentagewise, with depth, so there is little difference in the curves between 10 and 80 keV/μ. The peak of the Bragg curve for protons produces the well-defined peak at about 95 keV/μ. As all protons having an energy of ~80 keV or greater lose energy in this region, the peak is more pronounced where the spectrum is softened at greater depths. At both ends of the distributions, the curves shown were drawn to the average LET value obtained in the energy increment (i.e., 0 to 3.5 keV/μ on the low end and 200 to 1000

Table 14.2. Contributions from Individual Reactions to Average Dose in a Whole Anthropomorphic Phantom (^{252}Cf Source)

Reaction	Photon Energy (MeV)	Broad Beam[a]	Collimated Beam[a]
$H(n,n)H$		11.4294	0.14129
$C(n,n)C$		0.4318	0.00569
$N(n,n)N$		0.0257	0.00030
$O(n,n)O$		0.6361	0.00785
$C(n,n')^*C$; $^*C \rightarrow C + \gamma_1$	1.75	0.0008	0.00001
$C(n,n')^*C$; $^*C \rightarrow C + \gamma_2$	4.43	0.0389	0.00052
$C(n,n')^*C$; $^*C \rightarrow C + \gamma_3$	6.8	0.0006	
$N(n,n')^*N$; $^*N \rightarrow N + \gamma_1$	1.63	0.0001	
$N(n,n')^*N$; $^*N \rightarrow N + \gamma_2$	2.31	0.0005	0.00001
$N(n,n')^*N$; $^*N \rightarrow N + \gamma_3$	5.1	0.0006	0.00001
$N(n,n')^*N$; $^*N \rightarrow N + \gamma_4$	10.0		
$N(n,n')^*N$; $^*N \rightarrow N + \gamma_5$	11.0		
$O(n,n')^*O$; $^*O \rightarrow O + \gamma_1$	6.1	0.0239	0.00033
$O(n,n')^*O$; $^*O \rightarrow O + \gamma_2$	7.12	0.0069	0.00005
$O(n,n')^*O$; $^*O \rightarrow O + \gamma_3$	3.8	0.0025	0.00005
$O(n,n')^*O$; $^*O \rightarrow O + \gamma_4$	4.8	0.0002	
$C(n,\alpha_2)^*Be$; $^*Be \rightarrow Be + n$; $Be \rightarrow 2\alpha$		0.0007	
$C(n,n')^*C$; $^*C \rightarrow Be + \alpha$		0.0012	0.00001
$N(n,2n)N$			
$H^1(n,\gamma)H^2$	2.2	1.8933	0.02923
$C(n,\alpha_0)Be$		0.0030	0.00004
$N(n,\alpha_0)B$		0.0238	0.00028
$O(n,\alpha_0)C$		0.0707	0.00086
$C(n,\alpha_1)^*Be$; $^*Be \rightarrow Be + \gamma$	1.75	0.0002	
$N(n,\alpha_1)^*B$; $^*B \rightarrow B + \gamma_1$	2.1	0.0002	
$N(n,\alpha_2)^*B$; $^*B \rightarrow B + \gamma_2$	4.5	0.0005	
$N(n,\alpha_3)^*B$; $^*B \rightarrow B + \gamma_3$	5.0	0.0006	0.00001
$O(n,\alpha_1)^*C$; $^*C \rightarrow C + \gamma_1$	3.1	0.0041	0.00004
$O(n,\alpha_2)^*C$; $^*C \rightarrow C + \gamma_2$	3.8	0.0052	0.00007
$O(n,\alpha_3)^*C$; $^*C \rightarrow C + \gamma_3$	7.0	0.0006	
$N(n,p)^*C$		0.1221	0.00240
$O(n,p)^*N$; $^*N \rightarrow N + \gamma$	6.1	0.0003	
$N(n,t)C$		0.0007	0.00001
Total dose		14.7252	0.18906

[a]In units of 10^{-10} rad neutron^{-1} cm^2.

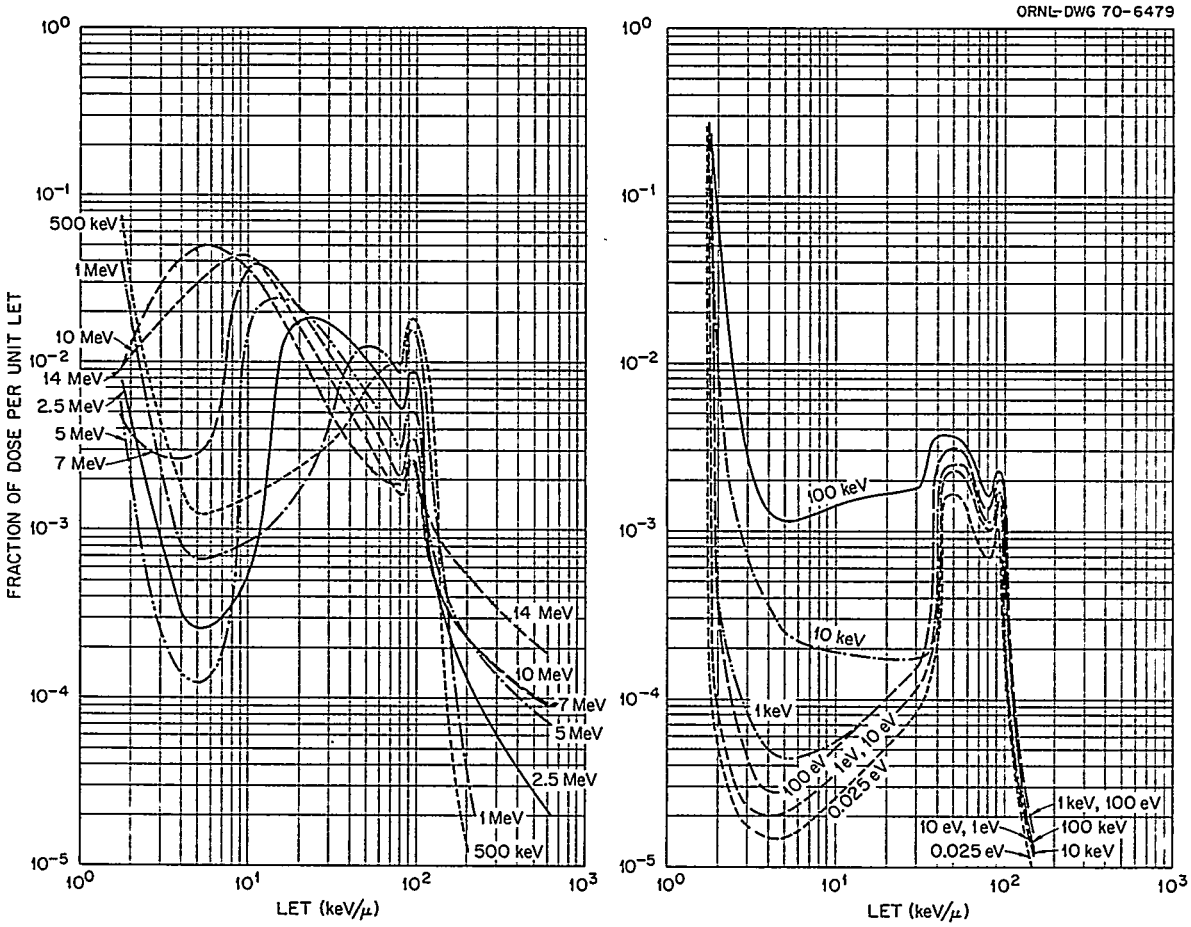

Fig. 14.16. Fraction of Dose per Unit LET at the Midpoint of a Rabbit-Sized Phantom (Radius = 6 cm, Height = 31 cm).

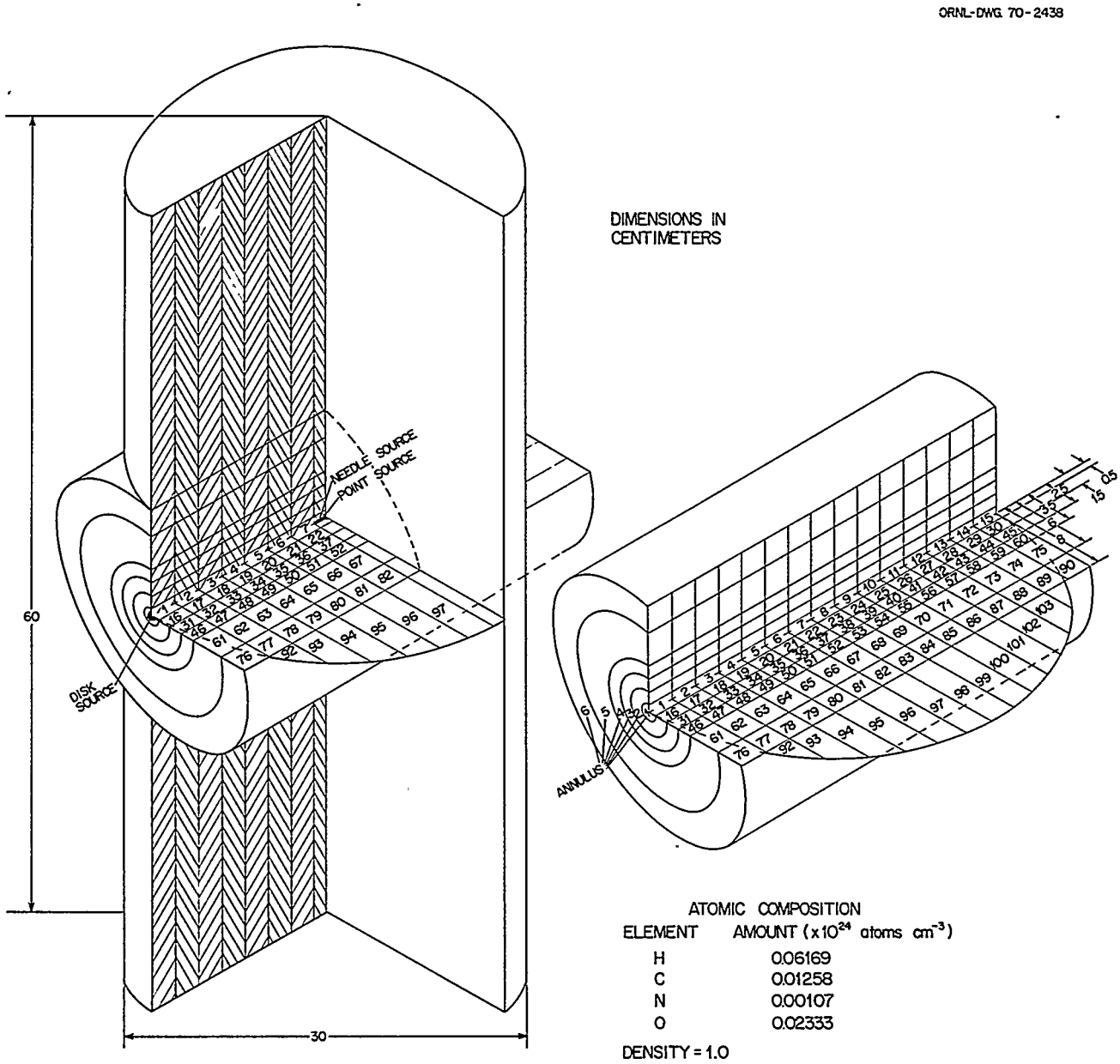

Fig. 14.17. Phantom Used to Study Dose and LET Distributions from Therapeutic Sources of ^{252}Cf.

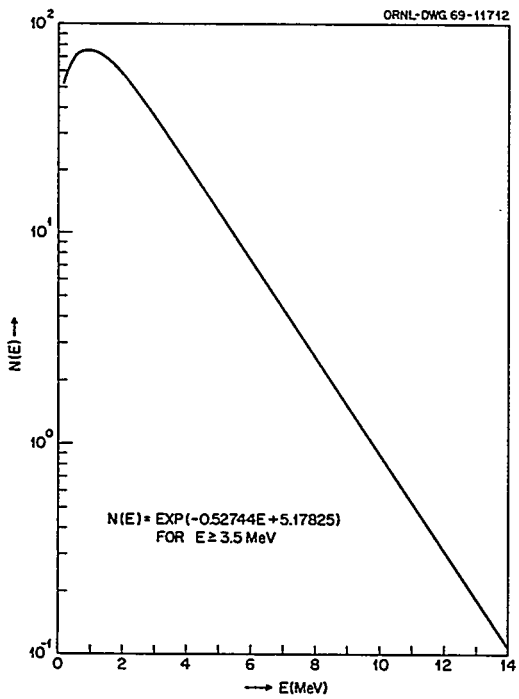

Fig. 14.18. Energy Spectrum from a ^{252}Cf Spontaneous Fission Source (Based on Hyde's Curve).

keV/μ on the high end). Although there is not much point in attempting additional manipulation of the data in this case, the procedure does perturb the shape of the curves in these areas due to the width of the interval. In addition, the high-LET portion of the curve, produced by ions heavier than hydrogen, is subject to greater statistical uncertainty, and consequently the curve for high-LET ions at the back of the phantom is unexpectedly high (i.e., it crosses the curve representative of the front of the phantom). However, the general trends are clear, and the accuracy is sufficient for general application. Similar observations apply to the collimated beam. For points at increasingly greater depths in the phantom and increasingly greater distances from the beam, the relative importance of the 0-to-3.5-keV/μ increment increases, but that for 200 to 1000 keV/μ decreases.

In therapeutics, ^{252}Cf source configurations of widespread interest are (1) internal sources concentrated at a point, emitting neutrons isotropically, (2) internal sources having the shapes of line segments corresponding to implanted needle sources of about 2 cm length (treated as a series of point sources), and (3) a small disk (0.25 cm radius) of ^{252}Cf located on the surface

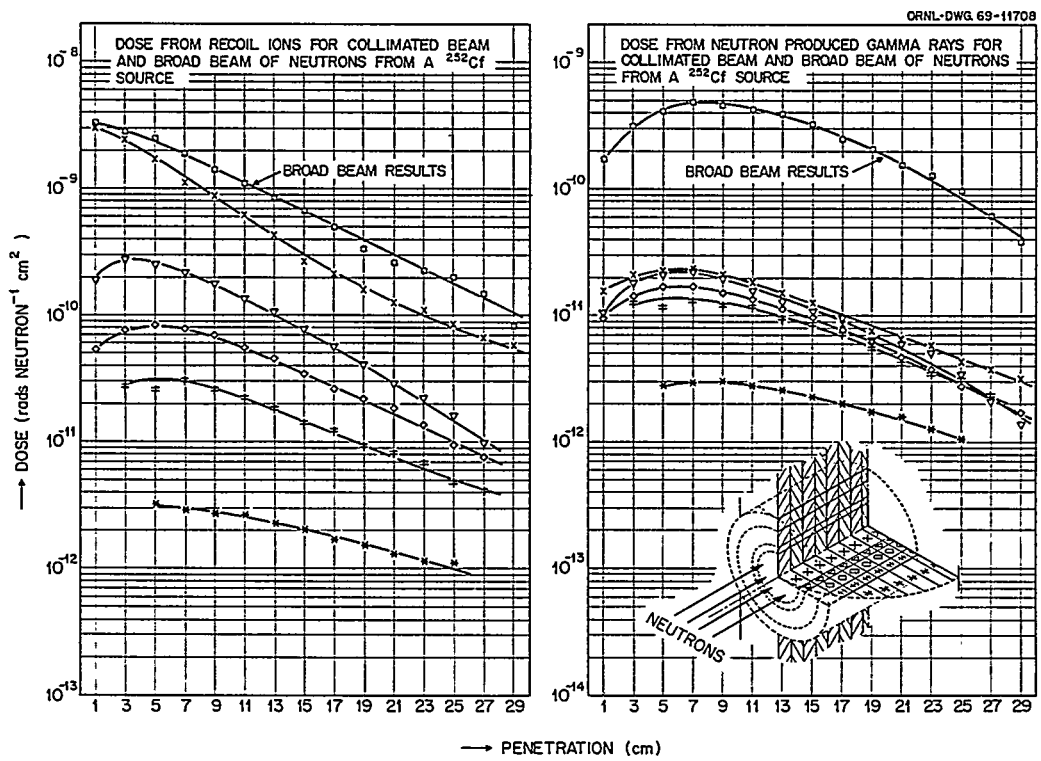

Fig. 14.19. Dose from Recoil Ions for Collimated Beam and Broad Beam of Neutrons from a ^{252}Cf Source and Dose from Neutron-Produced Gamma Rays for Collimated Beam and Broad Beam of Neutrons from a ^{252}Cf Source.

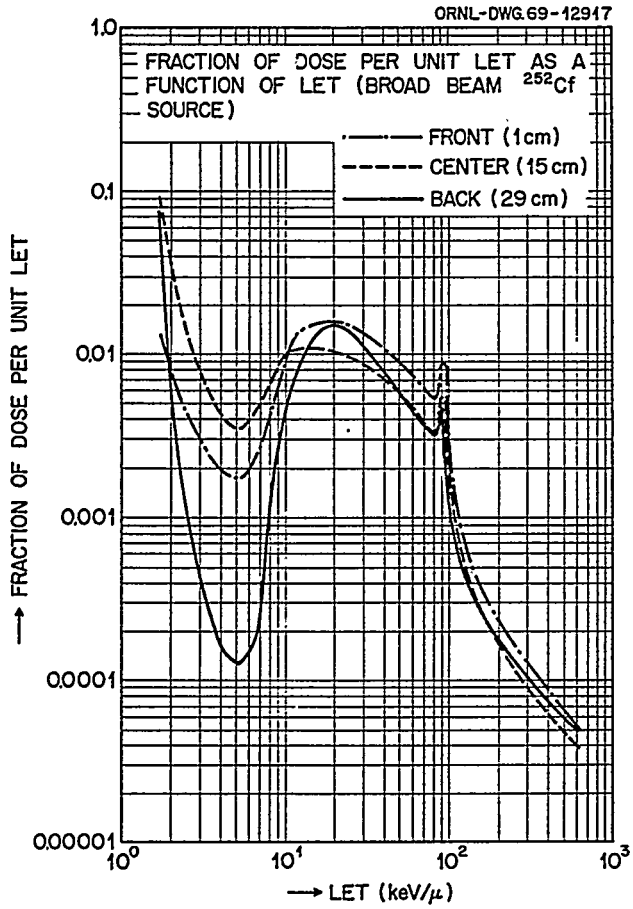

Fig. 14.20. Fraction of Dose per Unit LET as a Function of LET (Broad-Beam ^{252}Cf Source).

of a human torso.[13] The locations of these sources as used in these calculations are also shown in Fig. 14.18. Self-absorption by the source of neutrons is assumed to be negligible, and these calculations do not include gamma rays emanating from the source. Alpha and beta particles are absorbed in the source for all known encapsulating techniques that could be used in therapy. Distributions of dose equivalent were computed also, but as they are of interest to relatively few users of therapeutic sources, they are not included.

For the first two sources, calculational results were normalized to the total number of neutrons emitted, whereas for the disk, the results were normalized to the number of neutrons emitted in half space because the region of interest is approximately the 2π solid angle subtended by the phantom.

Figures 14.22 and 14.23 show dose contributions from recoil ions as functions of depth for the point and needle implanted sources. It is interesting to note that the dose values in the volume elements containing the two sources differ by about 15%, while variations in all other elements were less than the statistical uncertainty in the calculations. These source-containing volume elements were cylindrical and had a radius of 0.5 cm and a height of 2 cm. The difference in average dose in these source-containing volume elements is attributed to the fact that more neutrons from the point source have their first collision inside the source-containing element than do those from the needle source.

An equation of the form $D = \exp(A + BX + CX^2)$ was assumed to be compatible with the data, and least-squares solutions of the coefficients A, B, and C were obtained for each of the three basic therapeutic sources. In this equation, X is the distance of the centroid of the area element shown in Fig. 14.17 from the geometrical center of the source. It must be kept in mind that these equations are to be used only for X between 1 and 14 cm and most certainly will break down elsewhere.

Figure 14.24 shows dose as a function of perpendicular distance from three nonsimultaneous needle implanted sources. The results are all shown on this figure for comparison. From these results it is evident that the depth of the needle oriented normal to the surface does not significantly affect the distribution of dose in the surrounding tissue, so that the equations derived for the needle implanted source at the center of the phantom may also be used to predict dose values near an interface.

For the neutron-produced gamma rays, it was impossible to distinguish between the results for the two internal sources, and only one is included here (Fig. 14.25). These gamma dose distributions do not include those gamma rays originating in the source.

With these distributions given in functional form, it is easy to predict dose to a volume of interest from any configuration of implanted sources by either simple addition of evaluated results if the volume is quite small or by integration over the volume if it is large with respect to changes in the distribution functions. The absorbed dose from recoil ions for the disk source is shown in Fig. 14.26. As might be expected because of higher escape probabilities for the scattered neutrons, D falls off much more rapidly than for the internal sources, demonstrating the need to use these data for skin application and those for the point and line source

[13] T. D. Jones and J. A. Auxier, "Absorbed Dose and Linear Energy Transfer Distributions from Therapeutic Sources of ^{252}Cf," *Phys. Med. Biol.* (to be published).

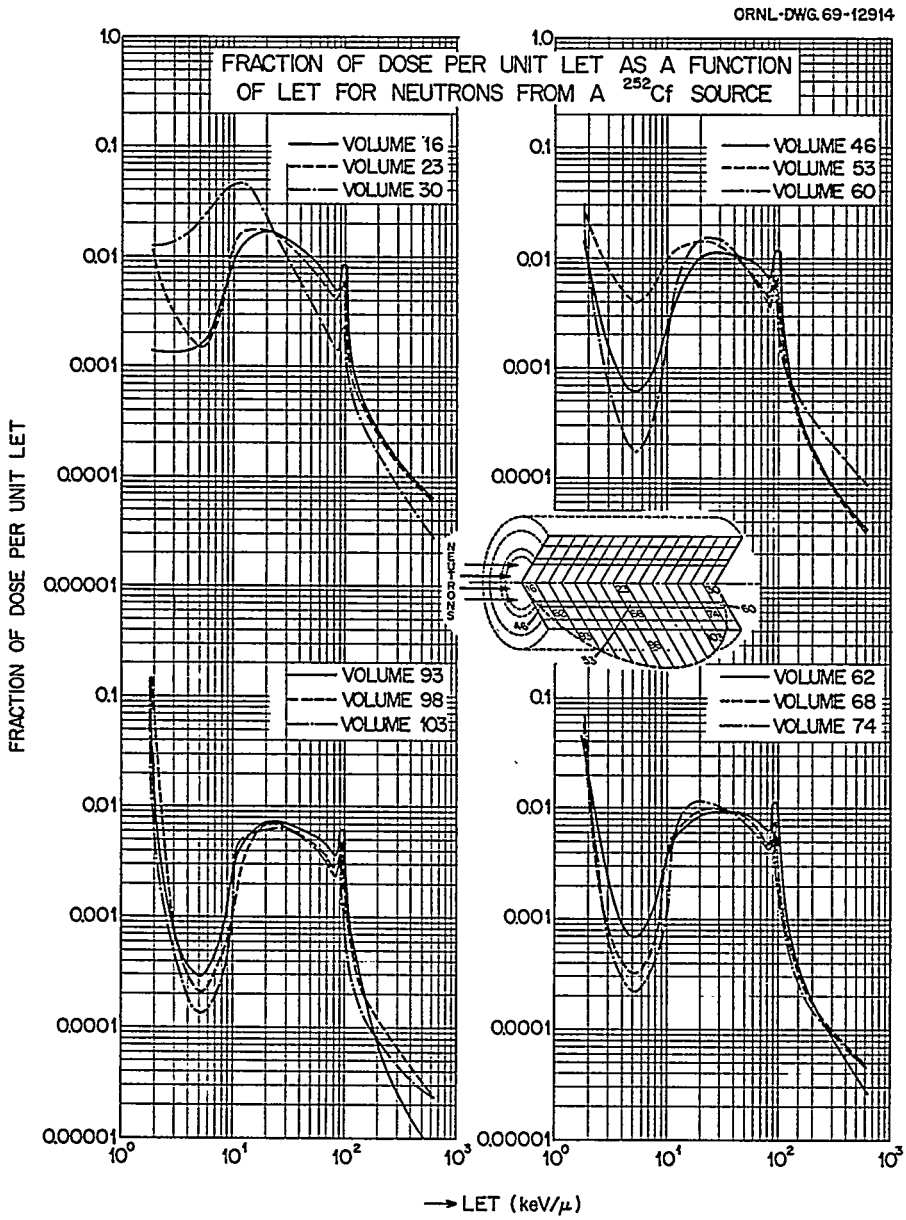

Fig. 14.21. Fraction of Dose per Unit LET as a Function of LET for Neutrons from a ^{252}Cf Source.

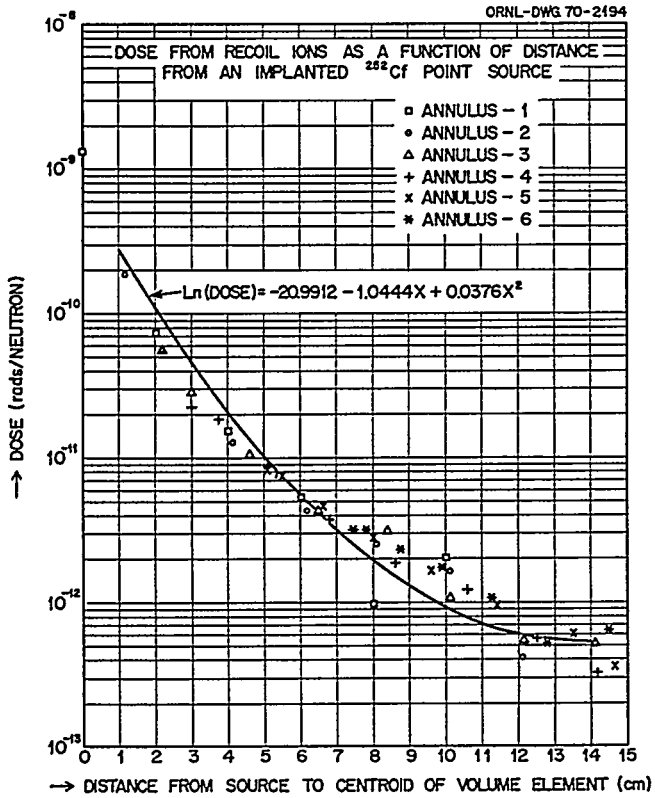

Fig. 14.22. Dose from Recoil Ions as a Function of Distance from an Implanted ^{252}Cf Point Source.

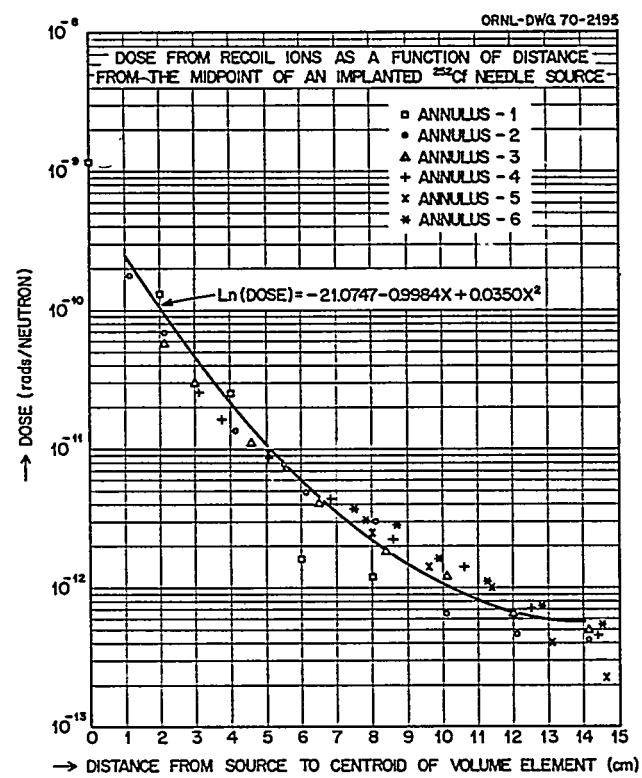

Fig. 14.23. Dose from Recoil Ions as a Function of Distance from the Midpoint of an Implanted ^{252}Cf Needle Source.

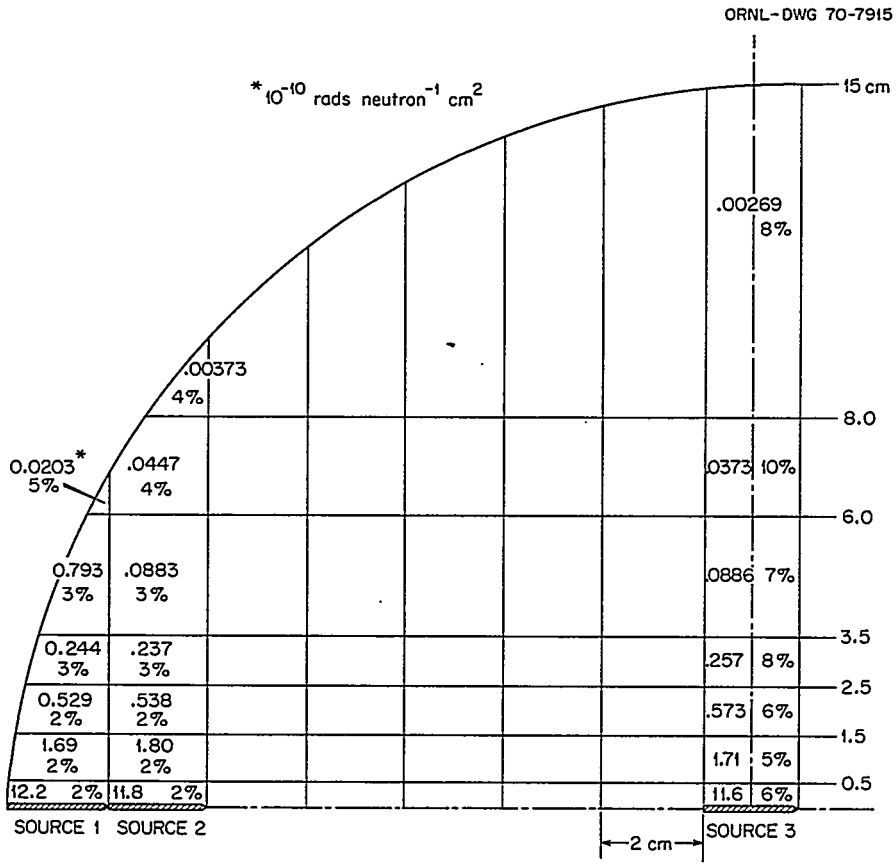

Fig. 14.24. Dose as a Function of Perpendicular Distance from a ^{252}Cf Needle. Three nonsimultaneous implants shown.

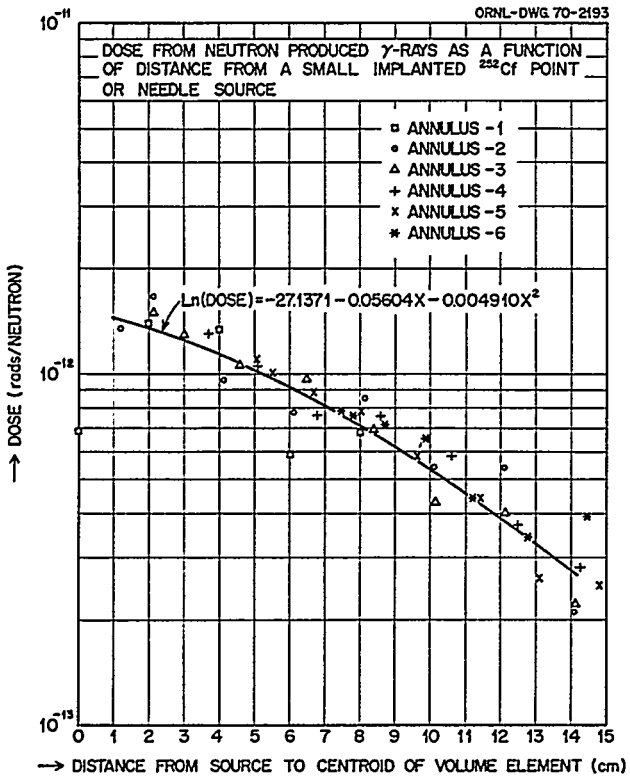

14.25. Dose from Neutron-Produced Gamma Rays as a Function of Distance from a Small Implanted ^{252}Cf Point or Needle Source.

for deep implants. Figure 14.27 shows the dose from neutron-produced gamma rays for the disk source; it is lower and it also falls more rapidly than do those for the internal sources.

Figures 14.28 and 14.29 give the fraction of dose as a function of LET and are indicative of the radiation quality at the given locations. Again, the difference between the point and needle sources was negligible except for the source-containing volume elements. At low values of LET (less than 10 keV/μ), a slight difference was noted, but the two curves converged at higher values of LET. The difference is shown graphically in Fig. 14.28. Figure 14.29 shows the wide variation in the LET spectra for selected volume elements exposed to radiation from the disk source.

The statistical uncertainties were, of course, dependent on the source configuration, the distance from the source to the volume element under consideration, and the type of radiation. For the recoil ion dose from the point and needle sources, the volume elements near the source were small, so that one standard deviation, σ, was in the range of 3 to 10% of the dose. For the most distant volume elements (i.e., up to 14 cm), σ remained less than 10% of the dose except for the smaller volume elements (e.g., 8, 16, and 24), wherein the uncertainty was as great as ±50% of the dose. Similar conditions held for the disk source except that at the distant volume elements (28 cm), σ was approximately ±20% of the dose for the large elements and ±100% of the dose for the smallest elements.

Statistical uncertainties for the neutron-produced gamma-ray dose were of a different pattern. Because the gamma-ray production increased with distance for several centimeters, σ varied from about ±15% of the dose close to the source to about ±2% of the dose for the larger volume elements at 14 to 28 cm; at 14 cm distance, σ for the smallest volume elements was about ±25% of the dose. Due to the number of points used, the uncertainties in the fitted curves are small and are dependent primarily on the form of the equation fitted to them.

The distributions presented should be of assistance in programming therapeutic exposures to the neutrons from the spontaneous fission of ^{252}Cf. The accuracy of the distributions of D and LET is more than adequate for such purposes. A more complex array of point and/or needle sources can be used and the dose distributions from each point or line source summed to obtain the total dose in any volume element of interest up to 14 cm from the source array.

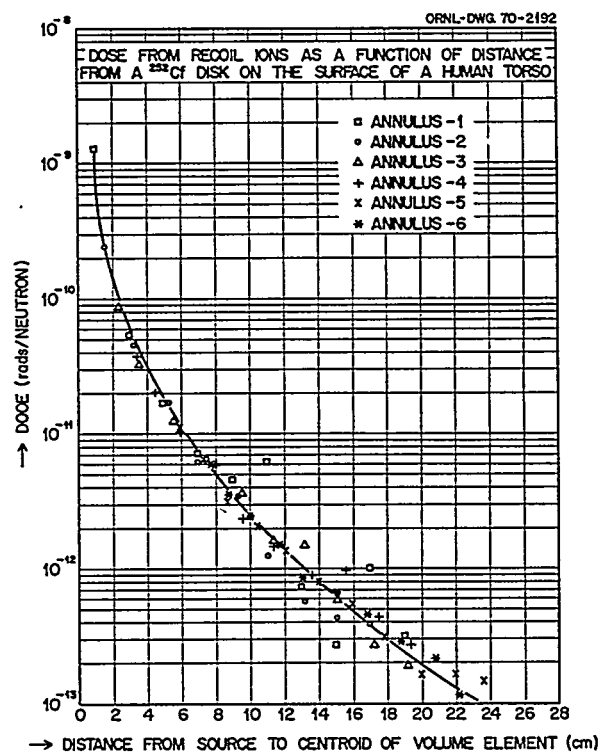

Fig. 14.26. Dose from Recoil Ions as a Function of Distance from a ^{252}Cf Disk on the Surface of a Human Torso.

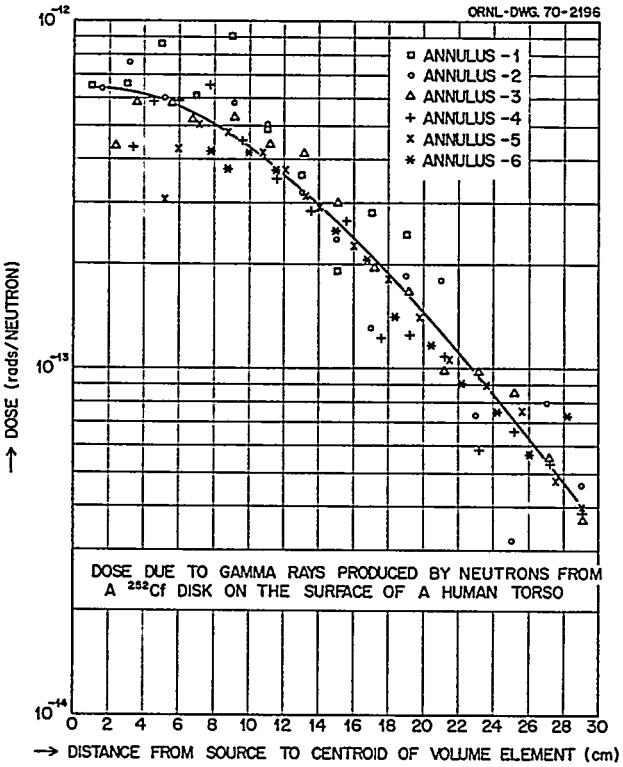

Fig. 14.27. Dose Due to Gamma Rays Produced by Neutrons from a ^{252}Cf Disk on the Surface of a Human Torso.

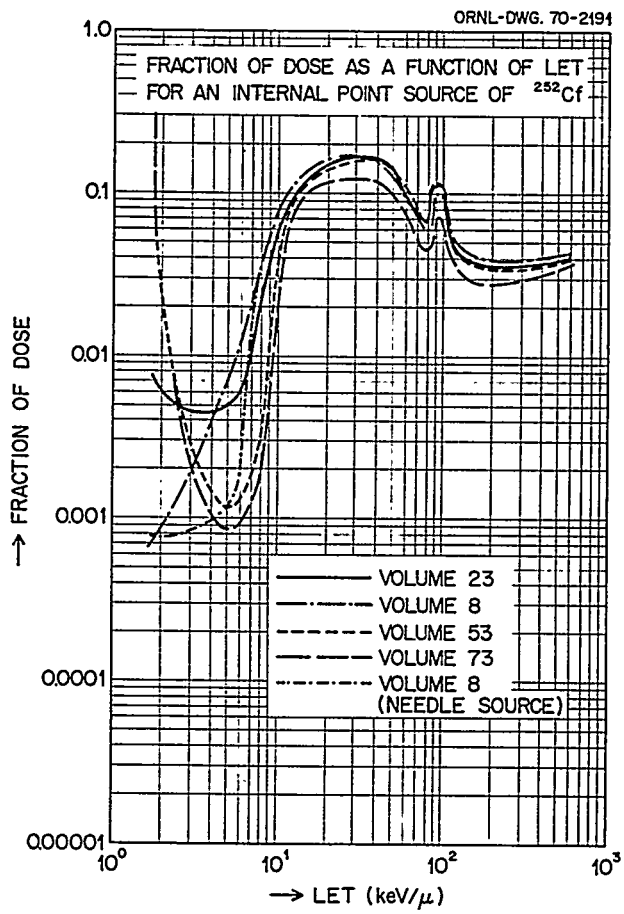

Fig. 14.28. Fraction of Dose per Unit LET as a Function of LET for an Internal Point or Needle Source of ^{252}Cf.

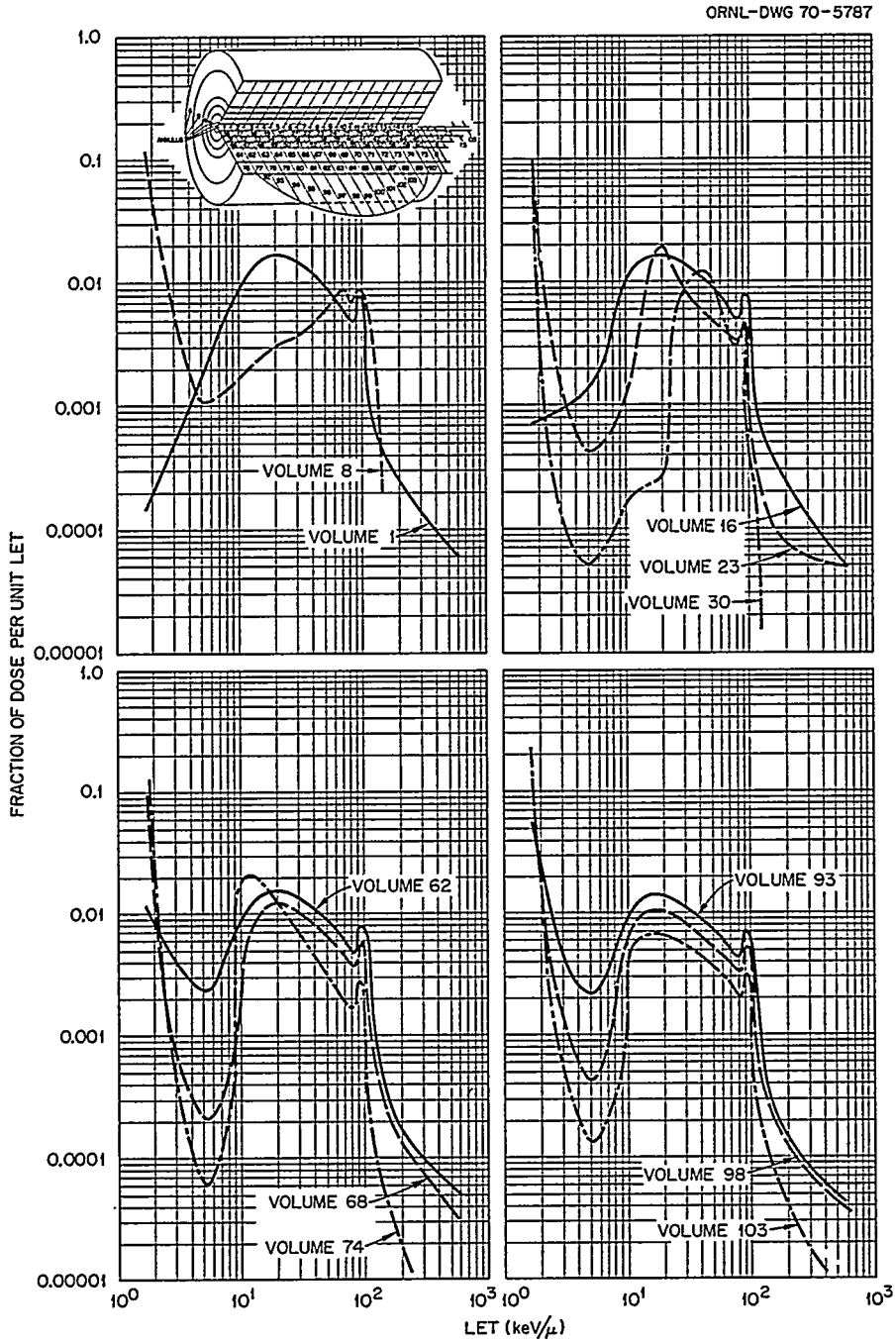

Fig. 14.29. Fraction of Dose per Unit LET as a Function of LET for a Disk of ^{252}Cf on the Surface.

15. Spectrometry Research and Development

J. W. Poston J. H. Thorngate[1]
M. D. Brown[2]
K. W. Crase[3]
P. T. Perdue
D. R. Stone[4]
Z. G. Burson[5]

AN EXTRAPOLATION CHAMBER FOR THE MEASUREMENT OF DOSE DISTRIBUTIONS AT BONE-TISSUE INTERFACES

A detector has been designed and fabricated which facilitates the measurement of dose distributions at bone-tissue interfaces at depth in a tissue-equivalent phantom. The detector relies upon the extrapolation ionization chamber principle suggested by Failla.[6] Basically, the chamber is a right circular cylinder 4.92 cm in diameter. The height of the cylinder is adjustable from about 6 to 12 cm. (See Fig. 15.1 for an exploded view of the chamber.) The sensitive volume is defined by two parallel plates with gap spacing adjustable from 0.05 to 2.54 cm. The outer ring and the body of the chamber are joined through precision threads (15.75 threads per centimeter) and allow accurate adjustment (±1%) of the gap spacing over its full range.

The detector features a guard ring around the collecting electrode, each of which is an integral part of the body of the detector. However, the collecting electrode is insulated from the guard ring and the body of the detector by 0.0178 cm of Teflon. Electrical and gas-flow connections to the collecting electrode are made through a conducting glue to the underside of the electrode. The high-voltage electrode is attached to, but insulated from, the movable ring. The electrical connection is also made to the top of the thin electrode with a conducting glue.

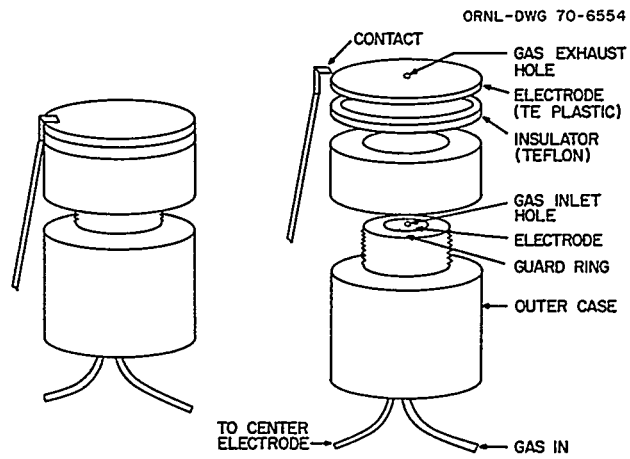

Fig. 15.1. Sketch of Extrapolation Chamber.

Six of these chambers have been fabricated, three from A-150 tissue-equivalent plastic and three from B-100 bone-equivalent plastic.[7] In each group, collecting electrodes of three different areas (1, 2, and 4 cm) are available.

Saturation characteristics have been determined over the expected range of electrode gap spacings. Figure 15.2 shows a typical set of saturation curves in the range of spacings 0.465 to 0.147 cm. These curves were "fitted" to straight lines above the applied voltage of

[1] Leave of absence.

[2] Part-time.

[3] AEC Predoctoral Fellowship.

[4] Present address: Chattanooga State Technical Institute, 4501 Amnicola Highway, Chattanooga, Tenn.

[5] E.G.&G., Las Vegas, Nev.

[6] G. Failla, "The Measurement of Tissue Dose in Terms of the Same Unit for All Ionizing Radiations," *Radiology* 29, 202–15 (1937).

[7] From Dr. F. R. Shonka, St. Procopius College, Lisle, Ill.

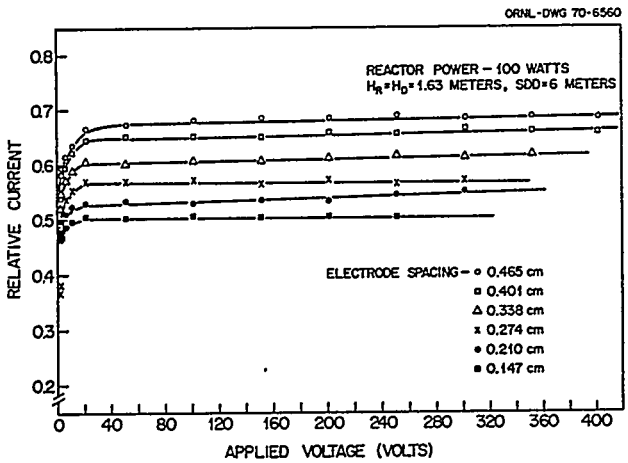

Fig. 15.2. Saturation Curves – 4-cm^2 TETE Chamber.

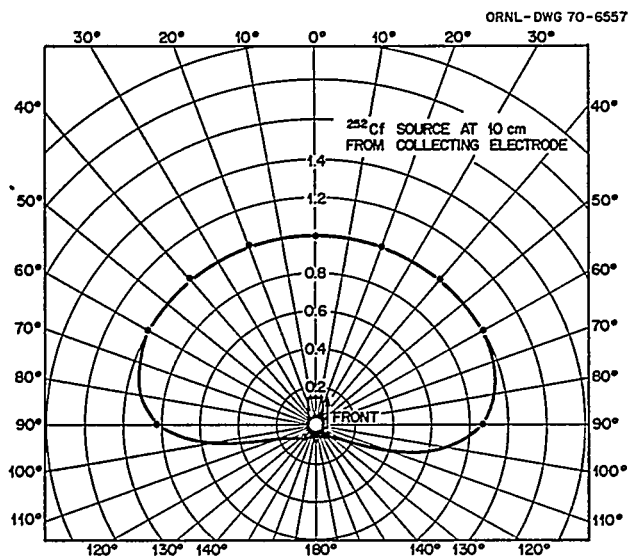

Fig. 15.3. Directional Response of 2-cm^2 TE Chamber.

+50 V. On the basis of these results, an operating voltage of +100 V was selected for this chamber for all gap spacings.

The directional response of a typical detector is shown in Fig. 15.3. The electrode spacing was 0.6 cm and the operating voltage was +300 V. The source of neutrons was ^{252}Cf located at 10 cm from the collecting electrode.

DOSE DISTRIBUTIONS AT BONE-TISSUE INTERFACES

Small extrapolation ionization chambers have been utilized to measure the distribution of dose across bone-tissue interfaces at depth in a tissue-equivalent phantom. Measurements have been completed in a phantom exposed to the leakage spectrum of the HPRR. The experiment arrangement (Fig. 15.4) consists of a standard cubical phantom[8] filled with tissue-equivalent liquid[9] and located at 6.0 m from the reactor. A Lucite tube, 5 cm in inside diameter with 0.635-cm-thick walls, is located along the center line of the phantom. This tube, which passes through the two parallel faces of the phantom, allows the movement of the ionization chambers through the phantom while isolating the detector from the liquid. Space in the tube not occupied by the detector is filled with tissue-equivalent material.

For the reactor exposures the ionization chamber was positioned remotely through the use of a positioning device. The position of the detector was noted by observing the experiment through closed-circuit television. Measurements were made in 5-cm steps from 5 cm behind the front face to 5 cm in front of the rear face of the phantom. These correspond to depths in the phantom of 5, 10, 20, and 25 cm.

Ionization current from the detector is measured through a semiautomatic electrometer (model Q-2102) designed and built at ORNL. This instrument is intended for use in measuring ionization currents at large distances (up to 500 m) from the detector unit. The electrometer features a matched pair of electrometer tubes (CK 5886), one located in a unit near the ionization chamber and a reference tube located at the instrument readout. Ionization in the detector produces a dc voltage at the grid of the remote electrometer tube. This results in a change in potential of the grid of one side of a cathode follower tube (6201) which is directly coupled to the anode of both the remote electrometer tube and the reference electrometer tube. The change induces an unbalance in the galvanometer circuit of a Brown recorder-amplifier. The balance motor in the Brown recorder serves as a mechanical feedback system acting through a precision voltage source to null the ionization current. The instrument features the ability to select remotely from a series of precision high-megohm resistors (located in the remote unit) for use in the feedback circuit. Thus the recorder deflection indicates the magnitude of the ionization current produced in the chamber.

---

[8] "Clinical Dosimetry," *Natl. Bur. Std. (U.S.) Handbook* 87, U.S. Department of Commerce, 1963.

[9] H. H. Rossi and G. Failla, "Tissue-Equivalent Ionization Chambers," *Nucleonics* 14, 32–37 (1956).

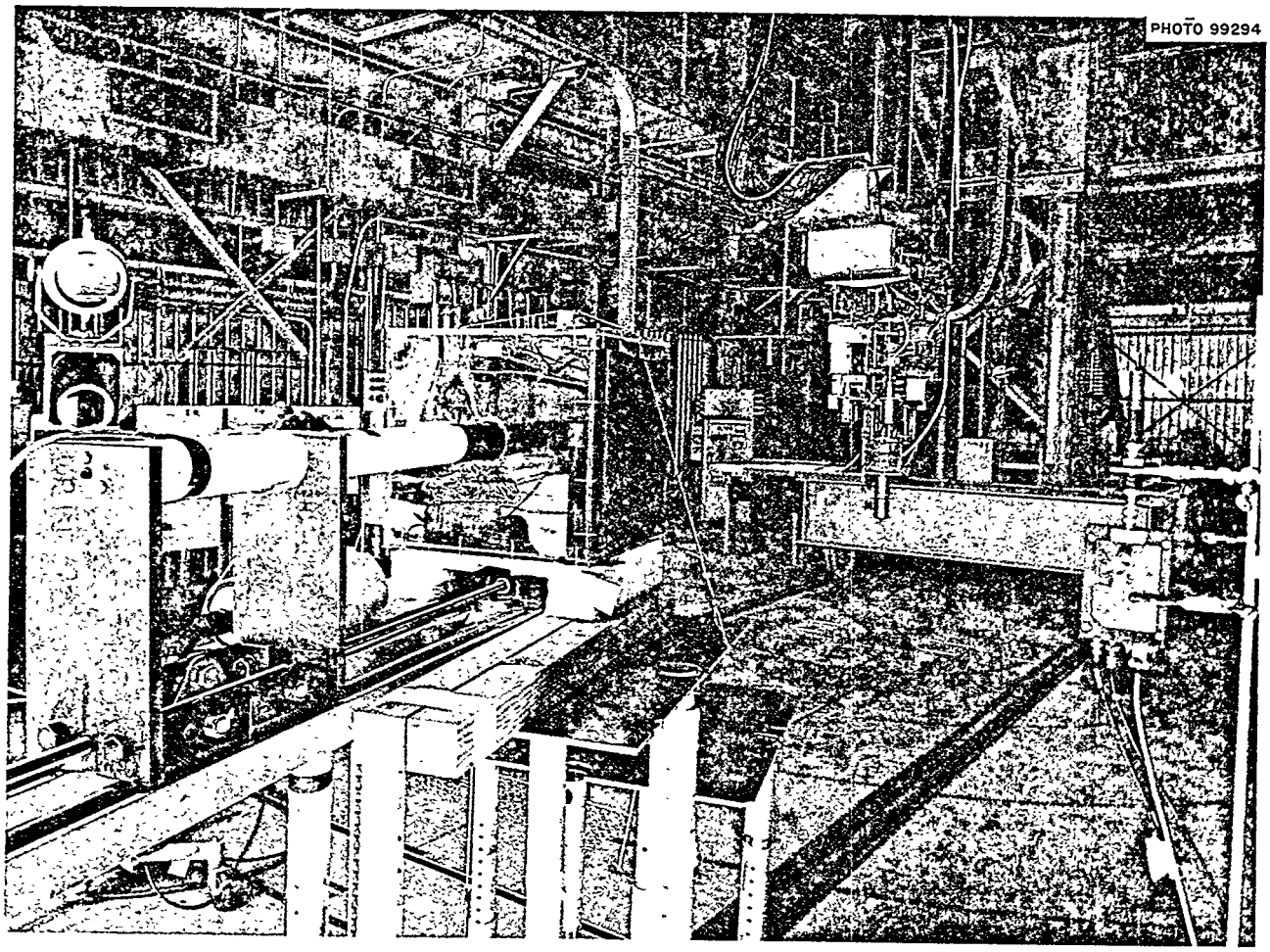

Fig. 15.4. View of the Experimental Arrangement Showing Phantom, Remote Positioner, Reactor, and Normalization Channel.

Measurements completed include: (1) measurement of dose distributions in bone-equivalent material as a function of distance from a bone-tissue interface and (2) measurement of dose distributions in tissue-equivalent material as a function of distance from a bone-tissue interface. The results of these measurements are shown in Figs. 15.5–15.9. As expected, the dose distribution shows an increase with increasing depth in tissue to the approximate equilibrium depth for neutrons in tissue. At this point, an equilibrium condition is reached. This distribution is the sum of both neutron and gamma-ray distributions at the interface. No attempt has been made to separate the individual components of the distribution. Such measurements, as well as measurements in bone-equivalent material, are under way and will be reported at a later date.

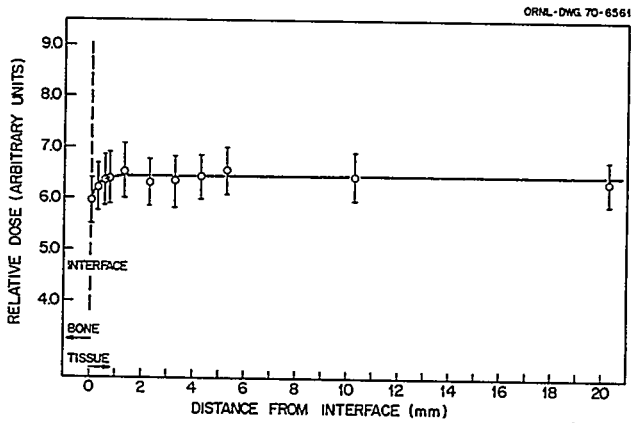

Fig. 15.5. Distribution of Dose at Bone-Tissue Interface. Fission neutrons from HPRR. Interface – 5 cm in tissue equivalent phantom.

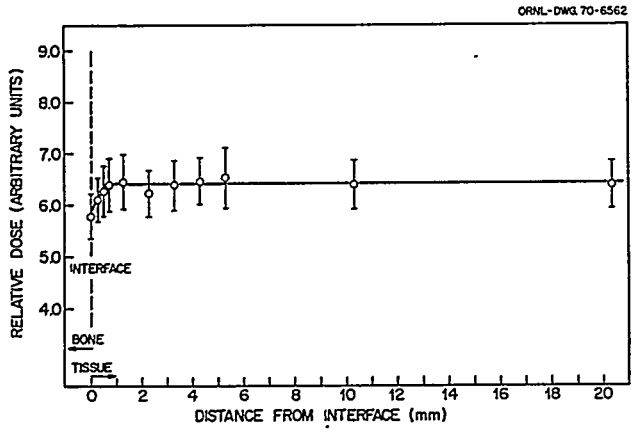

Fig. 15.6. Distribution of Dose at Bone-Tissue Interface. Fission neutrons from HPRR. Interface – 10 cm in tissue equivalent phantom.

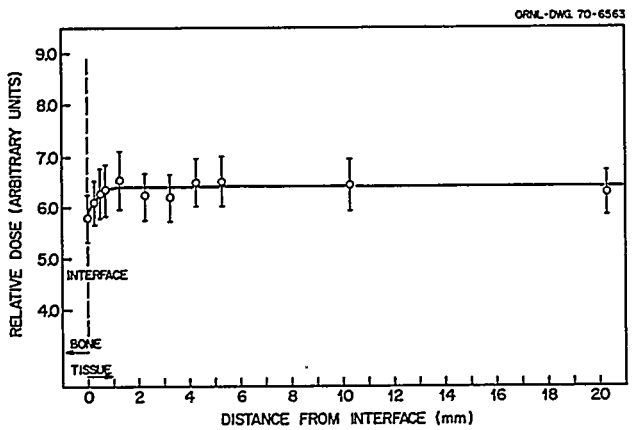

Fig. 15.7. Distribution of Dose at Bone-Tissue Interface. Fission neutrons from HPRR. Interface – 15 cm in tissue equivalent phantom.

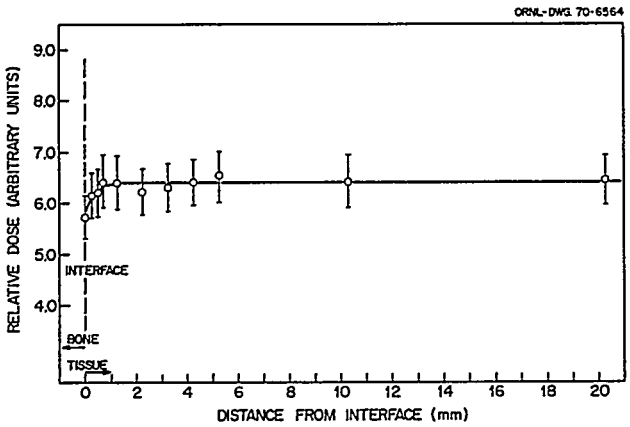

Fig. 15.8. Distribution of Dose at Bone-Tissue Interface. Fission neutrons from HPRR. Interface – 20 cm in tissue equivalent phantom.

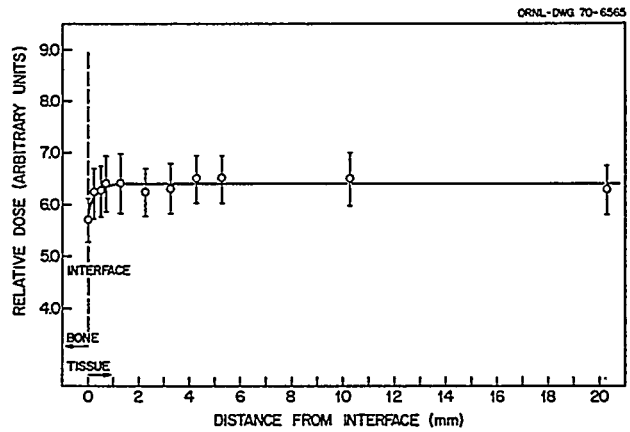

Fig. 15.9. Distribution of Dose at Bone-Tissue Interface. Fission neutrons from HPRR. Interface – 25 cm in tissue equivalent phantom.

PURIFICATION OF SULFUR BY ZONE REFINING

In conjunction with work related to the purification of organic scintillators, the same procedure has been extended to the purification of sulfur, which is used in the dosimetry program to detect high-energy neutrons. This purification process is carried out by means of zone refining, wherein a liquid zone is passed slowly through a solid cylindrical tube of sulfur approximately 70 cm long. The process used is actually a rotation convection zone refiner using ten liquid zones, each of which is gradually moved to one end of the tube (see Fig. 15.10). To date, there have been 2, 3, 4, 15, and 18 complete passes made on five different tubes of sulfur. The four-pass tube has been opened for analysis. Small samples from ten zones have been analyzed by activation analysis. There were five notable elements in the sulfur: ^{56}Mn, ^{24}Na, ^{197}Hg, ^{76}As, and ^{82}Br. The amounts of these materials in each zone are given in Table 15.1 relative to that amount of each activity occurring in zone 10, which is the region that impurities are moved toward. Further analyses are being made for the tubes having a larger number of passes, and these analyses are being compared with sulfur foils formed from distilled flowers.

EXPERIMENTAL MEASUREMENTS OF LET

The biological effect of the absorption in tissue of a given amount of energy is generally assumed to be related to the linear energy transfer (LET) of the radiation. Consequently, for several years there has been an interest in developing a procedure by which the LET distribution of the radiation can be determined.

PHOTO 94198

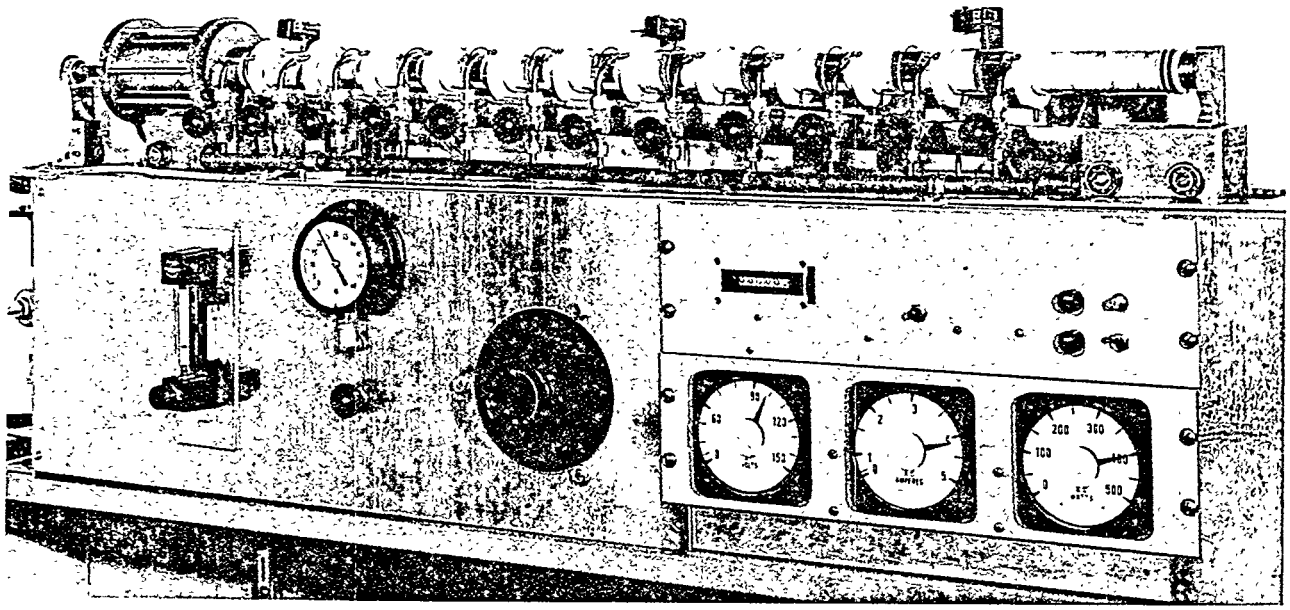

Fig. 15.10. Rotation Convection Zone Refiner.

Table 15.1. Activation Analysis for Impurities in Sulfur

Zone No.	^{56}Mn	^{24}Na	^{197}Hg	^{76}As	^{82}Br
1	0.30	0.47	0.24	0.21	0.31
2	0.47	0.08	0.25	0.22	0.45
3	0.30	0.31	0.33	0.30	0.64
4	0.33	0.25	0.25	0.18	0.65
5	0.81	0.55	0.24	0.32	0.47
6	0.39	0.61	0.33	0.40	0.94
7	0.18	0.13	0.32	0.26	0.63
8	0.70	0.28	0.13	0.19	0.45
9	0.95	0.43	0.56	0.54	0.70
10	1.00	1.00	1.00	1.00	1.00

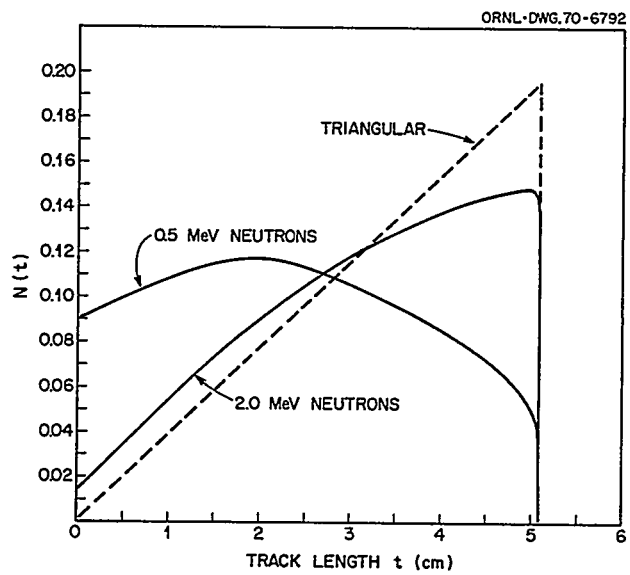

Fig. 15.11. Track Length Distributions.

The most common method for determining LET at present uses the Rossi counter,[10] a spherical proportional counter, and makes use of the theoretical triangular distribution of track lengths in a sphere in an isotropic radiation field to unfold the LET distribution from pulse-height measurements (see Fig. 15.11). However, the sphere is a particularly difficult geometry for a counter, and, in addition, the present method has certain other limitations as discussed in the Radiation Physics section (Part II) of this report. The cylinder is a much more convenient geometry for a counter, and work has begun, jointly with the Radiation Physics Section, to use a cylindrical proportional counter for determining LET distributions and also to eliminate some of the limitations of the Rossi method.

Pulse-height measurements have been made with both the Rossi spherical counter and the Hurst cylindrical

[10]H. H. Rossi, in *Radiation Dosimetry*, 2d ed., p. 77, F. H. Attix and W. C. Roesch, eds., Academic, New York, 1968.

counter in the radiation field of neutrons from the HPRR and from Am-Be. The Monte Carlo unfolding technique, developed jointly with the Radiation Physics Section, has been utilized to determine LET spectra from each pulse-height measurement. Figure 15.12 contains the LET distribution obtained by both counters for the Am-Be neutron source, and the agreement is quite good. However, the LET distributions shown in Fig. 15.13, obtained with the two counters for the HPRR neutron source, are not in agreement. Preliminary indications are that the lack of agreement may be attributed to the fact that the neutron flux from the reactor contains relatively more low-energy neutrons (below 1 MeV), and the assumption made in the analysis – that no recoil particles start or stop within the gas in the counter – becomes poor for low-energy particles. Work is under way to determine the reason for the discrepancy, to remove the limitations of the current method of determining LET distributions, and to determine conditions under which a cylindrical counter can be used.

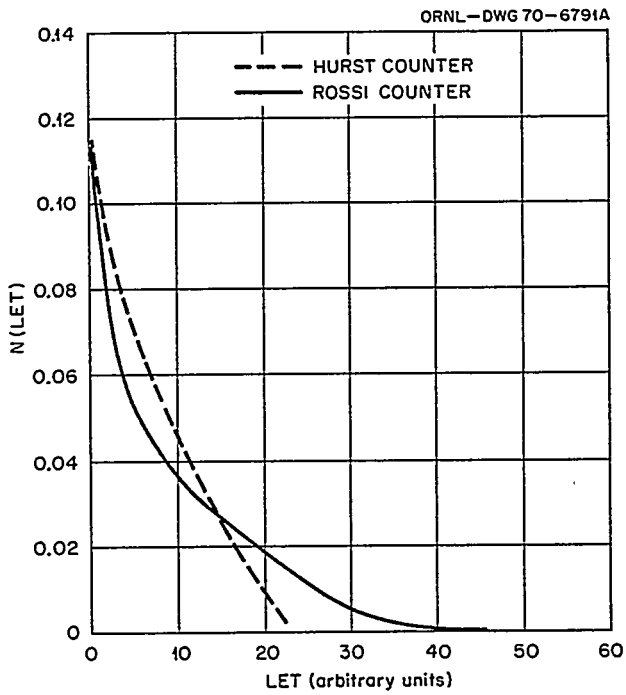

Fig. 15.13. LET Distribution for HPRR Neutrons.

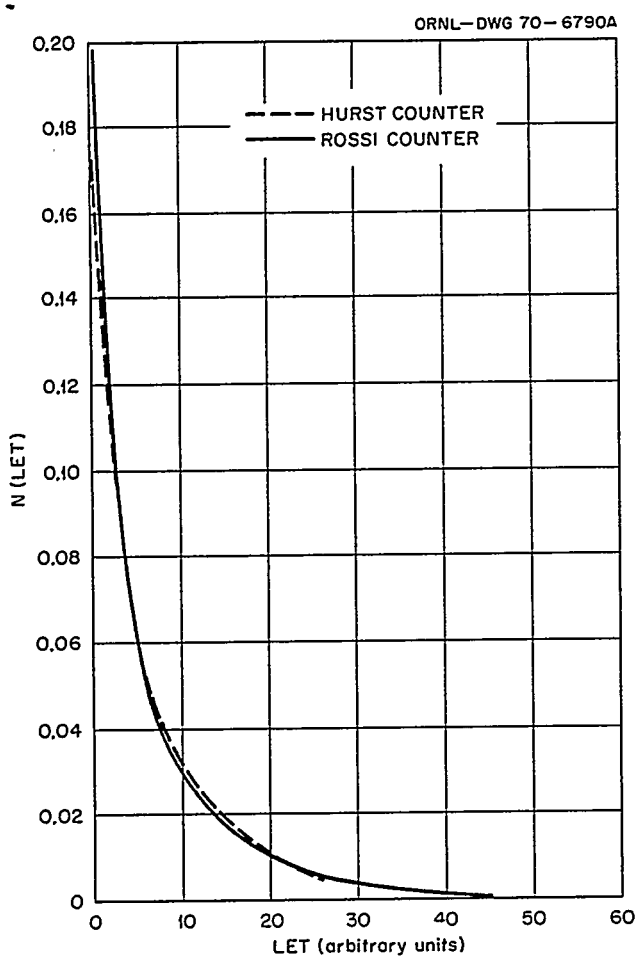

Fig. 15.12. LET Distribution for Am-Be Neutron Source.

UNUSUAL X-RAY SOURCES

For the period ending July 31, 1968, it was reported that certain high-vacuum switches and relays emitted x rays when operated under conditions where the voltage exceeded 10,000 V and the electrodes of the unit were in the open position. As one would expect, measurements made in a horizontal plane through the component's center indicate a nearly uniform radiation field; however, if the field is tilted 45°, there is a definite depression in the field behind the positive electrode. This may be seen in Fig. 15.14. There is a difference of approximately a factor of 9. The electrodes in this case were separated 3 mm, and the potential was 80 kV. This degree of absorption in the materials of the tube indicates that through careful engineering of the enclosure, much of the radiation could be eliminated. In addition, it was verified that x rays were emitted for ac voltages as well as for dc. Further, the radiation yield was dependent upon the electrode separation and the degree of usage of the equipment. A comparison of the x-ray yield of four different components, each with a 4-mm spacing between electrodes and with both ac and dc voltages

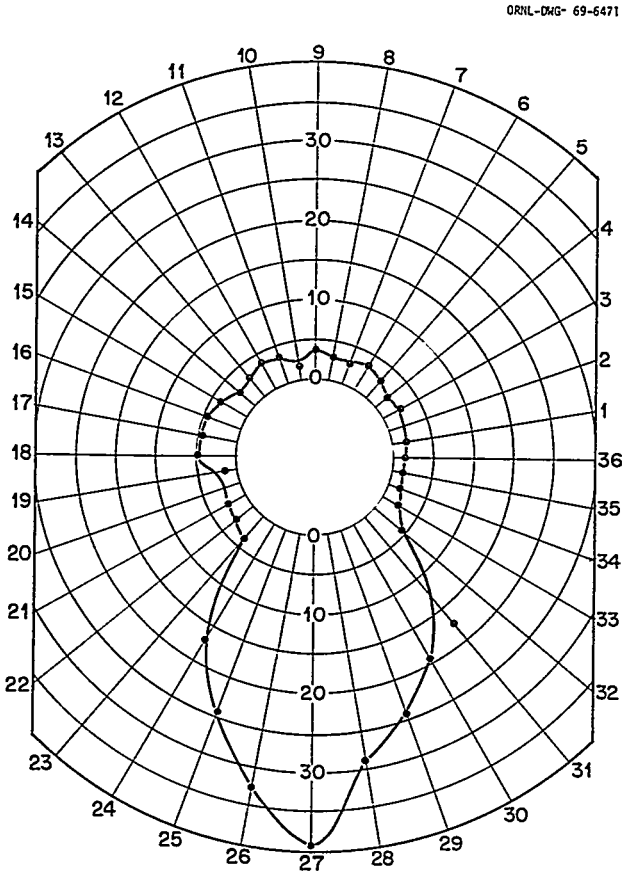

Fig. 15.14. Exposure at 50 cm from Center of Electrode Separation and in a Plane Which Passes Through Switch at 45°.

Table 15.2. X-Ray Yields as a Function of AC and DC Voltage

Unit	Ac (kv) (P-P)	mR/hr at 1 m	mR/hr at 2 m	Dc (kv)	mR/hr at 1 m	mR/hr at 2 m
B	45	0	0	45	3	~1
B	50	0	0	50	5	~1
B	56	1	0	56	8	2
B	62	2	0	62	12	3
				70	16	4
				80	35	8
C	45	3	1	45	4	0
C	50	22	6	50	6	~2
D	45	20	5	45	8	2
D	50	76	18	50	16	4
D	56	237	56	56	48	7
D	62			62	98	25
E	45	0	0	45	3	0
E	50	1	0	50	4	~1
E	56	2	0	56	4	~2
E	62	7	~2	62	8	2

applied, is given in Table 15.2. Alternating-current voltages appear to produce the larger field.

In order to demonstrate fully the x-ray hazard one might face in using switches similar to the one shown in Fig. 15.15, three of these units were connected first in series, then in parallel. For the test in series, ac voltages

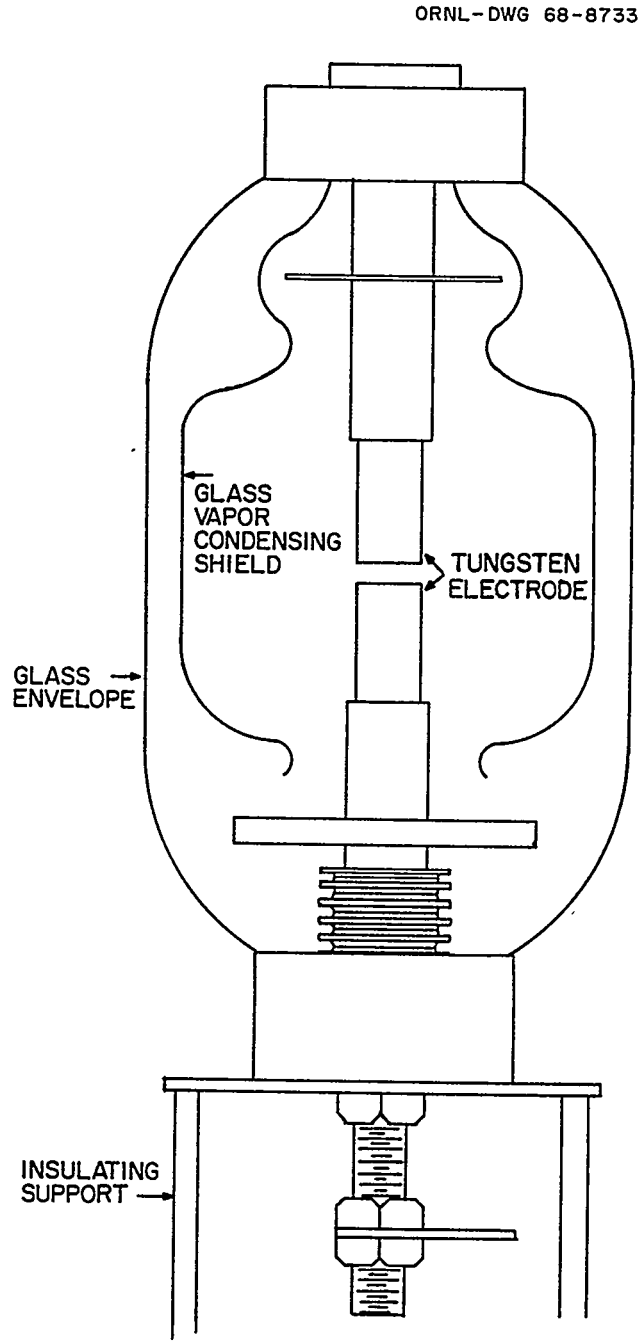

Fig. 15.15. Simplified Diagram of a High-Voltage Vacuum Switch Typical of the Ones Tested for Emission of X Rays.

to 62 kV were evenly divided across the three tubes. Exposure rates were less than 10 mR/hr at 1 m. But when the same three tubes were wired in parallel, which would simulate a set of three-phase distribution switches on standby, the exposures rates at 1 m reached 2.8 R/hr at 56 kV and 5.0 R/hr at 62 kV. The picture was nearly the same for dc voltages when wired in a similar fashion. For the parallel situation, exposure rates of 2.5 R/hr at 65 kV and 5.0 R/hr at 70 kV were measured at 1 m from the center on the assembly.

DESCRIPTION OF NEUTRON LEAKAGE FROM THE OPERATION HENRE NEUTRON GENERATOR

Operation HENRE, which was conducted at the Nevada Test Site during 1966 through 1968, was a large-scale field experiment including about 25 individual research projects, all of which obtained meaningful information pertaining to the propagation of neutrons and gamma rays in the atmosphere, shielding the interaction of radiation with matter, and to radiation effects. To make maximum use of these data and to allow rigorous comparison with calculations, a thorough description of the radiation output from the targets was required.[11]

As has been reported earlier,[12] the tritiated target substrate was made of copper and was 1 in. thick, 16 in. in diameter, and weighed about 40 lb. A 1000-cm^2 ErT_2 film was deposited in a ¾-in. depression in the substrate face, leaving a thick ring of copper for easy attachment to the accelerator drift tube. Neutrons were produced when a 400-mA deuterium beam accelerated to 150 kV interacted with the ErT_2 film. Approximately 10^{13} neutrons/sec were emitted over a 4π solid angle.

Calculations of the energy and angular distribution of neutrons emerging from the targets indicate that in the 0° direction (straight down), 80% of the neutrons were in the 13-to-15-MeV region, 5% were in the 5-to-13-MeV region, and 15% were in the 0-to-5-MeV region. At 88° the percentages were 67, 22.5, and 10.5 respectively (see Fig. 15.16). The calculated angular distribution of the 13-to-15-MeV component compares well with activation foil data (Fig. 15.17).

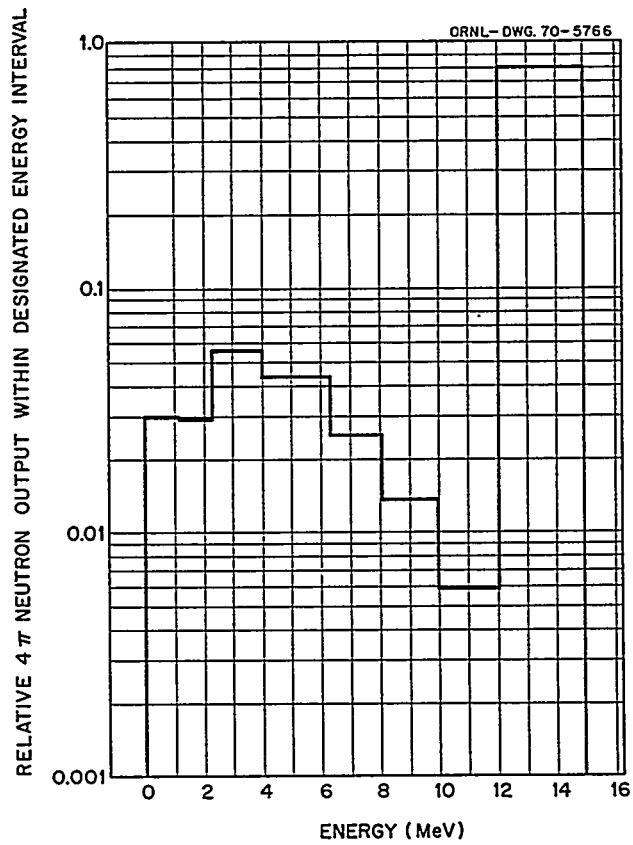

Fig. 15.16. HENRE 4π Neutron Spectrum.

Another set of activation foil data, taken at 0° and utilizing 14 different reactions, was studied in detail. Forty-seven trial spectra were chosen to evaluate the sensitivity of those foils to spectral changes. The spectrum giving the best fit was nearly the same as that predicted from calculations. This best spectrum is shown in Fig. 15.18.

ORGANIC SCINTILLATOR EXPERIMENT

As reported previously,[13] interest in the scintillation characteristics of the *para*-polyphenyls has continued. This interest derives from the measured characteristic of *para*-quaterphenyl, which appears particularly attractive for neutron detection and spectrometry in the energy region below 0.5 MeV. All scintillating materials exhibit a flattening of the dL/dE curve in the low-energy region. Thus the more efficient the photon production process becomes, the further down the energy scale the process of detection becomes feasible.

[11] Z. G. Burson, *Radiation Output Description from the $T(d,n)^4He$ Reaction in a Large Target (1000 cm^2) – Operation HENRE*, CEX-65.04 (to be published).

[12] F. F. Haywood, T. G. Provenzano, and J. A. Auxier, eds., *Operations Plan – Operation HENRE*, CEX-65.03 (September 1965).

[13] J. H. Thorngate *et al.*, *Health Phys. Div. Ann. Progr. Rept. July 31, 1969*, ORNL-4446, p. 245.

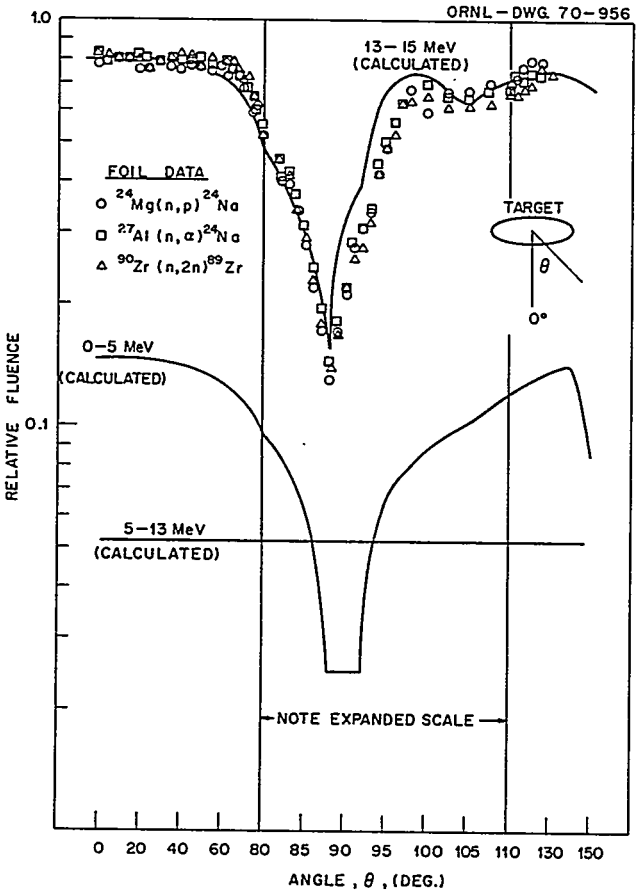

Fig. 15.17. Comparison Between Calculated and Measured Neutron Output as a Function of Angle Around the Target.

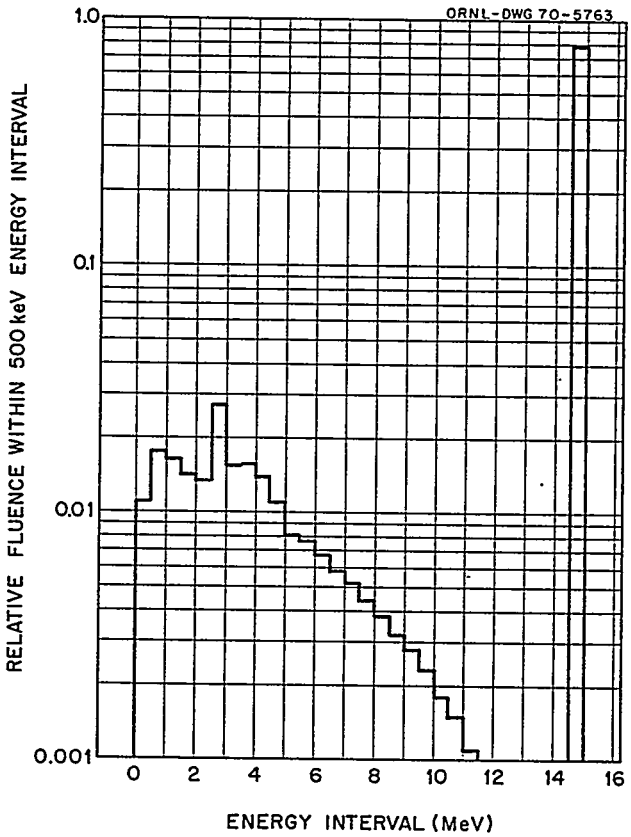

Fig. 15.18. HENRE Neutron Spectrum at 0°.

Repeated measurements have shown that *para*-quaterphenyl has slightly less than a factor of 3 larger response to Am-B neutrons than does *trans*-stilbene, apparently due to the larger macroscopic cross section of *para*-quaterphenyl. The Stokes shift of the two materials must also be considered, since the measurements were made in Pyrex glass with the RCA 8575 photomultiplier, which has a peak response at approximately 3850 Å.

More than 15 years ago, Sangster and Irvine[14] predicted theoretically that *para*-sexiphenyl would have more than twice the pulse-height response of anthracene to monoenergetic photons. The experimental work to date has tended to bear out this prediction.[15,16]

More recently,[17] a direct method of synthesis of *para*-sexiphenyl has become available which produces the material in good yield, based on the production of HCl. The production of scintillation-grade material from the crude product remains a formidable task. To date, vacuum distillation and zone refining appear to be the best methods of purification of the crude material.

Quite recently, modern polar solvents have been employed to remove highly colored impurities, which appear to be 4,4′-copper *para*-sexiphenyl complexes.[18] The results to date have been encouraging, but much of the chemistry of this compound remains to be done. This includes not only the identification and removal of impurities but investigations into the 4,4′ bonding of suitable organic radicals to make the scintillator more

[14] R. C. Sangster and J. W. Irvine, Jr., *J. Chem. Phys.* 24, 4 (April 1956).

[15] Tadashi Nozaki *et al.*, *Bull. Chem. Soc. Japan* 33(10), 1329 (1960).

[16] H. O. Wirth *et al.*, *Mol. Crystals* 4, 321 (1968).

[17] Peter Kovacic and Richard M. Lange, *J. Org. Chem.* 29, 2416 (1964).

[18] W. H. Baldwin, ORNL Chemistry Division, private communication.

soluble in organic solutes such as xylene and 2-ethylnaphthalene.[19]

Early in this year, it was discovered that the CDC 1604 computer would be retired, and since the original organic scintillator programs were written for this machine, a great deal of time was spent in rewriting these programs for the IBM 360 machines. Along with this project, several changes were made to the existing programs and new programs written to provide more information than had been available. A least-squares fitting program for the neutron data which allows plotting of the relative response of the various materials under conditions of near-optimum pulse-shape discrimination properties of the organic scintillators was written into machine programs for the IBM 360.

DOSAR PORTABLE SCALER MODIFICATION

During the past year, the gallium arsenide-phosphide light-emitting diode (LED) was developed to the point that it became feasible for use as indicators in counting equipment. Presently available diodes cost less than $2.00 each and produce a usable light output at 0.101 A (0.032 W input). The original DOSAR scaler used 10 V/0.10 A incandescent bulbs as indicators, as a compromise to reduce the cost of the Burroughs neon indicators.[20] This compromise was made at the cost of reducing the pulse-pair resolution of the instrument (originally 7 μsec). The modified circuit was not published, due largely to the necessity of matching the 2N1306 and 2N1307 germanium transistors used in the ring-counter decade stages.

Although a redesign of the scaler would presently employ the new matched integrated circuits, such as the RCA CD-4014/CD-4015 shift registers, the portability of the original instrument, as well as several other unique features, keeps the instrument in use. It has been found that LED's, such as the Monsanto MV-50, in series with the 680-Ω resistor to −12 V will provide indicators on each decade at a cost comparable with the cost of incandescent lamps. By reducing the 680-Ω resistor to 560 Ω, the original pulse pair resolution was restored. Some matching of the 2N1306/2N1307 transistors still is required, but the ring counters used in the decade stages are much less critical with the new light source.

The present design of the DOSAR scaler employs a unijunction transistor to set the timing interval and adjust the high voltage, both repeatable to less than 1%. These features are not yet available on laboratory instruments, so for these and other reasons, it may be desirable to update the design, employing the latest integrated-circuit devices. Such a course would not only retain all the original desirable features of the instrument but promises to reduce the cost as well. For the above reasons, the new circuit will not be published.

NUCLEAR DATA ANALYZER TAPE CONVERSION

The DOSAR has two ND-130 pulse-height analyzers which are used in various experiments to measure both dose and spectrum. These machines are used in conjunction with the Tally 420 tape punch to punch data on paper tape for data reduction on the computer. One of the problems with this method of data analysis is proper identification of the data. The conventional method is to write on the tape with white pencil and either have the computer operator enter some sort of identification manually or to arrange the data in some known order before recording the data on magnetic tape. Both methods are subject to errors.

The ND-130 machines punch paper tape in binary-coded decimal form, originally for reading back into the analyzer. The standard form for paper tape is now the American Standard Code for Information Interchange (ASCII). This code is now compatible with Teletypes and similar time-sharing equipment; in addition, computer programs are available to allow the introduction of data into the computer in this format.

During the past year an external interface for the ND-130 analyzer has been constructed which converts the original BCD code into the ASCII format. In addition, the interface allows manual entry of one or more six-number groups at the end of the data set for identification of the data in the computer. This conversion in no way affects the original outputs of the ND-130 analyzer. The method of making this conversion and the related circuits are the subject of ORNL-TM-2936.

The original intent in adding the extra number group at the end of each data set was for identification, but it was soon seen that it was possible to direct the computer to handle the data in a certain way, determined by the value of this added group. The majority of the gamma reduction codes now written are amenable to this method of direction, with some changes in the program. Since this extra group, or groups, is under

[19] J. G. Carter and L. G. Christophorou, *J. Chem. Phys.* 46(5), 1883 (1967).

[20] J. H. Thorngate and J. E. Parks, *Health Phys.* 12, 385 (1966).

control of the analyzer operator, the machine can be directed to reduce the data as a foreground, background, standard, unknown, time spectrum, etc. This allows a permanent decision to be made by the experimenter, at the time the data are taken, reducing the errors that often follow in transcription, card punching, and manual entry in the computer at the time the data are written onto magnetic tape.

TSEE AND SPARK-COUNTER PREAMPLIFIERS

Two preamplifiers, originally designed for use on Operation HENRE,[21] have been adapted for use on the TSEE and spark-counting equipment.

Although the TSEE counting chamber is operated at voltages high enough to achieve a Geiger-Mueller plateau and the pulse produced is of the order of 1.5 to 2 V, as viewed by a high-impedance oscilloscope (10 MΩ shunted by 10 pf), a special preamplifier was needed since most of the present counting equipment has a low-impedance input (2000 Ω or less) and the pulse produced in the counting equipment is small. The preamplifier shown in Fig. 15.19 has a gain of approximately 8 and presents a high impedance to the TSEE chamber with a low (91 Ω) impedance to the counting equipment. The output pulse varies up to about 10 V and is suitable for input to most scalers and count-rate meters.

The spark-counting technique for counting the etched holes in various plastic films requires the use of a special Pi-network on the input and is highly subjective. The version shown in Fig. 15.20 is that presently in use at ORNL.[22] Since a spark discharge produces a highly damped waveform, usually followed by several "after pulses," long time constants are used to integrate the pulse. The metal post over which the plastic foil is placed and the aluminum-coated Mylar backing become the plates of a capacitor, with the plastic foil as the

[21] J. H. Thorngate, unpublished data.

[22] D. R. Johnson, "Mechanisms and Applications of Nuclear Track Registration in Polymers," Ph.D. thesis, University of Kansas, 1970.

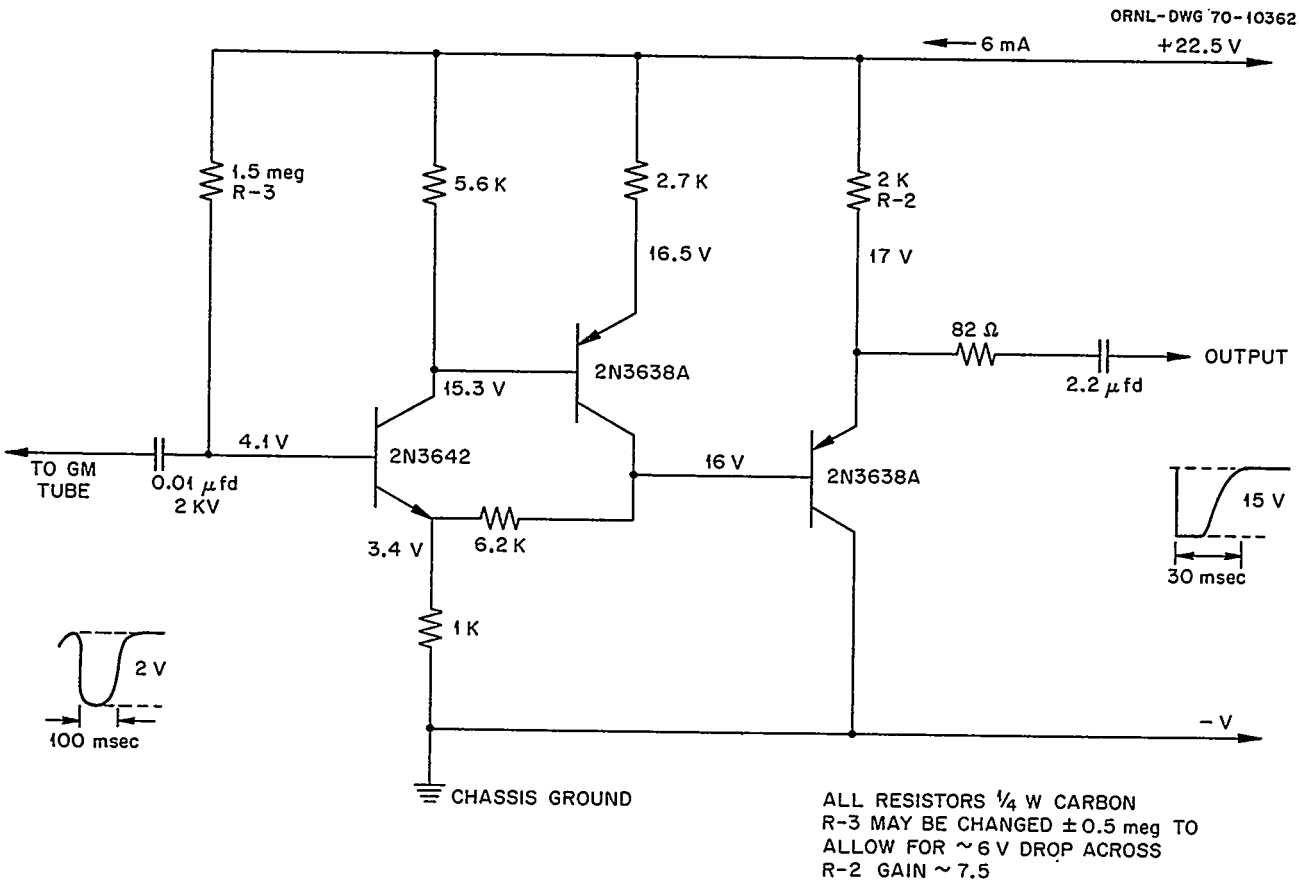

Fig. 15.19. TSEE Preamplifier.

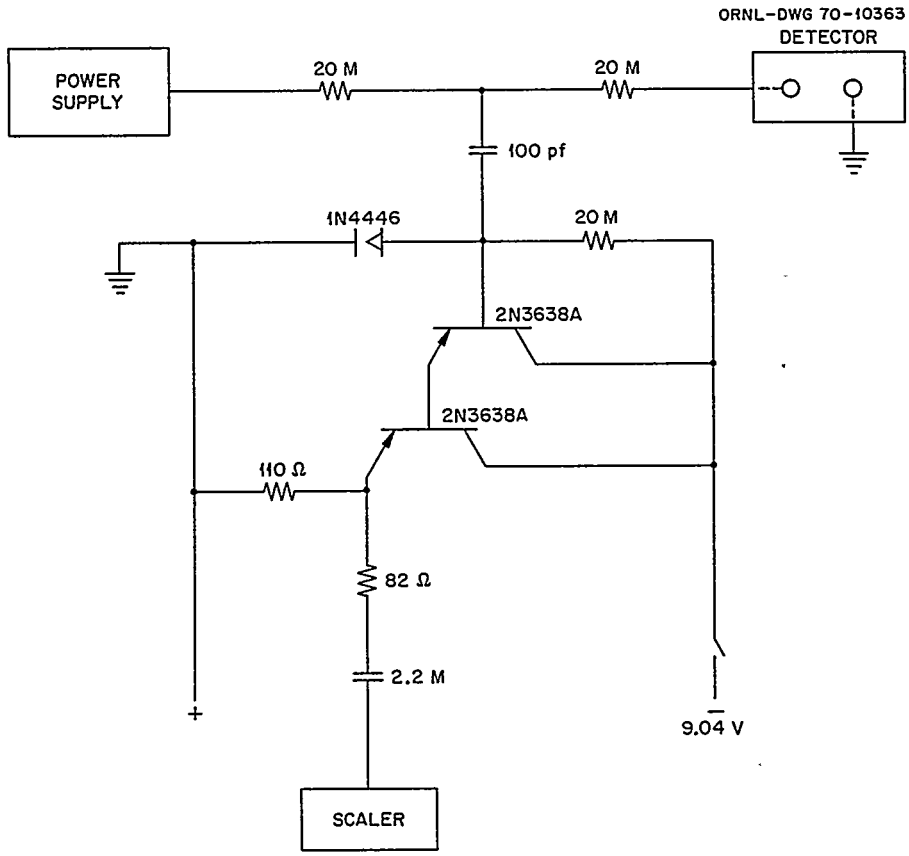

Fig. 15.20. Spark-Counter Schematic.

dielectric. The spark counter becomes the first capacitor in the Pi-network. The input capacitor to the preamplifier becomes the second capacitor in the network, with the second series resistor to the power supply (20 Ω) becoming the associated resistor in the second R-C network.

If a phase shift is produced by the coaxial cable between the counter and the resistance-divider network at the power supply, or in the preamplifier, oscillation results. Changes made in the diameter of the metal post used on the counter or plastic film thickness change the input capacitance of the preamplifier and/or changes in the resistance network. So far, efforts to use a single power supply for more than one counting system have not been successful, due to coupling between one counter and the other. Under reasonably uniform conditions, the pulse produced by the spark counter is ~15 V in amplitude and 10 to 25 msec in width, without large spikes at the peak or in the R-C decay.

The preamplifier used was originally designed to feed a Geiger-Mueller counter pulse over long lines[21] and presents a high impedance at the input. The emitter-follower design also does not cause significant phase shifts at the input and will tolerate large overload pulses. Power (8 to 12 V) is supplied to the preamplifier by a battery pack. The input resistor is chosen to produce a voltage drop across the output resistor of ~0.2 V, reducing the drain on the power supply. The diode on the input clips the positive pulses to protect the input transistor. Voltages used on the power supply are such that the preamplifier clips on the negative peaks, usually eliminating any ragged pulse peak that may be on the negative peak. This action presents a flat-topped pulse to the counting equipment. Output impedance is usually 91 Ω, depending on the series resistor.

Once the parameters of a given system have been optimized, repeatable results may be expected in multiple counts on a given plastic foil and continue until the geometry is changed. Any changes in the spark-counter geometry that result in capacitance changes require readjustment of the Pi-network parameters. Lengths of coaxial cable used should be as short as possible, but high-voltage power supplies and pulse-counting equipment are not usually critical.

MEASUREMENT OF THE NEUTRON SPECTRUM FROM THE HPRR BETWEEN 50 keV AND 450 keV

A proton-recoil telescope neutron spectrometer was developed to measure neutrons having energies between 50 and 450 keV.[23] The proton radiator was 17-μg/cm^2-thick anthracene film separated a distance of 83.82 cm from a ZnS detector. A magnetic analyzer was used between the radiator and detector to determine the momentum of the recoiling protons.

The ORNL 3-MV Van de Graaff accelerator was used to obtain the detector response as a function of proton energy, and the DOSAR Low Energy Accelerator was used to calibrate the magnetic field of the spectrometer.

Spectral measurements of neutrons with energies between 50 and 450 keV were made 50 cm from the HPRR. The results (see Fig. 15.21) agreed well with a portion of measurements made previously with an ^{6}Li spectrometer,[24] but the agreement with a calculated form of the Godiva II spectrum for this energy region was not as good. However, good agreement with the Godiva II spectrum for the energy region of interest would not be expected, since the Godiva II core configuration is smaller than the HPRR and the fuel is not alloyed with molybdenum as in the HPRR.

[23] D. R. Stone *et al.*, *The Development of a Spectrometer and the Measurement of the Neutron Spectrum from the Health Physics Research Reactor Between 50 kev and 450 kev*, ORNL-TM-2707 (November 1969).

[24] J. A. Auxier *et al.*, *Health Phys. Div. Ann. Progr. Rept. July 31, 1964*, ORNL-3697, p. 163.

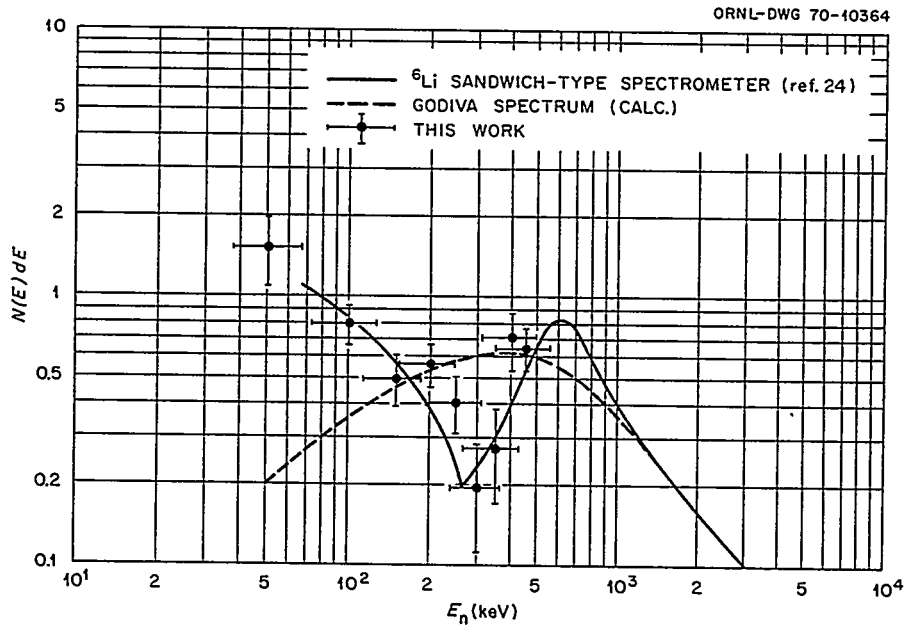

Fig. 15.21. HPRR Neutron Spectrum.

16. Applied Dosimetry Research

Klaus Becker
R. H. Boyett[1] R. B. Gammage
J. S. Cheka F. E. Gillespie[3]
K. W. Crase[2] D. R. Johnson[4]
J. F. Wilson[2]

TSEE RESEARCH

TSEE Instrumentation

TSEE dosimetry using a gas-flow G-M counter as an exoelectron detector can cover a wide dose range if detectors of varying sensitivity and varying heating rates are used in order to avoid dead-time losses at high count rates. With the development of ultrasensitive detector systems (see following section on detector development), however, it became increasingly desirable to develop special readers for high dose levels based on current instead of pulse measurements, and perhaps even to cover the whole range of interest in personnel, accident, and clinical dosimetry ($\sim 10^{-2}$ to 10^{4} rads) with one reader.

A reader using a flat plate collector and an electrometer has been tested successfully for the reading of metal-sensitized ceramic BeO detectors. The exoelectrons emitted from the detector during heating are accelerated to the thin gold collector plate by a 45-V battery. The current is measured using a Cary 401 vibrating-reed electrometer. A thin nickel foil is used to make contact to the top surface of the electron-emitting BeO disk and connects to the negative terminal of the battery. The positive terminal of the 45-V battery is connected to the chamber ground and to the ground connection of the vibrating-reed electrometer. Figure 16.1 illustrates the chamber and connections. The chamber is flushed with a mixture of 0.95% isobutane and 99.05% helium, as is used in the G-M counters. The area around the heater is water cooled in order to keep the temperature in the measuring volume down. Doses from 10 to 10^{6} rads, corresponding to the 10^{-14}-to-10^{-12}-A range, have been measured. A typical "glow curve" is given in Fig. 16.2. Current modifications on the instrument, for example, installation of a heater having better electrical shielding, are expected to extend the range to lower doses. Other instrumentation based on optical stimulation is under development.

Detector Development

Effect of Metal Diffusion on TSEE of Ceramic BeO

Kramer[5] first noted that making the exoelectron-emitting surface electrically conductive, thus preventing the buildup of local charges on the emitting surface which interfere with the emission process, improves the reproducibility and linearity of response. In most of the initial work on basic dosimetric properties of TSEE materials (such as linearity and reproducibility of response, fading stability, sensitivity of different materials as a function of purity and pretreatment, LET dependence of response, etc.), Kramer's technique of mixing the powdered substances with graphite and plating this mixture on graphite disks has been used for reasons of convenience and flexibility. It was, however, obvious that several other possibilities would deserve attention, in particular the impregnation of sintered

[1] Present address: Chattanooga State Technical Institute, 4501 Amnicola Highway, Chattanooga, Tenn.

[2] AEC Predoctoral Fellowship.

[3] On loan from Instrumentation and Controls Division.

[4] Present address: Texas Nuclear Corporation, Northwest Station, 9101 Highway 183, Austin, Tex.

[5] J. Kramer, *Z. Angew. Phys.* 20, 411 (1966).

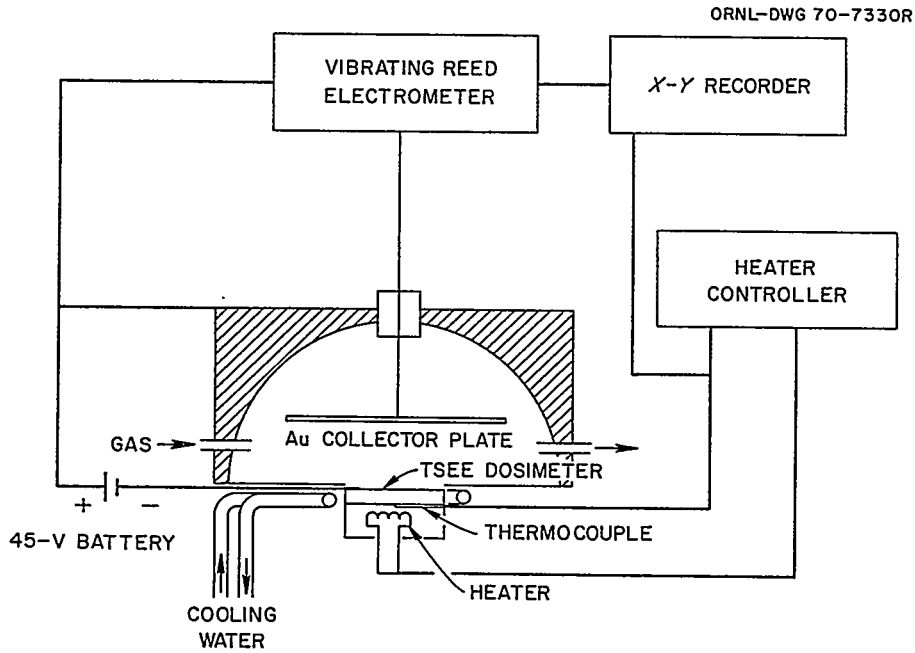

Fig. 16.1. Schematic Diagram of an Electrometer-Type Exoelectron Detector for High-Dose-Level TSEE Studies.

detector substances with a conducting material.[6] Diffusion of vacuum-deposited metals into the detectors turned out to be one of the more successful approaches. Preliminary experiments were carried out with a commercially available sintered beryllium oxide.[7] Some of the initial findings,[8] for instance, with regard to the distribution of the metal, the linearity of response, and the effect of protons, have, however, not been confirmed by subsequent more systematic studies.

During extended heating of a ceramic BeO on which a thin layer of an inert high-melting metal such as gold has been plated by vacuum deposition to temperatures in the 400 to 1200°C range, a more or less rapid diffusion of the metal into the matrix takes place. A change from the originally metallic appearance of the surface into a dull pink occurs within a few minutes. The pink becomes increasingly pale until, after extended heating, the BeO is almost as white as it was before the metal coating. Analogous processes occur during the heat treatment of BeO disks which have been coated with thin layers of other suitable metals which have to be (1) nonreactive with the TSEE emitter; (2) not subject to any substantial chemical change such as oxidation under the conditions of preparation, use, and readout; (3) nonvolatile at the temperatures involved. For example, samples coated with palladium or platinum change their appearance from shiny silver to a metallic gray (other metals, such as osmium or rhodium or mixtures of several metals, can be expected to exhibit a similar behavior). During the change in appearance the macroscopic electrical conductivity of the surface drops considerably.

The weight of the sample does not change measurably during the heat treatment, and studies on the metal depth distribution using an electron microscope confirm that the metal does not evaporate but actually impregnates into the sample. The diffusion speed depends on the temperature and time as well as on the diffusing metal and the substrate. The lattice of BeO is almost perfectly close packed in anions, which makes it likely that more metal migrates along grain boundaries (Fig. 16.3) than into the lattice itself.

If a preannealed detector is coated with a thin metal layer (50 $\mu g/cm^2$ Au), there is a small but definite radiation response even without any significant diffusion treatment. It seems, however, unlikely that

[6] K. Becker, "Some Studies on Radiation Dosimetry by Thermally Stimulated Exoelectron Emission (TSEE)," p. 200 in *Proceedings of Second International Conference on Luminescence Dosimetry*, September 23 through 26, 1968, Gatlinburg, Tenn., CONF-680920 (1968).

[7] Thermalox 995 and 998, available in different sizes and shapes from Brush Beryllium Corporation, Metal and Oxide Division, Elmore, Ohio.

[8] E. M. Robinson and M. Oberhofer, *Health Phys.* 18, 434 (1970).

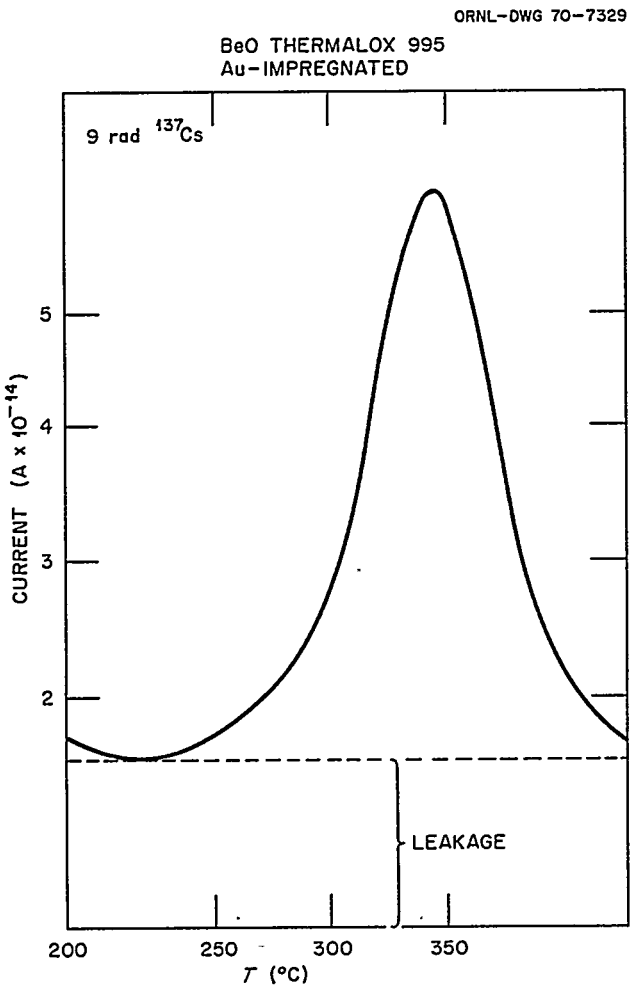

Fig. 16.2. TSEE "Glow Curve" of a Ceramic BeO as Measured in the Electrometer Reader.

exoelectrons are able to penetrate the intact conducting metal layer (this layer appears to contain numerous small perforations through which the emission may occur). Stepwise removal of the intact metal layer by the diffusion heat treatment greatly enhances the detector sensitivity. The relation between diffusion time and sensitivity has been studied in some detail.

In one set of experiments, ceramic BeO disks have been coated with equal quantities (50 $\mu g/cm^2$) of Pt, Pd, and Au.[9] The coated disks were then heated at either 550 or 650°C for various times, and the TSEE sensitivity after each time was measured by exposing them to a small gamma radiation dose and then reading them by recording the TSEE during heating at a constant rate of 1°C/sec inside a gas-flow G-M counter. If the total counts between about 200 and 500°C, including all three major TSEE peaks of this material for a given radiation dose, are plotted as a function of diffusion time (Fig. 16.4), a peak sensitivity of almost 10^4 counts/mR has been found in the Pd-treated detectors with an effective emitting surface area of about 3 cm^2. This makes it possible to measure doses in the microroentgen range. The sensitivity is subject to change in this particular detector type during consecutive heating cycles. The Au-coated sample, which did not exhibit a peak sensitivity but a steady decline in this experiment, was shown to go through a peak sensitivity too if the diffusion was done at a lower temperature.

The TSEE curve changes somewhat as a consequence of the metal treatment. In Fig. 16.5 the three peaks of a virgin sample are shown (the absolute location of the peaks is probably indicated in those graphs slightly too high due to a temperature gradient in the ceramic). Both sensitivity and peak location in the uncoated sample are poorly reproducible. After coating with 50 $\mu g/cm^2$ of Au, Pd, or Pt and heating of the samples for 20 min at 550°C, the main peak around 300°C is somewhat enhanced in the Au-treated samples and is considerably enhanced in the Pd- and Pt-treated samples. The two high-temperature peaks are depressed.

The changes that occur in the TSEE curve of a Pt-coated sample during the diffusion process are summarized in Fig. 16.6. Most of the sensitivity enhancement occurs in the first peak, while the high-temperature peaks are only subject to minor changes. After more than 3 hr at 550°C, the total sensitivity is as low as after only a few minutes of diffusion, but the TSEE curve exhibits three peaks instead of one. A similar behavior has been observed in other metal-treated detectors. In the Au-treated sample, for instance, the third peak stayed remarkably constant during the reduction of the first peak.

As an explanation for this effect it is suggested that a reduction in the work function, permitting a larger fraction of the detrapped electrons to leave the surface, occurs. Maximum sensitivity would result if the metal concentration at the emitting surface is high enough to reduce the work function sufficiently but low enough so that no significant absorption loss of the exoelectrons occurs. This model is supported by: (1) The fact that an increase of sensitivity is paralleled by a shift of the thermionic emission edge to lower temperatures and vice versa. (2) An experiment in which the photoelectron emission from two Pt-treated samples has been compared after different heat treatments; the detector

[9] K. Becker, J. S. Cheka, and R. B. Gammage, "Progress in Exoelectron Dosimetry," invited paper, International Symposium on Exoelectrons, Braunschweig, Germany.

Fig. 16.3. Grain Boundaries in a Ceramic BeO (Brush Thermalox 995). Scanning electron microscope. 1000X.

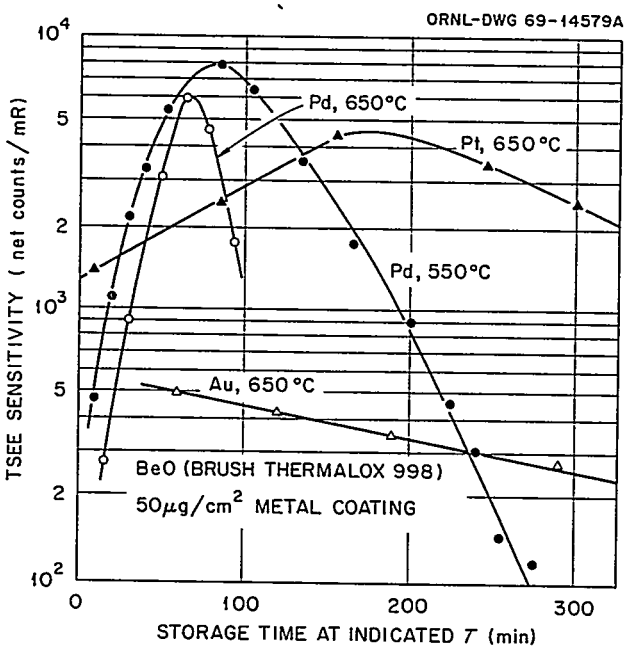

Fig. 16.4. Sensitivity (TSEE Counts over Background per Milliroentgen of Gamma Radiation) of Ceramic BeO After Vacuum Deposition of 50 $\mu g/cm^2$ of Pt, Pd, and Au as a Function of Diffusion Time at Indicated Temperatures.

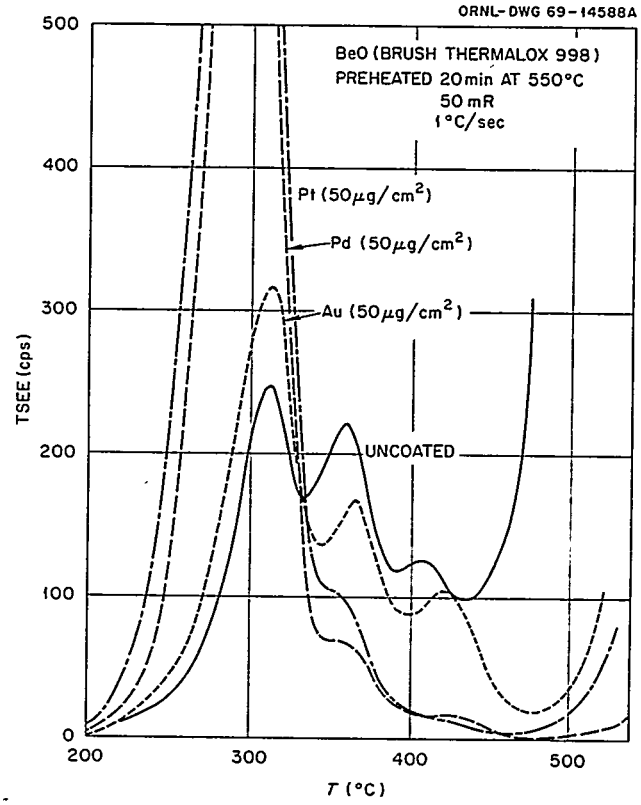

Fig. 16.5. TSEE from an Uncoated Ceramic BeO Disk During Heating at a Linear Rate of 1°C/sec and of Disks into Which 50 $\mu g/cm^2$ of Pt, Pd, and Au Have Been Diffused by a 20-min Heating at 550°C.

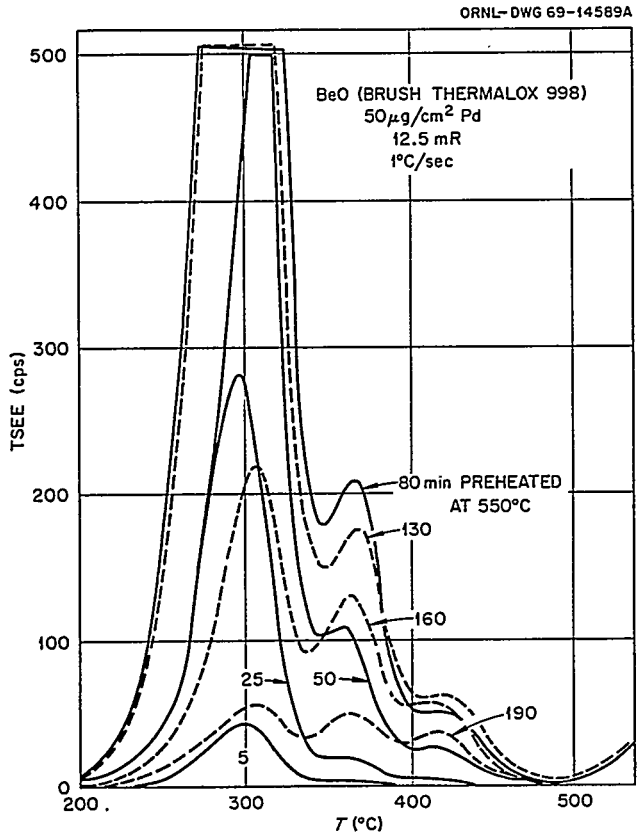

Fig. 16.6. Changes in the TSEE Curve Occurring During the Diffusion of Pd into BeO.

with the more pronounced photoelectron emission was also the more sensitive exoelectron emitter (the same has been found for Au-treated samples). The relatively stronger enhancement of the low-temperature peak may be explained by a different energy distribution of the exoelectrons from different peaks.

A disadvantage of this type of diffusion sensitization is the change that occurs in a detector's sensitivity during repeated use if the thermal diffusion is carried out at a temperature not much higher than that used for the reading and annealing of the detectors. A good consistency of the detector response during repeated use is, however, highly desirable. Further experiments have demonstrated that the thermal stability of the detectors can be considerably increased if the thickness as well as the diffusion temperature and/or time are increased. Plating detectors with 1 to 2 mg/cm^2 of platinum and heating for 10 to 20 hr at 1000 to 1200°C, for example, results in the same optimized surface concentration of platinum and high sensitivity as the treatment described above but a much deeper penetration of the metal into the bulk of the material. Frequent heating of such detectors to the temperatures used for the dosimeter evaluation (<700°) then does not alter their properties any more.

The optimum diffusion time and temperature depend on the initial thickness of the metal layer. In BeO samples coated with different amounts of Au, optimum sensitivity is obtained with a coating of 0.2 mg/cm^2 after three days at 800°C. If the same samples are further heated, a reduction of the surface Au concentration shifts the maximum to a higher initial Au thickness. The same effect has been found for Pt-coated samples. The "bulk diffusion" technique can, of course, be applied from both sides of a thin ceramic BeO.

There is another method for obtaining an optimized metal concentration in a thin surface layer which has the advantage of minimizing the amount of unnecessary "surplus" metal at the surface. This method consists in coating the ceramic BeO with a quite substantial amount of metal – 10 mg/cm^2 or more – followed by a heat-diffusion treatment as described above and a final step of removal of the remaining metal by "peeling." After this treatment the ceramic looks almost like the white untreated material with just a slight hue of pink. In Fig. 16.7, some detectors of this type before and after peeling are shown, as well as detectors of different sizes which have, for simplified handling and in order to avoid contamination or tribosignals, been semipermanently framed in a metal holder in which they remain for all irradiation, reading, or annealing sequences. This type of detector has been used for most of the consecutive experiments.

Consistency and Linearity of Response

The most serious problem in the initial work with the new type of detectors was poor reproducibility. A standard deviation of 10 to 20% and frequent erratic readings were common. With the present experience the main reasons for poor reproducibility and erratic results can be summarized as follows:

1. Tribo-TSEE is induced by touching or scratching the effective surface of the detector with any hard object such as tweezers; soft objects do not create any tribosignals.
2. Spurious peaks result from exposure to intense light, either by keeping the detectors close to an artificial light source or by exposing them to sunlight (as illustrated in Fig. 16.8, both tribo-TSEE and light-induced TSEE peaks normally do not occur at the same peak locations as the radiation-induced peaks).

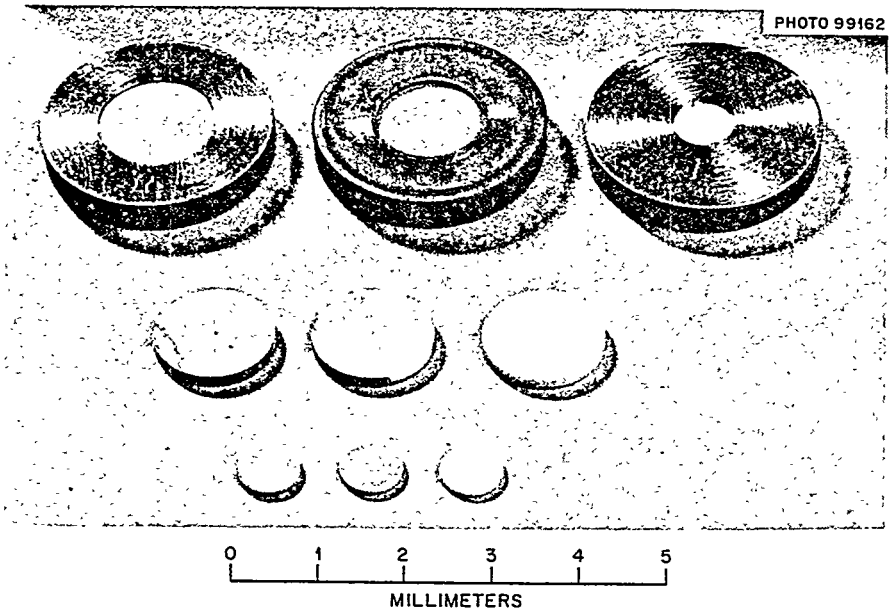

Fig. 16.7. Ceramic BeO of Different Sizes, With and Without Brass Holders for Simplified Handling, After Different Steps of Impregnation with Au, Pd, and Pt.

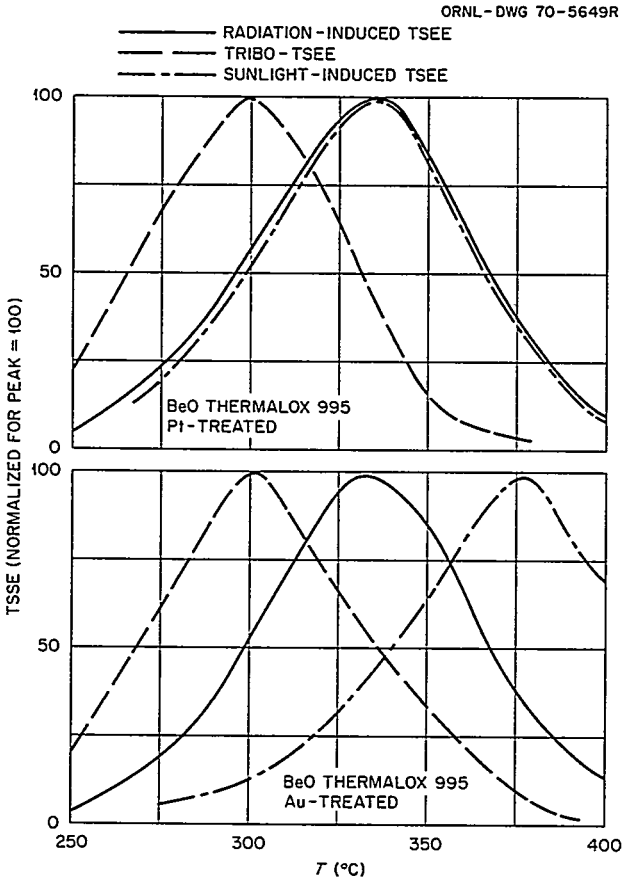

Fig. 16.8. Typical Radiation-Induced TSEE Peaks in Metal-Impregnated Ceramic BeO Compared with "Spurious" Tribo and Light-Induced Peaks.

3. Poor electrial and/or thermal contact either within the emitting surface, if the metal concentration becomes too small, or between the emitting substance and the frame or reader causes "bursts" of exoelectron emission.

If those sources of error are avoided by proper preparation and handling of the detectors, the reproducibility of at least 10 or 20 consecutive measurements is excellent (a standard deviation of 2% has been found with the peeled Au samples framed in brass holders). No special annealing procedure is required between reading and the next exposure: A reading either to about 375°C (lower peak) or to about 600°C (all peaks) completely anneals the signal.

A long-term drift in the detector response has been observed in some cases in which the same detector has been frequently used over long periods of time. This can be due either to a contamination of its surface, which usually can be removed by simple cleaning (e.g., with acetone or chloroform), or to an irreversible change in its surface properties.

All detectors investigated, independent of the type and amount of metal used, have exhibited a nonlinear radiation response. The sensitivity, expressed in counts per rad of gamma radiation, decreased with increasing exposure level, resulting in a linear relationship if the sensitivity is plotted against exposure on a log-log plot (Fig. 16.9). Sensitivity and slope of the curve are independent of the heating rate provided dead-time counting losses do not become significant. This calibra-

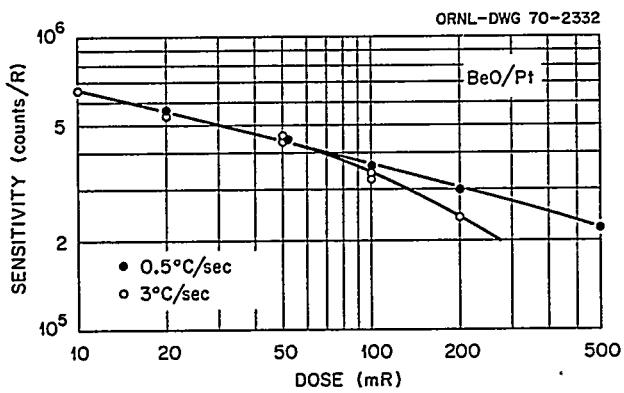

Fig. 16.9. Sensitivity of a Pt-Impregnated BeO as a Function of Exposure for Two Different Heating Rates. Nonlinearity of the 3°C/sec curve is caused by dead-time losses in the G-M counter.

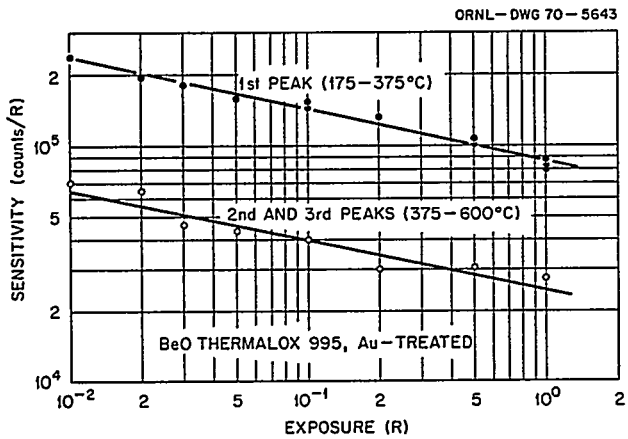

Fig. 16.10. Response of the Low-Temperature and the High-Temperature Peaks in Ceramic BeO as a Function of Gamma Radiation Exposure.

tion curve appears to be independent of the peak location; both low-temperature and high-temperature peaks show the same slope (Fig. 16.10).

There appears to be no exchange of electrons between the different trapping levels. Frequent annealing of the low-temperature peak during fractionation experiments did not create any deviation from the summation of the radiation effect in the high-temperature peaks. This is important for possible applications of such detectors in personnel dosimetry. Interval readings of low doses can be done by heating out the low-temperature peak, and doses accumulated over extended periods, or higher doses in accident dosimetry, can be read by heating up to the beginning of the thermionic emission edge around 600°C.

Thermal and Chemical Stability

Fading of TSEE detectors is a complex subject because it frequently does not consist simply of a release of electrons from a given trapping level whose rate corresponds to the difference between the activation temperature of the trap and the ambient temperature. Because of a multitude of physical and chemical processes which may occur at the emitting surface, leading to the creation or destruction of electron traps, secondary processes frequently complicate the annealing kinetics.[10] Such processes have even been observed occasionally in chemically and physically quite inert materials such as BeO. In agreement with earlier results on the fading of BeO/graphite mixtures, no fading at room temperature was observed during initial experiments.[11] Using another highly disperse BeO mixed with graphite, however, a quite significant fading of about 30% in three weeks at ~25°C was observed (Fig. 16.11). Changes in the relative humidity between 0 and 80% did not affect the fading rate, but samples kept over an open water surface showed in repeated tests an accelerated fading.

It can be assumed that the much denser surface of the sintered disks is more resistant to chemical changes; the metal impregnation may also contribute to a greater resistance. Indeed, no fading was observed in preliminary tests of those detectors at room temperature. It takes a considerably higher temperature to induce fading. As shown in Fig. 16.12, a fraction of the low-temperature peak around 300°C even survives 15 min of storage at 268°C.

Heating for 15 min to 305°C, which completely anneals this peak, does not visibly affect the high-temperature peaks. This is not necessarily so if the detector is heated in vacuo instead of air or oxygen. During half an hour of storage at 240°C in oxygen, the 300°C peak is substantially lowered, with no effect on the 575°C peak. Under the same conditions in vacuo, however, a much smaller reduction of the low-temperature peak is associated with a substantial fading of the high-temperature peak. Clearly, the fading is following different courses in oxygen and in vacuo.

The effect of the environment during isothermal annealing has been further studied in a series of experiments (Fig. 16.13). No fading was observed for

[10] K. Becker and N. Chantanakom, "On the Thermal Fading Characteristics of Some TSEE Dosimetry Materials," *Atompraxis* 16, 31 (1970).

[11] J. F. Wilson, M.S. thesis, University of Tennessee, to be published.

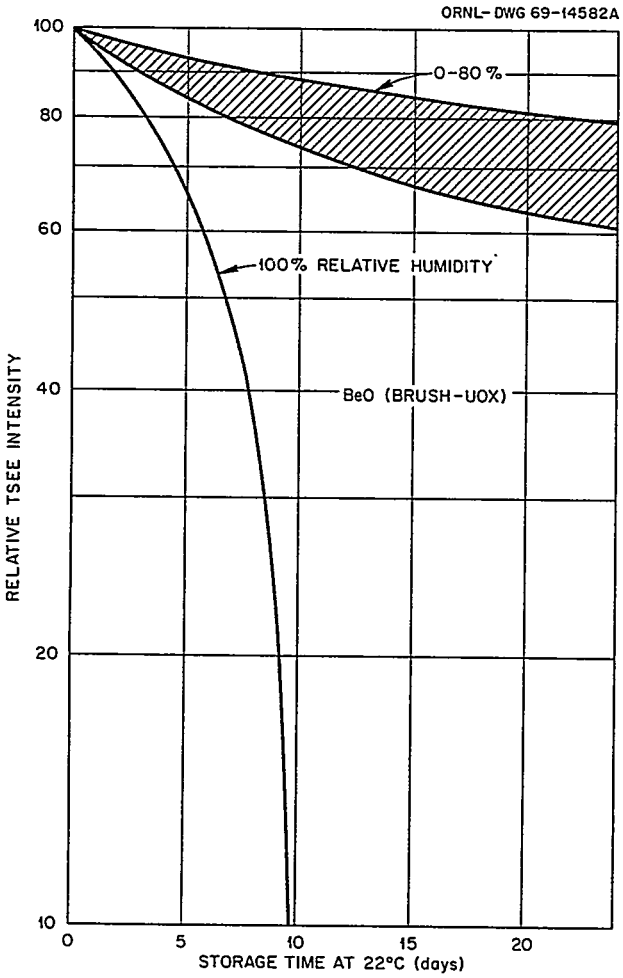

Fig. 16.11. Fading of Radiation-Induced TSEE in a BeO Powder/Graphite Mixture Plated on Graphite Disks at Different Relative Humidities During Storage at Room Temperature.

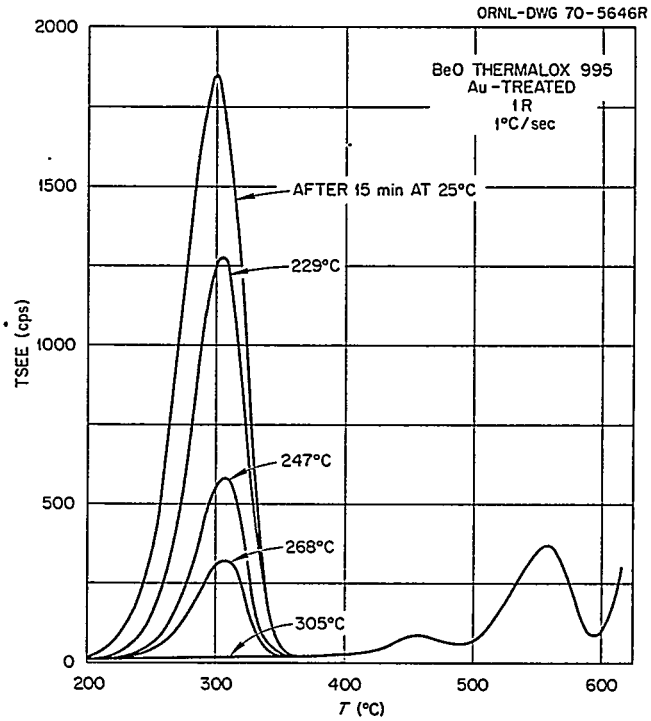

Fig. 16.12. Fading of the 300°C Peak in an Au-Impregnated ("Peeled") Ceramic BeO During Storage for 15 min at Various Temperatures.

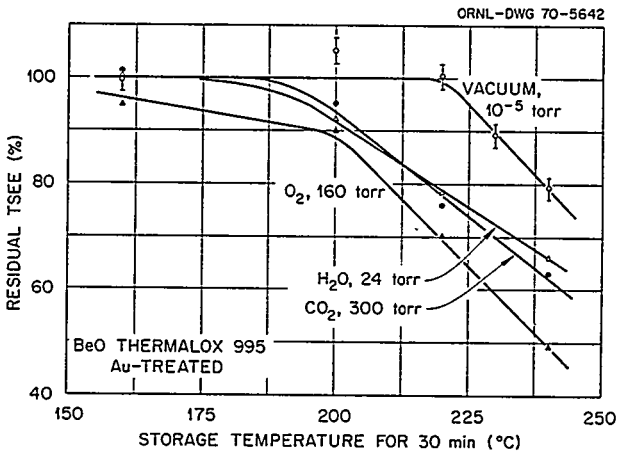

Fig. 16.13. Fading of TSEE in Au-Impregnated BeO During Storage for 30 min at Various Temperatures in Vacuo, H_2O Vapor, CO_2, and Oxygen.

samples heated in vacuo for 30 min up to 220°C. Under these conditions, 20% fading occurred in both H_2O vapor and CO_2 and 30% in O_2. There is no simple explanation of this complex behavior. Perhaps adsorption-desorption processes provide a means for discharging the surface region; O_2 and CO_2 are known to interact with S centers in irradiated oxide surfaces to give chemisorbed O_2^- and CO_2^- species. The different nature of the fading in vacuo (where desorption processes will predominate) may also be indicative of an important role played by chemisorbed entities.

Preliminary results on the fading of the detectors in liquids at normal temperatures point to quite rapid fading in water but little in alcohol or acetone. The markedly different behavior of the ceramic surface in the presence of liquid water as opposed to water vapor is probably tied to surface hydration events which for some oxides are often much more rapid in the liquid than the vapor (concentration and cooperative effects). The marked fading in liquid water is associated with a reduction of the detector sensitivity; heating to 1200°C, however, not only restores the initial sensitivity but may even lead to a sensitivity increase.

Photon Energy Response

Unlike most other solid-state dosimeters, in which the photon energy dependence of its response can be fairly easily calculated from the composition of the bulk of the material, surface-type TSEE detectors depend to a larger degree on the composition of other materials within photoelectron range of the sensitive surface layer. The calculated response of pure BeO shows a slight undersensitivity of about 18% in the 10-to-40-keV energy range. It was expected that the impregnation with high-Z metals would lead to a more or less pronounced oversensitivity for x rays.

The metal-impregnated detectors from which the excess metal had been removed by peeling, containing the smallest amount of heavy elements of all the detectors under study, exhibited an oversensitivity by a factor of ~2.5 around 45 keV if framed in a brass holder and exposed frontally to well-filtered x radiation (Fig. 16.14). Assuming that the brass could affect the energy response, the experiment was repeated using a carbon holder. Indeed, a considerably reduced energy dependence was observed.

In other experiments,[11] detectors into which larger amounts of heavy metals had been diffused by a high-temperature (800 to 1000°C) treatment have been studied. The highest oversensitivity by a factor of almost 22 at ~50 keV was observed in a sample containing 5 mg/cm^2 Au (Fig 16.15), but even with only 0.2 mg/cm Au the oversensitivity still amounts to 10 (all the measurements have been corrected for the nonlinearity of the sample response and the effect of the brass holder). In Pt-impregnated samples (Fig. 16.16), less energy dependence (oversensitivity of 7.5 with 2 mg/cm^2 Pt, ~1.5 with 0.2 mg/cm^2 Pt) has been observed, probably due to a smaller Pt concentration in the sensitive surface layer.

Other studies on the effect of a detector's environment on its energy response have also been carried out. According to Kramer (personal communication), the response of a TSEE dosimeter to soft x radiation rapidly increases with increasing Z of the gas between radiation source and detector. A similar experiment was

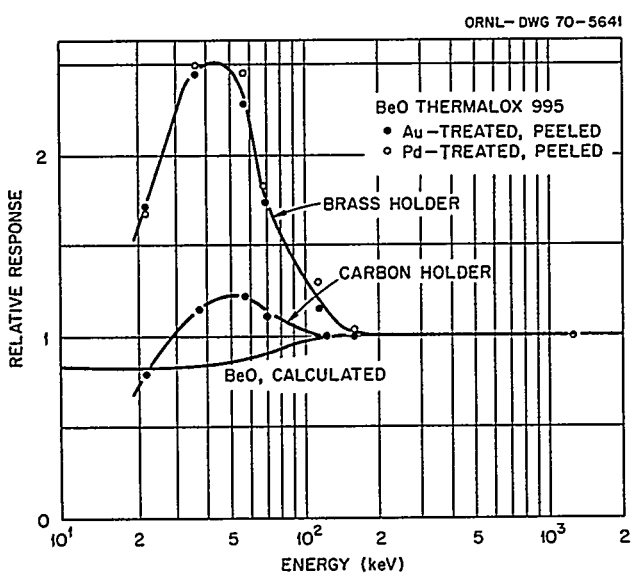

Fig. 16.14. Photon Energy Dependence of Pd- and Au-Impregnated Ceramic BeO Framed in Brass Holders and in Graphite Holders (Normalized for ^{60}Co), Compared with the Calculated Response for Pure BeO.

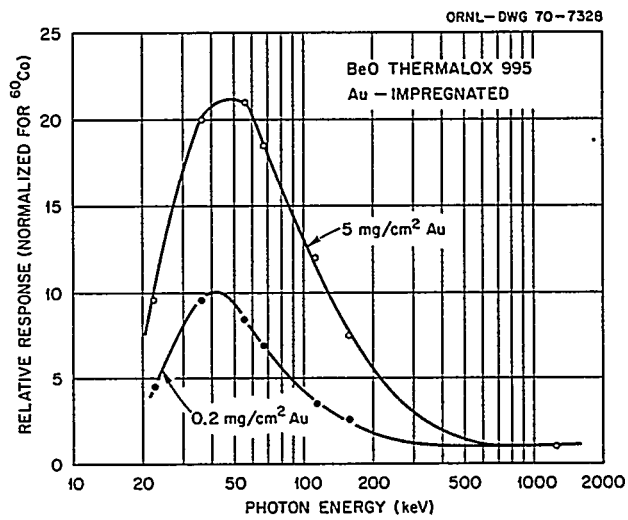

Fig. 16.15. Relative Response (Normalized for ^{60}Co) as a Function of Photon Energy in Ceramic BeO Impregnated with Different Amounts of Au.

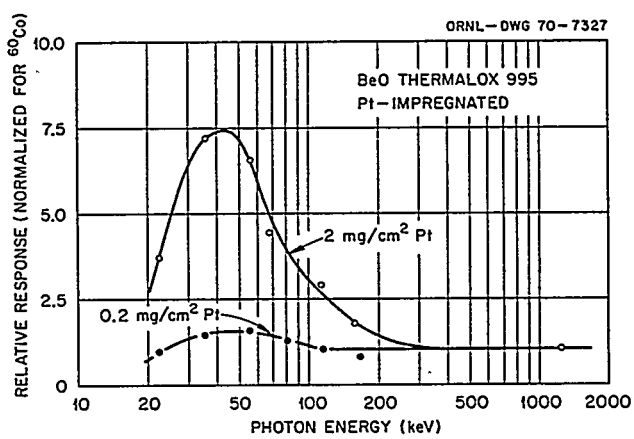

Fig. 16.16. Relative Response as a Function of Photon Energy in Ceramic BeO Impregnated with Different Amounts of Pt.

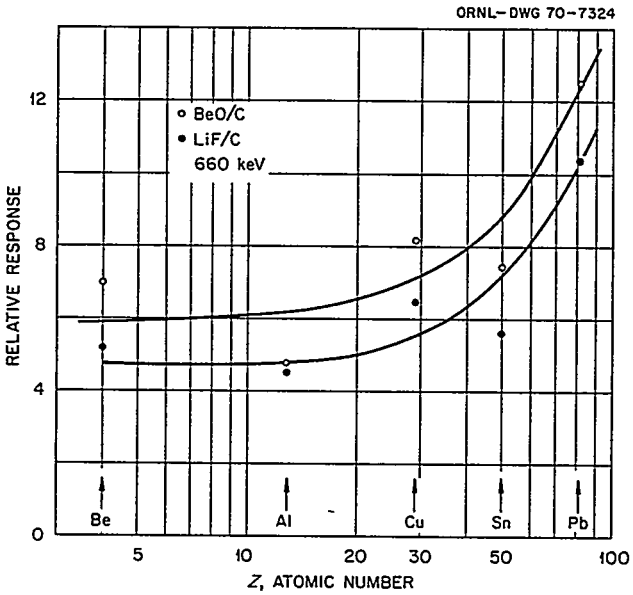

Fig. 16.17. Relative Response of LiF/Graphite and BeO/Graphite Detectors to 660-keV Photon Radiation as a Function of the Z of the Dosimeter Cover.

carried out with 660-keV gamma radiation, and layers of different Z covering the detectors. The thickness of the layer was sufficient to establish electron equilibrium but absorbed only a negligible fraction of the radiation. The results (Fig. 16.17) indicate a sensitivity increase only by about a factor of 2 due to the increase in Z from 4 to 82 in both LiF/C and BeO/C detectors.[11]

Neutron Response

The thermal- and fast-neutron sensitivity of BeO is very small. Impregnation with gold increases the thermal-neutron response slightly because of its activation. The integrated flux of fast neutrons can be measured in mixed neutron and gamma radiation fields with the following detection principle: Using a pair of identical detectors which are sensitive to both low- and high-LET radiation but have low inherent fast-neutron sensitivities due to the absence of hydrogen, one of the detectors is in intimate contact with a hydrogenous material, while the other is surrounded by a material having a small fast-neutron cross section. The difference between the number of exoelectrons released from the first detector, representing the sum of photon and recoil proton effect, and from the second detector, representing essentially only the effect of the photon (gamma or x-ray) dose, is a measure of the fast-neutron dose.

The recoil proton "radiator" can be a gaseous (e.g., an organic gas), liquid, or solid hydrogenous material. In most of the experiments, solid radiators have been used. Sets of gold-treated BeO detectors were covered with 1 mm of polyethylene and 1 mm of reactor-grade graphite, respectively, and exposed frontally to a fluence of 6×10^6 to 2×10^7 monoenergetic, monodirectional fast neutrons per square centimeter from the reactions $^7Li(p,n)$ (60 and 100 keV), $^3H(p,n)$ (0.2, 0.5, and 1 MeV), and $^3H(d,n)$ (16 MeV) at a distance of 10 cm from the target of a Van de Graaff generator. The fluence was determined by means of a calibrated long counter.

No significant absorption of recoil protons was anticipated in the thin air layer between radiator and detector in this energy range. For lower neutron energies, however, a more intimate contact with liquid or gaseous radiators is preferable. The detectors were read by heating each one at a rate of 1°C/sec up to 360°C, well above the ~285°C single peak in these detectors (Fig. 16.18). The net counts of the detectors were weighted by their calibration factors for ^{60}Co gamma radiation and averaged, and the difference was expressed in roentgens gamma response equivalent and then divided by the absorbed dose for fast neutrons in tissue as calculated from kerma. The results, as summarized in Fig. 16.19, indicate an increase in the fast-neutron sensitivity of this system from ~0.18 at 100 keV to ~0.28 of the gamma radiation response at 16 MeV. Depending on the neutron-gamma ratio, the neutron energy, the detector sensitivity, and the reproducibility of the detector response, the lower detection limit for fast neutrons in this dosimeter is between 10^{-5} and 10^{-3} rad.

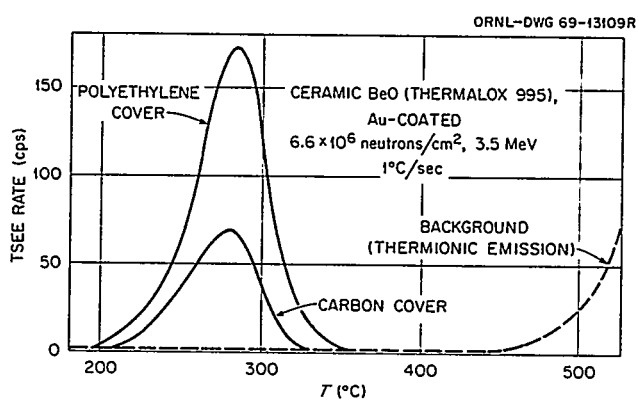

Fig. 16.18. TSEE Curve of Au-Treated BeO Detector Pairs Covered with Graphite and Polyethylene, Exposed in a Mixed Fast-Neutron/Gamma Radiation Field. Low-temperature peak location corrected for temperature gradient in sample.

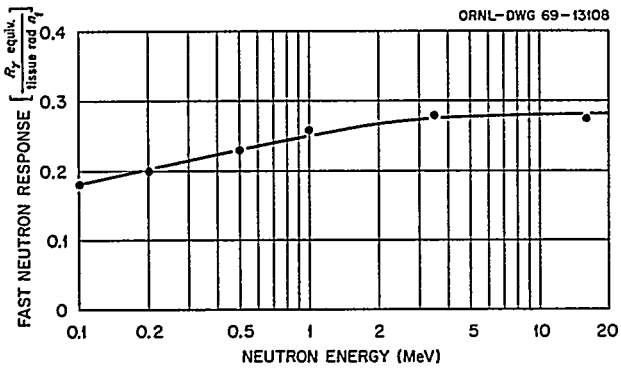

Fig. 16.19. Energy Dependence of the Fast-Neutron Response via Recoil Proton Registration of Polyethylene-Covered Au-Impregnated Ceramic BeO.

Metal-treated as well as graphite-mixed BeO is less sensitive to radiations of high LET, such as recoil nuclei and alpha radiation, than to low-LET gamma and electron radiation. No pronounced LET dependence of the TSEE peak locations and peak-height ratios comparable with that in other detector materials has been observed in the ceramic BeO. A number of other dosimetric properties of this material have not yet been studied. It can be expected that there will be little, if any, dose-rate dependence of response.

Miscellaneous TSEE Studies

As a part of a project to understand the mechanism of the different LET dependence of the radiation response in TSEE detectors and perhaps to find materials with such a pronounced LET dependence of the peak ratio that they can be used for discrimination against high- or low-LET radiations, the TSEE in several more "exotic" compounds has been tested. For example, extremely pure powdered samples of MoO_3, ZnS, $BaTiO_3$, BN, ZrO_2, La_2O_3, CdSe, CdS, CeO_2, ZnSe, ZnO, and Ag-activated ZnS exhibited only a very small, if any, TSEE sensitivity. More interesting but also not very sensitive were MgO and high-fired (1 hr at 1000°C) Al_2O_3.

Magnesium oxide (Fig. 16.20) exhibited a main peak around 400°C. If exposed to alpha radiation, an additional peak around 120°C appeared. Those experiments are presently being repeated with pressed and sintered ceramic MgO impregnated with metals. In an electron-exposed ceramic Al_2O_3, a small peak at 310°C and a large peak at 520°C have been observed (Fig. 16.21). This material appears to be particularly suitable for dosimetry at high temperatures. Metal sensitization and LET response of this material are presently under study.

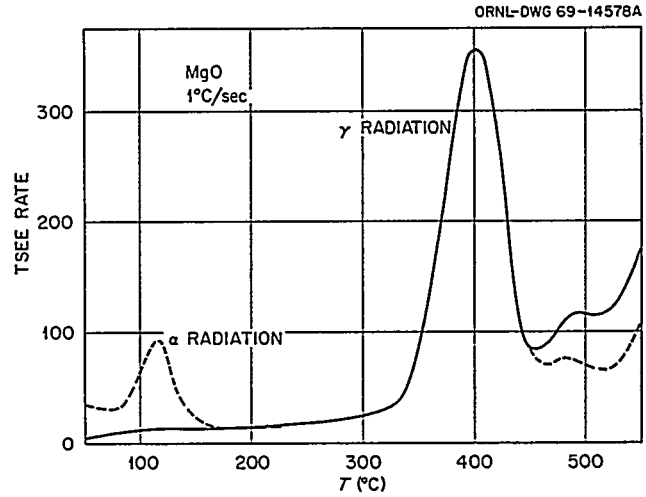

Fig. 16.20. TSEE in a Magnesium Oxide After Exposure to Gamma and to Alpha Radiation.

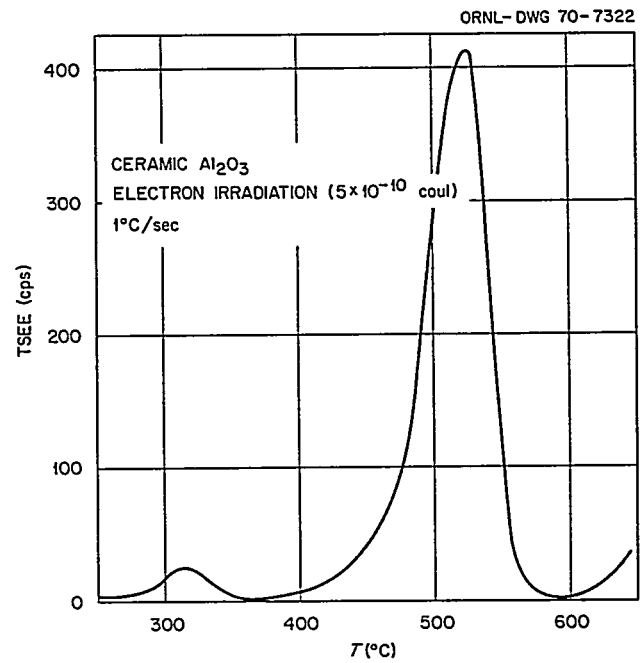

Fig. 16.21. TSEE in a Ceramic Al_2O_3 After Electron Exposure.

TSEE from Lunar Minerals

So far, most of the TSEE research has been concerned with relatively simple ionic crystals, in particular, metal oxides, halides, and sulfates. In only one paper to date,[12] describing TSEE and thermoluminescence (TL)

[12] D. R. Lewis, *Geol. Soc. Am. Bull.* 77, 761 (1966).

in limestone and halite, are possible applications of TSEE in geological research discussed. The author concludes that effects of tectonic activity, stored stress energy, mineral composition, and thermal history are reflected in TSEE curves. In view of the widespread application of TL in geological studies, it is surprising that the closely related technique of TSEE has not been used to a larger extent. TSEE appears to be superior to TL, primarily because:

1. TSEE can be much more sensitive.
2. TSEE seems to be a more widespread phenomenon than TL, and frequently more TSEE than TL peaks are observed in a given material.
3. Measurements do not, as in TL studies, become increasingly difficult at temperatures exceeding 300 to 400°C due to infrared emission, but are limited only by thermionic electron emission beginning, depending on a material's work function, around ~500 to 700°C, thus permitting studies of deeper and therefore thermally more stable trapping levels.
4. TSEE permits the study of extremely thin surface layers without (or with very little) interference from the bulk of the material.
5. TSEE is unaffected by light absorption in a material, which would cause a reduction in the TL output.

In order to check the TSEE from some terrestrial minerals, some tests with U.S. Geological Survey standard rock powders have been performed.[13] Dunite DTS-1, andesite AGV-1, granodiorite GSP-1, basalt BCR-1, and granite G-2 have been used. Of those, only basalt did not exhibit any peaks. The other minerals showed peaks around 150 and 250°C and/or around 450 to 500°C (Fig. 16.22). Thermionic (glow) electron emission increased the background rapidly above 580 to

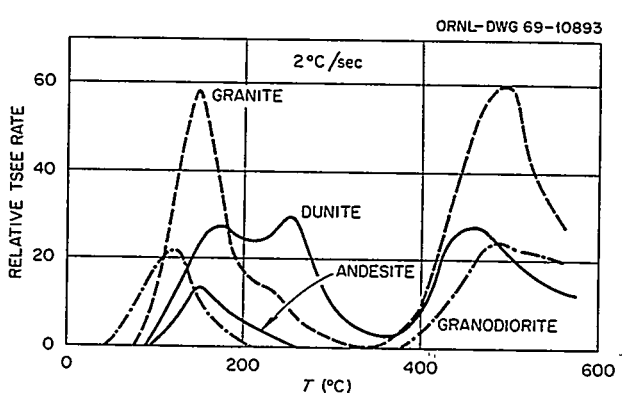

Fig. 16.22. TSEE from Different Rock Powders After Exposure to Gamma Radiation.

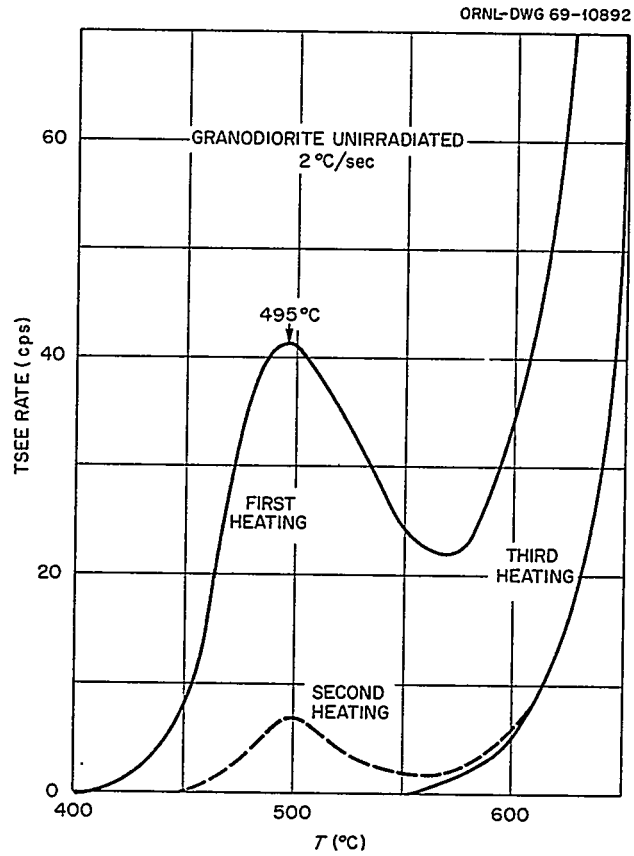

Fig. 16.23. TSEE from Unirradiated Virgin Granodiorite During Consecutive Heating Cycles.

660°C, depending on the material. At least one material, granodiorite, also exhibits a pronounced peak at 495°C in the unirradiated material (Fig. 16.23), probably due to the accumulated radiation dose in this material. As is to be expected from the thermal fading rate, only a slight peak at ~150°C was observed in the unirradiated granodiorite. If the heating was cut off at 650°C, a second heating cycle of unirradiated powder frequently produced a much smaller peak at ~500°C due to insufficient annealing during the first heating.

Based on these results, experiments with lunar minerals were initiated. It was thought that TSEE could be a more interesting tool than TL (which had been studied by several Principal Investigators in the Apollo Program) to study samples with respect to:

1. radiation history, for example, as a function of depth;

[13] K. Becker, "Thermally Stimulated Exoelectron Emission from Terrestrial and Lunar Minerals," ORNL-TM-2869 (1970).

2. thermal history (annealing of high-temperature peaks), with possible implications for the dating of the minerals;
3. surface trap density and radiation damage;
4. detection of small amounts of strong TSEE emitters;
5. phenomena related to mechanical deformation, stress, etc. ("tribo-TSEE"), which are known to affect TSEE.

A small sample (~10 mg) of slightly granular lunar fines which was thought to represent a reasonable cross section of the different minerals from Apollo 11, specified as No. 9, 10065-20, was used for the first TSEE experiments with lunar soil. The grain size was large enough to permit the reasonably homogeneous distribution in the central recess of a graphite sample holder, but small enough so that no significant distortion of the "glow" curves due to insufficient heat transfer was anticipated. The small size of the sample did, however, only permit a limited number of experiments.

During heating of the virgin, unirradiated material only a small (if any) increase of the background count was obtained. After exposure to a high gamma radiation dose (1.25×10^6 R ^{60}Co), an integral count of 1.15×10^4 over background at 600°C was obtained. This count did not decrease much with dose down to ~10^3 R.

The TSEE in preirradiated lunar material occurred in three distinct peaks (Fig. 16.24) which, for a heating rate of 1°C/sec, were located at 142, 268, and 465°C.

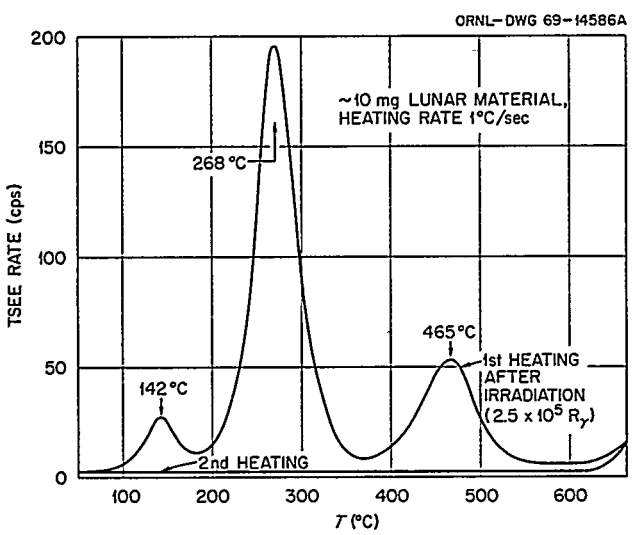

Fig. 16.24. TSEE Rate as a Function of Temperature During Linear Heating at 2°C/sec of Preirradiated Lunar Fines from Apollo 11.

Repeated heating of the same sample resulted in no increase in background. Thermionic electron emission began to occur around 625°C, depending somewhat on the heating rate. The location of all three peaks shifted, as expected, to higher temperatures with increasing heating rate. This shift, known as Randall-Wilkins shift in thermoluminescence research, can be used for determination of the activation energy.

A wider variety of lunar materials from Apollo 12 became available after approval of the TSEE research proposal by NASA, including fines from different locations, core tube samples from different depths, and several rock fragments including one, 12065,64, which exhibited two micrometeorite impacts. The more systematic investigation of TSEE from these samples is still in an early stage, and only a few preliminary results concerning surface fines 12033 and 12070 can be reported here.

In both samples, no TSEE was observed during the irradiation of the virgin material. In order to decide whether this was due to the annealing of the stored radiation effect by the combination of intense light and high temperatures during the lunar day or to an inherent "insensitivity" of the material, a virgin unheated sample of 10 mg 12033 was irradiated with 10^5 rads of ^{60}Co gamma radiation and heated. No TSEE was observed, indicating an insensitivity in addition to the annealing. After reirradiation of the same sample, however, a second heating cycle produced 5.5×10^4 net counts between 75 and 600°C with several distinct peaks (Fig. 16.25).

Further irradiation and heating cycles produced a continuous increase of sensitivity, in particular, if the temperature was held at 650°C in the counter (in an atmosphere consisting of 99.05% He and 0.95% isobutane) for longer than the normal heating cycle required. During consecutive irradiation/heating cycles, the peak locations did not vary and were, at a heating rate of 1°C/sec, at ~150, ~210, ~283°C, and about 490 and 560°C for the ill-resolved two high-temperature peaks. It was, however, observed that peaks grow with different speed during the heat treatment, and some peaks apparently reach a "saturation" level while others are still growing.

In another surface fine sample (12070) with a slightly brownish color (12033 was initially purely gray but became brownish during the heatings and irradiations), a similar behavior was observed (Fig. 16.26). The lower two peaks (~150 and ~210°C) are identical with those in 12033, but instead of the third peak a double peak occurs at ~290 and ~310°C. There seems to be only one high-temperature peak around 460°C. The different

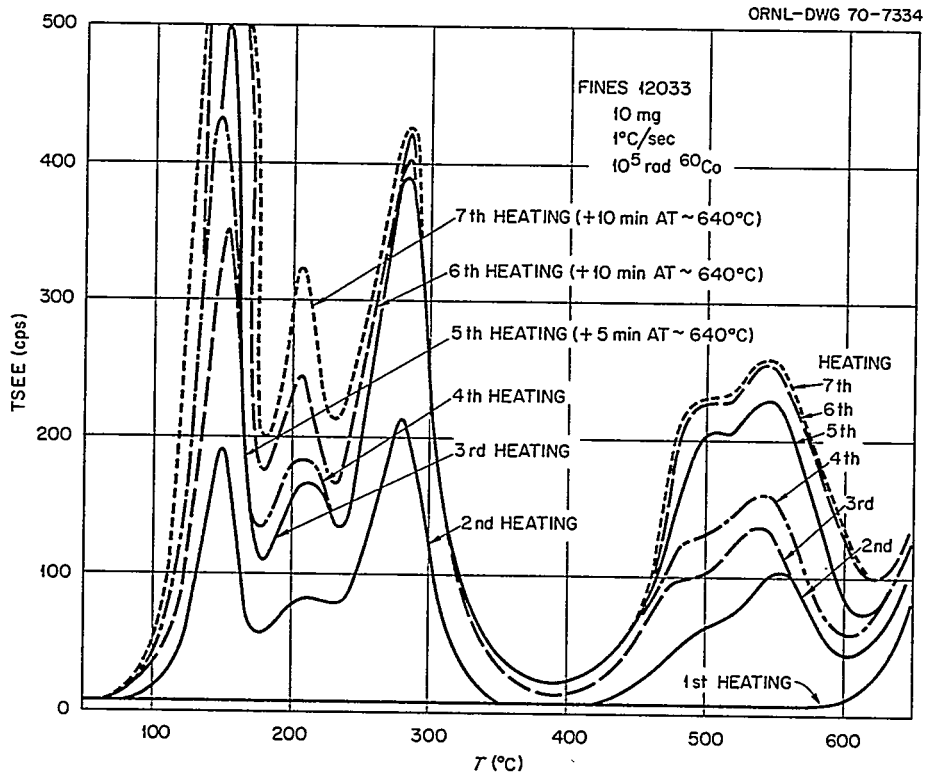

Fig. 16.25. TSEE from Preirradiated (10^5 Rads ^{60}Co) Lunar Fines from Apollo 12 (Sample 12033) During Consecutive Heating Cycles and More Extensive Heating to ~650°C.

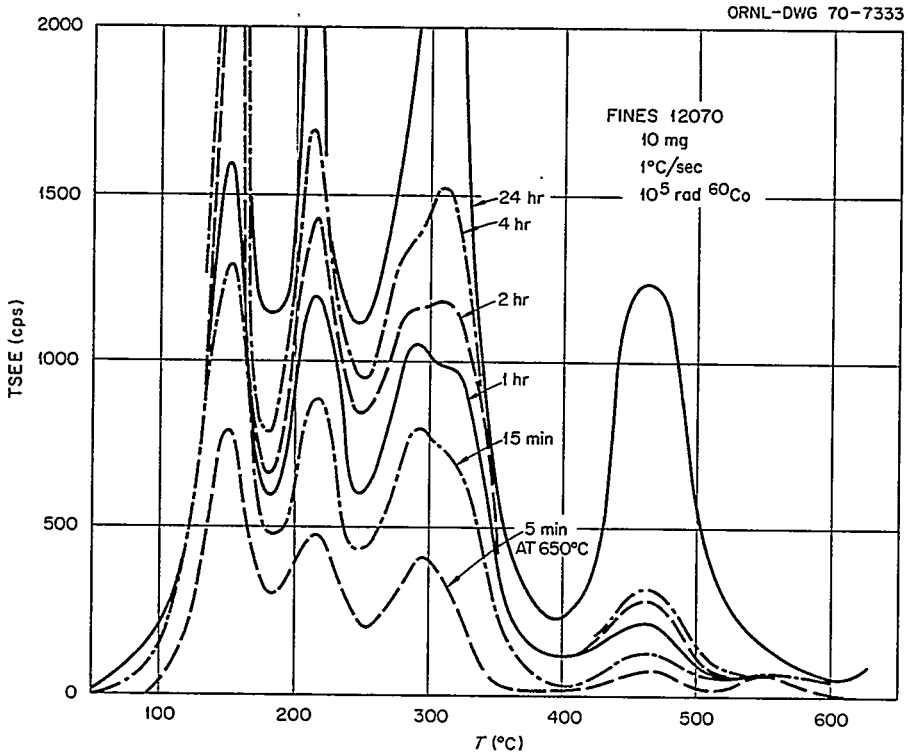

Fig. 16.26. Increase of TSEE in Preirradiated Lunar Fines 12070 During Consecutive Heating in Air at 650°C.

peak growth during heating is obvious in the development of the 290/310°C double peak. In this experiment the heating was carried out in air for extended periods. As illustrated in Fig. 16.27, the total sensitivity increase is a linear function of log heating time. Sample 12070 is more sensitive than 12033.

There are several possibilities to explain this behavior. It appears not to be related to humidity effects (the samples had been exposed to the atmosphere for at least several weeks), because a virgin sample that was stored for 17 hr at 10^{-5} torr at 100°C was after this treatment, which should have removed the physically absorbed water, still insensitive. Etching ("peeling") experiments will decide whether the insensitivity is caused by (1) the release of solar wind from the uppermost layers, which could interfere with the exoelectron emission process, or (2) the initial absence of exoelectron-emitting species in the sample, which are only formed by the heat treatment.

After extended heating, additional heating cycles have only little effect on the sensitivity, and the response becomes reproducible within a few percent. The response is a nonlinear function of exposure (Fig. 16.28). The peak ratio changes as a function of exposure, resulting in a different growth rate for the low-temperature and the high-temperature peaks. The peak temperature increases with increasing heating rate (Fig. 16.29). Preliminary results with sample 12070 indicate that both TSEE sensitivity and peak ratio depend on the size fraction.

In an attempt to measure the specific surface area, 50 mg of virgin 12033 fines were outgassed at temperatures up to 300°C at 10^{-5} torr. Negligible absorption of N_2 indicated the absence of submicron-size particles and any pore structure.

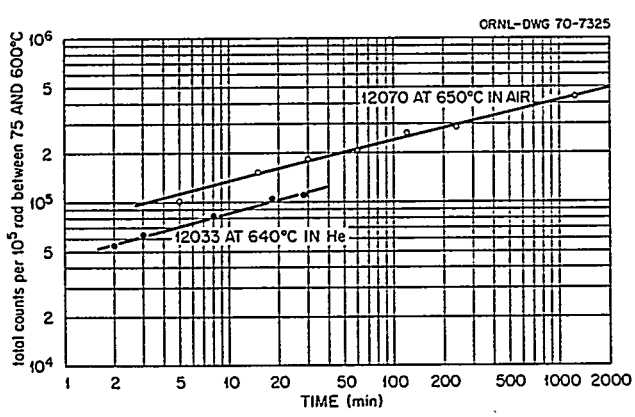

Fig. 16.27. Total Response (Net Counts Between 75 and 600°C) of Two Samples of Lunar Fines from Apollo 12 as a Function of Heating Time in Air or Counting Gas.

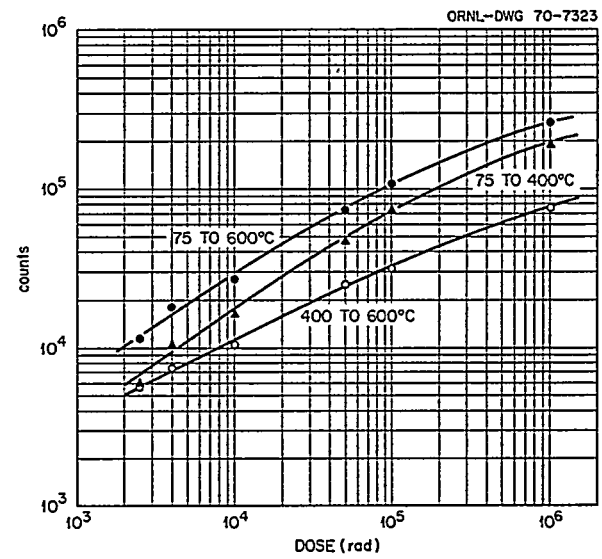

Fig. 16.28. Total Response and Growth of the Low-Temperature and the High-Temperature Peaks in a Preheated Lunar Fines Sample (12033) as a Function of the Gamma Radiation Dose.

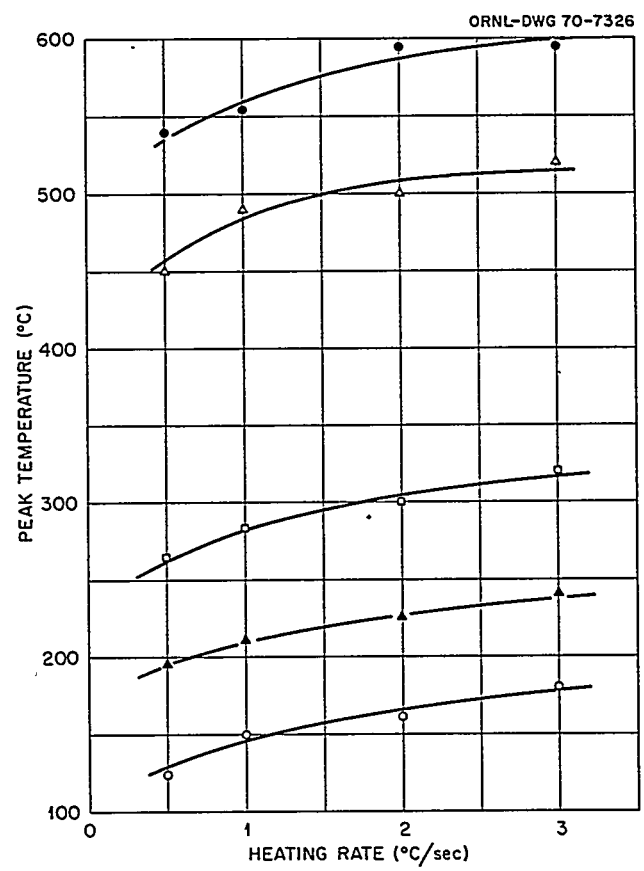

Fig. 16.29. Dependence of the TSEE Peak Location in Lunar Fines Sample 12033 on the Heating Rate.

NUCLEAR TRACK REGISTRATION IN POLYMERS

Neutron-Induced Autoradiography (NIAR)

It was already mentioned briefly in the last annual report[14] that, with a combination of two techniques: (1) alpha-particle or fission fragment registration in thin polymer foils by etching and (2) automatic counting and magnification of the etched perforations by local evaporation of a thin metal layer with an electric spark, the sensitivity of conventional photographic methods for determining quantity and spatial distribution of alpha emitters, fissile materials, and of elements undergoing (n,α) reactions can be drastically improved, without need for darkroom processing and microscopic evaluation. Further investigations of this technique[15,16] revealed that its use is not restricted to the measurement of the quantity and spatial distribution of small amounts of fissile elements in solids such as bone samples, but it can also be used for microanalysis of liquids and gases.

As an illustration of such an application, 1 cm^3 of distilled water and 1 cm^3 of Oak Ridge tap water were evaporated onto a detector film prior to exposure to a thermal-neutron fluence of 1.3×10^{15} neutrons/cm^2. The distilled water showed essentially background (150 counts), while the tap water sample exhibited 650 counts in a well-defined spot, which corresponded to 1.4×10^{-13} g of natural uranium per cubic centimeter of water (Fig. 16.30). The sensitivity, accuracy, and convenience of this method considerably exceeds microscopic counting because tracks in a much larger area can be completely counted in a short time. Using microscopic track counting, a detection limit of about 2×10^{-12} g/cm^3 was claimed for uranium,[17] whereas in the current experiments the sensitivity was at least a factor of 100 better with a further increase easily possible, mainly because of the spark-counting technique.

[14] J. A. Auxier *et al.*, *Health Phys. Div. Ann. Progr. Rept. July 31, 1969*, ORNL-4446, p. 266.

[15] K. Becker and D. R. Johnson, *Science* 167, 1370 (1970).

[16] D. R. Johnson and K. Becker, *Mechanisms and Applications of Nuclear Track Registration in Polymers*, ORNL-TM-2826 (1970).

[17] R. L. Fleischer and D. B. Lovett, GE-68-C-098 (1968).

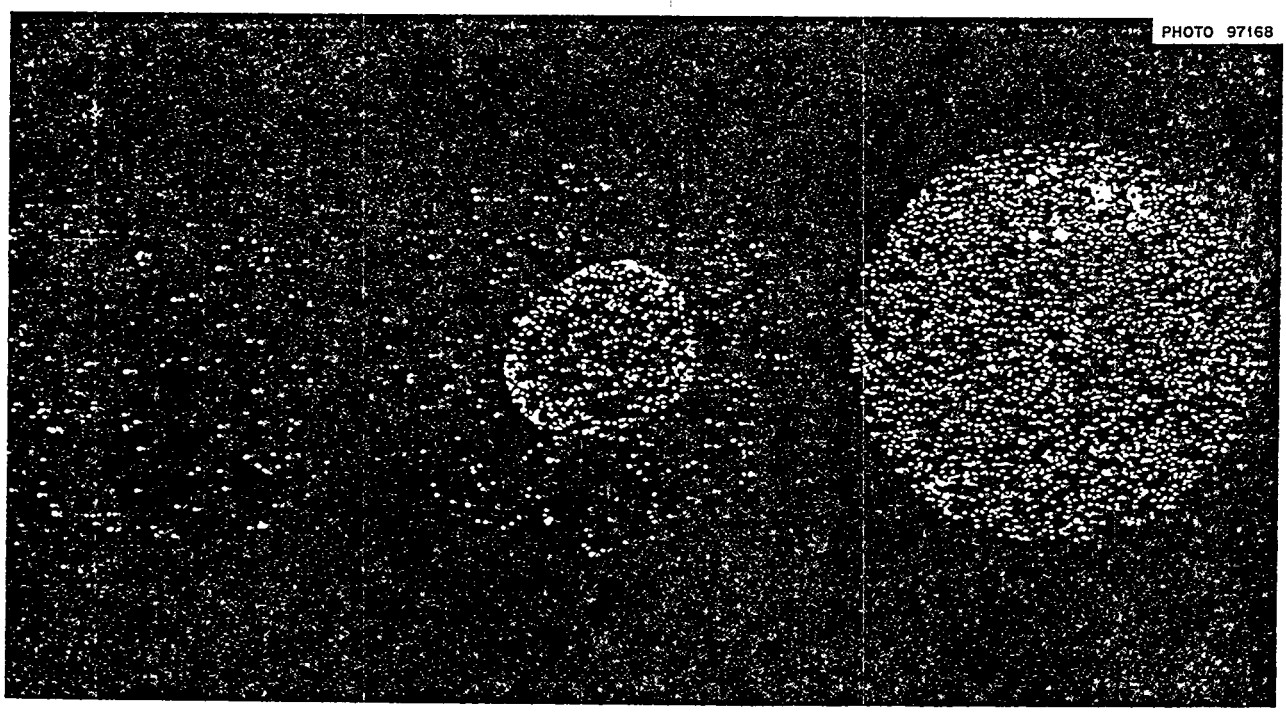

Fig. 16.30. Sparked "Replicas" of 1 cm^3 of Distilled Water (Left) and Oak Ridge Tap Water (Middle) Evaporated on a 10-μ Polycarbonate Foil, Irradiated with Thermal Neutrons, Etched, and Sparked; Replica of a Filter Through Which 8 m^3 of Air Passed (Field Diameter 20 mm), Right.

If untreated urine is evaporated on a detector film, a relatively thick layer of solid residue (mostly organic) remains, which causes self-absorption of the fission fragments. This difficulty can be overcome by destruction of the organic material prior to evaporation of the sample or by the use of smaller or diluted urine samples.

In Fig. 16.30 the sparked "image" of a standard piece of Whatman filter paper through which 8 m^3 of air had passed is also given. Obviously, the method is sensitive enough for accurate measurements of natural concentrations of fissile elements in air. Using alpha-sensitive films, samples can be analyzed in a similar manner for boron, lithium, or other elements which undergo (n,α) reactions with thermal neutrons. The high sensitivity of the method permits its use for tracer studies in hydrology, meteorology, and ecology.

Attempts have been made to use the different cross sections of fissile materials (or elements undergoing n,α reactions) at different neutron energies for the discrimination against certain elements, or for a determination of their ratio in samples, by exposing them to a high fluence of fast neutrons. Unfortunately, the usability of fast-neutron-induced reactions is limited by the following effect, which results in a breakdown (rapid dissolution) of thin foils during etching after exposure to a high fluence of fast neutrons.

It was known that the bulk etch rate of cellulose nitrate and polycarbonate foils in KOH is increased after gamma radiation exposures in the 10^7-to-10^9-rad range. In order to study the LET dependence of this effect,[18] foils of four different polymers have been irradiated under secondary particle equilibrium conditions with different doses of gamma radiation from a ^{60}Co source and with fast fission neutrons from the unshielded Health Physics Research Reactor. After irradiation, they were etched with 28% KOH at increased temperatures:

1. cellulose nitrate (15 μ, Hercules Pyro Smokeless) at 40°C,
2. cellulose triacetate (500 μ, Triafol T, Bayer) at 60°C,
3. polyethylene terephthalate (13 μ, Mylar, Kimberley-Clark) at 60°C,
4. dioxidiphenyl-propane polycarbonate (10 μ, Makrofol or Kimfol Bayer and Kimberley-Clark) at 60°C.

[18] R. H. Boyett and K. Becker, "LET Effects on the Chemical Resistance of Irradiated Polymers," *J. Appl. Polymer Sci.* 14, 1654 (1970).

The increase in etching speed has been expressed in percent weight loss per hour of etching in excess of that of the unirradiated control films and plotted as a function of dose (Fig. 16.31). Obviously, the neutron dose required for a given foil weight reduction is less than the gamma dose by a rather large factor. This factor depends on dose because the neutron radiation damage is a supralinear function of dose.

The considerable LET dependence may be explained by preferential etching along recoil particle tracks, which are produced by elastic neutron interaction throughout the polymer. Recoil protons (with the possible exception of those close to the Bragg peak in cellulose nitrate) are below the preferential etching threshold, but recoil carbon, oxygen, and nitrogen nuclei are above the threshold in all the polymers investigated. Based on previous experiments concerning the production of etchable recoil particle tracks in

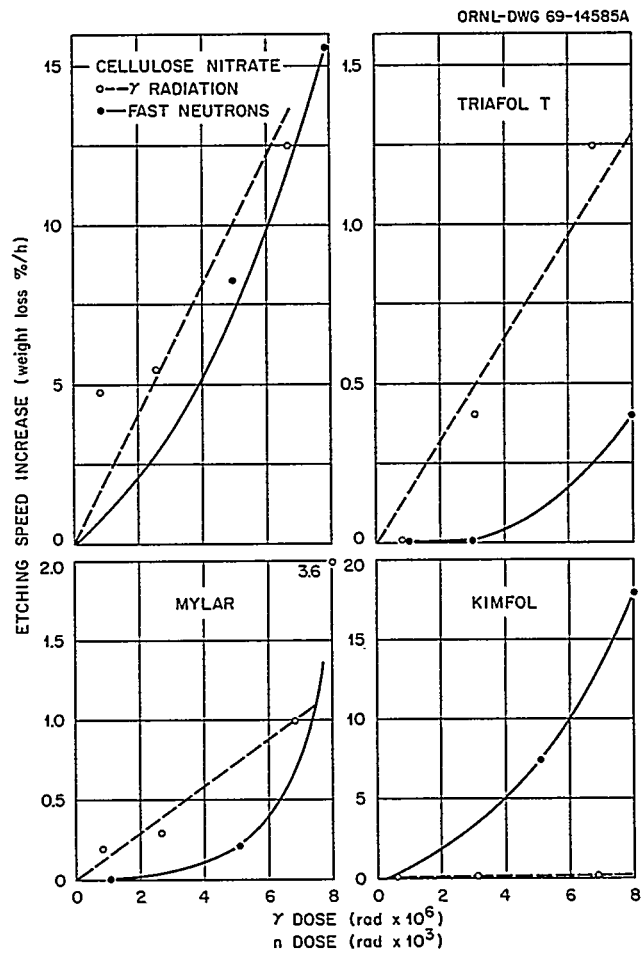

Fig. 16.31. Increase of Bulk Etching Rate in Gamma- and Fast-Neutron-Irradiated Polymers as a Function of Dose.

polymers by fission,[19] the density of recoil tracks can be estimated to be about 10^7 per square centimeter on each plane perpendicular to the direction of incident neutrons after a dose of 5000 rads (these experiments yielded 0.3×10^{-5} track per neutron in Makrofol and 1.1×10^{-5} track per neutron in cellulose nitrate). If one assumes a diameter of several microns for each preferential etch pit after the initial etching phase is completed (new tracks become accessible to the etchant continuously as the etching proceeds), a considerable increase in the bulk etching rate is understandable.

The rapid breakdown of polymers under attack by chemical etchants, which have been exposed to charged particles of high LET, is also of some interest with regard to the resistance of polymers in space radiation environments, nuclear weapons radiation effects, and in nuclear reactors or accelerators. Perhaps there are also applications to charged-particle dosimetry.

The principle of NIAR can also be used in a detector system for thermal- and fast-neutron radiography (imaging of neutron fluence distributions). A combination of a detector film with either a thin fissile converter foil or a material undergoing (n,α) reactions has been used in such experiments. The choice of additional, selective absorber foils such as cadmium permits the use of certain neutron energies. The high sensitivity of NIAR permits the use of low neutron fluences. If a ^{235}U converter foil is employed, as few as 10^7 fast or 10^5 thermal neutrons per square centimeter cause approximately 100 detector holes per square centimeter, resulting in sufficient contrast and resolution for many cases. Other advantages are that this detector system, unlike the widely used photographic film, is almost insensitive to gamma and beta radiation, it needs no darkroom processing, and many replicas can be made quickly from the original etched film by repeated sparking of new aluminized Mylar foils. The replicas can be used directly as slides or as "negatives" for photographic enlargements. A spark counter with a larger diameter has been used for neutron radiography experiments.

Alpha-Particle Registration in Cellulose Nitrate

In order to use the spark-counting technique for high-efficiency detection of alpha-particle tracks, the cellulose nitrate foil preparation techniques had to be further optimized. For example, the effect of a free-radical scavenger, diphenylpicrylhydrazyl (DPPH), on the foil sensitivity has been studied.[16] Although some "fading" (reduction of the DPPH concentration in the films during storage) occurred due to thermally induced free-radical production and/or addition reactions across the double bonds in the plasticizer used, the additive was generally compatible with the cellulose nitrate films and functioned well as a radical scavenger despite the restricted diffusion in the solid matrix. Films doped with DPPH at a concentration of 5×10^{-2} *M* and undoped controls were used to determine alpha track etching curves. Best results were obtained with films freshly annealed for 16 hr at 80°C.

If the cellulose nitrate foil was exposed to almost monoenergetic alpha particles of ~4 MeV and etched for various times in 30% KOH at 40°C, the resulting etching curve for DPPH-doped films was parallel to, but offset downward in sensitivity from, that for undoped films (Fig. 16.32). The DPPH-doped films showed a decrease in sensitivity, as would be expected from the neutralization of at least some of the free radicals

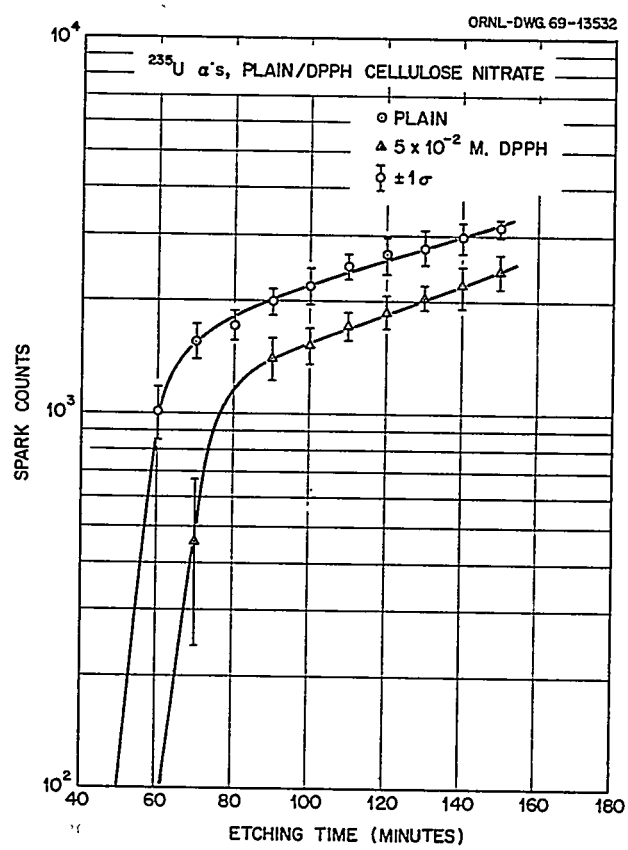

Fig. 16.32. Spark Counts vs Etching Time in 30% KOH at 40°C for Standard and DPPH-Containing Cellulose Nitrate Films.

[19] *Health Phys. Div. Ann. Progr. Rept. July 31, 1969,* ORNL-4446, p. 265.

generated in the tracks, thus substantiating the radiolytic damage mechanism of latent track formation in polymers.

One possible alternative explanation of the reduced sensitivity caused by DPPH is that it might act as an auxiliary plasticizer and augment the effect of the regular plasticizer, DOP, in reducing the bulk etch rate of cellulose nitrate films. The bulk etch rate was studied as a function of plasticizer concentration (the plasticizer in polymer track detectors slows the bulk etch rate and thus reduces the cone angle of etched tracks). Films containing 0, 20, 40, 60, and 80 mg of DOP, 5 mg of DPPH (the amount present in films containing 5×10^{-2} *M* DPPH), and 5 mg of DPPH plus 60 mg of DOP were prepared. The bulk etch rate R_b of each type of film was determined by measuring the elapsed time required for complete dissolution in the etchant. The results are summarized in Table 16.1.

It can be concluded that (1) ~60 mg of DOP per film is optimum because R_b goes through a minimum at this concentration, and (2) the plasticizing effect of 5×10^{-2} *M* DPPH amounts to a decrease in R_b of approximately 10%.

In other experiments the oxygen effect on the foil sensitivity, which is pronounced for microscopic track counting,[20] was studied with the spark-counting technique. No oxygen effect was discernible when spark counting was used for track counting. Studies using both a thick ^{238}U foil with a continuum of alpha particle energies as well as monoenergetic alpha particles from a thin point source of ^{241}Am failed to show any detectable oxygen effect, the criterion being the number of spark counts obtained after optimum etching from films exposed in air, compared with those exposed in an identical geometry, only in a pure nitrogen atmosphere (after several evacuation and flushing operations).

This is possibly due to the fact that the spark counter also serves as an active participant in the track development process (spark punching). The spark counter uniformly enlarges all tracks which are larger than a certain threshold size, whereas microscopic counting is strictly an analytical procedure having the added feature of being able to detect small differences in track dimension and shape. It is therefore possible that the changes in track density, size, and etching speed associated with the oxygen effect are too subtle to be detected reliably by spark counting. For practical applications, insensitivity to such environmental factors may be advantageous because, in general, the fewer the number of environmental factors that must be controlled, the more reliable a radiation detector becomes.

Table 16.1. Effect of Film Composition on the Bulk Etch Rate

Film Composition	Time Required for Dissolving (hr)	Bulk Etch Rate, R_b (μ/hr)
Plain cellulose nitrate	1	15.0
20 mg DOP/film	1.75	8.6
40 mg DOP/film	4	3.75
60 mg DOP/film	5	3
80 mg DOP/film	4	3.75
5 mg DPPH/film	1.5	10.0
60 mg DOP plus 5 mg DPPH	5.5	2.73

Detector efficiency for alpha particles from a thin ^{235}U source was essentially 100% after an optimum etching time of 2 hr. The useful dynamic range using the spark counter is limited to about 5000 tracks/cm^2 due to eventual loss of virtually all the aluminum of the aluminized Mylar during the sparking process (the evaporated spots are two orders of magnitude larger in area than the corresponding detector holes). The linearity of the system was quite good up to approximately 3000 tracks/cm^2, after which the precision became rather poor.[21] A somewhat smaller evaporated spot size was obtained using thicker-coated aluminized Mylar; however, there was an increased tendency toward multiple sparking through individual holes as the evaporated spot size was reduced.

In fission fragment spark counting with polycarbonate films, only a very small "background" count from unexposed etched films has been observed. For alpha-particle track counting in the more sensitive cellulose nitrate films, however, the background can be substantial due to two effects. First, preferential etching of imperfections in the plastic matrix such as dust particles, residual lint fibers, and miscellaneous debris seems to cause some of the background counts. These undesirable contaminants are readily visible to the naked eye and are remarkably difficult to remove from stock solutions prior to pouring films. Even fritted glass filtration of diluted stock solutions failed to remove all this debris. After an optimum etching of 2 hr at 40°C, a typical background of 50 to 100 counts/cm^2 is obtained. If etching is extended beyond 2 hr, the background count increases rapidly because the thresh-

[20] R. H. Boyett, D. R. Johnson, and K. Becker, *Radiation Res.* 42, 1 (1970).

[21] D. R. Johnson and K. Becker, *Health Phys.*, in press.

old thickness for electrical breakdown of the films is approached.

Second, it was observed that, when films had been stored for over a month, background counts of 300 to 500 resulted after optimum etching. This may have been due to the combined effects of alpha-emitting contaminants, either in the paper used to sandwich and store the films or in the air, and cosmic radiation. The fact that the increased background counts could be reduced to normal by thermally induced fading at 80°C (annealing) indicated that they represented latent tracks. Overnight annealing of all films prior to use is advisable for sensitive measurements.

Preirradiation of polymer foils with ultraviolet or low-LET ionizing radiation did not increase their track registration sensitivity. In some cases, it even caused a reduction in sensitivity. Postirradiation treatment with short-wavelength uv of cellulose nitrate resulted in some increase of the etching speed, but no enhancement of the alpha registration efficiency.

Alpha Autoradiography with Cellulose Nitrate

In alpha autoradiography studies of a beagle bone sample containing ^{226}Ra, a high-resolution good-contrast directly visible autoradiograph was obtained without sparking, if the sample has been exposed to a 15-μm cellulose nitrate film as long as required to obtain a photographic autoradiograph and etched for 2 hr in 28% KOH at 40°C (Fig. 16.33). The high alpha track density permits a significant reduction of ex-

PHOTO 97474

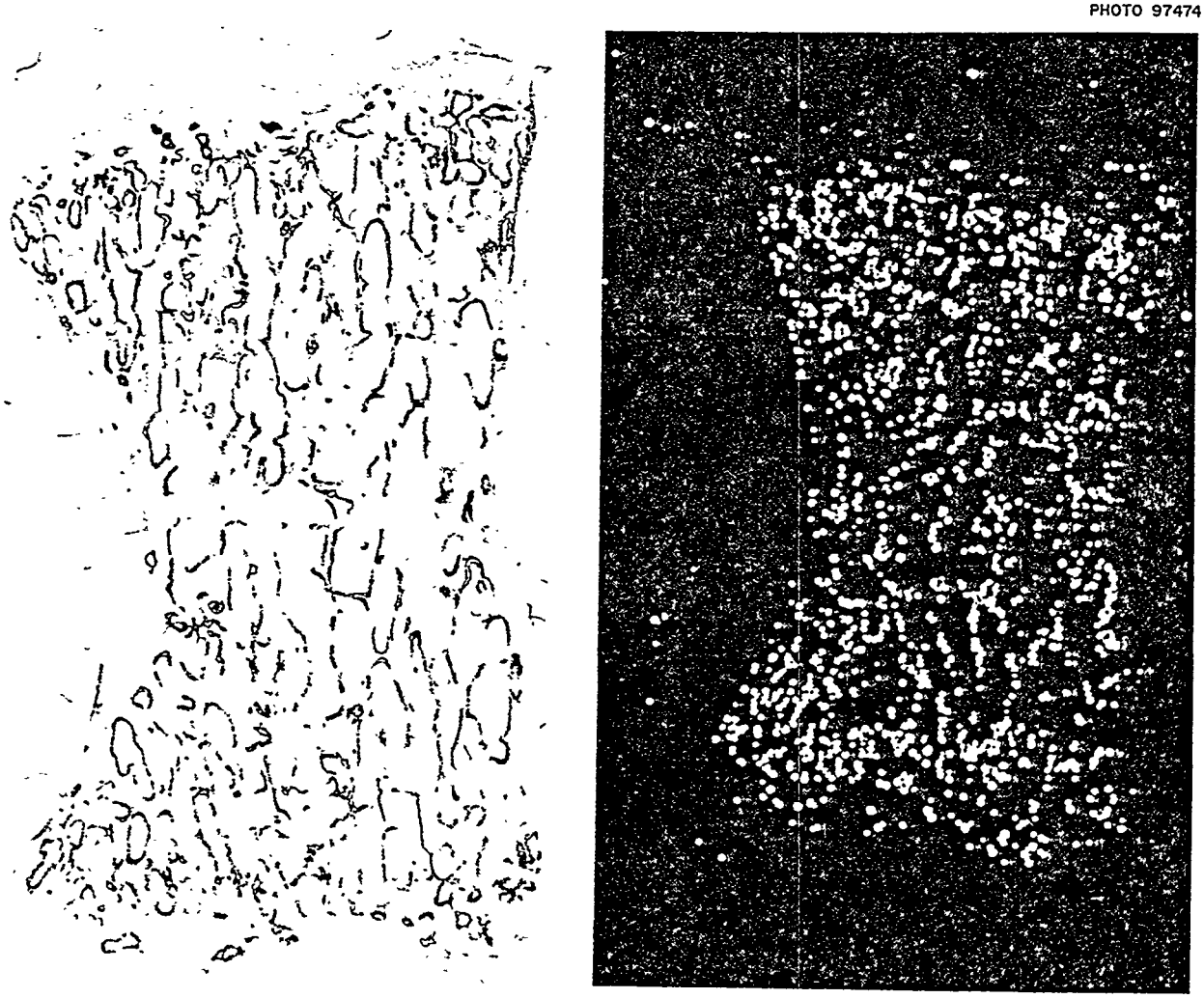

Fig. 16.33. Alpha Autoradiograph of a Beagle Bone Sample Containing ^{266}Ra in a 15-μm Cellulose Nitrate Foil. Left, after exposure time equivalent to that required for photographic alpha autoradiography and etching but without sparking; right, spark image of the sample after reduction of exposure time by a factor of 30.

posure time if the sample is to be sparked for evaluation. A reduction by a factor of 30, for instance, still results in a good spark image (Fig. 16.33), and the spark count (2200) is sufficient for an accurate determination of its ^{226}Ra content. Obviously, this technique permits a considerable reduction in exposure time (or increase in sensitivity), if high resolution is not required in quantitative experiments, and has the additional advantage of obviating the necessity for darkroom and microscope work. For samples containing fissile materials, it would replace exposure times of several months by an equal number of days, with no need for neutron exposure.

Radon Progeny Personnel Dosimeter

The principle of an "active" radon daughter product personnel dosimeter for uranium miners has been described briefly in a previous report.[22] Based on the results of tests of the prototypes carried out in cooperation with the AEC Health and Safety Laboratory, a larger number of an improved version was prepared for the final laboratory and actual mine tests. Among other changes the initial sensitivity had to be reduced by about a factor of 10 by a dense metal screen between the collecting filter and the detector foil, the motors were selected for constant speed, and the switching mechanism was improved. The whole system, consisting of the actual dosimeters, the charging unit, the foil cassette, and the spark counter, is pictured in Fig. 16.34.

Miscellaneous Track Studies

Cellulose nitrate films are also neutron sensitive because they record tracks of recoil nuclei produced in the films or in their immediate environment. The recoil

[22] *Health Phys. Div. Ann. Progr. Rept. July 31, 1969*, ORNL-4446, p. 266.

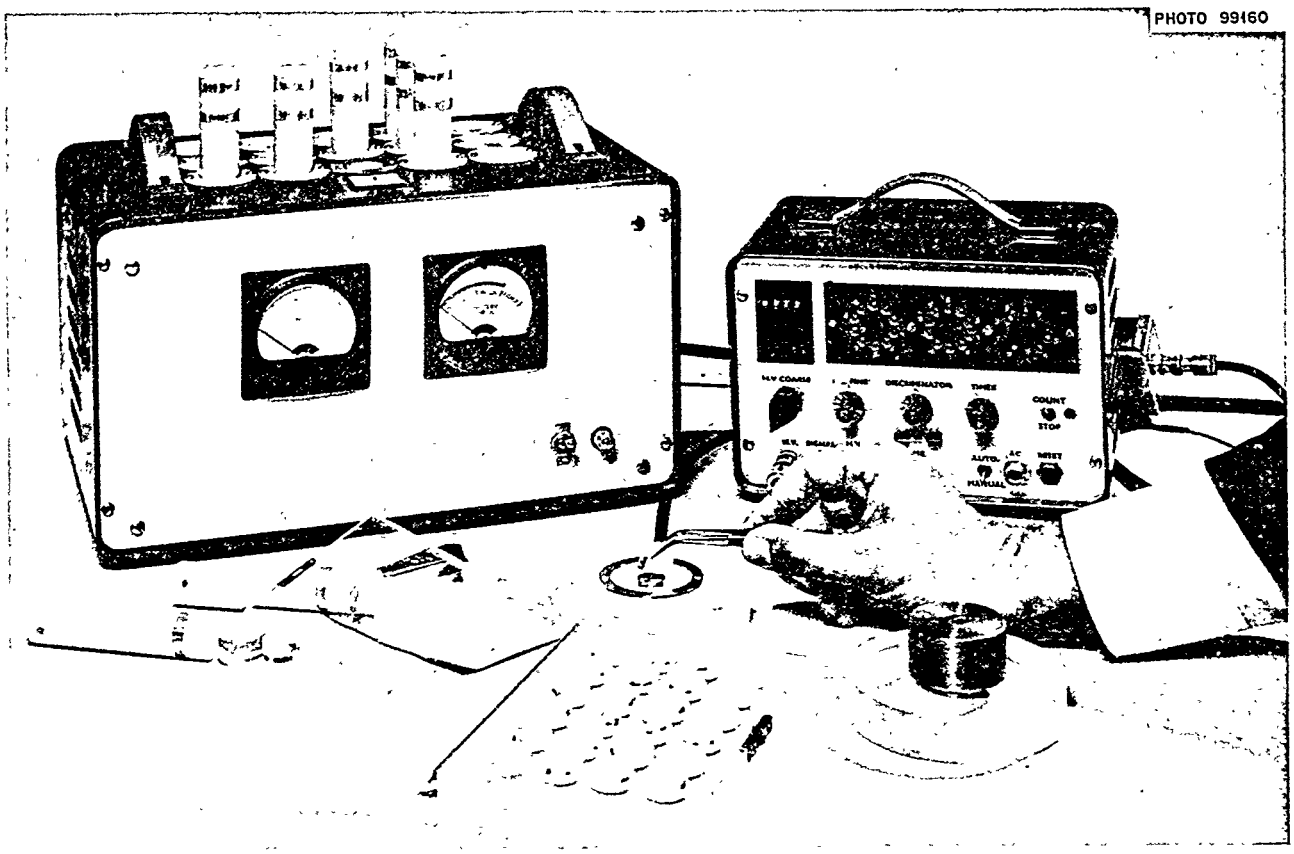

Fig. 16.34. Improved Prototype of the Radon Progeny Personnel Dosimetry System for Uranium Miners. Left front, exploded and closed monitoring unit to be attached to the miner's hard hat; left back, charging unit for 14 units; front middle, protective case for storing and mailing 24 detection foils in retainer rings; and middle and right, spark counter on which an etched foil is being placed for counting.

track sensitivity in cellulose nitrate films was determined by surrounding films with equilibrium thicknesses of various radiator foils including graphite (C), polyethylene $(CH_2)_n$, and cellulose nitrate $(C_6H_8N_2O_9)_n$, irradiating them in the same geometry to known fluences of fission neutrons from the Health Physics Research Reactor, and determining the number of tracks registered using the spark-counting technique. The neutron sensitivities obtained, 20, 22, and 32 counts cm^{-2} rad^{-1} for graphite, polyethylene, and cellulose nitrate radiator foils, respectively, were several orders of magnitude below the track density obtained using visual counting.[23] This can be explained by the short range of low-energy recoils as compared with fission fragments and alpha particles.

Some studies on the mechanism of the track formation during etching using a scanning electron microscope (Fig. 16.35) were initiated.

[23] K. Becker, *Health Phys.* 16, 113 (1969).

Fig. 16.35. Scanning Electron Micrograph of Fission Fragment Track in Lexane After 20 min Etching in 30% KOH at 60°C. 10,000×.

17. HPRR and Accelerator Operations

F. F. Haywood D. R. Ward[1]
C. P. Littleton[2]
J. W. Poston
E. M. Robinson
Z. G. Burson[3]

NEUTRON GENERATOR TARGET RESEARCH $D(d,n)^3He$ AND $T(d,n)^4He$ REACTIONS

There has been a major effort in this country for several years aimed at the ultimate goal of treating cancer and other diseases with fast neutrons. Research to support this investigation has centered on the topics of depth dose, oxygen enhancement ratio, incident beam dispersion in the body, shielding, and the machines available for use in hospitals and clinics. It has been considered generally that a neutron generator using tritium targets to produce 14-MeV neutrons [$T(d,n)^4He$] would provide the most useful means for such treatments. This opinion is based largely on studies with tumors in small animals. However, in order to use this reaction, there must be a considerable improvement made in the quality of targets both from the standpoint of yield and lifetime. Most clinicians maintain that a neutron generator must produce at least 5×10^{12} neutrons/sec for 40 hr in order to be economically feasible. Based on previous research and development for tritium targets within the Radiation Dosimetry Research Section, this criterion poses difficult engineering problems. Without utilizing a rotating-type target, no tritium targets have been operated such that 40-hr half-lives have been realized. In addition, the beam spot for targets used in therapy machines should not be larger than 2 cm in diameter because of the high dose to other parts of the body through attenuation and scattering in the first several centimeters of tissue. Such a beam spot would require the dissipation of about 20 kW of heat in an area of just over 3 cm^2. Because of this, it is obvious that significantly new approaches to target design are required. Considerable thought has been given to this problem recently. It was reported earlier[4] that deuterium bombardment of single crystals of metals such as copper resulted in larger neutron yields for the $D(d,n)^3He$ reaction. The idea was to load deuterium ions in the crystals through ion implantation. This was a very small-scale investigation and was conducted at voltages less than 100 kV. A decision was made to perform several studies for seeking new ways to make high-yield targets. These experiments were performed on the DOSAR Low Energy Accelerator. From the standpoint of normalization, it was necessary to establish a standard beam current density and energy. The beam was collimated just upstream from the target by a 1-cm^2 aperture. Standard conditions were 0.95 mA of beam current at 185 kV, with the beam defocused, so that a few percent of the charged particles were stopped at the collimator.

The first series of tests were for $D(d,n)^3He$ neutrons. Several targets loaded with deuterium were run in order to obtain a yield factor per unit beam current. Next, several materials including single crystals (110 major face) were placed in the target position, and deuterons were allowed to build up to a level neutron output. These data are shown in Fig. 17.1, and the data are expressed in Table 17.1. Specifically shown are the times required to reach 90% of the equilibrium neutron yield; and the yield is compared with a deuterium-loaded titanium target on copper, one taken to be a representative target of this type. Because of the

[1] On loan from Neutron Physics Division.

[2] On loan from Instrumentation and Controls Division.

[3] E.G.&G., Las Vegas, Nev.

[4] D. Schlafke, ORTEC, private communication, December 1969.

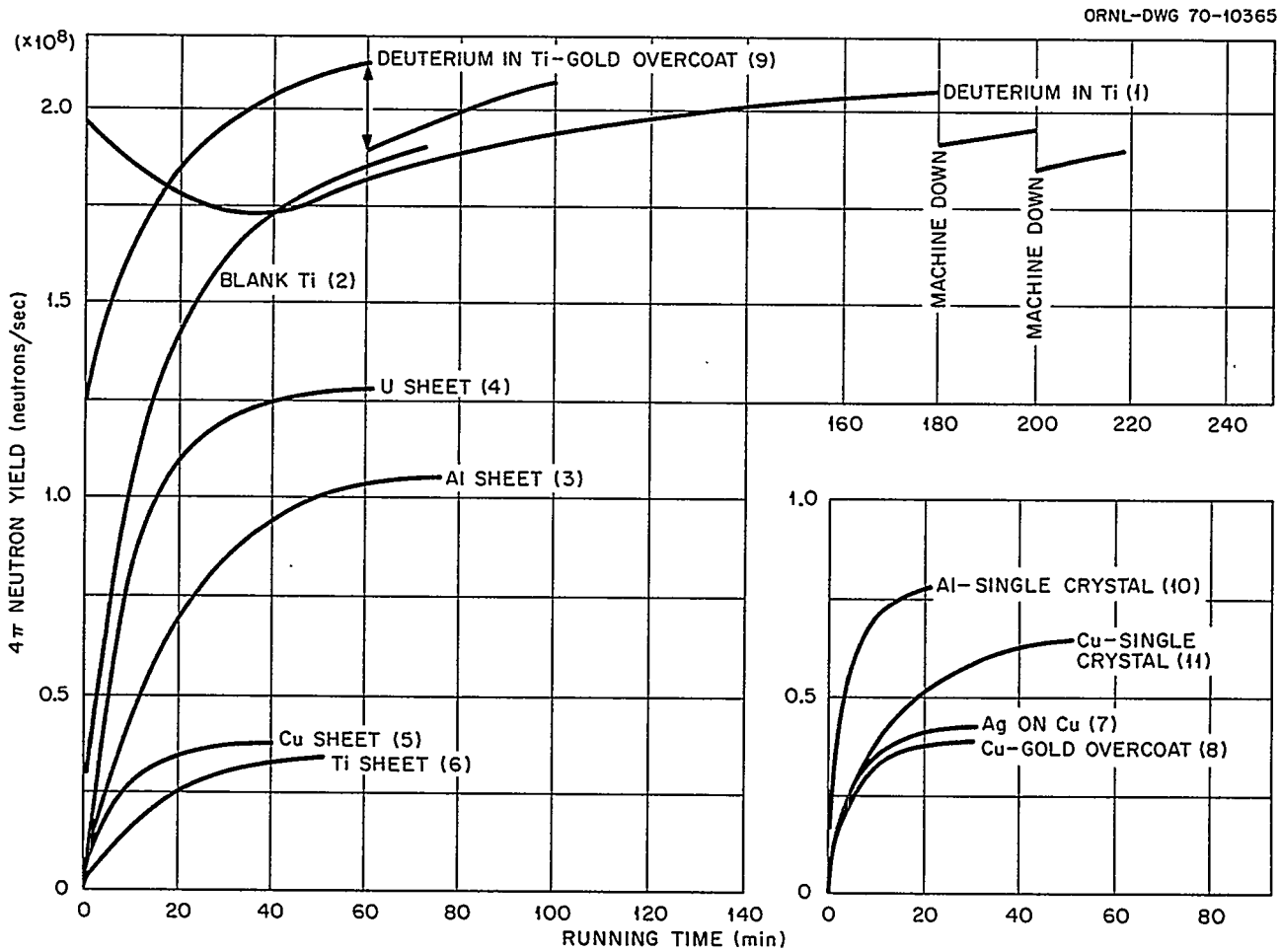

Fig. 17.1. Comparison of D-D Neutron Buildup in Various Metals as a Function of Time.

Table 17.1. Comparison of the Relative Neutron Yield as a Function of Bombardment Time for the $D(d,n)^3He$ Reaction in Several Materials

Target	Relative D-D Neutron Yield	Time to 90% Saturation (min)
Fully loaded deuterium target, Ti (1 mg/cm^2) on copper	100	
Blank titanium target, Ti (1 mg/cm^2) on copper	100	60
Plain aluminum sheet (40 mils thick)	48	25
Depleted uranium sheet	68	15
Plain copper sheet (13 mils thick)	19	5
Plain titanium sheet	17	30
Blank silver target (Ag, 306 μg/cm^2, on Cu)	23	7
Gold overlayer (100 μg/cm^2) over copper	21	10
Gold overlayer (132 μg/cm^2) over Ti on copper	113	
Aluminum single crystal (2 mm thick)	39	10
Copper single crystal (2 mm thick)	30	15

relatively poor performance of the single-crystal targets, the idea that tritium might be loaded into a single-crystal face through ion implantation and then used as a target for the production of 14-MeV neutrons seems to hold little or no promise of providing a high-yield long-lived target.

Although data are not available at this time, a new concept in targets will be explored soon. It involves the use of a tritium gas target which is expected to provide a nondepleting tritium target area for periods up to 30 to 40 hr. Specific investigations are to be concerned with neutron yield and target lifetime studies.

Calculation of HPRR Neutron Spectrum

The leakage spectrum of the HPRR was calculated using the DOT code.[5] This code is a two-dimensional discrete-ordinates code which incorporates anisotropic

[5] F. R. Mynatt, *A User's Manual for DOT, a Two-Dimensional Discrete Ordinates Transport Code with Anisotropic Scattering*, K-1694 (to be published).

ORNL-DWG 70-10366

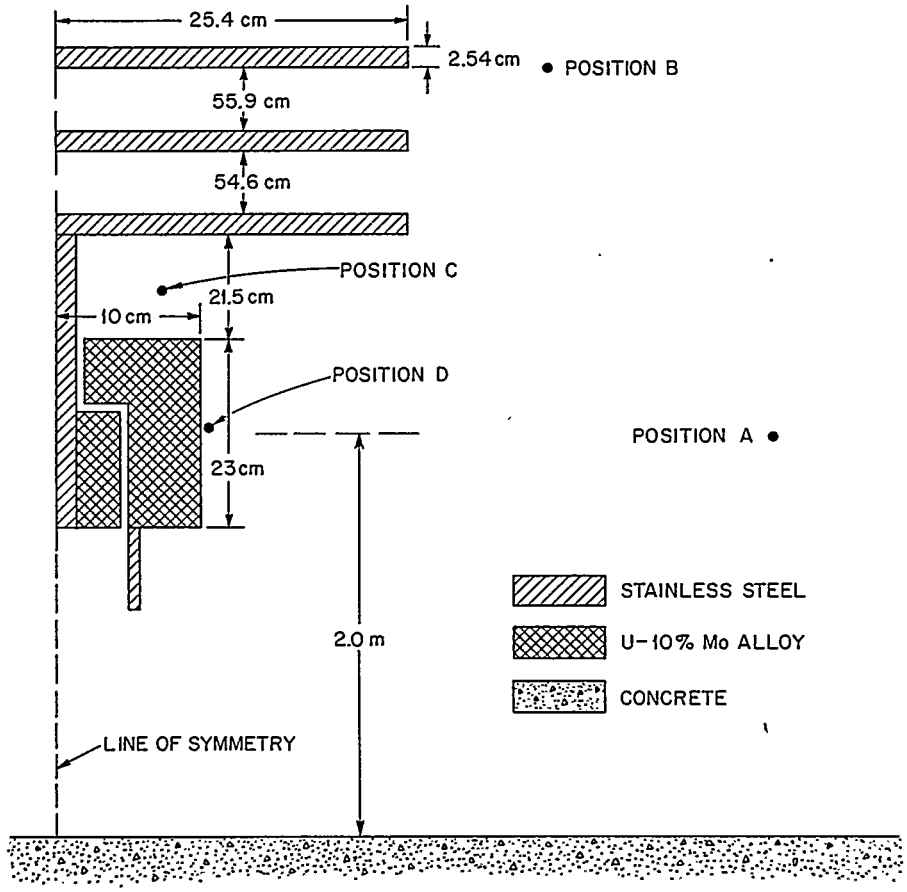

Fig. 17.2. Calculational Model of the HPRR.

scattering (a total of 664 angles were considered in the calculation). Cross sections used in the calculation were generated by the XSDRN code.[6] The energy spectrum was divided into 31 energy groups ranging from thermal to above 14 MeV. The groupings are given in Table 17.2. An idealized model of the core, which had cylindrical symmetry, was employed in the calculation (see Fig. 17.2). The neutron energy spectrum at a distance of 3 m from the core center line (position A) is shown in Fig. 17.3. Several spectra are also shown in this figure for comparison. These neutron spectra include the Godiva II spectrum,[7] the calculated spectrum for a position well above the concrete floor (position B), the spectrum for a position just above the reactor core (position C), and the spectrum for a position just off the core surface at the core center line (position D). The results shown for position D should accurately represent the leakage spectrum since this position is relatively uncluttered by reactor components which could perturb the energy distribution.

HPRR OPERATIONS

The HPRR was used extensively as a source of fission neutrons for health physics and radiobiological research activities. The reactor was employed, not only by the Health Physics Division, but by other Laboratory divisions, representatives of several foreign countries, many colleges and universities, and other Federal contractors and agencies. A summary of typical experiments is as follows:

[6] N. M. Greene and C. W. Craven, Jr., *XSDRN: A Discrete Ordinates Spectral Averaging Code*, ORNL-TM-2500 (July 1969).

[7] M. G. Chasanov and B. F. Wadding, *Analytical Fit for Godiva II Neutron Spectrum*, IBO-1584 (1958).

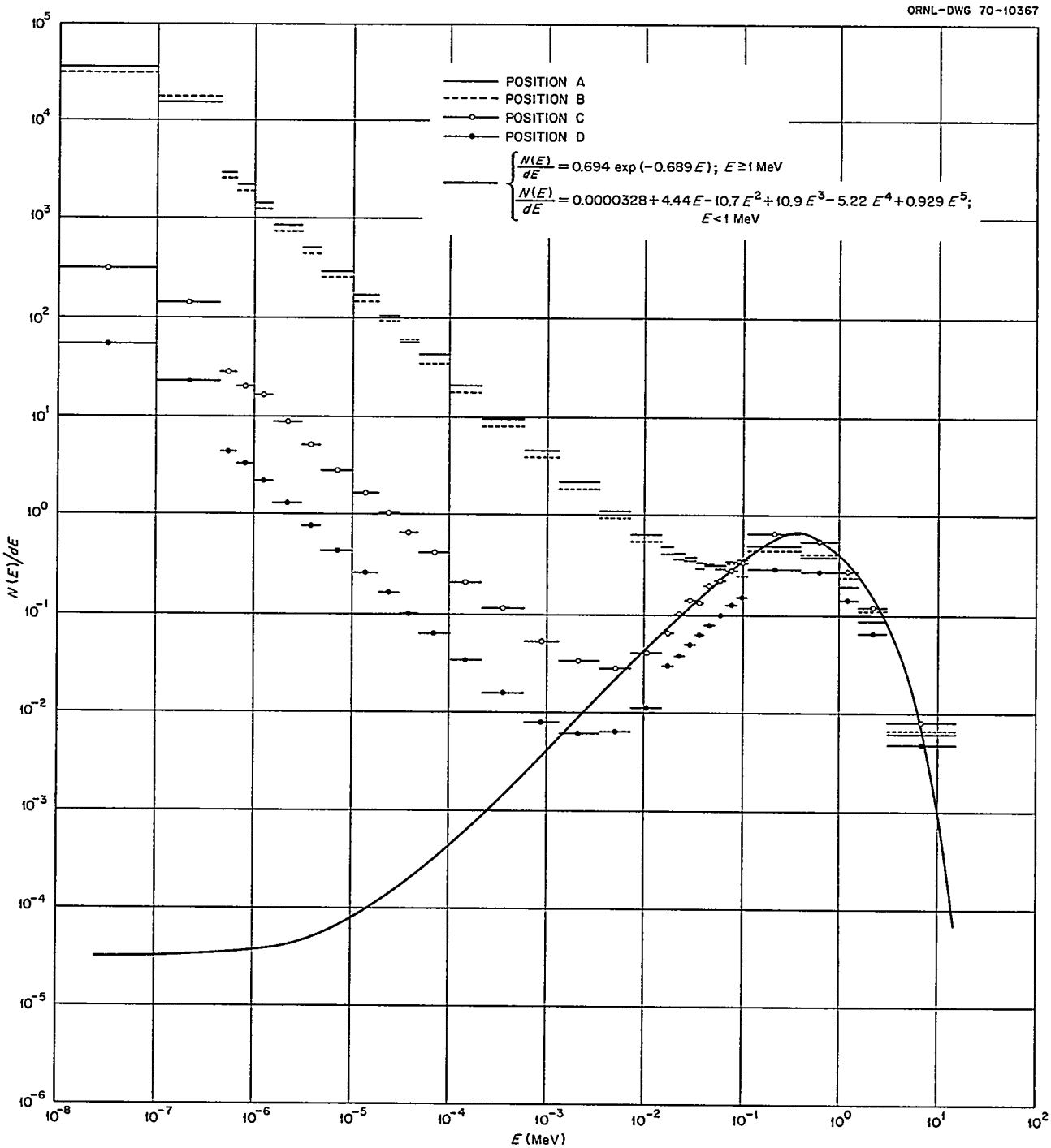

Fig. 17.3. Energy Spectral Distributions of the HPRR.

Table 17.2. Energy Groups for HPRR Spectrum Calculation

Group No.	Energy Range
1	14.92–3.01 MeV
2	3.01–1.50
3	1.50–0.91
4	0.91–0.41
5	0.41–0.11
6	110–87 keV
7	87–67
8	67–52
9	52–41
10	41–32
11	32–25
12	25–19
13	19–15
14	15–7.1
15	7.1–3.4
16	3.4–1.2
17	1200–580 eV
18	580–214
19	214–101
20	101–48
21	48–29
22	29–18
23	18–11
24	11–5.0
25	5.0–3.1
26	3.1–1.6
27	1.6–1.0
28	1.0–0.66
29	0.66–0.45
30	0.45–0.10
31	Thermal

1. determination of RBE of fission neutrons for the induction of lens opacities in mice,
2. study of the increased incidence of tumors in the mammary glands of Sprague-Dawley rats,
3. long-term effects of acute nonlethal doses of fission neutrons in mice,
4. determination of the effects of fission neutrons on 16- to 20-hr-old mice embryos,
5. interspecies comparisons of chromosome aberrations induced by exposure to fission neutrons and x rays,
6. effects of fission neutrons on developing embryos in swine,
7. radiosensitivity and mutation induction in agricultural and ornamental plants and seeds,
8. nuclear radiation pumping of a helium-neon gas laser,
9. determination of the HPRR leakage neutron spectrum in the region 50 to 450 keV,
10. determination of LET spectra of fission neutrons,
11. determination of dose distributions near a bone-tissue interface,
12. comparison of nuclear accident dosimetry systems used by licensees in the United States,
13. in support of students in the ORAU ten-week course in health physics,
14. preliminary investigations in the feasibility of employing the reactor as a source for neutron radiography.

No major modifications or changes in the reactor have been made in the past year. The annual inspection of the fuel and associated equipment showed no significant change in the condition of the reactor components.

INTERCOMPARISON STUDIES

The Sixth Intercomparison of Nuclear Accident Dosimetry Systems was held from July 8 through July 18, 1969. This study was designed primarily for participation by USAEC licensees. It was felt that the health physicists in private fuel fabrication and reprocessing plants should be given the opportunity to participate, testing their detectors and techniques against those which are commonly regarded as acceptable within the field of accident monitoring. There were 11 different groups participating in this study, 5 of which were holders of AEC special nuclear materials licenses. It was interesting to note that several of these groups utilized commercial services.

As is the custom, three pulses from the HPRR were used to provide the radiation fields. The first pulse was unshielded, the second was with a 23-cm-thick Lucite shield between reactor and detector station, and the third was with a 13-cm-thick steel shield. For each experiment all area-type detectors were placed along the circumference of a 3-m circle. All personnel-type dosimeters were placed on two phantoms which were also at 3 m. One of the phantoms was facing the reactor, and one was exposed side on. A typical arrangement of dosimeters is given in Fig. 17.4. Data collected at the 3-m station in free air are presented in Tables 17.3 through 17.5, and phantom data are presented in Table 17.6 for all three pulses.

During the last two intercomparison studies, it was noticed that there was a wide spread in the data

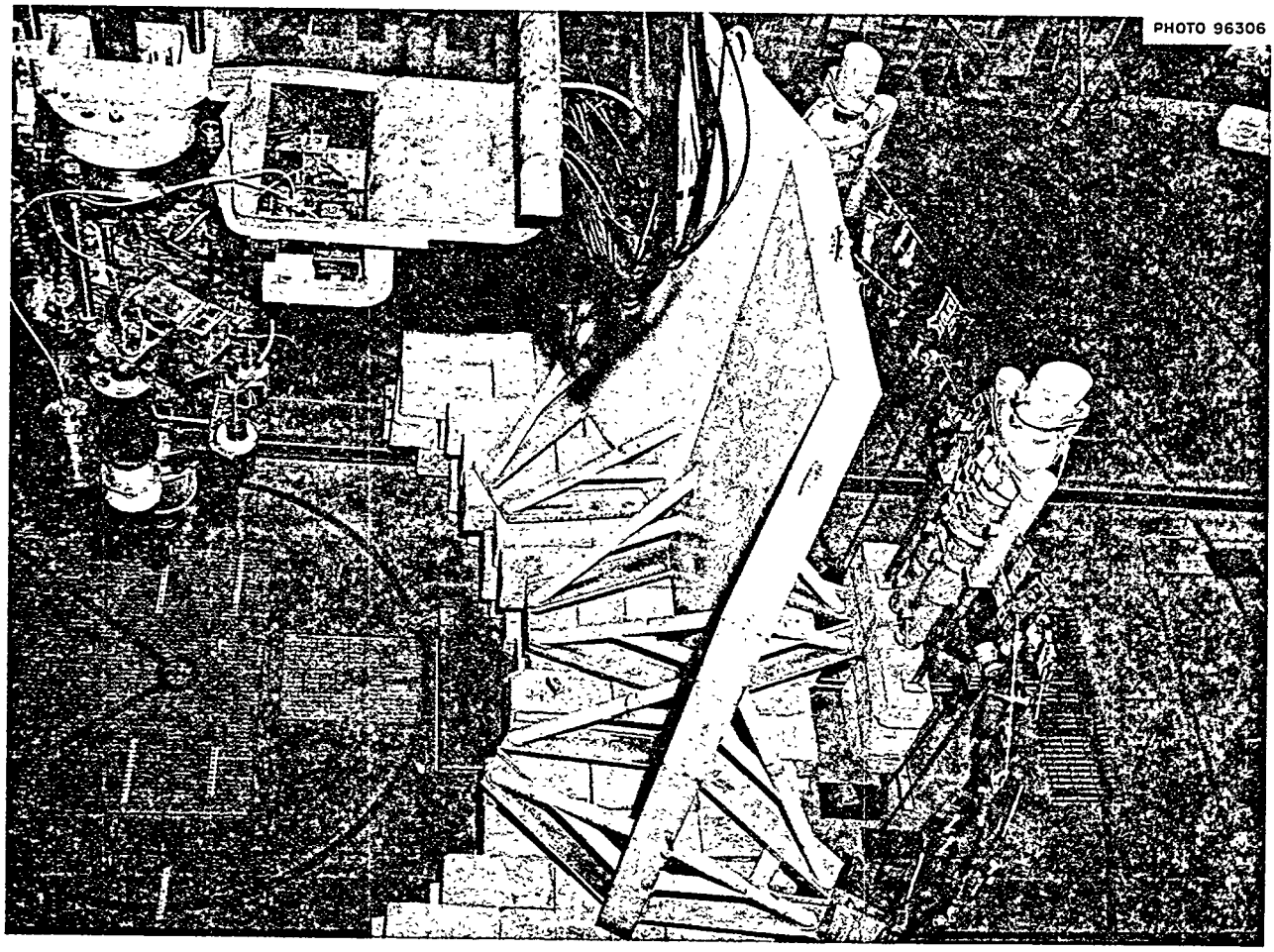

Fig. 17.4. Dosimeter Arrangement at 3 m Behind 13-cm Steel Shield.

reported for the pulse using the Lucite shield, especially between detectors near the edge and those behind the center. The shield provided so much attenuation that dosimeters placed near the edge were receiving a significant portion of their exposure by radiation scattered around and over the shield. Subsequently, this shield has been reduced to one-half its thickness, and its area has been doubled. The Lucite shield as it is now formed is shown in Fig. 17.5. The radiation field has been measured behind the modified shield, and the neutron spectrum as measured with threshold detectors is given in Fig. 17.6, being compared with the spectrum for the thicker Lucite, with the unmoderated field, and with the steel shield. It was interesting to note that the gamma-ray exposure at 3 m in free air is the same as that at 3 m behind the new Lucite shield. This may be explained simply; there is some shielding of the incident gammas, and there is production of others in the hydrogen of the Lucite. In all future intercomparisons, this modified shield will be used to provide one of the standard radiation fields.

One member of the section participated in an IAEA-sponsored intercomparison study at the Centre d'Etudes Nucleaires de Valduc facility called "Consequences Radiologiques des Accidents de Criticite" from June 15 through June 26, 1970. One week was devoted to experiments, while the second week was used for discussions, for reviews of accident monitoring systems, and for a critique of the first week's experiments. Results of this intercomparison are not available at this time. It is expected that as a result of this two-week study, the IAEA will sponsor another such experiment at ORNL during the summer of 1971.

The Seventh ORNL Intercomparison will be held from July 20 through 31, 1970. This study is comprised of several laboratories in this country and from France,

Table 17.3. ORNL Sixth Intercomparison of Nuclear Accident Dosimetry Systems July 8–18, 1969

Pulse No. 1 Unmoderated

Study Group	Neutron Dose (Rad)	n Detector System	Gamma Dose (Rad)	γ Detector System	D_n/D_γ	Neutron Fluence X 10^{-10} (n/cm^2) Au Thermal	Pu E > 1 Kev	Np E > 0.75 Mev	U E > 1.5 Mev	S E > 2.5 Mev	Cu	In	Position
Air Force Weapons Lab.	313	TDU	43.6	TLD	7.2	0.702	14.0[a]	7.39[b]	4.31	2.08[c]			Avg. of SE & NE
Batelle Memorial Institute	380	ACT	47.3[d] 64.0[e]	Film	8.0 5.9	0.47				1.7[f]	5.0[g]	5.4[h]	
Mound Laboratory	387[i]	ACT	51.9	TLD	7.5	0.63				1.97[f]	5.04[j]	8.0[h]	
NUMEC	No Free Field Data Reported – See Phantom Data												
ORGDP	284 311	TDU ACT	44.7	RPL	6.4 7.0	0.70	11.0	8.67	4.12	1.7[f]		5.0[k]	
ORNL-1	289 287	TDU MOD	44.7	RPL	6.5 6.6	0.41	11.4	8.7	4.3	2.4			
SRL	325 296[i]	ACT	45.6	TLD	7.1 6.5	0.89	14			1.6	6.2[l]	4.8[m]	
Y-12-1	308	TDU	49	Film	6.3	0.92	13.4	8.2	3.9	2.2			
Y-12-2	301	MOD	52	RPL	5.8	0.50			4.1	2.2			

[a] $E_n > 10$ Kev.
[b] $E_n > 0.6$ Mev.
[c] $E_n > 3.0$ Mev.
[d] Battelle's Commercial Service A.
[e] Battelle's Commercial Service B.
[f] $E > 2.9$ Mev.
[g] 0.5 ev–1.4 Mev.
[h] 1.4 Mev–2.9 Mev.
[i] Absorbed dose at 5 cm depth.
[j] Au(Cd) 0.4 ev–1 Mev.
[k] $E > 1.5$ Mev.
[l] 2 ev–1 Mev.
[m] 1 Mev–2.5 Mev.

Table 17.4. ORNL Sixth Intercomparison of Nuclear Accident Dosimetry Systems July 8–18, 1969

Pulse No. 2 Moderated by 23 cm Hydrogenous Shield

Study Group	Neutron Dose (Rad)	n Detector System	Gamma Dose (Rad)	γ Detector System	D_n/D_γ	Neutron Fluence X 10^{-10} (n/cm^2)							Position
						Au Thermal	Pu E > 1 Kev	Np E > 0.75 Mev	U E > 1.5 Mev	S E > 2.5 Mev	Cu	In	
Air Force Weapons Lab.	20.0	TDU	22.2	TLD	0.90	0.459	0.918[a]	0.48[b]	0.239	0.139 0.103[c]			Extreme Left, SE
Battelle Memorial Institute	20	ACT	25.4[d] 49.0[e]	Film	0.79 0.41	0.27				0.08[f]	0.64[g]	0.2[h]	Left
Mound Laboratory	10.6[i]	ACT	8.5	TLD	1.25	0.12				0.02	0.64[j]	0.05[h]	Right at 6 M
NASA			23	TLD									Left Center
NUMEC	No Free Field Data Reported – See Phantom Data												
ORGDP	9.73 11.6	TDU ACT	22.8	RPL	0.43 0.51	0.38	0.41	0.227	0.141	0.084[f]		0.17[k]	Left Center
ORNL-1	10.3–20.0 11	TDU MOD	23.6	RPL	0.44–0.85 0.47	.33–.37 .25	.42–.89 .51	.29–.54 .25	.15–.22 .14	.10–.13 .10			Far R.–Far L. R. Center
SRL	21.5	ACT	26.3	TLD	0.82	0.50	1.3			.08	1.0[l]	0.15[m]	Left Center
Y-12-1	17	TDU	24	Film	0.7	0.35	0.69	0.77	0.14	0.13			
Y-12-2	15	MOD	27	RPL	0.6	0.47			0.18	0.12			

[a] $E_n > 10$ Kev.
[b] $E_n > 0.6$ Mev.
[c] $E_n > 3.0$ Mev.
[d] Battelle's Commercial Service A.
[e] Battelle's Commercial Service B.
[f] E > 2.9 Mev.
[g] 0.5 ev–1.4 Mev.
[h] 1.4 Mev–2.9 Mev.
[i] Absorbed dose at 5 cm depth.
[j] Au(Cd) 0.4 ev–1 Mev.
[k] E > 1.5 Mev.
[l] 2 ev–1 Mev.
[m] 1 Mev–2.5 Mev.

Table 17.5. ORNL Sixth Intercomparison of Nuclear Accident Dosimetry Systems July 8–18, 1969

Pulse No. 3 Moderated by 13 cm Steel Shield

Study Group	Neutron Dose (Rad)	n Detector System	Gamma Dose (Rad)	γ Detector System	D_n/D_γ	Neutron Fluence X 10^{-10} (n/cm^2) Au Thermal	Pu E > 1 Kev	Np E > 0.75 Mev	U E > 1.5 Mev	S E > 2.5 Mev	Cu	In	Position
Air Force Weapons Lab.	121	TDU	10.1	TLD	12	0.315	6.61[a]	2.51[b]	0.876	0.407 0.301[c]			NE
Battelle Memorial Institute	131	ACT	14[d] 14.9[e]	Film	9.4 8.8	0.31				0.26[f]	3.0[g]	1.9[h]	
Mound Laboratory	189[i]	ACT	18.9	TLD	10	0.22				0.299[f]	2.34[j]	5.08[h]	
NASA			13.2	TLD									Center
NUMEC	No Free Field Data Reported – See Phantom Data.												
ORGDP	107 84	TDU ACT	12.3	RPL	8.7 6.8	0.44	5.18	2.72	0.771	0.27[f]			
ORNL-1	106 118	TDU MOD	12.3	RPL	8.4 9.6	.24 .31	5.07 6.44	2.77 2.10	.82 .73	.33 .36			
ORNL-2	99.6	TDU	14	RPL	7.1	0.50	4.70	2.65	0.74	0.35			
SRL	100	ACT	13.2	TLD	7.6	0.55	6.3			0.24			
Y-12-1	112	TDU	17	Film	6.9	0.51	5.3	3.3	0.81	0.30			
Y-12-2	108	MOD	19	RPL	5.7	0.55			0.76	0.29			

[a] $E_n > 10$ Kev.
[b] $E_n > 0.6$ Mev.
[c] $E_n > 3.0$ Mev.
[d] Battelle's Commercial Service A.
[e] Battelle's Commercial Service B.
[f] $E > 2.9$ Mev.
[g] 0.5 ev–1.4 Mev.
[h] 1.4 Mev–2.9 Mev.
[i] Absorbed dose at 5 cm depth.
[j] Au(Cd) 0.4 ev–1 Mev.

Table 17.6. ORNL Sixth Intercomparison of Nuclear Accident Dosimetry Systems Phantom Studies July 8–18, 1969

Study Group	Basis for Estimating Neutron Dose	Basis for Estimating Gamma Dose	Phantom Facing			Phantom at 90°		
			Neutron Dose (rad)	Gamma Dose (rad)	μCi ^{24}Na/mg ^{23}Na	Neutron Dose (rad)	Gamma Dose (rad)	μCi ^{24}Na/mg ^{23}Na
Pulse #1 (No Shield)								
Battelle Mem. Inst.	ACT Foils	Film	300	118*				
Mound Lab.	^{23}Na ACT	TLD	334	123*	7.55×10^{-4}			4.63×10^{-4}
NUMEC	^{23}Na ACT and ACT Foils	TLD	351	48.3*	4.88×10^{-4}			
ORGDP	^{23}Na ACT	n/γ From Area Dosimeter	295	48	7.48×10^{-4}			4.58×10^{-4}
ORNL-1	^{23}Na ACT		329		8.27×10^{-4}			4.95×10^{-4}
ORNL-2					7.55×10^{-4}			
SRL	^{23}Na ACT, SRL, TLD 600 + 700	TLD	317	81**	8.85×10^{-4}			
Y-12	^{23}Na ACT, TDU, Badge	Film, RPL	296	49*	5.68×10^{-4}			
Pulse #2 (Hydrogenous Shield)								
Battelle Mem. Inst.	ACT Foils	Film	14	37*				
Mound Lab.	^{23}Na ACT	TLD	8	32.9*	4.03×10^{-5}	13.1		6.74×10^{-5}
NASA		Film		19.7*				
NUMEC	^{23}Na ACT and ACT Foils	TLD	14.8	26.7*	8.79×10^{-5}			
ORGDP	^{23}Na ACT	n/γ From Area Dosimeter	11.2	25	4.54×10^{-5}			6.11×10^{-5}
ORNL-1	^{23}Na ACT		20		3.76×10^{-5}			4.86×10^{-5}
ORNL-2					3.76×10^{-5}			
SRL	^{23}Na ACT, SRL, TLD 600 + 700	TLD	(12),(20),(13)	30**	4.47×10^{-5}			
Y-12	TDU, Badge, ^{23}Na ACT	Film, RPL	17	24**	2.84×10^{-5}			
Pulse #3 (Steel Shield)								
Battelle Mem. Inst.	ACT Foils	Film	45	28*				
Mound Lab.	^{23}Na ACT	TLD	100	32.8*	3.83×10^{-4}	63	26.4*	2.37×10^{-4}
NASA		Film		36.6*				
NUMEC	^{23}Na ACT and ACT Foils	TLD	125	17.1*	1.26×10^{-4}			
ORGDP	^{23}Na ACT	n/γ From Area Dosimeter	103	17	3.78×10^{-4}			2.34×10^{-4}
ORNL-1	^{23}Na ACT		127		3.81×10^{-4}			2.35×10^{-4}
ORNL-2		Film		39*			27*	
SRL	^{23}Na ACT, SRL, TLD 600 + 700	TLD	(103),(103),(100)	36**	4.46×10^{-4}			
Y-12	TDU, Badge, ^{23}Na ACT	Film, RPL	133	16*	3.86×10^{-4}			

*Measured on front surface.
**Absorbed dose at centerline of phantom.

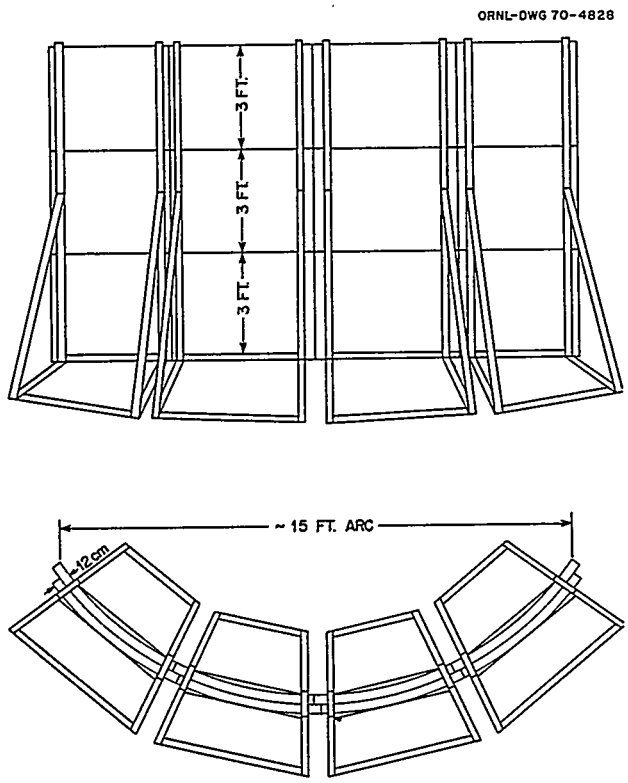

Fig. 17.5. Diagram of a Modified Hydrogenous Shield Used in the Intercomparison Studies.

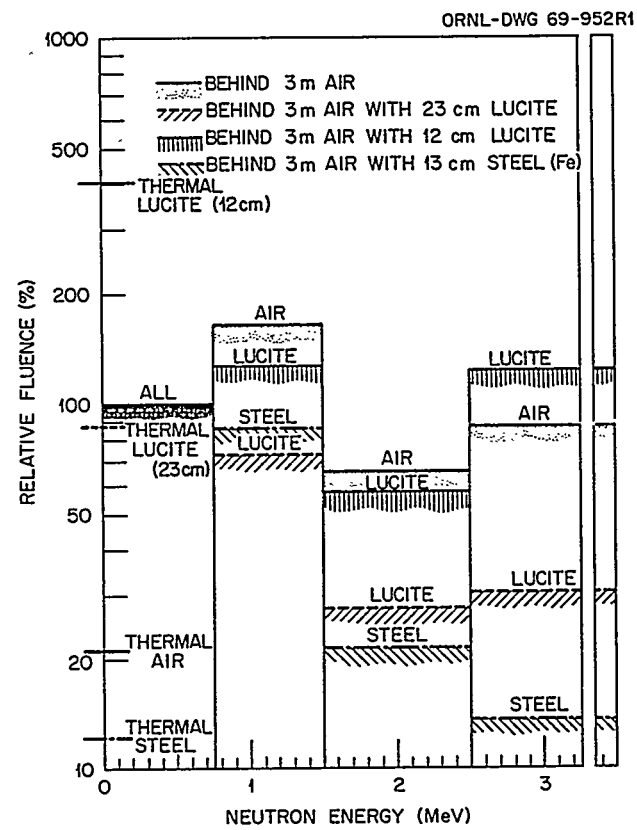

Fig. 17.6. HPRR Neutron Spectra Available for Comparing the Response of Criticality Dosimeters.

Canada, West Germany, and Yugoslavia. The HPRR will be pulsed once during the first week and twice the second; a critique will be held on July 31 to review experimental results.

VAN DE GRAAFF OPERATIONS

In addition to the DOSAR Low Energy Accelerator, the ORNL 3-MV Van de Graaff Accelerator is used for energy response studies, for direct irradiation of solid-state dosimeters with charged particles, and for other LET studies. A concentrated effort in the study of fundamental molecular physics was begun in June. It is expected that these experiments will comprise the majority of Van de Graaff operation during the next few years. Recently the Van de Graaff was utilized for the purpose of determining the LET dependence of various types of TSEE detectors. Of particular interest were ceramic BeO disks. Radiations employed were protons in the range 0.5 to 2.5 MeV and neutrons in the range 100 keV to 17 MeV. The Van de Graaff was also used to calibrate the energy scale of a newly developed recoil-proton magnetic analyzing spectrometer which was used to measure the low-energy neutron spectrum of the HPRR.

18. Interaction of Charged Particles with Matter

G. S. Hurst

D. M. Bartell[1] W. H. Shinpaugh
T. E. Bortner E. B. Wagner

An ORNL program on the interaction of charged particles with matter continues the objectives of a similar program conducted at the University of Kentucky during the past four years. The objectives are centered about the mechanism of and energy pathways following the interaction of protons with gases. To obtain a kinetic model representing energy pathways, the following measurements are made with the noble gases:

1. radiation intensities as a function of wavelength and pressure for the pure gases,
2. quenching of electromagnetic radiation by additive gases,
3. *W* values for the pure gases,
4. *W* values for the gas mixtures (i.e., Jesse effects),
5. lifetimes of continuous and resonance radiations,
6. absolute intensities of total radiation.

Figure 18.1 shows an experimental arrangement in which all these inputs can be determined in a single facility making use of the ORNL 3-MV Van de Graaff accelerator. Inputs 1 and 2 are determined by analysis of the spectrum of light leaving an emission cell. Inputs 3 and 4 are measured with a *W* cell to which a few of the protons are deflected by a thin gold foil. Input 5 is measured by pulsing the accelerator and making use of a TOF analyzer at the photodetector. Input 6 is measured with a simple geometry experiment where a CEM detector counts single photons.

At present, equipment is assembled and work is progressing on the installation and testing at the accelerator.

[1] University of Kentucky Summer Fellow and ORAU Fellowship.

ORNL-DWG 70-10895

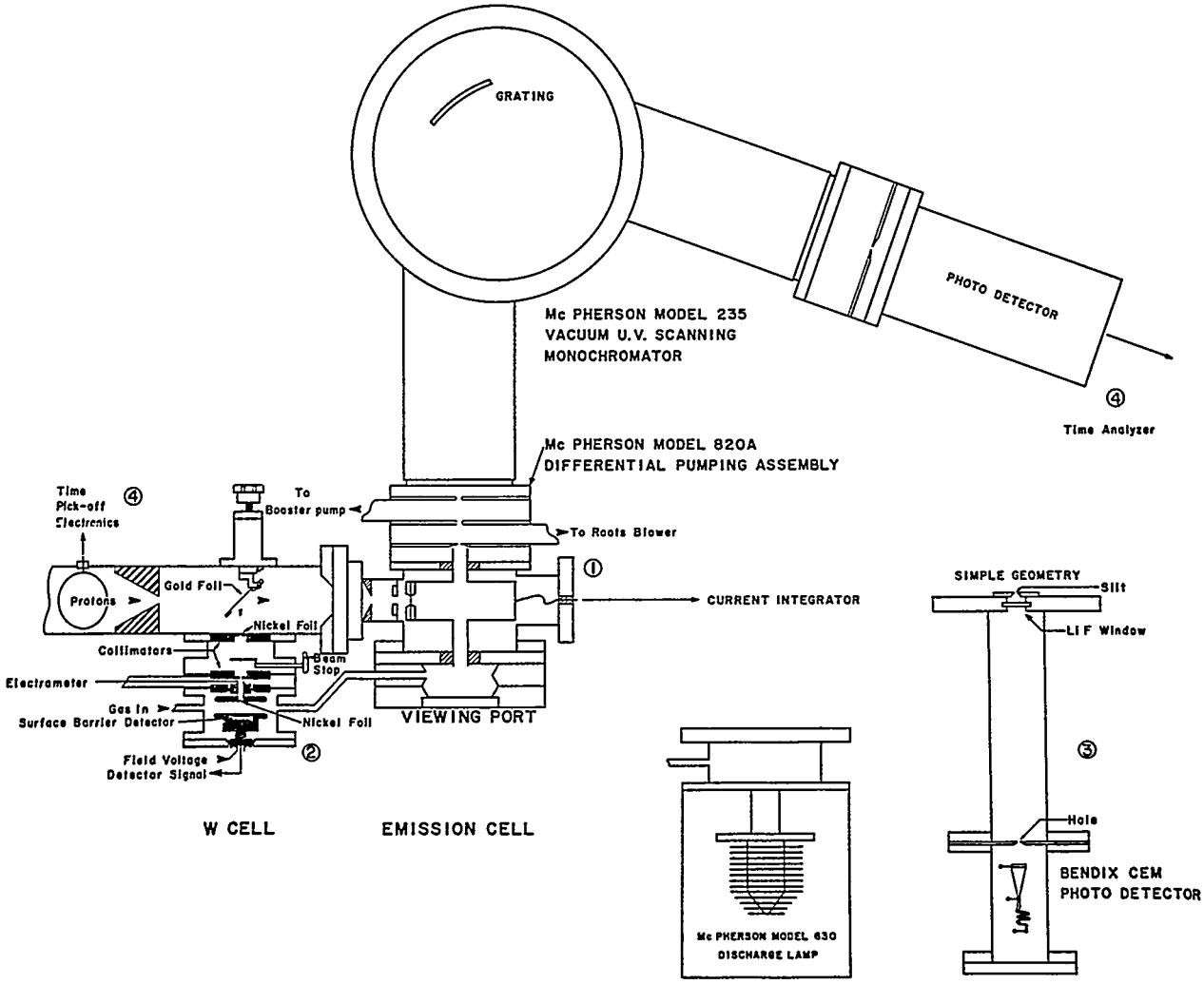

Fig. 18.1. Scattering Chambers and Spectrometer Arrangement for Installation on 3-MV Van de Graaff.

Part IV. Internal Dosimetry

W. S. Snyder

19. Internal Dose Estimation

ESTIMATES OF DOSE TO RED BONE MARROW FROM MONOENERGETIC SOURCES OF PHOTONS IN LUNGS AND OTHER ORGANS

M. J. Cook W. S. Snyder
G. G. Warner[1]

The International Commission on Radiological Protection (ICRP) has recommended lower dose limits for blood-forming organs than for the majority of other body organs – for radiation workers, 5 rems/year and for members of the public, 0.5 rem/year.[2] In view of the special category into which the ICRP has put the red bone marrow, it is important to have an accurate estimate of the dose to this tissue. Because of the complexity of the skeletal system and the red marrow, this is not an easy problem.

Two types of bone marrow may be distinguished in the adult, namely, red and yellow; however, the demarcation between the two is not sharply defined. Red bone marrow is hematopoietically active, while yellow marrow does not have any hematopoietic activity, being composed mostly of fat.

In the newborn, all of the bone marrow is red. An almost identical amount of red bone marrow is found in a child weighing 15 kg as in an adult weighing 70 kg. Although between the ages of 6 and 20 years there is a gradual replacement of red marrow by yellow marrow, the absolute quantity of red marrow remains essentially unchanged.[3] In this study only the adult is considered, although we plan to make similar studies for individuals of other ages.

Red bone marrow in the adult is located principally in the cavities of the ribs, sternum, skull, clavicles, vertebrae, and the proximal epiphyses of the femur and humerus. Because red bone marrow is scattered throughout the body, its weight has been difficult to obtain. For a 70-kg adult, ~1500 g has been assigned as the weight for the red bone marrow.[4]

A mathematical phantom has been designed which has the approximate form of the human body with 22 internal organs which are mathematical constructs of those in the living body.[5] The exterior form and some of the principal internal organs are shown in Fig. 19.1. For this study the phantom has been changed slightly to include scapulae and clavicles. These "bones" are specified by the following loci.

Clavicles – The clavicles are represented as two portions of a torus. The torus lies along the circular arc $x^2 + (y - 11.1)^2 = 20^2$, $z = 68.25$, and the smaller radius of the torus is 0.7883 cm. The clavicles include only the portion of the torus between the planes $11.1 - y = |x| \tan\theta$ with $8° \; 5.5' \leqslant \theta \leqslant 48° \; 12'$. The absolute value sign on x allows for both the right and left

[1] Mathematics Division.

[2] *Recommendations of the International Commission on Radiological Protection* (adopted Sept. 17, 1965), ICRP Publication 9, Pergamon, New York, 1966.

[3] Howard R. Bierman, "Homeostasis of the Blood Cell Elements," chap. 8, pp. 349–418 in *Functions of the Blood*, ed. by Robert G. MacFarlane and A. H. T. Robb-Smith, Academic, New York and London, 1961.

[4] William Bloom and Don W. Fawcett, *A Textbook of Histology*, 9th ed., p. 184, W. B. Saunders, Philadelphia, 1968.

[5] H. L. Fisher, Jr., and W. S. Snyder, "Distribution of Dose in the Body from a Source of Gamma Rays Distributed Uniformly in an Organ," *Health Phys. Div. Ann. Progr. Rept. July 31, 1967*, ORNL-4168, pp. 245–47.

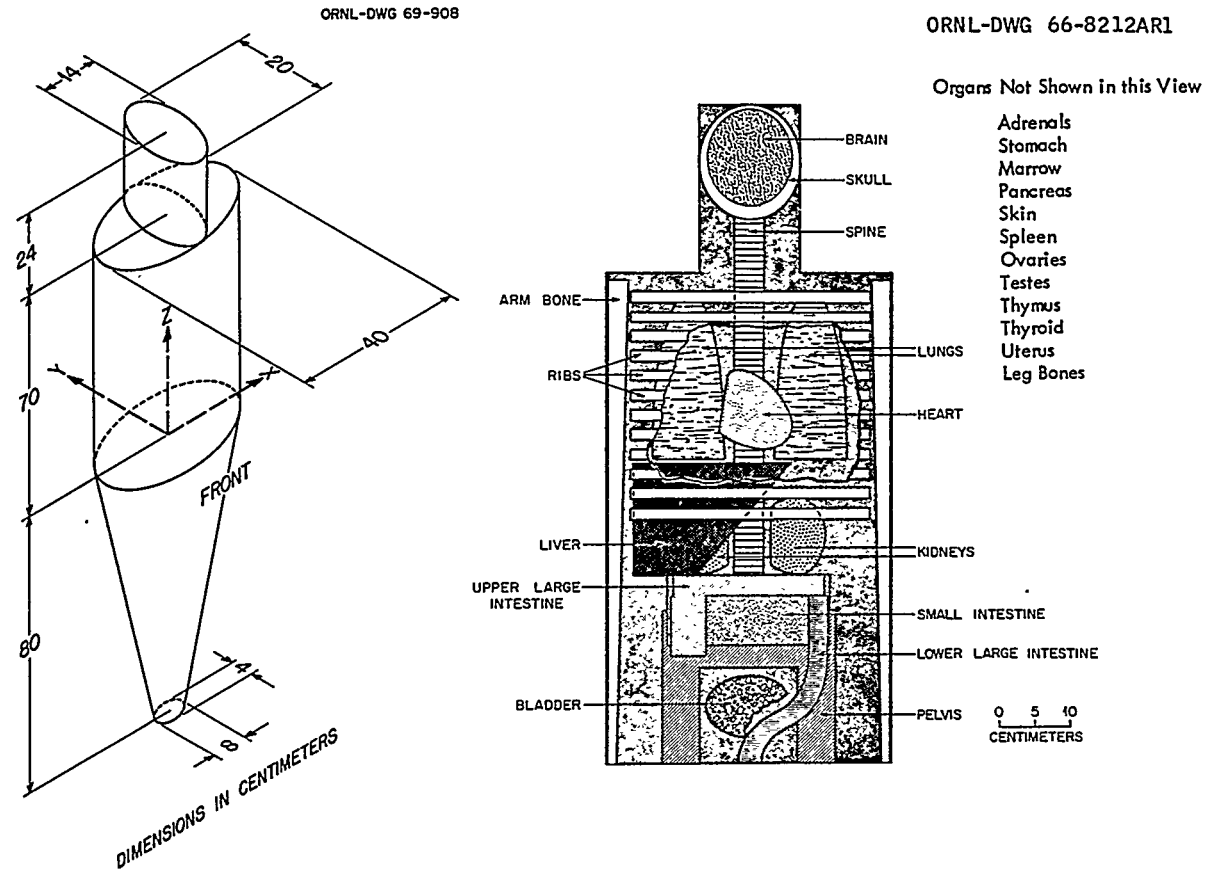

Fig. 19.1. The Adult Human Phantom, Showing an Anterior View of the Principal Organs in the Head and Trunk of the Phantom.

clavicles. The volume of both clavicles is 54.7 cm^3 and the mass is ~82 g.

Scapulae – The scapulae extend from the top of the 12th rib (z = 67.3 cm) to z = 50.9 cm. They lie between two elliptical cylinders,

$$\frac{x^2}{17^2} + \frac{y^2}{9.8^2} = 1 \text{ (outer surface of the rib cage)}$$

and

$$\frac{x^2}{19^2} + \frac{y^2}{9.8^2} = 1 \text{ (a somewhat larger cylinder)}.$$

The tapering shape of the scapulae has been ignored, and they are specified further as the volume between the above cylinders bounded by the planes $y = 0.25x$, $y = 0.80x$, and $50.9 \leqslant z \leqslant 67.3$. The volume of both scapulae is 100.7 cm^3, and the mass is taken as 151 g.

A computer code has been designed to compute random histories of photons which originate in one organ (the source organ) and to estimate the fraction of the photon's initial energy absorbed in each of the 22 target organs. This is essentially an application of the well-known Monte Carlo technique. In a previous report[6] estimates of the absorbed energy have been published for these 22 target organs when a monoenergetic source of photons is distributed uniformly in 16 different source organs. However, "marrow" as reported there includes both red and yellow. For this report the phantom and the computer code have been modified so that absorbed fractions for the red bone marrow are obtained.

In Fig 19.2 the stippled areas represent the red bone marrow in the phantom skeleton and in the drawing of an actual skeleton. Of the total 1500 g of red bone marrow, 13.1% is in the skull, 28.4% in the vertebrae,

[6]W. S. Snyder *et al.*, "Estimates of Absorbed Fractions for Monoenergetic Photon Sources Uniformly Distributed in Various Organs of a Heterogeneous Phantom," MIRD Pamphlet No. 5, Suppl. No. 3, *J. Nucl. Med.*, 7–52 (August 1969).

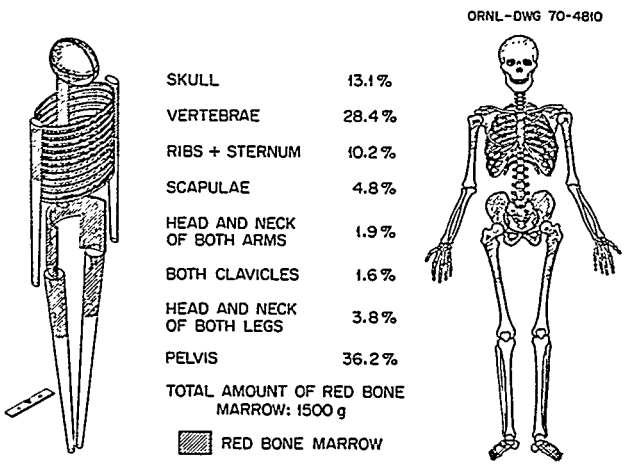

Fig. 19.2. Idealized Model for the Computer (Left) Showing Distribution of Red Bone Marrow in a Normal Adult (Right).

10.2% in the ribs and sternum, 4.8% in the scapulae, 1.6% in the clavicles, 36.2% in the pelvis, 1.9% in the proximal epiphyses of the humerus, and 3.8% in the proximal epiphyses of the femur. These data have been selected from Ellis,[7] although Hashimoto,[8] Russell *et al.*,[9] and others have given similar data. If the red marrow constitutes a fraction f of the total weight of a bone plus marrow, then the energy absorbed in the red marrow of that bone is taken as $f \times$ (energy absorbed in that bone plus marrow). Thus red marrow is assumed to absorb energy as efficiently per gram as do the other constituents of bone. One may use the code to compute the absorbed fraction with the source in any location, but for this study we are only reporting dose to the red bone marrow from a monoenergetic source of photons in the lung. We plan to obtain similar estimates with the source in other organs. The lung was chosen for these first calculations, because a considerable fraction of the red bone marrow is located close to these organs and inhalation is a frequent mode of exposure.

For this study 30,000 photons were programmed for each photon energy. The code provides estimates of average dose to the total red bone marrow, but since this dose would not be expected to be nearly constant, the code also provides separate estimates of dose for red bone marrow in ribs, three sections of the vertebral column, pelvis, arm bones, leg bones, clavicles, scapulae, and skull. A standard deviation and coefficient of variation are provided for each estimate.

As examples, in Fig. 19.3 are presented the dose to the total red bone marrow, three regions of the vertebral column (upper, mid, and lower), ribs and sternum, and pelvis. If the coefficient of variation was greater than 60%, the estimate was not included in this figure. The estimate plus or minus one standard deviation is shown unless the standard deviation was less than 10% of the estimate. The 12 different energies selected are 0.010, 0.015, 0.02, 0.03, 0.05, 0.1, 0.2, 0.5, 1.0, 1.5, 2.0, and 4.0 MeV. For 0.010 MeV the standard deviation of the estimate was always greater than 60%; therefore these data are not included in the figure.

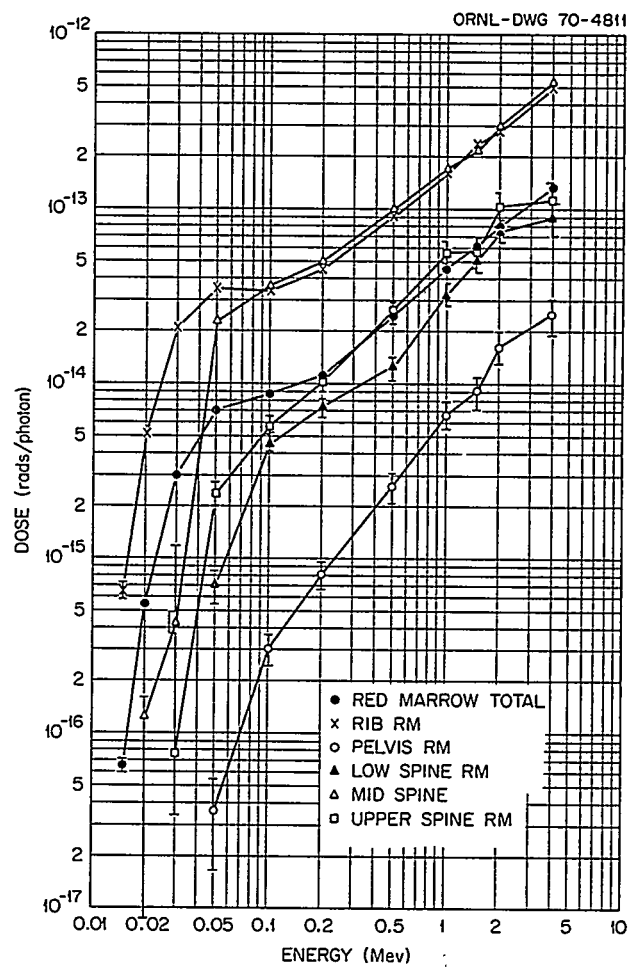

Fig. 19.3. Mean Dose per Photon to Red Bone Marrow and Portions of Red Bone Marrow from a Monoenergetic Source Uniformly Distributed in Lungs.

[7] R. E. Ellis, "The Distribution of Active Bone Marrow in the Adult," *Phys. Med. Biol.* 5, 255–58 (1961).

[8] Michio Hashimoto, "The Distribution of Active Marrow in the Bones of Normal Adult," *Kyushu J. Med. Sci.* 11, 103–11 (1960).

[9] Walter J. Russell *et al.*, "Active Bone Marrow Distribution in the Adult," *Brit. J. Radiol.* 39, 735–39 (1966).

With the source in the lungs, the ribs and sternum receive the highest dose. The midregion of the vertebral column receives almost the same dose as the ribs and sternum at the higher energies but less at energies below 0.1 MeV. Of the regions shown here, the red bone marrow of the pelvis receives the lowest dose, which is expected as it is farthest from the source in the lungs. The dose to the total red marrow falls about midway between these high and low values, as would be expected. In particular, the red bone marrow of the ribs and midvertebral column receives almost four times the average dose to the total red bone marrow. Of course, dose to the red bone marrow in the pelvis and leg bones is similarly low.

In this report the dose to various regions of the red bone marrow has been calculated when the source is distributed uniformly in the lungs of adults. Plans are under way to calculate the dose to these regions of red bone marrow when the source is in other organs such as the gastrointestinal tract, urinary bladder, etc., and to study the problem for various age groups.

ESTIMATION OF DOSE TO GONADS FROM GAMMA EMITTERS PRESENT IN THE BODY

W. S. Snyder Mary R. Ford
G. G. Warner[10]

The author and colleagues[11] have developed a Monte Carlo type computer code for estimating the specific absorbed fraction of photon energy $\Phi(X \rightarrow Y)$, that is, fraction of energy absorbed in Y per gram of that released in X, where X is an organ of the body containing a source of photons distributed uniformly therein and Y is a target organ. The code involves a mathematical anthropomorphic phantom whose organs approximate those of their prototypes in size, shape, composition, and density. Although results have been published[11] for 16 source organs X and some 20 target organs Y, the estimate is inaccurate sometimes because of poor statistics. This is likely to be the case when Y is a small organ and far from the source. In particular, the estimate of the specific absorbed fraction for the gonads frequently is found to have a large coefficient of variation. For this reason no estimates of the absorbed fraction for gonads were included in ref. 11 except when the gonads are a source organ. The present note is a first attempt to supply an approximate estimate of the specific absorbed fraction for the gonads.

Berger[12] has computed the buildup factor $B(\mu x)$ for photons emanating from a point source in an infinite medium of water, giving values for photon energies from 0.02 to 2 MeV and for $\mu X \leqslant 20$, μ being the mass attenuation coefficient for the photons. The specific absorbed fraction at distance x cm from a point source in the water is then given by

$$\Phi(X) = \frac{\mu_{ab} e^{-\mu x} B(\mu x)}{4\pi x^2}, \qquad (1)$$

where x represents the distance of the infinitesimal target volume from the point source and μ_{ab} is the mass absorption coefficient for the photons. If $\Phi(X)$ is used to estimate the fraction of energy absorbed per gram in the gonads at distance x from a point source in the body, one might expect the result to be an overestimate since $B(\mu x)$ was computed for an infinite medium so that buildup would be maximized. On the other hand, it is not easy to foresee what effect the differences in composition and density of the body might have in comparing buildup in the body with that in a homogeneous medium. Moreover, even if one suspects Eq. (1) will provide an overestimate of the specific absorbed fraction for distances in the body, it is desirable to know approximately the extent of the overestimate.

In an attempt to answer some of the questions raised, $\Phi(X)$ has been computed by the Monte Carlo methods of ref. 11 for certain subregions of the body much larger than the gonads, so that the statistical accuracy, while not always good, is nevertheless much better than for the gonads. These regions are "slices" shown in Fig. 19.4 and are numbered 1 to 5. The source has been placed in the thyroid, so that the distance from source to target is as large as can be attained in the trunk. Distance has been taken from a central point of the thyroid to the center of each slice. Clearly distance from the source to a point of the slice varies significantly at different portions of the slice, and thus a high degree of accuracy cannot be expected from the comparison. Figures 19.5–19.10 show the results for $\Phi(X)$ for photons of energies 2, 1, 0.5, 0.2, 0.1, 0.05 MeV as computed by the Monte Carlo calculation of ref. 11. For comparison, formula (1) with $B(\mu x)$ as

[10] Mathematics Division.

[11] W. S. Snyder *et al.*, "Estimates of Absorbed Fractions for Monoenergetic Photon Sources Uniformly Distributed in Various Organs of a Heterogeneous Phantom," MIRD Pamphlet No. 5, Suppl. No. 3, *J. Nucl. Med.*, 5 (1969).

[12] Martin J. Berger, "Energy Deposition in Water by Photons from Point Isotropic Sources," MIRD Pamphlet No. 2, Suppl. No. 1, *J. Nucl. Med.*, 15 (1968).

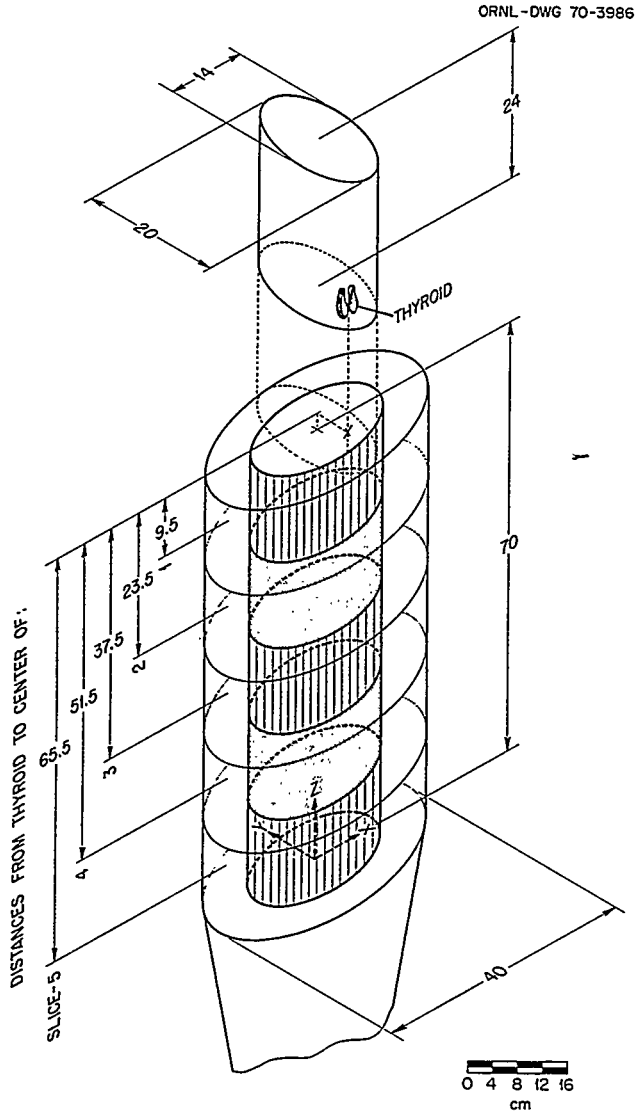

Fig. 19.4. The Human Phantom.

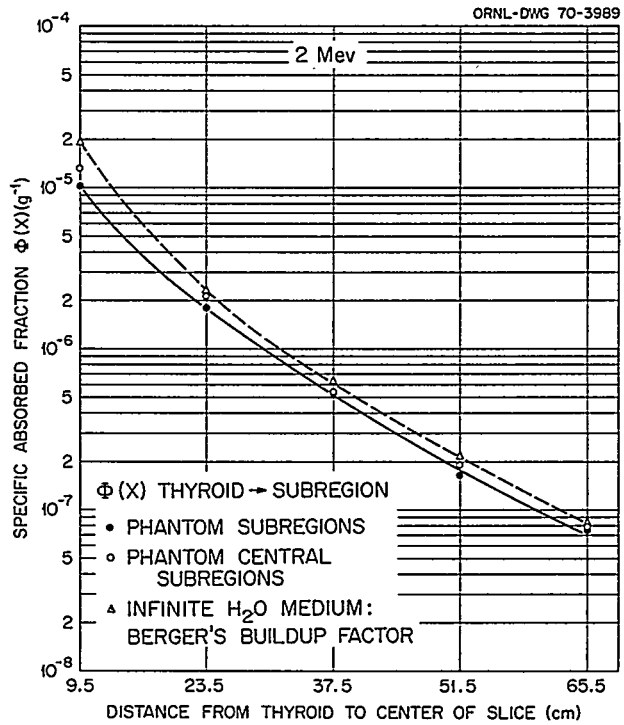

Fig. 19.5. Estimates of Specific Absorbed Fraction Φ for an Infinite Medium of Water and for Subregions of an Anthropomorphic Phantom. 2 MeV.

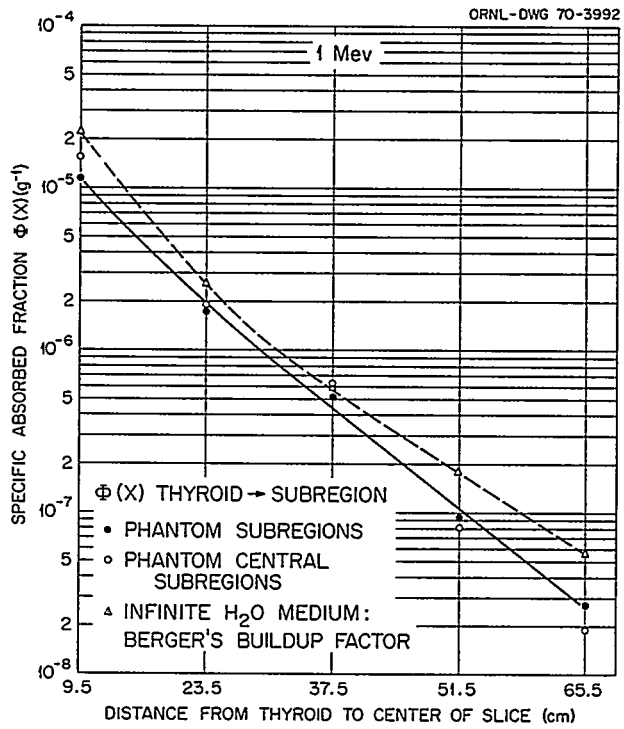

Fig. 19.6. Estimates of Specific Absorbed Fraction Φ for an Infinite Medium of Water and for Subregions of an Anthropomorphic Phantom. 1 MeV.

tabulated by Berger is shown also. It is seen that generally formula (1) is higher, as expected, and the cases when this does not hold might plausibly be due to either poor statistics or to the rather inaccurate characterization of the distance x. To test the influence of this distance factor, the value of $\Phi(X)$ has been computed also for the central portion of the slice (see Fig. 19.4), and it is evident that this generally improves the agreement of the estimate provided by this Monte Carlo calculation and that provided by Berger.

On the basis of the evidence presented here, it seems likely that the use of the buildup factor as given by Berger[12] and of formula (1) given here will generally overestimate $\Phi(X)$ but not by more than about a factor

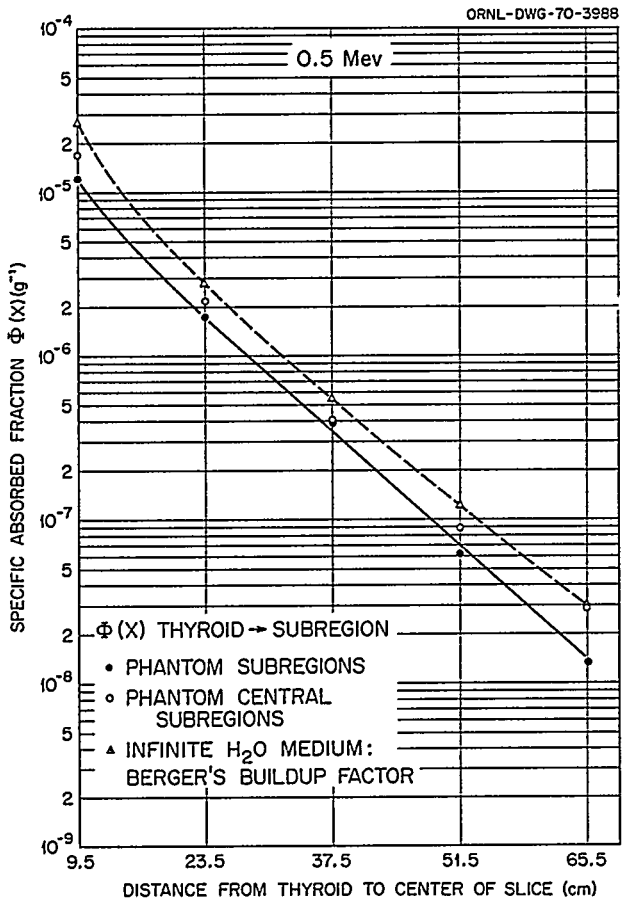

Fig. 19.7. Estimates of Specific Absorbed Fraction Φ for an Infinite Medium of Water and for Subregions of an Anthropomorphic Phantom. 0.5 MeV.

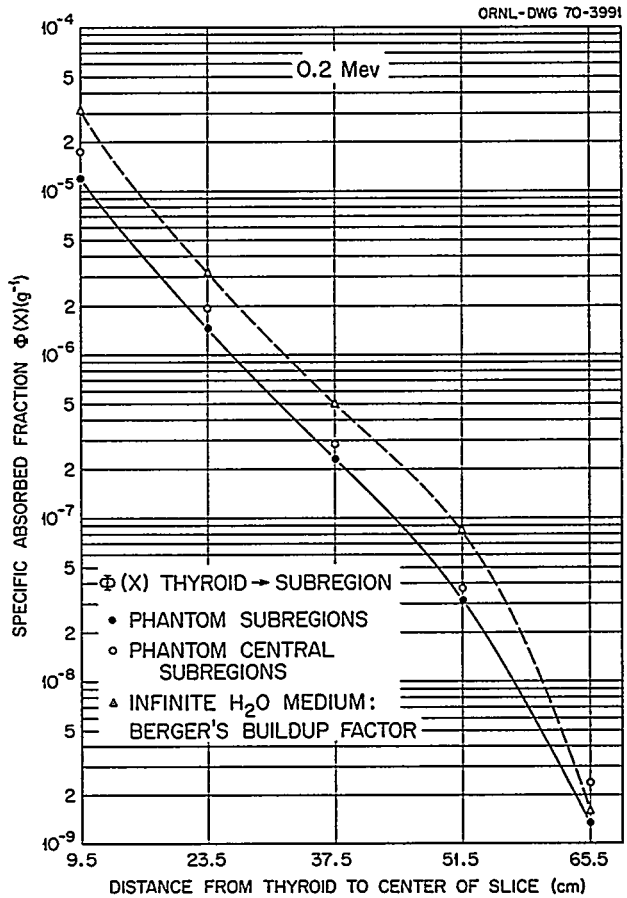

Fig. 19.8. Estimates of Specific Absorbed Fraction Φ for an Infinite Medium of Water and for Subregions of an Anthropomorphic Phantom. 0.2 MeV.

of 2. Such a margin of error is acceptable in view of the fact that alternative methods involve uncertainties of at least as much and are frequently much more difficult. It should be noted that the degree of accuracy obtained for formula (1) is roughly the same as can be attained by use of the reciprocity theorem (see ref. 13), namely, a factor of about 2.

It should be emphasized that the above comments apply only to the "point-source" formula. When the source is much more extended, for example, the lungs or stomach or liver, one should perform an integration over the source region and only then should one expect accuracy as indicated above. The use of a "representative point" for such large organs, say, a central point, will add an additional uncertainty. Moreover, when lungs are the source organ, the distance to the target organ probably should be taken in mass units. The influence of such corrections for the variable density of the body and the choice of "representative points" for source organs are matters which the author hopes to explore further in future studies.

Acknowledgment

The author owes much to his colleagues Gordon Warner, who has coded all these calculations for the computer; Mary Rose Ford, who has assisted in designing the code as well as in evaluating and analyzing the data; and James Hickey, who did the sometimes tedious tabulations necessary for this paper and for preparing the figures.

[13] W. S. Snyder, "Estimation of Absorbed Fraction of Energy from Photon Sources in Body Organs," *Proc. ORAU Symposium on Medical Radionuclides: Radiation Dose and Effects, December 8–11, 1969, Oak Ridge, Tennessee* (in press).

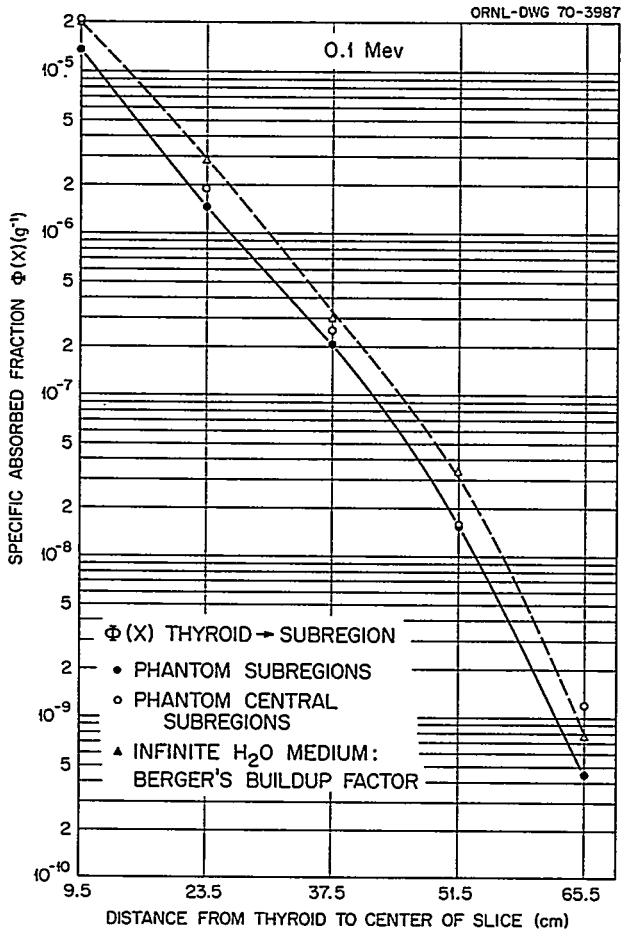

Fig. 19.9. Estimates of Specific Absorbed Fraction Φ for an Infinite Medium of Water and for Subregions of an Anthropomorphic Phantom. 0.1 MeV.

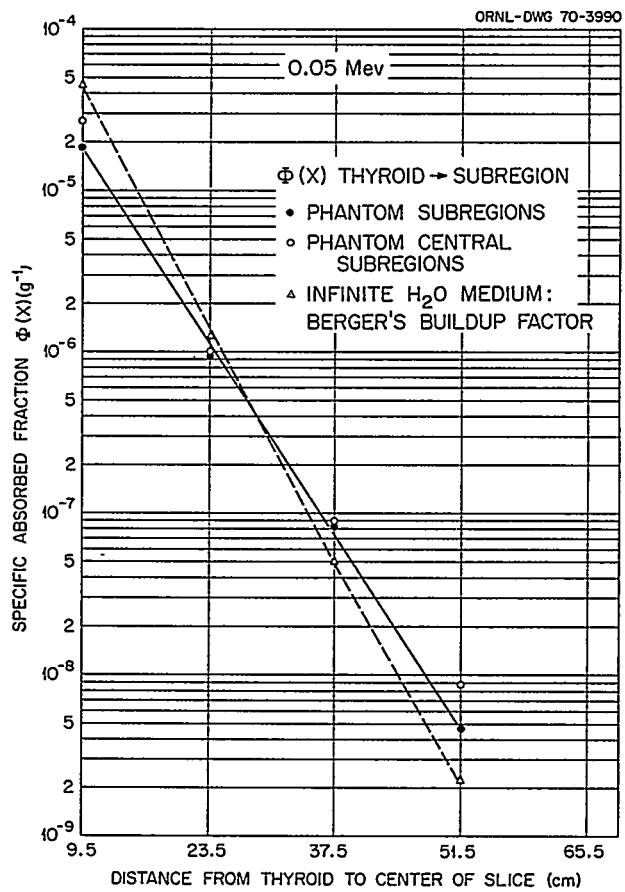

Fig. 19.10. Estimates of Specific Absorbed Fraction Φ for an Infinite Medium of Water and for Subregions of an Anthropomorphic Phantom. 0.05 MeV.

ESTIMATION OF DOSE AND DOSE COMMITMENT TO BLADDER WALL FROM A RADIONUCLIDE PRESENT IN URINE[14]

W. S. Snyder Mary R. Ford
G. G. Warner[10]

Estimation of dose to the bladder wall from a photon emitter present in urine is more complicated than in the case of most organs, because the dose per photon varies by almost an order of magnitude as the bladder fills, being largest for a nearly empty bladder.[15] This large variability implies that a dose estimate will depend significantly on the schedule of bladder voiding. Moreover, if some compartment is present which has an elimination half-time that is short compared with the time for a bladder filling, then the dose estimate will be influenced by whether this activity enters the bladder when it is nearly empty or nearly full. It is the purpose of this study to provide a basis for estimating the extent of the variability of dose to the bladder wall. The present study is concerned only with the dosimetric aspects of the problem. In a later study we hope to take into account certain patterns of urinary excretion which may be regarded as "typical" to provide bounds for variability of dose to the bladder wall as a consequence of other patterns.

The bladder is considered to be an oblate spheroid,

$$\left(\frac{x-x_0}{a}\right)^2+\left(\frac{y-y_0}{b}\right)^2+\left(\frac{z-z_0}{c}\right)^2=1\,,$$

[14] Presented at Health Physics Society Meeting, June 28–July 2, 1970, Chicago, Ill.

[15] W. S. Snyder, "Estimation of Absorbed Fraction of Energy from Photon Sources in Body Organs," *Medical Radionuclides: Radiation Dose and Effects*, p. 33, USAEC-DTI, Oak Ridge, June 1970.

where $(x_0, y_0, z_0) = (0, -4.5, 8)$ are the coordinates of the center in a Cartesian system of coordinates as chosen in MIRD Pamphlet 5,[16] that is, positive x axis to the left, positive y axis pointing toward the back, and positive z axis directed upward along the center line of the trunk with the origin at the base of the trunk. The semiaxes of the ellipsoid have the ratio $a:b:c = 4:3:3$, and this ratio is assumed to remain fixed as the bladder fills. The above equation may be considered to represent the inner wall of the bladder, and the exterior surface is represented by

$$\left(\frac{x-x_0}{\rho a}\right)^2 + \left(\frac{y-y_0}{\rho b}\right)^2 + \left(\frac{z-z_0}{\rho c}\right)^2 = 1\,, \quad (2)$$

where ρ is chosen so that

$$\frac{4}{3}\pi abc(\rho^3 - 1) = 45 \text{ g} \quad (3)$$

is the mass of the bladder wall. For different volumes of urine present in the bladder, the mass remains unchanged, and the value of 45 g has been chosen as typical.[17] In Fig. 19.11, a schematic diagram of the bladder is shown for three different situations, namely, empty and for content of 100 and 400 ml.

Define now a function $D_r(V)$ to be the average dose rate to the bladder wall, rads/μCi-hr, when the bladder content (urine content) is V ml. No mathematical formula for $D_r(V)$ is available; rather, its values may be obtained by use of the Monte Carlo method described in MIRD Pamphlet 5,[16] the only change being that the bladder content here is V ml and dose is estimated to the wall rather than averaged over wall and contents.

If one considers $D_r(V)$ as known, then formulas for the dose under any conditions of filling are easily written. Thus if $f(t)\,dt$ ml of urine enter the bladder in time interval dt (hr) and if $s(t)\,dt$ μCi of activity enter the bladder in time dt (hr), then the total dose (rads) from time 0 (commencement of bladder filling) to time T is given by

$$D(T) = \int_0^T dt \int_0^t d\tau\, s(\tau)\, e^{-\lambda_r(t-\tau)} \times D_r\left[\int_0^t d\tau\, f(\tau)\right]. \quad (4)$$

Formula (4) includes the special case where activity begins entering the bladder when it is partly filled; one need only assign $s(t) \equiv 0$ during this period.

Consider now a more special situation where

$$f(t) = \alpha\,, \quad s(t) = ua\lambda e^{-(\lambda+\lambda_r)t}\,. \quad (5)$$

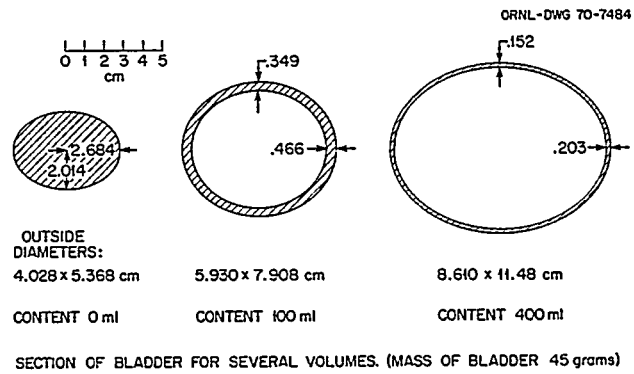

Fig. 19.11. Section of Bladder for Several Volumes.

Equations (5) represent the special, but unusual, case where bladder filling occurs at a constant rate, say, α ml/hr, and excretion is exponential in character [i.e., $a\lambda e^{-(\lambda+\lambda_r)t}$] with only a portion of the material excreted passing through the bladder. With this specialization, Eq. (4) becomes

$$D(T) = au \int_0^T dt\, e^{-\lambda_r t}(1 - e^{-\lambda t})\, D_r(\alpha t)$$

$$= \frac{au}{\alpha}\left[\int_0^{\alpha T} dx\, e^{-(\lambda r/\alpha)x}\, D_r(x) - \int_0^{\alpha T} dx\, e^{-(\lambda+\lambda_r)x/\alpha}\, D_r(x)\right]. \quad (6)$$

The latter integral of Eq. (6) is obtained by substituting $x = \alpha t$ as a new variable of integration.

The function $D_r(V)$ has been computed for $V = 0$, 50, 100, 200, 300, 400, 500 ml and for the same 12 monoenergetic sources of photons given in MIRD Pamphlet 5,[16] namely, 0.01, 0.015, 0.02, 0.03, 0.05, 0.1, 0.2, 0.5, 1, 1.5, 2, 4 MeV. The results are displayed in Fig. 19.12*a* for the four lowest energies and in Fig. 19.12*b* for the others. As will be noted the curves cross, and they are separated here to facilitate their use. This complex behavior seems to be due to the interplay of a number of factors, (1) amount of energy released, (2) changes in the mass absorption and mass attenuation coefficients with energy, and (3) thickness of the wall.

---

[16] W. S. Snyder, Mary R. Ford, G. G. Warner, and H. L. Fisher, Jr., "Estimates of Absorbed Fractions for Monoenergetic Photon Sources Uniformly Distributed in Various Organs of a Heterogeneous Phantom," MIRD Pamphlet No. 5, Suppl. No. 3, *J. Nucl. Med.* 10, 7 (1969).

[17] M. M. Nold, R. L. Hayes, and C. L. Comar, *Health Phys.* 4, 86 (1960).

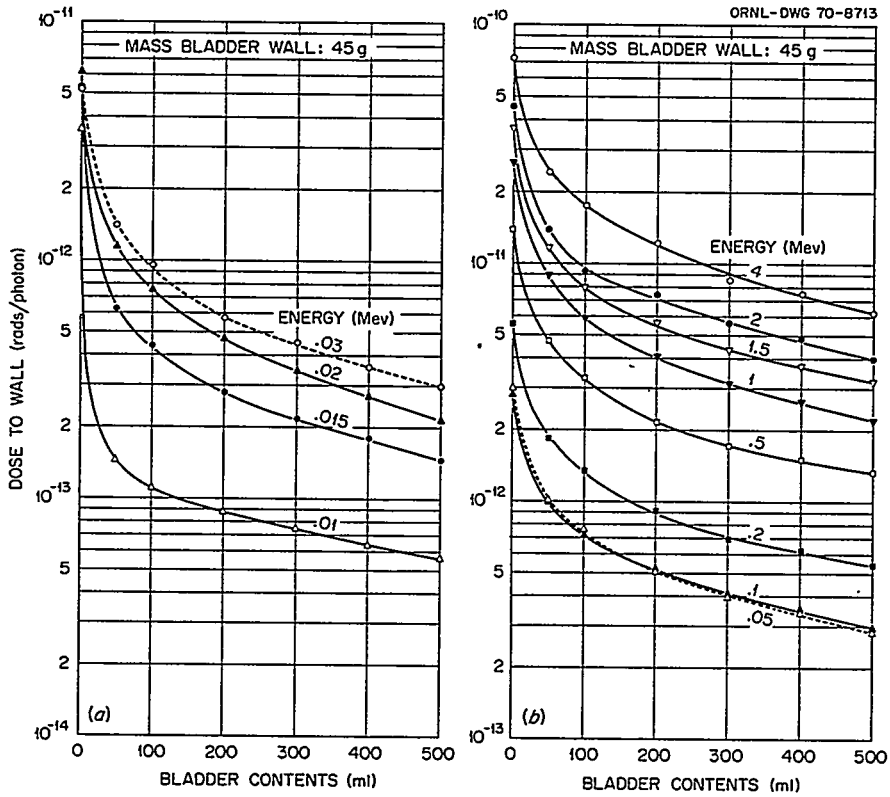

Fig. 19.12. Variation of Dose to Bladder Wall of a Photon Emitter in Urine as a Function of Photon Energy and Mass of Bladder Content. (*a*) Lower energies; (*b*) higher energies.

Where the mass absorption coefficient varies slowly (e.g., 0.1–4 MeV) the $D_r(V)$ decreases as photon energy decreases. but at still lower energies the increase in the mass absorption coefficient causes $D_r(V)$ to increase for small values of V; but for large V, attenuation predominates and $D_r(V)$ continues to decrease, although not regularly, as energy decreases. Also, the numerical values obtained by the Monte Carlo calculation are listed in Table 19.1 together with the coefficient of variation of each estimate, that is, coV = 100 (standard deviation)/estimate.

The data in Figs. 19.12*a,b* suggest a multiexponential form for $D_r(V)$. A two-exponential formula,

$$D_r(V) \approx ae^{-\lambda V} + be^{-\mu V} , \qquad (7)$$

has been found to fit the data with sufficient accuracy for practical purposes. The values of the parameters do change with photon energy sufficiently that no single formula applicable for the entire energy range is practical. The errors are not significantly less for a three-exponential form than for formula (7). The values of a, b, λ, and μ and the maximum percent deviation of the formula from the estimated value of $D_r(V)$ are given in Table 19.2. An average percent deviation and a maximum deviation are also given for each energy.

The development of formula (7) is due to P. Brindza, ORAU summer student from Marquette University on assignment to the Health Physics Division.

APPLICATION OF BERMAN'S TEN-COMPARTMENT MODEL FOR HUMAN IODINE METABOLISM TO ESTIMATION OF MICROCURIE-DAYS RESIDENCE OF ^{123}I, ^{124}I, ^{125}I, ^{126}I, AND ^{131}I

S. R. Bernard

A computer code for solving systems of linear differential equations (written by J. A. Carpenter, ORNL Mathematics Division) was employed to obtain the equations for retention and the residence times in the ten compartments of the model for iodine kinetics proposed by Berman.[18]

[18] M. Berman, *J. Clin. Endocrinol. Metab.* 28, 1 (1968).

Table 19.1. Dose to Bladder Wall from a Source in the Contents

Energy (MeV)	Dose (rads/μCi-hr) for Volume of Contents of													
	0 ml		50 ml		100 ml		200 ml		300 ml		400 ml		500 ml	
	Dose	Coefficient of Variation (%)	Dose	Coefficient of Variation (%)	Dose	Coefficient of Variation (%)	Dose	Coefficient of Variation (%)	Dose	Coefficient of Variation (%)	Dose	Coefficient of Variation (%)	Dose	Coefficient of Variation (%)
0.01	4.72×10^{-4}	0.027	1.90×10^{-5}	2.8	1.45×10^{-5}	3.2	1.18×10^{-5}	3.6	9.78×10^{-6}	3.9	8.43×10^{-6}	4.2	7.55×10^{-6}	4.5
0.015	7.04×10^{-4}	0.053	8.29×10^{-5}	1.5	5.83×10^{-5}	1.8	3.69×10^{-5}	2.3	2.99×10^{-5}	2.6	2.39×10^{-5}	2.9	1.92×10^{-5}	3.2
0.02	8.30×10^{-4}	0.20	1.51×10^{-4}	1.1	1.00×10^{-4}	1.4	6.25×10^{-5}	1.9	4.57×10^{-5}	2.2	3.60×10^{-5}	2.4	3.02×10^{-5}	2.7
0.03	6.93×10^{-4}	0.46	1.87×10^{-4}	1.0	1.27×10^{-4}	1.3	7.66×10^{-5}	1.6	6.01×10^{-5}	1.8	4.74×10^{-5}	2.1	3.94×10^{-5}	2.2
0.05	3.99×10^{-4}	0.77	1.32×10^{-4}	1.3	1.01×10^{-4}	1.4	6.77×10^{-5}	1.7	5.19×10^{-5}	1.9	4.56×10^{-5}	1.9	3.73×10^{-5}	2.1
0.1	3.71×10^{-4}	0.99	1.31×10^{-4}	1.6	9.52×10^{-5}	1.8	6.86×10^{-5}	2.1	5.41×10^{-5}	2.3	4.75×10^{-5}	2.4	3.97×10^{-5}	2.6
0.2	7.37×10^{-4}	1.1	2.43×10^{-4}	1.9	1.77×10^{-4}	2.2	1.22×10^{-4}	2.6	9.22×10^{-5}	2.9	8.30×10^{-5}	3.1	7.18×10^{-5}	3.3
0.5	1.84×10^{-3}	1.4	6.25×10^{-4}	2.4	4.41×10^{-4}	2.8	3.05×10^{-4}	3.3	2.28×10^{-4}	3.8	2.00×10^{-4}	4.1	1.77×10^{-4}	4.2
1.0	3.51×10^{-3}	1.6	1.18×10^{-3}	2.7	7.81×10^{-4}	3.3	5.35×10^{-4}	3.9	4.11×10^{-4}	4.5	3.49×10^{-4}	4.9	3.11×10^{-4}	5.2
1.5	4.86×10^{-3}	1.7	1.55×10^{-3}	3.1	1.05×10^{-3}	3.7	7.45×10^{-4}	4.3	5.75×10^{-4}	5.0	4.92×10^{-4}	5.3	4.26×10^{-4}	5.7
2.0	6.02×10^{-3}	1.8	1.86×10^{-3}	3.3	1.24×10^{-3}	4.0	9.79×10^{-4}	4.6	7.48×10^{-4}	5.2	6.46×10^{-4}	5.6	5.31×10^{-4}	6.2
4.0	9.70×10^{-3}	2.1	3.20×10^{-3}	3.7	2.34×10^{-3}	4.4	1.62×10^{-3}	5.2	1.13×10^{-3}	6.1	1.00×10^{-3}	6.7	8.28×10^{-4}	7.3

This model proposed by Berman is shown in Fig. 19.13. In all, 12 compartments, ten of them "body" compartments and two excretion compartments, are implied. The two excretion compartments are numbered 0 and 6. Note that there are six compartments (2, 5, 12, 13, 10, and 11) representing the thyroid. The remaining compartments (1, 8, 9, and 4) are not given a clearly defined anatomical location. In this report we take these compartments (1, 4, 8, and 9) as total-body (TB) compartments, while compartments 2, 5, 10, 11, 12, and 13 are taken as thyroid (T) compartments. We have computed microcurie-days residence at 50 years for each of the compartments of Berman's model except those for excretion. The sum of

Table 19.2. Parameter Values for Dose to Bladder Wall: $D_\gamma(V) = ae^{-\lambda V} + be^{-\mu V}$ (rads/photon)

E (MeV)	a	λ	b	μ	Deviation of Function and Data (%)	
					Average	Maximum
	$\times 10^{-12}$		$\times 10^{-12}$			
0.01	0.126	0.00168	3.474	0.0953	±2.51	+4.8
0.015	0.479	0.00252	4.811	0.0631	±4.28	+8.9
0.02	0.872	0.00292	5.301	0.0507	±4.44	+8.7
0.03	0.977	0.00248	4.162	0.0388	±3.83	+10.7
0.05	0.807	0.00218	2.172	0.0390	±3.65	+8.6
0.1	0.766	0.00195	2.022	0.0378	±2.30	−5.4
0.2	1.311	0.00187	4.124	0.0344	±4.04	+9.0
0.5	3.284	0.00192	10.471	0.0342	±3.66	−7.8
1.0	6.137	0.00213	19.916	0.0349	±2.56	−4.6
1.5	8.274	0.00199	28.293	0.0377	±3.03	−6.0
2.0	10.587	0.00198	34.723	0.0414	±2.04	−4.6
4.0	19.086	0.00235	53.210	0.0380	±5.08	−10.9

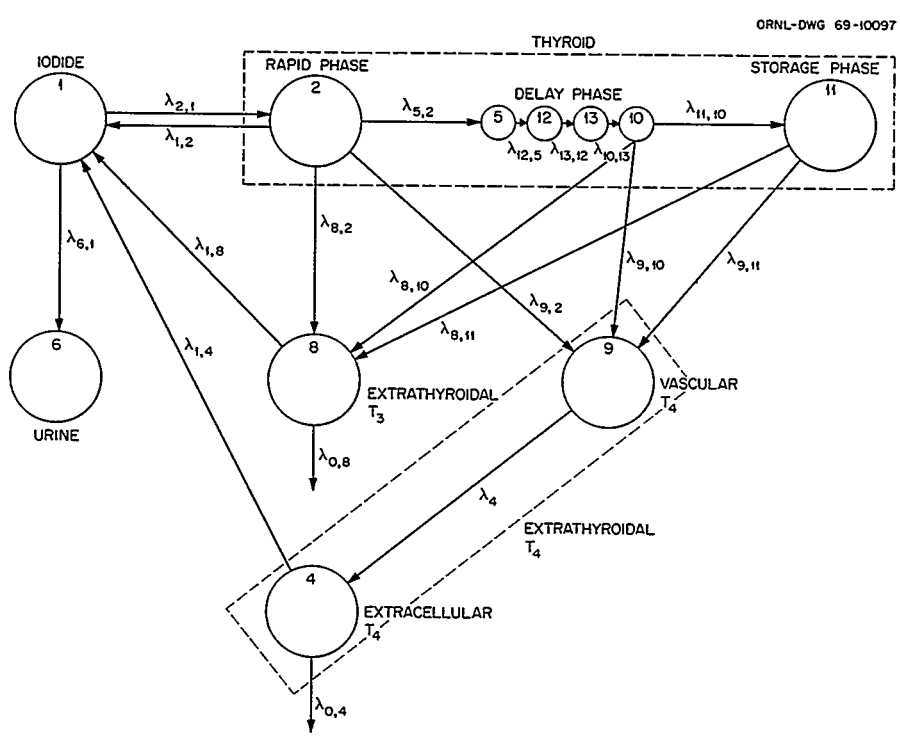

Fig. 19.13. Berman's Compartment Model for Iodine Metabolism.

the residence times for these compartments present in the thyroid (here designated by T) and the sum of the extrathyroidal compartments (here designated by TB) are given.

The equations for the amounts of iodine present in each compartment of the model, written in matrix notation, are

$$\dot{Y}(t) = -\Lambda\, Y(t)\,. \tag{1}$$

Here $Y(t)$ is a column vector of ten elements $y_j(t)$ (j = 1, ..., 10) corresponding to the amount of iodine in the jth compartment at time t; $\dot{Y}(t)$ is the derivative of the column vector $Y(t)$; $\Lambda = (\lambda_{jk})$ is a 10 by 10 matrix of transfer coefficients λ_{jk} ($j, k = 1, ..., 10$), and the values for a normal man have been specified by Berman. We do not list these here. They may be found in ref. 18. We do list the solution vectors we have obtained in our application of the computer code. It is unfortunate that these cannot be compared with those of Berman. In Table 19.3 are listed the eigenvalues corresponding to metabolism of stable iodine. Note these are generally complex numbers.

In order to explain the solutions which follow we have to discuss the solution of the differential equations (1). The computer is instructed to diagonalize the matrix Λ, that is, find P and D, where

$$\Lambda = P^{-1} D P \tag{2}$$

and where P is the matrix whose column vectors are left eigenvectors and D is a diagonal matrix whose diagonal elements are the eigenvalues and P^{-1} is just the inverse of P or the matrix of right eigenvectors. Now the solution can be shown to be

$$Y(t) = (P^{-1} e^{-Dt} P)\, Y(0)\,, \tag{3}$$

where

$$e^{-Dt} = \begin{pmatrix} e^{-d_1 t} & 0 \ldots 0 \\ 0 & e^{-d_2 t} \ldots 0 \\ \vdots & \\ 0 & 0 \ldots e^{-d_n t} \end{pmatrix} \tag{4}$$

and d_j is the eigenvalue. Here $Y(0)$ is the column vector of initial values. Now consider the special case where $Y(0)$ represents a vector with all elements equal to 0 except the first, that is, unit amount is present in compartment 1 at time $t = 0$. It is seen from Eq. (3) that the elements of the vector $Y(t)$, that is, the solutions for the amounts present in the various compartments, are linear combinations of the exponentials $e^{-d_j t}$ (j = 1, ..., n). If a vector E is defined to have its jth element equal to $e^{-d_j t}$ and if a diagonal matrix B is defined by $b_{jj} = p_{j1}$, then

$$Y(t) = P^{-1} B E = C E\,,$$

where $C = P^{-1} B$.

Let $R(C)$ and $I(C)$ be matrices formed of the real and imaginary parts of C and similarly let $R(E)$ and $I(E)$ be the vectors composed of the real and imaginary parts of E. Then the $R[Y(t)]$, the real part of $Y(t)$, is given by

$$R[Y(t)] = R(C)\, R(E) - I(C)\, I(E)\,. \tag{5}$$

Since $I[Y(0)] = 0$ and the differential equation is linear, this implies that $Y(t) = R[Y(t)]$. In Table 19.4 the elements of $R(C)$ and $I(C)$ are displayed. In our notation E is the vector with jth component $e^{-d_j t} = e^{-R(d_j)t}[\cos I(-d_j)t + i \sin I(-d_j)t]$. Explicit solutions

Table 19.3. Eigenvalues of the 10 × 10 Matrix of λ_{jk} for Stable Iodine

Compartment No. (This Paper)	Compartment No. (Berman's Paper)	$R(d_j)$	$I(d_j)$	$R(E_j)$	$I(E_j)$
1	1	+0.588	0.0	$e^{-0.588t}$	0
2	2	+0.134	0.0	$e^{-0.134t}$	0
3	4	+0.00720	0.0	$e^{-0.00720t}$	0
4	5	+1.71	0.0	$e^{-1.71t}$	0
5	8	+1.82	0.0	$e^{-1.82t}$	0
6	9	+2.43	0.0	$e^{-2.43t}$	0
7	10	+2.88	−0.585	$e^{-2.88t} \cos 0.585t$	$e^{-2.88t} \sin 0.585t$
8	11	+2.88	+0.585	$e^{-2.88t} \cos 0.585t$	$-e^{-2.88t} \sin 0.585t$
9	12	+3.47	−0.307	$e^{-3.47t} \cos 0.307t$	$-e^{-3.47t} \sin 0.307t$
10	13	+3.47	+0.307	$e^{-3.47t} \cos 0.307t$	$e^{-3.47t} \sin 0.307t$

Table 19.4. Real and Imaginary Parts of the Coefficient Matrix.

RL PT COEFFICIENT MATRIX

ROW	COLUMN 1	COLUMN 2	COLUMN 3	COLUMN 4	COLUMN 5
1	0.2202903630621784D-02	-0.2628739910498479D-03	0.9414137494319557D-03	-0.1776916959904730D 00	0.2614307215996C56D 00
2	0.2154827542922038D-02	-0.1780699016997300D-03	0.5873549545453755D-03	0.1847699865513981D 01	-0.1241375793875425D 01
3	-0.1542342916728187D-03	-0.7510475726783714D-02	0.1268307209734235D-01	-0.1490207528765254D 01	0.2190999317679779D 01
4	0.1339894185297667D-02	-0.9318996700046442D-04	0.2943837931695032D-03	0.2142126819772562D 01	-0.1578819610932594D 01
5	0.9324590065150744D-02	0.1159107588455794D-04	0.2713910858105051D-02	-0.3094057880365201D 00	0.2701801555524823D 00
6	0.3506432757204924D-04	0.2852307090214026D-05	0.7977784964504127D-03	0.1172174243766892D 01	-0.1848762558622262D 01
7	0.2535083059903394D-02	-0.1053843544401191D-03	0.2926022038795395D-03	0.2590318483669365D 02	-0.2513189173736854D 02
8	-0.1316495126706840D-01	0.2554574999017570D-02	0.3132683926680671D 00	-0.4581474391414412D 02	0.4164132140521593D 02
9	0.1666320289706315D-02	-0.9753888632107686D-04	0.2950918078079136D-03	0.4966940137447544D 01	-0.4015981906789934D 01
10	0.2072270585509028D-02	-0.1020907577390659D-03	0.2958015252735171D-03	0.1151682248747849D 02	-0.1021529664566137D 02

RL PT COEFFICIENT MATRIX

ROW	COLUMN 6	COLUMN 7	COLUMN 8	COLUMN 9	COLUMN 10
1	0.1400967857875574D 00	0.1965336303086761D 00	0.1965336303086756D 00	0.1901077422984768D 00	0.1901077422984767D 00
2	-0.1705689927283272D 00	-0.1206162596492902D 00	-0.1206162596492899D 00	-0.9854333610370820D-01	-0.9854333610370820D-01
3	-0.1729321845342983D 01	0.2595709989421396D 00	0.2595709989421387D 00	0.2521848482326469D 00	0.2521848482326465D 00
4	-0.4499311357529754D 00	-0.2468075273720453D 00	-0.2468075273720446D 00	0.1893489468228150D 00	0.1893489468228153D 00
5	0.4662977102224951D 00	-0.1760705111880101D-01	-0.1760705111880090D-01	-0.2019540337499978D 00	-0.2019540337499974D 00
6	0.1987293145766414D 01	-0.2473996866130562D 00	-0.2473996866130553D 00	-0.4083705764080239D 00	-0.4083705764080233D 00
7	-0.6172361559164910D 02	-0.5123840858913818D 01	-0.5123840858913812D 01	0.3559864095462117D 02	0.3559864095462110D 02
8	0.7647422803692686D 02	-0.3893587658609167D 01	-0.3893587658609150D 01	-0.3240814411359021D 02	-0.3240814411359015D 02
9	-0.2373679104060777D 01	0.1007020483084393D 01	0.1007020483084390D 01	-0.2965919829884042D 00	-0.2965919829884007D 00
10	-0.1252269967853077D 02	0.8317527272174222D 01	0.8317527272174197D 01	-0.2708073344493916D 01	-0.2708073344493899D 01

IM PT COEFFICIENT MATRIX

ROW	COLUMN 1	COLUMN 2	COLUMN 3	COLUMN 4	COLUMN 5
1	0.5944789086433186C-15	-0.9434260482664709D-16	0.1567019539997879D-16	0.9743077182853570D-16	0.0
2	0.5815050228362856D-15	-0.6390734321217755D-16	0.9776750034111276D-17	-0.1013118947405177D-14	0.0
3	-0.4162189943967395D-16	-0.2695427724600261D-14	0.2111146328139950D-15	0.8171010406703419D-15	0.0
4	0.3615858732542273D-15	-0.3344486153012353D-16	0.4900131917912344D-17	-0.1174557247831307D-14	0.0
5	0.2516347991088707D-14	0.4159910561426236D-17	0.4517409424951693D-16	0.1696513985562429D-15	0.0
6	0.9462512521013015C-17	0.1023661867732202D-17	0.1327933114724796D-16	-0.6427190682780230D-15	0.0
7	0.6841213523018066D-15	-0.3782129402056423D-16	0.4870476676194144D-17	-0.1420306828289600D-13	0.0
8	-0.3552713678800501D-14	0.9168090714103624D-15	0.5214473369130148D-14	0.2512084673287770D-13	0.0
9	0.4496757159527798D-15	-0.3500564118447020D-16	0.4911917094978889D-17	-0.2723440780505543D-14	0.0
10	0.5592260773292838D-15	-0.3663925813034604D-16	0.4923730616261635D-17	-0.6314830289128576D-14	0.0

IM PT COEFFICIENT MATRIX

ROW	COLUMN 6	COLUMN 7	COLUMN 8	COLUMN 9	COLUMN 10
1	-0.1877587587372098D-15	0.2439618644795124D-01	-0.2439618644795115D-01	0.9150484736031652D-02	-0.9150484736031222D-02
2	0.2285978380852420D-15	-0.7494545621335510D-01	0.7494545621335490D-01	-0.2113295148112063D-01	0.2113295148112040D-01
3	0.2317650053949898D-14	-0.3716986669467868D 00	0.3716986669467857D 00	-0.8363636303335570D-01	0.8363636303335620D-01
4	0.6030010688061382D-15	0.2572671644425348D 00	-0.2572671644425341D 00	0.1896576846934512D 00	-0.1896576846934507D 00
5	-0.6249356741570202D-15	0.2835944367001611D 00	-0.2835944367001603D 00	0.1132228019471667D 00	-0.1132228019471671D 00
6	-0.2663385117642051D-14	0.5856873801064639D 00	-0.5856873801064622D 00	0.1783685639623281D 00	-0.1783685639623289D 00
7	0.8272245064804340D-13	-0.4412533313698114D 02	0.4412533313698101D 02	-0.2381076054929703D 02	0.2381076054929709D 02
8	-0.1024913316239335D-12	0.4539078656952259D 02	-0.4539078656852246D 02	0.1775453428139476D 02	-0.1775453428139482D 02
9	0.3181222464980252D-14	0.1479985218563482D 01	-0.1479985218563477D 01	-0.1394087848654448D 01	0.1394087848654446D 01
10	0.1678301564495006D-13	-0.3407206465618726D 01	0.3407206465618718D 01	0.7079825380471367D 01	-0.7079825380471369D 01

for the retention function $Y_j(t)$ for the jth compartment are displayed below.

$$
\begin{aligned}
Y_1(t) = {} & 0.220 \times 10^{-2} e^{-0.588t} - 0.263 \times 10^{-2} e^{-0.134t} \\
& + 0.941 \times 10^{-3} e^{-0.00720t} - 0.178 \times 10^{0} e^{-1.71t} \\
& + 0.394 \times 10^{0} e^{-2.88t} \cos 0.585t \\
& + 0.380 \times 10^{0} e^{-3.47t} \cos 0.307t \\
& + 0.488 \times 10^{-1} e^{-2.88t} \sin 0.585t \\
& + 1.830 \times 10^{-2} e^{-3.47t} \sin 0.307t \,. \qquad (6a)
\end{aligned}
$$

$$
\begin{aligned}
Y_2(t) = {} & 0.215 \times 10^{-2} e^{-0.588t} - 0.178 \times 10^{-3} e^{-0.134t} \\
& + 0.587 \times 10^{-3} e^{-0.00720t} + 0.185 \times 10^{1} e^{-1.71t} \\
& - 0.124 \times 10^{1} e^{-0.82t} - 0.171 \times 10^{0} e^{-2.45t} \\
& - 0.242 \times 10^{0} e^{-2.88t} \cos 0.585t \\
& - 1.970 \times 10^{-1} e^{-3.47t} \cos 0.307t \\
& - 1.498 \times 10^{-1} e^{-2.88t} \sin 0.585t \\
& - 1.830 \times 10^{-2} e^{-3.47t} \sin 0.307t \,. \qquad (6b)
\end{aligned}
$$

$$
\begin{aligned}
Y_3(t) = {} & -0.154 \times 10^{-3} e^{-0.588t} - 0.751 \times 10^{-2} e^{-0.134t} \\
& + 0.127 \times 10^{-1} e^{-0.00720t} - 0.149 \times 10^{1} e^{-1.71t} \\
& + 0.219 \times 10^{1} e^{-1.82t} - 0.173 \times 10^{1} e^{-2.45t} \\
& + 0.520 \times 10^{0} e^{-2.88t} \cos 0.585t \\
& + 0.504 \times 10^{0} e^{-3.47t} \cos 0.307t \\
& - 0.744 \times 10^{0} e^{-2.88t} \sin 0.585t \\
& - 1.672 \times 10^{-1} e^{-3.47t} \sin 0.307t \qquad (6c)
\end{aligned}
$$

$$
\begin{aligned}
Y_4(t) = {} & 0.134 \times 10^{-2} e^{-0.588t} - 0.932 \times 10^{-4} e^{-0.134t} \\
& + 0.294 \times 10^{-3} e^{-0.00720t} + 0.214 \times 10^{1} e^{-1.71t} \\
& - 0.158 \times 10^{1} e^{-1.82t} - 0.450 \times 10^{0} e^{-2.45t} \\
& - 0.494 \times 10^{0} e^{-2.88t} \cos 0.585t \\
& + 0.504 \times 10^{0} e^{-3.47t} \cos 0.307t \\
& + 0.514 \times 10^{0} e^{-2.88t} \sin 0.585t \\
& + 0.380 \times 10^{0} e^{-3.47t} \sin 0.307t \,. \qquad (6d)
\end{aligned}
$$

$$
\begin{aligned}
Y_5(t) = {} & 0.932 \times 10^{-2} e^{-0.588t} + 0.116 \times 10^{-4} e^{-0.134t} \\
& + 0.271 \times 10^{-2} e^{-0.00720t} - 0.309 \times 10^{0} e^{-1.71t} \\
& + 0.270 \times 10^{0} e^{-1.82t} + 0.466 \times 10^{0} e^{-2.45t} \\
& - 0.352 \times 10^{-1} e^{-2.88t} \cos 0.585t \\
& - 0.404 \times 10^{0} e^{-3.47t} \cos 0.307t \\
& + 0.570 \times 10^{0} e^{-2.88t} \sin 0.585t \\
& + 0.226 \times 10^{0} e^{-3.47t} \sin 0.307t \,. \qquad (6e)
\end{aligned}
$$

$$
\begin{aligned}
Y_6(t) = {} & 0.351 \times 10^{-4} e^{-0.588t} + 0.285 \times 10^{-5} e^{-0.134t} \\
& + 0.798 \times 10^{-3} e^{-0.00720t} + 0.117 \times 10^{0} e^{-1.71t} \\
& - 0.185 \times 10^{1} e^{-1.82t} + 0.199 \times 10^{1} e^{-2.45t} \\
& - 0.494 \times 10^{0} e^{-2.88t} \cos 0.585t \\
& - 0.816 \times 10^{0} e^{-3.47t} \cos 0.307t \\
& + 1.172 \times 10^{0} e^{-2.88t} \sin 0.585t \\
& + 0.356 \times 10^{0} e^{-3.47t} \sin 0.307t \,. \qquad (6f)
\end{aligned}
$$

$$
\begin{aligned}
Y_7(t) = {} & 0.254 \times 10^{-2} e^{-0.588t} - 0.105 \times 10^{-3} e^{-0.134t} \\
& + 0.293 \times 10^{-3} e^{-0.00720t} + 0.259 \times 10^{2} e^{-1.71t} \\
& - 0.251 \times 10^{2} e^{-1.82t} + 0.199 \times 10^{1} e^{-2.45t} \\
& - 0.494 \times 10^{0} e^{-2.88t} \cos 0.585t \\
& - 0.816 \times 10^{0} e^{-3.47t} \cos 0.307t \\
& - 0.882 \times 10^{2} e^{-2.88t} \sin 0.585t \\
& - 0.476 \times 10^{2} e^{-3.47t} \sin 0.307t \,. \qquad (6g)
\end{aligned}
$$

$$
\begin{aligned}
Y_8(t) = {} & -0.132 \times 10^{-1} e^{-0.588t} + 0.255 \times 10^{-2} e^{-0.134t} \\
& + 0.313 \times 10^{0} e^{-0.00720t} - 0.458 \times 10^{2} e^{-1.71t} \\
& + 0.416 \times 10^{2} e^{-1.82t} + 0.765 \times 10^{2} e^{-2.45t} \\
& - 0.778 \times 10^{1} e^{-2.88t} \cos 0.585t \\
& - 0.648 \times 10^{2} e^{-3.47t} \cos 0.307t \\
& + 0.908 \times 10^{2} e^{-2.88t} \sin 0.585t \\
& + 0.356 \times 10^{2} e^{-3.47t} \sin 0.307t \,. \qquad (6h)
\end{aligned}
$$

$$
\begin{aligned}
Y_9(t) = {} & 0.167 \times 10^{-2} e^{-0.588t} - 0.975 \times 10^{-4} e^{-0.134t} \\
& + 0.295 \times 10^{-3} e^{-0.00720t} + 0.497 \times 10^{1} e^{-1.71t} \\
& - 0.402 \times 10^{1} e^{-1.71t} - 0.237 \times 10^{1} e^{-1.82t} \\
& + 0.202 \times 10^{1} e^{-2.88t} \cos 0.585t \\
& - 0.594 \times 10^{0} e^{-3.47t} \cos 0.307t \\
& + 0.296 \times 10^{1} e^{-2.88t} \sin 0.585t \\
& - 0.278 \times 10^{1} e^{-3.47t} \sin 0.307t \,. \qquad (6i)
\end{aligned}
$$

$$
\begin{aligned}
Y_{10}(t) = {} & 0.207 \times 10^{-2} e^{-0.588t} - 0.102 \times 10^{-3} e^{-0.134t} \\
& + 0.296 \times 10^{-3} e^{-0.00720t} + 0.115 \times 10^{2} e^{-1.71t} \\
& - 0.102 \times 10^{2} e^{-1.82t} - 0.125 \times 10^{2} e^{-2.45t} \\
& + 0.832 \times 10^{1} e^{-2.88t} \cos 0.585t \\
& - 0.542 \times 10^{1} e^{-3.47t} \cos 0.307t \\
& - 0.682 \times 10^{1} e^{-2.88t} \sin 0.585t \\
& + 1.416 \times 10^{1} e^{-3.47t} \sin 0.307t \,. \qquad (6j)
\end{aligned}
$$

It will be noted in Table 19.4 that certain elements of the matrix C are exceedingly small, less than 10^{-10}, and these have been interpreted to be 0. These occur in the imaginary parts of columns 1 through 6. Also, column 7 is the negative of column 8, and similarly for columns 9 and 10. It is also noted that only three digits have been used in the solutions $Y_1(t)$, ...,$Y_{10}(t)$. If additional digits (accuracy) are needed, then these can be obtained from Table 19.4.

The microcurie-days residence at 50 years were also computed in each of the ten compartments for injection of 1 μCi of ^{123}I, ^{124}I, ^{125}I, ^{126}I, and ^{131}I into compartment 1 and appear in Table 19.5. We mention that the correspondence between rows of the vector and Berman's compartment system is as follows:

Row No.	Berman's Compartment No.
1	1
2	2
3	4
4	5
5	8
6	9
7	10
8	11
9	12
10	13

Now the microcurie-days residence in the T and TB compartments mentioned earlier for each of these isotopes are shown in Table 19.6. Also shown are the estimates obtained by Snyder and Ford (unpublished data) in application of Riggs' three-compartment (*Pharmacol. Rev.* 4, 284, 1952) model as studied by Snyder, Fisher, and Boyd (ORNL-4007, p. 228). Here the inorganic and organic compartments are combined into the TB compartment. The point to note in this table is that there is only a slight difference in the microcurie-days residence given by either model. It is seen that the two models yield about the same residence times for these two compartments, namely, thyroid and total body, but in one case differ by a factor of about 2. This suggests that the three-compartment model of Riggs might be adequate for internal dose estimation for various isotopes of iodine injected into man.

APPLICATION OF A MAMMILLARY COMPARTMENT MODEL TO ESTIMATION OF MICROCURIE-DAYS RESIDENCE OF ^{232}Th, ^{228}Ra-^{228}Ac, ^{228}Th, AND ^{224}Ra IN MAN

S. R. Bernard C. F. Holoway

In a previous annual report[19] a mammillary model for distribution of thorium and radium in organs and tissues of man was presented, and the residence times for ^{232}Th and ^{228}Ra were estimated with this model. Two sets of residence times were computed. One calculation corresponded to the assumption of no recycling of radium daughter born in each of the compartments by decay of the thorium parent. Thus the radium daughter was assumed to be eliminated only by radioactive decay in situ. Another estimate of residence times was computed by the use of the other extreme assumption; namely, all of the radium daughter

[19] S. R. Bernard and C. F. Holoway, "Application of a Mammillary Compartment Model to the Estimation of Microcurie-Days Residence of ^{232}Th Parent and ^{228}Ra Daughter in Man," *Health Phys. Div. Ann. Progr. Rept. July 31, 1969*, ORNL-4446, p. 285.

Table 19.5. Microcurie-Days Residence at 50 Years in Each Compartment for Different Radionuclides per Microcurie Administered

Compartment No.	Microcurie-Days Residence for Isotope –				
	^{123}I	^{124}I	^{125}I	^{126}I	^{131}I
1	0.236×10^{0}	0.323×10^{0}	0.383×10^{0}	0.345×10^{0}	0.336×10^{0}
2	0.827×10^{-1}	0.182×10^{0}	0.237×10^{0}	0.207×10^{0}	0.198×10^{0}
3	0.125×10^{-2}	0.407×10^{-1}	0.614×10^{0}	0.162×10^{0}	0.933×10^{-1}
4	0.292×10^{-1}	0.863×10^{-1}	0.118×10^{0}	0.102×10^{0}	0.863×10^{-1}
5	0.152×10^{-2}	0.173×10^{-1}	0.148×10^{0}	0.478×10^{-1}	0.314×10^{-1}
6	0.863×10^{-3}	0.607×10^{-2}	0.444×10^{-1}	0.150×10^{-1}	0.102×10^{-1}
7	0.102×10^{-1}	0.726×10^{-1}	0.115×10^{0}	0.955×10^{0}	0.873×10^{-1}
8	0.242×10^{-1}	0.124×10^{1}	0.160×10^{2}	0.455×10^{1}	0.273×10^{1}
9	0.206×10^{-1}	0.818×10^{-1}	0.117×10^{0}	0.100×10^{0}	0.936×10^{-1}
10	0.145×10^{-1}	0.775×10^{-1}	0.117×10^{0}	0.984×10^{-1}	0.910×10^{-1}

Table 19.6. Comparison of Microcurie-Days Residence at 50 Years in Thyroid (T) Compartments and Total Body (TB) Compartments from Berman's Model and Riggs' Model

Lumped Compartment	^{123}I		^{124}I		^{125}I		^{126}I		^{131}I	
	Berman	Riggs	Berman	Riggs	Berman	Riggs	Berman	Riggs	Berman	Riggs
T	0.181	0.184	1.74	1.79	16.7	18.0	5.15	5.30	3.29	3.39
TB	0.240	0.277	0.387	0.416	1.19	2.60	0.596	0.786	0.471	0.567

formed by decay of the thorium parent was cycled to blood, where it was eliminated as would be the case with freshly injected radium. We tested these models against data of Stover *et al.*[20] on retention of ^{228}Th and ^{224}Ra in beagle dogs. They defined the fraction of radium daughter undergoing translocation in the body by

$$F_T(t) = \frac{1 - (^{224}Ra/^{228}Th)\ \text{body}}{0.3}$$

and reported that $F_T(t)$ decreased with time after injection (see Fig. 19.14). The fraction $F_T(t)$ was computed for the extreme cases of no recycling and for 100% recycling of the ^{224}Ra daughter using parameters appropriate for the beagle dog (see ORNL-4446), and results are plotted in Fig. 19.14. As can be seen the assumption of 0% recycling produces a lower estimate of $F_T(t)$ than the data of Stover *et al.* This lower $F_T(t)$ would correspond to higher estimates of dose commitment than the other case.

In this report we have made additional calculations corresponding to the cases of 50% recycling and 20% recycling, and the results are also plotted in Fig. 19.14. Here it can be seen that the case of 20% recycling of ^{224}Ra daughter corresponds to an $F_T(t)$ which more closely agrees with the experimental findings than the other cases shown in the figure. The case of 50% recycling overshoots the data at all times. Since the agreement with the dog data is better when 20% recycling is assumed, we shall assume in the following that this fraction also applies to man and compute corresponding estimates of microcurie-days residence in the various compartments of the mammillary model. In order to estimate microcurie-days residence in man, we use the data for the mammillary model given in the previous report. There we showed how to operate on total-body-retention equations to estimate parameters for the mammillary model. We only present here the final results in microcurie-days residence employing the parameters derived before for man.

Table 19.7 presents estimates of microcurie-days residence for ^{232}Th, ^{228}Ra-^{228}Ac, ^{228}Th, and ^{224}Ra following entry of ^{232}Th to blood. For comparison, estimates of microcurie-days residence are given using these assumptions: 0% recycling of all daughters, 20% recycling of the two radium daughters, and 100% recycling of all daughters. As can be noted, the long-term bone compartment has the highest microcurie-days, and the estimates of residence using 20% recycling of radium daughters is not much different than that using 0% recycling. Also, it can be noted that in the case of 100% recycling of all daughters the residence in blood is higher than it is in the other cases. Note too the microcurie-days residence in blood of ^{224}Ra is higher than the residence in bone when 100%

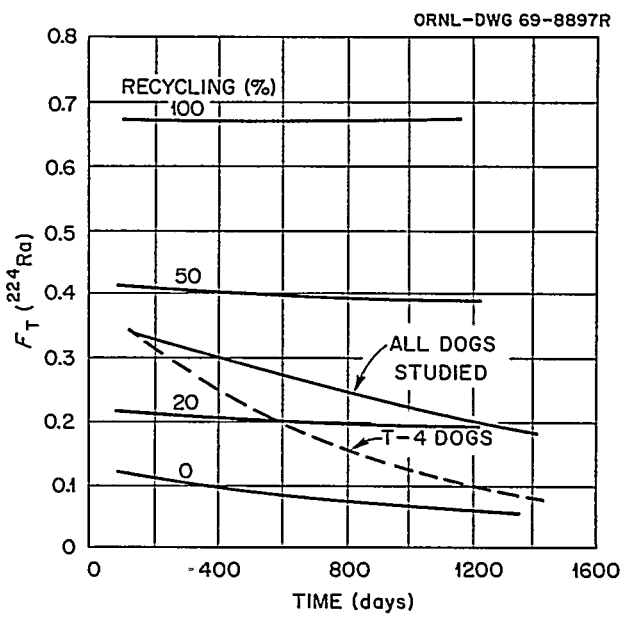

Fig. 19.14. Stover *et al.* Estimate of Fraction of ^{224}Ra Formed in the Dog Which Translocates Compared with Estimates Made with Model in Text.

[20] B. J. Stover *et al.*, "The ^{228}Th Decay Series in Adult Beagles: ^{224}Ra, ^{212}Pb, and ^{212}Bi in Blood and Excretion," *Radiation Res.* 26, 226 (1965).

Table 19.7. Microcurie-Days at 50 Years for ^{232}Th, ^{228}Ra-^{228}Ac, ^{224}Th, and ^{224}Ra Chain in Man for Cases of No Recycling, 20% Recycling to Blood of the Two Ra Daughters, and 100% Recycling

Radionuclide	Compartment	Microcurie-Days at 50 Years		
		0% Recycling	20% Recycling	100% Recycling
^{232}Th	Blood	1.267×10^{1}	1.267×10^{1}	1.267×10^{1}
	Bone, long term	1.014×10^{4}	1.014×10^{4}	1.014×10^{4}
	Bone, short term	1.425×10^{3}	1.425×10^{3}	1.425×10^{3}
	Soft tissues	6.229×10^{2}	6.229×10^{2}	6.229×10^{2}
^{228}Ra-^{228}Ac	Blood	3.642×10^{1}	5.406×10^{1}	1.195×10^{2}
	Bone, long term	6.962×10^{3}	5.513×10^{3}	1.331×10^{2}
	Bone, short term	1.382×10^{2}	1.148×10^{1}	2.792×10^{1}
	Soft tissues	6.085×10^{1}	5.086×10^{1}	1.375×10^{1}
^{228}Th	Blood	1.699×10^{0}	1.487×10^{0}	1.362×10^{0}
	Bone, long term	6.433×10^{3}	5.104×10^{3}	8.609×10^{1}
	Bone, short term	1.732×10^{2}	1.497×10^{2}	1.043×10^{2}
	Soft tissues	7.569×10^{1}	6.551×10^{1}	4.550×10^{1}
^{224}Ra	Blood	7.487×10^{0}	8.998×10^{2}	2.006×10^{2}
	Bone, long term	6.416×10^{3}	4.080×10^{3}	5.531×10^{-1}
	Bone, short term	1.702×10^{2}	1.218×10^{2}	8.825×10^{-1}
	Soft tissues	7.441×10^{1}	5.353×10^{1}	4.346×10^{-1}

recycling is assumed. The reason for this is that the shortest half-life for radium in blood is 20 days (see ORNL-4446, Tables 24.5 and 24.6), and hence ^{224}Ra with its 3.6-day half-life undergoes decay in the blood before reentering bone. This is the price one pays for approximating the power function with a sum of only three exponentials. Further study of this problem is indicated.

SCATTERED ENERGY SPECTRUM FOR A MONOENERGETIC GAMMA EMITTER UNIFORMLY DISTRIBUTED IN AN INFINITE CLOUD

L. T. Dillman[21]

Introduction

A basic problem in assessing the radiation dose received by various parts of the human body due to an external source of radiation distributed in a cloud is first of all to determine the spectrum of radiations incident upon the body. It is obvious that for a monoenergetic gamma emitter uniformly distributed in an infinite cloud there will be a continuous spectrum of scattered photons ranging in energy up to that of the initial photon. This spectrum results from Compton events in the scattering medium and also from the annihilation photons associated with pair production when this process is energetically possible. In addition, there will be a continuous spectrum of scattered electrons as a result of the photoelectric, Compton, and pair production events. For the case of an infinite unbounded medium it is clear from symmetry that there will be no angular dependence of the scattered photon and electron spectra but only energy dependence. This fact considerably reduces the complexity of the analysis of the problem, but a residual core of moderately complex equations remains. This report discusses analytic procedures which may be used to determine the scattered photon and electron spectra for the case of a monoenergetic gamma emitter uniformly distributed in an infinite unbounded cloud of air.

Several calculations of scattered photon spectra similar to those reported here have been made previously for the case of a water medium,[22] but the

[21] Consultant to ORNL from Ohio Wesleyan University.

[22] U. Fano, L. V. Spencer, and M. J. Berger, "Penetration and Diffusion of X-Rays," *Handbuch Der Physik*, S. Flugge, ed., vol. XXXVIII/2, pp. 660–817, Springer-Verlag, 1959.

technique employed was numerical solution of the moment equations rather than direct numerical integration of the integral equation, which is discussed in this report. Calculations of the scattered electron spectrum have not been reported previously in the literature.

Calculation of the Differential Photon and Electron Density Functions

The principal mathematical symbols used in this report are defined below.

E_0 = energy of initial photons in MeV,

$f(E')$ = differential photon density at energy E' (photons per initial photon per unit energy interval),

$\alpha_0 = E_0/m_0c^2$, the initial photon energy in terms of rest-mass energy units,

$K_p(E', E)\,dE'$ = probability that a photon of energy E will give rise to a Compton-scattered *photon* in the range of energy between E' and $E' + dE'$,

$K_e(E', E)\,dE'$ = probability that a photon of energy E will give rise to a Compton-scattered *electron* in the range of energy between E' and $E' + dE'$,

$P(E', E)\,dE'$ = probability that a photon of energy E will give rise to a pair-production electron *or* positron in the range of energy between E' and $E' + dE'$,

$\tau(E)$ = photoelectric cross section at energy E,

$\sigma(E)$ = Compton cross section at energy E,

$\kappa(E)$ = pair-production cross section at energy E,

$\mu(E) = \tau(E) + \sigma(E) + \kappa(E)$ = total cross section at energy E,

$g(E')$ = differential electron density at energy E' (electrons per initial photon per unit energy interval),

$\alpha = E/mc^2$, the energy E in terms of rest-mass energy units.

With these definitions the function $f(E')$ is determined from

$$f(E') = K_p(E', E_0) + \int_{E'}^{E_0} f(E)\,K_p(E', E)\,dE\,. \quad (1)$$

The first term on the right-hand side of Eq. (1) is the contribution to $f(E')$ due to the initial photons, and the second term is the contribution to $f(E')$ from the scattered radiation of energy higher than E'. The integral in the second term is required since all radiation of energy higher than E' has a finite probability of scattering with a resultant scattered photon energy of E'. Of course, the Compton scattering equations imply that $K_p(E', E) = 0$ if $E' < E/(1 + 2\alpha)$, and this discontinuity must be taken into account.

In this integral equation for $f(E')$, which is of the Volterra type, function $K_p(E', E)$ for an air medium, using MeV as the energy unit and all cross sections in cm^2/g, is given by

$$K_p(E', E) = 0.0755829 \left[1 + (1-x)^2 + \frac{\alpha^2 x^2}{1 + \alpha x}\right] \frac{1}{\alpha E'\,\mu(E)}\,, \quad (2)$$

where

$$x = \frac{E - E'}{\alpha E'}\,,$$

for

$$E' \geqslant \frac{E}{1 + 2\alpha}$$

and

$$K_p(E', E) = 0.0$$

if

$$E' < \frac{E}{1 + 2\alpha}\,.$$

The integral equation has been solved numerically using an iterative technique. This iterative technique makes use of the fact that the solution is given exactly by $K_p(E_0, E_0)$ when $E' = E$. One uses this result as a trial solution at E' slightly less than E_0 and performs the integration of the second term on the right-hand side to obtain a better approximation to the solution. This second approximation is then used in the integral on the right-hand side to obtain a still better approximation to the solution, etc., until the iterative procedure is terminated when the change in the iterated solution is less than 0.1% from the previous iteration. By this process one can work gradually downward in energy to obtain $f(E')$ at all desired energies.

In the computer implementation of Eq. (1), $f(E')$ was determined for 100 uniformly spaced energy increments between zero energy and the initial photon

energy, E_o. The numerical integration of the second term on the right-hand side of Eq. (1) was performed by quadrature using Simpson's rule, and the integration was terminated when the approximation to the integral changed by less than 0.1% in consecutive quadratures.

$$g(E') = f(E')\frac{\tau(E')}{\mu(E')} + K_e(E', E_0) + \int_{E'}^{E_0} f(E)\, K_e(E', E)\, dE + 2\left[P(E', E_0) + \int_{E'+2m_0c^2}^{E_0} f(E)\, P(E', E)\, dE\right] . \quad (3)$$

The first term on the right-hand side of Eq. (3) is due to photoelectric absorption of photons of energy E', the second term is due to Compton scattering of the initial photons which give rise to electrons of energy E', the third term is due to scattered photons which give rise to electrons of energy E', and the fourth and last term is due to pair-production events which give rise to electrons of energy E'. The factor of 2 in the fourth term is present because a positron and an electron are created with each pair-production event, and statistically over many such events the number of positrons of energy E' is the same as the number of electrons of energy E'. The fourth term has been separated into two parts, the first term being the contribution due to the initial photons and the second term being due to the scattered photons.

In Eq. (3) the function $K_e(E', E)$ for an air medium, using MeV as the energy unit and all cross sections in cm^2/g, is given by

$$K_e(E', E) = 0.0755829\left[1 + (1-x)^2 + \frac{\alpha^2 x^2}{1+\alpha x}\right]\frac{1}{\alpha E\, \mu(E)} , \quad (4)$$

where

$$x = \frac{E'}{\alpha(E - E')} ,$$

for

$$E' \leqslant \frac{2\alpha E}{1+2\alpha}$$

and

$$K_e(E', E) = 0.0$$

if

$$E' > \frac{2\alpha E}{1+2\alpha} .$$

Similarly the function $P(E', E)$ is given by

$$P(E', E) = 0.0012925TZ(1-Q)\, K(E)/\mu(E) , \quad (5)$$

where $Q = 0.135(T - 0.52)Z(1 - Z^2)$, with the restriction that Q is set equal to zero if this expression for Q is negative, and where

$$Z = 2[x(1-x)]^{1/2} ,$$

where

$$x = \frac{E'}{E - 2m_0c^2} ,$$

and

$$T = \frac{P^2}{2E_h{}^3}\left\{-\frac{1}{3} - \frac{E_h^2}{P^2} + \frac{m_0^2c^4E_h}{P^3}\epsilon - \frac{m_0^2c^4}{P^2}\epsilon^2 + 2\ln\left(\frac{E_h}{m_0c^2}\right)\left[\frac{E_h^2(E_h^4+P^4)}{P^6} - \frac{2E_h^2}{3P^2} - \frac{m_0^2c^4E_h}{P^2}\left(\frac{m_0^2c^4\epsilon}{P^3} + \frac{E_h{}^3}{P^4}\right)\right]\right\} ,$$

where

$$\epsilon = \ln\left(\frac{E_h + P}{m_0c^2}\right) ,$$

$$P = (E_h^2 - m_0^2c^4)^{1/2} ,$$

$$E_h = E/2 .$$

In addition to the above expressions for $f(E')$ and $g(E')$ the probability of obtaining annihilation radiation per initial photon, P_a, is

$$P_a = 2\left[\frac{K(E_0)}{\mu(E_0)} + \int_{2m_0c^2}^{E_0} f(E)\frac{K(E)}{\mu(E)}\, dE\right] , \quad (6)$$

where the integral is, of course, zero if $E_o \leqslant 2m_0c^2$. The probability of obtaining photoelectrons of energy equal to the initial photon energy, P_e, is

$$P_e = \frac{\tau(E_0)}{\mu(E_0)} . \quad (7)$$

The probability of obtaining photoelectrons of energy equal to the annihilation radiation energy, P_{ae}, is

$$P_{ae} = P_a\frac{\tau(m_0c^2)}{\mu(m_0c^2)} . \quad (8)$$

These equations have been applied to find the differential photon and electron densities for a source

of monoenergetic photons uniformly distributed in an infinite homogeneous cloud of *air*. The generated table of terms of $f(E')$ as a function of E' from Eq. (1) is used to evaluate $g(E')$. The integrals on the right-hand side of Eqs. (1), (3), and (6) must, in general, be evaluated by dividing the range of the integration into several smaller subranges of integration because of discontinuities in the functions $f(E)$, $K_p(E', E)$, and $K_e(E', E)$. For example, $f(E)$ is discontinuous at $E = E_0/(1 + 2\alpha_0)$, $K_p(E', E)$ is discontinuous at $E' = E/(1 + 2\alpha)$, and $K_e(E', E)$ is discontinuous at $E' = 2\alpha E/(1 + 2\alpha)$. The cross sections used in this work were computed from theoretical expressions given in Chap. 2 of *Alpha-, Beta- and Gamma-Ray Spectroscopy*,[23] but interpolation from National Bureau of Standards or comparable tables[24,25] would work equally well and provide greater speed.

ORNL-DWG 70-10368

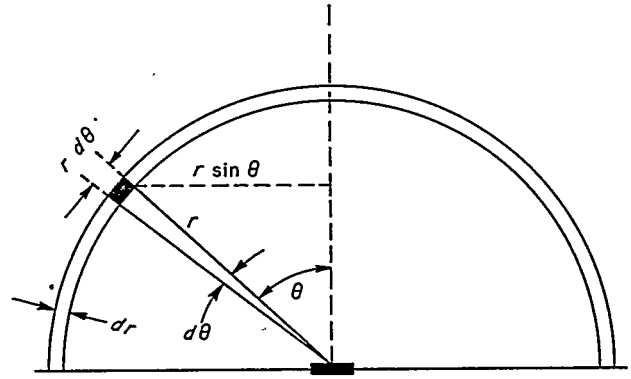

Fig. 19.15. Illustration of Geometric Parameters Involved in the Calculation of the Photon Flux.

Calculation of the Photon and Electron Fluxes

The equations discussed above may in turn be used to find the photon and electron fluxes which pass through any given cross-sectional area of the infinite cloud. Consider the volume element of the cloud, $r^2\, dr \sin\theta\, d\bar{\theta}$, which is illustrated in Fig. 19.15. The number of disintegrations per second in this volume element, dV, is $3.7 \times 10^4\ C\rho\, dV$, where $dV = \text{cm}^3$, $3.7 \times 10^4 = \text{dis sec}^{-1}\ \mu\text{Ci}^{-1}$, $C = \mu\text{Ci}$ per gram of air, and ρ = the density of air = $1.2929 \times 10^{-3}\ \text{g/cm}^3$. Thus disintegrations per second in volume $dV = 47.84C\, dV$. Now the solid angle subtended by an infinitesimal area dA as shown, for a point at dV is

$$d\Omega = \frac{dA \cos\theta}{r^2} ,$$

and so the fraction of radiations emitted from dV which start out in a direction such that they would pass through dA if undeflected or unabsorbed is

$$\text{fraction} = \frac{dA \cos\theta}{4\pi r^2} .$$

But the probability that the gamma rays survived to distance r is $e^{-\mu r}$, where μ is the linear absorption coefficient. Thus the number of gamma rays from volume element dV which pass through dA per second is

$$\frac{47.84C\, dV\, F\, dA \cos\theta\, e^{-\mu r}}{4\pi r^2} = \frac{3.807CF \cos\theta\, dA\, dV\, e^{-\mu r}}{r^2} ,$$

where F is the number of initial gamma rays per disintegration. Integrating over the half space which can contribute to photons passing through dA in one direction (i.e., integrating over the ranges $0 \leqslant \phi \leqslant 2\pi$, $0 \leqslant \theta \leqslant \pi/2$, and $0 \leqslant r \leqslant \infty$), we have

initial photons per second passing through dA in one sense

$$= 3.807CF\, dA \int_0^{2\pi} d\phi \int_0^{\pi/2} \cos\theta \sin\theta\, d\theta \int_0^{\infty} e^{-\mu r}\, dr = \frac{11.96CF}{\mu}\, dA .$$

Thus the number of initial photons per second per square centimeter of area is obtained by dividing this result by dA; so we have

$$\text{initial photons sec}^{-1}\ \text{cm}^{-2} = \frac{11.96CF}{\mu(E_0)} . \qquad (9)$$

Since we are dealing with an infinite medium, there are scattered photons associated with each initial photon. Let $f(E)$ represent the number of scattered

[23] C. M. Davisson, "Interaction of Gamma Radiation with Matter," *Alpha-, Beta- and Gamma-Ray Spectroscopy*, K. Siegbahn, ed., chap. 2, North-Holland, Amsterdam, 1966.

[24] G. W. Grodstein, "X-Ray Attenuation Coefficients for 10 keV to 100 MeV," *NBS Circular 583*, 1957; and R. T. McGinnis, *Supplement to NBS Circular 583*, 1959.

[25] J. H. Hubbell, "Photon Cross Sections, Attenuation Coefficients, and Energy Absorption Coefficients from 10 keV to 100 GeV," NSRDS-NBS 29, 1969.

photons per initial photon per MeV at energy E [see Eq. (1)]. Then the number of scattered photons $\sec^{-1}$ cm^{-2} MeV^{-1} at energy E is

$$\text{scattered photons sec}^{-1}\ \text{cm}^{-2}\ \text{MeV}^{-1} = \frac{11.96CF\,f(E)}{\mu(E)}. \quad (10)$$

In Eqs. (9) and (10), $\mu(E)$ = linear absorption coefficient in cm^{-1} rather than in cm^2/g as used previously. In addition, if the initial photon energy is above $2m_0c^2$, pair production will give rise to annihilation quanta. Let P_a be the probability of obtaining annihilation radiation per initial photon [see Eq. (6)]. Then the number of annihilation photons $\sec^{-1}$ cm^{-2} will be given by

$$\text{annihilation photons sec}^{-1}\ \text{cm}^{-2} = \frac{11.96CFP_a}{\mu(m_0c^2}. \quad (11)$$

Next we shall calculate the number of electrons $\sec^{-1}$ cm^{-2} MeV^{-1} which cross a unit cross-sectional area in one sense in the medium of air. The number of disintegrations per second per cubic centimeter of air is $3.7 \times 10^4\ \rho C = 47.84C$, where the units are as given previously. Thus the number of electrons per unit volume per second associated with a particular gamma ray and of energy equal to that of the gamma ray is

$$\text{initial photoelectrons sec}^{-1}\ \text{cm}^{-3} = 47.84CFP_e,$$

where F is the number of gamma rays per disintegration and P_e is the probability of obtaining photoelectrons of the energy equal to the initial photon energy as given by Eq. (7). Consider a volume of cross-sectional area A and thickness dr. The number of initial photoelectrons emitted per second by such a volume is $47.84CFP_eA\ dr$. Now $dE = S(E)\ dr$, where $S(E)$ is the stopping power; that is, $S(E) = dE/dr$ by definition. Hence the number of initial photoelectrons emitted per second by such a volume may be written as $47.84CFP_eA\ dE/S(E)$.

Half of these photoelectrons will pass through one surface of area A and the other half through the other surface. The number of photoelectrons which pass through surface A in one sense per second is $23.92CFP_eA\ dE/S(E)$. The number of initial photoelectrons per square centimeter per MeV is simply obtained by dividing this result by $A\ dE$. Letting $N(E)_p$ represent the number of initial photoelectrons per square centimeter per MeV in one sense we have

$$N(E)_p = \frac{23.92CFP_e}{S(E)}. \quad (12)$$

Because of scattering there will be a continuous distribution of Compton-scattered electrons and photoelectrons of energy lower than the initial gamma-ray energy. Now $g(E')$ in Eq. (3) represents the number of such electrons per initial photon per MeV. Any such electrons which initially start out with an energy greater than E will pass through energy E in the slowing-down process and thus contribute to the flux at energy E. Therefore the number of scattered electrons cm^{-2} sec^{-1} MeV^{-1}, $N(E)_c$, is

$$N(E)_c = \frac{23.92CF \int_E^{E_0} g(E')\,dE'}{S(E)}. \quad (13)$$

The total number of electrons cm^{-2} sec^{-1} MeV^{-1}, $N(E)$, is thus

$$N(E) = \frac{23.92CF}{S(E)}\left[P_e + \int_E^{E_0} g(E')\,dE'\right]. \quad (14)$$

This expression neglects the probability of obtaining photoelectrons of energy equal to the annihilation radiation energy, P_{ae}, which is negligible for air. To include this effect in the above equation one would merely add the term P_{ae} to the two terms in the brackets.

In Eqs. (12), (13), and (14), $S(E)$ is in units of MeV/cm. $S(E)$ was determined from the relativistic Bethe-Block equation.[26]

Discussion of the Results

The calculated photon and electron fluxes for initial photon energies of 0.1, 0.5, and 4.0 MeV are shown in Figs. 19.16, 19.17, and 19.18 respectively. The results are for a source intensity of 1 μCi per gram of air and assuming 1 photon per disintegration. The discontinuities in the photon flux curves occur at an energy corresponding to the fact that there is a minimum energy of the scattered photon equal to $E_0/(1 + 2\alpha_0)$ when the *initial* photon scatters. The discontinuity in the case of the 0.1-MeV initial energy photon curve is sufficiently severe that a small bump in the curve occurs at an energy value of approximately $E/(1 + 2\alpha)$, where $E = E_0/(1 + 2\alpha_0)$. This is precisely what one would expect.

The discontinuities in the slope of the electron flux curves occur at an energy complementary to that of the

[26] G. Knop and W. Paul, "Interaction of Electrons and Alpha Particles with Matter," *Alpha-, Beta- and Gamma-Ray Spectroscopy*, K. Siegbahn, ed., chap. 1, p. 12, North-Holland, Amsterdam, 1966.

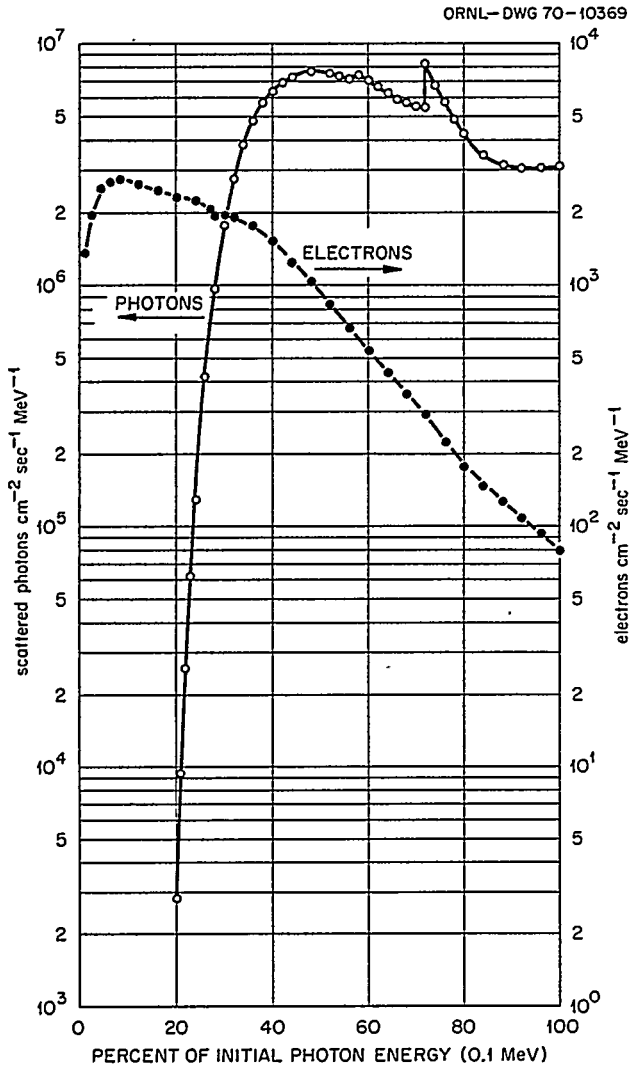

Fig. 19.16. Photon and Electron Fluxes in an Infinite Cloud of Air for a 0.1-MeV Photon Emitter Uniformly Distributed in the Cloud. Source intensity is 1 μCi per gram of air.

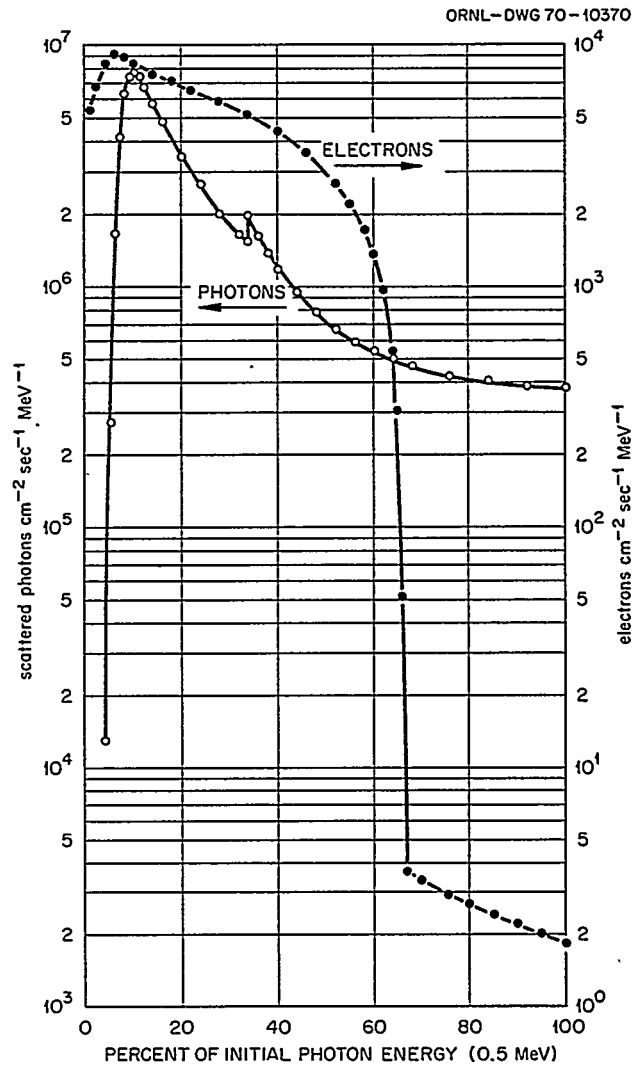

Fig. 19.17. Photon and Electron Fluxes in an Infinite Cloud of Air for a 0.5-MeV Photon Emitter Uniformly Distributed in the Cloud. Source intensity is 1 μCi per gram of air.

photon flux discontinuity, namely, at an energy value of $E_0 - E_0/(1 + 2\alpha_0)$.

The curves illustrated have been tested in several ways. The energy integral of the function $g(E)$ determined by Eq. (3) plus the energy associated with initial photoelectrons should equal the initial photon energy, since all of the photon energy is eventually delivered to electrons. The observed error increases slowly as the initial photon energy increases and amounts to 1.2% at 4.0 MeV, the highest energy used. At 0.5 MeV the error is 0.3%. One expects the error to increase with increasing initial photon energy because of the rapid variation of $g(E)$ at low energy values when the initial photon energy is high. The numerical integration of the function $g(E)$ over energy thus becomes less accurate.

Another test of the accuracy of the results presented here has been to obtain the curves by an alternate procedure.[27] The alternate procedure is only expected to be accurate at energies greater than approximately 20% of the initial photon energy, and the two methods agree to better than 1% in this region.

[27] L. T. Dillman, unpublished data, 1969.

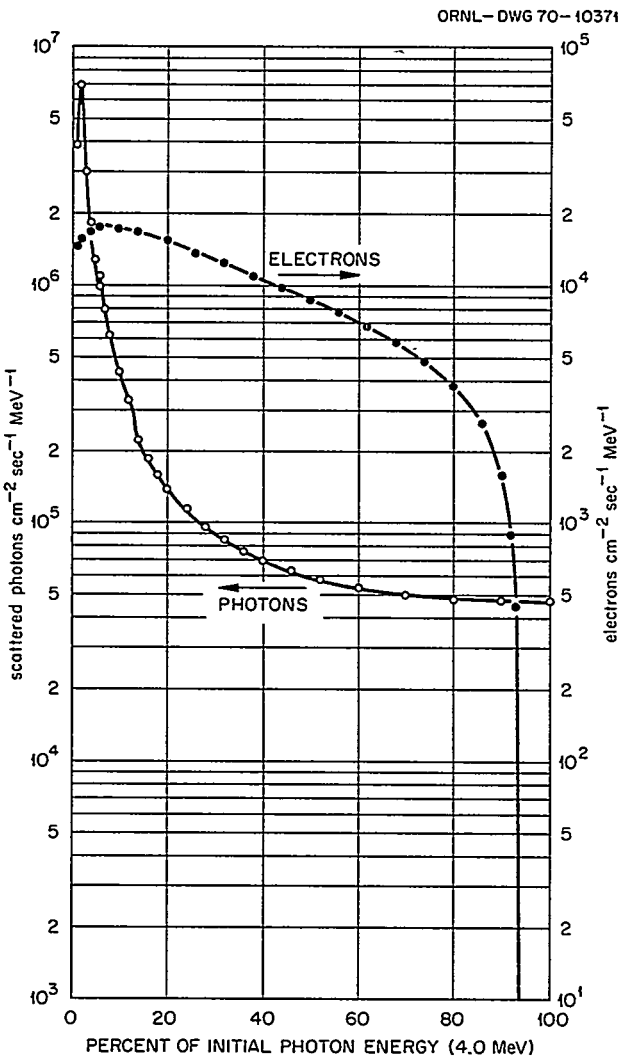

Fig. 19.18. Photon and Electron Fluxes in an Infinite Cloud of Air for a 4.0-MeV Photon Emitter Uniformly Distributed in the Cloud. Source intensity is 1 μCi per gram of air.

It is important to note that the photon fluxes illustrated in Figs. 19.16–19.18 are only for *scattered* photons. In addition, there are initial photon fluxes of 6.098×10^4, 1.055×10^5, and 2.997×10^5 photons cm^{-2} sec^{-1} for the 0.1-, 0.5-, and 4.0-MeV initial photon energy cases respectively. Furthermore, there is an annihilation quanta flux of 1.500×10^4 photons cm^{-2} sec^{-1} in the case of the 4.0-MeV initial photon energy case, where pair production is possible.

Work is presently in progress to apply these results to immersion dose problems. The most obvious application is to program the Monte Carlo gamma-ray code developed by Snyder and Fisher[28,29] for a source uniformly distributed on the surface of the phantom they use to represent standard man. Then if one picks initial photon energies according to the probability distribution implied by the photon fluxes calculated in this report and runs the Monte Carlo code for many photons, one may calculate the relative dose distribution to various organs of the body. A number of modifications must be considered so that photon and electron fluxes associated with finite and bounded clouds may be determined.

---

[28] H. L. Fisher, Jr., and W. S. Snyder, *Health Phys. Div. Ann. Progr. Rept. July 31, 1966*, ORNL-4007, p. 221.

[29] H. L. Fisher, Jr., and W. S. Snyder, *Health Phys. Div. Ann. Progr. Rept. July 31, 1967*, ORNL-4168, p. 245.

20. Stable Element Metabolism

ELEMENTAL INTAKE AND EXCRETION IN LONG-TERM BALANCE STUDIES

Isabel H. Tipton[1] Peggy L. Stewart[1]

This final year of the program for the study of trace elements in normal human beings has been spent for the most part in analyzing duplicates of the self-chosen daily diet and all excreta of a fourth adult male, subject F, for the period November 6, 1967, to November 14, 1968. This material has been ashed, and values for the concentrations of Cd, Ca, Mg, P, K, Na, and Zn have been determined by atomic absorption or flame photometry. Ashed samples have been excited in a dc arc, and photographic records of spectra have been made. Transmissions of appropriate lines of 16 elements (Al, Ba, Be, B, Cr, Co, Cu, Fe, Mn, Mo, Ni, Sr, Sn, Ti, V, and Zn) on the resulting films have been measured with a densitometer. Unfortunately there has not been time to convert these raw data into concentrations nor to calculate the daily intake and excretion from the concentrations already determined.

Descriptive statistics for a full year's data for subject E [see annual report 1969 (ORNL-4446)] have been prepared, and multiple regressions of diets and feces and diets and urine have been carried out [see annual report 1968 (ORNL-4316)]. Table 20.1 includes the mean daily elemental intake by ingestion and fecal and urinary excretion and Table 20.2 gives the mean daily gross dietary intake and gross fecal and urinary excretion.

Plots of daily intake and excretion (Fig. 20.1) brought to light an interesting circumstance for this subject. A marked elevation in the intake of magnesium, which began on the 148th day of the period and continued for 14 days, was followed by a similar elevation in fecal excretion on the 174th day which lasted for 17 days.

Regressions were run on fecal excretion over a 4-day period and intake over the same period, the previous 4-day period, 2 periods previous, and so on through 12 periods previous or covering a total of 48 days before excretion for the three subjects C, D, and E. For subjects C and D no significant relation between fecal excretion and intake by ingestion of magnesium was brought out by this statistical treatment. For subject E, however, this treatment indicated a high correlation between the 4-day amount of magnesium excreted in feces and the intake by ingestion during the two 4-day periods that included the 29th to 36th days previous. In fact, the multiple correlation coefficient R for this subject was 0.91, indicating that 83% (R^2) of the variability of magnesium in feces was due to the intake 29 to 36 days previously. The correlation coefficients for the periods 29–32 and 33–36 days previous were 0.43 and 0.26, indicating that for this subject 69% of magnesium ingested during an 8-day period was excreted after an elapse of about 4 to 5 weeks.

GROSS COMPOSITION OF BONE AND CARTILAGE

Isabel H. Tipton[1] Cyrus Feldman[2]
Mary Jane Cook

Samples of bone and cartilage, carefully collected by Alfred P. Stoholski, M.D., of the New York Medical Examiner's office, were analyzed at ORNL, and the results of the analyses were used to calculate the gross composition shown in Table 20.3.

The same rib and vertebra and a portion from the same region of costal cartilage, skull, and sternum were taken at autopsy, placed in polyethylene bags, and transported frozen to ORNL, where they were kept frozen until analysis.

Specific gravity was determined by the method of water displacement on thawed bone. Dry weight was determined first after the sample had been in a freeze-drying apparatus overnight at 50 μ pressure and

[1] Department of Physics, University of Tennessee.
[2] Analytical Chemistry Division.

Table 20.1. Mean Daily Intake by Ingestion and Fecal and Urinary Excretion

Subject E: October 5, 1964–October 5, 1965 (365 days)
All values except ratio in milligrams per day

Element	Diet, Mean (±S.E.)	Feces, Mean (±S.E.)	Urine, Mean (±S.E.)	Excreta, Sum of Feces plus Urine (±S.E.)	Balance (±95% Confidence Interval), Difference, Diet Minus Excreta (±2S.E.)	Urine/Excreta, F_u
Al	21(2)	13.(0.6)	0.56(0.03)	14(0.6)	7.(4.2)	0.040
Ba	1.0(0.1)	0.96(0.02)	0.021(0.007)	0.98(0.02)	0.02(0.13)	0.021
Be	0.043(0.003)	0.00034(0.0001)	0.00058(0.0003)	0.00092(0.0003)	0.042(0.006)	0.63
B	13.(1.)	0.30(0.006)	2.2(0.4)	2.5(0.4)	10.5(2.)	0.88
Ca	1100.(23.)	790.(17.)	230(5.1)	1000(18)	80.(60.)	0.23
Cd	0.14(0.004)	0.047(0.001)	0.075(0.004)	0.12(0.004)	0.02(0.01)	0.62
Cr	0.51(0.07)	0.12(0.001)	0.33(0.04)	0.45(0.04)	0.06(0.08)	0.62
Co	0.24(0.02)	0.047(0.003)	0.16(0.02)	0.21(0.02)	0.03(0.06)	0.76
Cu	4.1(0.2)	2.5(0.1)	0.031(0.004)	2.8(0.08)	1.3(0.4)	0.011
Fe	25.(0.8)	18.(0.4)	1.6(0.13)	20(0.4)	5(2)	0.080
Mg	380.(19.)	320.(14.)	70.(2)	330(14)	50(50.)	0.21
Mn	7.9(0.8)	2.5(0.1)	0.006(0.002)	2.5(0.1)	5.4(2)	0.0024
Mo	0.11(0.01)	0.052(0.001)	0.053(0.015)	0.11(0.01)	0.0(0.03)	0.48
Ni	0.88(0.25)	0.29(0.01)	0.084(0.016)	0.37(0.02)	0.51(0.5)	0.23
P	1900.(32.)	550.(14.)	1100.(25.)	1700(28)	200.(90)	0.65
K	3100(35.)	420(10)	2500(48.)	2900.(50)	200.(120)	0.86
Ag	0.095(0.008)	0.0037(0.0005)	0.010(0.002)	0.014(0.002)	0.081(0.02)	0.71
Na	4500.(63.)	210.(7.)	4300.(71.)	4500(72)	0(190)	0.96
Sr	2.2(0.1)	3.4(0.1)	0.21(0.011)	3.6(0.1)	−1.4(0.4)	0.058
Sn	15(0.8)	2.7(0.1)	0.066(0.018)	2.8(0.1)	12.(2.)	0.024
Ti	0.18(0.02)	0.26(0.01)	0.14(0.01)	0.40(0.02)	−0.22(0.06)	0.35
V	0.071(0.004)	0.053(0.002)	0.010(0.001)	0.063(0.003)	0.01(0.02)	0.16
Zn	14.0(0.3)	15.0(0.4)	0.52(0.02)	16.0(0.4)	2.0(0.3)	0.032
Zr	0.045(0.004)	0.032(0.002)	0.058(0.019)	0.090(0.02)	−0.045(0.04)	0.64

Table 20.2. Gross Daily Intake and Excretion (g/day)

Subject E: October 5, 1964–October 5, 1965
Mean ± standard deviation

Total daily intake by ingestion	3200 ± 520
Water content	2700 ± 580
Total daily fecal excretion	220 ± 72
Total daily urinary excretion	1100 ± 200

Table 20.3. Gross Composition of Bone and Cartilage

Number of subjects included in each determination indicated in parentheses

Tissue	Water (% ± S.D.)	Ash (% ± S.D.)	Fat (% ± S.D.)	Protein (% ± S.D.)	Specific Gravity
Cartilage (costal)	54.7 ± 6.2 (4)	2.1 ± 0.2 (4)	3.4 ± 0.9 (4)	32.1 ± 3.3 (4)	1.13 ± 0.001 (4)
Rib	25.9 ± 10.8 (4)	38.8 ± 6.6 (5)	9.0 ± 4.7 (4)	22.6 ± 6.9 (4)	1.40 ± 0.08 (4)
Skull	15.6 ± 6.8 (7)	50.2 ± 5.4 (7)	7.2 ± 4.1 (7)	20.4 ± 3.8 (7)	1.66 ± 0.116 (7)
Sternum	46.4 ± 8.2 (8)	13.0 ± 2.7 (8)	10.1 ± 3.0 (8)	27.4 ± 5.1 (8)	1.14 ± 0.028 (8)
Vertebra	45.3 ± 4.8 (4)	17.2 ± 3.8 (4)	22.2 ± 2.9 (4)	10.1 ± 2.0 (4)	1.17 ± 0.030 (4)
Rib plus vertebra	33.0 (1)	N.D.	10.8	24.1	1.25

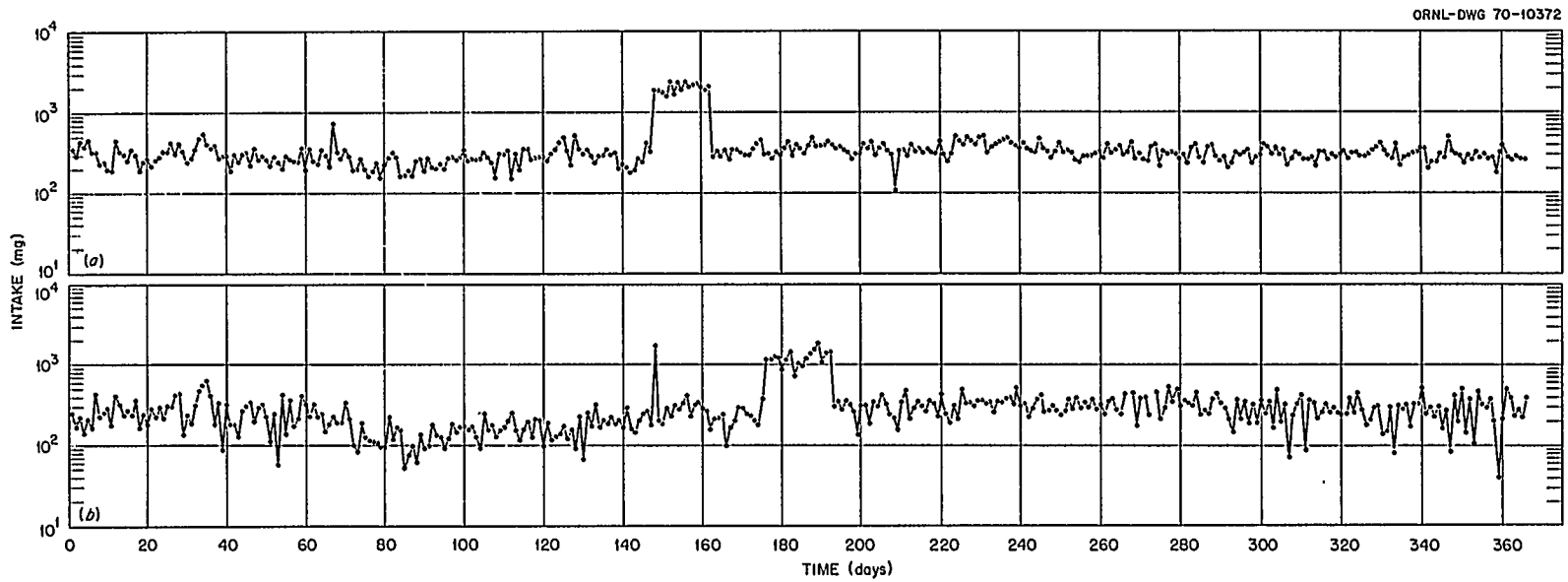

Fig. 20.1. (*a*) Daily Dietary Intake of Magnesium in Milligrams, Subject E, October 5, 1964–October 5, 1965; (*b*) Daily Fecal Excretion of Magnesium in Milligrams, Subject E, October 5, 1964–October 5, 1965.

again after the freeze-dried sample had been in a drying oven at 110° for 18 hr. The water content was determined on the basis of the weight after this final drying, An aliquot of the freeze-dried material was ashed in a muffle furnace at 450°C, and the weight of ash was related back to wet weight to determine ash percent of wet weight.

Each freeze-dried sample was finely divided in a special apparatus. Aliquots of this mealy material were taken for fat extraction by the Folch procedure [(*J. Biol. Chem.* 226, 479–509 (1967)] and total nitrogen determination by the Kjeldahl method. Total nitrogen values were used in calculating the protein in the total sample.

Theses, Papers, Publications, and Lectures

Theses

A. J. Braundmeier, Jr.
Plasmon Radiation from Electron Bombarded Aluminum Foils, ORNL-TM-2612 (December 1969).

A. J. Braundmeier, Jr.
Radiative Decay of Coulomb-Stimulated Plasmons in Al, Mg, and Be (in preparation).

Barbara Brooks
The Application of the Technique of Ellipsometry in the Determination of the Optical Constants of Sodium (in preparation).

E. L. Chaney
Electron Attachment to Polyatomic Molecules, ORNL-TM-2613 (January 1970).

A. A. Christodoulides
Resonant Electron Attachment Processes in Polyatomic Molecules (in preparation).

P. M. Collins
Investigation of Negative Ions with Electron Beams, ORNL-TM-2614 (in preparation).

J. J. Cowan
Surface Plasmon Resonance Effects in Grating Diffraction, ORNL-TM-2615 (November 1969).

C. E. Easterly
Study of Aromatic Hydrocarbons in Relation to Carcinogenesis, ORNL-TM-2616 (in preparation).

J. M. Elson
Collective Excitations in Inhomogeneous Plasmas (in preparation).

T. F. Gesell
Photoelectric Properties of Magnesium in the Vacuum Ultraviolet, ORNL-TM-2617 (in preparation).

J. T. Grissom
Electron Impact Excitation and Ionization Studies of the Rare Gases, ORNL-TM-2618 (March 1970).

W. F. Hanson
Optical Properties of Solids in the Extreme Ultraviolet (in preparation).

D. L. McCorkle
Interactions of Low-Energy Electrons with Polyatomic Systems (in preparation).

W. T. Naff
Transient Negative Ion States and Electron Excitation in Cyclic Molecules (in preparation).

S. J. Nalley
Charge Exchange Between Fast Atoms and Molecules, ORNL-TM-2620 (in preparation).

M. N. Pisanias
Inelastic Scattering of Slow Electrons by Organic Molecules (in preparation).

B. L. Sowers
Optical Properties of Organic Liquids in the Vacuum Ultraviolet (in preparation).

R. B. Vora
Stopping Power of Matter at Extreme Relativistic Energies, ORNL-TM-2621 (in preparation).

U. S. Whang
Optical Constants of Cesium for Photons of Energy 5 to 9.6 eV, ORNL-TM-2622 (March 1970).

Papers

E. T. Arakawa
Optical and Electronic Properties of Liquids in the Vacuum UV, Symposium on Recent Developments in Radiation Dosimetry, March 4, 1970, Dallas, Texas.

E. T. Arakawa and T. Gesell
High Current Exo-Electron Emission from Mg, American Physical Society, September 2–4, 1969, Honolulu, Hawaii.

J. A. Auxier, T. D. Jones, and H. H. Hubbell, Jr.
Review of Depth Dose Calculation and Experimentation, Symposium on Neutrons in Radiobiology, November 11–14, 1969, Oak Ridge, Tennessee.

K. Becker
New Imaging Techniques for Ionizing Radiation, Second International Conference on Medical Physics, August 11–15, 1969, Boston, Massachusetts.

Recent Progress in Solid-State Dosimetry, Symposium on Neutrons in Radiobiology, November 11–14, 1969, Oak Ridge, Tennessee.

Recent Progress in Solid-State Dosimetry (Refresher Course), 55th Scientific Assembly of the Radiological Society of North America, November 30–December 5, 1969, Chicago, Illinois.

Thermal Fading in TSEE Dosimeters, Radiation Research Society, March 2–5, 1970, Dallas, Texas.

Solid-State Microdosimetry, IVth International Congress of Radiation Research, June 28–July 4, 1970, Evian, France.

Klaus Becker, J. S. Cheka, and R. B. Gammage
Progress in Exoelectron Dosimetry, International Symposium on Exoelectrons, July 6–8, 1970, Braunschweig, Germany.

Klaus Becker and K. W. Crase
Gamma and Fast Neutron Response of Ceramic TSEE Dosimeters, Health Physics Society, June 28–July 2, 1970, Chicago, Illinois (presented by K. Becker).

K. Becker and D. R. Johnson
Some Dosimetric Applications of Nuclear Track Registration in Polymers, Radiation Research Society, March 2–5, 1970, Dallas, Texas.

S. R. Bernard
Use of Mathematics in Interpreting Bioassay Data, Health Physics Society Annual Meeting, June 28–July 2, 1970, Chicago, Illinois.

S. R. Bernard (and R. L. Hayes)
Dose to Various Segments of the Gastrointestinal Tract, ORAU Symposium on Medical Radionuclides: Radiation Dose and Effects, December 8–11, 1969, Oak Ridge, Tennessee.

R. D. Birkhoff
The Electron Flux Spectra and Radiation Yields in Solids Irradiated by Nuclear Radiation, IEEE Conference on Nuclear and Space Radiation Effects, July 7–11, 1969, University Park, Pennsylvania.

W. P. Bonner
Pollution of an Underground Aquifer in Florida, Annual Meeting of Florida Pollution Control Association and Florida Section of American Water Works Association, November 2–6, 1969, Miami Beach, Florida.

R. H. Boyett, D. R. Johnson, and K. Becker
On the Oxygen Enhancement of Alpha Particle Track Registration in Polymers, Second International Conference on Medical Physics, August 11–15, 1969, Boston, Massachusetts.

R. L. Bradshaw
Disposal of Solidified Power Reactor Wastes in Salt Mines, American Nuclear Society Meeting, December 2–4, 1969, San Francisco, California.

A. J. Braundmeier, Jr., and E. T. Arakawa
Emission of Photons by Nonradiative Surface Plasmons, American Physical Society, Southeastern Section, November 6–9, 1969, Gainesville, Florida.

Zolin G. Burson
Energy and Angular Distribution of Neutrons Emerging from the HENRE Targets, American Nuclear Society, June 28–July 2, 1970, Los Angeles, California.

E. L. Chaney and L. G. Christophorou
Electron Attachment to N_2O, Sixth International Conference on the Physics of Electronic and Atomic Collisions, July 26–August 2, 1969, Cambridge, Massachusetts.

E. L. Chaney, L. G. Christophorou, P. M. Collins, and J. G. Carter
Electron Attachment in the Field of the Ground and Excited Electronic States of the Azulene Molecules, 22nd Annual Gaseous Electronics Conference, October 29–31, 1969, Gatlinburg, Tennessee.

L. G. Christophorou
Electron Molecule Interactions, IBM Corporation Research Center, April 6, 1970, York Town Heights, New York.

Resonance Electron Attachment Processes in Polyatomic Molecules, Symposium on the Chemistry of Ions in the Gas State, May 24–29, 1970, Toronto, Canada.

Criteria for Scientific Research, Nuclear Research Center "Democritus," June 5, 1970, Athens, Greece.

Cross Section Functions for Slow-Electron Molecule Collision Processes, International Discussion on Progress and Problems in Contemporary Radiation Chemistry, June 22–25, 1970, Marianské Lázné, Czechoslovakia.

L. G. Christophorou, J. G. Carter, E. L. Chaney, and P. M. Collins
Long-Lived Parent Negative Ions Formed by Capture of Low-Energy Electrons (0–3 eV) in the Field of the Ground and Excited Electronic States of Organic Molecules, IVth International Congress of Radiation Research, June 28–July 4, 1970, Evian, France.

P. M. Collins, L. G. Christophorou, E. L. Chaney, and J. G. Carter
Electron Attachment Cross Sections and Negative-Ion Lifetimes for p-Benzoquinone and 1,4-Naphthoquinone, 22nd Annual Gaseous Electronics Conference, October 29–31, 1969, Gatlinburg, Tennessee.

Mary Jane Cook (W. S. Snyder, and G. G. Warner)
Estimates of Dose to Red Bone Marrow from Monoenergetic Sources of Photons in Lung and Other Organs, Second Congress of the International Radiation Protection Association, May 3–8, 1970, Brighton, England.

R. N. Compton
Mass Identification of Negative Ions Formed in Electron Swarm Experiments, Annual Conference on Mass Spectrometry and Allied Topics, June 14–19, 1970, San Francisco, California.

R. N. Compton, J. A. D. Stockdale, and H. C. Schweinler
Negative Ion Formation in Selected Hexafluoride Molecules, Sixth International Conference on the Physics of Electronic and Atomic Collisions, July 26–August 2, 1969, Cambridge, Massachusetts.

J. J. Cowan and E. T. Arakawa
Dispersion of Surface Plasmons in Dielectric-Metal Coatings on Concave Diffraction Gratings, American Physical Society, Southeastern Section, November 6–8, 1969, Gainesville, Florida.

K. E. Cowser and E. G. Struxness
Methods of Estimating Potential Dose Equivalents to Population Groups, 1969 Winter Meeting of American Nuclear Society, November 30–December 4, 1969, San Francisco, California.

Wallace de Laguna
Radioactive Waste Disposal by Hydraulic Fracturing, Third Annual National Pollution Control Conference, April 1–3, 1970, San Francisco, California.

Radioactive Waste Disposal by Hydraulic Fracturing, American Gas Association Conference on Underground Storage, April 13–15, Denver, Colorado.

Waste Disposal by Hydraulic Fracturing, American Institute of Chemical Engineers, August 26–28, 1969, Portland, Oregon.

Radioactive Waste Disposal by Hydraulic Fracturing, 25th Industrial Waste Disposal Conference, Purdue University, May 5–7, 1970, Lafayette, Indiana.

B. R. Fish
Particle-Particle and Particle-Surface Adhesion and Removal Forces and *Parametric Sampling of Gasborne Particles,* U.S.–Japan Seminar on Particulate Technology, October 5–11, 1969, Kyoto, Japan.

Mary Rose Ford (W. S. Snyder and)
Energy Absorbed in Body Organs from Internal Emitters, Health Physics Society Annual Meeting, June 28–July 2, 1970, Chicago, Illinois.

C. W. Francis
Soil Mineral Segregation Using Isopycnic Zonal Centrifugation, Annual Meeting of the American Society of Agronomy, November 9–13, 1970, Detroit, Michigan.

W. R. Garrett
Variational Method for Long Range Scattering Interactions, Sixth International Conference on the Physics of Electronic and Atomic Collisions, July 26–August 2, 1969, Cambridge, Massachusetts.

W. R. Garrett and V. E. Anderson
Electron Scattering by Polar Molecules, 22nd Annual Gaseous Electronics Conference, October 29–31, 1969, Gatlinburg, Tennessee.

T. F. Gesell
Contamination Effects on the Photoelectric Properties of Magnesium Films in the Vacuum Ultraviolet, Optical Contamination in Space, August 13–15, 1969, Aspen, Colorado.

J. T. Grissom, R. N. Compton, and W. R. Garrett
Electron Impact Excitation and Ionization Studies of He, Ne, and Ar, 22nd Annual Gaseous Electronics Conference, October 29–31, 1969, Gatlinburg, Tennessee.

R. N. Hamm, M. W. Williams, and E. T. Arakawa
Optical Properties of Organic Liquids in the Vacuum Ultraviolet. I. Analysis of Optical Data, American Physical Society, Southeastern Section, November 6–8, 1969, Gainesville, Florida.

W. F. Hanson and E. T. Arakawa
Optical Properties of MgO and MgF_2 in the XUV, American Physical Society, April 27–30, 1970, Washington, D.C.

S. Jablon, S. Fujita, K. Fukushima, T. Ishimaru, and J. A. Auxier
RBE of Neutrons in Japanese Survivors, Symposium on Neutrons in Radiobiology, November 11–14, 1969, Oak Ridge, Tennessee (presented by J. A. Auxier).

D. G. Jacobs
Consideration of the Radiological Impact from the Hypothetical Use of Contaminated Natural Gas from Nuclearly Stimulated Reservoirs, Second International Congress of the International Radiation Protection Association, May 3–8, 1970, Brighton, England.

A Preliminary Assessment of the Radiological Implications of Commercial Utilization of Natural Gas from a Nuclearly Stimulated Well, Fourth Plowshare Symposium, January 14–16, 1970, Las Vegas, Nevada.

T. D. Jones and J. A. Auxier
Dose, Dose Equivalent, and Linear Energy Transfer Distributions from Several Configurations of ^{252}Cf Sources of Neutrons, Health Physics Society, June 28–July 2, 1970, Chicago, Illinois.

C. E. Klots
Photosensitized Ionization of Molecules, 2nd U.S.–Japan Conference on Fundamental Processes of Radiation Chemistry, November 10–13, 1969, Hakone, Japan.

Fundamental Processes in Gas-Phase Radiolysis, Gordon Conference on Radiation Chemistry, July 14–18, 1969, New Hampton, New Hampshire.

Comparison of Photoabsorption and Resonance Energy Transfer Processes, IVth International Congress of Radiation Research, June 28–July 4, 1970, Evian, France.

C. E. Klots and D. R. Nelson
The Ratio of Transverse and Longitudinal Diffusion Coefficients, 22nd Annual Gaseous Electronics Conference, October 29–31, 1969, Gatlinburg, Tennessee.

W. T. Naff, R. N. Compton, and C. D. Cooper
Electron Attachment in Substituted Aromatic Hydrocarbons, 18th Annual Conference on Mass Spectrometry and Allied Topics, June 14–19, 1970, San Francisco, California.

S. J. Nalley, J. A. D. Stockdale, and R. N. Compton
Charge Transfer from Negative Halogen Ions to NO_2, 22nd Annual Gaseous Electronics Conference, October 29–31, 1969, Gatlinburg, Tennessee.

D. R. Nelson and F. J. Davis
Thermal Electron Attachment Rates of SF_6 for Different Carrier Gas Dilutants, Sixth International Conference on the Physics of Electronic and Atomic Collisions, July 26–August 2, 1969, Cambridge, Massachusetts.

Jacob Neufeld
An Alternative Approach to the Formulation of Quality Factor, Second International Congress of IRPA, May 3–8, 1970, Brighton, England.

Ambiguity of the Term "Quality Factor," Second International Conference on Medical Physics, August 11–15, 1969, Boston, Massachusetts.

R. H. Ritchie
Surface Plasmons in Solids, American Physical Society, September 2–4, 1969, Honolulu, Hawaii.

Surface Collective Modes in Solids, 4th Thin Films and Surface Conference, April 6–8, 1970, Reading, United Kingdom.

S. Y. Shieh and R. H. Ritchie
Simultaneous Generation of Transition Radiation and Bremsstrahlung from a Thin Foil, American Physical Society, January 26–29, 1970, Chicago, Illinois.

W. S. Snyder

The Use of the Reciprocity Theorem for Estimation of Dose, Second International Conference on Medical Physics, August 11–15, 1969, Boston, Massachusetts.

The Relation of Intake to Blood, Blood Activity, and Excretion of Plutonium at Early Times Post Exposure, 15th Annual Bioassay and Analytical Chemistry Meeting, October 9–10, 1969, Los Alamos, New Mexico.

Estimation of Absorbed Fraction of Energy from Photon Sources in Body Organs, ORAU Symposium on Medical Radionuclides: Radiation Dose and Effects, December 8–11, 1969, Oak Ridge, Tennessee.

Estimation of Dose to Gonads from Gamma Emitters Present in the Body, Second Congress of the International Radiation Protection Association, May 3–8, 1970, Brighton, England.

Estimation of Dose and Dose Commitment to the Bladder Wall from a Radionuclide Present in Urine, Health Physics Society Annual Meeting, June 28–July 2, 1970, Chicago, Illinois.

B. L. Sowers, R. N. Hamm, M. W. Williams, and E. T. Arakawa

Optical Properties of Organic Liquids in the Vacuum Ultraviolet. II. Saturated Hydrocarbons, American Physical Society, Southeastern Section, November 6–8, 1969, Gainesville, Florida.

J. A. D. Stockdale, R. N. Compton, and P. W. Reinhardt

Reactions of Low Energy O^- with Hydrocarbons, IVth International Congress of Radiation Research, June 28–July 4, 1970, Evian, France.

E. G. Struxness and P. S. Rohwer

An Approach to the Development of Guidelines for Plowshare, presented at 2nd Session of U.S.-U.S.S.R. Exchange Talks, Moscow, February 10–18, 1970.

Tsuneo Tamura

Soil Mineral Segregation Using Isopycnic Zonal Centrifugation, Annual Meeting of American Society of Agronomy, November 10–14, 1969, Detroit, Michigan.

J. E. Turner

Determination of Dose Equivalent for Monte Carlo Analysis of Pulse Height Spectra, Second International Conference on Medical Physics, August 11–15, 1969, Boston, Massachusetts.

J. E. Turner, R. D. Birkhoff, V. E. Anderson, E. B. Wagner, and H. A. Wright

Monte Carlo Method of Determining LET Spectra from Pulse-Height Measurements, Second Symposium on Microdosimetry, October 20–24, 1969, Ispra, Italy.

J. E. Turner, J. Dutrannois, H. A. Wright, J. Baarli, R. N. Hamm, and A. H. Sullivan

Calculation of Pion Depth-Dose Curves and Comparison with Experiment, IVth International Congress of Radiation Research, June 28–July 4, 1970, Evian, France.

J. E. Turner and H. A. Wright

Calculation of Dose from High-Energy Nucleons, Second International Conference on Accelerator Dosimetry and Experience, November 5–7, 1969, Stanford, California.

R. B. Vora and J. E. Turner

Stopping Power of Matter for Deuterons at Extreme Relativistic Energies, American Physical Society, Southeastern Section, November 6–8, 1969, Gainesville, Florida.

U. S. Whang, E. T. Arakawa, and T. A. Callcott

Optical Constants of Cesium for Photons of Energy 5 to 9.6 eV, American Physical Society, March 23–26, 1970, Dallas, Texas.

M. W. Williams, B. L. Sowers, R. N. Hamm, R. D. Birkhoff, and E. T. Arakawa

Optical Properties of Organic Liquids in the Vacuum Ultraviolet. III. Silicone Pump Oils, American Physical Society, Southeastern Section, November 6–8, 1969, Gainesville, Florida.

Harvel Wright and W. S. Snyder

Summability of the Derivates of Arbitrary Real-Valued Set Functions, 76th Annual Meeting of the American Mathematical Society, January 22–26, 1970, San Antonio, Texas.

H. A. Wright and J. E. Turner
Free-Nucleon Target Model Applied to Nucleon Penetration Through Matter, American Nuclear Society, November 30–December 4, 1969, San Francisco, California.

Publications

J. C. Ashley and R. H. Ritchie
"Double-Plasmon Excitation in a Free Electron Gas," *Phys. Status Solidi* 38, 425–34 (1970).

"The Mean Free Path of Relativistic Electrons for Plasmon Excitation," submitted for publication in *Physica Status Solidi.*

J. A. Auxier, J. S. Cheka, and T. D. Jones
Report of Trip to Japan During Period August 17 Through September 19, 1969, October 29, 1969 (internal memorandum).

K. Becker
Report of Trip to Germany, Belgium, and France April 28 Through May 13, 1969, July 11, 1969 (internal memorandum).

Thermally Stimulated Exoelectron Emission from Terrestrial and Lunar Materials, ORNL-TM-2869 (February 1970).

"Radiophotoluminescence Dosimetry Bibliography II," *Health Phys.* 17, 631–36 (1969).

"Application of the Track Etching Process in Radiation Protection," *Proceedings of International Topical Conference on Nuclear Track Registration in Insulating Solids, May 6–9, 1969,* Clermont-Ferrand, France (to be published).

"Recent Progress in Neutron Solid-State Dosimetry," *Proceedings of the Symposium on Neutrons in Radiobiology, November 11–14, 1969,* Oak Ridge, Tennessee (to be published).

"Principles of Thermally Stimulated Exoelectron Emission (TSEE) Dosimetry," to be published in *Atomic Energy Review.*

"Solid-State Dosimetry," to be published in *Critical Reviews in Radiological Sciences.*

K. Becker and N. Chantanakom
"On the Thermal Fading Characteristics of Some TSEE Dosimetry Materials," *Atompraxis* 16(1), 31–36 (1970).

Klaus Becker and K. W. Crase
"A Sensitive Integrating Fast Neutron Dosimeter Based on TSEE," to be published in *Nuclear Instruments and Methods.*

K. Becker and D. R. Johnson
"Non-Photographic Alpha-Autoradiography and Neutron-Induced Autoradiography," *Science* 167, 1370–72 (1970).

K. Becker, M. Oberhofer, and J. S. Cheka
"Thermally Stimulated Exoelectron Emission, Thermoluminescence, and Impurities in LiF and BeO," to be published in *Health Physics.*

G. M. Begun and R. N. Compton
"Threshold Electron Impact Excitation and Negative Ion Formation in XeF_6 and XeF_4," *J. Chem. Phys.* 51, 2367–70 (1969).

S. R. Bernard and R. L. Hayes
"Dose to Various Segments of the Gastrointestinal Tract," p. 295 in *Medical Radionuclides: Radiation Dose and Effects,* USAEC-DTIE, Oak Ridge, Tenn., June 1970.

R. D. Birkhoff
"Electron Flux Spectra and Radiation Yields in Solids Irradiated by Beta Rays," *IEEE Trans. Nucl. Sci.* 16(6), 233–41 (1969).

"Electron Flux Spectra and Radiation Yields in Solids Irradiated by Beta Rays," submitted for publication to *National Academy of Sciences–National Research Council.*

R. D. Birkhoff, J. E. Turner, V. E. Anderson, J. M. Feola, and R. N. Hamm
"The Determination of LET Spectra from Energy Proportional Pulse-Height Measurements. I. Track-Length Distributions in Cavities," *Health Phys.* 18, 1–14 (1970).

W. J. Boegly, Jr., D. G. Jacobs, T. F. Lomenick, and O. M. Sealand
The Feasibility of Deep-Well Injection of Waste Brine from Inland Desalting Plants, Research and Development Progress Report No. 432, U.S. Govt. Printing Office, Washington, D.C. (March 1969).

W. J. Boegly, Jr., W. L. Griffith, O. M. Sealand, and W. E. Baldry
Solid Waste Management Practices: An Annotated Bibliography and Permuted-Title and Key-Word Index, ORNL-HUD-12 (February 1970).

W. P. Bonner and Tsuneo Tamura
Walker Branch Watershed Project: Progress Report for the Period 1968–1969 on Characterization of Soil and Water and Their Possible Interactions (internal memorandum).

R. H. Boyett and K. Becker
"LET Effects on the Chemical Resistance of Irradiated Polymers," to be published in the *Journal of Applied Polymer Science.*

R. H. Boyett, D. R. Johnson, and K. Becker
"Some Studies on the Chemical Damage Mechanism Along Charged Particle Tracks in Polymers," *Radiation Res.* 42, 1-12 (1970).

R. L. Bradshaw, F. M. Empson, W. C. McClain, and B. L. Houser
"Results of a Demonstration and Other Studies of the Disposal of High Level Solidified, Radioactive Wastes in a Salt Mine," *Health Phys.* 18, 63–67 (1970).

R. L. Bradshaw, W. C. McClain, and F. M. Empson
"Disposal of Solidified Power Reactor Wastes in Salt Mines," *Transactions of 1969 Winter Meeting of American Nuclear Society, November 30–December 4, 1969, San Francisco, California* 12(2), 452 (1969).

R. L. Bradshaw and Florentino Sanchez
"Migration of Brine Cavities in Rock Salt," *J. Geophys. Res.* 74(17), 4209–12 (Aug. 15, 1969).

A. J. Braundmeier, Jr., and E. T. Arakawa
"Observed Radiation from 'Nonradiative' Surface Plasmons in Aluminum," submitted for publication in *Zeitschrift für Physik.*

A. J. Braundmeier, Jr., E. T. Arakawa, and M. W. Williams
"Intrinsic Damping Rate and Volume Plasmon Energy in Mg from Radiative Decay Measurements," submitted for publication in *Physics Letters.*

Daniel G. Brown, Donald F. Johnson, and John A. Auxier
"Unilateral and Bilateral Exposure of Swine to Fission Neutrons," to be published in *Health Physics.*

E. L. Chaney and L. G. Christophorou
"Electron Attachment to N_2O," *J. Chem. Phys.* 51, 883–93 (1969).

E. L. Chaney, L. G. Christophorou, P. M. Collins, and J. G. Carter
"Electron Attachment in the Field of Ground and Excited Electronic States of the Azulene Molecules," *J. Chem. Phys.* 52, 4413–17 (1970).

J. S. Cheka
Distribution of Radiation from a 14 MeV Neutron Source in and near Structures, CEX-65.13 (May 1969).

J. S. Cheka and K. Becker
"High Dose-Level Glass Dosimeters with Low Dependence on Energy," *Nucl. Appl.* 6, 163–67 (1969).

J. S. Cheka, E. M. Robinson, Leo Wade, Jr., and W. A. Gramly
"The UT-AEC Agricultural Research Laboratory Variable Gamma Dose Rate Facility," to be published in *Health Physics.*

L. G. Christophorou
Atomic and Molecular Radiation Physics, Wiley, Sussex, England, 1970.

L. G. Christophorou, J. G. Carter, E. L. Chaney, and P. M. Collins
"Long-Lived Parent Negative Ions Formed by Capture of Low-Energy Electrons (0 to 3 eV) in the Field of the Ground and Excited Electronic States of Organic Molecules," submitted for publication in *Proc. IVth International Congress of Radiation Research,* Gordon and Breach, Paris.

L. G. Christophorou, J. G. Carter, C. E. Easterly, and D. L. McCorkle
"Anomalous Emission from Liquid Benzene, Toluene, and Ethyl Benzene," submitted for publication in *Chemical Physics Letters.*

L. G. Christophorou and E. L. Chaney
"Electron Attachment to Gaseous Naphthalene," *J. Chem. Phys.* 52, 2165–66 (1970).

L. G. Christophorou, E. L. Chaney, and A. A. Christodoulides
"Electron Attachment and 'Carrier Gas' Energy Distribution Functions," *Chem. Phys. Letters* 3, 363–66 (1969).

L. G. Christophorou, D. L. McCorkle, and J. G. Carter
"Cross Sections for Thermal Peaking Electron Attachment Resonances," submitted for publication in the *Journal of Chemical Physics.*

L. G. Christophorou and D. Pittman
"Thermal Electron Scattering by Polar Molecules," submitted for publication in the *Journal of Physics B.*

T. G. Clark, B. R. Fish, W. H. Wilkie, J. L. Thompson, R. H. Boyett, and G. W. Royster
Biohazards of Aerospace Nuclear Systems, Final Report, SC-CR-69-3291 (December 1969).

P. M. Collins, L. G. Christophorou, E. L. Chaney, and J. G. Carter
"Energy Dependence of the Electron Attachment Cross Section and the Transient, Negative-Ion Lifetime for *p*-Benzoquinone and 1,4-Naphthoquinone," *Chem. Phys. Letters* 4, 646–650 (1970).

R. N. Compton and R. H. Huebner
"Collisions of Low-Energy Electrons with Molecules: Excitation and Negative Ion Formation," in *Advances in Radiation Chemistry* (ed. by J. L. Magee) (in press).

"Temporary Attachment of Electrons to Azulene-h_8 and Azulene-d_8," *J. Chem. Phys.* 51, 3132–33 (1969).

J. J. Cowan and E. T. Arakawa
"Dispersion of Surface Plasmons in Multiple Metal and Dielectric Layers on Concave Diffraction Gratings," *Phys. Status Solidi* (a) 1, 695 (1970).

J. J. Cowan, E. T. Arakawa, and L. Robinson Painter
"Time Studies of the Polarization Due to Gratings," *Appl. Opt.* 8, 1734–35 (1969).

J. J. Cowan, E. T. Arakawa, and R. H. Ritchie
"Dispersion of Surface Plasmons in Dielectric-Metal Coatings on Concave Diffraction Gratings," submitted for publication in *Zeitschrift für Physik.*

K. E. Cowser and E. G. Struxness
"Methods of Estimating Potential Dose Equivalents to Population Groups," *Transactions of 1969 Winter Meeting of American Nuclear Society, November 30–December 4, 1969, San Francisco, California* 12(2), 814–15 (1969).

K. E. Cowser, W. S. Snyder, and E. G. Struxness
"Application of ICRP Recommendations Relevant to Internal Dose," *Proceedings for the Symposium on Public Health Aspects of Peaceful Uses of Nuclear Explosives,* sponsored by the Southwestern Radiological Health Laboratory, Las Vegas, Nevada, April 7 through 11, 1969, U.S. Public Health Service (1969).

Julian Crowell and R. H. Ritchie
"Surface Plasmon Effect in the Reflectivity of a Metal," *J. Opt. Soc. Am.* **60**, 794–99 (June 1970).

F. J. Davis and D. R. Nelson
"Attachment Rate of Thermal Electrons to SF_6," to be published in *Chemical Physics Letters* (August 1970).

"Pseudo-First Order Attachment Rates of Thermal Electrons by SF_6 in Different Carrier Gases," *Chem. Phys. Letters* 3, 461–63 (1969).

Wallace de Laguna
"Control of Pollution from the Generation of Nuclear Power," *IEEE Trans. Geoscience Electronics* GE-7(4), 212–19 (October 1969).

Radioactive Waste Disposal by Hydraulic Fracturing (internal memorandum).

Hydraulic Fracturing Test in New York State (internal memorandum).

"Tracer Aids Interpretation of Pumping Test," *Water Resour. Res.* 6(1), 172–84 (1970), published by American Geophysical Union.

Wallace de Laguna and W. C. McClain
First Fracturing Test, West Valley, New York, Preliminary Report (internal memorandum).

C. E. Easterly, L. G. Christophorou, R. P. Blaunstein, and J. G. Carter
"Fluorescence from the Second Excited π-Singlet State of 1,2-Benzanthrane and 3,4-Benzopyrene in Solutions," submitted for publication in *Chemical Physics Letters.*

J. M. Elson and R. H. Ritchie
"Photon Surface Plasmon Coupling at a Dielectric Shield," submitted for publication in *Physics Letters.*

L. C. Emerson
"Induced Radioactivity" (book review), to be published in *Health Physics.*

Chester W. Francis, Gordon Chesters, and Larry A. Haskin
"Determination of ^{210}Pb Mean Residence Time in the Atmosphere," *Environmental Science and Technology* (in press).

C. W. Francis, Tsuneo Tamura, W. P. Bonner, and J. W. Amburgey, Jr.
"Separation of Clay Minerals and Soil Clays Using Isopycnic Zonal Centrifugation," *Soil Sci. Soc. Amer. Proc.* 34(2), 351–52 (1970).

F. W. Garber, M. Y. Nakai, J. A. Harter, and R. D. Birkhoff
"Low-Energy Electron Beam Studies in Thin Aluminum Foils," submitted for publication in the *Journal of Applied Physics.*

W. R. Garrett
"Critical Binding of an Electron to a Non-Stationary Electric Dipole," *Chem. Phys. Letters* 5, 393–97 (1970).

"Variational Method for Elastic Scattering Involving Long Range Forces," submitted for publication in the *Journal of Physics B.*

W. R. Garrett, J. E. Turner, and V. E. Anderson
Analysis of Ground-State Energy Eigenfunctions for Finite Dipole in Spherical Coordinate Systems, ORNL-4431 (February 1970).

"Spherical Coordinate Analysis of Ground State Energy Eigenfunctions for an Electron in the Field of a Finite Dipole," *Phys. Rev.* 88, 513–14 (1969).

T. F. Gesell, E. T. Arakawa, and T. A. Callcott
"Exo-Electron Emission During Oxygen and Water Chemisorption on Fresh Magnesium Surfaces," *Surface Sci.* 20, 174–78 (1970).

J. T. Grissom, R. N. Compton, and W. R. Garrett
"Electron Impact Excitation and Ionization of Helium near 60 eV," *Phys. Letters* 30A, 117–18 (1969).

V. G. Horton, E. T. Arakawa, R. N. Hamm, and M. W. Williams
"A Triple-Reflection Polarizer for Use in the Vacuum Ultraviolet," *Appl. Optics* 8, 667–70 (1969).

S. Jablon, S. Fujita, K. Fukushima, T. Ishimaru, and J. A. Auxier
"RBE of Neutrons in Japanese Survivors," *Proceedings of the Symposium on Neutrons in Radiobiology, November 11–14, 1969, Oak Ridge, Tennessee* (to be published).

D. G. Jacobs
"Isotope and Radiation Techniques in Soil Physics and Irrigation Studies" (book review), *Health Phys.* 18, 300 (1970).

D. G. Jacobs and M. J. Kelly
Fifth Quarterly Progress Report on the Theoretical Evaluation of Consumer Products from Nuclearly Stimulated Gas Wells, ORNL-TM-2862 (February 1970).

Fourth Quarterly Progress Report on the Theoretical Evaluation of Consumer Products from Project Gasbuggy, ORNL-TM-2721 (October 1969).

D. G. Jacobs, E. G. Struxness, and C. R. Bowman
"A Preliminary Assessment of the Radiological Implications of Commercial Utilization of Natural Gas from a Nuclearly Stimulated Well," p. 83 in *Proceedings of the ANS Topical Meeting, Engineering with Nuclear Explosives, Las Vegas, Nevada, January 1970,* CONF-700101, vol. I (1970).

D. R. Johnson, R. H. Boyett, and K. Becker
"Sensitive Automatic Counting of Alpha Particle Tracks in Polymers and Its Application in Dosimetry," *Health Phys.* 18, 424–25 (1970).

"Some Studies on the Chemical Damage Mechanism Along Charged Particle Tracks in Polymers," *Proceedings of International Topical Conference on Nuclear Track Registration in Insulating Solids, May 6–9, 1969, Clermont-Ferrand, France* (to be published).

D. R. Johnson, J. H. Thorngate, and P. T. Perdue
"A Sensitive Spectrometer for Fast Neutrons Using LiI(Eu)," *Nucl. Instr. Methods* 75, 61–65 (1969).

D. R. Johnson, J. A. Auxier, J. W. Poston, D. G. Brown, W. A. Gramly, W. D. Gibbs,
Harold D. Hodges, and D. R. Davy
" 'Total' and 'Exchangeable' Sodium Studies in Swine and Sheep Using Activation Analysis and Isotopic Dilution," *Health Phys.* 18, 729–30 (1970).

Larry D. Johnson
"Molecular Orbitals and Oscillation Strengths for Magnesium Porphin," submitted for publication in the *Journal of Chemical Physics.*

T. D. Jones and J. A. Auxier
"Absorbed Dose and Linear Energy Transfer Distributions from Therapeutic Sources of ^{252}Cf," to be published in *Physics in Medicine and Biology.*

"Neutron Dose, Dose Equivalent, and Linear Energy Transfer from ^{252}Cf Sources," to be published in *Health Physics.*

T. D. Jones, W. S. Snyder, and J. A. Auxier
"Absorbed Dose, Dose Equivalent, and LET Distributions in Cylindrical Phantoms Irradiated by a Collimated Beam of Monoenergetic Neutrons," to be published in *Health Physics.*

S. V. Kaye and P. S. Rohwer
Dose Estimation Studies Related to Proposed Construction of an Atlantic-Pacific Interoceanic Canal with Nuclear Explosives: Phase III, ORNL-4579 (in press).

C. E. Klots

"Bimolecular Association Reactions and Microscopic Reversibility," to be published in the *Journal of Chemical Physics.*

"Comparison of Direct and Photosensitized Ionization Efficiencies," to be published in *Proceedings IVth International Congress of Radiation Research,* Gordon and Breach, Paris.

C. E. Klots and P. W. Reinhardt

"Energy-Loss Rates of Slow Electrons in Hydrocarbons," *J. Phys. Chem.* (in press).

C. E. Klots and Harvel Wright

"Aspects of Degradation Spectra," *International Journal of Radiation Physics and Chemistry* (in press).

Vinod Krishan and R. H. Ritchie

"Anomalous Damping of Volume Plasmons in Polycrystalline Metals," *Phys. Rev. Letters* 24, 1117–19 (1970).

T. F. Lomenick and R. L. Bradshaw

"Deformation of Rock Salt in Openings Mined for the Disposal of Radioactive Wastes," *Rock Mechanics* 1, 5–30 (1969).

T. F. Lomenick and NSIC Staff

Earthquakes and Nuclear Power Plant Design, ORNL-NSIC-28 (July 1970).

W. C. McClain

"Disposal of Radioactive Wastes by Hydraulic Fracturing: Part V. Site Evaluations," *Nucl. Eng. Design* 9, 315–26 (1969).

W. C. McClain and R. L. Bradshaw

"Radioactive Wastes in Salt Mines," *Mines Mag.* 59, 11–14 (1969).

"Status of Investigations of Salt Formations for Disposal of Highly Radioactive Power-Reactor Wastes," *Nucl. Safety* 11(2), 130–41 (March–April 1970).

W. C. McClain and G. A. Cristy

Examination of High Pressure Water Jets for Use in Rock Tunnel Excavation, ORNL-HUD-1 (January 1970).

W. C. McClain and O. H. Myers

Seismic History and Seismicity of the Southeastern Region of the United States, ORNL-4582 (June 1970).

K. Z. Morgan

"Risks from Diagnostic X-Rays," *Amer. Radiography Technologist* 14(4), 15–22 (Winter 1969).

"History of the Health Physics Society," to be published as part of *The RSNA Symposium on the Critical History of American Radiology* (November 1970).

"History of the International Radiation Protection Association," to be published as part of *The RSNA Symposium on the Critical History of American Radiology* (November 1970).

"Tainted Radiation," *Sci. Technol.* No. 90, 46–50 (June 1969).

"You Can Drastically Cut X-Ray Exposure Below Today's Levels," reprinted from *Consultant,* March–April, 1970.

K. Z. Morgan and J. E. Turner

"Health Physics," submitted for publication in *American Institute of Physics Handbook.*

O. H. Myers

The ORNL Seismograph Station ORT: Operation from September 1, 1968, to February 28, 1969 (internal memorandum).

The ORNL Seismograph Station ORT: Operation from March 1, 1968, to August 31, 1968 (internal memorandum).

W. T. Naff, C. D. Cooper, and R. N. Compton

"Attachment of Electrons to Substituted Benzenes," submitted for publication in the *Journal of Chemical Physics.*

D. R. Nelson and F. J. Davis
"Determination of Diffusion Coefficients of Thermal Electrons with a Time-of-Flight Swarm Experiment," *J. Chem. Phys.* 51, 2322–35 (1969).

J. Neufeld
"Comments on Quality Factor," *Health Phys.* 17, 625–28 (1969).

"Dosimetric Field Quantities in Health Physics," submitted for publication in *Health Physics.*

"Radiation Quantities and Their Significance in Health Physics," *Health Phys.* (in press).

"Revised Formulation of the Macroscopic Maxwell Theory – I. Fundamentals of the Proposed Formulation," *Nuovo Cimento* 65B, 33–69 (1970).

"Revised Formulation of the Macroscopic Maxwell Theory – II. Propagation of an Electromagnetic Disturbance in Dispersive Media," *Nuovo Cimento* 66B, 51–76 (1970).

Revised Formulation of the Macroscopic Maxwell Theory. I. Fundamentals of the Proposed Formulation, ORNL-4406, part I (November 1969).

Revised Formulation of the Macroscopic Maxwell Theory. II. Propagation of an Electromagnetic Disturbance in Dispersive Media, ORNL-4406, part II (November 1969).

"Revised Formulation of the Kinetic Plasma Theory," *Intern. J. Electronics* 27, 301–17 (1969).

Revised Formulation of the Kinetic Plasma Theory, ORNL-4474.

"To Amend Refereeing," *Physics Today,* pp. 9–10 (April 1970).

J. Neufeld, W. S. Snyder, J. E. Turner, Harvel Wright, B. M. Wheatley, and Harold Wyckoff
"Radiation Dose from Neutrons and Protons in the Energy Range from 400 MeV to 2 GeV," *Health Phys.* 17, 449–57 (1969).

M. Oberhofer and E. M. Robinson
"A TSEE G-M Gasflow Counter," *Kerntechnik* 12(1), 34–38 (1970).

L. Robinson Painter, R. D. Birkhoff, and E. T. Arakawa
"Optical Measurements of Liquid Water in the Vacuum Ultraviolet," *J. Chem. Phys.* 51, 243–51 (1969).

P. T. Perdue and J. H. Thorngate
Conversion of the Nuclear Data 130A Pulse-Height Analyzer to ASC 11 Paper Tape with Manual Entry for Data Identification, ORNL-TM-2936 (May 1970).

J. W. Poston
Book review: "Fast Burst Reactors," *AEC Symposium Series 15,* Clearinghouse for Federal Scientific and Technical Information, Springfield, Virginia 22151, 646 pp., 1969, to be published in *Health Physics.*

R. H. Ritchie
"Optical Emission from Surface Plasmons," *Phys. Status Solidi* 39, 297 (1970).

R. H. Ritchie, F. W. Garber, M. Y. Nakai, and R. D. Birkhoff
"Low-Energy Electron Mean Free Paths in Solids," pp. 1–28 in *Advances in Radiation Biology,* vol. 3 (ed. by Leroy G. Augenstein, Ronald Masson, and Max Zelle), Academic, New York, 1969.

E. M. Robinson and M. Oberhofer
"A Sensitive Ceramic BeO-TSEE-Dosimeter," *Health Phys.* 18, 434–37 (1970).

A. S. Rogowski and T. Tamura
"Environmental Mobility of Cesium-137," *Radiat. Bot.* 10, 35–45 (1970).

"Erosional Behavior of Cesium-137," *Health Phys.* 18, 467–77 (1970).

P. S. Rohwer and E. G. Struxness
Quarterly Progress Report on Radiological Safety of Peaceful Uses of Nuclear Explosives: Development of Transient-Exposure Guides, ORNL-TM-2810 (May 1970).

T. Saigusa
"Calculation of Spectra of Energy Deposited by Recoil Heavy Particles," *Health Phys.* 18, 547–60 (1970).

H. A. Schroeder, A. P. Nason, and I. H. Tipton
"Essential Metals in Man – Magnesium," *J. Chronic Dis.* 21, 815–41 (1969).

H. C. Schweinler and E. P. Wigner
"Orthogonalization Methods," *J. Math. Phys.* (in press).

S. Y. Shieh and R. H. Ritchie
"Simultaneous Generation of Transition Radiation and Bremsstrahlung from a Thin Foil," submitted for publication in the *Physical Review.*

W. S. Snyder
"Estimation of Absorbed Fraction of Energy from Photon Sources in Body Organs," p. 33 in *Medical Radionuclides: Radiation Dose and Effects,* USAEC-DTIE, Oak Ridge, Tenn., June 1970.

"Estimation of Dose Within the Body on the Basis of Personnel Monitoring Data," p. 255 in *Progress in Nuclear Energy, Series XII, Health Physics,* ed. by F. Duhamel, Pergamon, London, 1969, vol. 2, part I.

J. A. D. Stockdale, R. N. Compton, and P. W. Reinhardt
"Reactions of O^- with Some Hydrocarbons in the Energy Region Between 0 and 2 eV," submitted for publication in the *International Journal of Mass Spectrometry and Ion Physics.*

"Studies of Negative Ion–Molecule Reactions in the Energy Region from Zero to Three Electron Volts," *Phys. Rev.* 184, 81–93 (1969).

J. A. D. Stockdale, R. N. Compton, and H. C. Schweinler
"Negative Ion Formation in Selected Hexafluoride Molecules," to be published in the *Journal of Chemical Physics.*

D. R. Stone, E. B. Wagner, T. D. Jones, and W. H. Shinpaugh
"Calculated and Experimentally Determined Neutron Dose Conversion Factor for Californium," *Health Phys.* 18, 69 (1970).

D. R. Stone, J. H. Thorngate, K. W. Crase, M. D. Brown, and D. W. Carver
The Development of a Spectrometer and the Measurement of the Neutron Spectrum from the Health Physics Research Reactor Between 50 keV and 450 keV, ORNL-TM-2707 (November 1969) (Master's thesis).

E. G. Struxness
Trip Report of Second Session of U.S.–U.S.S.R. Technical Talks Concerning Peaceful Nuclear Explosives Held in Moscow, February 10–18, 1970, internal memorandum, Mar. 10, 1970.

J. C. Sutherland, R. N. Hamm, and E. T. Arakawa
"Extinction Coefficient and Imaginary Part of the Dielectric Constant for Sodium and Potassium Above the Plasma Energy," *J. Opt. Soc. Am.* 59, 1581–83 (1969).

Tsuneo Tamura
"A Review of the Radiosensitivity of the Tissues in Bone" (book review), *Health Phys.* 18, 299–300 (1970).

Tsuneo Tamura and W. P. Bonner
Phosphorus in Land-Water Systems, ORNL-TM-2913 (1970).

William A. Thomas and Donald G. Jacobs
"Curium Behavior in Plants and Soil," *Soil Sci.* 108(4), 305–7 (1969).

J. H. Thorngate
"An Experimental Measurement of the High Energy Gamma Rays Produced by the Slowing Down of 14 Mev Neutrons in Air," *Health Phys.* 18, 339–46 (1970).

An Instrument That Provides Linear Temperature Ramps for Use with TSEE Experiments, ORNL-TM-2687 (October 1969).

J. H. Thorngate, D. R. Johnson, and P. T. Perdue
Energy and Angular Distribution of Neutrons and Gamma Rays – Operation HENRE, CEX-65.11 (August 1969).

I. H. Tipton
"Trace Elements in Human Tissue – a Need for Standards," *Amer. J. Clin. Nutr.* 23, 123 (1970).

I. H. Tipton and P. L. Stewart
"Long Term Studies of Elemental Intake and Excretion of Three Adult Male Subjects," *Develop. Appl. Spectros.* 8, 40 (1970).

J. E. Turner
"Calculation of the Penetration of Charged Particles Through Matter at Very High Energies," submitted for publication to National Academy of Sciences–National Research Council.

J. E. Turner and V. E. Anderson
"Relativistic Ground-State Energy Eigenvalues of the Electron-Dipole System," submitted for publication to *Nuovo Cimento.*

J. E. Turner, V. E. Anderson, R. D. Birkhoff, and D. R. Johnson
"The Determination of LET Spectra from Energy Proportional Pulse-Height Measurements. II. A Monte Carlo Unfolding Procedure," *Health Phys.* 18, 15–24 (1970).

J. E. Turner, R. D. Birkhoff, V. E. Anderson, E. B. Wagner, and H. A. Wright
"Monte Carlo Method of Determining LET Spectra from Pulse-Height Measurements," to be published in *Proceedings Second Symposium on Microdosimetry, Ispra, Italy, October 21–24, 1969.*

J. E. Turner and Hal Hollister
"RBE, LET, z, ν; Some Further Thoughts," *Health Phys.* 17, 356 (1969).

J. E. Turner, V. N. Neelavathi, R. B. Vora, T. S. Subramanian, and M. A. Prasad
"Contributions of Spin, Anomalous Magnetic Moment, and Form Factors to the Stopping Power of Matter for Protons and Muons at Extreme Relativistic Energies," *Phys. Rev.* 183, 453–57 (1969).

J. E. Turner, Patricia Dalton Roecklein, and R. B. Vora
"Mean Excitation Energies for Chemical Elements," *Health Phys.* 18, 159–70 (1970).

J. E. Turner and Harvel Wright
"Calculation of Dose from High Energy Nucleons," to be published in *Proceedings Second International Conference on Accelerator Dosimetry and Experience, Stanford, California, November 5–7, 1969.*

J. E. Turner, H. A. Wright, and J. H. Grossen
"A New Model for Calculation of High-Energy Nucleon Penetration Through Matter," *Health Phys.* 18, 80–82 (1970).

R. C. Vehse, E. T. Arakawa, and M. W. Williams
"Optical and Photoemissive Properties of Palladium in the Vacuum UV Spectral Region," *Phys. Rev.* B 1, 517–22 (Jan. 15, 1970).

R. B. Vora, V. N. Neelavathi, T. S. Subramanian, M. A. Prasad, and J. E. Turner
"Semiclassical Calculation of the Effect of Magnetic Moment (Spin) on the Slowing Down of Heavy Particles," submitted for publication in the *American Journal of Physics.*

R. B. Vora and J. E. Turner
"Stopping Power of Matter for Deuterons at Extreme Relativistic Energies," *Phys. Rev.* 1(5), 2011 (1970).

O. E. Wagner
"On the Temperature Dependence of Ovshinsky Type Devices," *J. Appl. Phys.* 40, 4212–13 (1969).

O. E. Wagner, L. G. Christophorou, and J. G. Carter
"Lifetimes of Liquid Benzene, Toluene, and Mesitylene Excited by a Pulsed-Electron Beam," *Chem. Phys. Letters* 4, 224–25 (1969).

Energy Pollution of the Environment, Health Physics Society Midyear Symposium, January 28, 1970, Louisville, Kentucky.

Acceptable Radiation Risk Concepts, UT-AEC Agricultural Research Laboratory, February 6, 1970, Oak Ridge, Tennessee.

Health Physics Profession – Where Do We Go from Here? East Tennessee Chapter of the Health Physics Society, August 4, 1969, Oak Ridge, Tennessee.

Acceptable Risk Concepts – ICRP, AEC Fellowship Students, ORNL, August 6, 1969, Oak Ridge, Tennessee.

Benefits and Risks of Diagnostic Radiation, Nashville Dental Society, September 23, 1969, Nashville, Tennessee.

O. H. Myers

ORNL Seismograph Station, Muskingum College Students, New Concord, Ohio, Oak Ridge National Laboratory, Building 3504, January 19, 1970, Oak Ridge, Tennessee.

P. S. Rohwer

CUE: A Guide for Transient Radiation Exposure, Seminar for Plowshare Program Personnel, Lawrence Radiation Laboratory, May 18, 1970, Livermore, California.

H. C. Schweinler

Molecular Potential Energy Curves by Klein's Method, Department of Chemistry, University of Tennessee, November 6, 1969, Knoxville, Tennessee.

W. S. Snyder

A Plutonium Exposure – Internal Dose, AEC Fellowship Program, ORNL, August 4, 1969, Oak Ridge, Tennessee.

Estimates of Dose from Photon Sources Within an Anthropomorphic Phantom, Southwestern Radiological Health Laboratory, October 13, 1969, Las Vegas, Nevada.

A Two-Exponential Model for Retention of Tritium and a Speculative Interpretation in Terms of Dose, Radiation Technology Class, University of Nevada, October 14, 1969, Las Vegas, Nevada.

Dose in a Homogeneous Phantom from Monoenergetic Beams of Neutrons with Energy Below 14 Mev, Lake Mead Chapter of the Health Physics Society, October 14, 1969, Las Vegas, Nevada.

Estimation of Dose from Photon Sources in the Body, Societe Francaise de Radioprotection, December 3, 1969, Paris, France.

Emergency Guidelines, Exposure Limits for Personnel, Contamination Guides, Fifth AEC-Sponsored Seminar on Medical Planning and Care in Radiation Accidents, December 16, 1969, Oak Ridge Associated Universities, Oak Ridge, Tennessee.

Health Physics Organizations and Journals, Ten-Week Course in Health Physics, January 16, 1970, Oak Ridge, Tennessee.

Monte Carlo Estimation of the Absorbed Fraction of Photon Energy for Organs in the Body, Comitato Nazionale per L'Energia Nucleare, May 19, 1970, Rome, Italy.

Dosimetry of the ICRP Models of the Lung and Gastrointestinal Tract, Comitato Nazionale per L'Energia Nucleare, May 20, 1970, Rome, Italy.

E. G. Struxness

The Interpretation and Application of ICRP Recommendations, Seminar at Lawrence Radiation Laboratories, June 18, 1970, Livermore, California.

Environmental Monitoring, Exhibits Managers' Training Course, ORAU, August 1969, Oak Ridge, Tennessee.

Environmental Monitoring, Oak Ridge High School, July 1969, Oak Ridge, Tennessee.

Tsuneo Tamura

Mineral Segregation by Zonal Centrifugation, Department of Agronomy, University of Tennessee, August 20, 1969, Knoxville, Tennessee.

Separation of Soils and Sediments by Zonal Centrifugation, 5th Nuclear Engineering Congress, Holiday Inn, April 7, 1970, Oak Ridge, Tennessee.

HEALTH PHYSICS DIVISION

SEPTEMBER 1, 1970

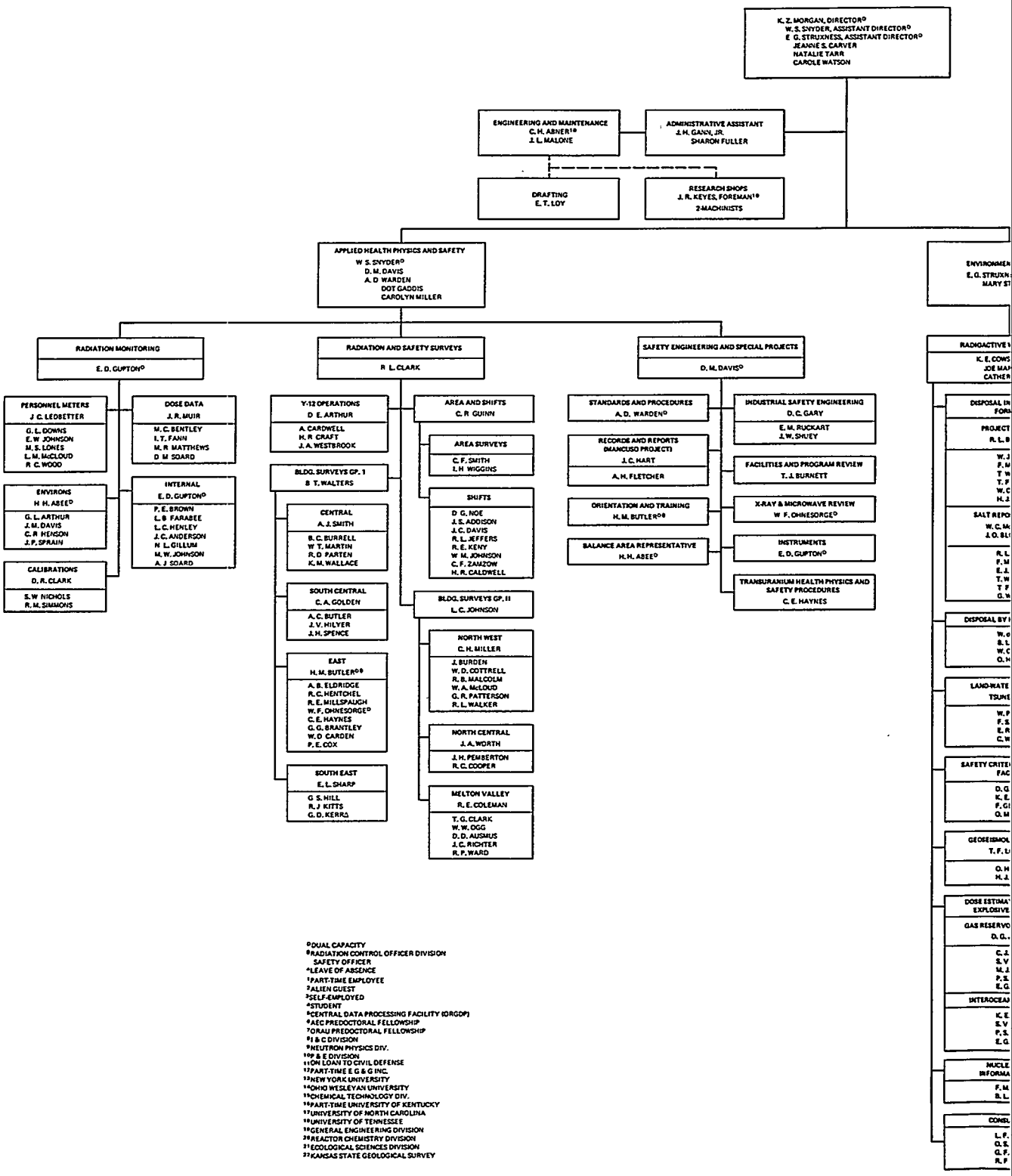

[D]DUAL CAPACITY
[9]RADIATION CONTROL OFFICER DIVISION SAFETY OFFICER
[A]LEAVE OF ABSENCE
[1]PART-TIME EMPLOYEE
[2]ALIEN GUEST
[3]SELF-EMPLOYED
[4]STUDENT
[5]CENTRAL DATA PROCESSING FACILITY (ORGDP)
[6]AEC PREDOCTORAL FELLOWSHIP
[7]ORAU PREDOCTORAL FELLOWSHIP
[8]I & C DIVISION
[9]NEUTRON PHYSICS DIV.
[10]P & E DIVISION
[11]ON LOAN TO CIVIL DEFENSE
[12]PART-TIME E G & G INC.
[13]NEW YORK UNIVERSITY
[14]OHIO WESLEYAN UNIVERSITY
[15]CHEMICAL TECHNOLOGY DIV.
[16]PART-TIME UNIVERSITY OF KENTUCKY
[17]UNIVERSITY OF NORTH CAROLINA
[18]UNIVERSITY OF TENNESSEE
[19]GENERAL ENGINEERING DIVISION
[20]REACTOR CHEMISTRY DIVISION
[21]ECOLOGICAL SCIENCES DIVISION
[27]KANSAS STATE GEOLOGICAL SURVEY

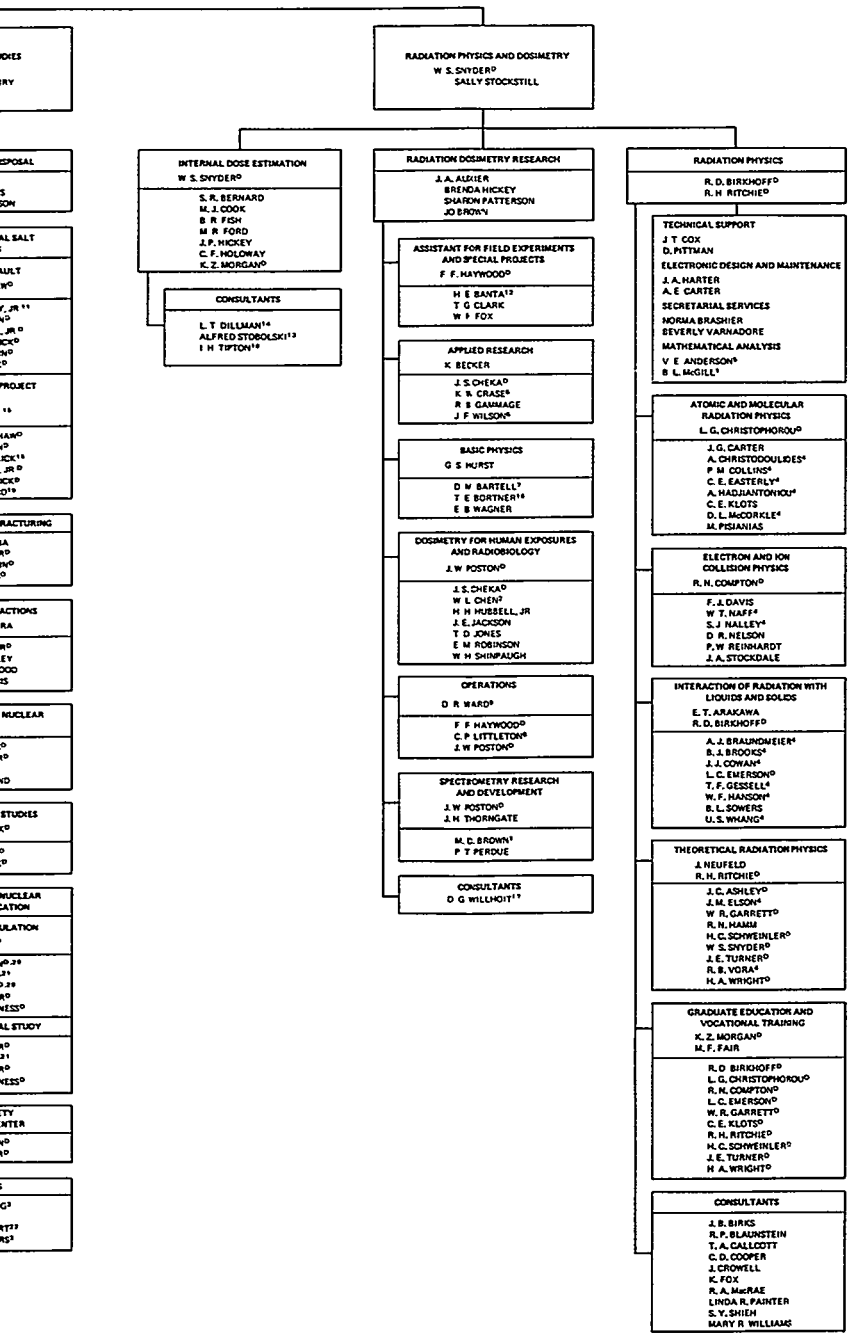
RADIATION PHYSICS AND DOSIMETRY
W S. SNYDER[D]
SALLY STOCKSTILL
INTERNAL DOSE ESTIMATION
W S. SNYDER[D]
S. R. BERNARD
M. J. COOK
B R FISH
M R FORD
J. P. HICKEY
C. F. HOLOWAY
K. Z. MORGAN[D]
CONSULTANTS
L T DILLMAN[14]
ALFRED STOBOLSKI[13]
I H TIPTON[10]
RADIATION DOSIMETRY RESEARCH
J. A. ALZIER
BRENDA HICKEY
SHARON PATTERSON
JO BROWN
ASSISTANT FOR FIELD EXPERIMENTS AND SPECIAL PROJECTS
F F. HAYWOOD[D]
H E BANTA[12]
T G CLARK
W F FOX
APPLIED RESEARCH
K BECKER
J. S. CHEKA[D]
K N. CRASE[6]
R B GAMMAGE
J F WILSON[6]
BASIC PHYSICS
G S HURST
D W BARTELL[7]
T E BORTNER[16]
E B WAGNER
DOSIMETRY FOR HUMAN EXPOSURES AND RADIOBIOLOGY
J.W POSTON[D]
J. S. CHEKA[D]
W L CHEN[7]
H H HUBBELL, JR
J. E. JACKSON
T D JONES
E M ROBINSON
W H SHINPAUGH
OPERATIONS
D R WARD[9]
F F HAYWOOD[D]
C. P LITTLETON[6]
J. W POSTON[D]
SPECTROMETRY RESEARCH AND DEVELOPMENT
J. W POSTON[D]
J. H THORNGATE
M. D. BROWN[7]
P T PERDUE
CONSULTANTS
D G WILLHOIT[17]
RADIATION PHYSICS
R. D. BIRKHOFF[D]
R. H RITCHIE[D]
TECHNICAL SUPPORT
J T COX
D. PITTMAN
ELECTRONIC DESIGN AND MAINTENANCE
J. A. HARTER
A. E CARTER
SECRETARIAL SERVICES
NORMA BRASHIER
BEVERLY VARNADORE
MATHEMATICAL ANALYSIS
V E ANDERSON[6]
B L. McGILL[5]
ATOMIC AND MOLECULAR RADIATION PHYSICS
L. G. CHRISTOPHOROU[D]
J. G. CARTER
A. CHRISTODOULIDES[4]
P M COLLINS[4]
C. E. EASTERLY[4]
A. HADJIANTONIOU[4]
C. E. KLOTS
D. L. McCORKLE[4]
M. PISIANIAS
ELECTRON AND ION COLLISION PHYSICS
R. N. COMPTON[D]
F. J. DAVIS
W T. NAFF[4]
S. J NALLEY[4]
D R. NELSON
P. W REINHARDT
J. A. STOCKDALE
INTERACTION OF RADIATION WITH LIQUIDS AND SOLIDS
E. T. ARAKAWA
R. D. BIRKHOFF[D]
A. J. BRAUNDMEIER[4]
B. J. BROOKS[4]
J. J. COWAN[4]
L. C. EMERSON[D]
T. F. GESSELL[4]
W. F. HANSON[4]
B. L. SOWERS
U. S. WHANG[4]
THEORETICAL RADIATION PHYSICS
J NEUFELD
R. H. RITCHIE[D]
J. C. ASHLEY[D]
J. M. ELSON[4]
W R. GARRETT[D]
R. N. HAMM
H. C. SCHWEINLER[D]
W S. SNYDER[D]
J. E. TURNER[D]
R. B. VORA[4]
H. A. WRIGHT[D]
GRADUATE EDUCATION AND VOCATIONAL TRAINING
K. Z. MORGAN[D]
M. F. FAIR
R. D BIRKHOFF[D]
L. G. CHRISTOPHOROU[D]
R. N. COMPTON[D]
L. C. EMERSON[D]
W. R. GARRETT[D]
C. E. KLOTS[D]
R. H. RITCHIE[D]
H. C. SCHWEINLER[D]
J. E. TURNER[D]
H A. WRIGHT[D]
CONSULTANTS
J. B. BIRKS
R. P. BLAUNSTEIN
T. A. CALLCOTT
C. D. COOPER
J. CROWELL
K. FOX
R. A. MacRAE
LINDA R. PAINTER
S. Y. SHIEH
MARY R WILLIAMS

ORNL-4584
UC-41 — Health and Safety

INTERNAL DISTRIBUTION

1. Biology Library
2–4. Central Research Library
5. Laboratory Shift Supervisor
6. ORNL, Y-12 Technical Library, Document Reference Section
7. MIT Practice School
8–62. Laboratory Records Department
63. Laboratory Records, ORNL RC
64. H. H. Abee
65. H. I. Adler
66. E. T. Arakawa
67. D. E. Arthur
68. J. C. Ashley
69. S. I. Auerbach
70–76. J. A. Auxier
77. C. J. Barton
78. S. E. Beall
79. K. Becker
80. S. R. Bernard
81. R. D. Birkhoff
82. W. P. Bonner
83. R. H. Boyett
84. R. L. Bradshaw
85. P. E. Brown
86. F. R. Bruce
87. T. H. J. Burnett
88. J. G. Carter
89. H. P. Carter
90. J. S. Cheka
91. L. G. Christophorou
92. R. L. Clark
93. T. G. Clark
94. W. E. Cohn
95. W. C. Colwell
96. R. N. Compton
97. M. J. Cook
98. K. E. Cowser
99. J. T. Cox
100. F. L. Culler
101. J. W. Curlin
102. Roger Dahlman
103. D. M. Davis
104. F. J. Davis
105. Wallace deLaguna
106. P. B. Dunaway
107. L. C. Emerson
108. F. M. Empson
109. M. F. Fair
110. L. B. Farabee
111. B. R. Fish
112. M. R. Ford
113. C. W. Francis
114. J. A. Gabbard
115. W. R. Garrett
116. D. C. Gary
117. J. H. Gillette
118. W. R. Grimes
119. C. R. Guinn
120. E. D. Gupton
121. R. N. Hamm
122. C. S. Harrill
123. J. C. Hart
124. J. A. Harter
125. F. F. Haywood
126. R. F. Hibbs
127. L. B. Holland
128. C. F. Holoway
129. H. H. Hubbell
130. G. S. Hurst
131. D. G. Jacobs
132. D. R. Johnson
133. L. C. Johnson
134. T. D. Jones
135. W. H. Jordan
136. M. T. Kelley
137. M. J. Kelly
138. R. F. Kimball
139. C. E. Klots
140. T. A. Lincoln
141. J. L. Liverman
142. R. S. Livingston
143. T. F. Lomenick
144. H. G. MacPherson
145. F. C. Maienschein
146. W. C. McClain
147. W. J. McConnell
148. A. J. Miller
149. K. Z. Morgan
150. O. H. Myers
151. D. J. Nelson
152. D. R. Nelson
153. Jacob Neufeld
154. J. S. Olson
155. R. V. O'Neill
156–157. R. B. Parker
158. G. R. Patterson
159. R. W. Peel
160. J. W. Poston
161. M. L. Randolph
162. D. E. Reichle
163. P. W. Reinhardt
164. R. H. Ritchie
165. E. M. Robinson
166. P. S. Rohwer
167. H. C. Schweinler
168. H. E. Seagren
169. M. J. Skinner
170. W. S. Snyder
171. J. A. Stockdale
172. E. G. Struxness
173. D. A. Sundberg
174. T. Tamura
175. E. H. Taylor
176. J. H. Thorngate
177. D. B. Trauger
178. J. E. Turner
179. E. B. Wagner
180. B. T. Walters
181. D. R. Ward
182. A. D. Warden
183. A. M. Weinberg
184. J. P. Witherspoon
185. H. A. Wright
186. Gale Young
187. John C. Frye (consultant)
188. Edward Gerjuoy (consultant)
189. John B. Hursh (consultant)
190. J. B. Birks (consultant)
191. R. P. Blaunstein (consultant)
192. W. Brandt (consultant)
193. Thomas Callcott (consultant)
194. C. D. Cooper (consultant)

195. J. Crowell (consultant)
196. Charles Eisenhauer (consultant)
197. K. Fox (consultant)
198. R. J. Lovell (consultant)
199. R. A. Macrae (consultant)
200. Linda R. Painter (consultant)
201. S. Y. Shieh (consultant)
202. G. E. Thoma (consultant)
203. I. H. Tipton (consultant)
204. Neil Wald (consultant)
205. Donald G. Willhoit (consultant)
206. M. R. Williams (consultant)

EXTERNAL DISTRIBUTION

207–443. Given external distribution
444. Laboratory and University Division, AEC, ORO
445. Patent Office, AEC, ORO
446–716. Given distribution as shown in TID-4500 under Health and Safety category (25 copies – NTIS)